UNIVERSITÉ DE STRASBOURG

ÉCOLE DOCTORALE des SCIENCES de la TERRE

Institut de Physique du Globe de Strasbourg

THÈSE

Présentée par :

Asem Salama

Soutenue le : 6 Novembre 2017

Pour obtenir le grade de : **Docteur de l'université de Strasbourg**

Discipline/ Spécialité:Géophysique

TITRE de la thèse

Recherche sur les traces et dépôts de tsunami le long de la côte méditerranéenne de l'Egypte: Contexte sismotectonique et modélisation

Active tectonics and Paleotsunami recordsof the Northern Coast of Egypt

---

THÈSE dirigée par :
Prof. MEGHRAOUI Mustapha   Directeur de Thèse, Université de Strasbourg

RAPPORTEURS :
Prof. Maria Ana Viana Baptista   Rapporteur Externe, Instituto Superior de Engenharia de Lisboa
Prof.Christophe Morhange   Rapporteur Externe,Université Marseille

---

AUTRES MEMBRES DU JURY:
Prof. Hesham Hussein   Examinateur, National Research Institute of Astronomy and Geophysics (NRIAG, Cairo)
Prof. Ahmet Yalciner   Examinateur, Middle East Technical University, (METU, Ankara)
Assoc. Prof. Mohamed El-Gabry   Examinateur, National Research Institute of Astronomy and Geophysics (NRIAG, Cairo)

FOREWORD

First, I would like to convey my sincere thanks to my thesis supervisor, Prof. Dr Mustapha Meghraoui and my adviser Dr. Mohamed El Gabry, whose advice and mentorship have been tireless, fair and of top-notch standards. I am grateful to my Prof. Dr Mustapha for teaching me the methodologies, problem-solving approaches, and sharing his experiences in active tectonics and his knowledge during the stages of my works, Dr Mohamed El Gabry, for his cooperation's and his continued assistance during my field work and PhD stages.

I would like to thank Profs.Ana Maria Viana Baptista, Christophe Morhange, Ahmet Yalciner, Hesham Hussein and Assoc.Prof. Mohamed El Gabry for their acceptance to be among the jury members. I would like to express my appreciation to Profs. Hatem Odah, Hesham Hussein for their scientific and logistic support during the field works and my work progress.I am grateful to Drs. Said Maouche, Assia Harbi, Saud Abdelhady, my NRIAG colleagues Sayed Mekhaimr, Hany Hassen, Adel Sami, Mohamed Maklad, Mohamed Sayedandmy friend Grant Wilson from New Zealand for their keen efforts and help during the development of this work.

I wish also to thank the Institut Français du Caire and the French-Egyptian IMHOTEP program for their interest and support. I would like to express my appreciation to central metallurgical research centre laboratory, for the geochemical analysis. Also, Thanks to the International Hydrographic Organization (IHO) and the Intergovernmental Oceanographic Commission (IOC) of UNESCO for providing me Bathymetry data 2014 of the Eastern Mediterranean which was helpful in the tsunami modelling. The scientific results of stress inversion in chapter III were obtained using Win-Tensor, a software developed by Dr Damien Delvaux, Royal Museum for Central Africa, Tervuren, Belgium.

I am also grateful to the French Centre d'études Alexandrines for providing their drilling equipment. Special thanks to Egyptian Armed Forces for issuing permissions and their support during field work. I am also thankful to my PhD students colleagues Souhila Bagdi-Issaad and Jugurtha Kariche for their support during my stay at the IPG Strasbourg.

This PhD thesis is conducted in the frame of the scientific cooperation between the National Institute of Geophysics and Astronomy (NRIAG, Cairo), and Ecole et Observatoire des Sciences de la Terre (EOST - IPGS) Université de Strasbourg, France, and the IMHOTEP bilateral French-Egyptian cooperation program (Campus-France) and European project ASTARTE. The NRIAG scientific foundation and the ASTARTE EC-funded project

support my research work in the field and at the laboratory. In addition, the IMHOTEP project (CMEP, Campus France) funded my stay at EOST during my study.

Last but not the least, my sincerest gratitude goes to my family; my father Mostafa, my mother Jehan and my wife Amal, who give me a deep support through all situations in my life to help me in my work progress.

September 2017   Asem SALAMA

Table of Contents   Pages

List of Figures

sand and mixed clay and organic matter. The layers with high values of magnetic susceptibility (especially for 1, 2 and 3) and organic matter are interpreted as deposits of tsunami origin

Pages

List of Tables

ABBREVIATIONS

Sh.min.: minmum shear (i.e.extension axis)

Sh.max.: maximum shear

XRD:X-ray diffraction

Lat.: Latitude

Long.:Longitude

GPS: Global Positioning System

CAIP: Central Africa Intra plate

EMRA:Egyptian Mineral Resources Authority

NRIAG: National Insitute of geophysics and Astronomy

NEIC: National Earthquake Information Center

ENSN:Egyptian National Seismology Network

CMT: Harvard Centroid Moment Tensor Catalog

GFZ: German Research Centre for Geosciences

GMT: Greenish Mean Time

IRIS: Incorporated Research Institutions for Seismology

EHA: Eastern Hellenic arc

WHA: Western Hellenic arc

Active tectonics and Paleo-tsunami records
of the Northern Coast of Egypt

SUMMARY

The aim of my thesis is: 1) to study of the main active and tsunamigenic zones in the Eastern Mediterranean and northern Egypt. The characterization of active faults has been identified from the Red Sea area in the east to Salloum in the west. Historical and instrumental data are used to determine the seismic activity of the faults. I also compile the geology and active faults, seismicity, focal mechanisms, and proceed with stress tensor inversions that help to 1) identify the present day stress field in northern Egypt and adjacent Mediterranean regions 2) to analyze the stratigraphy of tsunami deposits through trenching and coring in two selected sites; EL Alamein and Kefr Saber. Trenches and cores investigations enable us tocorrelate the paleotsunami deposits with the sequences of historical tsunamis documented in the historical seismicity catalogue; and 3) to model maximum wave height and travel times to the Egyptian coast from the worst case scenariosfrom the main seismic zones of the Eastern and Western Hellenic arc. This help in estimating the wave height and travel times as away for seismic hazard and risk assessment, and mitigate its effects in northern Egypt.

My thesis includes six chapters. The main items of these chapters are summarized as follows: -

Chapter I Introduction: This chapter introduces the steps and objectives of my study and the previous international methodology used in the active tectonics and paleo tsunamis studies all over the world in the last 20 years. The paleotsunami studies help in the identification of tsunami deposits thousands of years in the world. This chapter also includes the methodology used to study the seismotectoniccharacteristics and paleotsunami deposits. It also discusses the importance of this study in northern Egypt as the north of Egypt includes ancient Egyptian cultural heritage (i.e.Pharaohs archaeological sites) and the development of National strategic projects; in addition of the construction of new cities along the Egyptian coast. This chapter continues describing the basis of tsunami modelling to estimate the wave height and the travel time to the northern coast of Egypt and far-field effects from seismic sources of the Eastern and Western Hellenic arcs.

Chapter II Methodology: This chapter introduces the work methodologies. The methodology is classified into three stages. The first stage is a concern with seismotectonic, focal mechanisms and their parameters and the stress tensor inversion and its definition. The

parameters of the present day stress tensor deduced from focal mechanisms data are calculated using the Tensor program version 5.8.6 of 23 November 2016 for the six active zones. This method used as the Right Dihedron method and the Rotational Optimization method. The Rotational Optimization method has used in the determination of the four stress parameters, σ1, σ2, σ3 and stress ratio R = (σ2 - σ3)/(σl - σ3); used stress Tensor program to calculate these parameters (Delvaux and Sperner,1993). The second stage concern with Paleotsunami methodology, the main items to identify the tsunami deposits is by the tsunami signatures and the laboratories measurements include X-ray scanning , magnetic susceptibility, grain size analysis (i.e. mean size and sorting calculated according to Folk,1968 equations), sampling and macrofossil detections, XRD analysis to identify the minerals, total organic and inorganic matter measurements and carbon dating methodology and its history as effective tools for the scientists in dating. The third stage concerns with the tsunami modelling methodology. Modeling was which carried out using two worst sceneries to estimate the wave height and travel time across the Egyptian coasts.

The chapter III presents seismotectonic of the northern part of Egypt and show the tectonic and geologic framework of the active zones in northern Egypt and the Eastern Mediterranean. The historical and instrumental seismicity was collected from 2200BC to 2016 in the Eastern Mediterranean and northern Egypt. Six seismic tectonic sources are recognized in northern of Egypt: the Egyptian continental margin (Trend A and Trend B), Dahashour zone, Cairo-Suez zone, Northern Gulf of Suez, Southern Gulf of Suez, Gulf of Aqaba (subzones f and g). We also collected all focal mechanisms of earthquakes that occurred in active tectonics zones in and around the northern Egypt from 1951 to 2016. Focal mechanism solutions are for magnitude $M_L \geq 3.5$ for local earthquakes and $M_L \geq 4$ for the continental margin from the published data in different journals for the Egyptian territory. The inversion method of Delvaux and Sperner(2003) and Delvaux et al.(2010) is used for evaluating the stress field parameters in northern Egypt using the focal mechanisms of earthquakes.

The stress inversion results obtained in the northern Egypt active zones reflect an extensional stress regime with stress regime index value between 0.5 – 1, except for the trend B in the Egyptian continental margin zone A which shows the value 2.12 and acompressive regime index. The Tamsah and Baltim trend in the East continental margin is characterized by low seismicity data;where the stress orientation indicates N-S (Baltim trend) and NE-SW (Tamash trend) and a secondary E-W to NW-SE orientation observed from 11 petroleum wells Tingay et al. (2011). In this study, the present day stress map is

constructed based on the calculated stresses from collected focal mechanism data and the borehole breakout data in the study area and the GPS vector velocities calculated by Reilinger et al. (2006).

Chapter IV Paleotsunami: This chapter describes the effects of large historical tsunamis like 21 July 365, 8 August 1303, 24 June 1870 on the northern Egyptian coast and adjacent Mediterranean region coasts. The tsunami information's was preserved in the historical documents and recent catalogues like Ambrasey (2009) and Guidoboni (2009). The fieldwork was carried out using trenching and coring at Kefr Saber and El Alamein sites to distinguish and recognize the stratigraphy of tsunami deposits according to their characteristics and signatures. The two selected sites were chosen according to geomorphological and geological aspects. The two selected sites are located in the northwestern part of the Mediterraneancoast and northern part of the Western Desert which is covered mainly by a thin blanket of Miocene rocks forming a vast persistent limestone plateau. It extends from the western side of the Nile valley and delta in the east to El-Salloum in the west and from the Mediterranean coastal plain in the north to the Qattara and Siwa depression in the south (El-Bastwasy, 2008). This area is affected structurally by E-W trending faults and from the east and the south with Qattara – Alamein ridge and located in the north with Alamein faults NW-SE trends. The Egyptian coastlineis characterized by hummocky and rocky platforms and sand dunes along shorlines with variable heights ranging from 5 to 20 meters'maximum. The obtained chronology and dating results with the stratigraphic succession and tsunami signatures are summarized by two composite sections in Kefr Saber and El Alamein. The Kefr Saber site shows only one white tsunami layer with reworked broken shells compared with 21 July 365 tsunami event while the El Alamein site shows four tsunami layers which are compared with 1600 BC Santorini, 21 July 365, 8 August 1303 and the recent of 24 June 1870 tsunami events.

Chapter V consists in the tsunami modelling andscenarios in the northern Egypt.In this chapterI take as an example the significant recent tsunami modelling such as the massive tsunami generated by the major East Japan Tohoku earthquake of Mw 9.0 on March11, 2011, with a maximum wave height that reached 19.5 m at Sendai Plain (Mori et al., 2011). In my work, two simple scenarios are constructed using the Mirone software update version 2.7.0 last modified on 22 October 2016 (Luis, 2007) using the data from thetsunami deposits of 21 July 365 and 8 August 1303 AD. Two worst scenarios are chosen to estimated wave height and travel times depending on the historical information of the source locations and fault ruptures calculated by Stiros (2010) and Pagnoni et al. (2015).

The estimated fault mechanism depends on the recent large earthquakes events in the Hellenic zone.

Our worst scenario for the Eastern Hellenic arcshow that the wave arrival time to the Egyptian coast is 33 minutes and with maximum wave height ranging from 7-10 m at Kefr Saber while for the El Alamein area shows an expected arrival time of about 50 minutes. The Western Hellenic scenario shows much longer 66 minutes' arrival time with amaximum wave height of 0.88 – 1.76 m at Kefr Saber and 0.42-0.87 m wave height at El Alamein after 100 minutes. The simulation results agree well with Hassan (2013) in the estimated wave heights at Salloum, Alexandria and Domietta. However, our results show a higher estimated wave height at Matrouh and El Arish for the Eastern Hellenic arc scenario. In case of the Western Hellenic scenario, the estimated wave height coincides with Shaw et al. (2008) at Alexandria but itdiffers in the travel time arrival of the waves.

Chapter VI, this chapter is the final conclusive that show the final results obtained from seismicity, focal mechanisms, calculated stress inversion, geodetic data to identify the present day deformation and the main stress tectonic regime in the north Egypt and south eastern Mediterranean. The main result is that the whole northern Egypt is considered as a part of extensional regime except the Egyptian continental margin. Based on the paleotsunami study, the main tsunamigenic seismic sources with possible Mw > 8 in the Eastern Mediterranean region (eastern and western Hellenic arc) are taken into consideration. These arcs were considered as the the most hazaradous subduction zone and source segments of the possible future tsunamis in this region for northern Egypt. The results obtained from the trenching at Kefr Saber are correlatedwith 21 July 365 in Kefr Saber, while the four tsunami layers in cores at El Alamein site are correlated with the historical tsunami events of 1600 BC, 21 July 365, 8 August 1303, 24 June 1870. This chapter ends with the perspective for the seismotectonicsof Egypt including the study of El Alamein active Quaternary fault and more investigation of paleotsunamideposits. In this thesis, I also suggest warning messages depending on historical data, simulation data as a function of tsaunmigenic earthquake magnitudes to be provided for the decision-makers in case of tsunami hazard. A second recommendation includes the preparation of an Early warning system for tsunami hazards.

Recherche sur les traces et dépôts de tsunami le long de la côte méditerranéenne de l'Egypte: Contexte sismotectonique et modélisation

RÉSUMÉ

L'objectif de cette thèse consiste en : 1) l'étude des zones actives et tsunamigéniques de l'est méditerranéen et du nord de l'Egypte, incluant la caractérisation des failles actives et sismogènes et des données GPS depuis les bordures de la Mer Rouge jusqu'au Salloum et frontière avec la Libye. Une recherche sur la sismicité historique et instrumentale associée à des travaux sur les failles actives et mécanismes au foyer des principaux séismes avec une étude sur le tenseur de contrainte est utilisée afin de déterminer les caractéristiques de la déformation active du Nord de l'Egypte. 2) des travaux sur les dépôts côtiers pouvant receler des traces de tsunamis par le biais de tranchées et sondages carottées, notamment sur deux sites à Kefr Saber (localité située à l'ouest de Marsa Matrouh) et à El Alamein. Une corrélation des dépôts catastrophiques datés avec le catalogue de sismicité historique de l'Egypte et de l'est méditerranéen permet une reconnaissance des principaux tsunamis ayant affecté les régions côtières. 3) Une modélisation des tsunamis liés aux séismes majeurs de la zone de subduction hellénique jusqu'aux régions côtières de l'Egypte montre la hauteur de vagues potentielle et les implications sur l'aléa sismique.

Cette thèse est organisée suivant six chapitres que je résume comme suit :

Chapitre (I) Introduction: Ce chapitre présente les étapes et les objectifs de mon étude et la méthodologie internationale précédente utilisée dans les études de tectonique active et de paléotsunamis dans le monde entier au cours des 20 dernières années. Les études sur le paléo tsunami aident à identifier les dépôts de tsunamis depuis des milliers d'années dans le monde. L'identification des dépôts de tsunami par l'analyse des sédiments de surface (âge de l' Holocène) collectée à l'aide de carottages et par comparaison avec les dépôts actuels de tsunami observés ailleurs (Sicile, Algérie, Tohoku, Sumatra). La complexité de la dynamique côtière est prise en compte par l'étude des processus sédimentaires côtiers, paléoenvironnementaux et des fluctuations du niveau de la mer durant l'Holocène. En effet, l'existence de fossiles marins dans un environnement continental associé au développement d'espèces telles qu' ostracodes, diatomées, gastéropodes, plantes aquatiques peut indiquer des changements de salinité à long terme associés aux inondations soudaines du tsunami (Kortekaas et Dawson, 2007).

Par exemple, le long de la côte de Kiritappu au Japon, Nanayama et al. (2003) ont identifié des plaques de sable s'étendant sur 3 kilomètres à l'intérieur des terres, montrant de

grands tsunamis inondés tous les 500 ans en moyenne entre 2000 et 7000 ans. De même, une étude d'un record de 7000 ans dans un lac côtier de l'Oregon (ouest des Etats-Unis), Kelsey et al (2005) a identifié 12 dépôts de paléotsunami au cours des 4600 dernières années. D'autres enregistrements de tsunamis multiples ont été étudiés au Chili (Cisternas et al., 2005). Le long de la côte sud de l'île Andaman, en Inde, Malik et ses collaborateurs (2015) ont identifié trois séismes historiques et des tsunamis transocéaniques associés au cours des 1000 dernières années, en fonction de la stratigraphie des dépôts et des datations associées. En Méditerranée, parmi les études sur les paléo-tsunamis, De Martini et al. (2012) ont identifié deux dépôts de tsunamis au cours du premier millénaire avant J.-C. et un autre en 650-770 après J.-C. et ont estimé un intervalle de récurrence moyen pour les tsunamis forts d'env. 385 ans (en utilisant la chronologie comprennent C14, Pb 210 et Cs 13, OSL et téphrochronologie) le long de la côte orientale de la Sicile, en Italie. Le long de la côte algérienne, Maouche et al. (2009) ont identifié la présence de gros blocs de Tipaza à Dellys comme étant liée à des événements de tsunamis en 419 et 1700 en utilisant la datation au radiocarbone des bioindicateurs.

Les principales idées et fondements méthodologiques de mon travail y sont inclus mettant en évidence les implications sur l'évaluation du risque de tsunami sur le nord de l'Egypte, ceci tenant compte de l'importance des sites archéologiques des régions proches d'Alexandrie et du projet de centrale nucléaire de Dabaa. Des exemples de modélisation de tsunami et de hauteurs de vague sont également présentés. Ce chapitre continue de décrire les bases de la modélisation des tsunamis pour estimer la hauteur des vagues et le temps de trajet jusqu'à la côte nord de l'Égypte et les effets de champ lointain provenant des sources sismiques des arcs helléniques de l'Est et de l'Ouest. À la fin du chapitre I; il résume brièvement les idées principales des chapitres de thèse.

Le chapitre II montre les méthodes utilisées lors des travaux de cette thèse que je classe suivant trois principales approches. 1) L'analyse de la sismotectonique d'une zone active basée notamment sur les failles actives et les mécanismes au foyer des séismes majeurs associés. Ces travaux décrivent la détermination du champ de contrainte σ_1, σ_2 et σ_3 par le calcul d'un tenseur utilisant l'inversion des données des mécanismes de faille par la méthode « Right Dihedron ». Pour cela, j'utilise le programme TENSOR (Delvaux, 1993). Cette méthode consiste à séparer les données brutes du mécanisme focal collecté de 1951 à 2016 en sous-ensembles tout en optimisant le tenseur des contraintes à l'aide de la méthode « Right Dihedron » et de l'Optimisation rotationnelle pour chaque zone active. La méthode d'optimisation rotationnelle a été utilisée pour la détermination des quatre paramètres de contrainte, σ_1, σ_2, σ_3 et le rapport de contrainte $R = (\sigma_2 - \sigma_3) / (\sigma_1 - \sigma_3)$;

utilisé le programme Tensor de stress pour calculer ces paramètres (Delvaux et Sperner, 1993). L'indice du régime de contrainte (R ') est calculé numériquement avec le logiciel Tensor pour chaque zone sismique active du nord de l'Egypte. Il est défini en fonction de l'orientation de l'ellipsoïde de contrainte selon Delvaux et al (1997). Elle est exprimée en extension lorsque σl est verticale, en décrochement lorsque σ2 est verticale et en compression lorsque σ3 est verticale. R 'a des valeurs de 0-1 pour les régimes d'extension, 1-2 pour les régimes de décrochement, et 2-3 pour les régimes de compression. A cette recherche, j'associe une étude sur les données géodésiques GPS qui montre les principales directions et vitesses de la déformation active du nord de l'Egypte. 2) La recherche sur les enregistrements de tsunami dans les niveaux géologiques a été développées récemment. En effet, des travaux montrent la possibilité d'identifier des dépôts catastrophiques côtiers liés aux tsunamis. Pour cela, j'utilise des mesures de granulométrie en laboratoire avec utilisation des équations de Folk (1968) incluant la sélection de la taille des grains de sédiment, la détermination des espèces fossiles (notamment foraminifères, gastéropodes et lamellibranches, des analyse aux rayons X des dépôts de sondage carottés et détermination des contenus minéralogiques par la méthode XRD donnant des standards PDFs (obtenus à partir des radiation Cu$K\alpha$), des mesures des proportions en matière organique, et des mesures de susceptibilité magnétique des niveaux géologiques. Ces travaux sont complétés par un prélèvement d'échantillons de sable (avec proportion importante en quartz et feldspath), charbon, os, test de fossile, matière organique et pour des datations isotopique OSL-TL et C^{14} nécessaire pour la datation des niveaux géologiques. 3) La troisième étape concerne la méthodologie de modélisation des tsunamis. La modélisation du tsunami a été réalisée à l'aide du logiciel Mirone développé par Luis (2007) version mise à jour 2.7 la dernière mise à jour le 22 octobre 2016. Ce logiciel utilisait le code TINTOL (NSWING) pour effectuer le tsunami modélisation de la propagation et de l'inondation ". Le code modélise la propagation des tsunamis en utilisant la grille de bathymétrie (telle qu'utilisée dans cette étude des données de gebco 2014 de 30 secondes d'arc) et identifie la déformation initiale par le modèle d'Okada (1985). Un événement tsunamigène a été examiné pour étudier l'effet de l'emplacement, la direction, le temps de voyage et la hauteur vers la côte égyptienne. Les caractéristiques des tsunamis, telles que les temps de déplacement et la distribution de la hauteur des vagues, sont calculées, ce qui est utile pour évaluer le risque de tsunami. Ceci est fait en utilisant les zones d'inondation estimées et la comparaison avec la hauteur et le dépôt des vagues du tsunami pour aider à déterminer l'intensité des séismes tsunamigènes et leur impact sur la côte nord de l'Egypte.

Le chapitre III traite de la sismotectonique sismotectonique de la partie nord de l'Egypte et montre le cadre tectonique et géologique des zones actives du nord de l'Egypte et de la Méditerranée orientale. La sismicité historique et instrumentale a été collectée entre 2200 avant le siècle a' 2016 en Méditerranée orientale et au nord de l'Egypte. Six sources tectoniques sismiques sont reconnues dans le nord de l'Égypte: la marge continentale égyptienne (Tendance A et Tendance B), la zone Dahashour, la zone Le Caire-Suez, le nord du golfe de Suez, le sud du golfe de Suez et le golfe d'Aqaba. . Nous avons également collecté tous les mécanismes focaux des séismes survenus dans ces zones de tectonique active de 1951 à 2016. Les solutions du mécanisme focal sont de magnitude ≥ 3,5 pour les séismes locaux et ML ≥ 4 pour la marge continentale des données publiées dans différents journaux égyptiens. territoire.

J'ai compilé les solutions du mécanisme focal et calculé les inversions de contraintes du catalogue sismique de l'Egypte, recherché et cartographié les failles actives, et utilisé les données de forage pour développer une analyse sismotectonique de la distribution des contraintes dans ma région d'étude. Les données sismologiques et les mécanismes focaux associés sont considérés comme une excellente source d'informations sur la direction du stress dans la croûte, qui fournit des informations précises sur le champ de stress actuel dans la région de la Méditerranée orientale et le nord de l'Egypte. Plusieurs études portent sur les inversions sismotectoniques et de stress en Afrique du Nord et en Méditerranée orientale telles que (Bohnhoff et al., 2005, Delvaux, 2010, Heidbach et al., 2010, Tingay, 2011, Meghraoui et Pondrelli, 2012, Nocquet, 2012; et Hussein, 2013). L'installation de nouvelles stations GPS en Egypte complète l'image de la déformation active dans le coin nord-est du continent africain et du déplacement vers le nord de la Nubie nord-est par rapport à l'Eurasie (McClusky et al., 2000, Reilinger et al. 2006, Mahmoud et al., 2005, Saleh et Becker, 2015, Pietrantonio et al., 2016).

Nos travaux de collecte de solutions de plans de fautes et de calcul des inversions de contraintes des paramètres de défaut à l'aide du logiciel Tensor version 5.8.5 (version Windows, dernière mise à jour le 27/07/2016, http://www.damiendelvaux.be/Tensor/WinTensor/win-tensor.html) dans les six zones actives dans le nord de l'Egypte sont résumées comme suit:-

La première zone active dans le nord de l'Égypte; est la zone continentale égyptienne (A) qui était située au sud de la crête de la mer Méditerranée derrière la plaine abyssale d'Hérodote où le fond de la mer est occupé par l'éventail profond du Nil, le mont sous-marin d'Eratosthène et le bassin d'Hérodote. Il représente une zone de transition entre les croûtes continentales-océaniques où le champ de contraintes passe de la tension dominante à

l'intérieur des terres égyptiennes à la compression dominante le long de l'arc hellénique. Le cadre tectonique et la structure de la marge continentale égyptienne sont le résultat de l'interaction entre trois principales tendances de la faille: la zone Temsah nord-ouest-sud-est; la zone de Rosetta nord-est-sud-ouest et la direction est-ouest de la faille continentale ENE-WSW (Abdel Aal et al., 1994).

Les plus grands séismes historiques de la marge continentale égyptienne sont les tremblements de terre 320 et 956, tandis que le tremblement de terre instrumental le plus important a eu lieu le 12 septembre 1955 avec Ms 6.7 (Costantinescu et al., 1966) sur le plateau continental du delta du Nil. Les événements sismiques historiques des années 320 et 956 se sont produits au nord de l'épicentre du tremblement de terre du 12 septembre 1955 (Korrat et al., 2005). Ces tremblements de terre ont été suivis par d'autres grands événements survenus dans les 57 ans de l'événement du 19 octobre 2012 à 03: 35: 11.2, avec Mb 5.1 selon le Centre sismologique euro-méditerranéen (EMSC). Le séisme récent d'El Alamein s'est produit les 03 septembre 2015 ($M_L = 4.5$) et la faille d'El Alamein a été considérée comme une continuation de la zone de faille AL Qattara-EL Alamein qui s'étend de la zone de Rosetta dans la marge continentale.

Les résultats de 19 mécanismes focaux collectés dans la marge continentale égyptienne (Zone A, tendance A, B et zone adjacente montrent deux types de régimes tectoniques): Le premier groupe de mécanismes est représenté par NW Oblique (normal - dextrale) failles et la seconde est représentée par des failles EW à ENE (reverse - latéral gauche) L 'inversion de contrainte de notre étude de la zone marginale égyptienne est classée en deux tendances principales A, B. L' inversion de contrainte de la tendance A représente les contraintes dans la tendance de Rosetta et s'est poursuivie avec la distribution des contraintes d'Alexandrie à la marge d'El Alamein (Qattara - EL Alamein Ridge). L'inversion de contrainte de la tendance B comprenait 8 solutions de mécanismes focaux, ce qui représente les contraintes parallèles à la tendance de Rosetta jusqu'à la région de Mars Matrouh L'indice du régime de contrainte R 'de la tendance B est de 2.12 et montre une compression pure (TF) avec Tensor Quality B.

Les tendances de Tamash et Baltim à l'est de la marge continentale sont caractérisées par de faibles données de sismicité. L'orientation du stress de l'étude en petits groupes de Tingay et al. (2011) utilisant 11 puits sur le front du delta du Nil indique un N-S dominant à NE-SW Sh. orientation maximale et une orientation secondaire E-W à NW-SE. Nos résultats de stress ne concordent pas avec les données de trou de fracture de (Tingay et al., 2011) dans le cas de la tendance de Rosetta, car les données de forage ont une faible profondeur plutôt que la profondeur des séismes.

La deuxième zone active dans le nord de l'Egypte est la zone de Dahshour (B). Cette zone est située dans la partie nord du désert occidental et à l'ouest de la zone Le Caire - Suez. Le plus grand événement dans la zone de Dahshour avec M_L 5.9 est l'événement du 12 octobre 1992 qui a causé de gros dégâts principalement au Caire (voir le chapitre III pour des informations détaillées). 15 mécanismes focaux collectés dans cette zone montrent des failles normales avec des plans nodaux orientés NW-SE à E-W avec une composante décroissante (Maamoun et al., 1993; Hussein, 1999). L'inversion de contrainte calculée dans la zone de Dahshour résulte de 19 mécanismes focaux dans cette zone, produisant un régime de stress étendu caractérisé par des failles de tendance NE-SW avec N25° E Shmin. L'indice de contrainte R 'est de 0.69, ce qui est compatible avec le défaut normal et la composante de décrochement; la qualité du Tenseur est B. Ces résultats concordent avec l'inversion de contrainte calculée par Hussein et al. (2013).

La troisième zone active dans le nord de l'Egypte est la zone de Suez du Caire (C) située à l'ouest du golfe de Suez en suivant la route du Caire Suez et au nord du désert oriental. Les deux grands événements sismiques sont survenus les 29 septembre 1984, M_L = 4.5 et le 29 avril 1974 de M_L = 4.6. La plupart des mécanismes enregistrés montrent principalement des failles normales pures et une source oblique de la composante normale avec les tendances E-W et NWN-SES et NW-SE en accord avec la direction générale de la direction des failles exposées. Les inversions du tenseur des contraintes sont appliquées à 12 événements de mécanismes focaux pour la zone Cairo-Suez. L'inversion des mécanismes focaux des tremblements de terre dans cette zone produit un régime de contrainte étendu caractérisé par des failles de tendance NE-SW avec N18.7°E Sh-min. L'indice de contrainte est R'= 0.69 représentant un défaut normal avec une composante de défauts de frappe (transtensive) de qualité Tenseur A. L'optimisation rotationnelle des défauts réels montre un tenseur de contrainte de qualité A.

La quatrième zone active située dans le nord de l'Egypte est au nord de la zone du golfe de Suez (D) et est considérée comme un rift continental néogène qui a évolué comme un bras de la triple jonction du Sinaï avec le golfe d'Aqaba et la mer Rouge. . Dagett et al. (1986) l'ont considérée comme une zone active malgré l'absence de grands séismes dans cette zone. Les 15 solutions focales collectées sont caractérisées par des mécanismes de failles normales. Les avions nodaux ont des directions proches de NW-SE à NNW-SSE. Le reste des solutions présente des mouvements obliques ou purs de glissement. 14 événements de mécanismes focaux pour le nord du golfe de Suez sont appliqués aux inversions du tenseur des contraintes. L'inversion des mécanismes focaux des tremblements de terre dans

cette zone donne un régime de stress étendu pur caractérisé par des failles de tendance NE-SW avec N44E Sh-min. L'indice du régime de contrainte est R '= 0.64. Cette valeur est cohérente avec un régime normal de défaut et d'extension, où l'optimisation rotationnelle des défauts réels montre la qualité du Tenseur A.

La cinquième zone active dans le nord de l'Egypte est le sud du golfe de Suez (E). Les deux plus grands tremblements de terre sont enregistrés dans cette zone, à savoir les tremblements de terre de l'île de Shadwan le 31 mars 1969 (ML = 6.1); et le 28 juin 1972 (ML = 5.0). Les 29 mécanismes de failles normales du mécanisme focal collecté avec les tendances NW-SE. Les inversions du tenseur des contraintes ont été appliquées à 28 mécanismes focaux du sud du golfe de Suez. L'inversion des mécanismes focaux des tremblements de terre dans cette zone donne lieu à un régime de stress important caractérisé par des failles de tendance NE-SW avec N27.8 ° E Sh-min. L'indice du régime de contrainte est R '= 0.51 et la qualité du Tenseur A.

La sixième zone active dans le nord de l'Egypte est la zone du golfe d'Aqaba (sous-zones F, G) considérée comme une région source d'activité intense qui constitue la principale limite de la plaque tectonique entre l'Afrique (Sinaï) et l'Arabie. Le plus grand séisme enregistré (Mw = 7.2) est survenu le 22 novembre 1995. Les 36 solutions focales présentent des failles normales avec un décrochement latéral gauche ou un décrochement avec une composante normale mineure, tandis que certains événements reflètent un mécanisme de failles normal. . La plupart des événements montrent des axes T approximativement dans la direction NNE à N-S et NW. Les inversions du tenseur des contraintes ont été appliquées à 7 événements de mécanismes focaux pour la zone F de la zone du golfe d'Aqaba. Cette zone est située au nord de 29° de latitude. L'inversion des mécanismes focaux dans cette zone montre des failles normales, où l'indice du régime de contrainte est R '= 0.89, N72.3ºE pour Sh-min et Tensor qualité A. La sous-zone G est située au sud de 29 ° de latitude, où le stress les inversions tensorielles sont appliquées à 27 mécanismes focaux. L'indice du régime de contrainte est R'= 0.98, avec N 59.3° E Shmin et Tensor Qualité A. L'inversion des mécanismes focaux des tremblements de terre dans cette zone donne un défaut normal avec la composante décroissante.

Pour compléter l'image de la déformation et de la direction des contraintes, j'ai également compilé dans le chapitre III: a) les vecteurs de vitesse GPS pour estimer le taux de déformation (Reilinger et al., 2006); b) l'inversion de contrainte calculée dans cette étude en utilisant la version 5.8.6 du programme Tensor du 23/11/2016 (Delvaux et al., 2010); c) les contraintes calculées par les études sur les forages de puits de pétrole (Tingay, 2011); d)

les contraintes de la carte mondiale des contraintes (http://www.world-stress-map.org/) dans la région de la Méditerranée orientale et le nord de l'Egypte pour avoir une image complète de la distribution actuelle des contraintes. La principale conclusion des résultats du stress montre que l'ensemble de l'Égypte septentrionale est soumise à un régime de stress d'extension, à l'exception de la marge continentale égyptienne qui montre des tendances à la compression. Ce régime de stress fonctionne actuellement dans la plupart des régions du nord de l'Egypte comme des failles normales et des glissements avec des tendances Shmin N-NNE.

Chapitre IV Paléontunami: Ce chapitre décrit les effets de grands tsunamis historiques comme le 21 juillet 365, le 8 août 1303, le 24 juin 1870 sur la côte égyptienne septentrionale et les côtes méditerranéennes adjacentes. Les informations sur le tsunami ont été conservées dans les documents historiques et les catalogues récents comme Ambrasey (2009) et Guidoboni (2009). À l'heure actuelle, les données du paléosunami n'existent que pour un nombre limité de régions sismiquement actives du monde. L'arc hellénique et la zone de subduction connexe sont considérés comme la source dangereuse des tsunamis qui ont pu affecter la côte nord égyptienne dans le passé et générer des tsunamis dans le futur. On supposait que la ville de Thonis - Heracleion avait sombré à cause d'un tsunami survenu dans le passé (??). Cette ville a été fondée en 331 avant J.-C et était un port d'entrée en Egypte et le Nil pour tous les navires venant de la région grecque. Un fort tremblement de terre s'est produit le 21 juillet 365 dans le segment ouest de l'arc hellénique, avec des signes de soulèvement et de basculement jusqu'à 9 m dans l'île de Crète (Stiros, 2010). Cet événement a provoqué un tsunami qui a dévasté la ville d'Alexandrie en Égypte et a envoyé un mur d'eau à travers la Méditerranée vers la côte nord-africaine et toute la Méditerranée orientale, y compris le sud de l'Italie (Ambraseys, 2009). Les navires dans le port à Alexandrie ont été renversés pendant que l'eau près de la côte a reculé soudainement. Les rapports indiquent que beaucoup de gens se sont précipités pour piller les navires malheureux (cela a été mentionné par Ammianus Marcellinus qui a vécu pendant ce temps à Ambrayses (2009) .La vague de tsunami s'est ensuite précipitée dedans et a porté les navires au-dessus des murs de mer. A Alexandrie, environ 5000 personnes ont perdu la vie et 50 000 maisons ont été détruites Le tremblement de terre du 8 août 1303 a été considéré comme le deuxième plus grand séisme et tsunami de la côte égyptienne. les effets effrayants de ce raz de marée sismique exceptionnel (tsunami) qui a frappé de nombreuses localités du bassin méditerranéen (Ambrayses 2009) Guidoboni et Comastri (2005) ont suggéré que cette vague de mer étendue a été causée par un tremblement de terre et son épicentre entre les îles de Crète et Rhodes.

A partir de l'étude des événements sismotectoniques et paléotsunami d'origine sismique en Egypte orientale et septentrionale, quatre zones actives sont identifiées comme étant à l'origine d'éventuels tsunamis. L'arc hellénique oriental, l'arc hellénique occidental, l'arc cyprien, la marge continentale égyptienne. Les arcs helléniques de l'Est et de l'Ouest sont considérés comme les zones tectoniques les plus actives à longue distance et une source majeure de tsunamis qui peuvent frapper les côtes égyptiennes et les régions méditerranéennes adjacentes. Le catalogue historique de sismicité rapporte trois événements sismiques significatifs de la zone de subduction hellénique avec des tsunamis majeurs qui ont affecté la côte méditerranéenne de l'Egypte:

1) Le tremblement de terre et l'événement tsunamigène du 21 juillet 365 (Mw 8,3 - 8,5; Stiros et Drakos, 2006; Shaw et al., 2008),

2) Le tremblement de terre et l'événement tsunamigène du 8 août 1303 (Mw 7,8 - 8,0) (Abu El Fida, 1329)

3) Tremblement de terre et tsunamigène du 24 juin 1870 (ML 7 -7.5) (Ben Menahem, 1979). Les trois événements ont causé de grands dégâts sur la côte égyptienne et ont particulièrement affecté la ville d'Alexandrie avec des inondations côtières et des inondations. l'eau dans le nouveau port d'Alexandrie a éclaboussé sur le quai (Ambraseys 1961).

Les deux autres zones des sources de tsunamis moins actives sont l'arc chypriote et la marge continentale égyptienne. La magnitude la plus élevée rapportée dans les catalogues de tremblements de terre pour Chypre est de 7,5 et se réfère au séisme du 11 mai 1222, AD. Ce tremblement de terre a été suivi par de faibles impacts de tsunami le long de la zone côtière égypto-méditerranéenne Ambraseys (1995). Les séismes les plus importants se sont produits dans la marge continentale égyptienne, par exemple le tremblement de terre d'Alexandrie en mer, le 6 septembre, le 6 septembre 1955 (Hussein et al., 2005). Il est situé dans le cône sédimentaire du Nil qui présente un potentiel de glissements de terrain tsunamis (Garziglia et al., 2008).

Trois travaux de terrain ont été réalisés en utilisant des tranchées et des carottages sur les sites de Kefr Saber et El Alamein en juin 2014, août 2015 et octobre 2015 dans la côte nord de l'Egypte. Le but de ce travail de terrain était de 1) étudier la géologie et la géomorphologie de la côte nord de l'Egypte. 2) Etudier l'enchaînement successif de la stratigraphie dans les sites sélectionnés d'EL Alamein et de Kefr Sabre et 3) caractériser l'âge des couches possibles de tsunami en fonction de la chronologie des datations au carbone et des signatures des tsunamis.

Pour la sélection du site paléotsunami,, les critères géomorphologiques et topographiques ont été pris en compte ainsi que l'accessibilité afin d'éviter l'urbanisation et le remodelage artificiel des sols. Les critères géomorphologiques sont:

Le premier est la présence de gros rochers observés le long de la côte dans le nord de l'Egypte dans des localités telles que Ras El Hekma -Ras ELAlam Rum -Mersa Matrouh - Est Mersa Matrouh (Kefr Saber) avec une riche teneur en fossiles de Dendropoma. La datation calibrée de l'échantillon de Dendropome à Kefr Saber est 940-1446 AD qui peut être corrélée avec une vague forte et élevée (> 5m) à la côte de Kefr Sabre probablement durant ce tsunami du 8 août 1303. Ce résultat coïncide avec celui de Shah-Hosseini et al., (2016) le long du même littoral.

Les deuxièmes critères géomorphologiques sont la présence de dunes côtières le long de la côte égyptienne. Elles sont composées de sables carbonatés blancs et blancs, délavés, provenant de la dégradation des dorsales côtières oolithiques de 2 à 20 mètres de hauteur. Derrière ces dunes de sable, les troisièmes critères de géomorphologie sont les lagunes ou marais salés que l'on trouve entre des crêtes disséquées avec parfois une élévation inférieure au niveau de la mer à l'ouest de Marsa Matrouh.

Cinq tranchées ont été réalisées à Kefr Saber ~ 32 km à l'ouest de Marsa-Matruh. 12 sondages carottés ont été réalisées dans le deuxième site sélectionné d'El Alamein. Les sondages carottés ont été réalisés en utilisant un instrument de forage cobra. La taille des tranchées était ~ 2 x 1 mètre avec ~ 1.5-m-profondeur et la profondeur maximale des noyaux est ~ 2.6 m.

Les tranchées sont enregistrées et photographiées avec une description détaillée et un échantillonnage pendant les travaux sur le terrain à Kefr Saber. Alors que les carottes réalisées sur le site d'ElAlamein étaient divisées en deux dans le laboratoire NRIAG avec Fisher Wire. Un pour les archives et l'autre pour l'analyse de la sédimentation et du contenu. Le noyau étudié comprend la collecte d'échantillons pour la datation, la photographie, les descriptions stratigraphiques détaillées, le balayage des rayons X, l'analyse géochimique et la susceptibilité magnétique. L'objectif principal est d'identifier les dépôts de Paleotsunami dans les grumes stratigraphiques en fonction des signatures des tsunamis.

Des radiographies radiographiques ont été effectuées sur des carottes en utilisant un laboratoire de radiographie médicale avant d'être ouvertes pour identifier les détails des sédiments et des microfossiles. Des rayons X très intensifs ont été utilisés pour pénétrer dans les sédiments afin de montrer les détails dans les sédiments. Trois radiographies de 40 cm de long ont été prises pour chaque noyau de 1 m de long avec un chevauchement d'au moins 5 cm.

Les carottes et les tranchées ont été décrites en fonction de leur longueur, de leur couleur, de leur texture (granulométrie, tri), des structures sédimentaires (naturelles ou dues à des carottages), du type de contact sédimentaire (acéré ou dégradé). Les carottes et les tranchées ont ensuite été photographiées à l'aide d'un reflex numérique à reflex numérique (Appareil photo reflex numérique à objectif unique) en sections de 25 cm de long, avec un chevauchement d'au moins 2 cm. Ces images ont été assemblées pour reconstruire une seule image pour chaque section de base.

La susceptibilité magnétique a été mesurée avec des intervalles de 3 cm le long des carottes en utilisant un système Bartington MS-2. Des échantillons d'une dimension de 2 cm de long ont été collectés tous les 15 cm pour la minéralogie en vrac, la taille des grains, l'analyse organique et inorganique totale qui a été réalisée au laboratoire d'un institut central de recherche métallurgique (CMRDI) à Helwan.

La datation au radiocarbone des échantillons a été réalisée dans trois laboratoires (laboratoire de Poznan - Pologne, CIRAM à Bordeaux, France et Beta Analytical Laboratory, USA) pour assurer des résultats cohérents et de haute qualité. Les échantillons prélevés étaient constitués de charbon de bois, d'os, de gastéropodes, de coquilles et de matières organiques. Les résultats de datation au radiocarbone du charbon et de la matière organique ont été étalonnés en utilisant une courbe d'étalonnage récente (Reimer et al., 2013) et le logiciel Oxcal pour la fonction de densité de probabilité de chaque âge d'échantillon avec incertitude 2σ (Bronk-Ramsay, 2009); de plus, les gastéropodes et les coquilles ont été corrigés par rapport aux effets du réservoir.

Deux sections composites ont été construites pour résumer les stratigraphes et les couches de tsunami reconnues sur le site de Kefr Sabre et EL Alamein avec la chronologie et la simulation des événements historiques paléotsunamis 1600 avant J.-C, 21 juillet 365, 8 août 1303 et un tsunami plus récent le 24 juin 1870 Les troncs stratigraphiques des tranchées de Kefr Saber montrent principalement une couche de sable et de gravier mélangés à des tsunamis, et des coquilles brisées à une profondeur d'environ 35 cm et une épaisseur de 20 cm comparable aux dépôts de tsunami du 21 juillet 365. Les carottes d' El Alamein montrent quatre couches principales caractérisées par un sable fin et grossier mélangé à des fragments de coquilles brisées qui indiquent la présence de dépôts sédimentaires à haute énergie dans l'environnement du lagon côtier.

Les diagraphies stratigraphiques dans les carottes montrent quatre couches principales de tsunami; A) La première couche a ~ 7.5 cm d'épaisseur à ~ 19 cm de profondeur et est faite de dépôts de sable blanc mal triés avec des gastéropodes brisés et des fossiles de lamellibranches. La valeur élevée de la matière organique et le pic élevé de

susceptibilité magnétique reflètent une teneur riche en carbonates et en quartz. B) La deuxième couche est d'environ 13 cm d'épaisseur à 50 cm de profondeur, caractérisée par des dépôts sableux blancs intercalés de sable brun grossier avec stratification horizontale, de mauvais sédiments de triage, riches en matière organique totale et un fort pic de susceptibilité magnétique. C) La troisième couche ~ 18 cm d'épaisseur à 89 cm de profondeur est faite de sable jaune mélangé avec des intercalations de sable blanc, avec des laminations au fond des dépôts, directions gastropodes verticales et horizontales reflètent le courant de haute vague, fragments de coquilles brisées, riches dans la matière organique totale et la pyrite montrant un pic élevé de susceptibilité magnétique. D) La quatrième couche de tsunami est à 151 cm de profondeur avec une épaisseur de 19 cm. Il est caractérisé par du sable jaune pâle, moyen à fin, avec des fragments de coquilles brisés et un tri extrêmement pauvre, avec un haut pic de susceptibilité magnétique, et un haut pic de matière organique > 5.5% en poids et une quantité élevée de gypse.

Le chapitre V, je prends comme exemple la récente modélisation significative des tsunamis telle que le tsunami massif généré par le tremblement de terre majeur de Tohoku de Mw 9.0 le 11 mars 2011, avec un hauteur maximale des vagues atteignant 19.5 m dans la plaine de Sendai (Mori et al., 2011). Dans mon travail, deux scénarios simples sont construits en utilisant la mise à jour du logiciel Mirone version 2.7.0 modifiée le 22 octobre 2016 (Luis, 2007) en utilisant les données des dépôts de tsunami du 21 juillet 365 et du 8 août 1303. Les deux pires scénarios simples avec des sources de tsunami actives à haute possibilité ont été construits en créant la vague initiale de ruptures de failles calculées pour les arcs helléniques occidentaux et helléniques orientaux. La hauteur des vagues et les temps de parcours ont été calculés dans ces deux scénarios en fonction de l'historique des localisations sources, par exemple le 21 juillet 365 (Stiros, 2010) et le 8 août 1303 (Abu Fida, 1329; Guidoboni et Comastri, 2005). en testant les ruptures de failles calculées par Stiros (2010) et Pagnoni et al. (2015).

Les amplitudes des tremblements de terre ont été estimées égales ou supérieures à la magnitude la plus élevée enregistrée à l'époque historique (tableau 4). Les données de bathymétrie utilisées sont la grille de 30 secondes d'arc à partir des données GEBCO disponibles en ligne, et ceci en l'absence de la résolution plus détaillée (1 seconde d'arc ou moins) des données de bathymétrie côtière dans ma zone d'étude.

Les incertitudes sont calculées pour la géométrie de la faille (longueur, largeur et glissement) utilisée dans les arcs helléniques est et ouest en comparaison avec les études précédentes. De plus, les incertitudes sont calculées en hauteur des vagues (m) selon les 5

scénarios testés résultant en une hauteur de vague de ± 5 m dans le cas du scénario de l'est et de ± 1.5 m dans le scénario de l'ouest de l'arc hellénique

Dans le scénario hellénique oriental, la propagation d'onde calculée est effectuée toutes les 0, 33, 50, 66, 80 minutes. Après 30 minutes, la vague initiale arrive et après 50 minutes, la vague maximale atteint 7 à 10 mètres dans les sites de Kefr Saber et El Alamein. Dans le scénario Hellénique de l'Ouest, la propagation de l'onde de tsunami est calculée à 0, 33, 66, 100, 150 minutes. La hauteur des vagues atteint 4-10 m à l'heure d'arrivée 33 minutes sur la côte libyenne. La vague arrive à la côte égyptienne après 66 minutes avec une hauteur de vague légèrement inférieure à celle de la côte libyenne. La hauteur de la vague arrive à la côte égyptienne avec 0.8 – 1.7 m à Kefr Saber et avec une hauteur de vague de 0,4 à 0,8 m à El Alamein après 100 minutes. Les vagues du tsunami couvrent toute la côte égyptienne après 150 minutes du scénario de l'ouest de l'arc hellénique.

Mes résultats sont comparés avec des études antérieures de (Hamouda, 2006) pour la côte égyptienne ; (Hassan, 2013, Pagnoni et al., 2015) dans le cas du scénario de l'arc hellénique oriental et pour l'arc hellénique occidental (Hamouda, 2009, Shaw et al., 2008, et Pagnoni et al., 2015). Mes résultats sont en accord avec la modélisation de (Hassan, 2013) pour la hauteur des vagues à Salloum, Alexandrie, Damiette en cas de scénario oriental et semblent être différentes du résultat de (Hamouda, 2005 et Pagnoni et al., 2015) . Mes résultats concordent bien avec la taille de l'onde de tsunami déduite du modèle de Shaw et al., (2008) hauteur des vagues à Alexandrie dans le cas du scénario de l'ouest de l'Hellénisme.

Chapitre (VI), ce chapitre est le dernier concluant qui montre les résultats finaux obtenus par la sismicité, les mécanismes focaux, l'inversion de contrainte calculée, les données géodésiques pour identifier la déformation actuelle et le régime tectonique de stress principal dans le nord de l'Egypte et sud-est méditerranéen. Le résultat principal est que toute l'Egypte du nord est considérée comme faisant partie du régime d'extension sauf la marge continentale égyptienne. Sur la base de l'étude du paléotsunami, les principales sources sismiques tsunamigènes avec des potentiels Mw> 8 dans la région de la Méditerranée orientale (arc hellénique oriental et occidental) sont prises en compte. Ces arcs ont été considérés comme la zone de subduction la plus dangereuse et les segments sources des futurs tsunamis possibles dans cette région pour le nord de l'Egypte. Les résultats obtenus lors du creusement à Kefr Saber sont corrélés au 21 juillet 365 à Kefr Saber, tandis que les quatre couches de tsunami dans les carottes du site d'El Alamein sont corrélées avec les événements historiques du tsunami de 1600 avant J.-C , 21 juillet 365, 8 août 1303, 24 Juin 1870. Ce chapitre se termine par la perspective de la sismotectonique de l'Égypte, y

compris l'étude de la faille quaternaire active d'El Alamein et d'autres recherches sur les dépôts paléotsunamis.

Mes recommandations dans le chapitre VI sont 1) l'heure d'arrivée minimum pour que les vagues du tsunami arrivent à la côte égyptienne étant 30 minutes dans le cas de l'arc hellénique oriental et 66 minutes dans l'arc hellénique occidental cela laisse assez de temps pour prendre mesures de protection et d'envoyer des alarmes à la défense civile et la côte égyptienne et sauver des vies. J'ai construit un tableau pour suggérer des messages d'alerte possibles en fonction des données historiques, des données de simulation en fonction des grandeurs de séismes multisystémiques à fournir aux décideurs en cas de risque de tsunami. Les messages d'alerte nécessitent une coopération étroite avec les centres d'études sur les tsunamis turcs et grecs et sont classés en fonction de l'échelle locale, régionale et du bassin. Par exemple, selon (Salamon et al., 2010), les messages peuvent être liés à des distances locales ($\leq$100 km), ou régionales (100-400 km) ou à l'échelle du bassin ($\geq$400 km). Dans le cas des zones côtières égyptiennes, nous considérons que l'arc hellénique oriental (EHA) et l'arc hellénique occidental (WHA) sont le message régional de 100-400 km.

2) L'ensemble de la zone hellénique de subduction représente un risque sérieux de tsunami pour la Méditerranée orientale et comme preuve des dépôts de tsunami analysés dans cette étude. L'activation probable de l'arc hellénique ou même de l'arc cyprien avec un séisme majeur Mw> 8 va générer un fort tsunami sur la côte égyptienne. Par conséquent, la première étape pour la protection civile est la préparation du système d'alerte précoce et le plan d'évacuation pour un probable probable tsunami sur les côtes égyptiennes.

Mes perspectives sont suggérées pour les études sismotectoniques et paléontunami comme suit:

Premièrement, il n'a pas été possible d'effectuer des études de terrain détaillées sur les zones sismiques actives et les failles actives du Quaternaire. Cependant, des failles dans la zone du Caire-Suez et des failles d'EL Alamein ont été réalisées lors des premières investigations en octobre 2015 et des reconnaissances ont été effectuées. Il n'y a jamais de problème pour effectuer des mesures de champs détaillées pour la faille quaternaire active d'El Alamein pour la perspective future.

Deuxièmement pour l'étude paléontunami,

a) Des investigations sur le terrain sont prévues sur le site de la ville de Thonis Heracleion, ancienne cité historique égyptienne située dans l'embouchure canopique du Nil, à 32 km au nord-est de la côte d'Alexandrie. Cette ville aurait été inondée apparemment à la suite d'un tsunami majeur

b) Compléter le carottage et les investigations précédentes dans d'autres sites situés de Kefr Sabr à Salloum pour déterminer une éventuelle inondation du tsunami historique à l'intérieur des terres le long de la côte nord de l'Egypte.

c) Créer un scénario potentiellement pire pour l'heure d'arrivée et la hauteur des vagues du tsunami pour les projets stratégiques construits sur la côte égyptienne tels que la ville de New El Alamein et la centrale nucléaire égyptienne.

دراسة عن النشاط التكتوينى و السجلات الجيولوجية للرواسب
الطوفانات البحرية فى شمال مصر

الملخص العربى

أولا أهداف الدراسة :-

دراسة المناطق التكتونية النشطة في شرق البحر المتوسط وشمال مصر. وقد تم تحديد المناطق النشطة فى شمال مصر من منطقة شمال البحر الاحمر الى حافة الاقليم القارى المصرى و انتهاء بالسلوم غربا. و قد استخدمت بيانات النشاط الزلزالى المسجلة و التاريخية فى تحديد ستة أماكن نشطة فى شمال مصر. و قد تم دراسة الجيولوجيا و النشاط الزلزالى و حلول ميكانيكية البؤرة بالاضافة الى حساب معاملات الإجهاد السيزمى و بالتالى حساب اتجاه العام للإجهاد فى مناطق شرق البحر المتوسط و شمال مصر .

دراسة الطبقات الناتجة عن رواسب التسونامى باستخدام منهجية الخنادق و الابار في الموقعين اللذين تم اختيارهما في الدراسة الحقلية فى منطقة العلمين وكفر صابر. وسوف تساعد هذه الطريقة على ربط تسلسل رواسب الطوفانات البحرية مع الاحداث الطوفانات البحرية التاريخية المحددة سابقا في الكتالوجات التاريخية.

دراسة السيناريوهات لتحديد الحد الاقصى لإرتفاعات الامواج ووقت وصولها إلى الساحل المصري و خاصة فى المناطق المختلفة للطوفانات البحرية التى تم تحديد الرواسب الجيولوجية بها مما قد يساعد فى تحديد الخطورة الناجمة على تلك الطوفانات على الشاطىء المصرى و كيفية الاستعداد لها فى حالة حدوث حدوثها فى المستقبل.

و قد أشتملت الدراسة على خمسة أبواب بألاضافة الى مقدمة الدراسة :-

الباب الأول :-

و يتناول المقدمة حيث تشرح مراحل عمل الدراسة و الاهداف الأسياسية المرجو تنفيذها فى مكان الدراسة بالاضافة الى مقدمة عن الدراسات المستخدمة فى مجال الحركة التكتونية النشطة و دراسات رواسب الطوفانات البحرية دوليا و أقليميا . خاصة و ان دراسة الطوفانات البحرية القديمة ساهمت بشكل كبير فى التعرف على الكثير من رواسب الطوفانات البحرية القديمة فى خلال الاف السنين حول العالم.

كما يحتوى هذا الباب ايضا على اهمية الدراسة و خصوصا انها تقام بالشمال المصرى حيث يتميز الشمال المصرى بإقامة عدد من المشاريع الاستراتجية و الحيوية على طول الساحل. و قد تم وصف الأسياسات التى يعتمد عليها عمل السيناريو و تقدير وصول و ارتفاع الامواج بالاضافة الى زمن وصول الموجة الى الشاطىء المصرى من القوسى الهلينى الشرقى و الغربى لإنهم يمثلان المصدر التواجد الرواسب الشمالية فى كفر صابر و العلميين.

الباب الثانى:-

يتناول الباب الثانى منهجية و طرق العمل المستخدمة فى الدراسة وقد قسمت على ثلاثة مراحل. المرحله الاولى اهتمت بدراسة السيزموتكتونية و ذلك عن طريق دراسة ميكانيكية البؤرة الزلازليه و حساب الاتجاهاتلإجهاد السيزمى . بالاضافة الى دراسة الاجهاد السيزمى و تعريفة و الطريقة المستخدمة فى حسابه معاملات الاجهاد الاربعة $\sigma1$، $\sigma2$، $\sigma3$ ونسبة الإجهاد $R = (\sigma2 - \sigma3) / (\sigma1 - \sigma3)$ وحيث تم استخدم برنامج (2003) Delveaux فى حساب معامل الأجهاد العام و تحديد نوع و حركة الاجهاد السيزمى .

أما المرحلة الثانية فتتعلق بمنهجية دراسة الجيولوجية الرواسب اللطوفان البحرية ، ومن العناصر الرئيسية لتحديد رواسب تسونامي هي بصمات لها متعارف عليها دوليا، وتشمل قياسات المسح بالأشعة السينية والقابلية المغناطيسية وأخذ العينات للكشف عن الحفريات الكبيرة و التعرف عليها و على البيئة الخاصة بها ،كما تم عمل تحليلات كميائية و تشمل الحيود الاشعة السينية (XRD) و ذلك لتعرف على المعادن بالاضافة الى حسابنسبة هذه المعادن فى الرواسب و التعرف على مصدرها و ايضا النسبة النوعية لكمية الكربون العضوى و الغير عضوى وتحليل حجم الجزيئات للرواسب (من حيث الحجم الحبيبى ودرجة الفرز المحسوبة وفقا لمعادلات (1968) Folk، و بعد تحديد الرواسب الجيولوجية للطوفانات البحرية تم تحليل عينات الكربون المشع للتعرف على عمر هذه الطبقات و مقارنتها بالطوفانات القديمة المسجلة فلا المراجع التاريخية.

وتتعلق المرحلة الثالثة بمحاكاة و نمذجة الطوفانات البحرية و التعريف بطريقة عمل هذه النمذجة. حيث تم عمل 10 سيناريوهات لكل من منطقة شرق اللوح اللهلينى الغربى و الشرقى و اختيار الانسب من حيث توقع ارتفاع الامواج و أماكن المصدر للطوفانات عن طريق الكالتوجات التاريخية.

الباب الثالث :ـ

يتناول هذا الباب دراسة للجيولوجيا العامة لكل من شرق البحر المتوسط و المناطق النشطة للوح الهلينى الشرقى و الغربى بالاضافة الى اللوح القبرصى وصولا الى اللوح القارح شمال مصر و خطورة هذه الالوح من حيث خطر الطوفانات البحرية و تحديد ألاماكن الجيولوجية فى شمال المصر. و لتحديد الاماكن النشطة زلزاليا فى كل من شرق البحر المتوسط و الشمال المصرى. و تم تجميع بيانات الزلازل التاريخية و المسجلة من 2200 قبل الميلاد الى العام 2016 في شرق البحر المتوسط وشمال مصر.كما تمتحديد ستة مصادر تكتونية فى شمال. و هى كالتالى1 - الحافة الشمالة القارية المصرية، 2ـ منطقة دهشور ، 3- منطقة القاهرة -السويس، 4-خليج السويس الشمالي، 5- خليج السويس الجنوبي، 6- خليج العقبة. و تم ايضا تجميع البيانات البؤرية الزلازلية لهذا المناطق من البيانات المنشورة في الكتالوجاتالدولية المختلفة و خاصة البيانات الزلزالية ذات القوة من 3.5 بمقياس ريختر وأكبر من أو يساوي 4 للحافة القارية. و قد تم حساب اتجاهات الاجهاد السيزمى عن طريق البرنامج (Tensor v.5, Delveaux 2010), و قد تم تقييم معاملات الاجهاد في المناطق النشطة بالشمال المصرى .إن نتائج الإجهاد السيزمى للطبقات المختلفة للطبقات داخل الأراضى المصرية منطقة الدهشور- منطقة القاهرة –السويس-خليج السويس الشمالي- خليج السويس الجنوبي - خليج العقبة و هو نظام اجهاد شد يتخذ إتجاه العام شمال شرق - جنوب غرب بإستنثناء الحافة القاريه حيث تظهر إتجاه ضغط فى شمال شرقى – جنوب غربى . بينما إتجاه التمساح وإتجاه البلطيم في الحافة القارية الشرقية تتميز بإنخفاض بيانات الزلازل لذا تم الإستعانة بدراسات شركات البترول) لمعرفة قمة الإجهاد بها حيث تمثل قيمة تتضاغطية فى كل من الإتجاهات شمال ـ جنوب (اتجاه بلطيم) و الشمال الشرقى الجنوب الغربى (اتجاه التمساح).

و فى نهاية هذا الباب تم عمل خريطة مجمعة لجميع معاملات الاجهاد السيزمى فى شمال مصر بالإضافة الى شرق البحر المتوسط من حلول البؤرة الميكانيكية و من الاجهاد السيزمى المحسوب عالميا بالإضافة الى القيمة المحسوبة عالميا من قياست و اتجاهات الحركة من GPS .

الباب الرابع :ـ

يقدم هذا الباب ملخصا لأثار الطوفانات البحرية التاريخية الكبيرة مثل 21 يوليو 365 و 8 أغسطس 1303 و 24 يونيو 1870 و اثار هذه الطوفانات البحرية على الشمالى المصرى و سواحل المناطق المجاورة لشرق البحر المتوسط .حيث تم أخذ هذه المعلومات من الوثائق التاريخية حيث تم تجميعا بوسطة (2009), Ambrasey و Guidoboni (2009). و قد تم عمل عدد ثلاث زيارات حقلية ميدانية بدءا بتحديد أماكن الدراسة الى عمل أبار تربة

آختبارية و حفر خنادق لدراسة رواسب الطوفانات البحرية فى الشمال المصرى. و قد تم اختيار الاماكن بناءا على جيمورفلوجية و جيولوجية المكان.

ويقع الموقعان المختاران في الجزء الشمالي الغربي من ساحل البحر الأبيض المتوسط، ويعتبر الجزء الشمالى من الصحراء الغربية و المغطى أساسا بطبقة من عصر المايوسين التي تشكل هضبة من الحجر الجيري لهضبة المرماريكا . يمتد من الجانب الغربي من وادي النيل والدلتا في الشرق إلى السلوم في الغرب وساحل البحر الأبيض المتوسط في الشمال إلى منخفض القطارة وسيوة في وتأثرت هذه المنطقة بشكل عامبأتجاه التكتونى شرق-غرب واتجاه فالق العلمين شمال غرب - جنوب شرق . وتتميز السواحل المصرية بتجمعات كتل صخريةتأخذ شكل الإتجاه شمال —جنوب كما يتميز الموقع بالكثبان الرملية التي تتفاوت من 5 إلى 20 مترا كحد أقصى بالإضافة الى وجود بعض المستنقعات خلف الكثبان الرملية .

و تتلخص نتائج الحفر و أبار التربة الاختبارية و نتائج التاريخ بالكربون المشع الى وجود طبقة بيضاء اللون فى منطفة كفرصابر غرب مدينة مرسى مطروح و تتمتز بوجود كثيف للحفربات المتكسرة و قد قورنت هذه الطبقة ذات السمك 20 سم بالطوفان البحرى 21 يوليو 365. بينما يظهر فى موقع العلميين 4 طبقات مميزة لطوفانات تم مقارنتها بالتحليل السابقة الذكر من القابلية المغناطيسية و الاشعة السينية و الكربون المشع . و قد وجد انها للطوفانات البحرية القديمة 1600 قبل الميلاد سانتوريني، 21 يوليو 365، 8 أغسطس 1303 و مؤخرا 24 يونيو 1870.

الباب الخامس :-

يقدم الباب الخامس بعض الامثلة من الطوفانات البحرية التى حدثت فى الزمن الحديث في العالم مثل طوفان اليابان (2011). ويعتبر هذا الطوفان البحرى الهائل الناتج من زلزال شرق اليابان في 11 مارس 2011 فى الوقت 14:16 هو الأكبر من حيث الحجم حيث كانت قوته 9.0 و قد قدر أقصى ارتفاع للموجة إلى 19.5 مترا في سهل سينداي وأثرت على امتداد كيلومترين من ساحل المحيط الهادئ لشرق اليابان.

و قد تم عمل 2 سيناريو اعتمدا على وجود طبقات للرواسب الجيولوجية فى منطقة كفر صابر و العلميين و استخدم برناج (2.7) Mirone تحديث 22 أكتوبر 2016 (Luis 2007) و قد قدر ارتفاع الامواج من خلال عمل نمذجة لكل من المصدر الهلينى الشرقى و الغربى كا قدر زمن وصول الإمواج إلبالشاطىء المصرى .

وتوضح هذه النمذجة أسوأ السيناريوهات بناءا على عدد 10 اختبارات . وقد تم حساب زمن وصول الموجة الاولى الساحل المصري و هو 33 دقيقة، مع وصول أقصى أرتفاع للموجة 7-10 متر في كفر صابر والعلمين بعد 50 دقيقة في حالة سيناريو القوس الهيلينيى الشرقي. في حين أن السيناريو اللوح الهلينى الغربى يظهر وقت أكبر من وقت وصول الموجة الاولى هو 66 دقيقة مع أقصى ارتفاع موجة 0.88 - 1.76 متر في كفر صابر و 0.87-0.42 متر في العلمين بعد 100 دقيقة. وقد تمت مقارنة نتائج المحاكاة مقارنة بدراسات السيناريوهات السابقة وتظهر نتائج المحاكاة و النمذجة الى توافق مع (2013) Hassan لإرتفاعات الموجات المقدرة في السلوم والإسكندرية ودمياط ولكن نتائج الدراسة الحالية تظهر ارتفاع الموجة المحسوبة في مطروح والعريش لسيناريو قوس الهيلينيى الشرقي. في حالة السيناريو الهيليني الغربي يتزامن مع ارتفاع الموجة المقدرة مع (2008).Shaw et al في الإسكندرية ولكن يختلف في وقت وصول الأمواج .

و قد تم مقارنة نتائج المحاكاة ايضا بهذه الدراسة مع السيناريوهات السابقة (2006) Hamouda (2015) Hamouda(2009), Shaw et al., (2008), Hassan (2013), Pagnoni et al على للسواحل المصرية

في شرق وغرب قوس الهيلينية. وتبين أن هذه السيناريوهات تختلف في قيمة ارتفاع الموجة وأوقات وصولها الى المدن المختلفة بالسواحل المصرية.

الباب السادس:-

وتظهر استنتاجات الباب السادس النتائج النهائية التي تم الحصول عليها من الدراسة السيزميةو حساب الاتجاهات من ميكانيكية البؤرة بالاضافة الى تحديد معامل الاجهاد السيزمى لتحديد التشوه الحادث فى المناطق الستة النشطة والنظام التكتوني الرئيسي للإجهاد السيزمى في شمال مصر وشرق المتوسط. ويعتبر الساحل المصري كله جزءا من النظام التمدديه باستثناء الحافة القارية المصرية.

و كما تعرض فى هذا الباب نتائج ما تم التوصل إليه من تواجد للطبقات الرئيسية للطوفانات البحرية القديمة فى منطقة كفر صابر و العلميين . وقد تم تحديد اللوح الهيلينى الشرقى و اللوح الهيلينى الغربى كمناطق رئيسية للخطورة الزلزالية المتسببة فى الطوفانات البحرية ويليهم اللوح القبرصى (و قد تم تسجيل شواهد تاريخية لزلزال يعقبه طوفان بحرى صغير فى 11 مايو 1222) بالإضافة الى الحافة القارى لقابليتها لعمل انزلاق أرضى بالرغم من عدم تسجيل لطوفان بحري قديم بها و حيث أن خطورتهم الزلزالية أقل من اللوح الهيلينى الشرقى و الغربى .

كما اظهرت النتائج التى تم الحصول عليها من الخنادق و الابار الاختبارية فى كفر صابر و العلميين وجود اربع طبقات روسبية من طوفانات البحرية القديمة و مقارنة بالاحداث التاريخية 1600 قبل الميلاد و 21 يوليو 365 و 8 أغسطس 1303 و 24 يونيو 1870 بينما تواجد طبقة واحد مميزة للروسب الطوفان البحرى فى كفر صابر غرب مدينة مطروح و تم مقارنته بالطوفان البحرى ل 21 يوليو 365 وقد يرجع سبب اختفاء روسب الطوفانين البحريين 8 أغسطس 1303 و 24 يونيو 1870 الى ان المصدر الشرقى الهيلينى اقرب لمنطقة العلميين عن منطقة كفر صابر .

و ينتهى هذا الباب بعدد من التوصيات و التطلعات التى يمكن العمل عليها فى المستقل . إن وجود روسب الطوفان البحرية جيولوجيا فى الشمال المصرى تأكيد على حدوث الطوفانات البحرية فى الماضى لذا و جب الإعتداد لها فى المستقبل بالتحضير و التجهيز لعمل انظمة انذار مبكر فى الشمال المصرى للحد من خطورة الطوفان البحرية التى قد تحدث فى المستقبل نتيجة لنشاط فى اللوح الهيلينى او حتى المصادر الاخرى الإقل احتمالا مثل اللوح القبرصى او الإنزلق صخرى فى حاقة اللوح القارح المصرى . و قد أشار نظام المحاكاة الى وجود زمن كافى للوصول الموجة من المصدر حتى الشوطىء المصرية .

لذا تم الإعداد لجدول يعطى انظمة تحذيرية نتيجة قوة الزلازل المترتب عليها طوفانات بحرية لاستخدمه لصانعى القرار. و قد تم تصنيف الجدول اعتمادا على المعلومات التاريخية و معلومات التى تم الحصول عليها فى هذه الدراسة و قوة الحدث و البعد عن المصدر .

كما توصى الدراسة بإستكمال العمل فى الساحل الشمالى المصرى لدراسة الامتدادات الجيولوجية لطبقات الطوفانات البحرية القديمة بالشمال المصرى بالاضافة الى عمل دراسات للبحث فى سبب غرق مدينة هراقلين بالساحل الاسكندرية غرب فرع الكينوبى القديم و معرفة السبب الحقيقى وراء غرق المدينة .

Chapter I

Introduction

The understanding of seismotectonic, earthquake faulting and the recurrence of paleotsunami in northern Egypt is the first step in seismic hazard assessment and risk mitigation. The instrumental and historical seismicity catalogues of the Eastern Mediterranean and northern Egypt help to identify the main seismic and tsunamigenic zones. Numerous destructive earthquakes and tsunamis have occurred in northern Egypt and where seismicity was studied by Sieberg, 1932; Ismail, 1960; Maamoun et al., 1984; Kebeasy, 1990; and Abou Elenean, 1997. The seismic activity is reported to occur in narrow belts (Levant-Aqaba, Northern Red Sea, Gulf of Suez, Eastern Mediterranean and the Egypt continental margin) that represent the major tectonic trends in northern Egypt (Fig.1).

According to (Papazachos, 1990; Ambraseys et al., 2005 and Riad et al., 2003), several kinds of disasters were caused in Syria and Egypt, especially in Alexandria where a house was ruined and 60 m of the city wall with 27 towers were destroyed (this was mentioned in the Arabic historical documents (Abu El Fida, 1329). Damage was also seen in Peloponnese in the northwest of Crete and islands in the Aegean sea. The sea struck the city with strong force destroying the building and killing theinhabitants in the capital city of Heraklion in the northeastern Crete. This damage happened during the earthquake which was followed by a strong tsunami on 8 August 1303. The other example of a large damaging earthquake was on 21 July 365 which was also followed by a strong tsunami with the biggest damage reported in Greece, southwest Crete and Alexandria in the Nile Delta. The houses were destroyed and human lives were lost and the ships were driven by strong flooding in Alexandria city.

As the first objective of this thesis, I compiled the focal mechanism solutions and calculated the stress inversions from the seismicity catalogue of Egypt, searched for and mapped active faults, and used borehole data to develop a seismotectonic analysis from the stress distribution in my study region. The seismological data and related focal mechanisms are considered as an excellent source of information on the stress direction in the crust, which gives accurate pieces of information on the present-day stress field in the Eastern Mediterranean region and northern Egypt. Several studies deal with the seismotectonic and stress inversions in North Africa and Eastern Mediterranean such as (Bohnhoff et al., 2005; Delvaux, 2010; Heidbach et al., 2010; Tingay, 2011; Meghraoui and Pondrelli, 2012; Nocquet, 2012; and Hussein, 2013). The installation of new GPS stations in Egypt

completes the picture of the active deformation in the north-eastern corner of the African continent and on the northward motion of northeast Nubia with respect to Eurasia (McClusky et al., 2000; Reilinger et al., 2006; Mahmoud et al., 2005, Saleh and Becker, 2015, Pietrantonio et al., 2016).
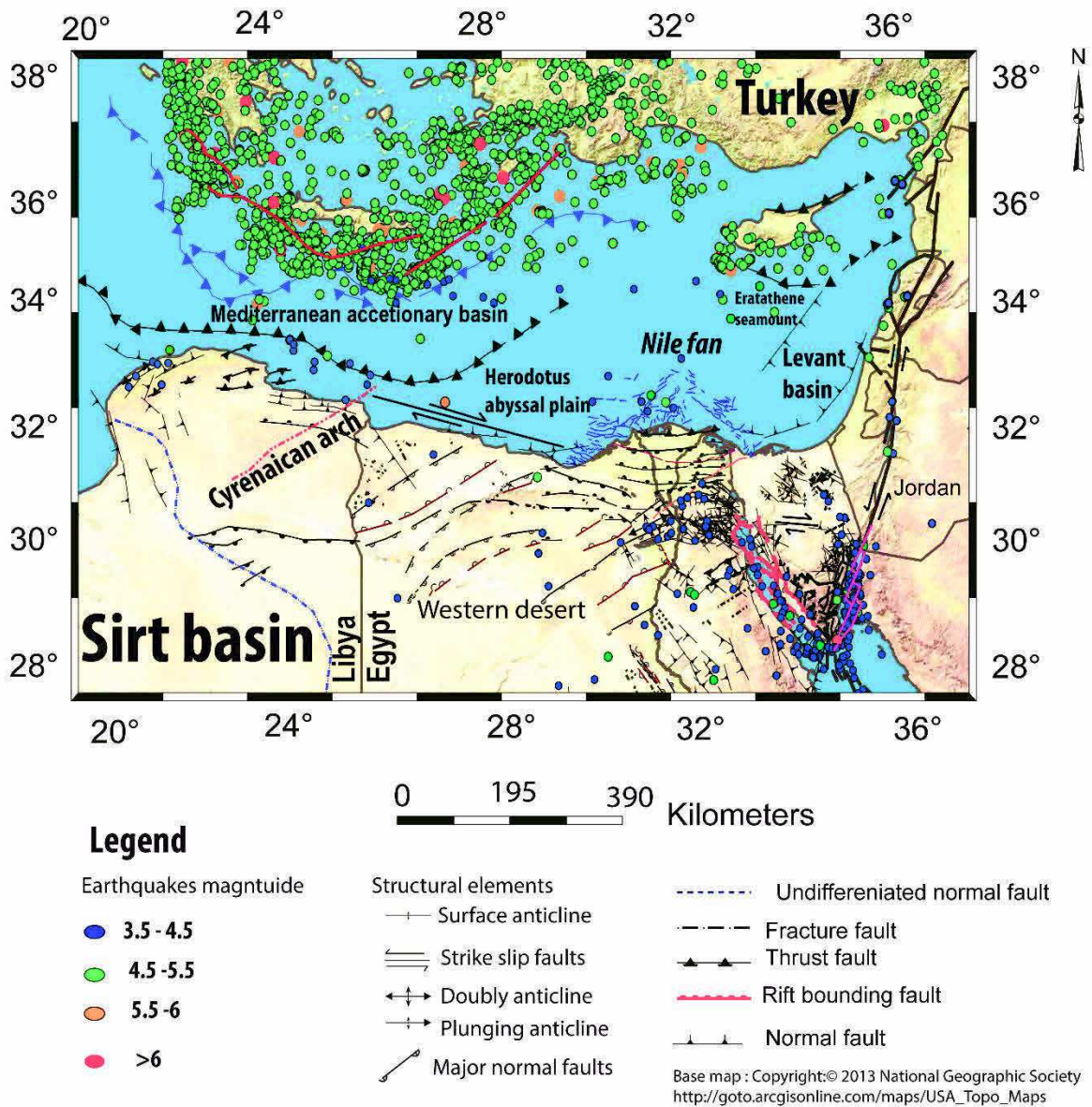
Fig. 1 : Seismic activity and tectonic map based on (a geological map of Libya, 1985; geological map of Egypt EMRA, 2008;Bathworth, 2008) and seismicity data for north Egypt of NRIAG bulletin from 1997-2016 and the seismicity data of the Eastern Mediterranean from IRIS bulletin (http://ds.iris.edu/ds/nodes/dmc/data/types/events/).

The north of Egypt has been affected by large earthquakes like in Cairo in 1992 (Mw 5.8), Shadwan, 1969 (Mw=6.1), Gulf of Aqaba, 1995 (Mw=7.2) and by other historical large earthquakes and tsunamis from the Eastern Mediterranean region. The largest earthquakes are recorded in historical documents and an updated catalogue of the events of

Santorini ~1600 BC, 21 July 365, 8 August 1303, and 24 June 1870. Since the beginning of the 20th century, many efforts have been directed towards the establishment of a reliable catalogue of historical seismicity based on the retrieval and assessment of original sources of information e.g. (Poirier and Taher, 1980; Soloviev et al., 2000; Ambraseys, 2009; Guidoboni and Ebel, 2009).

The second main objective of this work is the identification of tsunami deposits by analyzing surface sediments (Holocene age) collected using core drill holes and by comparison with current tsunami deposits observed elsewhere (Sicily, Algeria, Tohoku, Sumatra). The complexity of the coastal dynamics is taken into account by the study of coastal sedimentary processes, paleoenvironmental and sea level fluctuations during the Holocene. Indeed, the existence of marine fossils in a continental environment associated with the development of species such as ostracods, diatoms, gastropods, aquatic plants may indicate long-term salinity changes associated with sudden tsunami floods (Kortekaas and Dawson, 2007).

The research of paleotsunami deposits consists in the identification and dating of tsunami deposits developed through testing, systematization and formalization. This work is usually carried out following a multidisciplinary approach testing several methodologies. Interesting and promising results are expected from an original combination of geomorphology, geology with coring of deposits, macrofossils determination, X-ray scanning, geochemical analysis, microscopic, magnetic susceptibility measurements, etc.

Several studies have been developed for the identification of paleotsunami in the last 20 years using different methodologies. For example, along the coast of Kiritappu, Japan, Nanayama et al.(2003) identified sand sheets, extending 3 kilometres inland, that show large tsunamis with coastal inundation every 500 years on average, between 2000 and 7000 years ago. Similarly, a study of a 7000-year-long record in a coastal lake in Oregon (western USA), Kelsey et al.(2005) identified 12 paleotsunami deposits over the past 4600 years. Other long records of multiple tsunamis have been studied in Chile (Cisternas et al., 2005). Along the coast of South Andaman Island, India, Malik et al.(2015) identified three historical earthquakes and associated transoceanic tsunamis during the past 1000 years, depending on the stratigraphy of deposits and related dating. In the Mediterranean, among paleo-tsunami studies, De Martini et al. (2012) identified two tsunamis deposits during the first millennium BC and another one in 650-770 AD and estimated an average recurrence interval for strong tsunamis of ca. 385 years (using chronology include C14, Pb 210 and Cs 13, OSL and tephrochronology) along the eastern coast of Sicily, Italy. Along the Algerian Coast, Maouche et al. (2009) identified the presence of large boulders in Tipaza to Dellys to be related to tsunami events in 419 AD and 1700 AD using radiocarbon dating of

bioindicators. Along the Egyptian coast, Shaha-Hosseini et al. (2016) identified coastal boulder accumulations between Alexandria to Marsa Matrouh and with boulders weighing up to 23 metric tons. By C^{14}dating of (Vermetidae and Dendropoma) shells found in these the large boulders, it was found that they were transported by the historical tsunami of 8 August 1303 AD.

It seems that Egypt is lack of tsunami investigations for the tsunami deposits which are well documented historically. The field surveys of the coastal landscape all around the Mediterranean coasts should allow 1) the recognition of paleo-tsunami deposits and landforms, 2) the evaluation of tsunami intensity and frequency, and 3) the propagation direction that may constrain the tsunamigenic source area.

At the present, paleotsunami data exist only for a limited number of seismically active regions of the world. The Hellenic arc and related subduction zone are considered as the hazardous source for tsunamis that may have affected the northern Egyptian coast in the past and would generate tsunami events in the future. It was supposed that the Thonis - Heracleion city sunk due to a tsunami event that occurred in the past (??). This city was founded in 331 BC and was a port of entry to Egypt and Nile River for all ships coming from the Greek region. A strong earthquake occurred on 21 July 365 located in the western segment of the Hellenic arc with evidence of up to 9 m of uplift and tilting in Crete Island, (Stiros, 2010). This event caused a tsunami that devastated the city of Alexandria, Egypt and sent a wall of water across the Mediterranean Sea toward the north African coast and the entire eastern Mediterranean including southern Italy (Ambraseys, 2009). Ships in the harbour at Alexandria were overturned as the water near the coast receded suddenly. Reports indicate that many people rushed out to loot the hapless ships (this was mentioned by Ammianus Marcellinus who lived during that time in Ambrayses (2009). The tsunami wave then rushed in and carried the ships over the sea walls, many landing on top of buildings. In Alexandria, approximately 5,000 people lost their lives and 50,000 homes were destroyed. The earthquake on 8 August 1303 was considered the second largest earthquake and tsunami that affected the Egyptian coast.Old documents describing the disaster of the 1303 tsunami event, concentrate on the frightening effects of that exceptional seismic tidal wave (tsunami) which struck many localities in the Mediterranean basin (Ambrayses 2009). Guidoboni and Comastri(2005) suggested that this extensive sea wave was caused by an earthquake and with its epicenter between the islands of Crete and Rhodes.

Therefore, the fieldwork, which includes coring and trenching, was carried out to identify the tsunami deposits along the coast of two investigated sites: El Alamein and Kefr

Saber. The low topography and limited human occupation of this region favour the preservation of tsunami deposits, especially west of Alexandria. The field investigations were multidisciplinary and include geomorphology and geology, coring with X-ray, petrochemical and magnetic susceptibilities measurements. The dating was done for collecting samples of organic matter, fossils, charcoal, plant remains and roots.

Tsunami modelling was carried out using Mirone software developed by Luis (2007) update version 2.7 the last update on 22 October 2016. According to Luis (2007) in the Mirone manual software, *''This software used* TINTOL (NSWING) *code to perform tsunami modelling of propagation and inundation. The code models the tsunami propagation by using the bathymetry grid (as used in this study of gebco data 2014 of 30 arc seconds) and identify the initial deformation by the Okada (1985) model. The code used the linear theory in deep sea and with the shallow sea theory and on land with constant grid length in the whole region. The computation of tsunami wave* velocity was done according to the shallow water equation v = where g is the gravity acceleration and h is the water column depth''*. A tsunamigenic event was examined to study the effect of location, direction, travel time and height towards the Egyptian Coast. Computed tsunami features such as travel times and wave height distribution are calculated, which are useful in the evaluation of the tsunami hazard. This is done using the estimated flood zones and comparison with the tsunami wave height and deposition to help determine the intensity of tsunamigenic earthquakes and their impact on the northern Egypt coast.

Paleo-tsunami studies in northern Egypt are important because of the following reasons:- 1) the region includes archaeological monuments found along the Egyptian coast like the Citadel of Qaitbay, Ruins of the Temple of the King, the Pharaoh Ramesses II (1200 BC) temple, the Rommel's hideout and the Library of Alexandria; 2) the development of new Cities along the Egyptian coast like New EL Alamein city and 3) the construction of a nuclear power plant in the area of El-Dabaa on the Egyptian coast. As the Egyptian coastline was badly damaged in the past, a hazard assessment and mitigation plan need to be developed for the protection of these sites from future tsunamis.

The chapters of my thesis present three key items: 1) the seismotectonic in the Eastern Mediterranean and northern Egypt; 2) the paleotsunami works in the northern Egypt through identifying the tsunami layers; and 3) the modelling of two expected tsunami scenarios that faced the northern Egypt in the past and may affect it in the near future.

The first chapter introduces and presents the importance and the aim of my study. While the second chapter introduces the methodologies used in this study and the main definitions in seismotectonic, paleotsunami, modelling and scenarios for tsunamis.

The third chapter I calculated the present day stress regime in northern Egypt from the collected focal mechanisms using Tensor software version 5.8.5 developed by Delvaux et al. (2003, 2010).

The fourth chapter discusses the paleotsunami records in the north Egyptian coast during successive fieldwork trips. In addition to, using the laboratories analysis and different measurements to find the tsunami signatures.

The fifth chapter deals with the numerical modelling of two worst-case scenarios built up and processed by Mirone software developed by Luis(2007) update version 2.7 the last update on 22 October 2016. The snapshots were saved with specific wave travel times until they arrived at the Egyptian shoreline where wave heights were recorded. In addition to my modelling, I compared my results with different modelling other authors developed in northern Egypt.

The sixth chapter presents the final conclusions of my work in the view of identification of the main seismic active zones in northern Egypt and the tsunami sources in the Eastern Mediterranean. Also, my concerns about final conclusions of tsunami layers recorded in northern Egypt and the wave progradation. I end the chapter with perspective and recommendation items.

Chapter II

Methodology

1-Seismotectonic methodology

seismotectonics consists of the study of active tectonics and their relationships with earthquakes, active faulting and deformation along faults or active regions. It seeks to correlate the active faults with seismic activity in a certain region through the analysis of combined regional tectonics, recent instrumentally recorded events, accounts of historical earthquakes, focal mechanisms, stress tensor and geodynamics. The compilation of such information helps to identify the main active zones and the possible tsunamigenic zones that may affect northern Egypt. In this study, the steps of the seismotectonic analysis were carried out as follows:

1) Collection of the seismicity data and focal mechanisms of magnitude $M_L \geq 4$ for the continental margin and $M_L \geq 3.5$ for the local zones in the north of Egypt from updated earthquake catalogue.

2) Tracing of active faults and geological units from Egyptian geological structural maps EMRA, (2008) using ArcGIS V10.2 to identify the active tectonic zones.

3) Stress tensor inversion is calculated using Stress Tensor inversion Wintensor software version 5.8.5 (Delvaux et al.,2003, 2010).

4) Construction of a stress field pattern and GPS map of the study area.

Among the steps of my seismotectonic study, I will briefly describe my procedure to calculate the stress inversion method in northern Egypt. While the main definition and details in the methodology of focal mechanisms and stress inversion (i.e Right Dihedron method and the Rotational Optimization method) will be described in Appendix F.

1.1.Stress inversion

According to Ramsay et al. (2000) *"Stress tensor was identified as an inverse method for distinguishing the stresses from fault – slip data obtained from outcrops, borehole cores or active seismic clusters".* Stress field studies were developed recently by adding in situ measurements, fault slip data and the focal mechanisms of earthquakes. Researchers have estimated regional stresses using different methods, for example, using direct inversion, iterative and grid search methods. These methods help in the reconstruction of past and present stresses from fault kinematics and/or earthquake focal mechanism data (Angelier, 1979, 1984; Reches, 1987; Vasseur et al., 1983; Gephart and Forsyth, 1984; Carey-Gailhardis and Mercier, 1987).

In my study area, I calculated the stress inversion of the six main active seismic zones in northern Egypt using the Delvaux method Delvaux and Sperner(2003) and Delvaux and Barth(2010). I used the Tensor inversion software version 5.8.5 Delvaux (2003) last updated on 27 July 2016 to calculate the four parameters of the Stress tensor: the principal stress axes σl (maximum compression), σ2 (intermediate compression) and σ3 (minimum compression) and the stress ratio R = (σ2 - σ3)/(σl - σ3).

My first step starts with separating the raw data of the collected focal mechanism from 1951 to 2016 (Appendix A) into subsets while optimize the stress tensor using improved Right Dihedron method and the Rotational Optimization for each active zone (see Chapter III for the stress inversion calculation). The stress regime index (R') is calculated numerically with the Tensor software for each active seismic zone in northern Egypt. It is defined as a function of the orientation of the stress ellipsoid according to Delvaux et al.(1997). It is expressed as extensional when σl is vertical, strike-slip when σ2 is vertical and compressional when σ3 is vertical. R' has values of 0-1 for extension regimes, 1-2 for strike-slip regimes, and 2-3 for compressional regimes.

Many items are taken into consideration when using the Tensor program in the study area, including 1) minimization of deviation (α∘) between observed and theoretical slips on the fault planes; and 2) maximization of the shear stress magnitude on every fault plane. This is done in the Tensor program by using the function (F5). The amplitude of rotation angle value of R (the stress ratio) is tested and progressively reduced until the Tensor is stabilized. Moreover, the focal planes whose slip deviation α is more than 30∘ are removed. This stress tensor study was considered as an extension and update of previous studies using inversion of focal mechanism data like (Abou Elenean, 1997; Hussein, 2013; Emad Mohamed et al., 2015).

2. Paleotsunami, methodology

In 1980, the tsunami researchers around the world speculated that tsunamis do not leave deposits. However, the reports of several pre-1980s surveys indicated that tsunamis eroded and deposited sediments, not only sand but also responsibly large boulders and coral debris. Since the 1990s, and certainly, since 2004, there is no doubt that tsunamis erode and deposit sediments in the stratigraphy records. In the 1990s, post-tsunami surveys started to take observations on geological tsunami deposits e.g., (Dawson et al. 1996; Minoura et al., 1997; Bourgeois et al., 1999; Matsutomi et al., 2001; Gelfenbaum and Jaffe, 2003; Rothaus et al.,2004).

Since 1900 (the beginning of instrumental location of earthquakes), most tsunamis have been generated in Japan, Peru, Chile, New Guinea and the Solomon Islands (Clague et

al., 1994; Sato et al., 1995; Nishimura and Miyagi, 1995; Dawson and Shi, 2000). Some historic tsunami events have also been identified in the Atlantic Ocean/northwest Europe (Haslett and Bryant, 2007). A much smaller number of tsunamis have been generated in the Atlantic and Indian Oceans.

In the Indian Ocean, the Indo-Australian plate is being subducted beneath the Eurasian plate at its eastern margin (Gunathilake, 2005) with the Indian plate moving northeast at around 6 cm per year at an oblique angle to the Java Trench with Sumatra sliding over the top of the subducting Indian oceanic plate (Sandiford et al., 2005; Richards et al., 2007; Mosher et al., 2008). Large magnitude earthquakes occur as a result of this convergence. Field surveys outline the geological and geomorphic effects of the 26 December 2004 Indian Ocean tsunami including Szczucinski et al. (2005, 2007) studies of the environmental and geological impacts of the tsunami on the Thailand coast. Kurian et al.(2006) describe inundation and geomorphological impacts of the tsunami on the SW coast of India, documenting before and after beach profiles and quantifying erosion and deposition by the tsunami. Kench et al.(2006) describe geological effects of the tsunami on the Maldives, a set of low-lying, mid-ocean coral islands, where deposition dominated erosion.

The December 2004 tsunami has generated a new view of geological and geomorphological studies, many using techniques not available when other great tsunamis occurred, for example, like Alaska 1964, Chile 1960, and Kamchatka 1952, and addressing questions about the tsunami deposits.

In a number of historical cases, seaward-directed flow and evidence of seaward flow such as flopped-over plants have been observed on the coastal plain. The drawdown phase of the tsunami is typically slower than the uprush, however, outflow tends to be concentrated in topographic lows such as channels. Terrestrial debris from tsunami outflow has been observed and photographed in the nearshore region in many historical cases. It is likely that on the shelf, a tsunami deposit looks similar to and might be confused with a deposit from a flooding river mouth e.g., Wheatcroft and Borgeld(2000), or a storm-surge return flow e.g.,Aigner and Reineck(1982).

Several criteria, based on tsunami signatures, are used to identify tsunami deposits in the sediment cores and trenches. The following summarizes the most common tsunami signatures in sediments as evidenced from previous tsunami studies :

a) A sharp lower contact is a common feature found in high-energy wave deposits regardless of the exact hydrodynamic process.

b) Ripped-up clasts of underlying strata are very common in tsunami sediments (Bridge, 2008; Wang & Horwitz, 2007).

c) Concentrations of major heavy minerals such as tourmaline or zircon are entirely sited dependent (Jagodziński et al., 2009); other observations rely on reduced heavy mineral content (Dahanayake & Kulasena, 2008).

d) The macro and microfaunal assemblages (benthic foraminifera, ostracods, gastropods, shells) within tsunami deposits tend to contain many broken reworked fossils from a wide range of marine, brackish and even freshwater habitats (Kortekaas & Dawson, 2007).

e) The geochemical pattern of an overwash sediment body solely proves marine flooding but does not represent a criterion to distinguish between tsunami or storm origin (Chagué-Goff., 2010).

f) The measurements of magnetic susceptibility may provide definite signatures of paleo-tsunami deposits. According to Font et al. (2010), the magnetic susceptibility data indicate that the tsunami deposits were characterized by a very low magnetic susceptibility values linked to amounts of sand (i.e. paramagnetic) originated from the littoral dunes and mixed with inland sediments with tsunami wave reworked.

2.1. Examples of cores and trenching in tsunami and paleotsunami research

Some recent tsunami events, for example, the 26 December 2004 Indian Ocean tsunami or the 11 March 2011 Tohoku Japan tsunami, have provided a valuable view for future studies on old tsunamigenic deposits (Paris et al., 2007).

These two recent tsunamis resulted in more than ~ 184,167 deaths, and the total or partial destruction of more than 250,000 buildings, including harbours, seawalls, and other coastal protection structures (Nandasena et al. 2011). Fatalities from the Indian Ocean tsunami and earthquake in Indonesia alone totalled 128,645, with more than 37,063 persons missing and 532,898 persons displaced (USAID 2005).

Ishimura et al.(2015), studied historical and paleotsunami deposits during the last 4000 years including deposits of the 2011 Tohoku tsunami. In their study, they used canal trenches which were 2 m deep and 300 m from the shoreline. The 2011 Tohoku tsunami had a maximum runup height of 26-29.4 m at Koyadori and minimum run-up height of 5.8-8.9 m at Osawa (Haraguchi and Iwamatsu, 2011). The resulting tsunami deposit was recognized by beach and beach ridge sourced sand and gravel found up to 600 m inland in December 2012. Tsunami deposits were identified at by their grain composition, size, and roundness, which widely differed from those of the background deposits (e.g., peat and debris flow deposits). They also used the radiocarbon dating and tephra analysis to establish the

geochronology in the KYD-trench wall sediments and to correlate tsunami deposits with historical tsunami events.

Borrero et al.(2006) examined the tsunami deposits of 2004 Indian Ocean event in pits and trenches along 800 km of the shoreline from Breuh Island to Teluk Bandera in Batu Islands three months after this event. They examined the paleotsunami deposits by push cores. Bent vegetation, within or at the base of tsunami deposits, was used to determine flow direction. These tsunami deposits were composed primarily of sand and their thickness varied from site to site. Deposits were usually composed of multiple layers; the total thickness may reflect deposition during multiple waves and/or during uprush and return flow. The causes of the observed variability in grading include differences in the processes of deposition suspension versus bed load and in the spatial and temporal gradients in transport. The typical thickness was 5-20 cm, while the greatest thickness was 70 cm. The maximum tsunami runup height was 13 m at the northern Simeulue Island.

Polonia et al. (2013) examined the paleotsunami tributaries in cores in Malta and western Crete Island. Their results depend on the changes of sedimentology and geochemical pattern in the stratigraphy of cores. The radioactive dating shows the presence of the 21 July 365 in the Malta and western Crete cores.

My studies of tsunami deposits from coring and trenching described as follows:-

2.2. a. X-ray scanning

The x-ray scanning method used in chest scanning was used as an effective tool to identify small-scale sedimentary structures (e.g. sharp contacts, convoluted layers, etc.) which were not clearly detected through sedimentological changes, as well as the presence of bioturbation, or a fining upward of grain size and possibly erosional, basal contact like in paleotsunami studies such as (Bertrand et al. 2005; Gerardi et al., 2012).

In this study, 12 cores of a total of 24 tubes were scanned in the Royal Scanning Laboratory in Helwan, Cairo. Each 40 cm of the tube was scanned with a different level of radiation (the x-ray spectra ranged from 80-100 KV until the best contrast at the lowest radiation dose was achieved).

Each 40 cm of the tube were scanned with overlaps of 5 cm and then pasted together with Adobe Illustrator V. 6 software. Details like fossil content arrangements and stratigraphic markers like contacts, grain size were recognized along the cores in my studied area and indicate tsunami layers (see Chapter V). Moreover, the tube of unclear x-ray scanning may reflect high sedimentation rate.

2.2.b. Magnetic susceptibility

According to Handely(2000) "*The magnetic susceptibility of a mineral is defined as the measure of its 'magnetizability' in the presence of a small magnetic field. In mathematical terms, the volume magnetic susceptibility (κ) is defined as the ratio between induced magnetization per volume unit of the measured sample (M), an applied magnetic field intensity (H):*

$$\kappa = M/H$$

Since M and H have the same SI units (A/m), κ is a dimensionless number. However, it is common practice to report volume susceptibility in what are known as 'SI units' (and often omitting the 10-5 multiplier!)".

Magnetic susceptibility (MS) measurements were used as a good tool in identifying the plaeotsunami deposits for example Bertrand et al.(2005); Font et al. (2010); Polonia et al. (2013). The main idea of these works of MS measurements is that it detects a tsunami layer as having the lowest magnetic susceptibility values with peak values reflecting sediments rich in carbonates and high organic matter. In addition, low MS values, give evidence that a core is characterized by a higher sedimentation rate and high fossil content.

Magnetic susceptibility measurements provide a quantifiable, nondestructive and economic method for inter-correlation between cores. The MS variations of marine and lacustrine sediments indirectly reflect the proportion of biogenic (carbonates and silica) to lithogenic (clay and detrital) components (Sangode et al. 2001). In my study, magnetic susceptibility measurements were carried out using a Bartington MS-2 system (Fig. 2) to measure cores with a sampling rate of 3 cm. The measurements were carried out in the Geomagnetic Laboratory of the National Research Institute of Geophysics and Astronomy (NRIAG, Helwan).

Corrections for air were done using drift during the measurement period being linear and each measurement in the sequence is corrected by subtracting the estimated air reading at that time. The correction air value estimated for each point as:

Air value = first air + (final air * n/N)

Where n= the reading number (1, 2, 3….etc.) and N = number of reading +1

The correction is done using the Multisus software supplied by Bartington instruments.

Fig. 2: Bartington MS-2 Magnetic Susceptibility measurements.

2.2.c. Sampling and Macrofossil detections

We collected samples in this study as follows, first, 120 samples were collected from core tubes every 15 cm for the geochemical analysis (Fig. 3) including grain size, bulk mineralogy and totally organic and inorganic matter. Each sample was 25 grams, weighed using a sensitive balance. Then the samples are sent to Central Metallurgical Research Center Laboratory, Cairo, Egypt. This procedure of the sample analyses is described in detail in the next section. Second, sampling was used for macrofossils detection and carbon dating. The sediments contain several species of gastropods and bivalves (broken or in fragments) bones, charcoal, minerals (crystals like anhydrite that reflect the lagoon environment) and unidentified constituents (Fig. 4). Identified gastropods species are Conus and Tympanotonos fuscatus species, which reflect the lagoon environment. The collected samples helped to: (1) recognize sedimentary layers containing particles transported by tsunami (broken shells are more likely to be transported); and (2) to reconstruct the origin of the shells, as some of them are from lagoon environment and others are transported by waves and boulders to the shoreline like the Dendropoma (Fig. 4 N, O).

13

Fig. 3: Collected samples in this study of 25 grams for grain size and X-ray diffraction and totally organic and inorganic measurements

A,B,C is Mollusk species
A: found at depth 53 cm at core 3
B: found at depth 47 cm at core 3
C: found at depth 60 cm at core 3
D: Bone found at depth 60 cm at core 3
E,F,G,H,I,J,K,M,N,O gastropods family
E,F: found at depth 115 cm at core 3
G: Crystalline gastropod found at depth 48 cm at core 5
I: found at depth 2.2 cm at core 1
K: found at depth 53 cm at core 6
J: Tympanotonos fuscatus found at depth 130 cm at core 4
M: Fulguropsis radula found at depth 45 cm at core 6
N,O Dendropoma found at the boulders in Kefr Saber and Ras El Hekma sites had dating 940-1446 AD, 681-7597 AD respectively

P: Hexagonal crystal system of Quartz
Q: Magnesite sample

Fig. 4: Photos of the collected samples from cores and trenches in the studied area.

2.2. d. Geochemical analysis

The geochemical pattern was traced across the cores to define the paleotsunami deposits. The 120 collected samples in 24 core tubes were analysed using grain size, X-ray

14

diffraction, totally organic and inorganic matter measurements. The geochemical analysis will be described in brief as following:-

Grain size analysis

       The samples were collected from the cores and weighed before being sent to Central Metallurgical Research Center Laboratory, Cairo. The procedures include separating the weighed samples through a series of sieves (or screens) from 0.75 to 1000 microns. The distribution of size particles is determined by weighing the material remaining on each of the sieves and dividing these weights by the total weight of the sample. A correction is made for the moisture content of the sample so that all calculations are based on dry weight. The method requires drying, washing, during a series of separations.

I calculated the grain-size distribution statistics with gun plot software and excel 2013 (see Appendix D). Grain-size statistical parameters and graphic representations are given in φ units. Converting from microns to mm (as 1 micron = 10^{-3} mm) to Phi units using the following equation: -

$$\varphi = - \log_2 (d) \quad \text{where d is grain diameter in millimetres}$$

       The calculated grain size analyses distribution parameters have been calculated following Folk and Ward (1957) to determine to mean grain size, sorting, skewness, Kurtosis (see Appendix F for detailed equations). The most useful parameters of grain-size analysis for this study are the mean grain size and sorting. Extremely poor sorting reflects tsunami layers. Also, the high mean grain-size of sediments, which means coarser grain size, reflects high rich organic matter in cores analyses (see the section of coring analyses and interpretation in Chapter IV).

Total organic and organic matter

       TOC content can be measured directly or can be determined if the total carbon content and inorganic carbon contents are measured according to the following equation (Jones 1925).

       In soils and sediments, the total carbon means, (Total Carbon = Inorganic Carbon + Organic Carbon)

       In this study, the total organic and inorganic carbon are calculated by weight percent in cores. Organic carbon (Corg) in the sediments was analyzed at Central Metallurgical Research Center Laboratory, Cairo, Egypt using treatment with hydrogen peroxide H_2O_2. This treatment was unlike combustion methods and it would not be expected to affect the combined water content or change of weight of the inorganic material (Jones,1925).

The samples were treated with hydrogen chloride HCl to calculate the inorganic carbon by note the loss of weight before and after treatment.

X-ray diffraction

According to (Pecharsky et al., 2009), X-ray diffraction (XRD analysis) is a very useful tool for the identification of bulk mineral phases in powder specimens in the form of powder thin-film samples. The key for identifying materials by this method is their unique crystalline structure.The XRD instrument was called an X-ray diffractometer see Appendix F for the details of methodology and theory.

In cooperation with the Central Metallurgical Research Center Laboratory, Cairo, the collected samples were mounted in X-ray specimen holder on glass slides. The powder specimens were stuck on a glass slide using double-sided tape or Vaseline. The machine is equipped with a Philips PW 1730 X-ray diffractometer (Fig. 5) to measure the samples in the studied area under target Fe, filter Mn, KV 30, Ma 20, with speed 1 degree.

The data were analyzed in a semi-quantitative way following Cook et al. (1975). The intensity of the most intense diffraction peak of each mineral (see AppendixB) was measured and the identification of crystalline substance and crystalline phases in a specimen is achieved by comparing the specimen diffraction spectrum with spectra of known crystalline substances (Table 1). X-ray diffraction data from a known substance (called fingerprint) are recorded as a powder diffraction file (PDF).

Most PDFs were obtained with Cu$K\alpha$ radiation Standard diffraction published by the International Centre for Diffraction Data (ICDD) and summarized in Table 1, and they are updated and expanded from time to time.

Fig. 5: Philips PW 1730 X-ray diffractometer used in the study.

Table 1: Diffraction standard main peak identify minerals according to (ICDD)

Minerals	Principal diffraction peak (Å)
Gypsum (CaSo4.2H2O	7.56
Quartz	3.34
Calcite	2.92
Dolomite (CaMg(Co3)2	2.89
Feldspar (Albite)	3.1875
Feldspar (Orthoclase)	3.3193
Aragonite	3.3985
Halite	2.81
Goethite	4.19
Pyrite (FeS)	2.7090
Illite	10
Montmorillonite	15

2.2.e. Radiocarbon dating

Radiocarbon is a defined as an isotope of carbon which is radioactive with and has a half-life of about 5730 years and has the symbol of C^{14} (Bowman, 1990).

The C^{14} is produced by the interactions of cosmic rays with the atmosphere. The resulting radiocarbon combines with the atmosphere which is incorporated into plants and then by animals after they eat plants containingC^{14}. When an organism dies, carbon stops being absorbed. As the C^{14} radioactively decays to nitrogen, the remaining percentage remains as C^{14}. Samples older than about 50,000 years have a C^{14} concentration that is in practice too small to measure; so they cannot be dated via C^{14}.

The C^{14} dating of the samples in the natural environment should be corrected for the variations in the in the C^{14}/C^{12} ratio of the atmosphere, ocean, or another reservoir the sample was formed. Numerous calibration curves have been introduced by many authors in the last few years such as Reimer et al. (2009, 2013).

In my study, 46 samples were collected from cores and trenches in both study areas (see Tables 1 and 2 in Appendix E) for collecting samples and calibration dating curve using Oxcal,Bronk Ramsay 2013) for dating the paleotsunami deposits. These samples were sent to two laboratories (Poznan laboratory, Poland and Beta Analytical Laboratory, USA) for radiocarbon dating to identify dates of the historical tsunami layers. The collected samples were made of charcoal, plants (Fig. 6), bones, gastropods, shells and organic matter. The

radiocarbon dating results of charcoal and organic matter were calibrated using Oxcal software (Bronk-Ramsay, 2009) with the IntCal13 calibration curve.
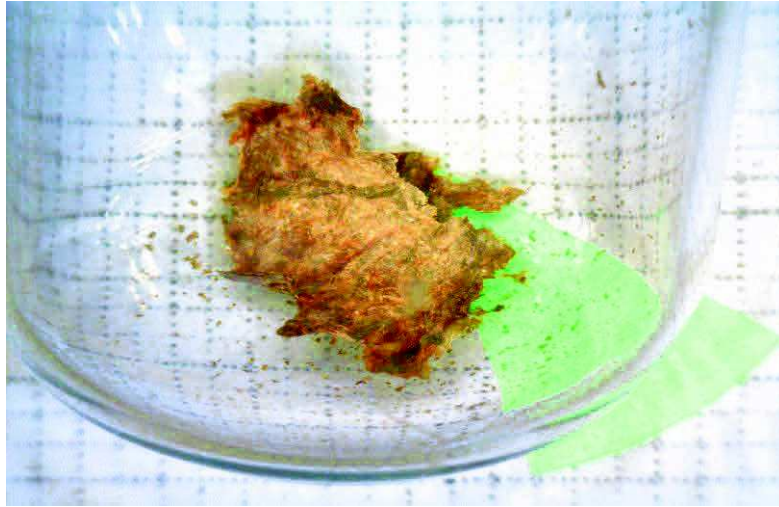
Fig. 6: Photo of plant remains that were dated in our study in the Beta Analytical laboratory.

3.Tsunami modelling

According to Power (2013)*''Tsunami modelling was defined as a set of mathematical formula that describes the physical characteristics of the tsunami to evaluate and predict the evolution of tsunami waves and their coastal impact. Tsunami models can be used to estimate the probable arrival times of tsunami, their amplitudes, inundation ranges, flow depths and/or current speeds. There are two main types of tsunami models: numerical models (i.e., computer-derived models) and empirical models''*.

When creating a numerical simulation, consideration should be given to the source mechanism and bathymetry grid in order to produce realistic and accurate results. As an example, there is a difference between using source parameters for local and far-field tsunamis to identify the local and far-field tsunamis run up. For far-field tectonic tsunamis, the line on the fault or even a point is sufficient to identify the runup height averaged over large distances. In contrast, local tsunamis require a full source identified by rupture area as well as consideration of temporal and spatial changes in the source parameters of the earthquake.

Numerical simulations have been developed and progressed during the past 30 years. The ongoing research into developing the numerical tsunami models is aimed at giving better and faster computing of the origin of tsunami wave propagation, inundation or impact on the coastal zone. Examples of common modelling used are: submarine mass failure

18

model by Hampton et al. (1996); the Antonio Baptista model by Baptista (1995); 'TSUNAMI-N2' developed by Goto et al. (1997); the most famous model used in the world, Tsunami propagation and inundation model (Geowave) by Madsen et al. (2002), Fuhrman and Bingham (2004); and Method of Splitting Tsunami (MOST) by Burwell et al.(2007). The most important task of the propagation modelling was to estimate the arrival time and wave heights. In addition, these models help us in understanding the behaviour of tsunamis, and to estimate the damage and tsunami risk.

My procedure in this study is to develop two simple scenarios based on the geological evidence observed at the paleotsunami investigation sites of Kefr Saber and EL Alamein (see Chapter IV). These two scenarios started from the Eastern and Western Hellenic arc tsunamigenic zone and affected the northern Egypt (see Chapter VI for estimated wave height and travel times). The scenarios were developed using Mirone software version 2.70 (updated by 22 October 2016; Luis, 2007), the software was created by the MATLAB tool and using TINTOL code. We create the initial wave by using two selective fault parameters for the eastern and western Hellenic arc sources (see chapter VI for details of the fault ruptures used i.e. location, length, width, depth, rake, slip). The Okada (1985) model are used to identify the co-seismic displacement in the Mirone software.

Five possible scenarios for both the eastern and western Hellenic arcs were developed and the best two scenarios were chosen based on recent large focal mechanism earthquakes in the Hellenic region with increasing the magnitude to reaches the magnitude of historical events of 21 July 365 and 8 August 1303. Then I compute the tsunami wave according to shallow wave theory numerical shallow water equation v= √Gh; where g is the acceleration of gravity, v is propagation velocity and h is depth (See details of equation in Appendix F) and using Mirone software to spread the tsunami across the bathymetry grid (30 arc seconds) in the study area (available from http://www.gebco.net/; Gebco 2014).

4. Concluding remarks

For the seismotectonic methodology, we collected instrumental and historical earthquake recordings, surface faults, tectonic and geological setting, and earthquake focal mechanisms data and GPS velocity vectors to give a general picture of the seismotectonic in the northern Egypt and adjacent areas of Eastern Mediterranean. We used the stress inversion method to calculate the present-day stress of six main active zones in the north of Egypt as a part of a study of the seismotectonic setting. To begin, we prepared a dataset of focal mechanisms from 1951 to 2016. We then used the right dihedron method and the rotational optimization method to calculate the four parameters of the Stress tensor: the principal stress axes σl (maximum compression), σ2 (intermediate compression) and σ3

(minimum compression) and the Stress Ratio R = (σ2 - σ3)/(σl - σ3) and evaluate the stress index regime.

For the paleotsunami methodology, different methods are used in my study to identify the paleotsunami deposits such as 1) X-ray scanning which used an x-ray spectra range of 80-100 KV to identify the broken shell fragments or identify the sharp contacts or sedimentation rate. 2) magnetic susceptibility measured by a Bartington MS-2 system with a sampling rate of 3 cm. The peak of magnetic susceptibility with values close to zero reflects the richness of organic matter and carbonates in paleotsunami deposits. 3) geochemical methods useful in determining the changes along the cores by grain size analysis to determine the mean and sorting using Folk and Ward (1957); bulk mineralogy used the x-ray diffraction method to identify the minerals and to determine the abrupt changes in mineral compositions and related source environment; total organic carbon is determined by treating with H_2O_2 to identify the organic matter enrichment in the tsunami deposits.

For the tsunami numerical modelling, we test five scenarios for both the Eastern and Western Hellenic arc based on our main findings of deposits of the 21 July 365 and 8 August 1303 tsunamis. We used Mirone software developed by Luis (2007) and this program used the TINTOL model code to compute travel time and the wave height in the study area.

There are some problems and limitations in the applying these methodologies. The uncertainties in stress inversion determination were due to geological and mechanical errors which generally fall in the range of measurement errors (Dupin et al., 1993 and Pollard et al., 1993). Moreover, a numerical quality index was evaluated to measure the accuracy of the results in the Tensor program based on the total number of data, the average slip deviation (α∘), the number of solutions kept (Delvaux and Sperner, 2003). Although, the solution of the stress axes parallel to the fault plane was removed to increase the accuracy the solutions.

There are also some limitations and problems in the paleotsunami methodology. The radiocarbon dating method may have some uncertainty related to mixing or reworking of surrounding plant materials in the cores. The shells from both marine and land organisms consist almost entirely of calcium carbonate which often dissolves and recrystallize which could give errors in the dating of shell samples. The correction of reservoir effects was applied to shells and collected gastropods samples in my study area using (Oxcal, Bronk Ramsy 2013) software. We calculated ΔR from the 50 nearest points in the Eastern Mediterranean database of dated shells and we applied this value ΔR = 103 and uncertainty= 161 to correct the samples dating against reservoir effect in my studied area.

With respect to the tsunami modelling, most propagation models assumed that coastlines behave as perfect reflectors of tsunami waves. This assumption omits the natural dissipation of tsunami energy which occurs when they run-up against the shore (Dunbar et al., 1989). This leads to a gradual reduction of the accuracy of the model. This is a particular problem for modelling the effect of a tsunami from distant sources, as incoming waves may arrive over the course of several hours and interact with earlier waves, especially in locations where tsunami waves may become 'trapped' within bays and inlets as an area between Alexandria and El Alamein.

Moreover, the characterization of the tsunami source and the resolution of the bathymetry data may represent uncertainty for tsunami modelling. The tsunami source problem is due to little source information availability. We overcome this problem because of the diversity of historical information and studies for the source locations for 21 July 365 and 8 August 1303 tsunami events.

Chapter III

Seismotectonic of northern Egypt

3.1. Introduction

Egypt is part of the northern African continent. It is affected by tectonic movements due to the proximity of the tectonic boundaries of the Eurasia, African and Arabian plates and significant seismic activity such as the Hellenic subduction zone. Northern Egypt is affected by the opening of the Red Sea and tectonic movement along the Gulf of Suez and Gulf of Aqaba- Dead Sea transform fault.

The seismicity of northern Egypt was studied by many authors among them Sieberg, 1932; Ismail, 1960; Gergawi and El Khashab, 1968; Maamoun et al., 1984; Kebeasy, 1990; Abou Elenean 1997; Ambraseys et al., 2005. In their studies, the seismic activity is reported in narrow belts (Levant-Aqaba, Northern Red Sea, Gulf of Suez, Eastern Mediterranean, and Egypt continental margin) which represent the major tectonic trends in northern Egypt. While the Western Desert and Nile Delta are characterized by low-level seismicity.

The seismicity data and focal mechanisms used in this chapter are collected for magnitude $M_L \geq 4$ for the continental margin and for $M_L \geq 3.5$ for inland in northern Egypt from the updated Egyptian earthquake catalogue (see references Tables 2, 4, 6, 8, 10 and 12 of focal mechanism solutions in Appendix A). The seismicity catalogue is divided into historical (pre-1900 AD) and instrumental with different level of completeness. Instrumental earthquakes during the period 1900 to 2016 were collected from (IRIS) (http://ds.iris.edu/seismon/) and an online bulletin provided by the National Earthquake Information Center (NEIC) for the period from 1950 to 2016 (http://earthquake.usgs.gov/earthquakes/), and Egyptian Research Institute of Astronomy Bulletins of the Egyptian National Seismic Network for events which occurred after 1997 in Egypt. Additionally, published data on historical earthquakes was also considered e.g. (Ambraseys et al. 2005; Guidoboni et al. 2009, and Ambraseys 2009).

In order to study the recent stress field of northern Egypt, we first collect all focal mechanisms in a catalogue and study the active faulting distribution. Secondly, we perform stress inversion using the Tensor program Delvaux and Sperner (2003). This procedure depends on two major assumptions for the study region: a) the stress field is uniform and invariant in space and time, and b) earthquake slip occurs in the direction of maximum shear stress (Bott, 1959).

The aim of this chapter is to study the seismotectonic setting of the active seismic zone of northern Egypt through the analysis of late Quaternary geological and tectonic structures, their main faults trends, the seismicity through historical and instrumental data, focal mechanisms with stress distribution and active deformation with GPS data. This chapter will also deal with the geology and tectonics of the Eastern Mediterranean and the possible tsunamigenic sources in the Eastern Mediterranean active zones, which will be discussed in Chapter IV.

3.2. Geological and tectonic settings of the Eastern Mediterranean and the Egyptian continental margin

The present-day geological configuration of the Mediterranean region is the result of the opening and subsequent consumption of two major oceanic basins, the Paleo-Theys (mostly Paleozoic) and the Neotethys (Late Paleozoic-Mesozoic) and additional smaller oceanic basins (e.g. the Atlantic Alpine Tethys). This has occurred within an overall regime of prolonged interaction between the Eurasian and African-Arabian plates (Robertson and Dixon, 1984; Stampfli et al., 2001).

The Eastern Mediterranean is a tectonically complex basin and is a relic of the Mesozoic Neotethys Ocean (Garnfunkel, 2004) with its evolution strongly related to the active subduction along the Hellenic arc. The present tectonics of the Eastern Mediterranean was developed by the northward convergence of the African plate relative to the Eurasian at a rate of 1cm/yr while the Aegean Sea represents an extensional basin with opening rates in the order of 3.5-4 cm/year (McKenzie, 1972; McClusky et al., 2000). The African plate oceanic lithosphere is nowadays subducted along the two small Hellenic and Cyprian arcs.

The Hellenic Trench (Fig. 7) is parallel to the Hellenic Arc which consists of an outer sedimentary arc and an inner volcanic arc. The average distance between them is 120 km. The sedimentary arc (Hellenides Mts, Ionian Islands, Crete, Rhodos) connects Dinarides and Hellenides mountains to the Tauride mountains in southwestern Turkey (Benetatos et al., 2004). Between the sedimentary and volcanic arcs South of Crete, the sea has a maximum depth of 2 km. The African oceanic lithosphere is subducting under the continental Aegean Sea lithosphere as part of the collision process of the Africa–Eurasia plates. This leads to the formation of an inclined seismic zone —a Benioff zone dipping to the NE to a depth of about 150–200 km (Papazachos, 1990).

The Hellenic zone subduction appears to have been activated continuously since the late Cretaceous (Arsenikos et al., 2013). According to Benetatos et al. (2004), the distribution of focal mechanisms along the Hellenic Arc shows that:

1) Along the central Mediterranean rise, a general NE-SW to NNW-SSE compression trend exists in the outer part of the Hellenic Arc. It starting south of Zante and up to the coast of Turkey, is deforming through high angle reverse mechanisms. These faults mechanisms are responsible for the rapid uplift in the western coast of Crete

2) At the inner part of the Hellenic Arc, a narrow zone is developed along the whole extent of the Arc which is characterized by the presence of N–S trending normal faults. This zone consists of an accretion prism up to the volcanic arc and is deforming by normal faulting with the T-axes having an almost E–W direction. The normal faulting does not occur deeper than 35 km and is underlain by active shortening result from gravitational collapse.

3) Along-arc extension continuous up to the coast of southern Turkey following the Taurides Mountain range. The back-arc area, starting north of the volcanic arc deforms by normal faulting where the T-axes have the N–S direction at the Aegean Sea. The western coast of Peloponnese is deforming by strike-slip faulting where, if the NE–SW trending planes are selected as the fault planes, then this faulting is parallel to the Cephalonia strike-slip fault and the sense of strike-slip motion is dextral (Fig. 7, Scordilis et al., 1985).

The island of Crete represents an emergent high at the fore-arc of the subduction zone, indicating the transition between the African and Eurasian plates. The Hellenic arc is associated with moderate arc-parallel extension and strong compression perpendicular or oblique to it. Three successive fault groups occupy the Crete Island. The first represents E-W trending faults of kilometric scale, mainly cutting the basement rocks or bound basement rocks and Miocene sediments. The second group consists of large and moderate scale N-S striking faults, cutting the previously mentioned group. The third group comprises kilometric scale faults striking NE-SE, which appear to be youngest faults occurring on Crete Island (Fig. 7, Kokinou et al., 2008).

East of the Eastern Mediterranean region, the Cyprian arc forms a plate boundary between the Anatolian plate in the north and the Nubian and Sinai plates in the south. It has been deformed in late Cenozoic (Ben Avraham et al., 1988; Kempler and Garfunkel, 1994).It is connected to the Hellenic arc in the west, and the Dead Sea Transform Fault and East Anatolian Fault in the east. A northward subduction of the African Plate beneath the Anatolian Plate indicates the existence of convergent mode along the western segment of the Cyprian arc (Ben Avraham et al., 1988). The Anatolian block escapes from the collision between Eurasia and Arabia by moving south-westwards forming the Hellenic and Cyprian Arcs (McKenzie, 1984). The geological structure in Eastern Mediterranean region is observed in the following bathymetry and structural map (Fig.8).
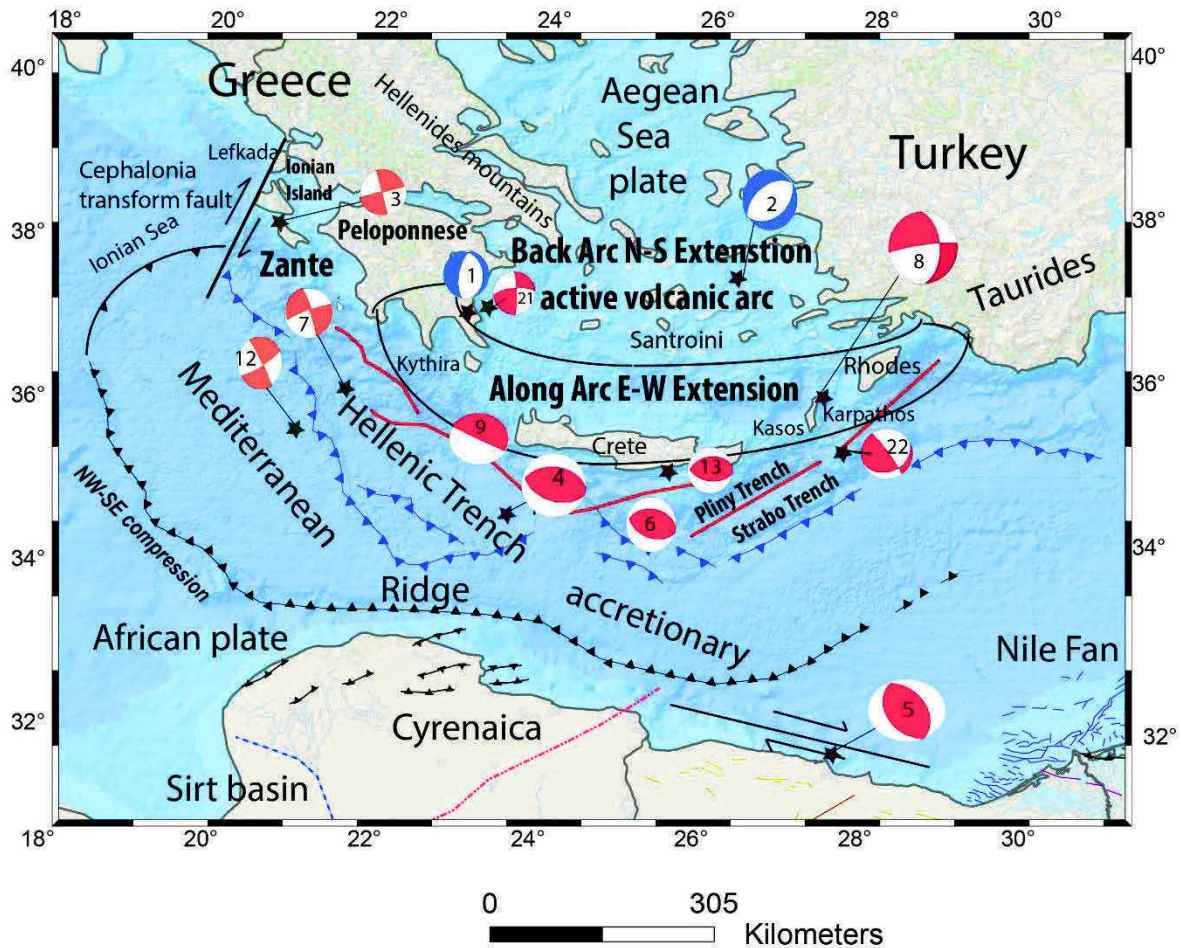
Legend

Reverse fault mechanism

Normal fault mechanism

Strike slip fault mechanism

Epicenter of earthquakes

Fault trends

Strike slip faults

Thrust fault

Base map: Bathymetry data of GEBCO_08 Grid (copy right: British Oceanographic Data Centre (BODC))

Fig. 7: Summary of the distribution of focal mechanisms for earthquakes along the Hellenic trench constructed based on (Cavazza et al., 2004; Billi et al., 2011; Benetatos et al., 2004), (see reference Table 14,15 of focal mechanisms data in Appendix A).
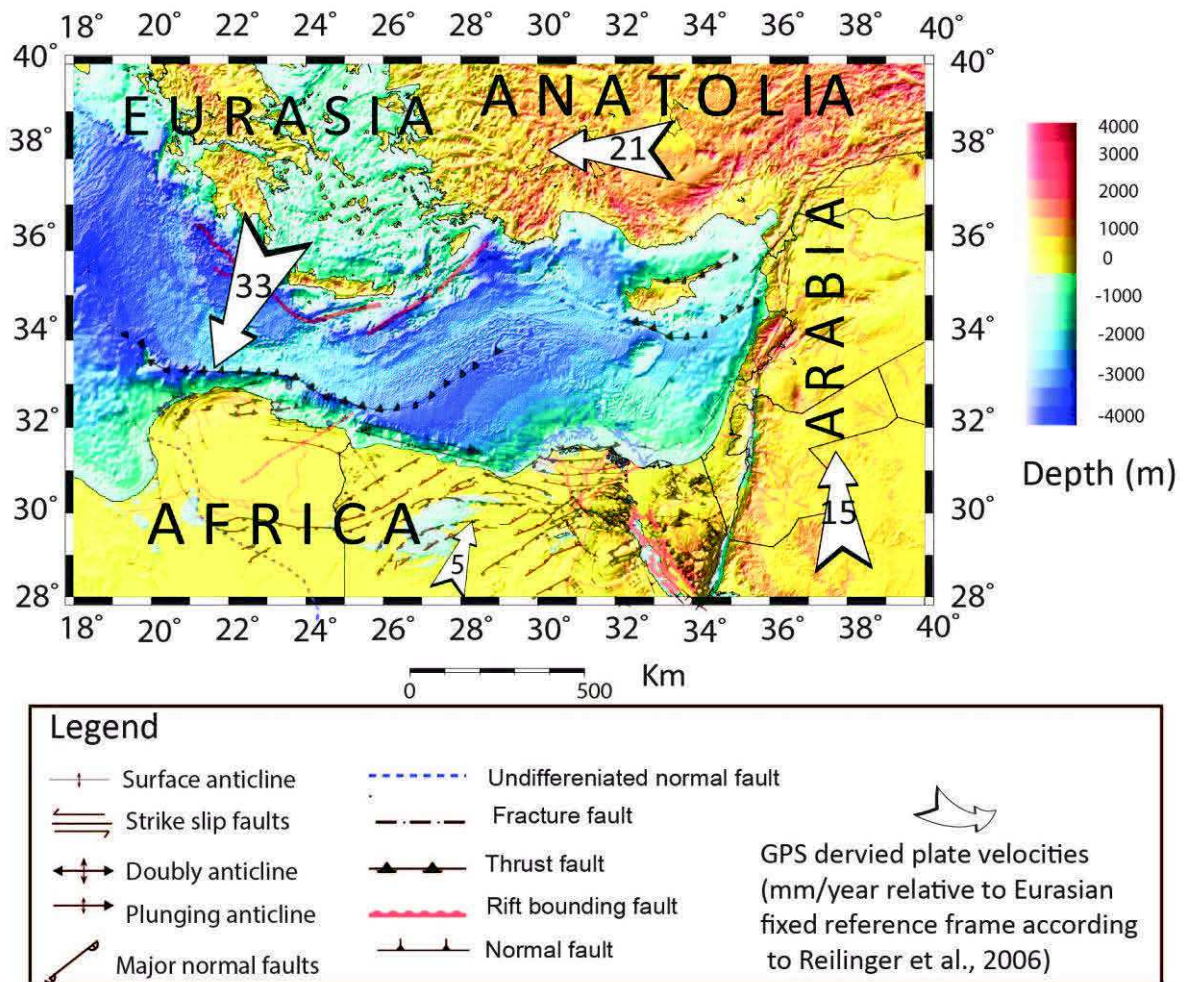
Fig.8: Morphotectonic map of the Mediterranean with major, simplified geological structures offshore constructed based on bathymetry data of ETOPO1 (1 min arc-minute global relief model of Earth's surface; https://www.ngdc.noaa.gov/mgg/global); Reilinger et al., 2006).

The Egyptian continental margin (Fig. 9) is located to the south of the Mediterranean Sea ridge behind the Herodotus abyssal plain where the sea floor is occupied by the Nile Deep-Sea fan, Eratosthenes Seamount, and Herodotus basin. It represents the transition zone between the continental-oceanic crusts where the stress field changes from dominant tension over Egyptian territory to dominant compression along the Hellenic Arc convergence zone (experiencing north-south compression), as demonstrated in several studies (Abu Elenean, 1997; Korrat et al., 2005; Abou Elenean and Hussein, 2007; Bosworth, 2008). The Herodotus abyssal plain (Fig. 8) is behind the Mediterranean Ridge. It is characterized by mud and salt diapers where rapid loading of shale and salt horizons by the clastics provided by the Nile River resulted in a progressive gravitational gliding of sedimentary wedge toward the North, coeval with the development of listric faults.

The tectonic framework and structural pattern of the Egyptian continental margin (Fig. 9) are the results of the interplay between three main fault trends: the northwest-southeast Temsah zone; the northeast-southwest Rosetta zone; and the east-west to ENE-WSW continental fault trends (Abdel Aal et al., 1994). These tectonic trends seem to belong to the reactivation of the basement faults. Other secondary fault trends are mapped and delineated in the west-northwest–east-southeast and east-northeast–west-southwest tectonic directions (Selim, 2012) in addition to the north-south Baltim fault trend (Mosconi et al., 1996; Abdel Aal et al. 2000).
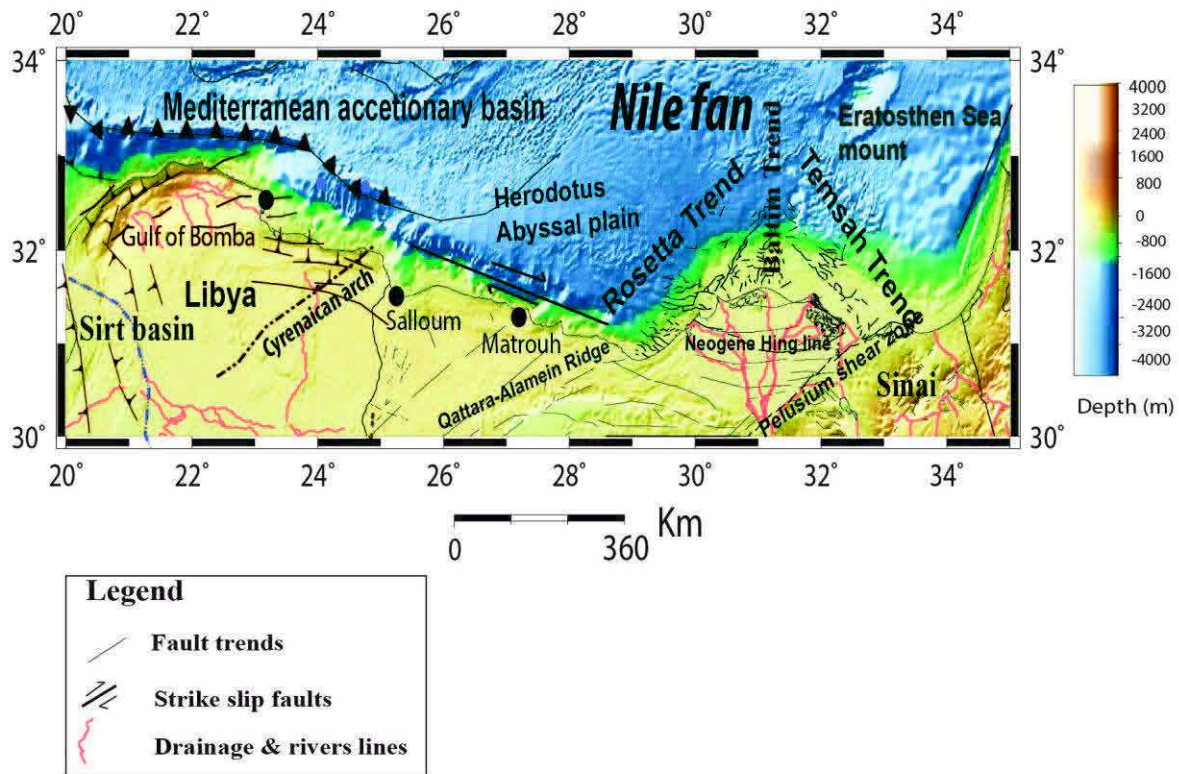
Fig. 9: Map of the Egyptian continental margin with major simplified geological structures onshore and offshore based on tectonic tectonics structures elements from (Abdel Aal et al. 1994; Egyptian geological map EMRA, 2008; bathymetry data of ETOPO1 (1 min arc-minute global relief model of Earth's surface; https://www.ngdc.noaa.gov/mgg/global/)).

The physiographic elements of the coastal zone and adjacent seafloor is shown in Fig. 9. The Mediterranean Ridge and the Nile Deep-Sea Fan are the major morphostructral domains in the southeastern Mediterranean Sea. The Mediterranean Ridge is a long accretionary prism between the Africa and Alpine belt, consisting of sediments which are scraped off from the subduction plate. The Nile Deep Sea Fan is the largest sedimentary clastic accumulation within the Eastern Mediterranean Sea. The interpretation of the marine geophysical survey PRISMED II conducted over a large area of the Nile Deep-Sea Fan explained the morphostructure in and around it (Mcclusky et al., 2000; Loncke et al. 2002;

28

Gaullier et al., 2000). The Nile Deep Sea Fan is bounded by the Dead Sea shear zone to the east and the Cyprus convergent zone and the Mediterranean Ridge to the north.

The continental margin bordering the Eastern Mediterranean Sea is characterized by a narrow continental shelf extending from the shoreline seaward to the shelf edge at about 15–20 km. However, the shelf in the region between Rosetta mouth and Bardawil Lagoon becomes wider, where it ranges from 48 to 64 km (Ross and Uchupi, 1977). The continental shelf in the western part is affected by a series of WNW trending faults. The present steep faulted continental slope, which has a rectilinear WNW orientation, varies in width from 34 to 56 km off western Egypt to about 20 km seaward of the Nile Delta. The coastal and continental shelf margin is offset abruptly to the WNW at several places, especially at the Gulf of Salloum and Gulf of Bomba.

In the area immediately seaward of the Nile Delta, the slope shows a fairly well-developed stratification with many closely spaced normal faults (Korrat et al., 2005). In principle, the continental margin can be considered a zone of weakness which experienced thinning of the crust during the Triassic period (Sofratome, 1984).

3.3. Geology and tectonics setting of Northern Egypt

The Mesozoic to the Tertiary tectonic history of northern Egypt had a significant effect on the formation of the Nile Delta, Cairo-Suez, Gulf of Suez, Gulf of Aqaba, and Sinai.

According to Abdel Aal et al. (1994) using 2D seismic profiles; the tectonic history of northern Egypt is divided into three main phases based on 2D seismic profiles wells data:

''*The first phase, a thick wedge of Early and Middle Mesozoic sediments was deposited. The southern edge of this sequence is north of a late Paleozoic and Early Mesozoic E-W trending faulting zone which bisects the Sinai* (Abdel Aal et al., 1992)*and bounded the intracratonic Abu Gharadig basin in the central northwestern desert. The deep structures in the Nile Delta show that the hinge line bisected the delta parallel to pre-existing E-W fault trends* (Fig.13). *During the Triassic and Jurassic, the opening of Tethys Sea led to a left lateral motion of Eurasia relative to Africa* (Robertson & Dixon, 1984*). This movement resulted in a system of NE-SW to ENE-WSW trending faults either normal faults or strike-slip faults with left lateral motion in northern Egypt, including northern Sinai* (Mesherf, 1990). *These faults are parallel to the PelusiumMegashear system* (Fig.10, Neev and Hali, 1982). *The NE trending Rosetta fault is parallel to Pelusium and the Jurassic NE to ENE faults along the extension of northwestern desert "Qattara- Alamein"*

ridge. These probably resulted in the right lateral oblique–slip movement along the Rosetta fault during the Early Miocene (Abdel Aal et al., 1994).

The second phase, during the late Cretaceous-early Tertiary, the NW-SE oblique compression related to the closing of Tethys Sea as a result of Eurasia moving southeast relative to Africa (Orwig, 1982). *The oblique compression resulted in a series of an echelon NE-SW trending, double anticline belt (Syrian Arc structures) in northern Sinai and in Alamein and Abu Roash in the Western Desert, and NW to NNW extension faults parallel to the major contraction force that affected northern Egypt. The compressional stresses generated NW to NNW extension faults parallel to major compressional stresses that affected northern Egypt* (Abdel Aal et al., 1994).

The third tectonic phase started from the late Eocene and up to recent times. At the beginning, the northeastward motion of the Arabian Peninsula yielded the opening of the Red Sea; subsequently, the rifting propagated toward the Gulf of Suez area. The rifting is thought to be cumulative in the early – middle Miocene when stresses of the Red Sea rift were transferred along the Aqaba-Levant area generating a left – lateral transform fault that extends through the Gulf of Aqaba northeastward to the Dead Sea, with a minor extensional component (Steckler et al., 1988). *The dominated motions were affected by three fault trends during Late Eocene-Miocene. The first trend is the Gulf of Suez NNW trending normal faults observed in the central Nile Delta. The second is the NNE faults trend related to the development of the Gulf of Aqaba rift which is formed from the Miocene up to recent by left lateral oblique slip movement. The third is the NS Baltim fault* (Fig.9,13) *trend which is thought to be formed by rejuvenation and reactivation of the older pre-Tertiary structure during the early Miocene* (Abdel Aal et al., 1994)*''.*

The main structural elements and the geology of the Northern Egypt can be summarized as the follows according to (Said, 1962; Abdel Aaal, 1994 and Moustafa, 1995):

3.3. a. Northern Egypt fold-fault Belt

The North Egypt fold-fault includes NE-SW oriented folds that affect the Mesozoic and older rocks in north Egypt. These folds are well exposed in the north Sinai (Moustafa and Khalil, 1989) as well as the northern parts of the Eastern and Western Desert. This belt comprises:

i-The North Sinai folds and associated faults

This belt is described in detail in Moustafa and Khalil, 1989, 1990; Abdel Aal, 1992. The belt is oriented NE-SW doubly plunging fold and is well exposed in north Sinai (Fig. 10). The right lateral reverse diagonal slip faults are parallel or sub-parallel to the folds of

the north Sinai. These folds extend eastward to the Dead Sea fault with the gradual rotation of their axes toward the northeast. The North Sinai fold belt is bounded on the south by the Tih plateau, where flat-lying upper Senonian to Middle Eocene rocks crop out.

Fig. 10: Tectonic geological map of Sinai constructed based on Egyptian geology map EMRA (2008) using ArcGIS map version 10.2 Software.

31

ii - Faults and folds in the north Western Desert

The Western Desert stretches from the Nile valley border to the Libyan border and southwards from the Mediterranean coast to the Sudanese border. The main tectonic trends affecting the northwestern Desert are E-W (or Tethyan a major one), NE-SW and NW-SW (Meshref, 1990).

The North Sinai type folding affects the Cretaceous formation in the northern and western Desert. The Bahariya and Abu Roash anticlines in the western Dessert, are bordered by NE-SW normal faults as a typical structure of the Upper Cretaceous through the late Eocene Syrian Arc belt (Said, 1962) and further dissected by mostly E-W faults. The El-Fayum, Wadi El-Natrun, Qattara and Siwa depressions, the existing folds that were intersected by NW-SE and E-W faults causing the removal of the loose section of Holocene and the Miocene fractured limestone, then the excavation of the Oligocene shales constituting low parts (Oases or depressions) through the karstification phenomenon.

The Alamein fault lies at 65 km to the south of El Alamein village. It is one of the faults that was splayed from the east-west oriented faults that extend from Wadi El Natrun area to the western end of Qattara Depression. The fault bounds the northern side of a relatively high plateau lying south of El Hamra Oil Field, while Razzak Oil Field lies on the top of the plateau. To the south, El Alamein fault has two segments: the first is the NW segment while the second one is longest and has the WNW trend (Fig. 11). The two segments have a total length of 58 km. The footwall of this fault is built up of the Moghra formation which is free of faults, whereas its hanging wall is mainly made up of the Moghra beds as well as some of the Marmarica Limestone that forms several scattered tableland formations. The Pliocene beds cap the upper surfaces of the Moghra Formation in several parts.

According to Abd-Allah (2009), the maximum displacement south of the Alamein fault is 72 m which measured at its middle part of the west-northwest segment. The displacement decreases toward the northwest segment to become zero at its southeastern end. Both segments of this fault have high angle (71° to 80°) fault planes with rakes 83° measured from slickenside striations. In some places, the fault consists of several planes that are separated by very small distances and bind together to form a fault zone.

3.3. b. The northeast Desert (Cairo–Suez area)

The Cairo-Suez area is located in the northern part of the Eastern Desert of Egypt and extends from the northern end of the Suez rift to the Nile valley. The Cairo-Suez area is affected by late Oligocene–early Miocene deformation related to the opening of the Suez rift. As shown in the tectonic geological map (Fig. 12), this deformation is responsible for

the E-W and NW-SE oriented normal faults (Said 1962; Abd-Allah,1992) associated with gentle folds affecting the upper Eocene and Miocene strata.

The south Cairo- Suez area is characterized by six slightly tilted fault blocks that affected the Middle Eocene formation. These blocks are Gebel Ataqa, Gebel Akheider, Gebel El Ramilya, Gebel Abu Trefia, Gebel Abu Shama, and Gebel Mokattam blocks.
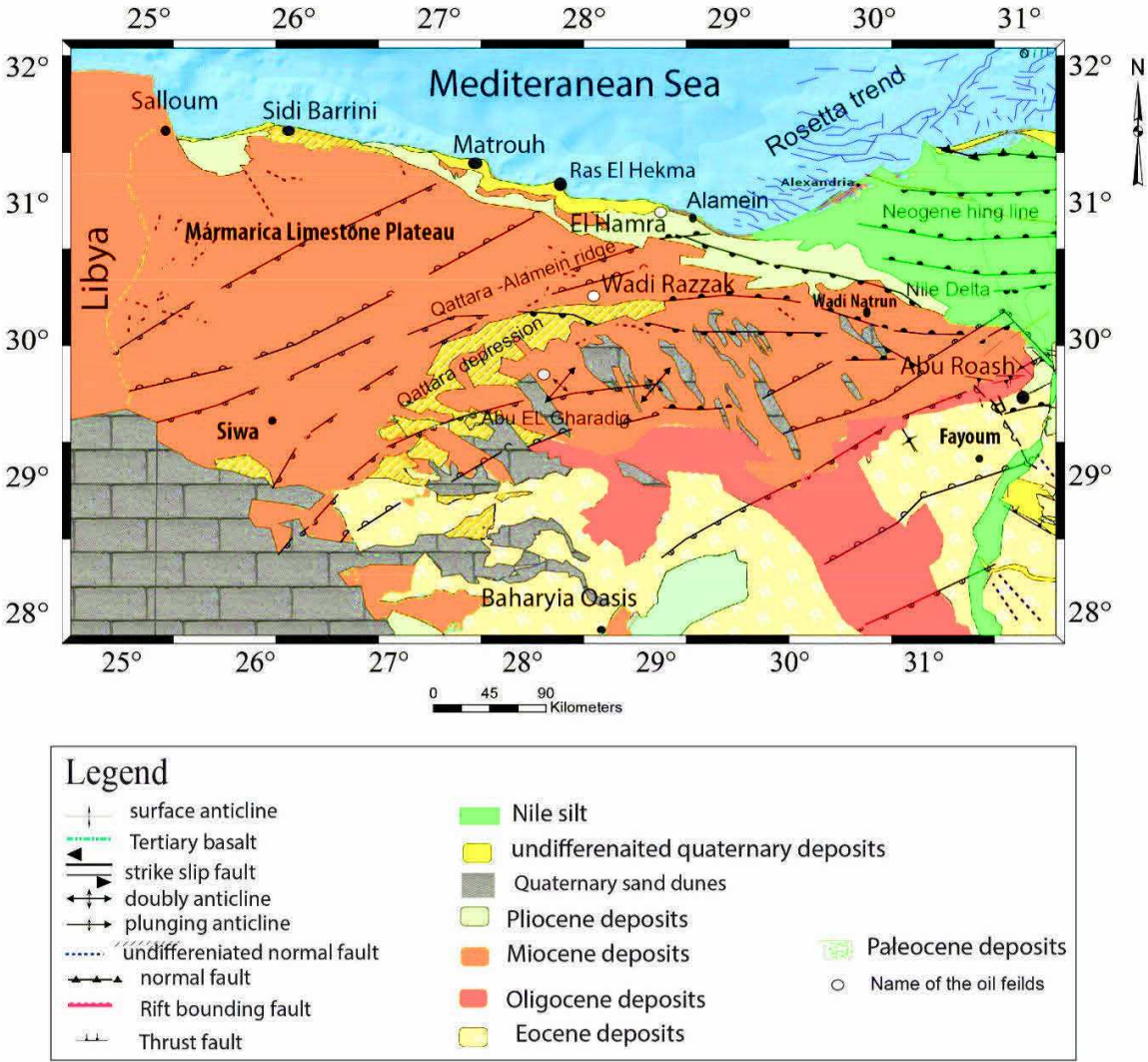
Fig. 11: Tectonic geology map of the northwestern Desert constructed based on Egyptian (geological survey EMRA, 2008) using ArcGIS map version 10.2 Software.
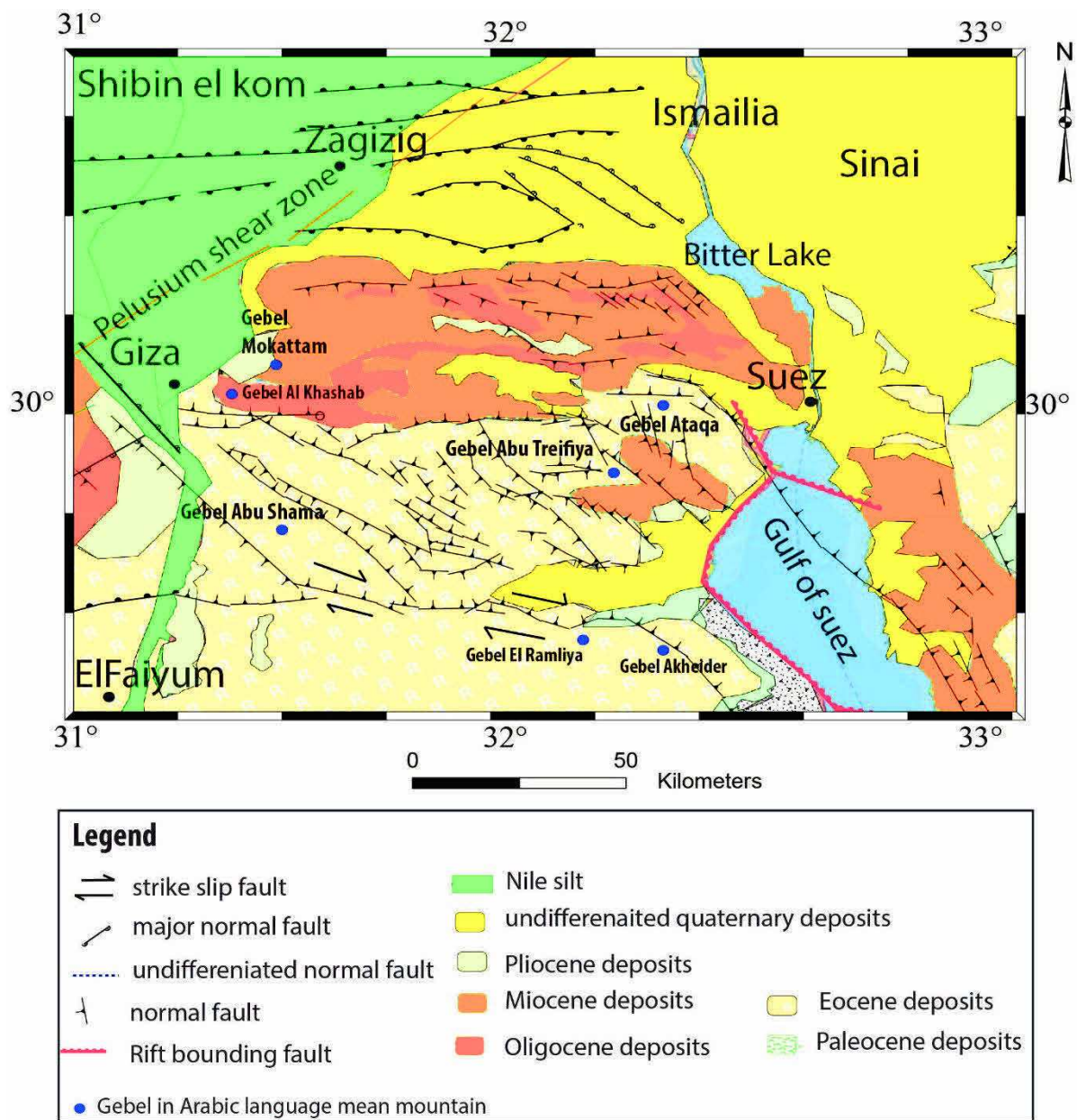
Fig. 12: Tectonic geological map of Cairo–Suez zone based on compiled structures elements from (Abdel Aal et al., 1994; geology map EMRA, 2008) using ArcGIS map version 10.2 Software.

3.3. c. The Nile Delta

The Nile Delta area is totally covered by the Quaternary deposits consisting of Nile silt, clay, sandy clay, sand, and gravel (Fig. 13). The Quaternary sediments in the Nile Delta have been classified into two rock units: a) Mit Ghamr formation (Baltim formation), which is overlain by the Bilqas formation (Rizzini et al., 1978); and b) Mit Ghamer formation composed of thick layers of quartzitic sand and pebbles that belongs to the Early to Middle Pleistocene and overlies the late Pliocene clay of the El- Wastani formation (Said, 1962). The thickness of Mit Ghamr formation (pre-Nile sediments) ranges from 250 m near Cairo

34

to more than 1000 m north of the Nile Delta. The Bilqas formation is composed of medium to fine-grained sand, silt, clays and peats (New-Nile sediments; Said, 1962).

The Neogene history of the Nile Delta area is much better known than the history of the older units. Two major unconformities of regional extent subdivide the Miocene and Pliocene intervals. A thick sequence of Miocene fluviomarine and shallow marine deposits is present in the northern portion of the Nile Delta basin. The thickness exceeds 2000 m near the coast but decreases rapidly southward (Said, 1962).

The Pliocene-Quaternary sediments uncomfortably overlay the Eocene-Miocene rocks throughout the Nile Delta and Valley. Generally, these sediments are composed of fluvial sands and clays with several gravel lenses. The surface agricultural clay layer caps these sediments inside the Nile Delta and Valley with variable thicknesses and alluvial – fluvial lithology (Said, 1962). This layer has a thickness varying from less than 10 m to more than 28 m inside the Nile Valley and is more than 70 m thick in the Nile Delta. Also, the sandy to silty clay lithology of this layer in the Nile Valley changes into pure clay lithology mainly to the North of the Nile Delta. The Quaternary sediments in the Nile Delta increase in thickness northward, from about 100 m to more than 900 m in the offshore part of the delta forming the Nile cone (Said, 1962). The agricultural layer also increases to the north and shows interfingering features with the underlying sand body.

The tectonic history of northern Egypt from the Mesozoic through to the Tertiary had a significant effect on the formation of the Nile Delta. The seismic reflection profiles (from oil field data), reflected six major structural trends which delineate the present Nile Delta (Abdel Aal et al., 1994). These trends have developed during the three main phases of the tectonic history of northern Egypt and described above (Figs. 9 and 13).

1) East-West Neogene Hinge Line.
2) Northeast-trending Rosetta fault trend.
3) Northwest-trending Temsah structural trend.
4) Northwest-trending Red Sea-Gulf of Suez fault trend.
5) Northeast trending Pelusium megashear structural trend.
6) North-South Baltim fault trend.

These structural trends are schematically represented in Fig. 13.
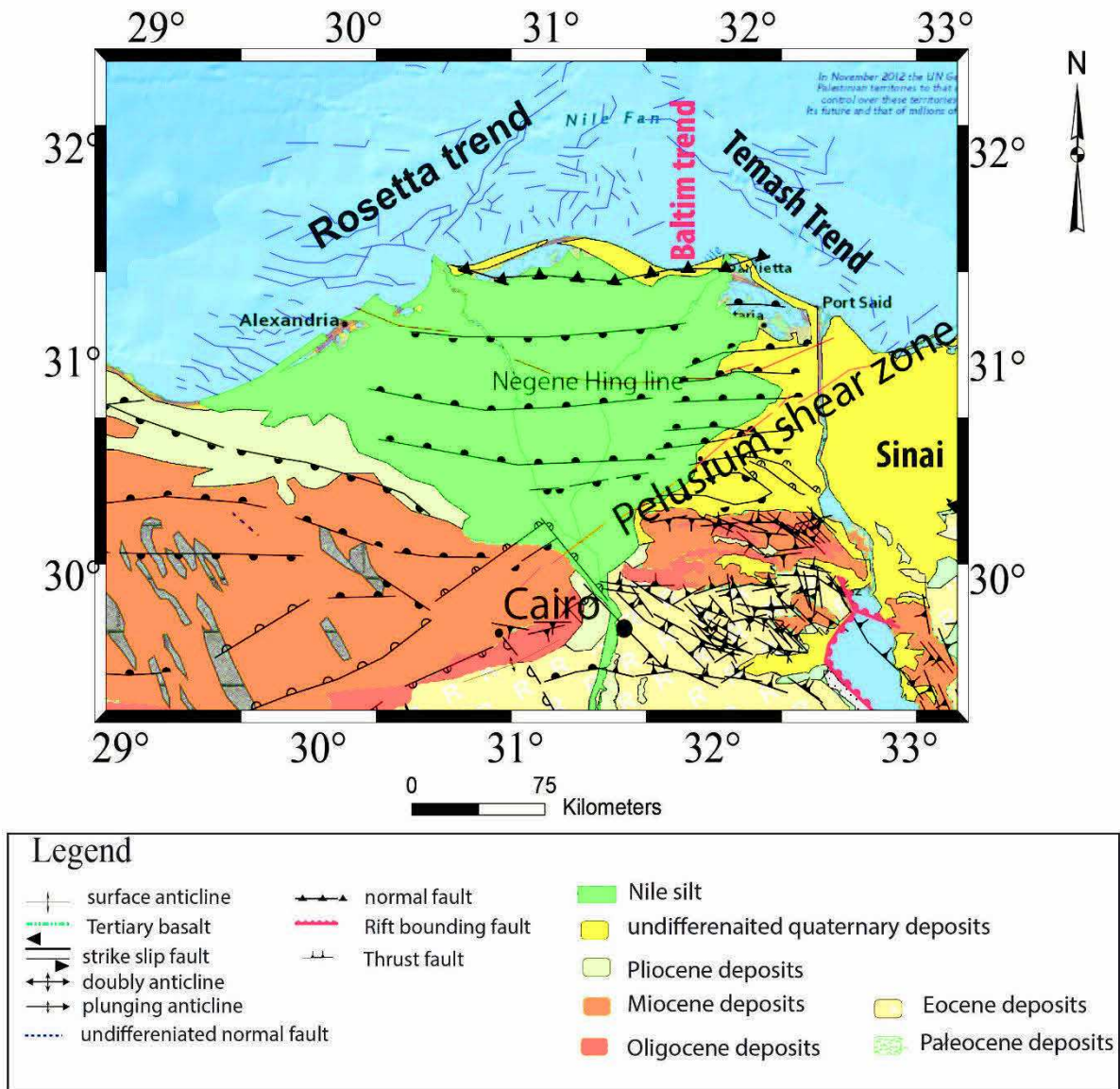
Fig. 13: Tectonic geological map of Nile Delta based on compiled structures from (Abdel Aal et al. 1994; geologic map EMRA, 2008) using ArcGIS map version 10.2.

3.3.d. The Suez Rift

The Suez Rift is located between Sinai and the northern part of the Eastern Desert (Fig. 10). This rift basin has a width of about 50-90 km and length of about 350 km and is occupied by the Gulf of Suez in the middle part. This has been traditionally referred to as the ''Clysmic'' rift, after the ancient Roman settlement of Clysma that occupied the present city of Suez (Robson, 1971). The Suez rift is dominated by NW-SE oriented normal faults and tilted fault blocks. The opening of the Suez rift resulted from the extension between the African and Arabian plates, leading to separation of the Arabian plate in the late Oligocene or Early Miocene (Moustafa, 1993). The dip direction of the tilted blocks of the Suez rift changes from N-S to SW-NE and back to SE and implies the formation of three distinct

provinces. These dip provinces represent three half grabens of opposite tilt directions (Moustafa, 1993), separated by two accumulation zones. The Suez rift faults extend into the Cairo-Suez fault systems but with smaller amounts of throw (Moustafa and Abd Allah 1992).

3.3.e -The Dead Sea fault and Gulf of Aqaba fault system

The Dead Sea Fault (DSF, Fig. 14) is a boundary between the Sinai microplate and the northwestern part of the Arabian plate (Garfunkal et al., 1981). It consists of a narrow belt of NNE oriented, left lateral strike-slip faults which include the Gulf of Aqaba, the Dead Sea, and Lake Tiberias (Youssef, 1968). The Dead Sea deformation zone along the Dead Sea fault is about 45 km wide, while the DSF extends for about 1000 km from the Gulf of Aqaba to the Antachia triple junction (south Turkey; Mahmoud et al., 2013).

In the Sinai region, the Gulf of Aqaba constitutes the eastern branch of the Red Sea, which is about 180 km long and 25 km wide, south of the DSF or Levant fault (Hartman, 2014). The Gulf of Aqaba appears as a succession of pull-apart basins bounded to the east by the Hejaz Mountains (Saudi Arabia) and to the west by the Sinai Mountains (Egypt), which shows a large inherited system of faults mostly parallel to the Gulf (Frieslander 2000; Ten Brink et al. 2007).

The pull-apart tectonic model of Fig. 31 a, and b; Hartman et al., 2014 shows that the Gulf of Aqaba has dominant left lateral strike-slip motion along the main faults parallel to the main axis of the Gulf, and normal slip along the traversing faults. From north to south, the Gulf includes the Eilat, Aragonese and the Dakar basins, respectively. These observations are results from the geological evidence and seismic reflections study of (Hartman et al., 2014).
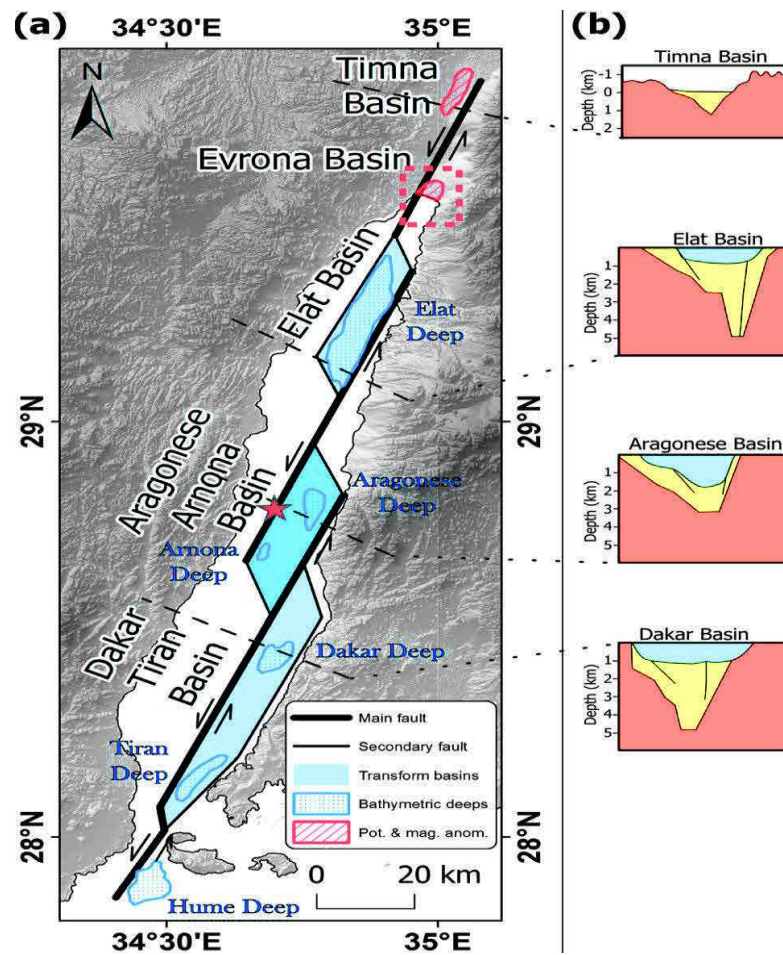
Fig. 14 : (a) Generalized tectonic settings of the Aqaba by Hertman (2014). The Evrona and Timna basins are mapped from bathymetric, gravimetric and magnetic data (Frieslander, 2000; Ten Brink et al. 2007). (b) Schematic models of the deep section of the basins (Ben Avraham, 1985; Ten Brink et al. 1999).

3.4. Seismicity and active tectonic zones

3.4.1. Historical earthquakes

The historical earthquakes in northeast Egypt and the Eastern Mediterranean, which occurred in the period from 2200 BC till 1899 AD are compiled by Maamoun et al.(1984) and Ambraseys et al. (2005). We have analyzed the seismological literature, which covers about four thousand years of seismic history of northern Egypt and the eastern basin of the Mediterranean, through the catalogues of (Guidoboni and Comastri, 2005; Guidoboni et al., 2009 and Ambraseys, 2009).

Catalogues of (Maamoun et al., 1984; Ambraseys, 2005) are also based on the Al-Suyuti (1445 – 1511) work titled "Kashf El-Salsala and wasf El-Zalzala ("*the sequential discovery from the description of earthquakes*") contains a list of earthquakes

38

between 712 AD and 1499 AD (translated into English by Springer in 1843 from the Arabic manuscript of the National Library of Paris).

From the historical documents dealing with earthquakes, it can be concluded that Egypt is one of the few regions of the world where evidence of historical earthquake activity has been recorded during the past 4200 years. Most of this information about historical earthquakes that have been felt in Egypt was collected from the annals of ancient Egyptian history, Arabic and European literature culturally flourishing (Badway et al., 1999). Therefore, the nature and type of the documentary sources in which its history was preserved are essential.

The historical earthquakes of Egypt were collected during the period from 2200 BC to 1899 AD (Fig. 15 and see the Table 13 of the historical earthquakes in Appendix A). The most significant earthquake damage in the Eastern Mediterranean and in northern Egypt are described briefly in the following lines:

A - 320 AD event

The epicentre is located in the Egyptian continental margin as shown in Fig. 15. It is, therefore, more likely that it is coming from an offshore earthquake near Alexandria. The 320 AD event damaged many houses in Alexandria and many people were injured (Ambraseys et al., 1994).

B - 956 AD event

The event was felt with maximum intensity of VI based on the MSK scale in Alexandria city and caused the collapse of the upper 22-meter part of the lighthouse (Ambraseys et al., 2005). The 320 and 956 events occurred north of the epicentre of the September 12, 1955 (Ms = 6.8) earthquake. There are large events that cannot be distinguished clearly in the period before 1900 due to the variability in the felt effects from event to event.

C - The 21 July 365 event

The quake was located west of Crete at the plate boundary of the Hellenic Arc and quickly sent a wall of water across the Mediterranean Sea toward the Egyptian Coast (Fig. 15,Ambraseys et al.,2005; Guidoboni et al., 1994; Stiros, 2001; Shaw et al., 2008).The 365 AD event is qualified as a "great" earthquake with magnitude M > 8, as manifested by up to 9 m uplift in western Crete. It was probably responsible for the reported or observed destruction in ancient towns of West Cyprus and Libya. Historical and archaeological data

also support the hypothesis that the fourth to the sixth centuries AD was a period of clustering seismicity in the Eastern Mediterranean region (Pirazzoli et al., 1996).

The fact that the AD 365 coseismic uplift occurred in a single movement suggests the occurrence of an extensive seismic sea wave that can be modelled according to the inferred fault parameters (Stiros and Drakos, 2006; Shaw et al., 2008). On the Nile Delta, the sea wave caused temporary changes in the coastline, and in the region of Al- Manazala, east of Nile Delta between Damietta and Port Said, the previously rich land became a desert, presumably due to flooding (Ambraseys, 2009).

D - The 8 August 1303 event

The epicenter of the 8 August 1303 event is located in the Eastern part of the Hellenic arc as shown in (Fig. 15, Guidoboni and Comastri, 2005; Ambraseys, 2009). According to Ambraseys (2009), this major earthquake caused serious damage in Crete, Rhodes, including other eastern Mediterranean coastlines in Cyprus, Palestine and Egypt.

In Egypt, the damage occurred at Abyar, Damanhur, al Wahsh and Sakha in the Nile Delta; in Alexandria, part of the city walls collapsed and the famous light houses were destroyed (Abu-El Fida, 1329). In southern Egypt, houses collapsed at Al-Minya (historical reports in Ambraseys et al. (2009)). In Cairo (which is ~150 km south of the Mediterranean coastline), ground movements were slow (probably due to surface waves), making it difficult for people to walk, while those on horseback were thrown down (historical reports in Ambraseys et al.(2009)).

Many houses suffered some damage and local contemporaneous witnesses report that the earthquake caused panic and women ran into streets without their veils (Ambraseys, 2009). Streets littered with fallen parapets and free standings walls slowed down the evacuation of the city, whose inhabitants encamped that night outside Cairo. The mosques of Al-Azhar, Al-Hakim and Amr Ibn-al-Ass at Fustat partly collapsed and had to be pulled down and rebuilt.

E - The 24 June 1870 event

Three shocks were noted in Alexandria at 18 h 25 which seemed to be directed from south-east to northwest and were accompanied by a hollow rumble (Soloviev et al., 2000).Three shocks, each about 5s long, were also felt in Ismailia at 18 h 25. These events were also felt in Cairo approximately at 18 h 30. The first one was very weak and only a few inhabitants noticed it. Two minutes later, a very strong shock occurred, and the third one that caused panic, came immediately (few seconds) after. The two main shocks were also felt in Beirut and Naplus at 18 h with an interval of 5 min and it was recorded in the earliest

recording at the Observatory of Naplus (Ambraseys, 2009); the second shock was stronger than the first one. The second earthquake was felt in the vicinity of Beirut, in the town of Zebdani and in the Anti-liban range at 18 h 15 m and on the eastern shore of the Red Sea (Soloviev et al., 2000). The strong shocks were felt in the sea and in the ports and ships sustained severe damage.
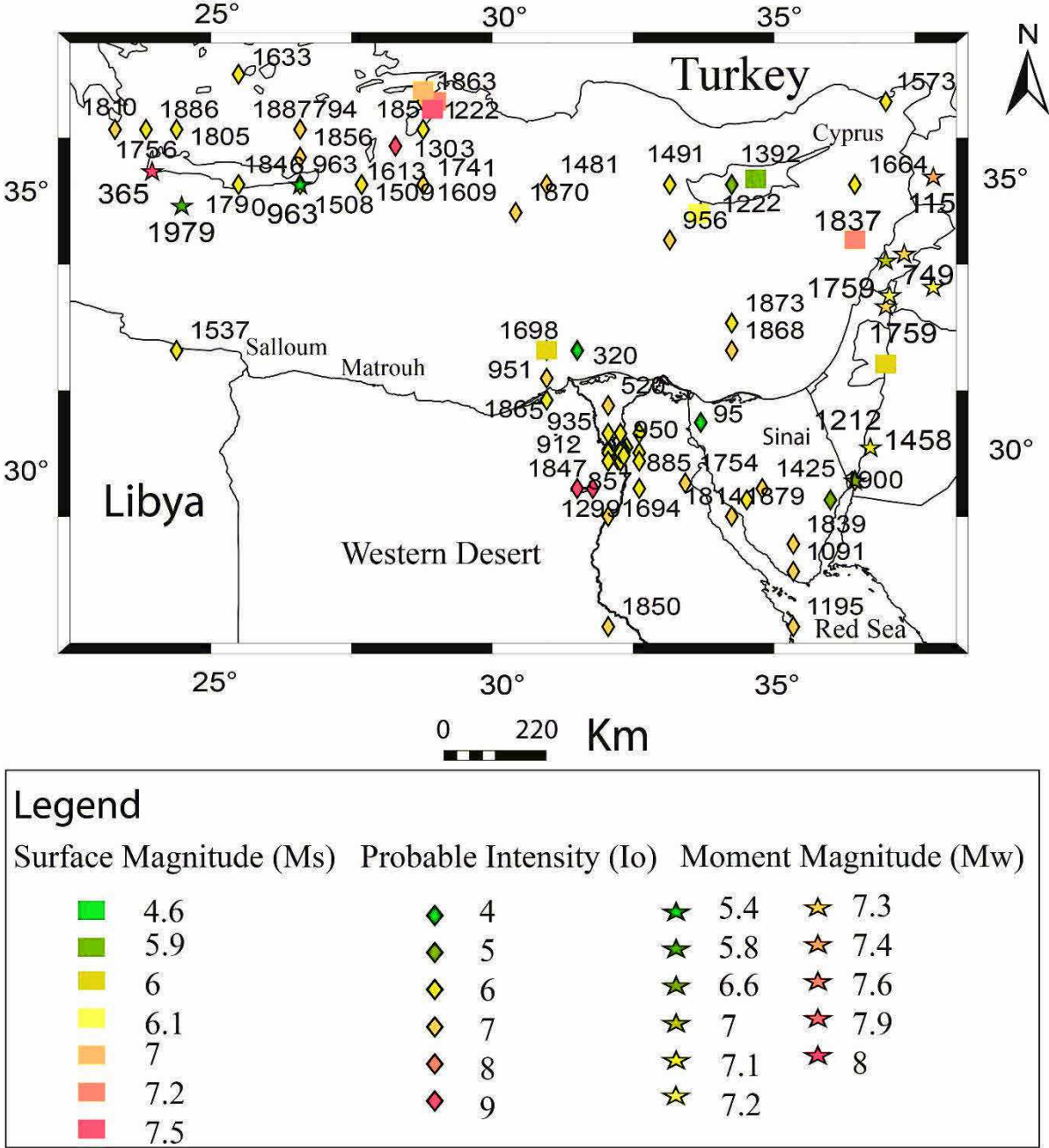
Fig. 15: Historical earthquakes in Eastern Mediterranean and North Egypt (see historical earthquakes references Table 13 of the historical earthquakes in Appendix A).

3.4.2. Instrumental Seismicity

The seismicity of Egypt was studied by many authors e.g., (Sieberg, 1932; Ismail 1960; Gergawi and El Khashab, 1968; Maamoun et al. 1984; Kebeasy, 1990; Ambraseys et

al., 2005; Abou Elenean, 1997). In their studies, the seismotectonic characteristics were addressed based on the regional geological structures and sometimes implying the dominant tectonic stress.

In 1997, the Egyptian National Seismological Network (ENSN) project started to cover all Egyptian territory (Fig. 16). The installation of new stations (ENSN) network has significantly enhanced the old seismicity distribution of the Egyptian region and the Red Sea.

The history of instrumental recording of earthquakes started in Egypt as early as 1899 at Helwan (Hlw) by an E-W component Milne Shaw seismograph. While another N-S component of Milne –Shaw and vertical component of Galitzin- Willip seismographs were initiated in 1922 and 1923, respectively. In 1955, another set of short period Sprengnether seismographs were also added. In May 1962, the system was replaced by the Benioff short period and Sprengnether long period seismographs with the photographic recording system and Helwan became one of the World Wide Standardized Seismograph Network (WWSSN) stations. In December 1972, a Japanese three-component short period component seismograph system with analogue recording system was installed.

In 1975, another three permanent seismological stations with photographic recording system were installed at Aswan, Abu Simbel and Mersa Matrouh. These stations have three component short period seismometers. In 1990, a broadband station (KEG) was installed at Kottamyia as a part of the Mednet project. In cooperation with the International Institute of Seismology and Earthquake Engineering (IISEE) of Japan, the National Research Institute of Astronomy and Geophysics (NRIAG) has installed a network of 10 telemetered seismic stations, which was operational in August 1994 around the southern part of Gulf of Suez. All these stations have the same seismograph system which consists of L4C (Mark – product) vertical component seismometer. Only one station of this network was equipped with a horizontal component.

In 2008, NRIAG started the construction of strong motion network (Fig.16) along the highly populated Nile Delta in the northern Egypt. These strong motion network reached 10 stations with the end of 2016.
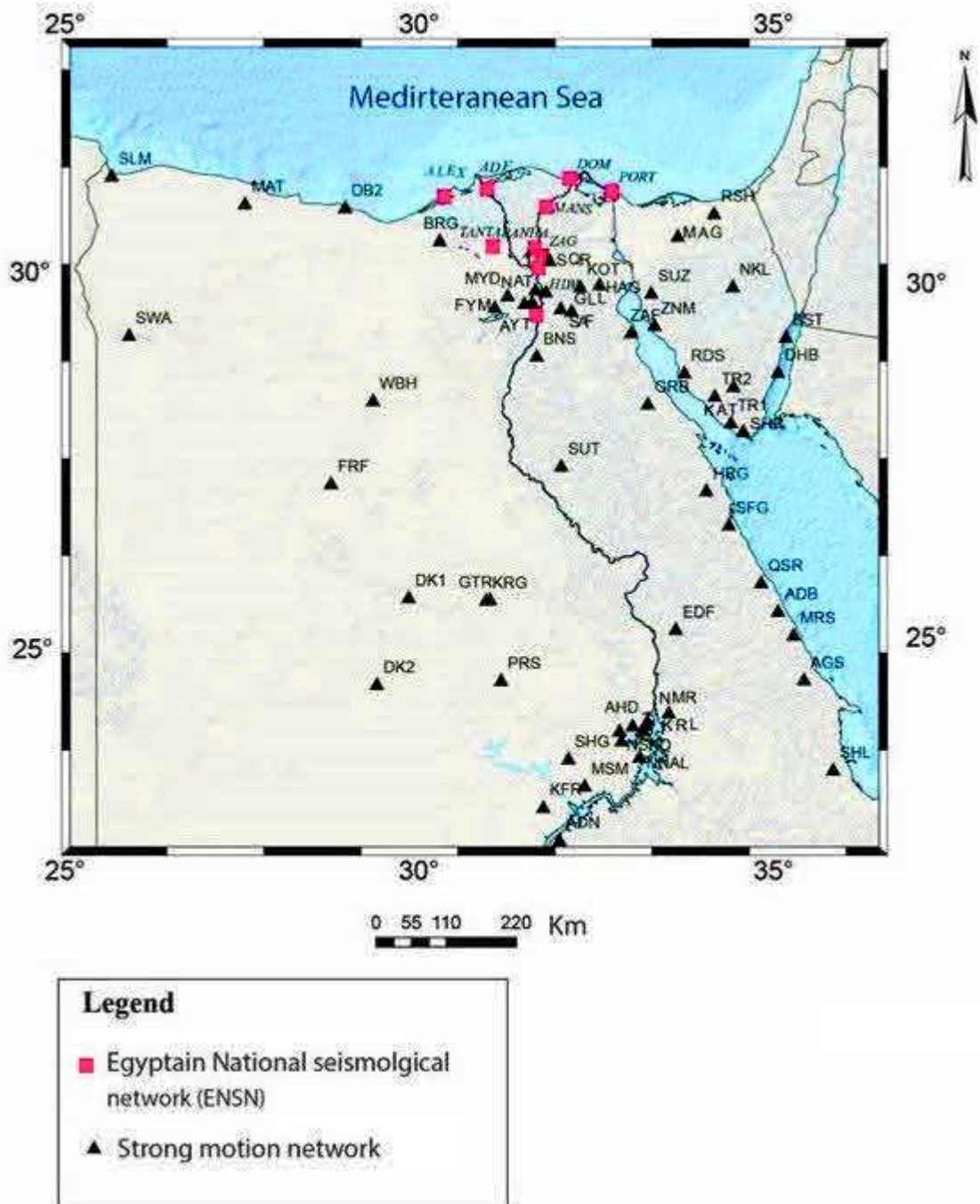
Fig. 16: The Egyptian National Seismological Network (ENSN) and the Nile Delta strong motion stations in Egypt

In our work, the most significant earthquakes which sometimes caused damage in the Eastern Mediterranean region and northern Egypt are taken into consideration. The seismicity data for the period from 1970 to 2016 (Fig. 17) was obtained from the IRIS bulletin. The seismicity of this region was not complete before the installation of the ENSN because there were only two permanent stations Helwan (HLW) and Kottamyiabroad band Station (KEG) that have been installed close to our study area.

The most recent instrumentally recorded earthquakes with severe damage in northern Egypt are described briefly as follows Table 2; Maamoun et al. (1984); Hussein (1989):

Table 2: The earthquakes parameters and stress axes of the significant earthquakes in northern Egypt.

No.	Date	Time	Location (º)		Depth (Km)	Mag. (Mb)	P axis		T axis		References
			Lat.	Long.							
a	12/09/1955	06:09:24	32.20	29.60	33	6.7	346	06	251	32	Hussein (1989)
b	31/03/1969	07:15:54	27.61	33.91	6.2	6.1	019	82	203	08	Hussein (1989)
c	12/10/1992	13:09:55	29.76	31.14	22	5.8	175	61	293	49	CMT
d	22/11/1995	04:15:11	28.76	34.66	9.0	7.3	159	31	062	12	CMT
e	28/05/1998	18:33:28	31.45	27.64	10	5.5	67	43	243	47	Huessein (2008)

a-The September 12, 1955, Alexandria earthquake (Ms = 6.7)

It occurred offshore in the Egyptian continental margin at 06:09 (GMT). It was strongly felt in Egypt and causing large amounts of damage between Alexandria and Nile Delta. The epicenter was located about 120 km NW of Alexandria (Maamoun et al., 1984). Eighteen people were killed, 89 injured, 40 houses collapsed completely and 420 houses ruined.

b-The March 31, 1969, Shadwan Earthquake (Mb = 6.1)

It occurred in Shadwan Island, the Red Sea at 07:15 (GMT) with Ms= 6.8 (Abu Elenean, 2007). The effect of this earthquake on the island caused fissures and cracks in the area south of Shadwan and extend a few kilometres towards the North (Saker et al., 2011).The main direction of this fault is an NW-SE direction, the same orientation of the Gulf of Suez. The coral reefs in the Red Sea appeared a few meters above the sea level after the earthquake, probably due to the uplifted sea floor. In Sharm El Sheikh and Hurghada cities, people ran outdoors, although had difficulty balancing and some mud brick houses were damaged in Ras Ghareb city (130 km north of Shadwan Islands). In the Nile Delta area, the event was very slightly felt at Kefrel Sheikh, Dakhalyia, Domiatta, Alexandria and the effects were stronger in the upper stories of the building (Maamoun et al., 1984).

c-The October 12, 1992, Cairo (Dahshour) earthquake (Mb = 5.8)

The earthquake epicenter was located at coordinates of 29.75°N and 31.13°E, at the outskirts of Dahshour village (SW Cairo, Fig. 17). The event affected Cairo and the northern part of the Nile Valley and caused much damage. Being close to the Cairo urban area, this

earthquake was one of the single most expensive natural disasters in the history of Egypt. It was felt all over Egypt from Alexandria to Aswan (Hussein et al.,1996); also discussed by Abd El-Aal.(2008). It was estimated that about 8300 dwellings were destroyed, 561 people were killed, and 6500 were injured. An official investigation revealed that 1343 schools were damaged beyond any repair, 2544 need major repair and 2248 need maintenance-type repairs (Khater, 1992; Thenhaus et al. 1993).

Tectonically, the faults of this area are trending E-W to NW-SE parallel to the Tethyan trend, or NW-SE parallel to the Gulf of Suez trend (Mesherf, 1990). The NW-SE to E-W structures are in agreement with the coseismic surface features and related liquefaction features observed near the earthquake epicenter and mainly in the late Quaternary alluvial Nile deposits.

d- The November 22, 1995, Gulf of Aqaba earthquake (Ms = 7.2)

It occurred in the Gulf of Aqaba and at least 8 people were killed and 30 were injured in the epicenter area. The earthquake occurred along the Dead Sea transform (DST) fault system; the epicenter was located 60 km south of the Gulf of Aqaba. The heaviest damage occurred in the town of Eilat where seven hotels and 50 buildings were damaged. In Saudi Arabia, two people died and five others died in Egypt, three of them in the town of Nuweiba.

3.4.3. Active tectonic zones

Many attempts were made to partition Egypt into different seismotectonic zones and structural trends (Youssef, 1968; Maamoun and Ibrahim, 1978; Ibrahim and Marzouk, 1979; Maamoun et al. 1984; Kebeasy et al. 1987; Kebeasy, 1990; Abu Elenean, 1997). The layout of these studies is made on basis of all available geology, geomorphology, geophysical, tectonic history, tectonic structures and seismicity.

In this study and on the basis of instrumental and historical earthquake catalogue, surface faults, tectonic and geological setting, and earthquake focal mechanisms of northeast Egypt, Six seismotectonic (Fig. 17) zones are recognized in northern Egypt:

a- The Egyptian continental margin (Trend A and B)

b- The Dahashour zone

c- The Cairo-Suez zone

d- The Northern Gulf of Suez zone

e- The Southern Gulf of Suez zone

f- The Gulf of Aqaba zone (subzones F and G)
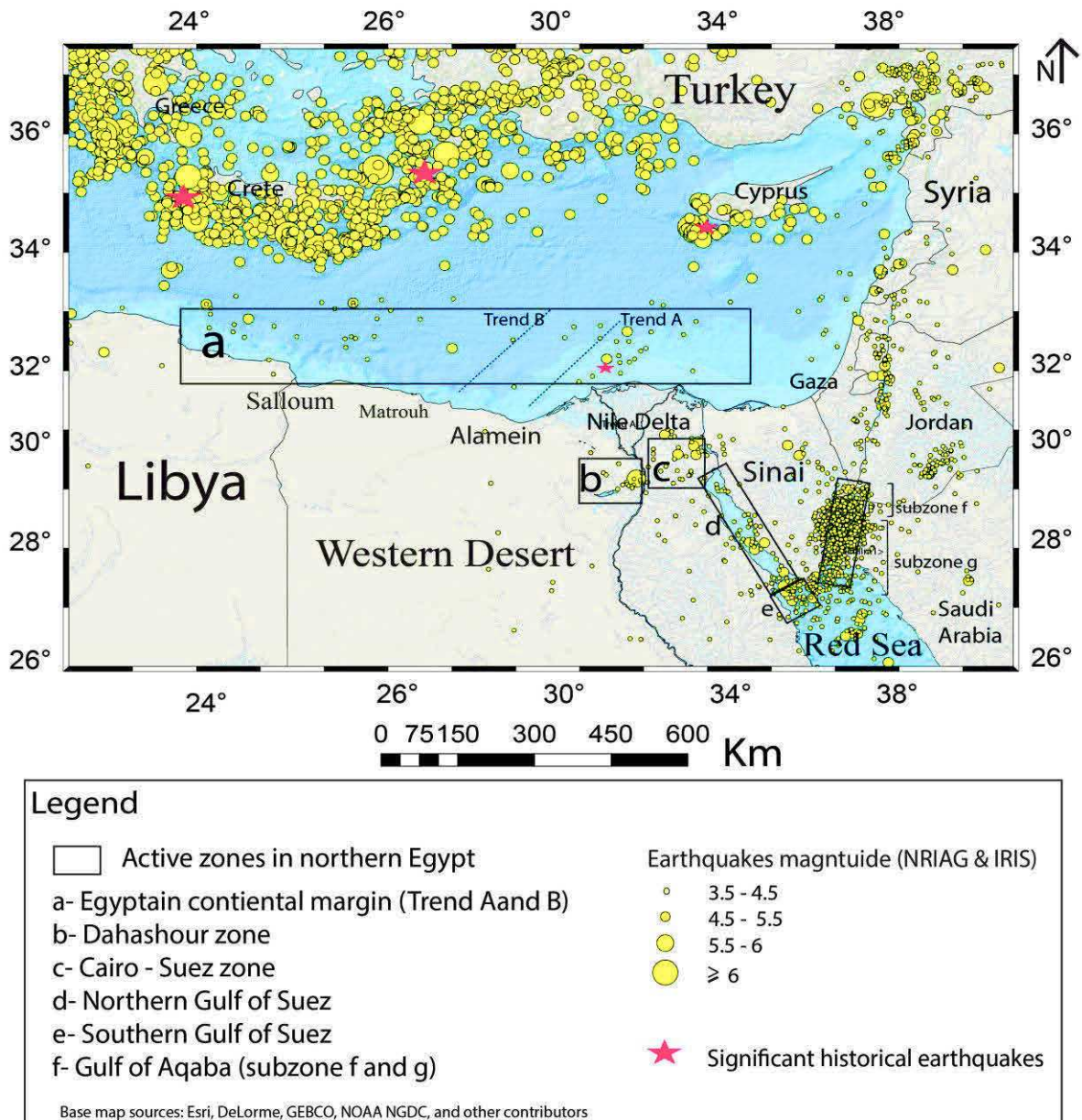
Fig. 17: The seismicity in north Egypt (Mag. ≥ 3.5) and Eastern Mediterranean region (Mag. ≥ 4.5) constructed based on NRIAG and IRIS bulletins. The active zones in the northern Egypt based on the (Abu Elenean, 1997) and this study: a) Egyptian continental margin, b) Dahashour zone, c) Cairo-Suez zone, d) Northern Gulf of Suez, e) Southern Gulf of Suez, and f) Gulf of Aqaba.

3.5. Focal mechanisms data

Earthquake source mechanisms are of prime importance in monitoring local, regional and global seismicity.

Our work was carried out by collecting all focal mechanisms of earthquakes that occurred in active tectonics zones in and around northern Egypt from 1951 to 2016. We constructed a comprehensive catalog for the focal mechanism solutions, including the data

published in different journals for the Egyptian territory which cover the period from 1951 until the end of 2016 of magnitude $M_L \geq 3.5$ for local earthquakes and $M_L \geq 4.0$ for the continental margin (see Tables 2, 4, 6, 8, 10, 12 in Appendix A). The results are the focal mechanism solutions based on the polarity of the first P-wave motion e.g. (Maamoun, 1976; Hussein, 1989 & 1999; Megahed and Dessokey, 1988; Badawy and Horvath, 1999; Abdel Fattah, 1999; Abou Elenean, 1997; Hussein and Korrat, 2001; Salamon et al., 2003; Hofstetter et al., 2003; Abou Elenean et al. 2004; Egyptian National Seismological Network (ENSN), 1998–2004) and solutions based on the waveform inversion (Hussein, 1999; Abou Elenean et al. 2004; Abdel Fattah et al., 2006).

In addition to the available first motion solutions, the solutions of the global catalogues of CMT Harvard and the National Earthquake Information Center NEIC, as well as the regional CMT catalogues (RCMT) in the Mediterranean Sea region, are also collected. These catalogues include the European Mediterranean Net (Med Net) of the National Institute of Geophysics and Volcanology of Rome, ZUR-RMT of the Institute of Technology of Zurich (ETHZ), German Research Centre for Geosciences (GFZ).

In the following paragraphs, I will present and discuss the focal mechanisms solutions and fault trending in the active tectonic zones of Egypt which include the Egyptian continental margin, Dahshour zone, and Cairo-Suez area, Northern Gulf of Suez, South Gulf of Suez, and Gulf of Aqaba.

3.5. a. Egyptian continental margin

19 focal mechanisms solution of magnitude $M_L \geq 4.0$ from previous works were collected (Fig. 18, see references to the focal mechanism data Tables 1 and 2 in Appendix A). The results from focal mechanisms show two types of tectonic regimes: the first group of mechanisms is represented by NW Oblique (normal–dextral) faults (blue beach ball); and the second is compressive, represented by E-W to ENE (reverse–sinistral) faults (red beach ball).

The largest event occurred in the Egyptian continental margin on September 12, 1955, with Ms 6.7 (Costantinescu et al., 1966) in the continental shelf of the Nile Delta. This event indicates a strike-slip faulting mechanism with a considerable reverse component along an NE-SW or ESE-WNW striking plane (Korrat et al., 2005). The ESE-WNW striking plane yields a right-lateral motion whereas the NE-SW fault plane indicates left-lateral offset.

The October 19, 2012 event occurred at 03:35:11.2, (GMT) with Mb 5.1 according to the Euro-Mediterranean Seismological Centre (EMSC) and represents the second largest

offshore significant seismic event that occurred within 57 years in the continental margin of the Nile delta.

In front of the Nile Delta, the continental slope shows a fairly well-developed stratification with many closely spaced normal faults. In principle, the continental margin can be considered a zone of weakness which experienced thinning of the crust during the Triassic period (Sofratome, 1984). This zone of transition between the faulted continental crusts and oceanic domain might be predestined by its orientation to be reactivated with dextral strike-slip and reverse components (Sofratome, 1984).
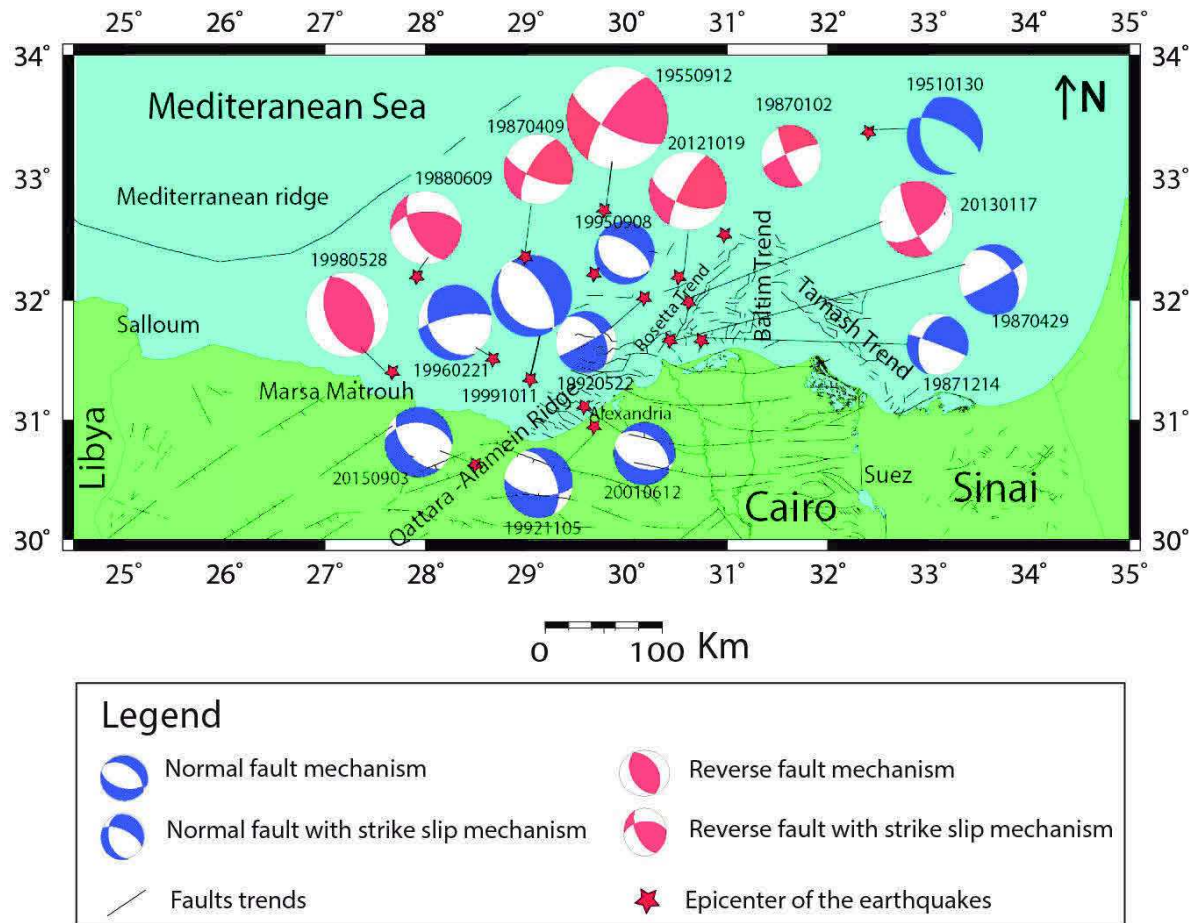
Fig. 18: Focal mechanisms of 19 events with $M_L \geq 4.0$ at the continental margin (see reference Tables 1 and 2 of focal mechanism solutions in Appendix A).

3.5.b. Dahshour zone

This zone is located in the northern part of the Western Desert and in the west of the Cairo – Suez zone.

The epicenter of 19 collected focal solutions with $M_L \geq 3.5$ are obtained from previous work (Fig. 19; see Appendix A, Tables 3 and 4) which are situated at the unstable shelf (Said, 1962) underlain by high basement relief due to block fault and effect of minor

compressional folding. The largest event in the Dahshour zone with $M_L5.9$ is the famous October 10, 2017event: black beach ball in Fig. 19. This event shows normal faulting mechanisms and its nodal planes trending NW-SE with some strike-slip component (Maamoun et al.,1993; Hussein, 1999).

Most studied events indicate normal faulting with two nodal planes E-W to WNW-WSE in agreement with normal faults observed in the tectonic and geological map as shown in Fig. 11.

Fig. 19: Focal mechanisms of 19 earthquakes $M_L \geq 3.5$ at the Dahshour area (see reference Tables 2 and 4 in Appendix A).

3.5.c. Cairo –Suez zone

Twelve focal solutions of earthquakes with $M_L \geq 3.5$ were collected from previous work (Fig. 20, see Appendix A Tables 5 and 6). This zone extends between the northern end of Suez rift to the Nile Valley in the northern Eastern Desert. The structural framework is

dominated by two main sets of faults oriented E-W and NW that have the same age (see tectonic and geological map Fig. 12).

The mechanisms of large two events of September 29,1984 and April 29, 1974, of M_L 4.6 in the Cairo shear zone show normal faulting with a strike-slip component along nodal planes trending nearly E-W to NE-SE. Most of the mechanisms of other events show mainly pure normal faults and oblique source of the normal component with E-W and NWN-SES and NW-SE trends in accordance with to the general strike direction of exposed faults.

Generally, these solutions confirm the suggestion of a reactivation of pre-existing E-W and NW-SE faults due to a partial transfer of rifting deformation from the Red Sea – Gulf of Suez along these trends.
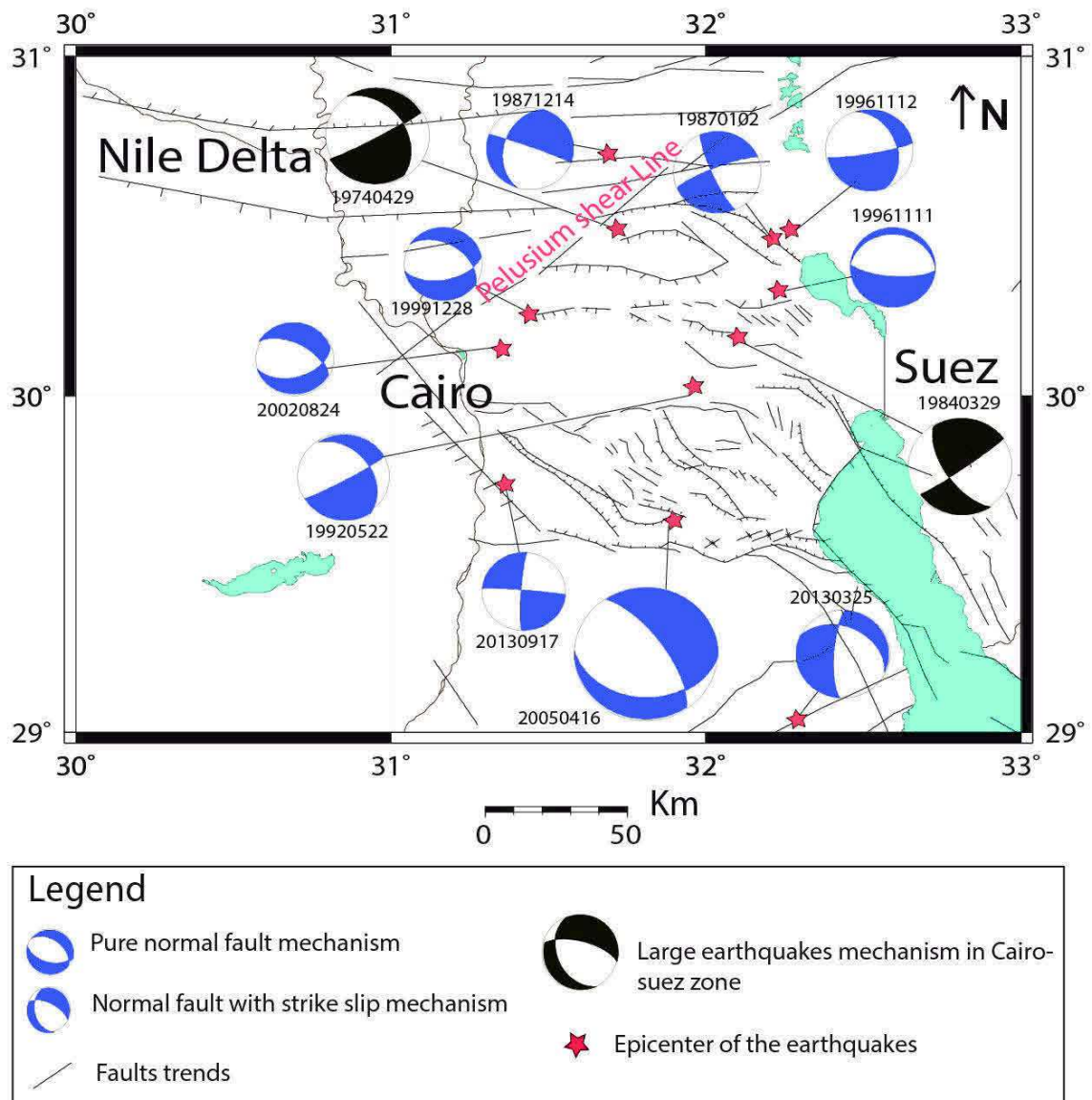
Fig. 20: Focal mechanisms of 12 earthquakes with $M_L \geq 3.5$ magnitude in Cairo-Suez area (see reference Tables 5 and 6 in Appendix A).

3.5.d. Northern Gulf of Suez zone

The Gulf of Suez is a Neogene continental rift which has evolved as one arm of the Sinai triple junction together with the Gulf of Aqaba and the Red Sea. Although there are no significant earthquakes in the northern Gulf of Suez, it can be considered as one of the active seismic zones (Dagett et al., 1986). The 15 collected focal solutions of earthquakes with $M_L \geq 3.5$ in the northern Gulf of Suez are shown in Fig. 21 (see Appendix A, Tables 9 and 10). These solutions are characterized by normal faulting mechanisms. The nodal planes have directions close to NW-SE to NNW-SSE. The rest of solutions exhibit either oblique or pure strike-slip motion. The sense of strike-slip component along the NW-SE trends were a subject of debate among previous studies. Garfunkel and Bartov (1977) and Chenet et al. (1985) supposed a left lateral movement while (Maamoun et al. 1980; Moustafa and Abd-Allah, 1992; Moustafa, 2002) assumed a right lateral movement.

The interaction of the northern tip of the Red Sea - Suez rift with the Mediterranean margin, suggests a high strength of oceanic lithosphere and the start of seafloor spreading south of the Arabian plate in the Gulf of Aden, Moustafa and Abd-Allah 1992; Moustafa and Khalil, 1994; Moustafa, 2002 attribute the northern termination of the Suez rift to the transfer of slip into the E-W faults pre-rift (Suez-Cairo faults) in the northeastern Desert. They also indicate an ending of the NNW-SSE faults along the western Sinai against the E-W themed fault.

3.5.e. South Gulf of Suez zone

The largest two significant earthquakes of Shadwan Island occurred on March 31, 1969 ($M_L = 6.7$) and June 28, 1972 ($M_L = 5.0$) along the southern part of the Suez Gulf. These solutions indicate normal faulting mechanisms with NW-SE with strike-slip mechanism. Moustafa 2001 have identified some structural trends with a left lateral strike-slip motion in the southern Gulf of Suez zone. The 29 collected focal solutions in the southern Gulf of Suez of $M_L \geq 3.5$ are shown in Fig. 22 (see Appendix A Tables 11 and 12). The majority of solutions indicates predominate NW-SE trending normal faulting with strike-slip. They reflect normal faulting mechanisms with some strike-slip component and their nodal planes trending parallel to the main trend of the Gulf of Suez.
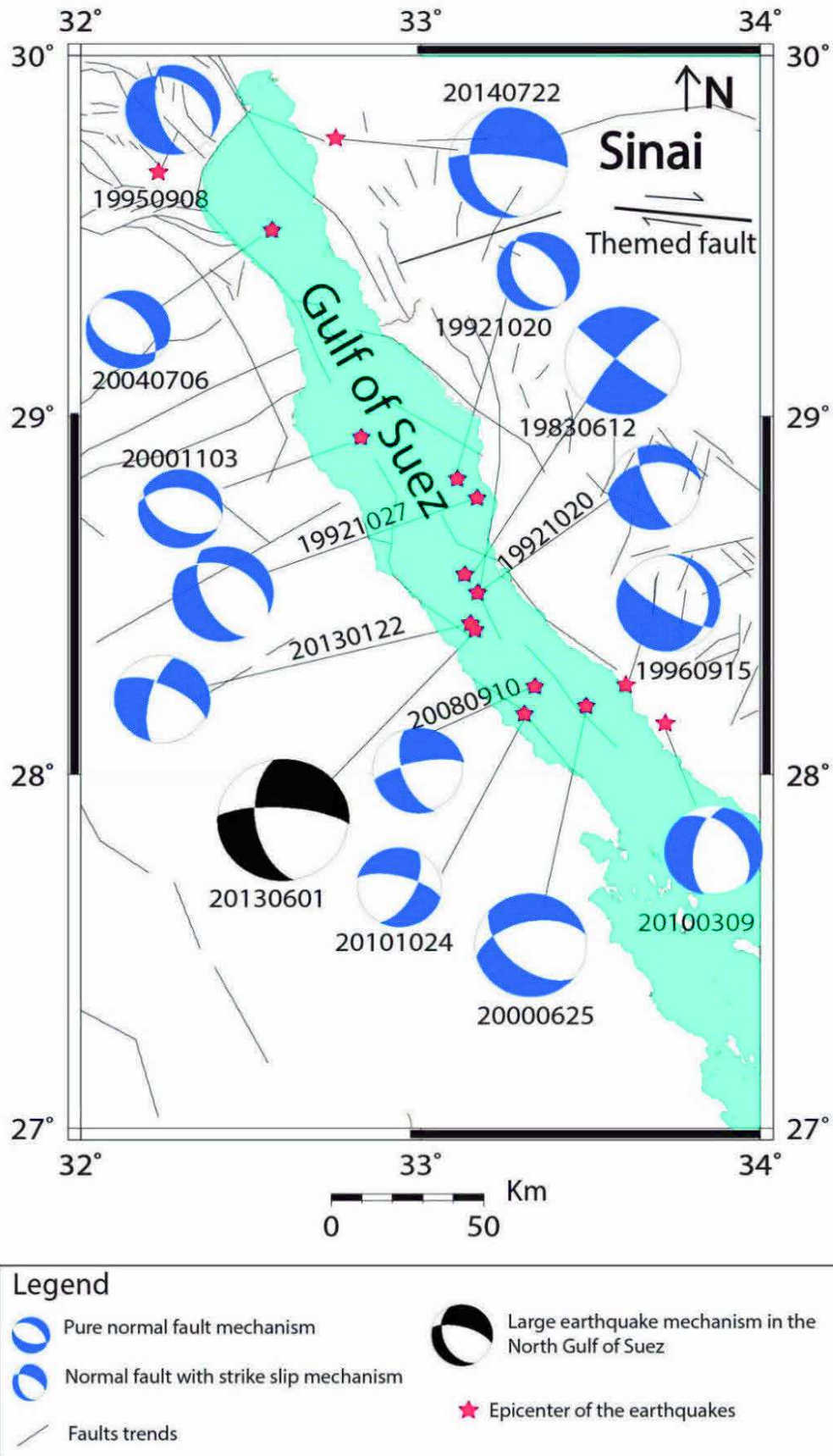
Fig. 21: Focal mechanisms of 15 earthquakes with $M_L \geq 3.5$ magnitude in the northern of Gulf of Suez (see reference Tables 9 and 10 in Appendix A for the focal mechanism solutions).
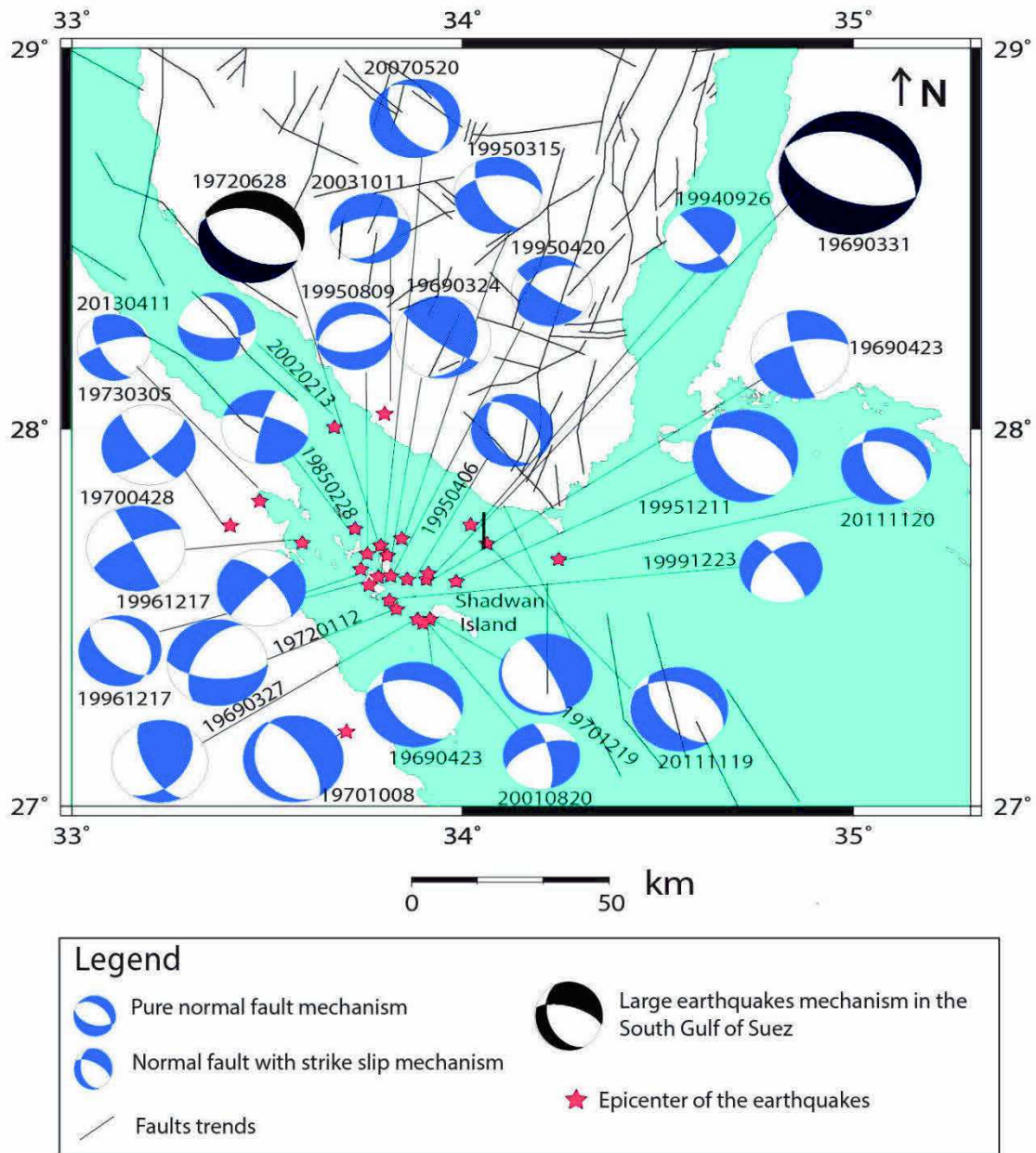
Fig. 22: Focal mechanisms of 29 earthquakes $M_L \geq 3.5$ magnitude in south Gulf of Suez (see reference Tables 11 and 12 in Appendix A for focal mechanism solution).

3.5.f. Gulf of Aqaba

The Gulf of Aqaba is a source region of intense activity which forms the main tectonic plate boundary between Africa (Sinai) and Arabia. The movement along this transform boundary caused some significant historical and instrumental earthquakes (Ambraseys, 2009). The largest recorded and strongest earthquake (Mw = 7.2; Hussein and Abu Elenean 2008) in this region is that of November 22, 1995.

The CMT-Harvard fault plane solutions of the November 22, 1995 large event give normal fault mechanism with a slight strike-slip component along the nodal planes trending NNE to N-S and NW. The NNE to N-S nodal planes show slight left lateral component appears to be consistent with the mechanisms of the two foreshocks of August 3, 1993: M_L = 6 at 12:43 and M_L = 5.7 at 16:33 respectively. These three large events are shown as black beach balls in Fig. 23 (see Appendix A Tables 7 and 8). These mechanisms are consistent with the extensional regime of rhomb-shape grabens within the Gulf, and with the NNE-SSW trend of the aftershocks of the August 1993 earthquake (Abdel-Fattah et al., 2007).

The epicenters of 36 focal solutions with ML ≥ 3.5 obtained from previous studies (see reference Table 8 in Appendix A for the focal mechanisms solutions) are shown in Fig. 23 and reveals the distribution of previous fault plane solutions in the Gulf of Aqaba. They reflect normal faulting with left-lateral strike-slip component or strike-slip fault with a minor normal component, while some events reflect a normal faulting mechanism.Most of the events show T-axes approximately in the ENE-WSW to E-W direction.
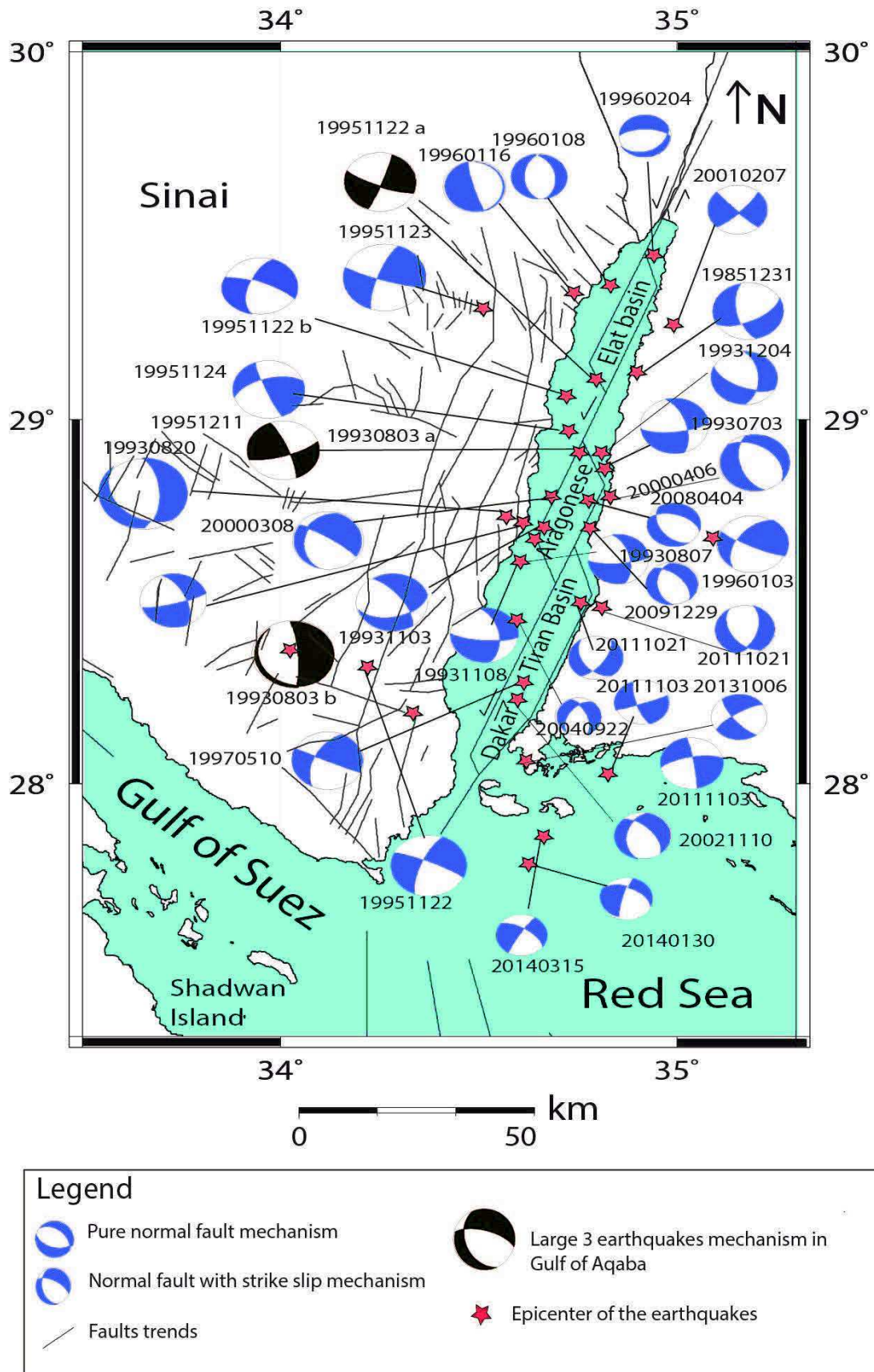
Fig. 23: Focal mechanisms of 36 earthquakes with $M_L \geq 3.5$ magnitudes in Gulf of Aqaba (see reference Table 8 in Appendix A for the focal mechanisms solutions)

3.6. Stress inversions

Many researchers have attempted to estimate regional stresses using a wide variety of direct inversion, iterative and grid search methods adapted for the reconstruction of past and present stresses from fault kinematics and/or earthquake focal mechanisms data e.g. (Angelier, 1984; Reches 1987; Vasseur et al., 1983; Gephart and Forsyth 1984; Carey-Gailhardis and Mercier, 1987).

In this study, the inversion method of Delvaux and Sperner,(2003) and Delvaux and Barth, (2010) is used for evaluating the stress field parameters in northern Egypt, using focal mechanisms of earthquakes collected from different sources as mentioned above. The inversion of fault-slip data gives the four parameters of the reduced stress tensor: the principal stress axes $\sigma 1$ (maximum compression); $\sigma 2$ (intermediate compression); $\sigma 3$ (minimum compression); and the Stress Ratio $R = (\sigma 2 - \sigma 3)/(\sigma 1 - \sigma 3)$. The two additional parameters of the full stress tensor are the ratio of extreme principal stress magnitudes ($\sigma 3/\sigma 1$) and the lithostatic load, however, these two parameters cannot be determined from fault data only.

We refer to Angelier (1989, 1991, 1994) for a detailed description of the principles and procedures of fault-slip analysis and paleo-stress reconstruction using focal mechanism data. In this work, we used the Stress Tensor inversion software, version 5.8.5 (Windows version; last updated on July 27, 2016. It allows us not only to obtain the first estimation of the principal stress axes orientations and also estimate the stress ratio R and stress regime index R' for the fault kinematics and to filter out the focal mechanisms that may not be compatible with the stress tensor. The angle between the calculated shear stress τ and the slip vector d is the fit angle α.

Thus, the corresponding misfit function to be minimized for each earthquake i is the misfit angle α:

$$F (i) = \alpha (i)$$

Within the WinTensor software, we process the data using the Right Dihedron method, a graphical method to determine the range of possible $\sigma 1$ and $\sigma 3$ orientations which are independent of the choice of the nodal plane (Angelier, 1984). The initial result is used as a starting point for iterative grid search "Rotational optimization" procedure using the misfit function F5 in the Tensor program.

In the following paragraphs, we will apply the stress inversions in the Egyptian continental margin and northern Egypt seismic zones (summarized in Table 3) using Stress Tensor inversion software (version 5.8.5).

3.6. a. The Egyptian continental margin (Zone A, trend A and B)

The Egyptian continental margin was classified into two types according to the mechanisms revealed from the earthquake data. The first group of mechanisms is represented by NW Oblique (normal–dextral) faults considered as Trend A and the second group of mechanisms is compressive represented by E-W to ENE (reverse–left-lateral) faults considered as Trend B.

Table 3: Parameters of the present day stress tensor deduced from focal mechanisms in this study.

Seismic zone	σ1		σ 2		σ 3		R	α°	α ° max	n/nt	R'	Shmax.°	Shmin°
	Az.	Pl.	Az.	Pl.	Az	Pl.							
Continental margin Zone A Trend A	74	168	13	313	09	45	0.79	18.4	33.4	14/18	0.67	136	39.2
Continental margin Zone A Trend B	10	67	04	336	79	255	0.12	6.1	20.8	8/16	2.12	79	165
Dahshour Zone B	67	125	23	292	05	24	0.83	18.3	22.4	24/34	0.69	114	N25E
Cairo- Suez Zone C	63	286	27	108	01	18	0.79	10.7	20.8	15/36	0.69	108	N18.7E
North Gulf of Suez Zone D	61	130	29	317	03	225	0.64	12	24.9	15/28	0.64	134	44
South Gulf of Suez Zone E	77	97	11	311	07	219	0.68	11	23.8	24/56	0.51	128	27.8
Gulf of Aqaba sub zone F	45	170	44	338	06	74	0.9	13.5	26.8	10/14	0.89	164	72.3
Gulf of Aqaba sub zone G	09	212	09	336	14	68	0.89	11.4	38.6	24/54	0.98	161	59.3

N=is the number of data explained by stress tensor
Nt the total population of fault solutions
α : mean slip deviation for all focal mechanisms used

R': stress regime index
Shmax. maximum shear
Shmin. minmum shear

shmin. minimum shear

The stress tensor inversion is applied to 10 focal mechanisms events from Trend A (Table 3, Fig. 24). The inversion in Trend A show normal faulting N39.2E with strike fault component including the Rosetta trend and extend to Qattara- EL Alamein trend and the value of stress regime index is 0.67. The data set of eight focal mechanisms events for Trend B (Table 3, Fig. 25). Trend B show compressive with shmax. = 79° by trending NE-SW reverse faulting and with stress regime index value = 2.12.

These data and results of Trend A and Trend B covered the stresses in the Rosetta trend and reveal the stress distribution from Alexandria to El Alamein margin.

The Tamash and Baltim trend in the continental margin is characterized by low-level seismicity data. There are two main Sh max orientations observed in oil wells above the Messinian evaporates in both trends. The stress orientation of the continental margin in the front of the Nile Delta observed from 11 wells (Tingay et al., 2011) indicates a dominate N-S to NE-SW Sh max orientation and a secondary E-W to NW-SE orientation observed in six wells in the central region. These trends are also observed in Fig. 32.
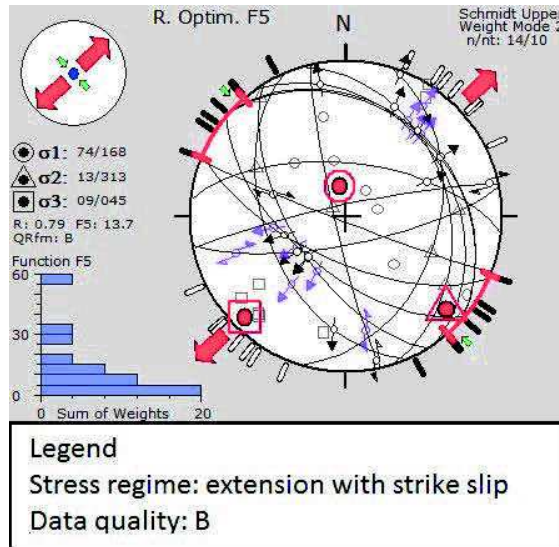
Fig. 24: Rotational optimization method of the present day stress tensor deduced from focal mechanisms data at continental margin Zone A, Trend A (see Table 3).
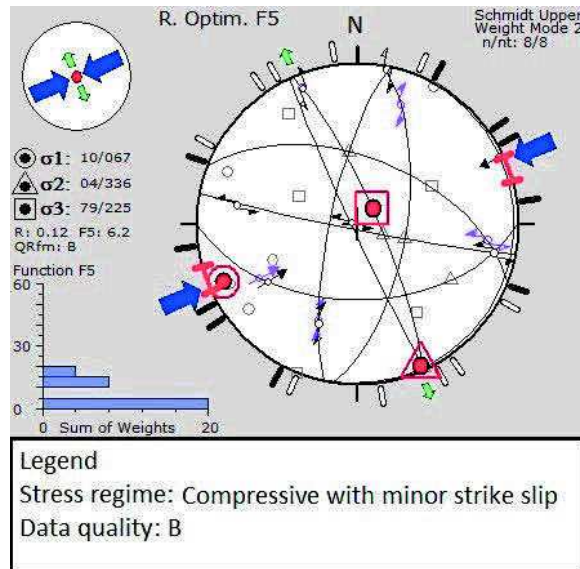
Fig. 25: Rotational optimization method of the present day stress tensor deduced from focal mechanisms data at continental margin Zone A, Trend B (see Table 3).

3.6.b. The Dahshour Zone (Zone B)

This zone acts as the source of the October 12, 1992 (Mw = 5.8) event, the most recent damaging earthquake in Egypt. This event provides key earthquake parameters for the study of active tectonics in the Dahshour area (Hussein, 1999). Two main fault trends WNW-ESE to E-W and NW-SE dominate in this area (Sehim et al., 1992; Mesherf 1990; Maaamoun et al., 1993). The stress tensor inversions were applied to 17 focal mechanisms of the Dahshour zone (Table 3, Fig. 26). The inversion of focal mechanisms in this zone yields an extensive stress regime characterized by E-W and WNW-SES trending faults with N25°E Sh-min. The stress regime index R' is 0.69, consistent with normal faulting mechanism with a strike -slip component. The rotational optimization of actual faults shows quality index A. These results agree with Hussein et al.(2013).

3.6. c. The Cairo Suez zone (Zone C)

The dominant structural trend in this zone consists of two main sets of faults oriented E-W and NW with the same age (Said, 1962). The stress tensor inversions are applied to 18 focal mechanisms events for Cairo-Suez zone (Table 3, Fig. 27). The inversion of focal mechanisms of the earthquakes in this zone yields a pure extensive stress regime characterized by E-W and WNW-SES trending faults with N18.7°E Sh-min. The stress regime index is R'=0.69, representing a normal fault with a strike-slip mechanism (extensional component). The Tensor solutions in this zone show quality index A.
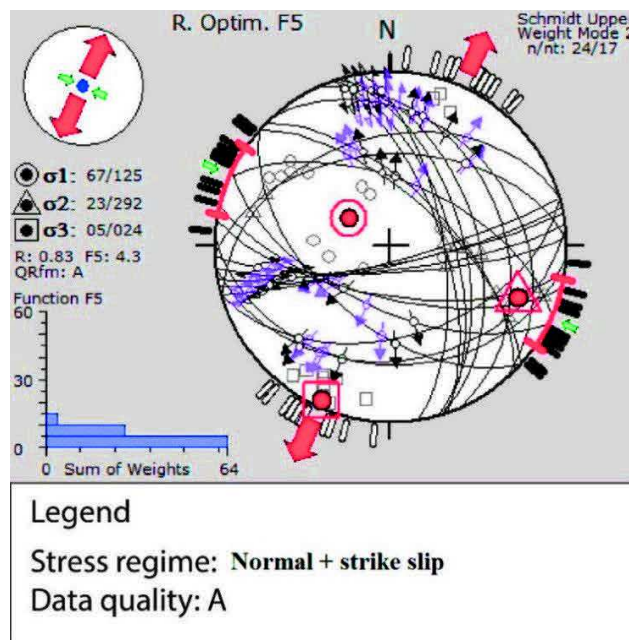
Fig. 26: Rotational optimization method of the present day stress tensor deduced from focal mechanisms data at Dahshour Zone Zone B (see Table 3).
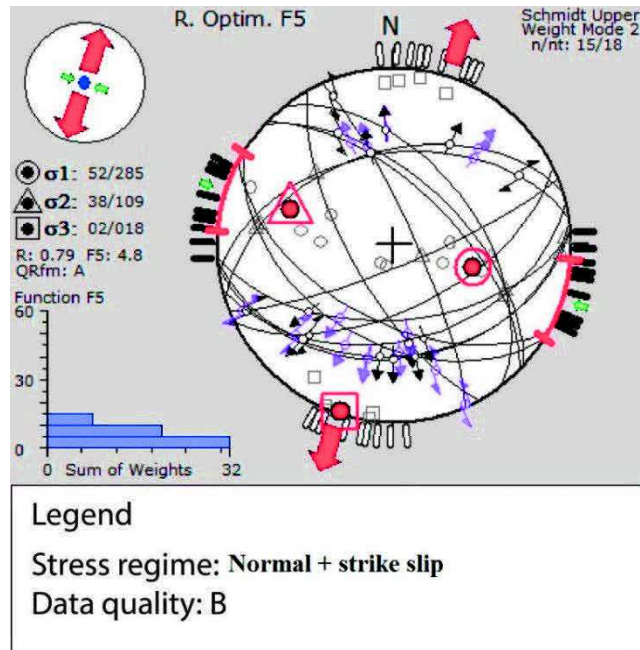
Fig.27: Rotational optimization method of the present day stress tensor deduced from focal mechanisms data at Cairo-Suez zone, Zone C (see Table 3).

3.6.d.Northern Gulf of Suez zone (Zone D)

The stress tensor inversions were applied to 14 focal mechanisms events for the northern Gulf of Suez (Table 3, Fig. 28). The inversion of focal mechanisms of earthquakes in this zone yields extensive stress regime characterized by NW-SE to NNW-SSE trending faults with N44ºE Sh-min. The stress regime index is R'=0.64, consistent with a normal faulting and extensional regime, where the rotational optimization of the actual faults show quality A stress tensor.
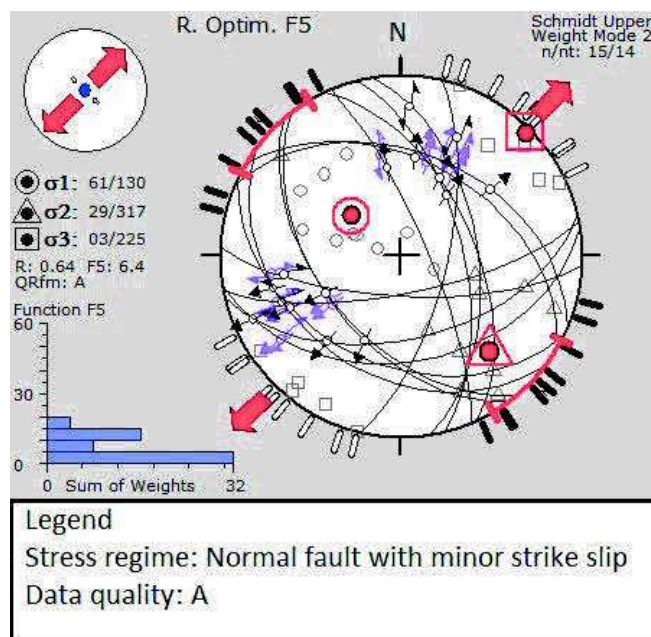
Fig. 28: Rotational optimization method of the present day stress tensor deduced from focal mechanisms data at Northern Gulf of Suez, Zone D (see Table 3).

3.6.e. South Gulf of Suez zone (Zone E)

The stress tensor inversions were applied to 28 focal mechanisms of the south of the Gulf of Suez zone (Table 3, Fig. 29). The inversion of focal mechanisms of earthquakes in this zone yields pure extensive stress regime characterized by NW-SE trending faults with N27.8ºE Sh-min. The stress regime index is R'=0.51, consistent with a pure extensional regime, where the rotational optimization of actual faults shows quality A stress tensor.
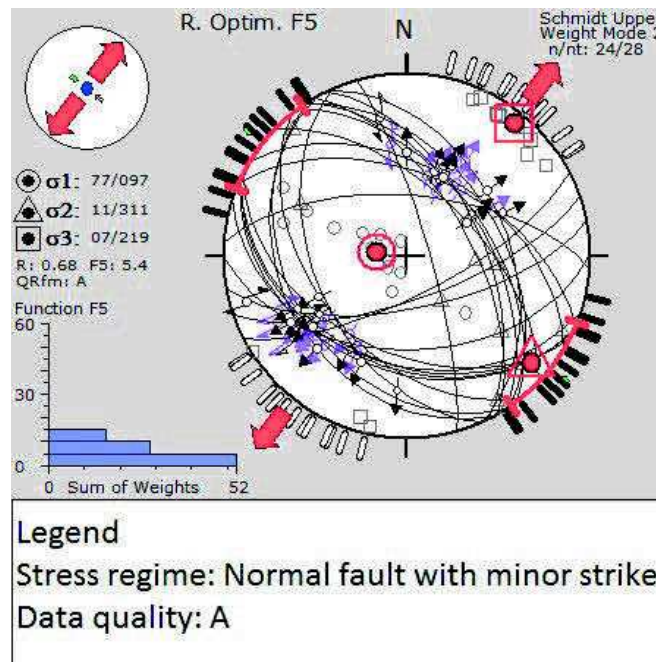
Fig. 29: Parameters of the present day stress tensor deduced from focal mechanisms data at Southern Gulf of Suez, Zone E (see Table 3).

3.5.5.e. Gulf of Aqaba subzone (subzone F)

The dominated structural trend in Gulf of Aqaba transform fault is a left-lateral strike slip movement with major normal component Garfunkel et al., (1981). The main structural trends of Gulf of Aqaba are N-S to NNE-SSW and NW-SE fault zone (Ben Avraham, 1985; Abdel Fattah et al., 1997).

The stress tensor inversions were applied to seven focal mechanisms events for the Gulf of Aqaba subzone F (Table 3, Fig. 30). This zone is located north of 29° latitude. The inversion of focal mechanisms in this zone yields an extensional regime, with the stress regime index equal to R'=0.89, N72.3ºE Sh-min and the rotational optimization of actual fault shows Tensor quality index A.

3.6. f. Gulf of Aqaba subzone (subzone G)

This subzone is located to the south of 29° latitude, where the stress tensor inversions are applied to 27 focal mechanisms of Gulf of Aqaba subzone G (Table 3, Fig.

31). The stress regime index is R'=0.98, with N59.3°E Shmin. The inversion of focal mechanisms of earthquakes in this zone yields a normal with a strike-slip regime with the noticeable extensional regime. The rotational optimization of actual fault shows quality B stress tensor.
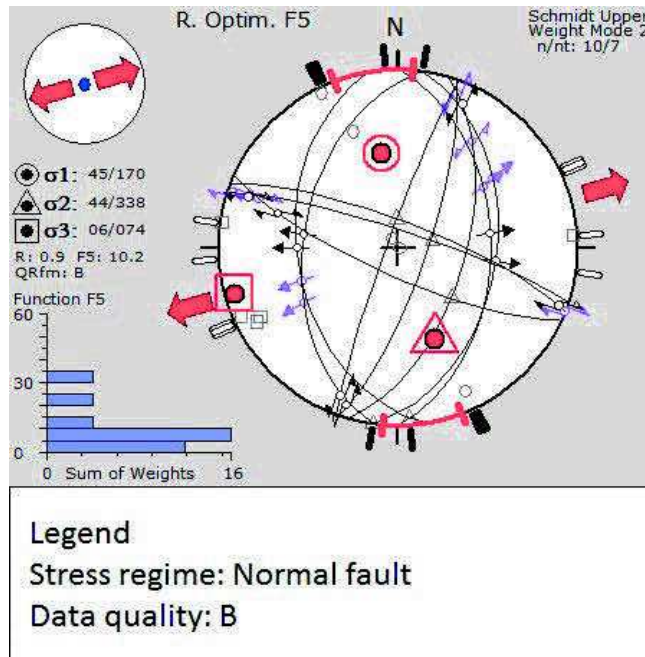
Fig. 30 : Parameters of the present day stress tensor deduced from focal mechanisms data at Gulf of Aqaba, subzone F (see Table 3).
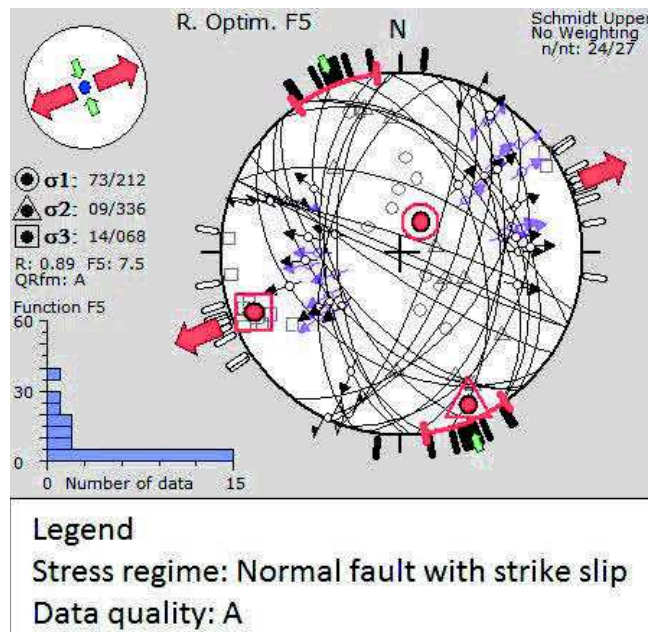
Fig. 31: Parameters of the present day stress tensor deduced from focal mechanisms data at Gulf of Aqaba, subzone G (see Table 3).

3.7. Stresses field pattern and GPS results

The present-day tectonics is related to the collision of the African and Eurasian plates, in some regions with the Arabian- Eurasian convergence and displacement of the Anatolian-Aegean sub-plate. The boundary between the African and the Anatolian-Aegean sub-plate is delineated by the Hellenic arc, the Pliny –Strabo trench, the Florence and Cyprus trench in the west (Aksu et al., 2005). The subduction zone between Nubia and Eurasia and activities along the Red Sea, Gulf of Suez and Gulf of Aqaba may control the surface deformation in the north-eastern corner of the African continent.

Furthermore, the boundary between the Arabian plate and the Anatolian plate is characterized by predominantly left-lateral strike-slip motion with contraction and convergence and possibly in some regions a small amount of extension (Mahmoud et al., 2013). These kinematic results explain the tectonic mechanisms linked with the present-day westward motion and counter-clockwise rotation of the Anatolian plate (Reilinger et al., 2006). The increasing rate of motion toward the Hellenic and Cyprus trenches, suggests to us that the primary forces responsible for the westward motion of Anatolia, and perhaps a counter-clockwise rotation of Arabia, are associated with slab rollback along the Hellenic and Cyprus trenches (Reilinger et al., 2006). Counter-clockwise rotation of the Arabian plate, with respect to the Anatolian block, may also be enhanced by slab pull from the NE-directed subduction beneath the Makran and possibly the south Zagros (Bellahsen et al., 2003). A direct corollary of this proposed dynamic hypothesis is that rifting in the Red Sea and the Gulf of Aden is a response to plate motions induced by the active subduction. This interpretation implies that continuing subduction of the African and Arabian oceanic lithosphere (i.e., Neotethys), is driving the plate motions and interplate deformation throughout the zone of interaction between the African, Arabian, and Eurasian plates.

Previous studies indicate the northward motion of northern Nubia with respect to Eurasia by about 5mm/yr (McClusky et al., 2000; Reilinger et al., 2006). Mahmoud et al.(2005) defined Sinai as a separate sub-plate "*sandwiched*" between the Arabian and African plates. Mohamoud et al.,(2005) suggested that Sinai sub-plate bounded by the Gulf of Aqaba–Dead Sea fault, Gulf of Suez and Cyprus Arc with a motion of 1.4 ± 08 mm/yr northward and 0.4±0.8mm/yr eastward relative to the stable Nubia plate. Saleh and Becker, (2015) used 16 permanent GPS stations in combination with 47 non-permanent stations covering Egypt for the period 2006–2012. Their GPS results show relative motion between Nubia and Eurasia of about 6.5±1 mm/yr which may increase toward the Hellenic trench, 8.2±0.8 mm/yr in Sinai Peninsula, 14.2±1.4 mm/yr in the north on the of the Arabian plate, and 22.3±0.7mm/yr in eastern and central Anatolia.

The main differences between Reilinger et al., 2006 and Saleh and Becker 2015 that the last estimated that the GPS results relative motion in Nubia was 6.5±1 mm/yr higher than estimated by Reilinger et al., 2006 which is 5 mm/yr. Also, Saleh and Becker 2015 estimated the motion of Sinai plate with 8.2±0.8 mm/year as separate motion from Nubia plate.

Recently, Pietrantonio et al., 2016 suggested that the Sinai moved in a counterclockwise rotation with respect to Africa plate fixed with tangential velocities of ~2 mm/yr. This proposed model predicts a small extension (from 0 to ~2 mm/yr moving from north to south) in the Gulf of Suez with left-lateral strike-slip motion along the Gulf margin of ~1 mm/yr. They estimated the strain rate field by velocity interpolation on a regular grid equal to rate of 40-50×10^{-9}/yr in the Sea, the Nile Delta region with the largest deformation along the Dead Sea Transform fault, where the shear prevails with strain rate values up to 90×10^{-9}/yr (Pietrantonio et al., 2016). The direction of the main strain rate axes is consistent with the direction of the Red Sea opening and with the left-lateral shear zone along the Dead Sea fault.

The stress results from this study in northern Egypt indicate that this tectonic domain is under an extensional stress regime. This stress regime is presently dominating in most of Egypt as normal with minor strike faults of extension trending N to NNE. The northern parts of Egypt have been extensively explored for hydrocarbons, particularly in the Gulf of Suez, Nile Delta (offshore and onshore), and the basins of western Desert. A small number of exploratory wells have also been drilled in the Red Sea and southern Nile Valley. Therefore, abundant material exists for the development of breakout and well-bore stress field studies. Bosworth and Taviani, (1996) analyzed sub-Miocene salt breakouts in wells from the southern Gulf of Suez and found a consistent N75°W orientation for SH (one small anomalous area was identified at ~27°45'N, 33°45'E). Badawy (2001) used additional wells and came to a similar conclusion with SH N70°W, although his analysis of earthquakes gave ENE-WSW SH with a fairly broad range of uncertainty. The breakout results are somewhat surprising, as they indicate a propensity for nearly N-S shallow crustal extension highly oblique to the axis of this rift. This is supported by the occurrence of several large recent earthquakes in the southern Gulf of Suez that showed normal movement and NNE-SSW striking T-axes. The breakout data from the southern Gulf of Suez suggest that the stress field of Central Africa Intra Plate (the CAIP) extends from Congo to Sudan to north most Egypt and Libya where the maximum horizontal stress is E-W and it is related to far effects of ridge in the Atlantic and Indian Ocean (Bathworth 2008). The stress regime of CAIP is a

mixture of strike-slip and thrust faulting in the south and strike-slip and normal faulting in the north.

Along the transition zone between the northern Egypt continental and oceanic crust, the stress field changed from a dominate tension to a prevailing compression linked to the N-S compression of the Mediterranean convergence zone as manifested in several studies (Abou Elenean and Hussein, 2007; Bathworth, 2008). The Egyptian continental margin is the zone of transition between the faulted continental crust that might be predetermined by its orientation to be reactivated with dextral strike-slip and reverse components (Sofratome, 1984). The Cyprian and Hellenic arcs are dominated by compression, whereas to the east of Cyprus, a left-lateral motion exists (Mahmoud et al., 2013). Bohnhoff et al. (2005) performed a stress tensor inversion in the subduction Hellenic trench which indicated a uniform N-NNE direction of relative plate motion between the Ionian Sea and Rhodes, resulting in orthogonal convergence in the western forearc and oblique (40-50°) subduction in the eastern forearc. There, the plate boundary migrates towards the SE, resulting in left-lateral strike-slip faulting that extends to onshore Eastern Crete. Normal faulting, trending N110°E, in the Aegean plate as back-arc structures are in agreement with this model (the along-arc extension is observed on Western Crete). The fault plane solutions of earthquakes within the dipping African lithosphere indicate that slab pull is the dominant force within the subduction process and is interpreted to be responsible for the roll-back of the Hellenic subduction zone.

Fig. 32 summarizes the stress distribution in northern Egypt and the Eastern Mediterranean region obtained from the stress inversions of this study. In addition to the stresses determined from the oilfield boreholes and the data of the World Stress Map (http://www.world-stress-map.org/) and the GPS velocity vectors after (Reilinger et al., 2006).
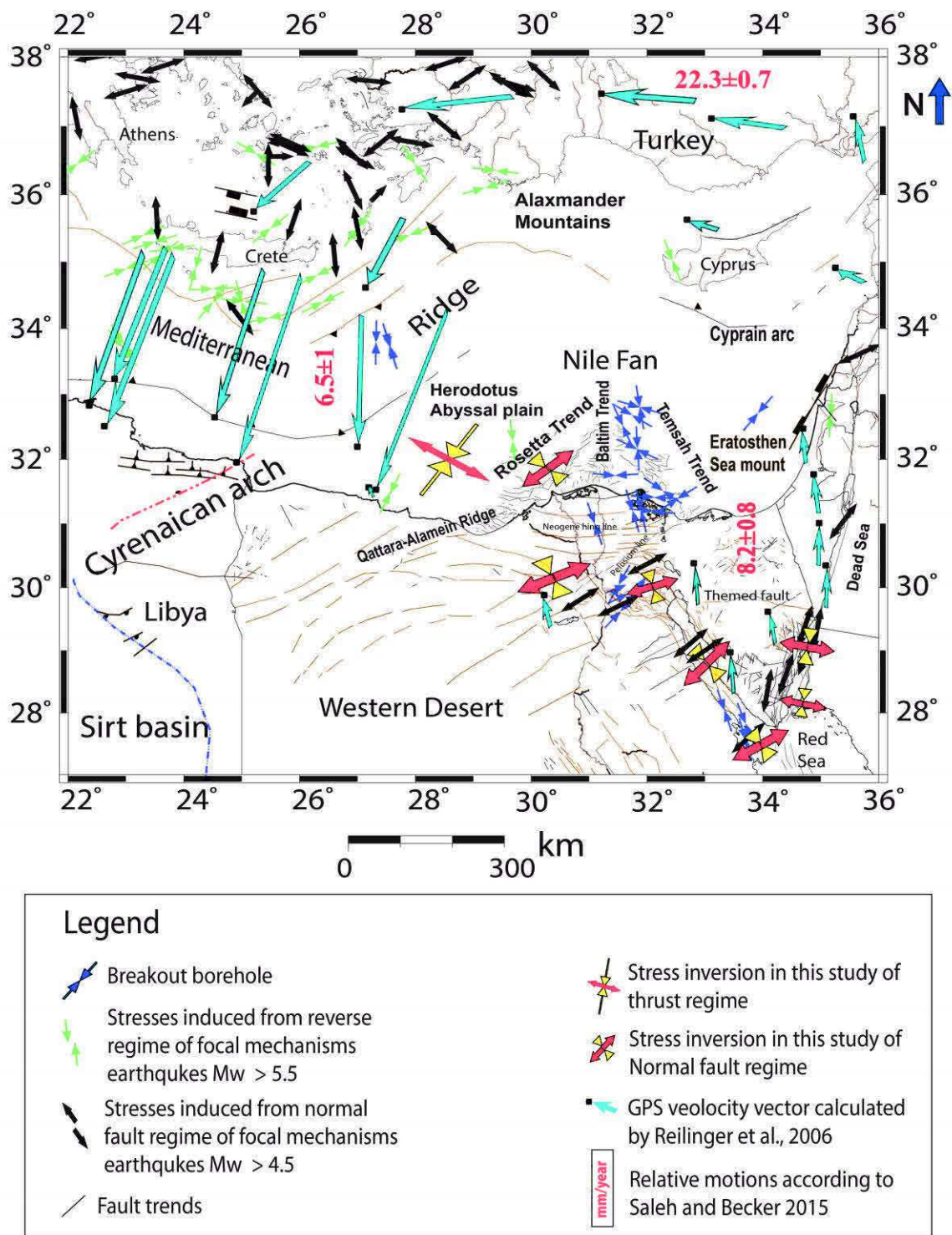
Fig. 32: Stress map of the North Egypt and Eastern Mediterranean region (this map is constructed based on data from the calculated stress inversion in this study, tensor and world stress data (http://www.world-stress-map.org/), Egyptian geological map (EMRA, 2008), Reilinger et al. 2006, Saleh and Becker, 2015).

Chapter IV
Paleotsunami records in Northern Egypt

4.1. Introduction

The seismotectonic study of the Eastern Mediterranean and northern Egypt presented in the previous chapter helps in the identification of the active seismic source of tsunami events through the study of historical and instrumental seismicity and related tectonic zones. The major source of large earthquakes with M≥8 in the Mediterranean region is the Hellenic subduction zone ; that can be divided into the Eastern and Western segments. Large shallow earthquakes associated with thrust faulting beneath the Hellenic trench can generate tsunamis in this area.

The largest magnitude reported in earthquake catalogues for the Hellenic Arc is Mw 8.3 – 8.5 and refers to the July 21, 365 earthquake(Stiros and Drakos, 2006; Shaw et al., 2008). The hypocenter of this earthquake was probably located offshore of western Crete, along with a major thrust fault parallel to the Western Hellenic trench. The earthquake generated a large coseismic uplift and tsunami that was very likely destructive along the western Crete coast and is known to have destroyed most of the harbours and the Nile Delta area along the Egyptian coastline (Stiros, 2001; Stiros and Papageorgiou, 2001; Dominey Howes, 2000; Papadopoulos et al., 2007). The second large paleotsunami event generated by an earthquake source in the Eastern segment of the Hellenic Arc area is that of August 8, 1303, event. The estimated magnitude of this earthquake is 8.0 (Papazachos, 1996). The Cyprian Arc is the third tsunamigenic source, which is the closest subduction zone to the Egyptian-Mediterranean coast but is smaller and less active than the Hellenic Arc. The largest magnitude reported in the earthquake catalogues for Cyprus is 7.5, from the May 11, 1222 earthquake.

The continental margin of Egypt is considered to have no potential for tsunamigenic earthquakes. Large earthquakes (with M>6) or landslides that produce local tsunamis also originate from time to time from the Egyptian coast, but no significant basin-wide tsunami is known to have originated from this region. Although M≥6.5 earthquakes such as the offshore Ms 6.7 Alexandria earthquake on September 12, 1955, have already occurred in the continental margin (Korrat et al., 2005). It was close to the sedimentary cone of the Nile that poses the potential for tsunamis (Garziglia et al. 2008).

In this Chapter, I will present the significant historical tsunamis that affected northern Egypt and the East Mediterranean region, the paleotsunami research study conducted along the Egyptian coastline by means of trenching and coring at EL Alamein

and Kefr Saber sites. The study includes the description of cores and trenching at both sites, the analysis and interpretation of geochemical and magnetic susceptibility measurements with the chronology of events using C^{14} dating of the coastal sedimentary layers.

4.2. Historical paleotsunamis of northern Egypt:

Large earthquakes caused most of the historical tsunamis in the Mediterranean region. Although, there is a low possibility of landslide tsunamis occurring offshore of the Nile Delta due to the high slope of the continental margin. Yalciner, (2014) estimated a landslide volume of 500 km^3, which may trigger a tsunami with wave height ranging from 0.4 to 4 m, that would affect major cities of the northern coast of Egypt (Alexandria, Damietta, Port Said). The recent example of landslide tsunamis in the Mediterranean was associated with the eruption of Stromboli volcanic, December 30, 2002 (Tinti et al. 2005).

The preserved historical documents and archives are the principal sources of macro seismic data for historical earthquakes and tsunamis. Since the beginning of the 20th century, much effort has been undertaken towards the establishment of a reliable catalogue of historical seismicity based on the retrieval and assessment of original sources of information e.g. (Poirier & Taher, 1980 ;Maamoun, 1984 ; Soloviev et al. 2000 ;Ambraseys, 2009 ;Guidoboni, 2009).

Guidoboni (1994) and Ambraseys (2009) report several large earthquakes with tsunamis that caused damage in the eastern Mediterranean region and in particular in the coastal metropolises of Egypt (Table 4). Among these events, the tsunamis of 21 July 365, 8 August 1303 and 24 June 1870, local and contemporaneous reports describe wave heights with inundations and severe damage to the city of Alexandria as well as the Mediterranean coast of Greece, Sicily, Libya, Cyprus, Syria, Lebanon and Palestine. The three events were most likely triggered by major earthquakes in the Hellenic subduction zone (Papadopoulos et al., 2014).

Table 4: Historical earthquakes and tsunamis effect on the north Egyptian coast

Date	Epicentre	Estimated Mag.	Comment	Reference
~1410 B.C.	Santorini volcanic eruption	-	Inundation in Alexandria	Cita et al. (1996)
21 July 365	Western Crete	Mw 8.3 – 8.5	Tsunami northern Egypt	Stiros and Drakos, (2006); Shaw et al. (2008)
18 January 746	Dead Sea Fault	7.5	Tsunami eastern Mediterranean	Sieberg, (1932) Ambraseys, (1962)
881 - 882	Palestine	?	Tsunami in Alexandria & Palestine	Galanopoulos A., (1957)
4 January 1033	Jordan Valley Fault	7.4	Tsunami northern Egypt	Ambraseys, (1962)
18 January 1068	Northern Lebanon	6.9	Waves in northern Egypt	Ambraseys, (1962), Soloviev et al.(2000)
8 August 1303	Rhodos	8	>8-m	Abu al-Fida (1329), Ambraseys (2009) Hamouda (2006)
24 June 1870	Hellenic Arc	ML 7.2	Inundation in Alexandria harbour	Ben-Menahem (1979) ; Soloviev et al. (2000)

The following is a short description of the three most significant tsunamis triggered by large earthquakes that affected northern Egypt :

a-The 365 tsunamigenic event

Historian Ammianus Marcellinus in Guidoboni et al., (1994) a Roman historian who lived in the fourth century (325–391 AD), reported the tsunami event 13 years after in 378 AD. He documented the devastating effects of the tsunami hitting Alexandria with comments such as "*The solidity of the earth was made to shake…and the sea was driven away*", "*The waters returning when least expected killed many thousands by drowning*", "*huge ships… perched on the roofs of houses… hurled miles from the shore…*''. Other settlements around the Mediterranean were hit at roughly the same time.

Reports indicate that ships in the harbour of Alexandria were overturned as the water near the coast receded suddenly and that many people rushed out to loot the hapless ships. The tsunami wave then rushed in and carried the ships over the sea walls, landing many on

top of buildings. In Alexandria, approximately 5,000 people lost their lives and 50,000 homes were destroyed. The surrounding villages and towns suffered even greater destruction and many were virtually wiped off the map. Outside the city, 45,000 people were killed. In addition, the inundation of salt water rendered farmland useless for years to come. Slowly, but steadily, the buildings of Alexandria's Royal Quarter were overtaken by the sea following the tsunami. It was not until 1995 that archaeologists discovered the ruins of the old city off the coast of present-day Alexandria.

A review of historical accounts (Hamouda 2002 ; Ambraseys, 2009) of a notable earthquake, such as that of 21 July AD 365 indicates that this event destroyed nearly all towns in Crete and was followed by a tsunami, which had devastating effects on coastal areas of the eastern Mediterranean.

The study of paleo-shorelines that fringes the coast of western Crete and Antikythera, first described by Captain Spratt RN in 1851, who noted many 'sea marks' up to 10m above present sea level in southwest Crete. Because these marks run through the remains of a Roman harbour at Phalasarna at 6m above sea level, he deduced that the land must have been raised during or after the Roman era. Pirazzoli et al. (1992) showed that this shoreline that extends in all western Crete had a C^{14} age of around 2,000 yr BP and attributed its uplift to an earthquake; this earthquake was subsequently linked to the AD 365 event. Pirazzoli et al. (1992) also indicate the existence of small subsidence events in between large uplifts.

Shaw et al., (2008), using radiocarbon dates, refer to the uplift of western Crete in AD 365 but with an age uncertainty. The field observations also show slow uplift during short intervals in a series of rapid small events. The authors inferred that either uplift of western Crete and its surrounding sea floor took place slowly within a few decades of AD 365 and some other event caused the tsunami that destroyed Alexandria in AD 365, or the two events are connected. Shaw et al., (2008) also model the tsunami wave propagation across the eastern Mediterranean and infer the occurrence of 0.6 m wave heights reaching the Egyptian coast.

b-The 1303 tsunamigenic event

On 8 August 1303, a major earthquake with magnitude ~Mw 8 occurred in between Crete and Rhodos islands and generated a tsunami that greatly damaged the coastal cities of eastern Mediterranean, in particular, the cities of Candia and Heraklion (Crete), and Alexandria with the Nile delta was flooded (Ambraseys, 2009 ; Papadopoulos et al., 2014). In Greece, it resulted in destruction in the islands of Rhodos, Crete and the Peloponnesus.

According to detailed contemporaneous reports, many houses were damaged in Cairo and northern Egypt, ships were torn apart and many of them were carried inland due to tsunami waves (the detailed description of this earthquake and its effect in Egypt is in the contemporaneous Arabic source of Abu-El Fida born 1273 – died 1331 (1329)).In Alexandria, the sea spilt over into the harbour, inundating the shore, carrying sailing ships and boats onto the land and with the fall of Alexandria lighthouse. Houses were ruined and 70 m of the city wall together with 27 towers were destroyed. However, Abu-El Fida report that the worst damage was caused by the combination of the earthquake, the sea and high winds, which drove ships onto the coast and demolished part of the ramparts, killing 46 people.

c- The 24 June 1870 tsunamigenic event:

A large earthquake was felt throughout the eastern Mediterranean followed by tsunami waves on Alexandria. It is reported that the location of this earthquake is probably either the Eastern Hellenic arc (i.e., the same location as of 8 August 1303 earthquake) or the May 11, 1222 earthquake in the Cyprian Arc. In Alexandria, three successive shocks were felt with no earthquake damage. Everyone along the coast of Nile Delta felt the earthquake and it was reported from Port Said to Suez Canal. In the new Port area, the sea flooded the quay and the shock was felt on board ships in both the old and new ports.

The strong shocks were felt in the sea and in the port where ships also underwent severe shocks. The three shocks lasted for about 5s each were also felt in Ismailia at 18 h 25m, but they were very strong. The three shocks also occurred in Cairo at approximately 18 h 30 m. The water in the new port of Alexandria splashed out onto the quays.

4.3. Paleotsunami investigations

The paleotsunami investigations are classified into fieldwork and laboratory analysis. Three successive field campaigns were carried out in June 2014, August 2015, and October 2015. The aim of these field investigations was to choose the best locations that triggered tsunami deposits from geological and geomorphological evidence.

The work was carried out by trenching and coring in the two selected sites of Kefr Saber (Marsah Matrouh) and El Alamein (Fig. 33) and the sampling collection includes charcoal, gastropods, shells, roots samples in trenches and cores. In the laboratory, different core analyses were undertaken including collecting samples for dating after opening the cores, photography, detail stratigraphic descriptions, X-ray scanning, geochemical analysis, Magnetic susceptibility (methods are described in detail in Chapter II).
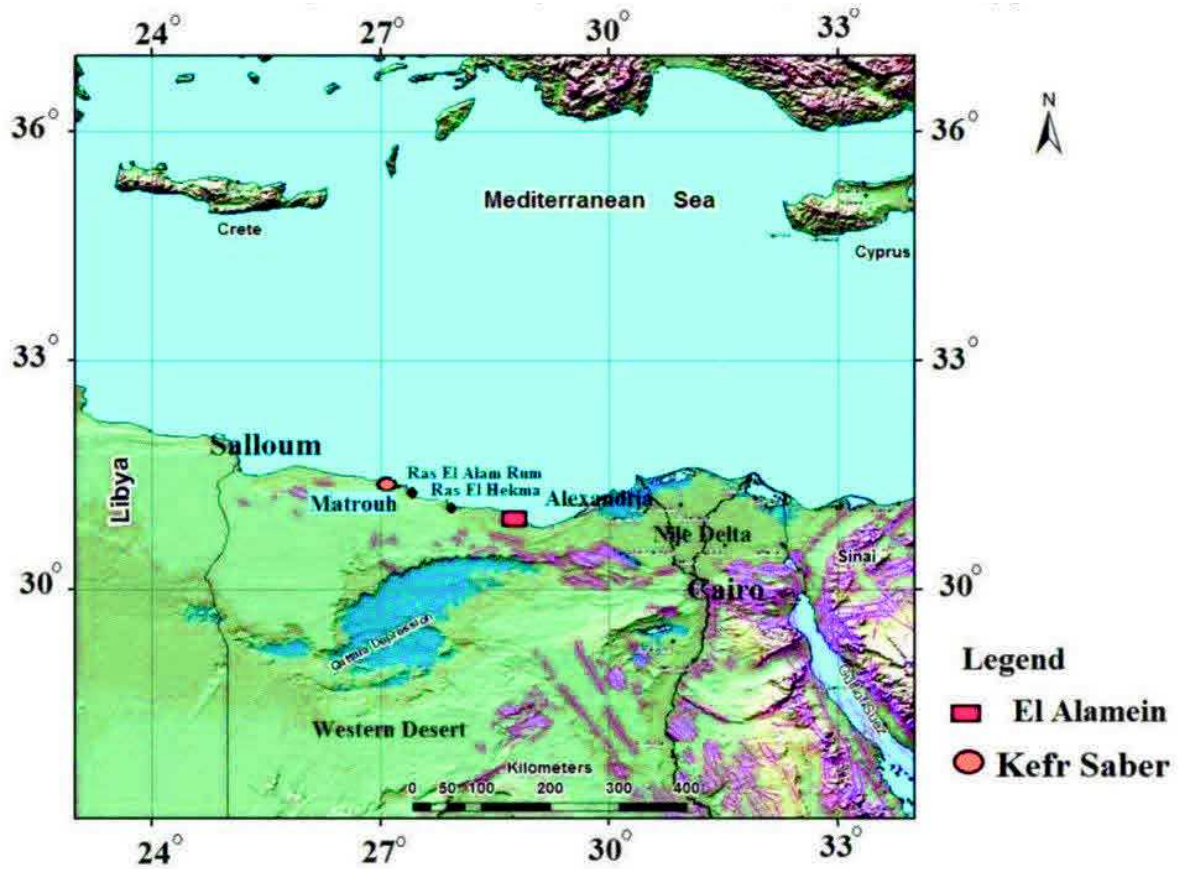
Fig. 33: The location map of the studied areas in northern Egypt.

The following briefly describes the geomorphology features in the studied area including the chosen investigation of two sites according to some geomorphologic paleo-tsunami evidence and my field steps including coring and trenching and the laboratory measurements and the core and trenching description :

4.3. a. Geomorphology features of the studied areas

From the structural geology and tectonic point of view, these areas are selected according to the reasons developed in previous chapters and mainly on the seismotectonic setting in northern Egypt and location of major tsunami sources. The two selected sites are located along the Mediterranean coast and in the northwestern part of the Western Desert, which consists mainly of a thin blanket of Miocene rocks forming a vast persistent limestone plateau (Fig. 34). It extends from the western side of the Nile valley and delta in the east to El-Salloum in the west and the Mediterranean coastal plain in the north to the Qattara and Siwa depression in the south (El-Bastwasy, 2008). This area is affected structurally by E-W to WNW-ESE trending faults associated with the Qattara – Alamein ridge and in the north with the NW-SE trending El Alamein faults.

The geomorphology and surface geology of the study areas is essentially dominated by sedimentary rocks of Tertiary and Quaternary ages. The Quaternary is exposed in coastal

plains, lagoons, wadis and raised beaches. The Pliocene and Miocene of the Tertiary are exposed, for its major part, in the coastal platforms and tableland, with the Miocene limestone forming the surface beds of the tableland. The geological units are characterized by the presence of Tertiary Miocene, mainly composed of limestone and sandstone reaching the shoreline in several areas. The coastal zone and related Miocene plateau are covered by Quaternary deposits. These deposits are mainly represented by the Holocene units of coastal sand dunes, lagoonal and alluvial deposits and the Pleistocene oolitic limestone ridges and old lagoonal deposits. The Quaternary carbonate ridges in the present area are cemented into moderately hard limestone, except for the coastal ridge which is mostly less cemented Zahran, (2008).

The area includes a narrow coastal plain, followed by sand dunes in some areas to the south. South of the dunes, the plain rises gradually until the altitude of the plateau reaches 50 to 250 meters above sea level. The coastal plain stretches in a generally east-west direction, bounded by the sea to the north and a pediment plain to the south. Controlled by the geologic formations, the pediment plain width varies from some meters to about 10 km. This plain mainly consists of alluvial fans, descending from the plateau, rivers (wadis) extensions, rocky plains, salt lagoons (sabkhas), sand sheets and sand dunes. Besides the aeolian sediments, other sediments were transported to form alluvial fans and floodplains, and the subsoil layers are formed locally from marine limestone (El-Bastwasy, 2008). The area is characterized by rich archaeological remains such as Ramses II (1303 – 1213 BC) temple ~20 km west of Marsa-Matrouh city.

The first field investigations were carried out in June 2014 along the north coast of Egypt from Alexandria to Salloum border coast.

Several criteria were applied to select the sites, taking into account geomorphological and topographic setting, accessibility in order to avoid urbanization and artificial soil reworking. The criteria are 1) the presence of large boulders; 2) sand dunes; and 3) Lagoons environment and salt marshes. Two sites, 160 km apart, met the selection criteria for site investigation: 1) Kefr Saber, and 2) El Alamein site (Fig.33).
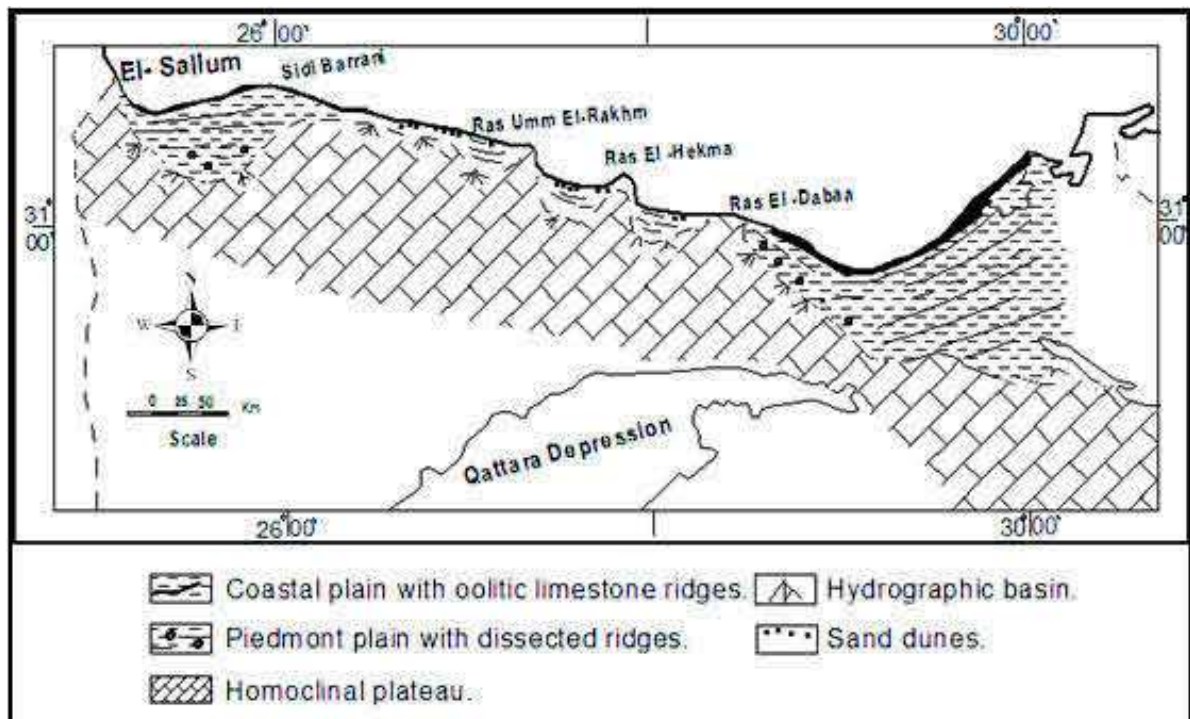
Fig. 34: The location and geomorphology landforms map in the studied area after Raslan (1995).

The geomorphology of the area characterized by geomorphologic features include the following :

a- Coastal dunes

The coastal dunes (Fig. 34, 35) are found close to the beach within synclinal areas; they are well developed and recent ridges extended parallel to the present beaches. They are composed of loose white oolitic carbonate sands washed from the degradation of oolitic coastal ridges, almost the foreshore dunes are impeded by plants.The frontal dunes generally extend as ridges parallel to the shoreline

b- Large boulders

The accumulation of large boulders (Figs. 36 and 37) noticed in this study have a N-S trend near the shoreline of large width along the Egyptian coast. These large boulders are related to probable tsunami origin from the Mediterranean.This accumlation of boulders are noticed and studied by (Dalal et al., 2013; Shaha-Hosseini et al., 2016)

Shaha-Hosseini et al., (2016) studied the accumulation of boulders between Alexandria and Mersa Matrouh along the Egyptian coast. They concluded that these boulders were transported by a tsunami wave 2.6 m height or by storm waves about 10 m height. Their C^{14} dating of Dendropoma in boulders was compared with 8 August 1303 AD tsunami.

Fig. 35: Sand dunes along Mediterranean coast west Mersa Matrouh.

We have noticed that accumulation of boulders in the (Ras El Hekma –Ras ELAlam Rum –Mersa Matrouh - East Mersa Matrouh (Kefr Saber) during the fieldwork, however, it was not possible to conduct detailed work during my study. These boulders reflect the force of the waves responsible for transferring large blocks in the direction of the coast. Two samples of Dendropoma species in the boulders were chosen in this study for dating in Kefr Saber and Ras El Hekma (Table 1 in Appendix E).

Fig. 36: Large boulders in Kefr Saber.

Fig. 37: Large boulders in Ras EL Hekma.

c-Salt Marshes and lagoons

Salt marshes and lagoons are found between dissected ridges with a lower elevation below sea level than West Matrouh are formed due to surface erosion by drainage lines. Many lagoons and sabkhas are distributed along the North Western Coast at El Dabaa and Ras El Hekma. This surface is mostly covered with carbonate dunes (Fig. 38).

Fig. 38: Show lagoons behind the sand dunes.

4.3.b. Cores and trenching

Coring and trenching act as effective tools which allow us to recognise paleo-tsunami deposits and landforms, e.g. (De Martini et al., 2012 and Malik et al., 2015). In this study, trenching and cores were undertaken within the two selected studied areas along the

northern coast of Egypt in Kefr Saber and EL Alamein sites. This was done in order to study the sedimentary succession and to identify the possible tsunami deposits and correlate them with historical tsunamis records.

Trenches, ~2 x 1 m and ~1.5 m deep, were dug in both selected sites. The underground water infiltration was treated using a water pump (Fig. 39).The cores (Fig. 40 and Fig. 41) were collected in both sites using a Cobra digging instrument. The tube's has a diameter of 2 inches and 1m long. The cores were taken up to depths of 2.6 m.

Fig. 39: Pumping machine to discharge the underground water.

Fig. 40: Photo core dug using Cobra instrument.

Fig. 41: The end of core tube.

4.3.c. Laboratory analysis

The cores were then opened (Fig. 42) with a Fisher wire in the Laboratory of the National Institute of Geophysics and Astronomy (NRIAG), then labelled. The first half of the cores have been named and archived, while the other part was used for measurements and sampling.

X-ray radiographs were carried out on cores using medical X-ray scan laboratory before they were opened to identify the details of sediments and microfossils. Very intensive

X-ray was used in order to penetrate the sediments to show the details in sediments. Three 40 cm-long x-ray pictures were taken for each 1 m long core with an overlap of least 5 cm.

The cores and trenches were described according to their length, colour, texture (grain-size, sorting), sedimentary structures (natural or due to coring disturbances), type of sedimentary contacts (sharp or gradient). The cores and trenches were then photographed using DSLR (Digital Single-Lens Reflex camera) in 25 cm long sections, with an overlap of at least 2 cm. These pictures were assembled together to reconstruct a single image for each core section.

A number of different measurements were taken from the cores (Fig. 43); the magnetic susceptibility was measured with 3 cm intervals along the cores using a Bartington MS-2 system. Samples with a dimension of 2 cm long were collected every 15 cm for bulk mineralogy, grain size, total organic and inorganic analysis which was carried out at the laboratory of a central metallurgical research institute (CMRDI) in Helwan.

Fig. 42: The preparation of core.
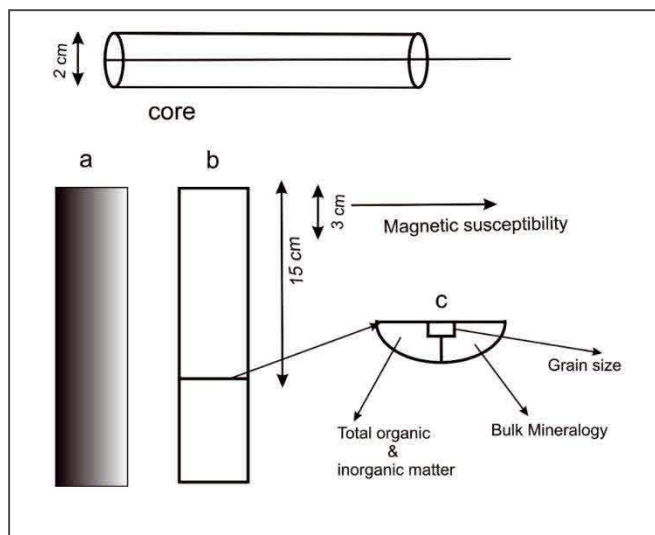
Fig. 43: Sampling sketch of the split cores: a) the archive core part; b) the working core part; and c) the measurement analysis each 2cm slices divided into 3 small part.

The radiocarbon dating of samples was carried out in three laboratories (Poznan laboratory - Poland, CIRAM in Bordeaux, France and Beta Analytical Laboratory, USA) to ensure consistent and high quality results (Table 1 and 2 in Appendix E). The collected samples were made of charcoal, bones, gastropods, shells and organic matter. The radiocarbon dating results of charcoal and organic matter were calibrated using a recent calibration curve (Reimer et al., 2013) and Oxcal software for the probability density function of each sample age with 2σ uncertainty (Bronk-Ramsay, 2009); furthermore, the gastropods and shells were corrected against reservoir effects.

4.3.d. Trenching and coring description in the investigated sites

In the following, a description for trenching and coring in the two selected areas of Kefr Saber and El Alamein is presented, with the analysis procedures and interpretation performed along the northern coast of Egypt.

i. Kefr Saber site

This site is located ~32km west of Marsa-Matruh city in an area characterized by a lagoon depression protected from the sea by 2 to 20 m high sand dunes (Figs. 44 a, b and c). The area also shows big rocky boulders rich in Dendropoma along the nearby shoreline that testify for past tsunami deposits. Five trenches dug in June 2014 (Fig. 44 c). The trenches were dug perpendicular to the E-W trending coast in a dry lagoon.

The sizes of trenches are ~2 x 1 m and ~1.5m deep. The trenches dug to figure out the deposits and find the geological evidence for the tsunami deposits. The detailed description and photography were done in the field (see Figs. 45, 46, 47, 48 and 49).
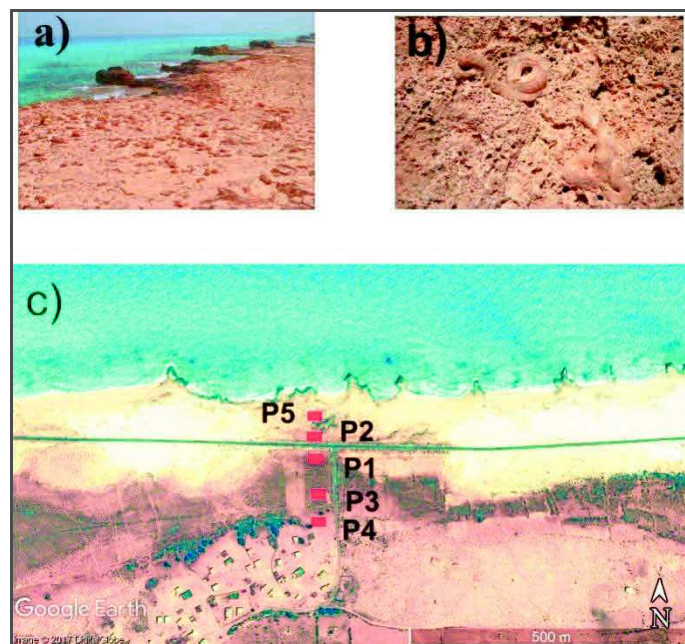
Fig. 44: a) Coastal zone at Kefr Saber rich in boulders, b)Dendropoma fossils rich in the boulders, and c)the location of the five trenches P1 to P5 at Kefr Saber.

The five trenches dug in Kefr Saber (Fig. 44c) were numbered according to the time they were dug. The following is the description of tsunami layers found in trenches located in Fig. 44 c:

Trench no.1

Located 152 m from the shoreline, this trench shows a succession of soft sedimentary layers made of sandy-silt, sandy-clay and fine gravel layers. A layer of mixed sand and gravel, and broken shells (Fig. 45) is found at 35 cm depth, but with a variable thickness from 2 to 10 cm in trench walls. This layer is characterized by rich broken shell fragments and is interpreted as of tsunami origin. Two samples of charcoal are chosen in Trench 1 at Kefr Saber for dating (Table 1 in Appendix E). The first is of modern age at 35 cm depth. The other charcoal sample is at 53 cm depth and aged between 39000-38250 BC. This sample is found below the stratigraphic tsunami layer. This sample is transported from deepest sediments due to the high wave current tsunami.
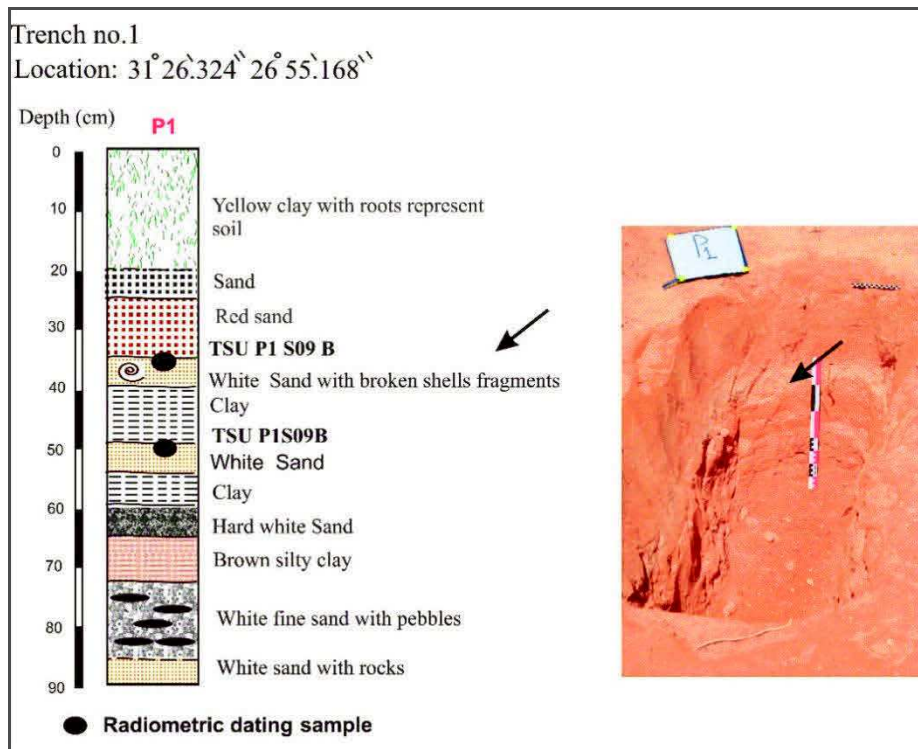
Fig. 45: Description of trench no.1.The arrow reflects tsunami layer 1 which is rich in broken shell fragments.

Trench no. 2

It is located at ~100 m distance from the shoreline. Three phases of flooding with pebble and gravel deposits at 25, 40 and 100 cm depth were found on trench walls. The reasons for the presence of the boulders may be related to tsunami or storm flooding. The trench is closer to the shoreline with respect to Trench 1. The same layer at Trench 1of

mixed sand and gravel and broken shells continued in Trench 2. It was found at 24 cm with a 16 cm thick layer of white sandy reworked and broken shell fragments (Fig. 46).

Trench no.3

It is located at 177 m from the shoreline. The same layer at Trench 1of mixed sand and gravel and broken shells extend into Trench 2 and Trench 3. It occurred at a depth of 44 cm (Fig. 47) in Trench 3 with a 6 cm thick layer of highly reworked fossils and broken shell fragments. The bottom of this trench is also characterized by white sand mixed with clay and marine sea water.

Two charcoal samples are chosen at depths 73 and 100 cm in Trench 3 at Kefr Saber for dating. The first charcoal sample is at 73 cm depth and has a date of 50-70 AD. This sample is below the tsunami layer 1 (Table 1 in Appendix E). The other charcoal sample is at 100 cm depth and has a date of 5300-5070 BC. This sample is transported from deepest sediments due to the high wave current tsunami.
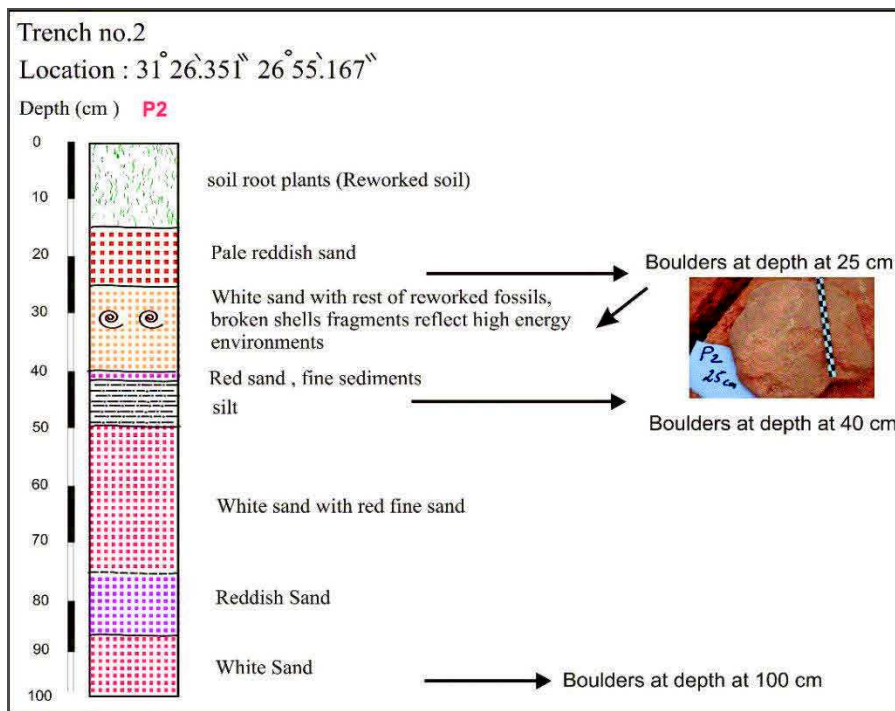
Fig. 46: Description of trench no.2.The arrow reflects tsunami layer 1 which is rich in broken shell fragments.
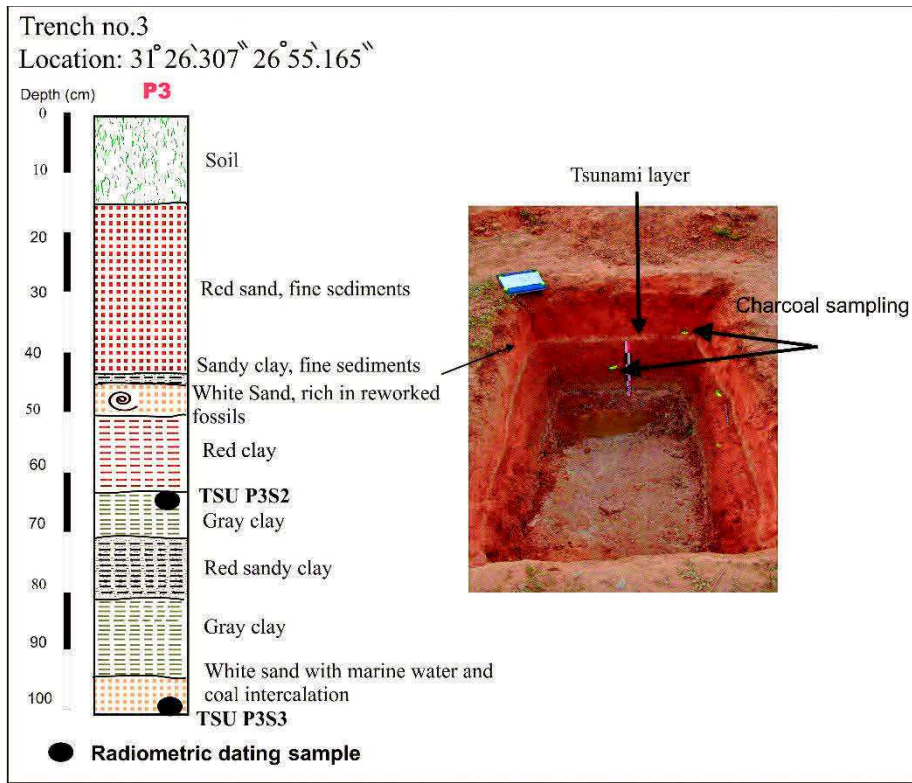
Fig. 47: Description of trench no.3.The arrow reflects tsunami layer 1 which is rich in broken shells fragments.

Trench no.4

This trench is located at 210 m from the shoreline. The same layer at Trench 1 of mixed sand and gravel mixed with broken extends into Trench 2, Trench 3 and Trench 4. This layer is found at 55 cm depth in Trench 4 (Fig. 48) with lateral variation from 1 to 5 cm in thickness and is characterized by reworked shells and gastropods.

Five charcoal samples are chosen for dating in Trench 4. The first sample is at 15 cm depth and is from the modern age. The second sample is at 20 cm depth and has a date of 1700- 1920 AD. The charcoal at 40 and 61 cm depth have a modern age and may be transported from shallow to deep depth due to a contamination of farming in this area. The last charcoal sample is at 60 cm depth and has a calibrated age of 17200- 15900 BC (Table 1 in Appendix E). These samples are located within the tsunami deposits in Trench 4 and are transported from deepest sediments of high energy current waves during the tsunami of 21 July 365.

Trench no.5

This trench is located at 72 m from the shoreline is the closest to the sea (Fig. 44 c). The mixed white sand with reworked fossils reached the maximum thickness near the shoreline and is found at a depth of 22 cm (Fig. 49). Two phases of boulder accumulation were found at depths of 25 and 40 cm. The first phase of the boulders has an angular surface, while the second phase of boulders and pebbles is more elliptical and smoothed.

Four charcoal samples are chosen for dating in Trench 5 (Table 1 in Appendix E). The first charcoal is found at 12 cm depth and has an age of 360-50 BC for the transported sediments. The second sample is found at 17 cm depth with and age 30- 180 AD. The third and fourth charcoal samples are found at depths of 33 and 37 cm and have calibrated dates of 350-1050 BC and 2400-4000BC, respectively. These last two samples, found in the thicker tsunami layer in Trench 5, resulted from transport due to high energy currents during tsunami waves.
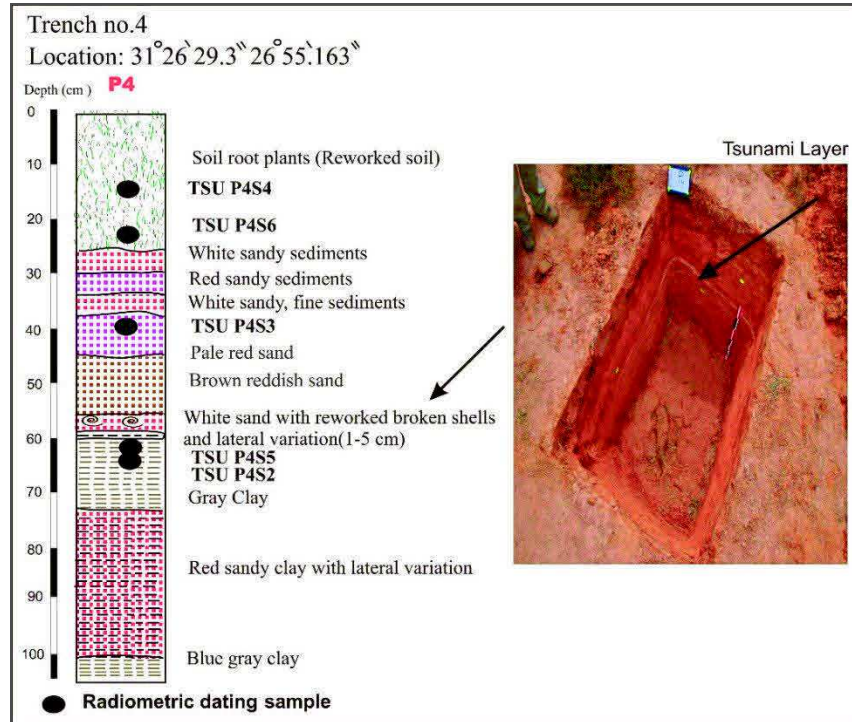
Fig. 48: Description of trench no.4.The arrow reflects tsunami layer 1.
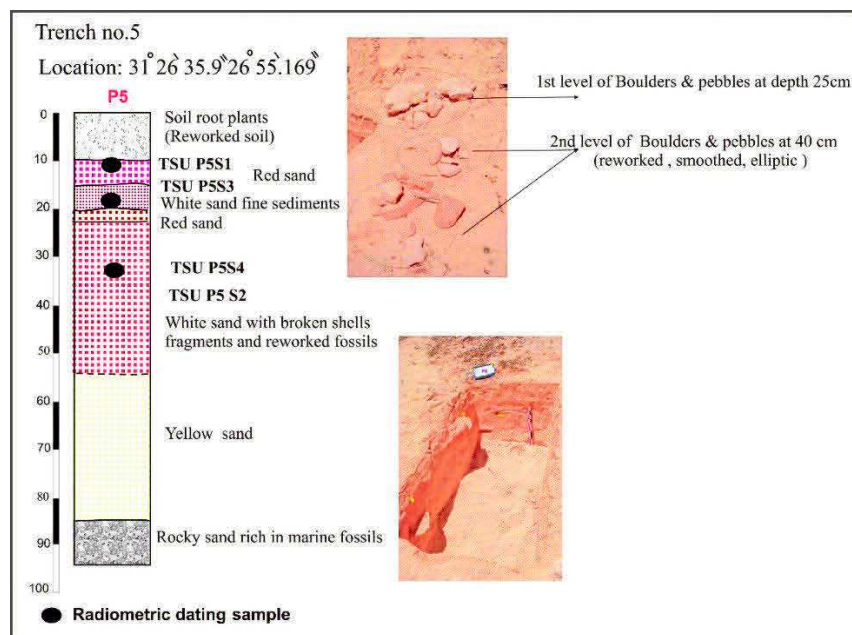
Fig.49: Description of trench no.5.

ii. El-Alamein site

This site is located ~10 km northwest of El Alamein village and immediately north of the German World War II graveyard (Figs. 50 a and b). We proceeded with 12 cores at the site (Figs. 50). The cores were carried out using the Cobra instrument and the maximum~2.4 m depth was reached at core 12.

The photography and sedimentary markers in the detail log description, X-ray scanning, magnetic susceptibility, measurements and the geochemical analysis in 12 cores at El-Alamein site help us to identify the stratigraphy of the tsunami layers. The following is the description and interpretation of tsunami layers in cores from the El Alamein site (see Fig. 50 for core location) :
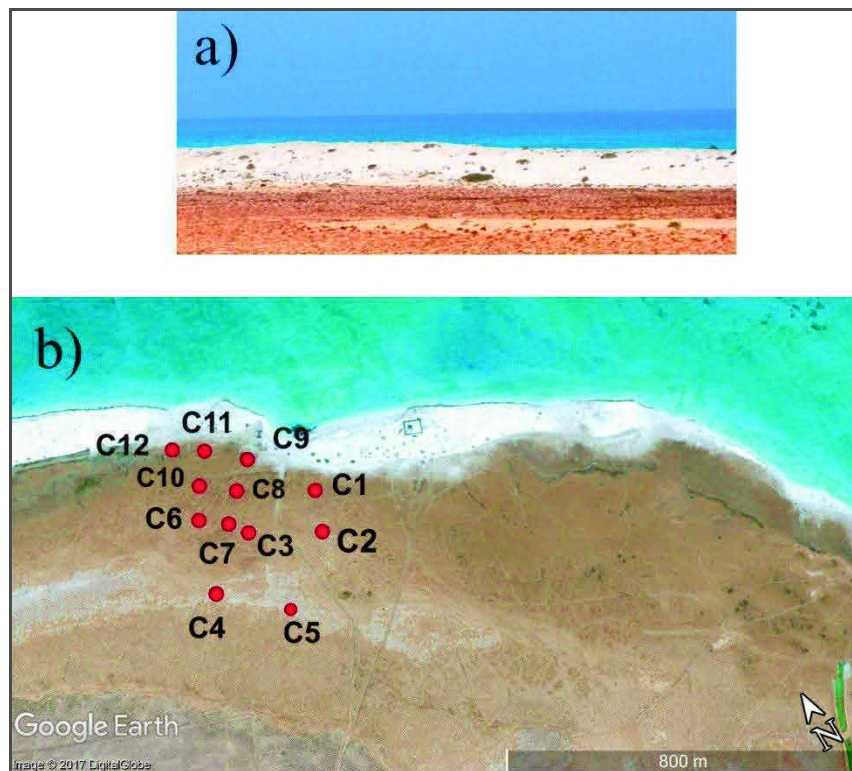
Fig. 50: a) Dunes;b) Paleoseismic site at El Alamein with white sand dune deposits along the coast site (Google Earth image). Dune heights may reach 40 m, but northeast of core C9 the outlet of seawater corresponds to the area of minimum dune heights.

Core 1

This core is located 166 m from the shoreline, east of the study area behind the sand dunes and near the outlet of the seawater. The core depth is 2.14 m and the stratigraphic section consists of 11 stratigraphic units of sand and clay sediments with varying amounts of minerals content. Three tsunami layers are recognized (Figs. 51,52) :

The first layer is at 12.5 cm depth with 34.5 cm thick, brown clay sediments with extremely poor sorting, fine grain sediments, with an observable peak in magnetic susceptibility, rich in organic matter, and the X-ray image reflects clear lamination.

The second layer at 70 cm depth is 5 cm thick. It is characterized by highly broken shell fragments with the extremely bad sorting of sediments. The third layer at 75 m depth is 22 cm thick as is a pale yellow sand with the extremely bad sorting of sediments, with an observable peak in magnetic susceptibility. The chemical analysis shows the presence of gypsum and minor goethite.

A possible fourth tsunami layer at 160 cm depth is a 20 cm thick, brown silty clay with extremely poor sorting, with a peak in magnetic susceptibility, rich in broken shell fragments and high organic matter.

Two samples are chosen for dating in core 1. The first charcoal sample is at a depth of 40 cm and has a calibrated date of 13985-14415 BC (Table 2 in Appendix E). The second is a bone sample from a depth of 50 cm and has a calibrated age of 403-603 AD. The first sample is transported from deep sediments as this sample is located in first stratigraphic tsunami layer. This sample is transported due to high current waves because of tsunami waves. The second sample is between two tsunamis in stratigraphic succession 1 and 2. This sample reflects the probable tsunami of 8 August 1303 above and 21 July 365 below.

Core 2

As shown in Fig. 50 b, core 2 is 90 cm deep located south of core 1 at 264 m from the shoreline. Two tsunami layers are recognized as shown in (Fig.53). The first tsunami layer, of brown clay sediments, is at 12.5 cm depth and is 12.5 cm thick with extremely bad sorting, corresponding to a small peak at magnetic susceptibility. The layer is rich in organic matter (> 1 weight %) compared with other layers of this core; the geochemical analysis shows minor component of goethite.

The second layer is at 50 cm depth and is 15 cm thick and is made of yellow sand with silty-clay pockets, rich with broken shell fragments, extremely poor sorting with peak magnetic susceptibility. It is rich in organic matter compared to other layers, and the geochemical analysis shows minor component of halite.

Two samples are chosen for dating in core 2. The two gastropod samples are at depths of 75 and 77 cm and have calibrated dates of 32971-34681 and 34362-36931 BC, respectively (Table 2 in Appendix E). These two samples are located at the bottom of tsunami stratigraphic layer 2. These samples are transported from the deepest sediments due to high current waves of the tsunami.

Core 3

This core is located 270 m from the shoreline and the outlet of sea water as shown in Fig. 50 b.

The first tsunami layer is at 25 cm depth and corresponds to a 26 cm thick pale brown clay with poorly sorted sediments. It is characterized by highly broken shell fragments and is rich in organic matter. The second layer, at 70 cm depth, is 17.5 cm thick and is characterized by white sand with laminations at the top and fine sediments at the bottom, with a peak of magnetic susceptibility near zero value, and with high organic matter > 2. The third tsunami layer at 106 cm depth is 32 cm thick, characterized by yellow sand with minor illite and broken shells fragments as shown in (Fig. 54).

Two samples are chosen for dating in core 3. The two shell samples are at depths of 37 and 45 cm and have calibrated dates of 43618 BC and 34218-37224 BC, respectively (Table 2 in Appendix E). These two samples are located in stratigraphic tsunami layer 2. These samples are transported from the deepest sediments due to high energy current waves of the tsunami.

Core 4

It is located 435 m from the shoreline. It characterized by two tsunami layers (Fig. 55). The first tsunami layer is white sand at 12.5 cm depth and is 7 cm thick with highly sorted sediments. It also shows highly broken shell fragments with organic matter > 2. The third tsunami layer is a 35 cm thick pale yellow sand at 102 cm depth. It is also characterized by yellow sand with a minor amount of illite and gypsum and broken shell fragments.

One sample is chosen for dating in core 4. The shell sample is at a depth of 37 cm and has a calibrated date of 32887-34447 BC (Table 2 AppendixE). This sample is located in stratigraphic tsunami layer 1. This sample is transported from the deepest sediments due to high energy current waves because of the tsunami.

Core 5

This is the southernmost core in the El Alamein site and is 490 m from the shoreline (Fig. 53 b). It does not contain any tsunami layers (Fig. 56). It may mean that core 5 fixes the limit of inundation in the area with respect to the first and second tsunami layers.

One sample is chosen for dating in core 5. The gastropod sample is at a depth of 50 cm and has a calibrated date of 442182-448237 BC (Table 2 in Appendix E). This sample is transported due to high current waves from the deepest sediments.
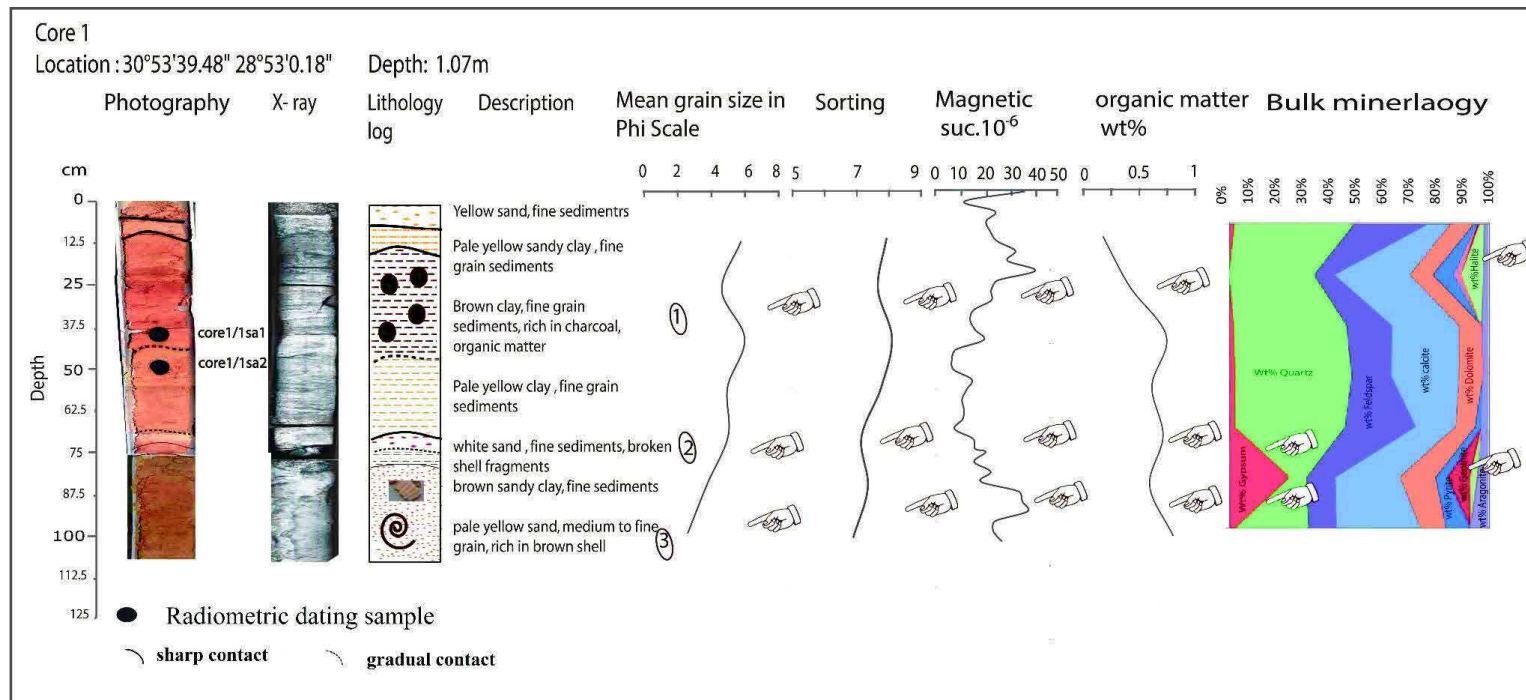
Fig. 51: Description of core no.1 with photography, x-ray scanning, detail description of lithology, mean grain size, sorting, total organic and inorganic matter and bulk mineralogy. The core is at 166 m from the shoreline and reveals 3 main layers (see numbers and pointed hands) of high energy deposits with coarse sand and mixed clay and organic matter. The layers with high values of magnetic susceptibility (especially for 1 and 3) and organic matter are interpreted as deposits of tsunami origin
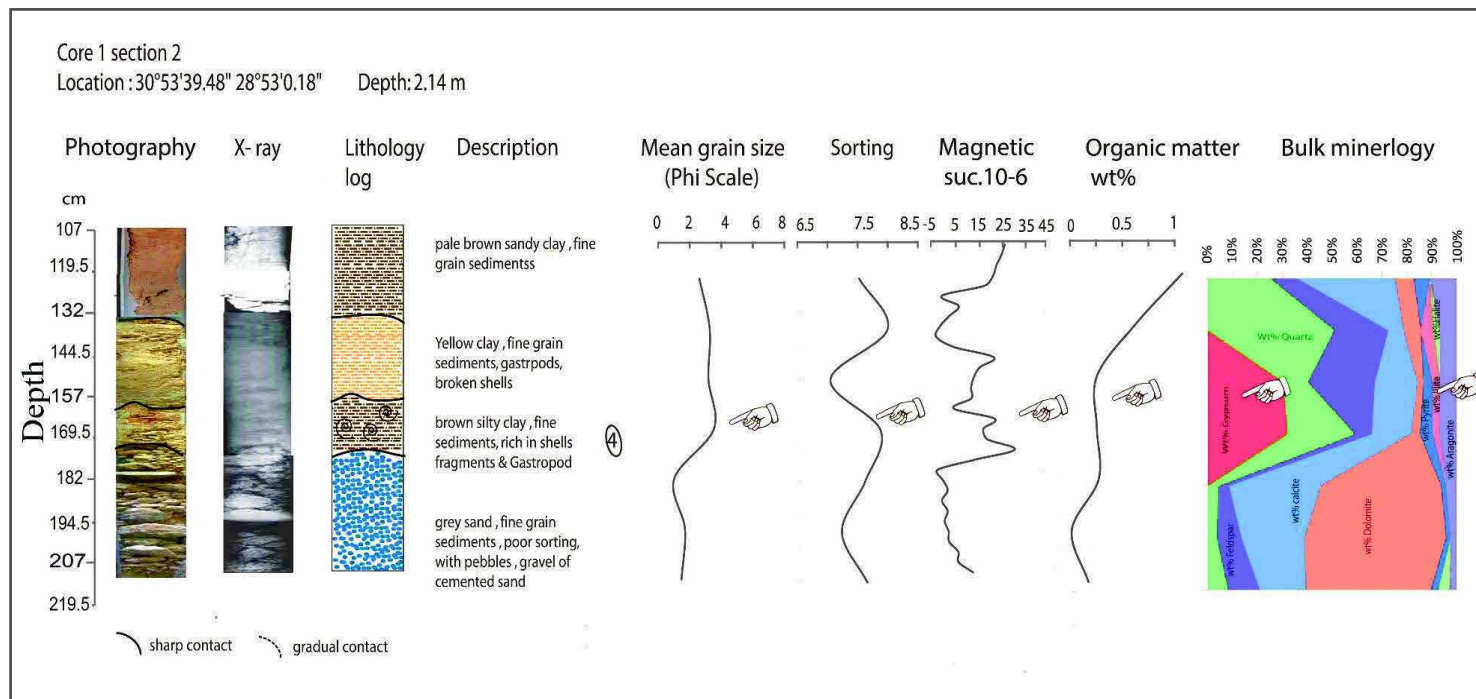
Fig. 52: Description of core no.1 section 2 with photography, x-ray scanning, detail description of lithology, mean grain size, sorting, total organic and inorganic matter and bulk mineralogy. The fourth layer (see numbers and pointed hands) of high energy deposits with coarse sand and mixed clay and organic matter. The layers with high values of magnetic susceptibility and organic matter are interpreted as deposits of tsunami origin
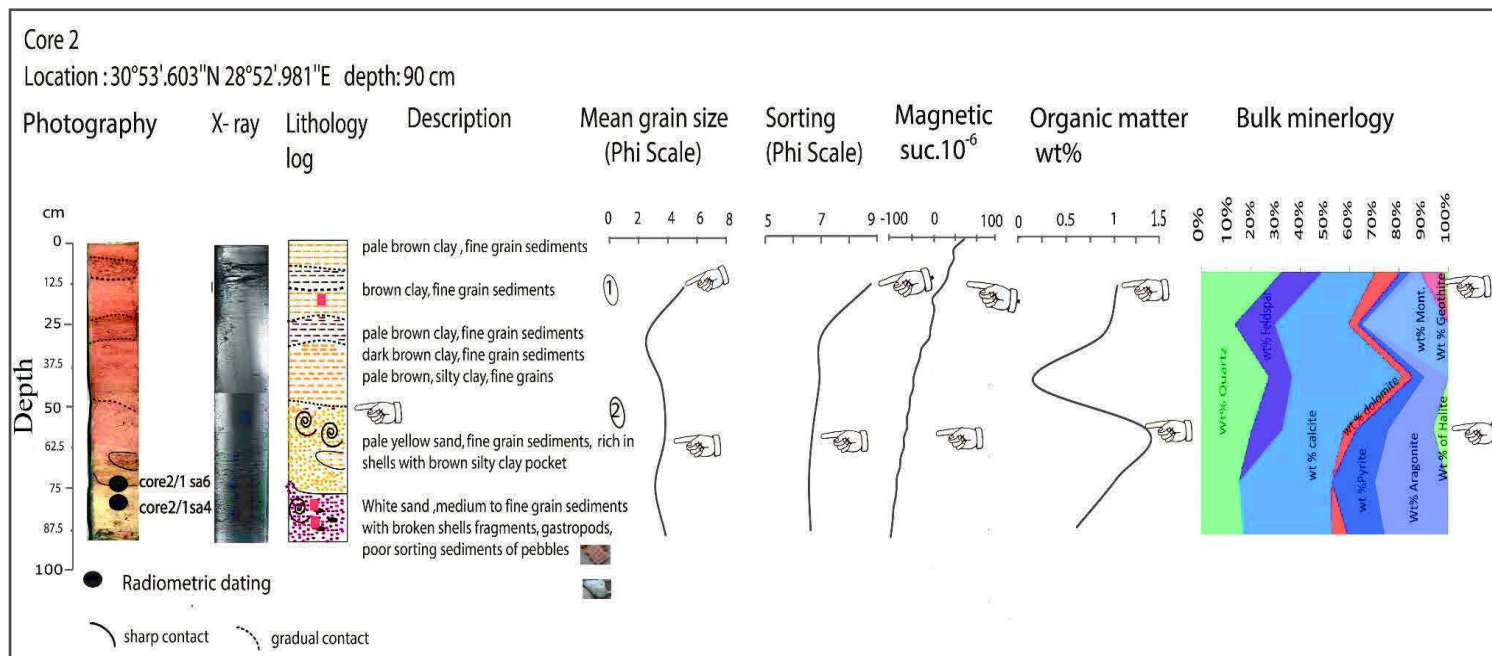
Fig. 53 : Description of core no.2 with photography, x-ray scanning, detail description of lithology, mean grain size, sorting, total organic and inorganic matter and bulk mineralogy. The core is at s ~90 cm deep located south of core 1 at ~264 m from the shoreline. It reveals 2 main layers (see numbers and pointed hands) of high energy deposits with coarse sand and mixed clay and organic matter. The layers with high values of magnetic susceptibility (especially for 1 and 2) and organic matter are interpreted as deposits of tsunami origin.
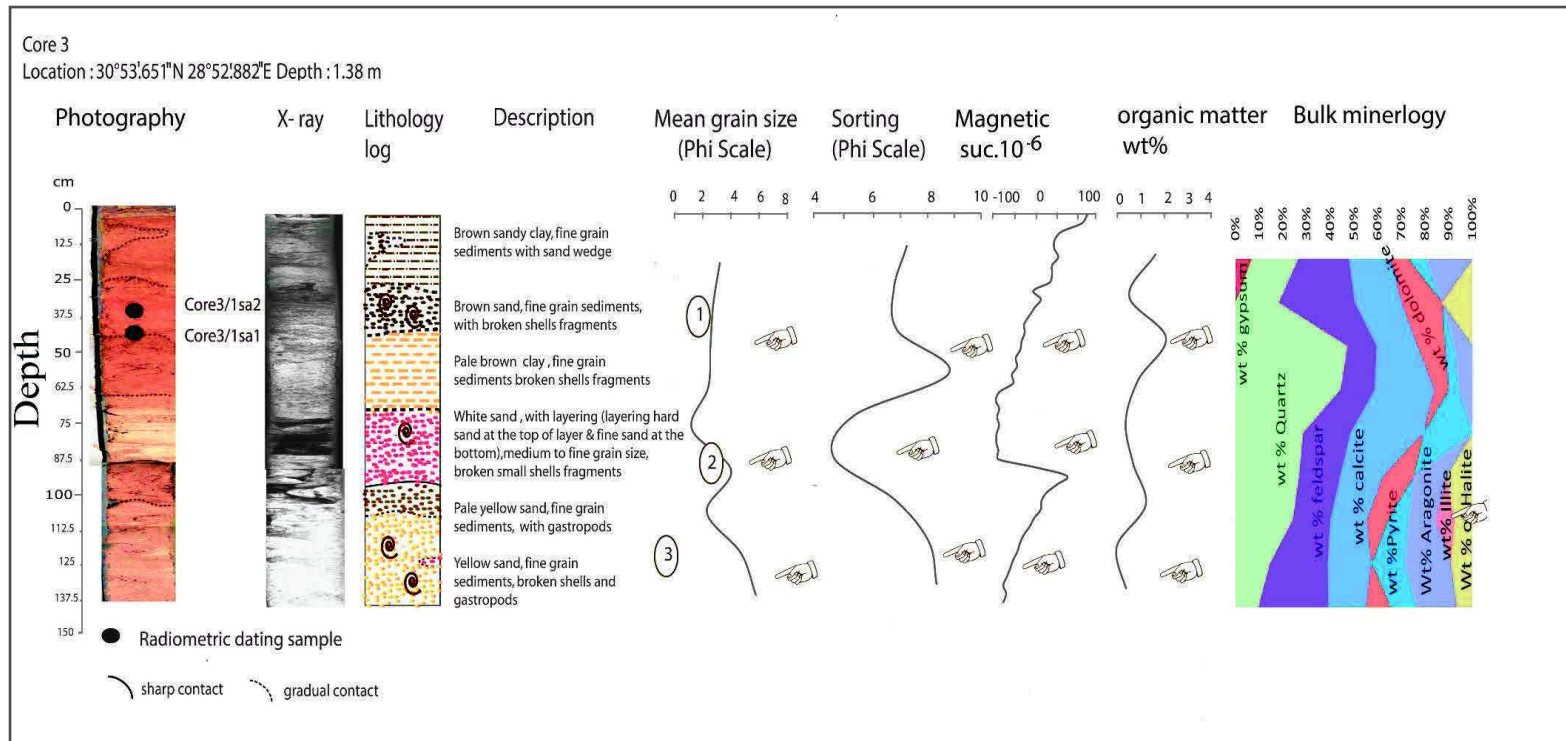
Fig. 54 : Description of core no.3 with photography, x-ray scanning, detail description of lithology, mean grain size, sorting, total organic and inorganic matter and bulk mineralogy. The core is at located at 270 m far from the shoreline and the outlet of seawater. It reveals 3 main layers (see numbers and pointed hands) of high energy deposits with coarse sand and mixed clay and organic matter. The layers with high values of magnetic susceptibility (especially for 1 and 2 and 3) and with laminations at 2 and high organic matter are interpreted as deposits of tsunami origin.
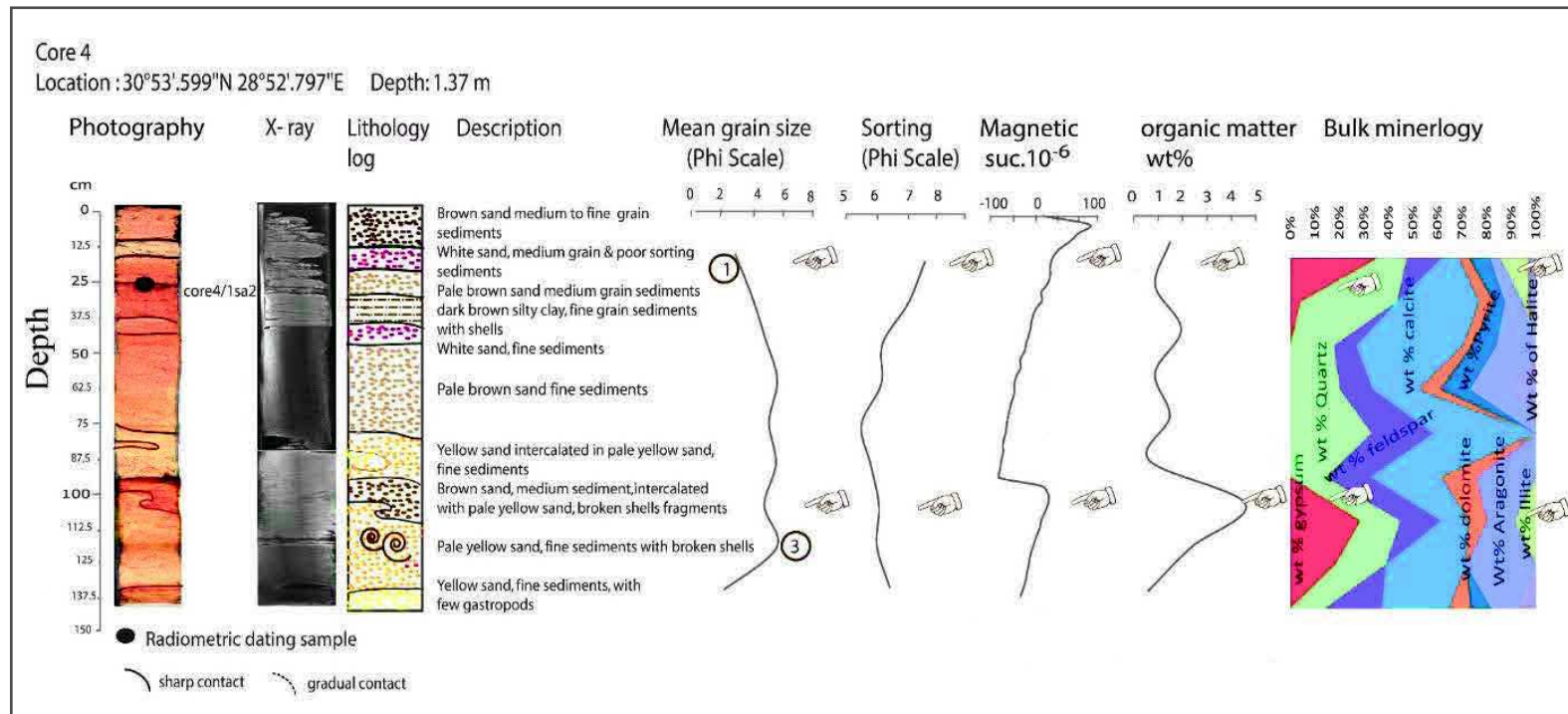
Fig. 55: Description of core no.4 with photography, x-ray scanning, detail description of lithology, mean grain size, sorting, total organic and inorganic matter and bulk mineralogy. The core is at 435 m from the shoreline 166 m from the shoreline. It reveals 2 main layers (see numbers and pointed hands) of high energy deposits with coarse sand and mixed clay and organic matter. The layers with high values of magnetic susceptibility (especially for 1 and 3) and organic matter are interpreted as deposits of tsunami origin.
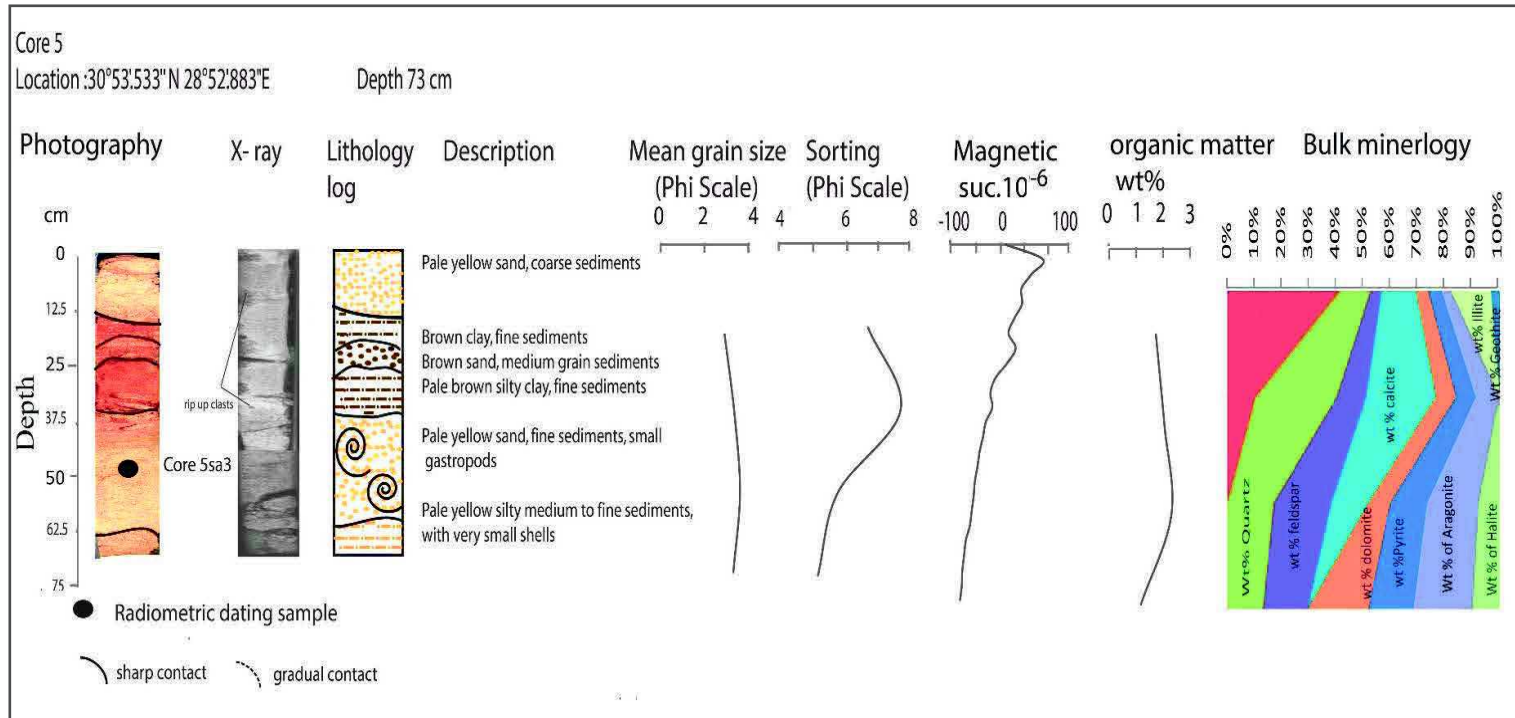
Fig. 56: Description of core no.5 with photography, x-ray scanning, detail description of lithology, mean grain size, sorting, total organic and inorganic matter and bulk mineralogy. The core is at 490 m distance from the shoreline and the sedimentary succession does not show any possible sedimentary high-energy sedimentary layer of tsunami origin.

Core 6

This core is located south of the sand dunes, 320 m from the shoreline. It is characterized by three tsunami layers (Fig. 57). The first tsunami layer is a pale yellow sand with broken shell fragments at 5 m depth and is 24 cm thick with highly sorted sediments rich in an organic matter > 2.5. The second tsunami layer is at 58 cm depth and is 18.5 cm thick and is characterized by yellow sand with a minor amount of gypsum and Illite. The third tsunami layer at 130 cm depth is 20 cm thick and is characterized by white sand with a minor amount of goethite and broken shell fragments. It is very rich in the total weight of organic matter >3 weight %.

Three samples are chosen for dating in core 6. The first gastropod sample is at a depth of 45 cm and has a calibrated date of 35002-37441 BC. The second coral sample is at a depth of 60 cm and has a calibrated age of 42776-69225 BC. The third coral sample is at a depth of 80 cm and has a calibrated age of 1620AD (Table 2 in Appendix E). The first sample was above the stratigraphic tsunami layer 2 while the second sample was within the stratigraphic tsunami layer 2. These samples are transported due to high current waves of the tsunami. The last sample may be transported due to old farming which occurs up to depths of 80 cm.

Core 7

This core was located 273 m from the shoreline. It characterized by three tsunami layers(Fig. 58). The first tsunami layer is a 6 cm thick brown sand with broken shell fragments at 14 cm depth with highly sorted sediments. It is characterized as being rich with organic matter > 2 and a noticeable peak of magnetic susceptibility and the presence of gypsum from the lagoonal environment and a minor amount of Illite and goethite. The second tsunami layer, at 50 cm depth, is a 20 cm thick layer characterized by pale brown clay with pebbles at the bottom. The third tsunami layer, at 115 cm depth, is a 15 cm thick layer characterized by white sand, bad sorting of sediments with a minor amount of pyrite. One sample is chosen for dating in core 7. The sample is at a depth 17 cm and has a calibrated date of 293-1113 BC.

Core 8

This core is located 214 m from the shoreline. Three tsunami layers are recognized as shown in (Fig. 59) in this core. The first tsunami layer is a pale silty clay at 14 cm depth and 16 cm thick with high organic matter and a minor amount of Goethite. It is characterized by highly broken shell fragments and is rich in organic matter. The second layer, at 52 cm depth, is 22 cm thick and is characterized by pale yellow silty-clay, with a low peak of magnetic susceptibility and high organic matter >2.5. The third tsunami layer at 128 cm

depth is 9 cm thick and characterized by pale yellow sand with highly angular gravel sediments, badly sorted and broken shell fragments.

Core 9

It is located 130 m from the shoreline. Three tsunami layers are recognized within the core (Fig. 60). The first tsunami layer is a white sand at 16 cm depth. It is 13 cm thick, with high organic matter and rips up clasts that appear in X-ray scanning and characterized by highly broken shell fragments and is rich in organic matter. The second layer, at 67 cm depth, is 22 cm thick and is characterized by white sand, with a peak of the magnetic susceptibility high content of organic matter > 5. The third tsunami layer at 139 cm depth is 14 cm thick and is characterized by broken shell fragments and white sand with highly angular sediments that reflect the bad granulometric sorting.

Two samples are chosen for dating in core 9 (Table 1 in Appendix E). The first gastropod sample is at a depth of 24 cm and has a calibrated date of 1052-1888 BC. The second bivalve sample is at a depth of 55 cm and has a calibrated age of 40521-43169 BC. The first sample was found in the stratigraphic tsunami layer1 while the second sample was below the stratigraphic tsunami layer 1 and above stratigraphic tsunami layer 2. These samples are transported due to high current waves of the tsunami.

Core 10

It is located 245 m from the shoreline. Three tsunami layers are recognized (Fig. 61). The first tsunami layer is a brown silty clay at 19 cm depth. It is 9 cm thick, with high organic matter and with rip up clasts and lamination that appear in X-ray scanning. It is characterized by highly broken shells fragments and is rich in an organic matter > 4. The second layer at 48 cm depth is 38 cm thick and is characterized by brown sand with broken fragments of shells, with a peak of magnetic susceptibility and high organic matter > 1.5 at the bottom of the layer. The third tsunami layer, at 101 cm depth, is 28 cm thick and characterized by pale yellow sand rich in organic matter and sediments that reflect the bad sorting.

Two samples are chosen for dating in core 10. The first shell sample is at a depth of 24 cm and has a calibrated date of 2623-3521 BC. The second bone sample is at a depth of 70 cm and has a calibrated age of 41256-46581 BC (Table 2 in Appendix E). The first sample was found in the stratigraphic tsunami layer 1 while the second sample was within stratigraphic tsunami layer 2. These samples are transported due to high current waves of a tsunami from the deepest sediments.
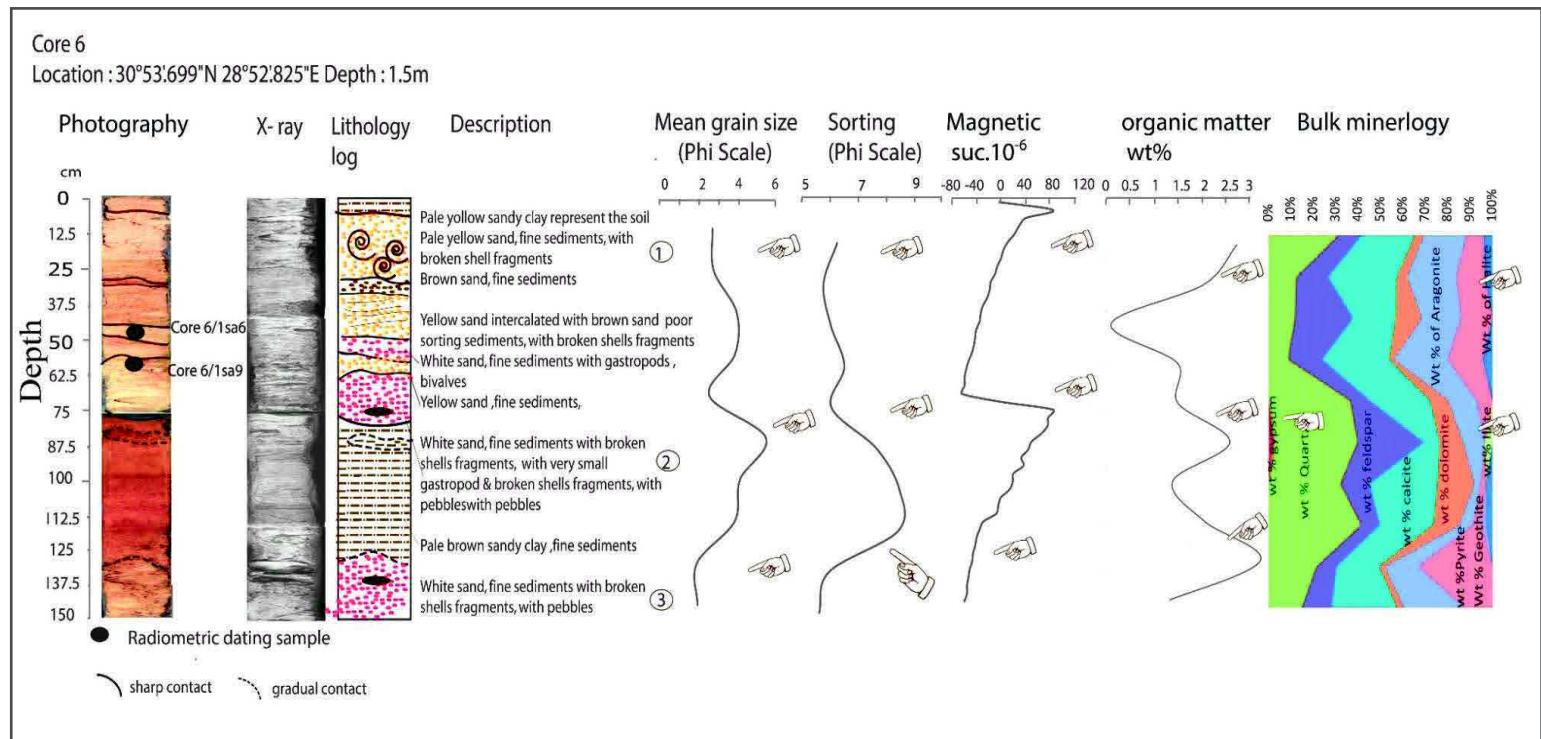
Fig. 57: Description of core no.6 with photography, x-ray scanning, detail description of lithology, mean grain size, sorting, total organic and inorganic matter and bulk mineralogy. The core is at 320 m from the shoreline and reveals 3 main layers (see numbers and pointed hands) of high energy deposits with coarse sand and mixed clay and organic matter. The layers with high values of magnetic susceptibility (especially for 1 and 2) and organic matter are interpreted as deposits of tsunami origin.
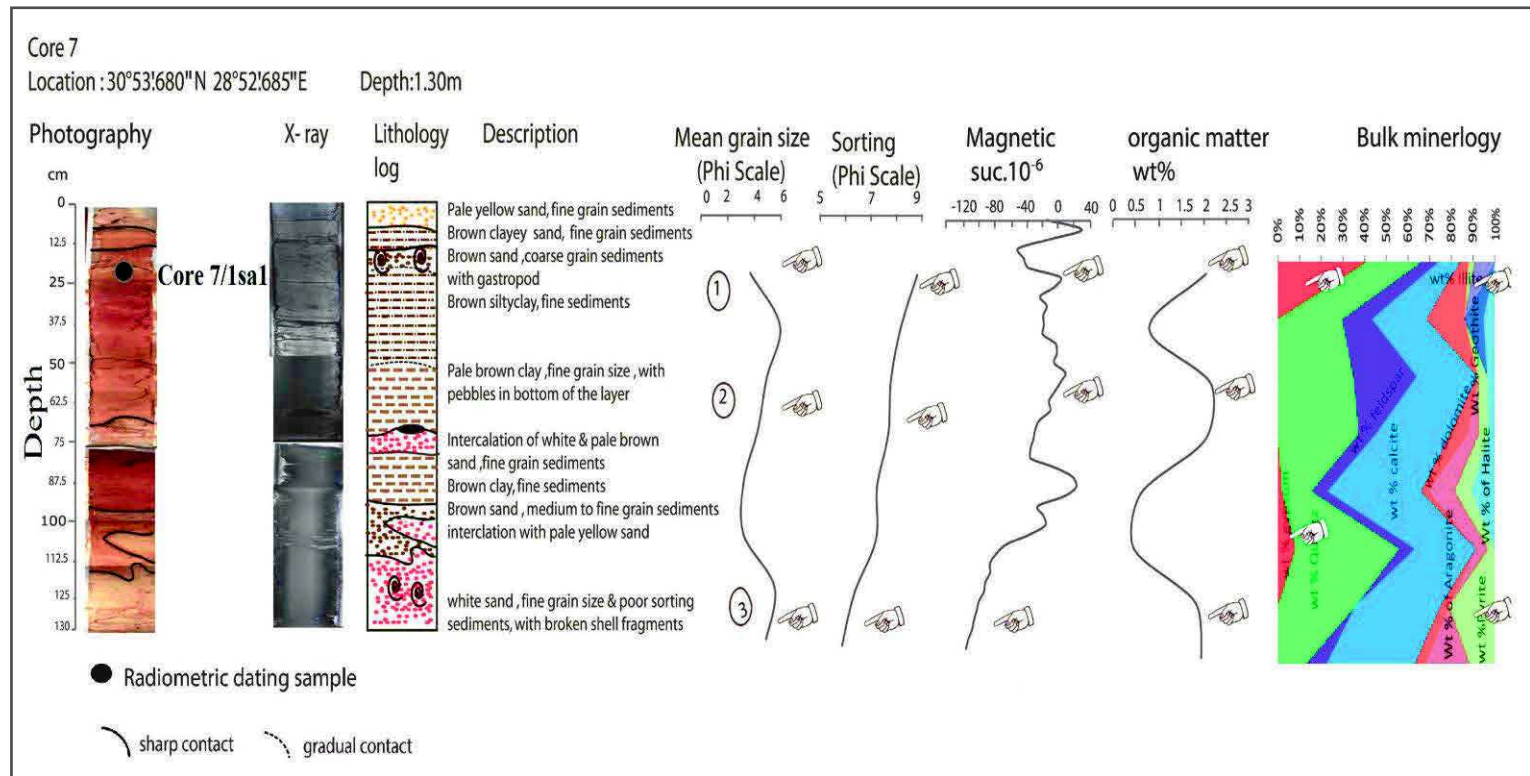
Fig. 58: Description of core no.7 with photography, x-ray scanning, detail description of lithology, mean grain size, sorting, total organic and inorganic matter and bulk mineralogy. The core is at 273 m from the shoreline and reveals 3 main layers (see numbers and pointed hands) of high energy deposits with coarse sand and mixed clay and organic matter. The layers with high values of magnetic susceptibility (especially for 1 and 2) and organic matter are interpreted as deposits of tsunami origin.
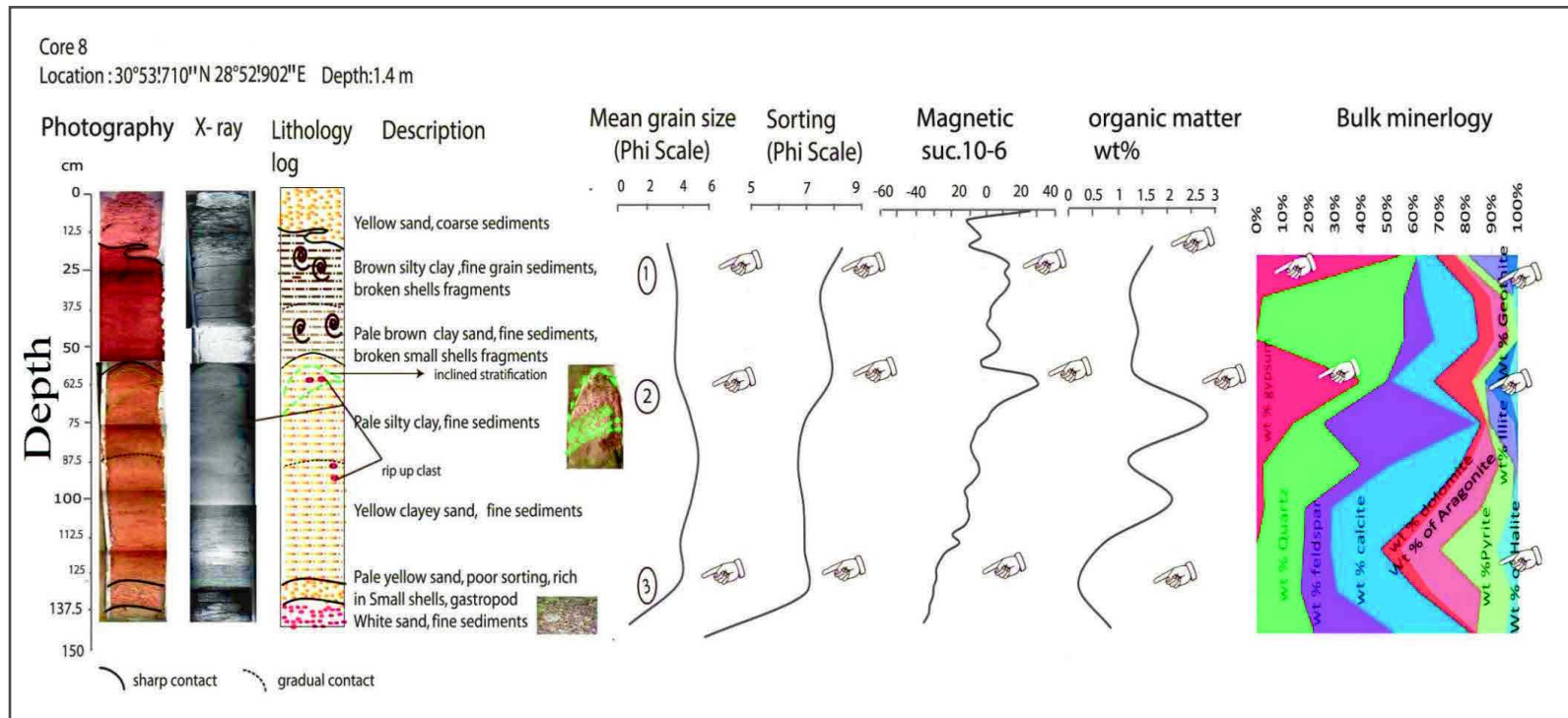
Fig. 59: Description of core no.8 with photography, x-ray scanning, detail description of lithology, mean grain size, sorting, total organic and inorganic matter and bulk mineralogy. The core is at 214 m from the shoreline and reveals 3 main layers (see numbers and pointed hands) of high energy deposits with coarse sand and mixed clay and organic matter. The layers with high values of magnetic susceptibility (especially for 1, 2 and 3) and organic matter are interpreted as deposits of tsunami origin.
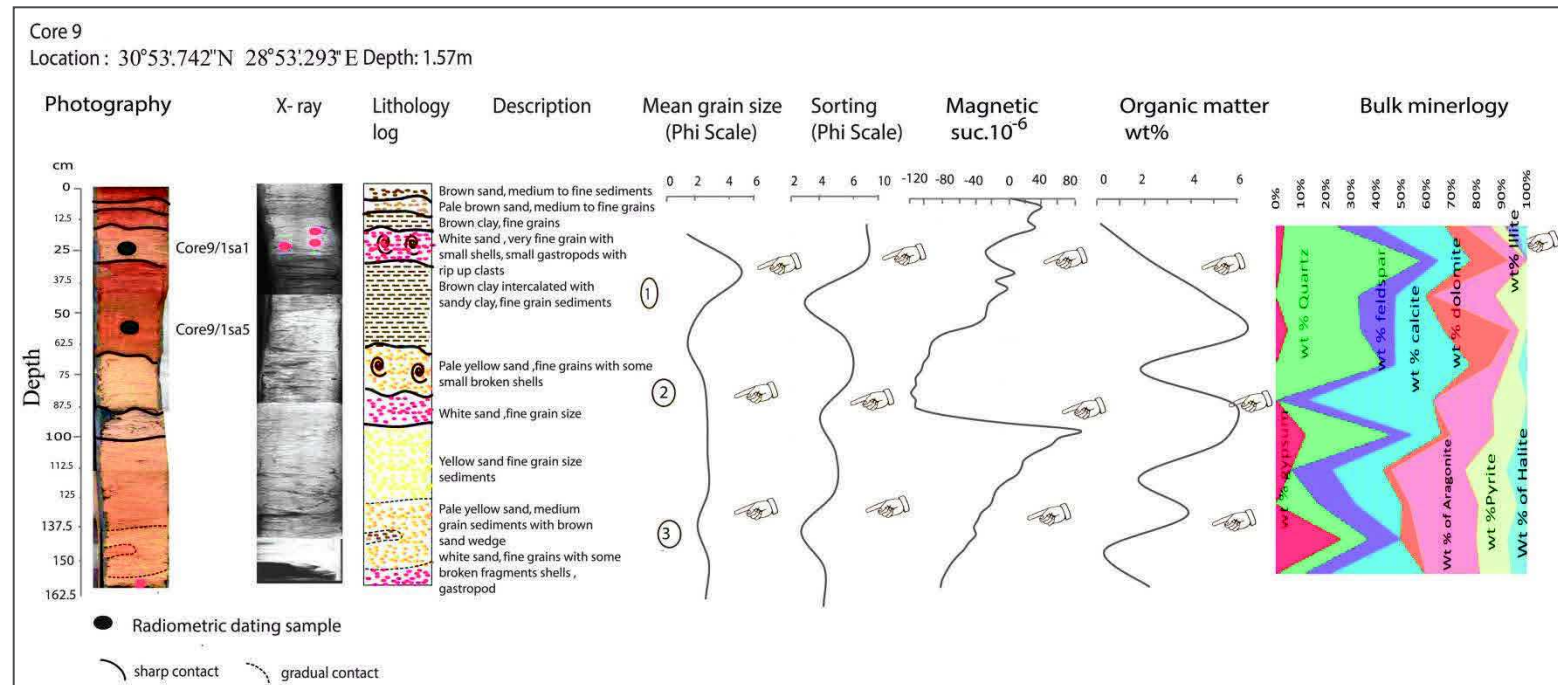
Fig. 60: Description of core no.9 with photography, x-ray scanning, detail description of lithology, mean grain size, sorting, total organic and inorganic matter and bulk mineralogy. The core is at 130 m from the shoreline and reveals 3 main layers (see numbers and pointed hands) of high energy deposits with coarse sand with highly broken shells fragments and rich in organic matter. The high values of magnetic susceptibility and organic matter point to the white coarse sands with broken shells interpreted as tsunami deposits.
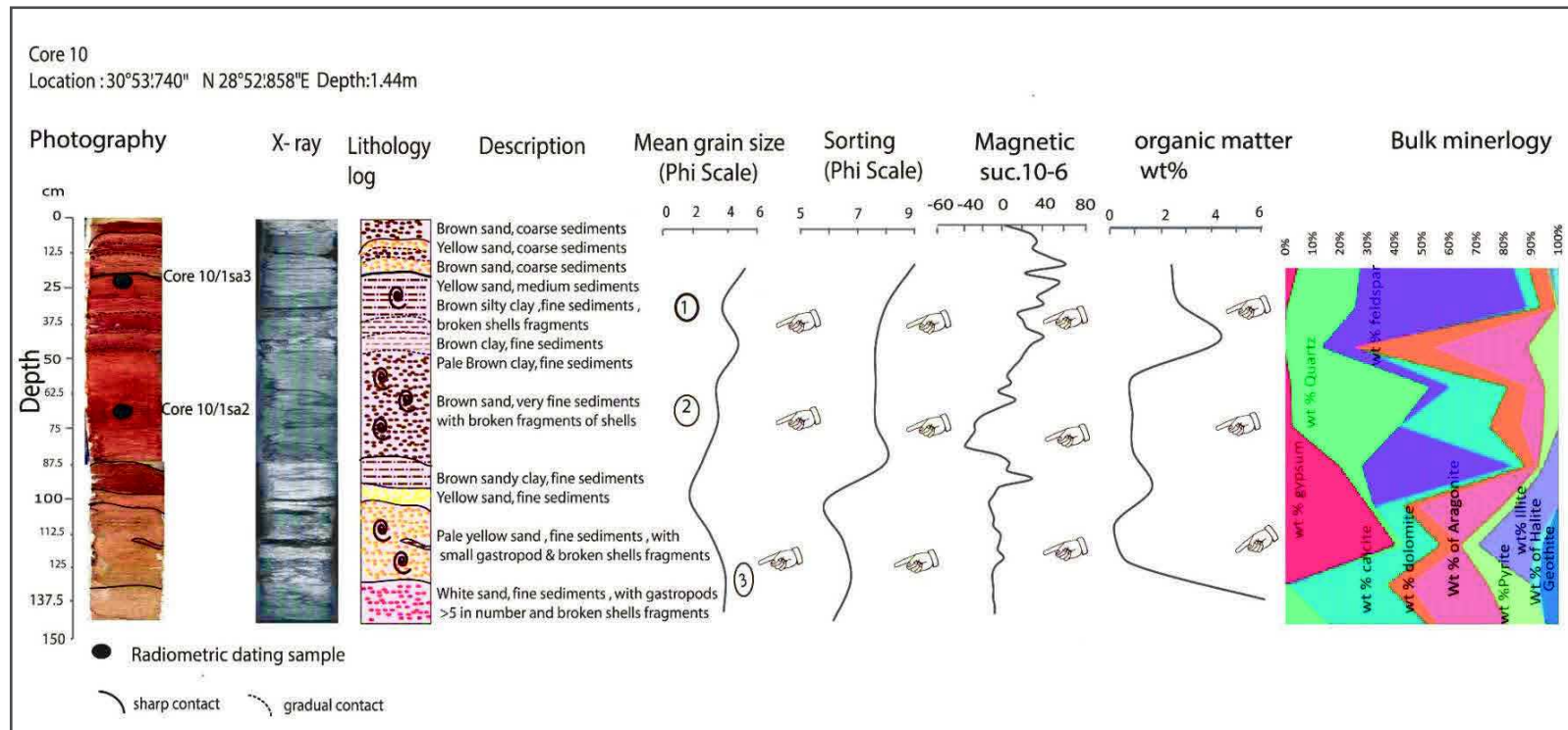
Fig.61: Description of core no.10 with photography, x-ray scanning, detail description of lithology, mean grain size, sorting, total organic and inorganic matter and bulk mineralogy. The core is at 245 m from the shoreline and reveals 3 main layers (see numbers and pointed hands) of high energy deposits with coarse sand and mixed clay and organic matter. The layers with high values of magnetic susceptibility (especially for 1, 2 and 3) and organic matter are interpreted as deposits of tsunami origin

Core 11

It is located 151 m from the shoreline. Three tsunami layers are recognized (Fig. 62). The first tsunami layer is a white sand at 19 cm depth. It is 10 cm thick and characterized by highly broken shells fragments and rich in an organic matter > 4 with a high weight% of gypsum. The second layer at 76 cm depth is 9 cm thick and characterized by white sand, with broken fragments of shells, with a peak of magnetic susceptibility and high organic matter > 1.5. The third tsunami layer at 107 cm depth is 21 cm thick and is characterized by grey silt and sediments which reflect the bad sorting and high organic-rich matter with a minor amount of Illite and gypsum.

Eight samples are chosen for dating in core 11. The first gastropod sample is at a depth of 20 cm and has a calibrated date of 3638-4328 BC. The second shell sample is at a depth of 62 cm and has a calibrated date of 3710-3943 BC (Table 2 in Appendix E). These two samples are found in the stratigraphic tsunami layer 1 and 2, respectively. They are transported from the deepest sediments by high wave current of the tsunami.

The third gastropod sample is found at a depth of 116 cm and has a calibrated date of 2619-3386 BC. The fourth gastropod sample is found at a depth of 121 cm and has a calibrated date of 2457-3366 BC. The fifth gastropod sample is found at a depth of 126 cm and has a calibrated date of 2477-3368 BC. The sixth shell sample is found at a depth of 152 cm and has a calibrated date of 33294-36120 BC. The seventh root sample is found at a depth of 139 cm and has a calibrated age of 2666-2817 BC. The eighth charcoal sample is found at a depth of 180 cm and has a calibrated date of 3710-3943 BC (Table 2 in Appendix E). From the third to eighth samples, except the sixth sample, are arranged chronologically within the second meter in the core from 2457 to 3943 BC. The sixth sample seemed to be transported by high wave current of the tsunami.

Core 12

It is located 127 m from the shoreline. Four tsunami layers are recognized (Figs. 63 and64). The first layer is variable in thickness,but~7.5cmthick at ~19cmdepth. It is made of poorly sorted white sandy deposits, and highly broken gastropods and lamellibranch fossils. This layer is characterized by a high value of organic matter and the high peak of magnetic susceptibility reflect rich carbonates. The second layer is ~13cm thick at ~32.5cmdepth and is characterized by white sandy deposits intercalated with coarse brown sand horizontal lamination, poorly sorted sediments, rich in total organic matter and the high peak of magnetic susceptibility. The third layer is ~25cmthick at 89cmdepth and is made of grey sandy clay, with laminations at the bottom of deposits, vertically aligned gastropods, broken shell fragments, rich in total organic matter and pyrite showing a high peak of magnetic susceptibility. The fourth tsunami layer is at 151 cm depth and is 17.5 cm thick. It is

characterized by pale yellow medium to fine-grained sand with broken shell fragments and extremely poor sorting, with the high peak of magnetic susceptibility, the high peak of organic matter > 5.5 and high amount of gypsum.

Five samples are chosen for dating in core 12. The first gastropod sample is found at a depth of 44 cm and has a calibrated date of 3367-3366 BC. The second shell sample is found at a depth of 108 cm and has a calibrated age of 3097-3950 BC (Table 2 in Appendix E). The third gastropod sample is found at a depth of 114 cm and has a calibrated date of 3331-4050. The fourth shell sample is found at a depth of 117 cm and has a calibrated age of 39560-40811 BC. The fifth gastropod sample is found at a depth of 135 cm and has a calibrated age of 3365-4071 BC (Table 2 in Appendix E). The first and fourth samples seem to be transported from deep sediments due to high energy wave current. The other samples were found within the second meter of the core sediments and this coincides with the calibrated ages in core 11; as it indicates the second meter of the sediments belonged to 2457 to 4071 BC ages.
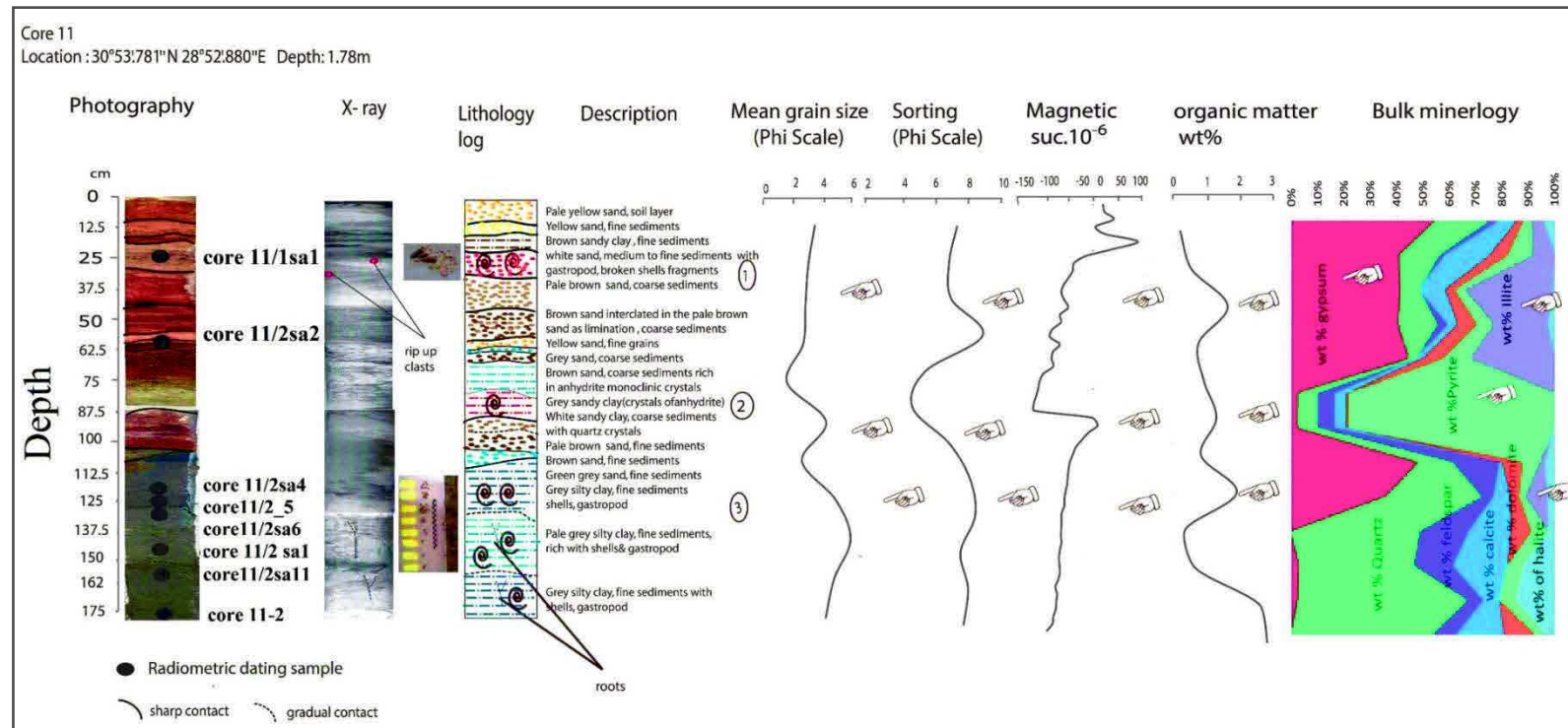
Fig. 62: Description of core no.11 with photography, x-ray scanning, detail description of lithology, mean grain size, sorting, total organic and inorganic matter and bulk mineralogy. The core is at 151 m from the shoreline and reveals 3 main layers (see numbers and pointed hands) of high energy deposits with coarse sand and mixed clay and organic matter. The layers with high values of magnetic susceptibility (especially for 1 and 2) and organic matter are interpreted as deposits of tsunami origin
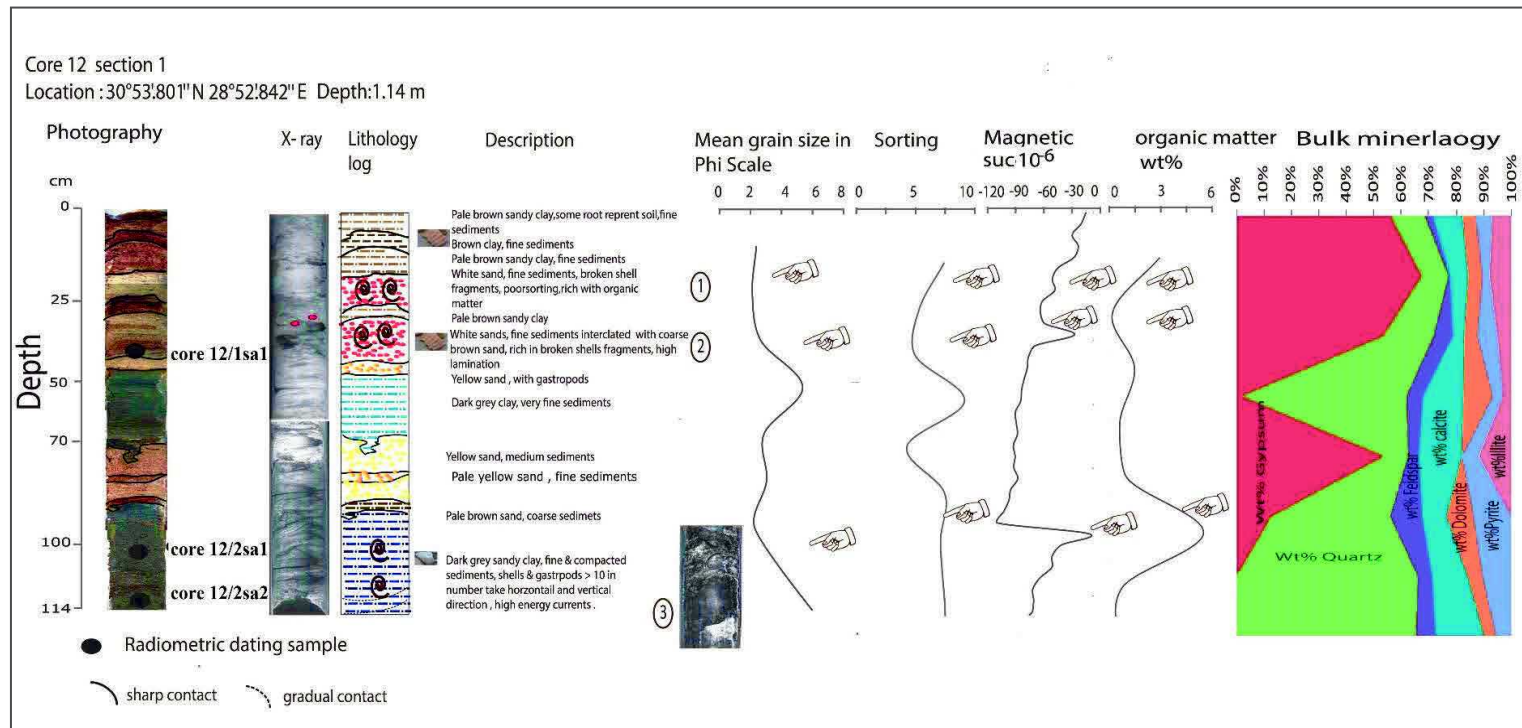
Fig. 63 : Description of core no.12 section 1 with photography, x-ray scanning, detail description of lithology, mean grain size, sorting, total organic and inorganic matter and bulk mineralogy. The core is at 151 m from the shoreline and reveals 3 main layers (see numbers and pointed hands) of high energy deposits with coarse sand and mixed clay and organic matter. The layers with high values of magnetic susceptibility (especially for 1, 2 and 3) and organic matter are interpreted as deposits of tsunami origin
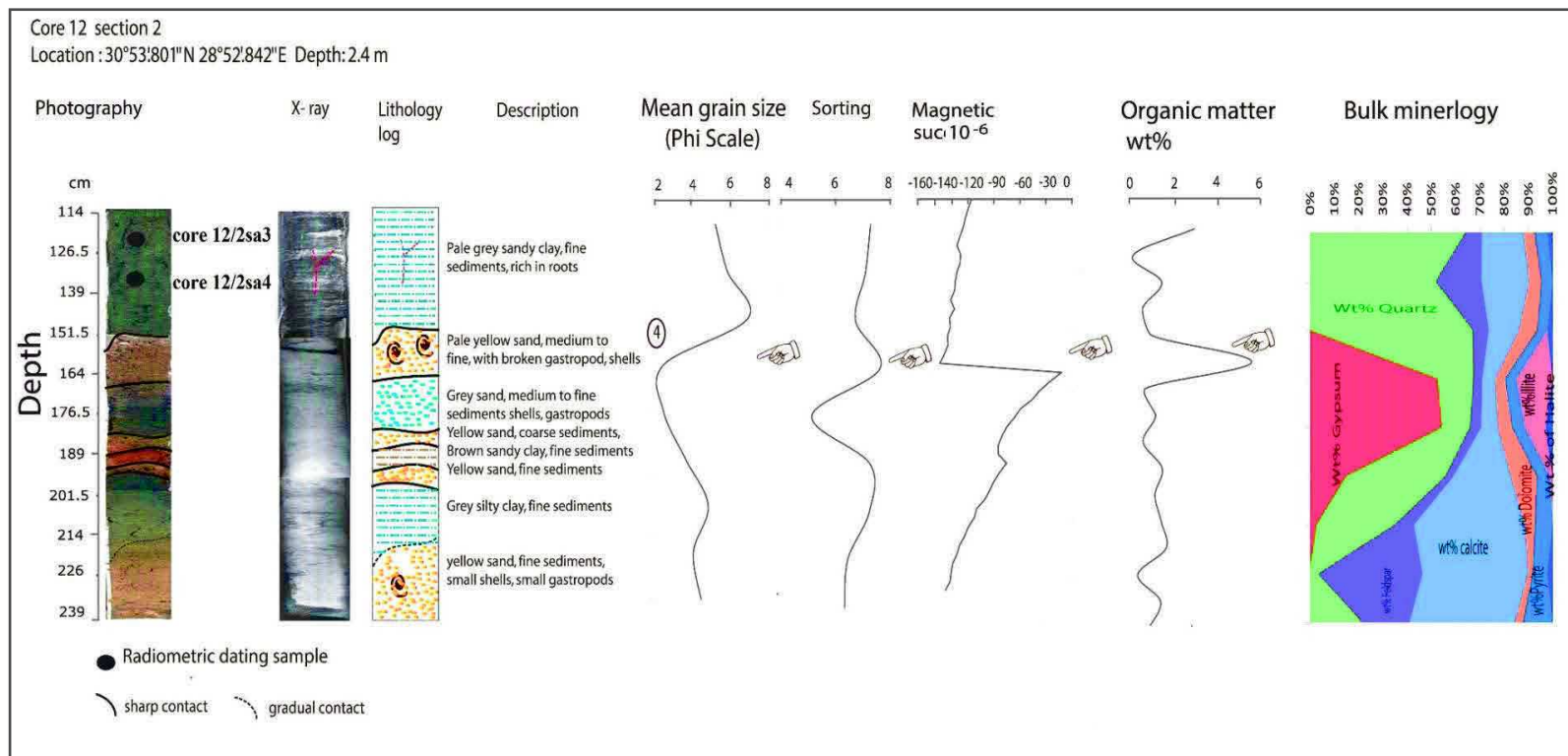
Fig. 64: Description of core no.12 section 2 with photography, x-ray scanning, detail description of lithology, mean grain size, sorting, total organic and inorganic matter and bulk mineralogy. The fourth layer (see numbers and pointed hands) of high energy deposits with coarse sand and mixed clay and organic matter. The layers with high values of magnetic susceptibility and organic matter are interpreted as deposits of tsunami origin

4.4. The composite section and chronology sequence of the tsunami layers

The correlation between trenches and cores in both sites helps to construct two composite sections from both sites using the chorology from the dated samples. The stratigraphic position of the tsunami layers was identified in the sediments of cores and trenches based on the grain size, sedimentary structures and the nature of the contact (sharp or gradual), fossils content, and geochemical and magnetic susceptibility. The composite stratigraphic section of 1 m of sediments from trenches in Kefr Saber with chronology dating are summarized in Fig. 65 and the composite section for the cores in El Alamein are summarized in Fig. 66.

The sedimentary units in Kefr Saber trenches were identified as nine stratigraphic units (Fig. 65) in the composite section. The tsunami layers are characterized by stratigraphic signatures probably related to one tsunami. The tsunami layer is at a depth of ~35 cm with thickness varying along the trenches from 2 to 20 cm. The tsunami layer appears as a homogeneous white sandy layer that exists in trenches P1, P3 and P4 located in a middle of the lagoon. The tsunami deposits are composed of white sand with oolitic carbonate similar to the nearby sand dunes. The white sandy layer is rich in reworked fossils and broken shell fragments with a high percentage of carbonate.

The sedimentary units of the cores at El Alamein site were identified by 11 stratigraphic units in the composite section (Fig. 66). The first tsunami layer has an average thickness of7.5 cm and is found at a depth of 13.5 cm. It is made of poorly sorted white sandy deposits with highly broken gastropods and lamellibranch fossils. The observable peak in magnetic susceptibility is a low value close to zero which reflects a rich carbonate content in the tsunami layer. The X-rays correlation between cores shows laminations and rip up clast in this layer. The second tsunami layer is ~15cmthick and is 50 cm deep. It is characterized by white sandy deposits intercalated with coarse brown sand horizontal lamination, poor sorting sediments, rich in total organic matter and the high peak of magnetic susceptibility. The bottom of this layer is characterized by pebbles.This layer also shows inclined stratifications. The third tsunami layer is ~25 cm thick and the depth is 89 cm. It is made of grey sandy clay to pale yellow sand, with laminations at the bottom of deposits. We also observe vertical and horizontal gastropods direction, broken shell fragments, rich in total organic matter and pyrite and goethite, showing a high peak of magnetic susceptibility. The fourth tsunami layer has an average thickness of 20 cm and a

depth which varies from 151 to 160 cm with highly poorly sorted sediments. It is also characterized by brown silty clay with broken shell fragments.

By dating the samples (see Table 1 and 2 in Appendix E) it reflects multiple effects that a tsunami wave can have on deep sea and coastal sedimentation in a Mediterranean type basin. Moreover, the transportation of samples in depths, not its real depths due to high energy wave current resulted from tsunami or old age storm. The C^{14} isotopic dating of tsunami deposits has allowed the correlation with known historical earthquakes of the Eastern Mediterranean region. Compared with other Mediterranean coastal regions, our results show the identification of one tsunami stratigraphy markers in Kefr Saber and four tsunami stratigraphic deposits at the El Alamein site.

The chronology of sediments in cores in El Alamein was constructed with the Bayesian simulation provides the dating of the four tsunami deposits using the Oxcal software Bronk-Ramsay (2001). The tsunami layers are comparable with the four historical events :simulated tsunami event (W, 1600 BC(Santorini tsunami ?) ;simulated tsunami event (X, 21July365) ; (simulated tsunami event Y, 8 August 1303) ; (simulated tsunami event Z, 24 June 1870), as shown from the probability density function (PDF) of the Oxcal program as shown in Fig. 66. One recognized stratigraphic tsunami layer at Kefr Saber compared with the 21 July 365 tsunami (simulated tsunami event X) as shown in Fig.65
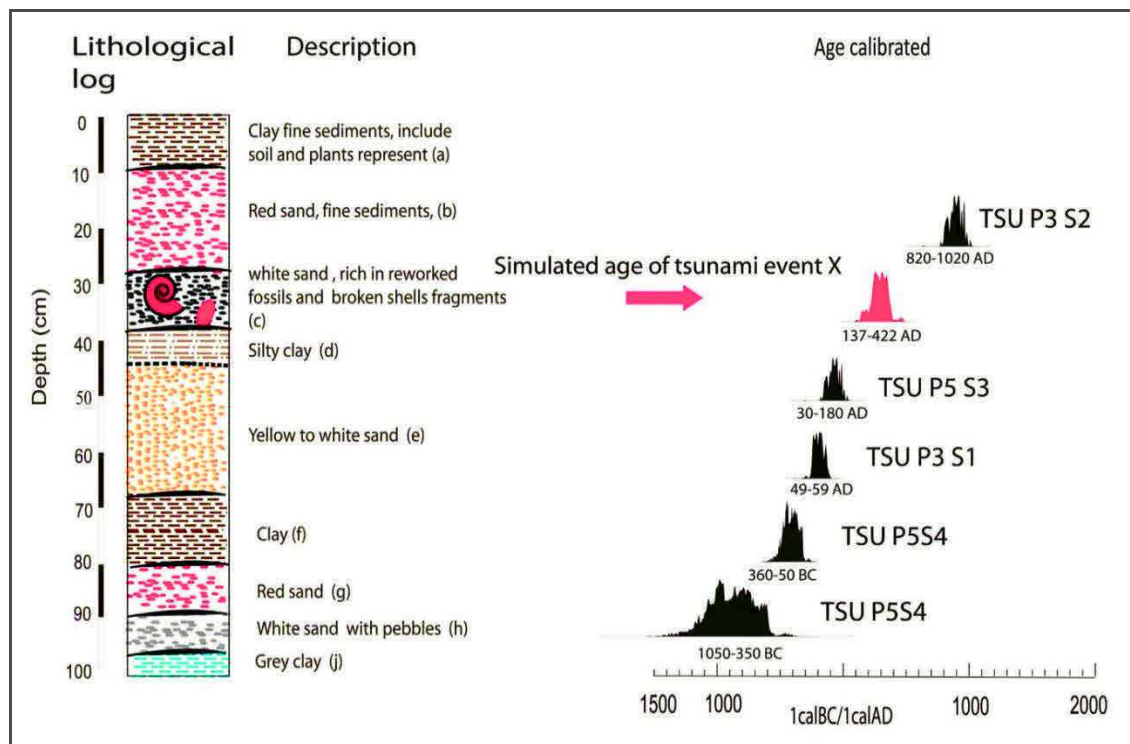
Fig. 65: Composite section for the trenches in Kefr Saber.
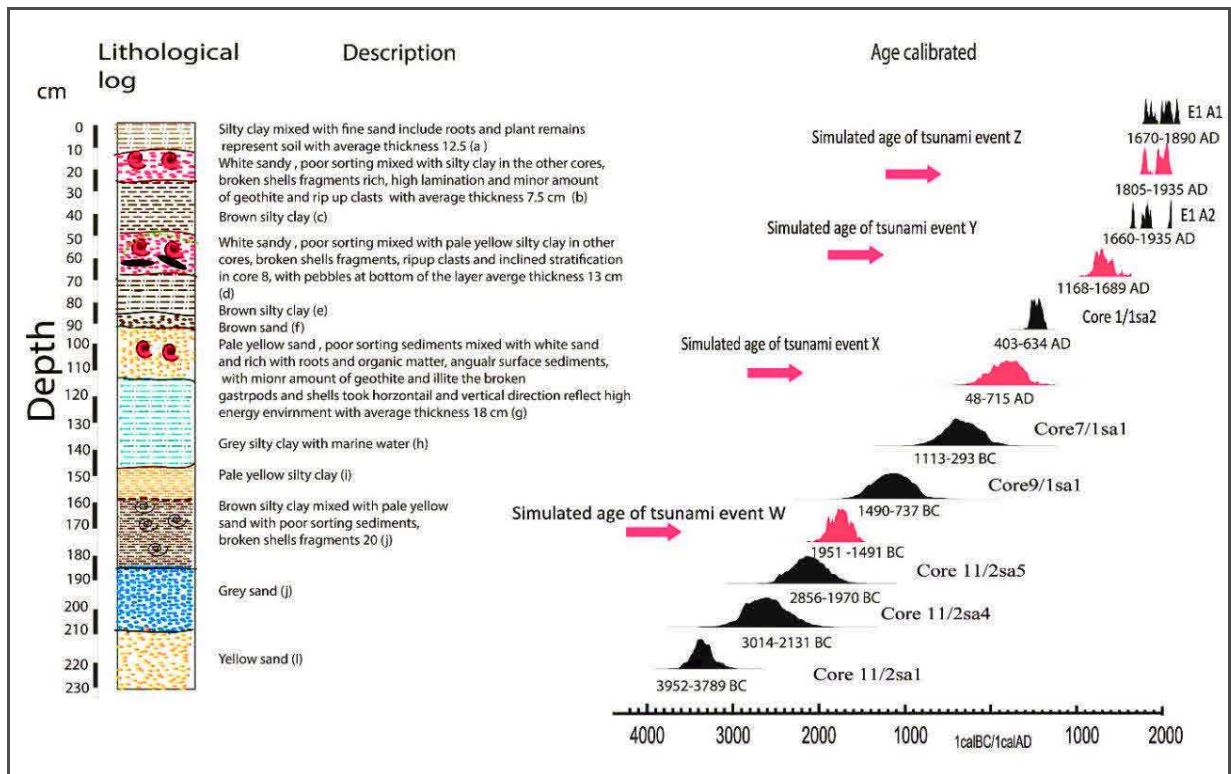
Fig. 66: Composite section for the cores in El Alamein.

4.5 Conclusion and Summary of results:

The geomorphological landforms along the northern Egyptian coast are characterized by sand dunes, accumulation of large boulders, lagoons. The large accumulation of boulders extends along the Egyptian coast particularly in Ras EL Hekma and Kefr Saber which have boulders rich in Dendropoma species. Although the detailed study of boulders is not included in this study, two Dendropoma species were sampled (see Table 1 in Appendix E) in the Ras ELHekma and Kefr Saber for dating. Our dating result of Dendropoma in Ras el Hekma has a calibrated date of 6812-7597 BC. This means that these boulders may have been transported as a result of a strong storm or tsunami during the old ages (6812-7597 BC). The calibrated date of Dendrompa at Kefr Saber was a 940-1446 AD. This Dendropoma sample date coincides with the 8 August 1303 tsunami and these results agree with Shah-Hosseini et al., (2016).

The cores and trenches in both the Kefr Saber and Alamein sites were dug during three fieldworks to identify the tsunami deposits according to their interpreted sedimentary tsunami signatures (see details of trenches and cores above). The stratigraphic log of the trenches in Kefr Saber mainly show one tsunami layer of mixed sand and gravel, and broken shells at a depth of ~ 35 cm (see the composite section in Fig. 65). The cores in El Alamein show four main layers, characterized by fine and coarse sand mixed with broken shell fragments that indicate the occurrence of high energy sedimentary deposits in the coastal

107

lagoon environment(see the composite section in Fig. 66). A remarkable observation is the similarity of the white layers of sand with broken shells observed in trenches and cores at both sites ~200 km apart. We interpret these as tsunami deposits due to their sedimentary signatures (see details of core descriptions above).

From the composite sections and dating chronology in Kefr Saber and El Alamein sites and the results of our paper entitled ''Paleotsunami deposits along the Northern coast of Egypt correlate with historical earthquake records of eastern Mediterranean'', it appears that the tsunami deposits of the 365 AD tsunamigenic earthquake have a larger thickness at Kefr Saber site than at the El Alamein site. However, the opposite trend is seen for the 1303 AD and 1870 AD sedimentary layers which are thicker at the El Alamein site. These observations can be justified by the proximity of the tsunamigenic source in western Crete and 365 AD earthquake with respect to the Kefr Saber site, and the proximity of the 1303 AD and 1870 AD seismic sources in the east Hellenic Arc with regards to the El Alamein site.

Chapter V

Tsunami modelling and scenarios in the northern Egypt

5.1. Introduction

The analysis of tsunami scenarios is a very useful approach for the evaluation of tsunami hazard and risk for any given region. It is the first step in the frame of tsunami mitigation and preparedness for a sustainable coastal zone development. Few countries around the world took serious notice of tsunamis until the occurrence of the Indian Ocean tsunami following the Mw 9.1 earthquake of December 26, 2004, in Sumatra (Indonesia). The massive tsunami generated by the Great Tohoku earthquake Mw 9 in East Japan on 11 March 2011 had a maximum wave height that reached to 19.5 m at Sendai Plain (Mori et al., 2011) and impacted a 2000km stretch of the Pacific coast of eastern Japan. The tsunami propagated more than 5km inland.

These significant events around the world brought the problem of tsunami hazard and risk assessment to the attention of the scientific community and showed the urgent need for tsunami hazard assessment for other seismogenic regions. The assessment is important for the Eastern-Mediterranean countries that are known to have been affected by earthquakes, volcanic eruption or landslides and related tsunamis events throughout history. Major historical tsunamis in the eastern Mediterranean region that affected northern Egypt are triggered by large earthquakes (Papadopoulos et al., 2014) but the possibility of landslide tsunami associated with local earthquakes (El-Sayed et al., 2004; Yalciner et al., 2014). However, the effects of landslide tsunami are limited to the nearby coastline as shown by the recent examples of landslide tsunamis in the Mediterranean associated with the eruption of Stromboli volcanic eruption of 30 December 2002 (Tinti et al., 2005).

Egypt is one of these countries that have experienced strong tsunami impacts in the past (e.g., 21 July 365 and 8 August 1303 AD tsunamis) and has geological records along coastlines. The Eastern Mediterranean area is characterized by very complex tectonics that can be generally described in the frame of the convergence of the African plate towards Eurasia. The problem is particularly urgent for the Mediterranean countries that are known to have been affected by tsunamis in the past, several of which had catastrophic size and impacts. A detailed description of the seismotectonic processes responsible for tsunamis taking place in the Eastern Mediterranean region and possible tsunami sources are described in Chapter III & Chapter IV. The record of paleotsunami events presented in the previous

chapter indicates the location of two large historical tsunami events of 21 July 365 and 8 August 1303.

The aim of this chapter is to develop two simple scenarios for the main far field tsunami-genic in the eastern and western Hellenic arcs which have geological records in this study. we test five scenarios of eastern Hellenic arc and five scenarios of western Hellenic arcs using different focal mechanisms of large recent earthquakes of the same historical location information of the 21 July 365 and 8 August 1303 (Stiros, 2010; Guidoboni and Comastri, 2005) and we used the calculated fault ruptures of eastern Hellenic arc (Stiros, 2010) and for eastern Hellenic arc (Pagnoni et al., 2015). The magnitude of the earthquakes were enlarged to be equal or larger than the largest magnitude recorded in historical times.

Then we simulate the ensuing tsunamis using the Mirone version 2.70 (updated by 22 October 2016; Luis (2007)), highlighting the basic features of the wave propagation and roughly identifying the coastal sectors that are expected to suffer the largest tsunami impacts. The following describes the two scenarios used in the eastern and western Hellenic arcs :

5.2. The eastern Hellenic arc scenario

In the first scenario, we consider a Mw 8.9 earthquake generated on the eastern segment of thrust fault running parallel to Eastern Crete on the 1303 AD west Rhodos segment (Figs.67 and 72). The fault rupture geometry at the eastern segment of Crete Island used in this scenario is shown in Table 5 and consists in a thrust fault that belongs to the Hellenic subduction zone. The initial tsunami conditions for this first case are plotted in Fig. 67. The maximum positive and negative initial water elevations are > 15 m and -16 m at the tsunami source, respectively.

In the following analysis of computed wave propagation, snapshot images show the tsunami fields every 0, 33, 50, 66, 80 minutes after the tsunami initiation (Figs. 68, 69, 70,71 and 72). The scenario describing the tsunami propagation after 50 minutes indicates that the wave arrives at the Kefr Saber and El Alamein investigated sites on the Egyptian coast with a wave height between 7-10 m (Fig. 70). The modelling results show that the entire Egyptian coast is affected by the tsunami triggered in the eastern Hellenic arc with a variation of the wave heights and arrival time.

Table 5: Fault geometry and parameters (see Fig. 67) in the east Hellenic arc used for our modelling and scenario modified after Pagnoni et al., 2015.

Fault parameters	Values	Uncertainty	Measured value
Length	124 km	±65	116±65
Width	47 km	±9	37±9
Slip	8 m	±1.5	7±1.5
Depth (at the bottom of fault)	57 km		
Rigidity	3×10^{11} dyne/cm^2		
Seismic moment (Mo)	1.4×10^{28} dyne.cm		
Mw	8.0 dyne.cm		
Strike	54°		
Dip	55°		
Rake	90°		
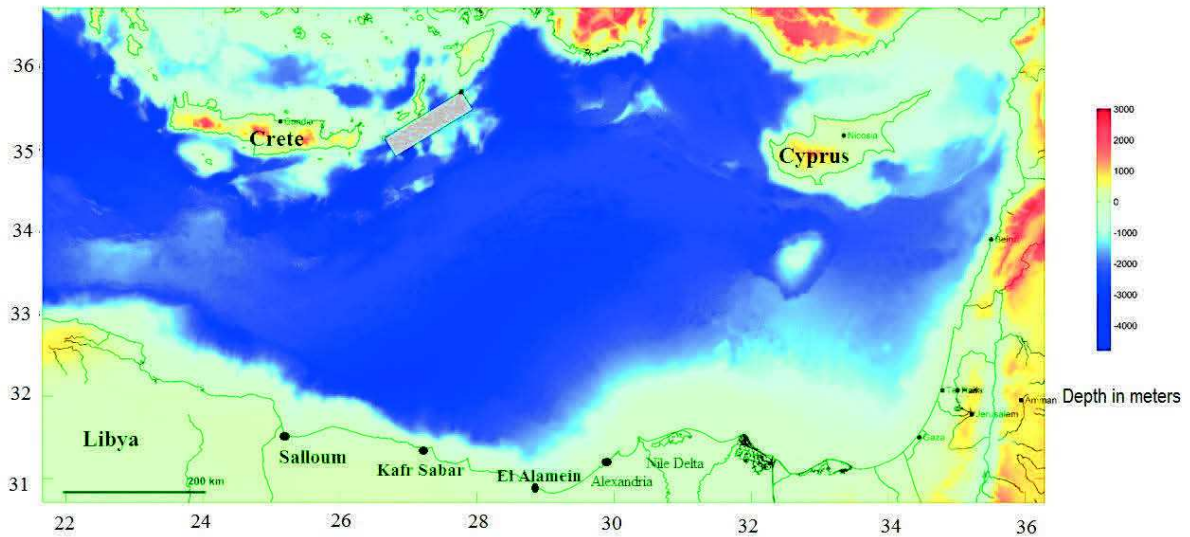
Fig. 67: Bathymetry data from Gebco (2014) (30 arc seconds) with the location of the fault rupture zone (box) along the Hellenic subduction between Crete and Rhodos as the seismic source for the first scenario.
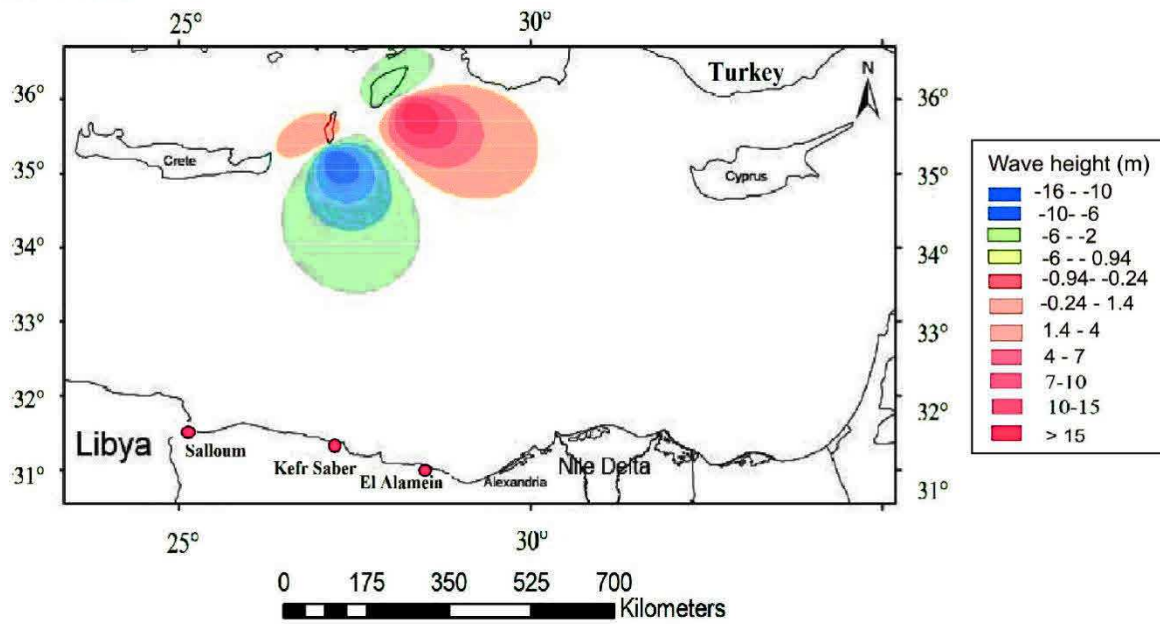
Fig. 68: Initial wave of the eastern Hellenic arc scenario (see seismic source parameters in Table 4 and location in Fig.67).

Time = 33 minutes
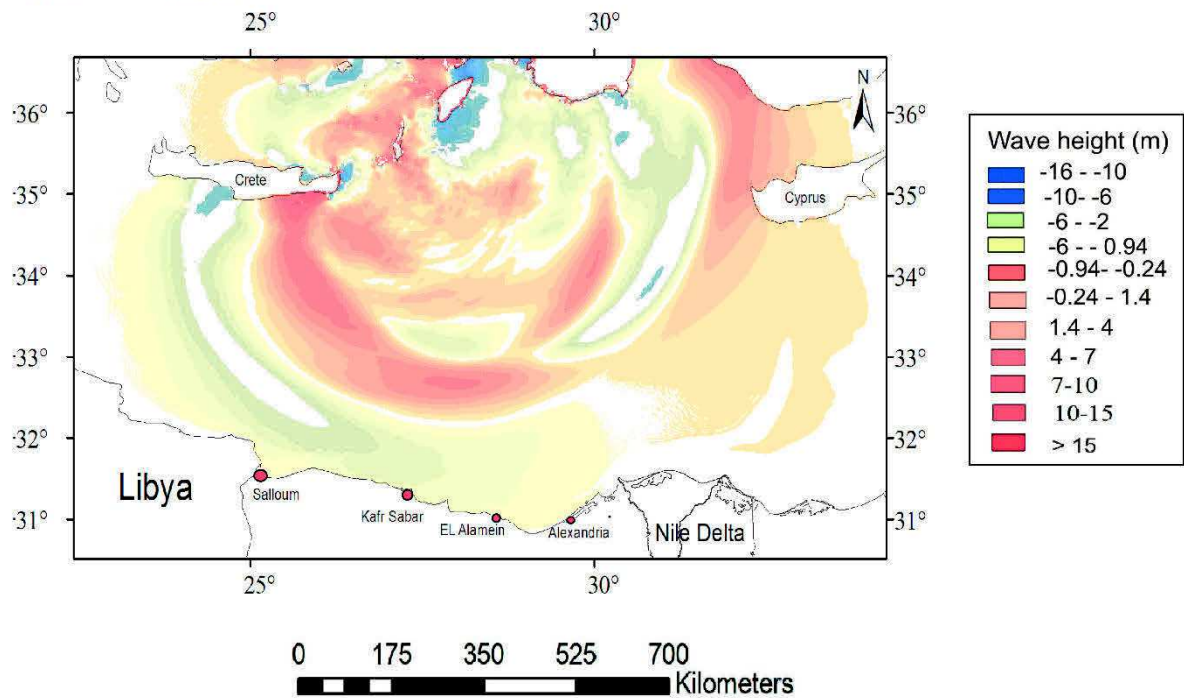
Fig. 69: Wave propagation at min 33 after the tsunami was triggered by an EH source.

112
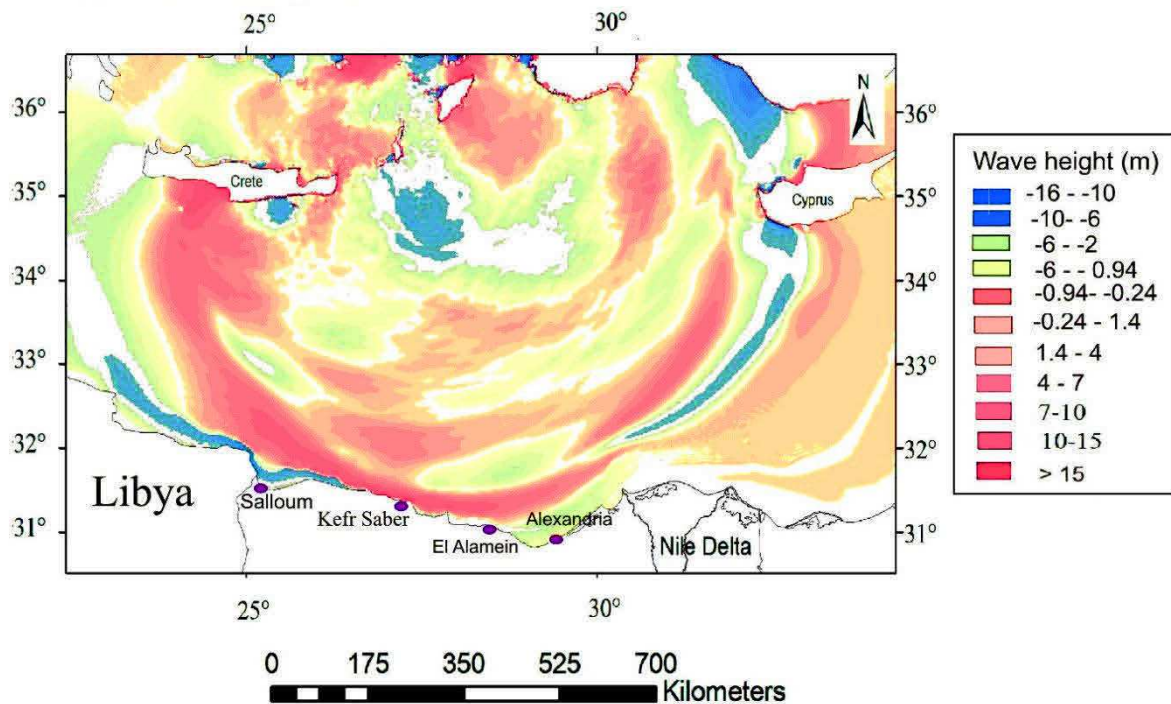
Fig. 70: The wave height after 50 minutes of wave propagation in the eastern Hellenic arc scenario. Wave heights of 10 m reach northern Egypt.

Time = 66 minutes
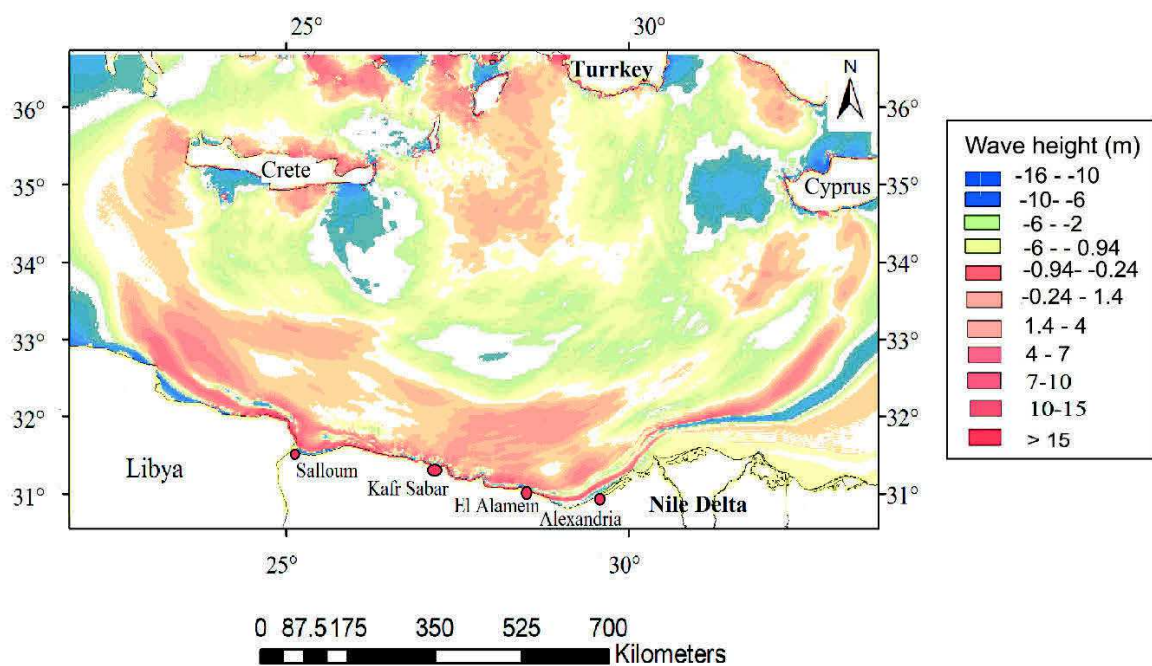
Fig. 71: The wave height after 66 minutes of wave propagation in the eastern Hellenic arc scenario. Wave heights of 7 m reach northern Egypt.

113
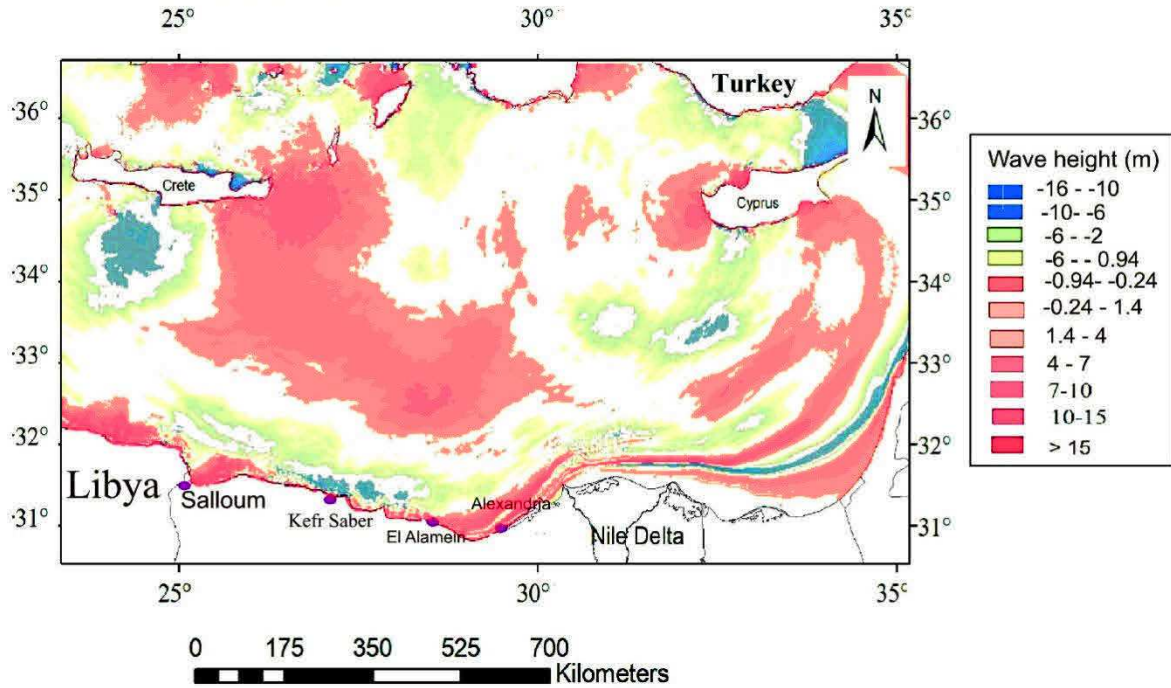
Fig. 72: The wave height after 80 minutes of wave propagation in the eastern Hellenic arc scenario. Wave heights of4 m reach northern Egypt.

5.3. The western Hellenic arc scenario

In the second scenario, we consider a Mw 8.8 earthquake generated in the western segments of thrust fault running parallel to western Crete (Table 6 and Fig.73). The initial tsunami condition for this second scenario is plotted in Fig. 74 and show the maximum positive and negative initial water elevations at the tsunami source are 11 m and -5.0 m, respectively.

The following snapshot images in Figs.74 to 78 show the tsunami wave propagation computed at different arrival times i.e. 0, 33, 66, 100, 150 minutes, after the tsunami initiation. Our observation is that the entire Egyptian coast is affected by the tsunami of the western Hellenic arc, but with a relatively long time of wave propagation with regards to the eastern Hellenic scenario.

The image snapshot of the tsunami propagation after 33 minutes shows that the wave arrives on the Libyan coast with a 4-10 m wave height (Fig. 75). The wave arrives at the Egyptian coast after 66 minutes (Fig. 76) with slightly lower wave height compared with the wave on the Libyan coast. The image describing the tsunami propagation after 100 minutes indicates that the waves arrive at the Egyptian coast with a 0.86-1.76 m wave height at Kefr Saber and a 0.44-0.87 m wave height the at El Alamein (Fig. 77). The tsunami waves from the western Hellenic arc source and scenario cover the entire Egyptian coast after 150 minutes (Fig. 78).

114

Table 6: Fault configuration (see Fig. 73) in the west Hellenic arc used for our modelling and scenario modified after Stiros, 2010.

Fault geometry	Values	Uncertainty	Measured value
Length	115 km	±73	125±73
Width	45 km	±35	63±45
Slip	16 m	±7.5	17±7.5
Depth (at the bottom of fault)	40 km		
Rigidity	3×10^{11} dyne/cm^2		
Seismic moment (Mo)	2.484×10^{28} dyne.cm		
Mw	8.2 dyne.cm		
Strike	133.5°		
Dip	45°		
Rake	90°		
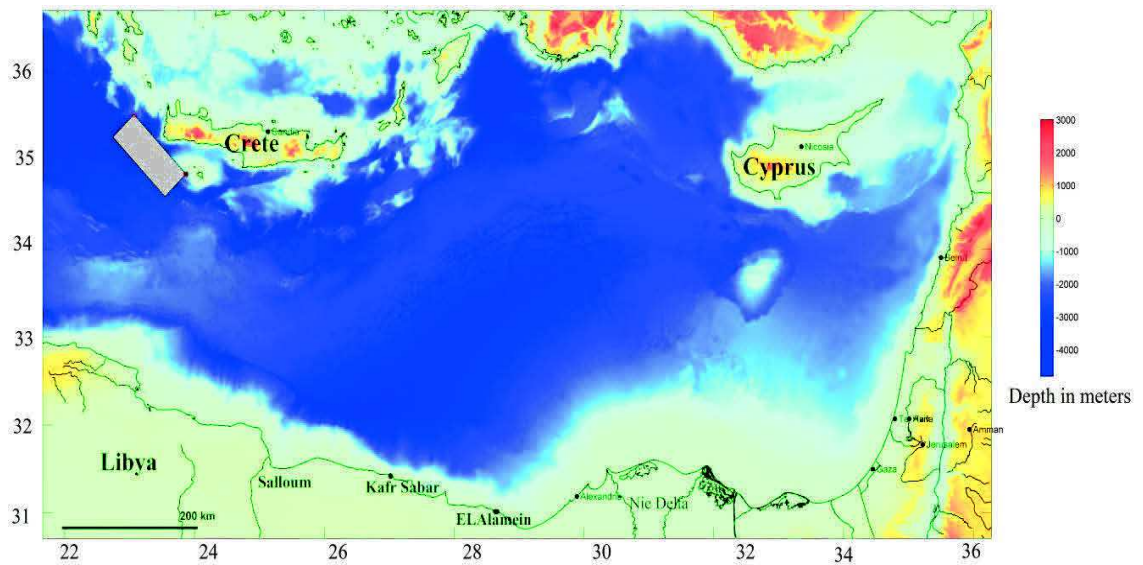
Fig. 73: Bathymetry data from Gebco (2014) (30 arc seconds) with the location of the fault rupture zone (box) along the Hellenic subduction west of Crete as the seismic source for the second scenario.
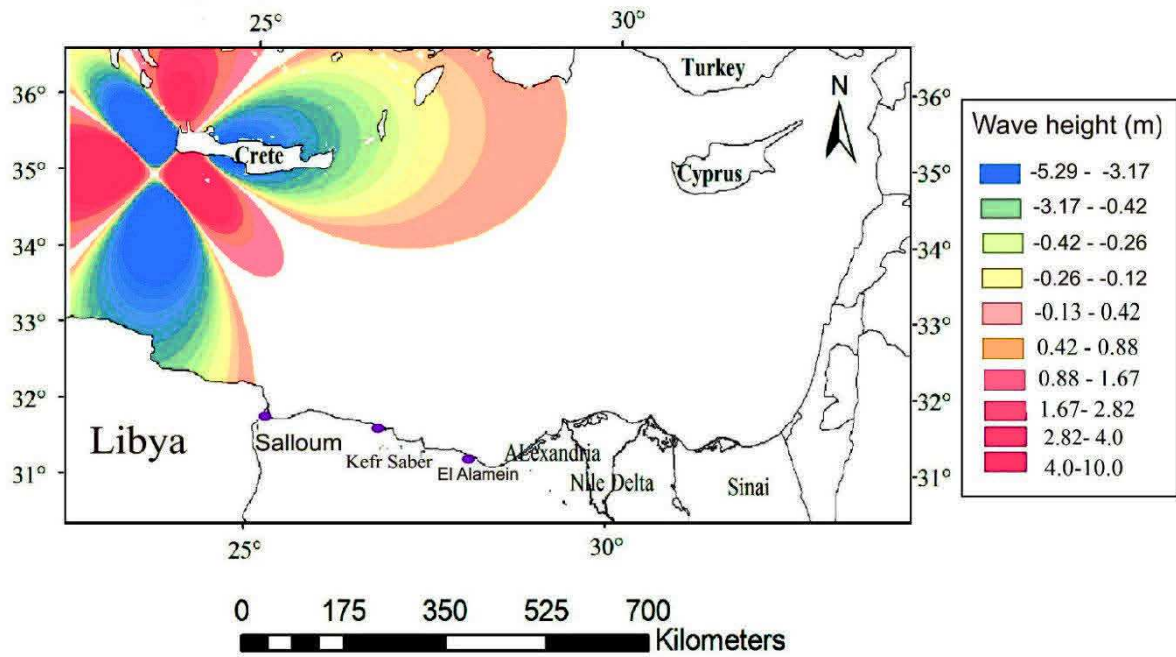
Fig. 74: Initial wave of the Western Hellenic arc scenario.

Time = 33 minutes
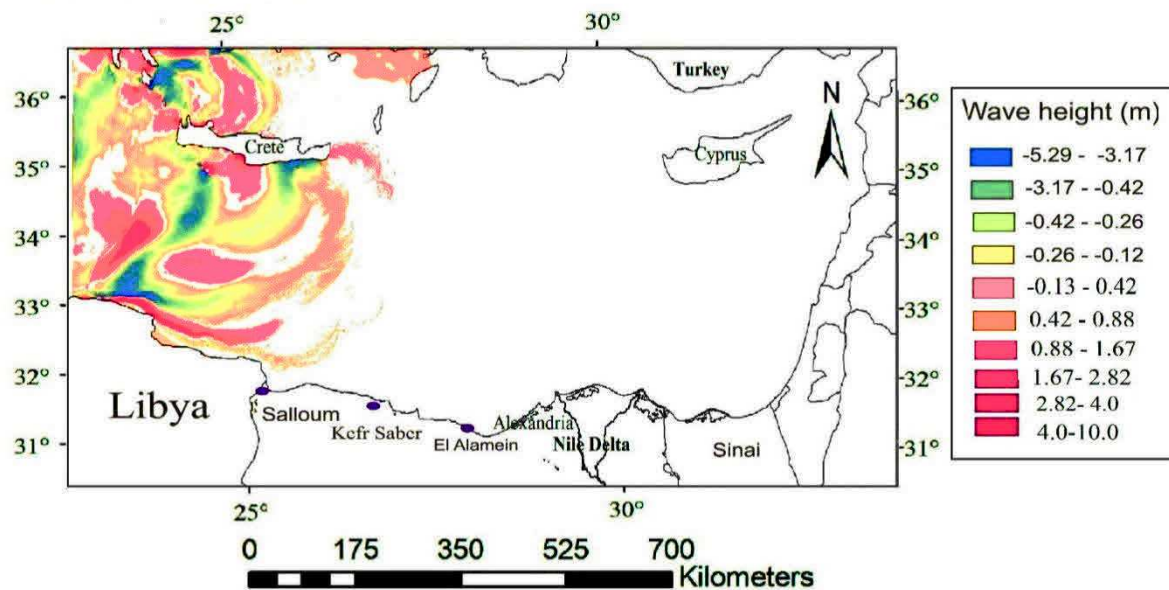
Fig.75: The wave height after 33 minutes of wave propagation in the Western Hellenic arc scenario.

Time = 66 minutes
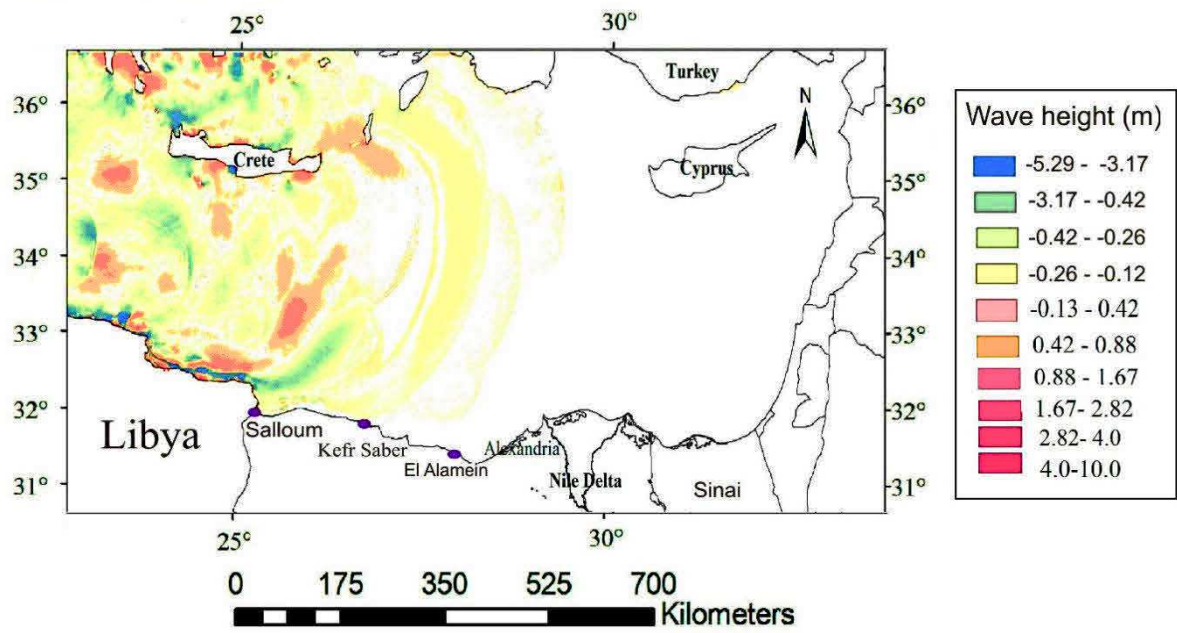
Fig.76: The wave height wave after 66 minutes of wave propagation in the Western Hellenic arc scenario.

Time = 100 minutes
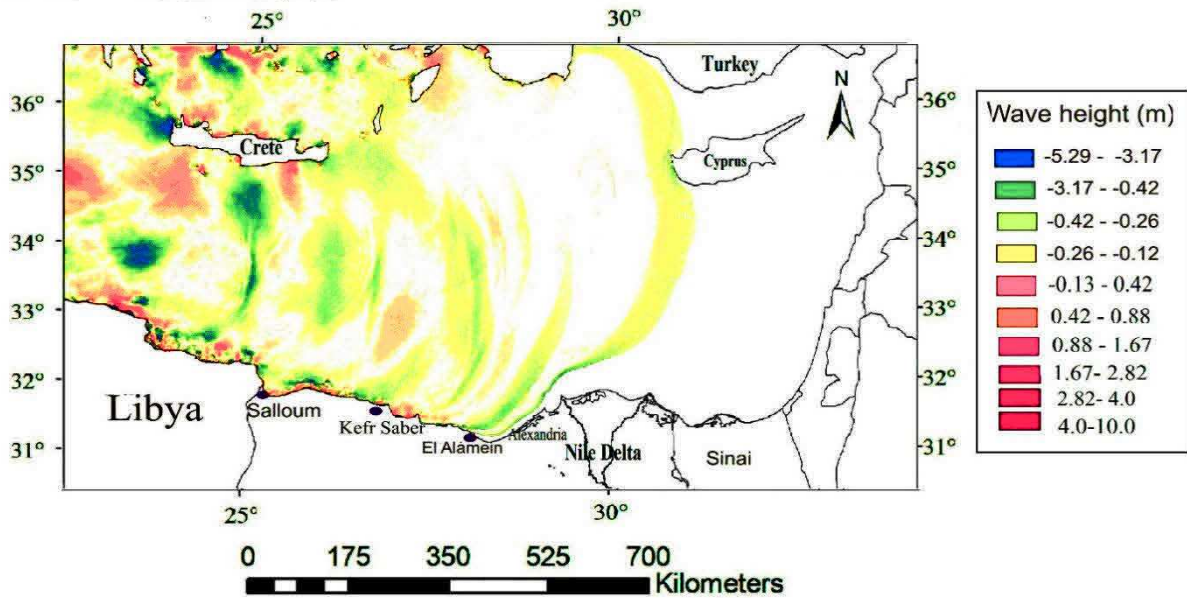
Fig.77: The wave height after 100 minutes of wave propagation in the Western Hellenic arc scenario.
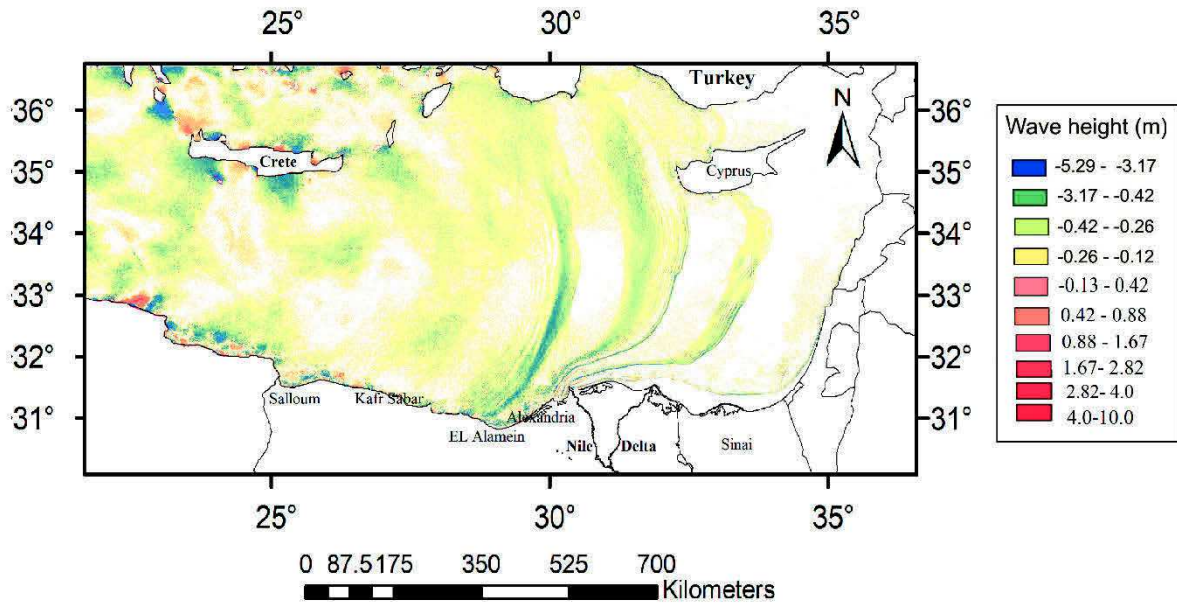
Fig.78: The wave height after 150 of wave propagation in the Western Hellenic arc scenario.

5.3. Comparing my two scenarios with previous studies

Various numerical studies of tsunami modelling and estimation of the wave height run-up and wave propagation have been conducted for the eastern Hellenic arc (Hamouda, 2006 ; Hassan, 2013 ;Pagnoni et al. 2015), and for the western Hellenic arc (Hamouda 2009, Shaw et al., 2008, Pagnoni et al. 2015). Those studies have obtained different results with respect to the wave heights and the time of wave arrival on a given coastline. The differences arise because of a) the bathymetry data used the modelling has different resolutions, and b) various different fault rupture and surface deformation parameters have been used. The wave height run-up and wave propagation of these studies are summarized in Table 6.

Comparing my results with others studies helps to imagine all possible scenarios and how to deal with each in the case of a tsunami in the future (Table 7). My simulation results of the estimated wave heights at Salloum, Alexandria, Damietta well agree with Hassan, (2013) however, my results show higher estimated wave heights at Matrouh and El Arish for the Eastern Hellenic arc scenario (Table 7). Hamouda (2006, 2009) have the highest wave height of 9.4 m at Alexandria in the western Hellenic arc scenarios. Simulated results of Shaw et al., (2008) offshore of Alexandria shows wave heights of ±0.6 m which is in agreement with my results at Alexandria in case of Western Hellenic arc scenario. The first arrival time of my simulations is similar with Pagnoni et al. (2015), especially for Alexandria and Matrouh in the eastern Hellenic scenario.

Table 7: Summary of different tsunami wave propagation and arrival time scenarios in the Eastern Mediterranean from historical earthquake data.

Study reference		Salama This study		Hamouda (2009)	Hamouda (2006)	Hassan (2013)		Shaw et al. (2008)	Pagnoni et al (2015)	
Tsunami event		WHA	EHA	21July 365	8 August 1303	21July 365	8 Aug. 1303	21 July 365	WHA	EHA
First arrival of tsunami (minutes)	Salloum	60	30	50	28	62	39	50	40	30
	Matrouh	66	33	64	31	61	29	60	60	40
	Alexandria	120	40	83	43	140	98	70	80	60
	Damietta	150	68	98	62	143	100	_	120	100
	EL Arish	160	80	115	73	170	123	_	140	140
Max. Wave height (m)	Salloum	0.8	4-7	2.1	1.8	3.5	5.0	0.5	4.0	2.0
	Matrouh	1.6	7-10	2.2	2.0	3.3	4.0	0.4	3.0	2.0
	Alexandria	0.4-0.8	2-4	9.4	8.9	3.0	3.0	0.6	2.5	3-4.0
	Damietta	0.4	1.4-4	6.1	5.6	1.4	1.0	_	1-2	3.5
	EL Arish	0.26	1.4	1.9	1.2	1.3	0.6	_	0.5	1.5

5.4. CONCLUSION AND DISCUSSION

The two main seismic sources of the tsunami were the eastern and western Hellenic arcs in the Eastern Mediterranean. These sources are responsible for two large historical earthquakes and subsequent tsunamis, which affected Egypt on 21 July 365 and 8 August 1303 (Ambrayses, 2009). While the third seismic source is Cyprus zone and it was considered as a low potentiality of the tsunami.

I tested two programs of tsunami wave propagation in Eastern and western Hellenic arc with scenarios using NAMIDANCE beta V.9.0, (Velioglu et al., 2016) and Mirone v. 2.7 (Luis, 2007). I succeeded to create an initial wave from Mirone v.2.7, 22 October 2016 updated. Two-tsunami scenario were developed with sources in the eastern and western Hellenic arcs. These tsunami events were based on the geological tsunami records in Kefr Saber and EL Alamein (see chapter IV for details about the historical events and tsunami deposits). The uncertainties of these two models depending on the chosen fault rupture data, the quality of the bathymetry data and the accuracy of the model used. The fault ruptures used in this study for the western Hellenic scenario are those calculated by Stiros (2010) and used in Pagnoni et al. (2015) study with changes in these fault parameters. The uncertainties are calculated for the fault geometry (i.e length, width, and slip) used in east and west Hellenic arcs as it compared with the previous studies (see tables 5 and 6). Also, the uncertainties are calculated in wave height (m) depend on the tested 5 scenarios

resulted in ±5 m in wave height in case of east Hellenic arc scenario and ± 1.5 m in wave height in case of west Hellenic arc scenario.

We chose highest resolution bathymetry data available (30 arc seconds, Gebco 2014) to reduce any uncertainties. Although, the irregularities along the Egyptian coast shape i.e syncline bays in Alexandria or and in front of Kefr Saber or Ras El Hekma, will require high-resolution coastal bathymetry of 1-3 arc seconds to reduce uncertainties in simulated wave height. Two worst scenarios were chosen based on historical damage information and effective possible wave height along the Egyptian coast resulting from testing 10 scenarios with changing in the fault parameters. The simulations were carried out using the Mirone software Luis (2007) which computed the wave propagation and identified the coastal sectors that are expected to suffer the largest tsunami effects along the northern Egypt coast.

From a tsunami hazard assessment point of view, these simulations show detailed information about the travel time and wave height of tsunamis. From the western Hellenic source zone, the Egyptian coast can expect a maximum wave height 1.7 m tsunami at Kefr Saber after 66 minutes as shown in Fig.79a, 0.5 m after 100 minutes at ElAlamein as shown in Fig.79 b while Alexandria has 0.8 m after 100 minutes as shown in Fig.79 c. For Eastern Hellenic zone, the Egyptian coast has the maximum wave heights of 7-10 m at Kefr SaberandEl Alamein as shown in Fig.79 e, f. While Alexandria the maximum wave height is 4m at 120 minutes as shown in Fig.79 d. Therefore, the East Hellenic zone is considered as a high hazard location. The travel times of these simulated results are sufficient enough for evacuation plans to be implemented to save people's lives (see Table 8 in Chapter VI). In addition, these simulations can help in the protection of the strategic projects and a number of archaeological sites (e.g. New El Alamein city, Ramses II temple) along the Egyptian coast
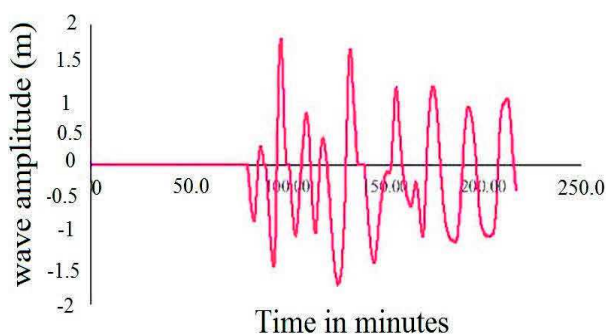
Fig.79 a. Synthetic tide gauge at Kefr Saber in case of west Hellenic scenario
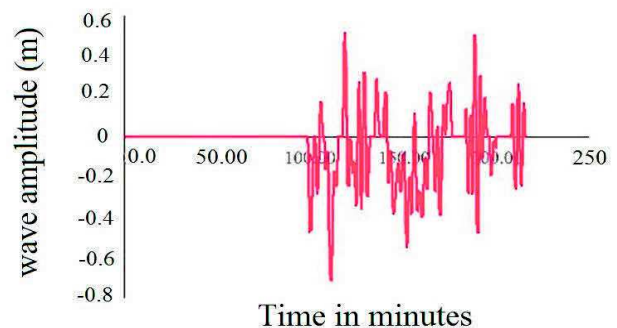
Fig.79 b. Synthetic tide gauge at El Alamein in case of west Hellenic scenario
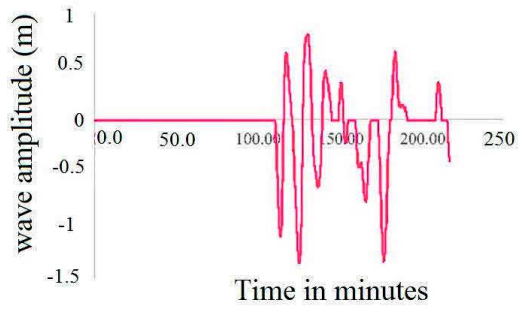
Fig.79 c. Synthetic tide gauge at Alexandria in case of west Hellenic scenario
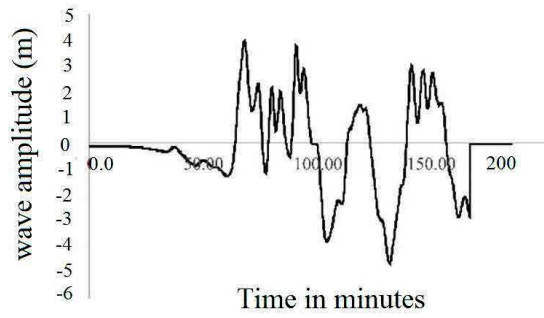
Fig.79 d. Synthetic tide gauge at Alexandria in case of east Hellenic scenario
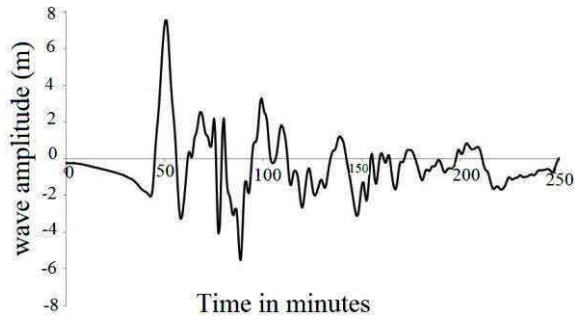
Fig.79 e Synthetic tide gauge at Kefr Saber in case of east Hellenic scenario
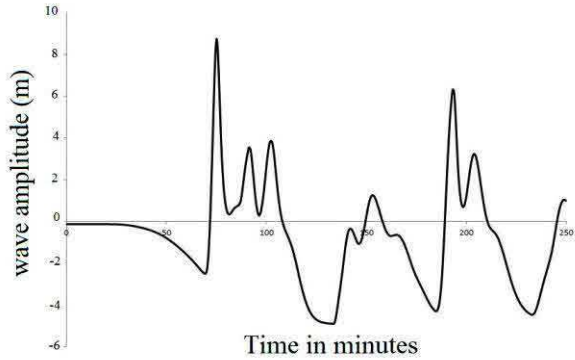
Fig.79 f. Synthetic tide gauge at at EL Alamein in case of east Hellenic scenario

Chapter VI
CONCLUSIONS

The study of historical and instrumental seismicity, the focal mechanisms, stress inversions, GPS velocity vectors and the tectonic geology help me to characterize the seismotectonic of the Eastern Mediterranean and study the impact of past tsunami in the northern Egypt.

Firstly, the Eastern Mediterranean region is considered as a complex tectonics domain that can be studied in the frame of the collision between the Eurasian and African plates. In Eastern Mediterranean, the African plate subducts underneath Eurasia along the Hellenic Arc at a rate of about 0.5-1 cm/year, while the Aegean Sea represents an extensional basin with opening rates in the order of 3.5-4 cm/year (McClusky et al., 2000). In the eastern Mediterranean region, the Cyprian Arc is the expression of the convergence between the Africa plate and the Anatolia microplate and characterized by the formation of Eratosthenes Seamount. It has been deformed in late Cenozoic (Ben Avraham et al.,1988; Kempler and Garfunkel, 1994). The Cyprian arc connected to the Hellenic arc in the West, and Dead Sea Transform Fault and East Anatolian Fault in the East. A northward subduction of oceanic material related to the African Plate beneath the Anatolian Plate indicates the convergent mode along the western segment of the Cyprian arc (Ben Avraham et al.,1988).

Secondly, six seismic active zones are identified from the study of seismicity and tectonic geology in the north of Egypt. The six zones are the Egyptian continental margin, Dahashour zone, Cairo-Suez zone, Northern Gulf of Suez, Southern Gulf of Suez, Gulf of Aqaba. My works include the collecting of fault plane solutions of earthquakes in the six active seismic zones of northern Egypt and calculating the stress inversions of the fault parameters in these active zones using the Tensor software version 5.8.5 (Windows version; last updated on 27/07/2016, http://www.damiendelvaux.be/Tensor/WinTensor/win-tensor.html).

The first active zone in the north Egypt; is the Egyptian continental zone (A) which was located to the south of the Mediterranean Sea ridge behind the Herodotus abyssal plain where the sea floor is occupied by the Nile Deep-Sea fan, Eratosthenes Seamount, and Herodotus basin. It represents a transition zone between the continental–oceanic crusts where the stress field changes from dominant tension inland of Egypt to dominant compression along the Hellenic Arc. The tectonic framework and structural pattern of the Egyptian continental margin are the results of the interplay between three main fault trends:

the northwest-southeast Temsah zone; the northeast-southwest Rosetta zone, and the east-west to ENE-WSW continental fault trends (Abdel Aal et al., 1994).

The largest historical seismic events of the Egyptian continental margin are the 320 and 956 AD earthquakes, while the largest instrumental earthquake occurred on September 12, 1955 with Ms 6.7 (Costantinescu et al., 1966) in the continental shelf of the Nile Delta. The historical AD 320 and 956 seismic events occurred north of the epicenter of September 12, 1955 (Ms =6.8) earthquake (Korrat et al., 2005). These earthquakes were followed by other large events that occurred within 57 years on the October 19, 2012 event at 03:35:11.2, with Mb 5.1 according to the Euro-Mediterranean Seismological Centre (EMSC). The EL Alamein recent earthquake occurred on September 03, 2015 (M_L = 4.5) and the fault of El Alamein was considered as a continuation of AL Qattara–EL Alamein fault zone which extends from the Rosetta area in the continental margin.

The results of 19 collected focal mechanisms in the Egyptian continental margin (Zone A, trend A, B (Fig.18) and adjacent area show two types of tectonic regimes: The first group of mechanisms is represented by NW Oblique (normal –dextral) faults and the second is compressive represented by E-W to ENE (reverse – left-lateral) faults. The stress inversion of in our study of the Egyptian continental margin zone is classified in two main trends A, B. The stress inversion of trend A of 10 collected focal mechanism with normal faulting with strike-slip components stress regime index R ' = 0.67 of the Tensor quality is B. The trend A represents the stresses in the Rosetta trend and continued with the stress distribution from Alexandria to El Alamein margin (Qattara EL Alamein Ridge). The stress inversion of trend B included 8 focal mechanism solutions. This trend represents the stresses parallel to the Rosetta trend until Mars Matrouh area. The stress regime index R' of trend B is 2.12 and shows pure compressive (TF) with Tensor Quality B.

The Tamash and Baltim trends in the east of continental margin are characterized by low-level of seismicity data. The stress orientation from breakout study of Tingay et al. (2011) using 11 wells in the front of the Nile Delta indicates a dominant N-S to NE-SW Sh. max orientation and a secondary E-W to NW-SE orientation. Our stress results do not agree with break hole data of (Tingay et al., 2011) in case of Rosetta trend this due to that the borehole data have a shallow depth rather than the depth of the earthquakes.

The second active zone in northern Egypt is Dahshour zone (B). This zone is located in the northern part of the Western Desert and in the west of the Cairo – Suez zone. The largest event in the Dahshour zone with M_L 5.9 is the 12 October 1992 event which has great damage mainly in Cairo (see chapter III for detail information). 15 collected focal mechanisms in this zone show normal faulting with nodal planes trending NW-SE to E-W with strike-slip component (Maamoun et al., 1993; Hussein, 1999). The stress inversion

calculated in the Dahshour zone results from 19 focal mechanisms in this zone yielding extensive stress regime characterized by NE-SW trending faults with N25°E Shmin. The stress index R' is 0.69 with consistent with normal faulting and strike-slip component; the Tensor quality is B. These results agree with stress inversion calculated by Hussein et al. (2013).

The third active zone in the northern Egypt is the Cairo Suez Zone (C) located West the Gulf of Suez following the Cairo Suez road and north of the Eastern Desert. The two large earthquakes events occurred on September 29, 1984, $M_{L=}$ 4.5 and 29 April 29, 1974 of M_L=4.6. Most of the mechanisms recorded mainly show pure normal faults and oblique source of the normal component with E-W and NWN-SES and NW-SE trends in accordance with the general strike direction of exposed faults. The stress tensor inversions are applied to 12 focal mechanisms events for the Cairo-Suez zone. The inversion of focal mechanisms of earthquakes in this zone yields extensive stress regime characterized by NE-SW trending faults with N18.7°E Sh-min. The stress index is R'=0.69 representing a normal fault with strike faults (transtensive) component with Tensor quality A. The rotational optimization of actual faults shows quality A stress tensor.

The fourth active zone located in the northern Egypt is north of the Gulf of Suez zone (D) and it is considered as a Neogene continental rift which has evolved as one arm of the Sinai triple junction together with the Gulf of Aqaba and the Red Sea. Dagett et al. (1986) considered it as an active zone in spite of no large earthquakes occurred in this zone. The 15 collected focal solutions are characterized by normal faulting mechanisms. The nodal planes have directions close to NW-SE to NNW-SSE. The rest of solutions exhibit either oblique or pure strike-slip motions. 14 focal mechanisms events for the northern Gulf of Suez are applied to stress tensor inversions. The inversion of focal mechanisms of earthquakes in this zone yields pure extensive stress regime characterized by NE-SW trending faults with N44E Sh-min. The stress regime index is R'=0.64. This value is consistent with a normal faulting and extensional regime, where the rotational optimization of the actual faults show Tensor quality A.

The fifth active zone in the northern Egypt is the southern Gulf of Suez (E). Two largest earthquakes are recorded in this zone which is the Shadwan Island earthquakes on 31 March 1969 (M_L=6.1); and 28 June 1972 (M_L=5.0). The 29 collected focal mechanism normal faulting mechanisms with NW-SE trends. The stress tensor inversions were applied to 28 focal mechanisms of the south of the Gulf of Suez. The inversion of focal mechanisms of earthquakes in this zone yields extensive stress regime characterized by NE-SW trending faults with N27.8°E Sh-min. The stress regime index is R'=0.51 and Tensor quality A.

The sixth active zone in northern Egypt is the Gulf of Aqaba zone (F, G subzones) considered as a source region of intense activity which forms the main tectonic plate boundary between Africa (Sinai) and Arabia. The largest recorded and strongest earthquake (Mw=7.2) occurred on November 22, 1995. The 36 focal solutions show normal faulting with left-lateral strike-slip component or strike-slip fault with minor normal component, while some events reflect normal faulting mechanism. Most of the events show T-axes approximately in the NNE to N-S and NW direction. The stress tensor inversions were applied to 7 focal mechanisms events for Gulf of Aqaba zone subzone F. This zone is located north of 29° latitudes. The inversion of focal mechanisms in this zone shows normal faulting, where the stress regime index is R'=0.89, N72.3ºE for Sh-min and Tensor quality are A. The subzone G is located south of 29° latitudes, where the stress tensor inversions are applied to 27 focal mechanisms. The stress regime index is R'=0.98, with N 59.3° E Shmin and Tensor Quality A. The inversion of focal mechanisms of earthquakes in this zone yields a normal faulting with strike-slip component.

To complete the picture of the deformation and direction of stresses, I compiled: a) GPS velocity vectors to estimate the strain rate (Reilinger et al., 2006); b) stress inversion calculated in this study using Tensor program version 5.8.6 of 23/11/2016 (Delvaux et al., 2010); c) the stresses calculated by petroleum boreholes breakout studies (Tingay, 2011); d) the stresses of the world stress map (http://www.world-stress-map.org/) in the Eastern Mediterranean region and northern Egypt to have complete picture of the present-day stress distribution. The main conclusion of stress results shows that the whole northern Egypt is under extensional stress regime except for the Egyptian continental margin which shows compressive trends. This stress regime is presently operating in most of the northern Egyptian regions as normal faulting and strike-slip with Shmin trending N-NNE.

From the study of seismotectonic and paleotsunami events of seismic origin in the Eastern and northern Egypt, four active zones are identified to be the source of possible tsunamis. The eastern Hellenic arc, Western Hellenic arc, Cyprian arc, Egyptian continental margin. The Eastern and Western Hellenic arcs are considered as the highest active far-field tectonic zones and a major source of tsunamis that may strike the Egyptian coasts and adjacent Mediterranean regions. The historical seismicity catalogue reports three significant earthquake events of the Hellenic subduction zone with major tsunamis that have affected the Mediterranean coast of Egypt:

1) The earthquake and tsunamigenic event of 21 July 365 (Mw 8.3 – 8.5; Stiros and Drakos, 2006; Shaw et al., 2008),

2) The earthquake and tsunamigenic event of 8 August 1303 (Mw 7.8 – 8.0) (Abu El Fida, 1329)

3) The earthquake and tsunamigenic event of 24 June 1870 (M_L 7 -7.5)(Ben Menahem, 1979).The three events have generated great damage in the coast of Egypt and affected especially the Alexandria city with coastal flooding and inundations (The reported as the water in the new port of Alexandria splashed out onto the quay (Ambraseys 1961).

The others two zones of the less active tsunamis sources are the Cyprus arc and the Egyptian continental margin. The highest magnitude reported in earthquake catalogues for Cyprus is7.5 and refers to the 11 May 1222, AD earthquake. This Earthquake was followed by low tsunami impacts along the Egyptian-Mediterranean coastal zone Ambraseys (1995). The largest earthquakes have occurred in the Egyptian continental margin as example offshore Alexandria earthquake Ms 6.7 on September 12, 1955 (Hussein et al., 2005). It is located in the sedimentary cone of the Nile that poses the potential for landslides tsunamis (Garziglia et al., 2008).

Three successive field works were carried out in June 2014, August 2015, and October 2015 in the northern Egyptian coast. The aim of this field works was to 1) investigate the geology and geomorphology of the north coast of Egypt. 2) To study the successive sequence of the stratigraphy of the in the both EL Alamein and Kefr Saber selected sites and 3) characterize the age of the possible tsunami layers depend from the carbon dating chronology and tsunami signatures.

For the paleotsunami site selection, geomorphological and topographic setting criteria were taken into accounts as well as accessibility in order to avoid urbanization and artificial soil reworking. The geomorphological criteria are:

The first is the presence of large boulders noticed along the coastline in northern Egypt in localities such as Ras El Hekma –Ras ELAlam Rum –Mersa Matrouh - East Mersa Matrouh (Kefr Saber) with rich content of Dendropoma fossils. The calibrated dating of Dendropoma sample at Kefr Saber is 940-1446 AD which may be correlated with a strong and high (> 5m) wave to Kefr Saber coast possibly during that8 August 1303 tsunami. This result coincides with that ofShah-Hosseini et al., (2016) along the same coastline.

The second geomorphological criteria are the presence of coastal sand dunes along the Egyptian Coast.They are composed of loose white oolitic carbonate sands washed from the degradation of oolitic coastal dune ridges with height from 2 to 20 meters. Behind these sand dunes, the third geomorphology criteria are the lagoons or salt marshes found between dissected ridges with sometimes a lower elevation below sea level as West of Marsa Matrouh.

Five trenches were carried out in Kefr Saber ~32-km west of Marsa-Matruh city. 12 cores were carried out in the second selected site of El Alamein. The cores were carried out

using cobra drilling instrument. The size of the trenches were~2 x 1 meter with ~1.5-m-depth and the maximum depth of cores is ~2.6 m.

Trenches are logged and photographed with detailed description and sampling during the field works in Kefr Saber. While the cores carried out in ElAlamein site were split in two half in the NRIAG Laboratory with Fisher Wire. One for archive and the other for the analysis of sedimentation and content. The studied core includes the collection of samples for dating, photography, detail stratigraphic descriptions, X-ray scanning, geochemical analysis and magnetic susceptibility. The main target is to identify the Paleotsunami deposits in the stratigraphic logs according to tsunami signatures.

Two composite sections were constructed to summarize the stratigraphic logs and recognized tsunami layers in Kefr Saber and EL Alamein site with chronology and date simulation of paleotsunami historical events 1600 BC, 21 July 365, 8 August 1303 and a more recent tsunami event on 24 June 1870.

The stratigraphic logs of the trenches in Kefr Saber show mainly one tsunami layer of mixed sand and gravel, and broken shells at depth ~ 35 cm with thickness 20 cm comparable with the 21 July 365 tsunami deposits. The cores in El Alamein show four main layers characterized by fine and coarse sand mixed with broken shells fragments that indicate the occurrence of high-energy sedimentary deposits in the coastal lagoon environment.

The stratigraphic logs in cores show four main tsunami layers; A) The first layer is ~7.5-cm-thick at ~19cm-depth and is made of poorly sorted white sandy deposits with high broken gastropods and lamellibranch fossils. The high value of organic matter and the high peak of magnetic susceptibility reflect a rich content in carbonates and quartz. B) The second layer is ~13-cm-thick at ~50-cm-depth characterized by white sandy deposits intercalated with coarse brown sand with horizontal lamination, poor sorting sediments, rich in total organic matter and a high peak of magnetic susceptibility. C) The third layer ~ 18 cm-thick at 89-cm-depth is made of yellow sand mixed with white sand intercalations, with laminations at the bottom of deposits, vertically and horizontal gastropods directions reflect high wave current, broken shells fragments, rich in total organic matter and pyrite showing a high peak of magnetic susceptibility. D) The fourth tsunami layer is at 151 cm depth with thickness 19 cm. It is characterized by pale yellow sand, medium to fine, with broken shells fragments and extremely poor sorting, with a high peak of magnetic susceptibility, and a high peak of organic matter > 5.5 weight percentage and high amount of gypsum.

Two worst simple scenarios with high possibility active tsunami sources were built up by creating the initial wave of calculated fault ruptures for the Western Hellenic and

Eastern Hellenic arcs. This modelling depends on the presence of geological record of 21 July 365 and 8 August 1303 in the northern Egyptian coast in Kefr Saber and El Alamein.

The location of Eastern and Western Hellenic arc scenarios depends on historical tsunami information for 21 July 365 (Stiros, 2010) and 8 August 1303 (Abu Fida, 1329; Guidoboni and Comastri, 2005). The chosen fault parameters depended on the calculated western Hellenic arc (Stiros, 2010) and of eastern Hellenic arc (Pagnoni et al., 2015) with scenario tests to the focal mechanisms of large earthquakes in the recent time. The magnitudes of earthquakes were estimated to be equal or larger than the highest magnitude recorded in historical times (Table 4). Then we simulate numerically the ensuing tsunamis using the Mirone software (Luis, 2007). The used bathymetry data is the 30 arc seconds grid from the available GEBCO data online, and this in the absence of the more detail resolution (1 or fewer arc seconds) of coastal bathymetry data in my study area.

In the Eastern Hellenic scenario, the computed wave propagation is performed every 0, 33, 50, 66, 80 minutes. After 30 minutes, the initial wave arrives and after 50 minutes where the maximum wave heightreaches7- 10 meters in Kefr Saber and El Alamein sites. In the Western Hellenic scenario, the tsunami wave propagation is computed at 0, 33, 66, 100, 150 minutes. The wave height reached 4-10 m at the arrival time 33 minutes on the Libyan coast. The wave arrives at the Egyptian coast after 66 minutes with slightly low wave height compared with the wave on the Libyan coast. The wave's height arrives at the Egyptian coast with 0.8 – 1.7 m at Kefr Saber and with 0.4 -0.8 m wave height at El Alamein after 100 minutes. The tsunami waves cover the entire Egyptian coast after 150 minutes from the western Hellenic arc source scenario.

My results are compared with previous studies of (Hamouda, 2006) for the Egyptian coast;(Hassan, 2013; Pagnoni et al., 2015) in case of Eastern Hellenic arc scenario, and for the western Hellenic arc (Hamouda, 2009; Shaw et al., 2008, and Pagnoni et al., 2015). My results are in agreement with modelling of (Hassan, 2013) for the wave height at Salloum, Alexandria, Damietta in case of Eastern scenario and appear to be different from the result of (Hamouda, 2005; andPagnoni et al., 2015). My results agree well with the size of tsunami wave inferred from the model of Shaw et al., (2008) wave height to Alexandria in case of the Western Hellenic scenario.

Some perspectives are suggested in this thesis for the seismotectonic and paleotsunami studies as follows:

First, it was not possible the seismotectonics study to do detailed field investigations of the active seismic zones and active Quaternary faults. However, field to Cairo-Suez zone and EL Alamein faults were carried out as primary investigations in October 2015and

reconnaissance were conducted. Neverless, there is no problem to carry out detail field measurements for the El Alamein active quaternary fault for the future perspective.

Secondly for paleotsunami study,

a) Field investigations are planned at the site of sinking Thonis Heracleion city, an old Egyptian historical city located in the Canopic mouth of the Nile, 32 Km northeast from the Alexandria coast. This city was supposedly flooded apparently following a major tsunami

b) Complete the coring and previous investigations in other sites located from Kefr Sabr to Salloum to determine a possible inundation of the historical tsunami inland along the northern Egyptian coast.

c) Creating a possible worst scenario for the arrival time and height of tsunami waves for the strategic projects constructed on the Egyptian coast such as the New El Alamein city and the Egyptian nuclear power plant.

My recommendations are1) the minimum arrival time for the tsunami waves to arrive at the Egyptian coast being 30 minute in case of the Eastern Hellenic arc scenario, and 66 minutes in case of Western Hellenic arc this leaves enough time to take protective measures and send alarms to the civil defence and Egyptian coast and save people lives. The following Table 8, Fig. 80 summarizes the data for decision makers. The warning messages are requiring a close cooperation with the Turkish and Greek Centers of Tsunami studies and are classified according to local, regional, basin-wide. For instance, according to(Salamon et al., 2010) the messages may be related to local (≤100 km), or regional (100-400 km) or basin-wide (≥400 km) distances. In case of the Egyptian coastal zones, we consider the east Hellenic arc (EHA) and Western Hellenic arc (WHA) are the regional message of 100-400 km.

2) The whole subduction Hellenic zone represents a serious tsunami hazard for the eastern Mediterranean and as evidence from tsunami deposits analyzed in this study. The probable activation of the Hellenic arc or even the Cyprian arc with a major earthquakes Mw >8 will generate a strong tsunami on the Egyptian coast. Therefore, the first step for civil protection is in the preparation of the early warning system and evacuation plan for a probable near future tsunami effects on the Egyptian coasts.

Table 8: Summary of the possible warning tsunami message, EHA and WHA are the most dangerous tsunami sources.

Depth	Location	Mw	Tsunami Potential	Tsunami Message Type			Possible Tsunami sources	Compared with historical events	Comments in the Egyptian coast
				Local	Regional	Basin Wide			
< 100 Km	Under the Sea	7 – 7.5	Potential Destructive local tsunami	Watch	Advisory	Information	Off shore of Nile Delta (possible simulated volume 41 km3 simulated land slide)	None	22 minutes' arrival time of the initial wave of 2.3 m wave height at Ras at Tin 37 minutes' arrival time of intail wave of 4.0 at Rasheed Yalciner et al. (2014)
		7.5-8.0	Potential Destructive for regional Tsunami	Watch	Watch	Advisory	Cyprus Arc	11 May 1222	0.6 m wave height of the initial arrival time 66 minutes Hassan (2013)
							EHA, WHA, Cyprus, Egyptian continental margin	24 June 1870	Only historical information of wave at the Alexandria harbour
		>8	Potential for a very Destructive Regional Tsunami	Watch	Watch	Watch	EHA	8 August 1303	7-10 m wave height of arrival time wave 33 minutes intial arrive at Egyptian coast (This study)
							WHA	21 July 365	1.7 m wave height of arrival time wave of 66 minutes at the Egyptian coast (This study)
	Inland	>7.0	No potential tsunami	Information	Information	Information	--------	-------	----
>100 km	Under sea or in land	>7.0	No potential tsunami	Information	Information	Information	-------	-------	------
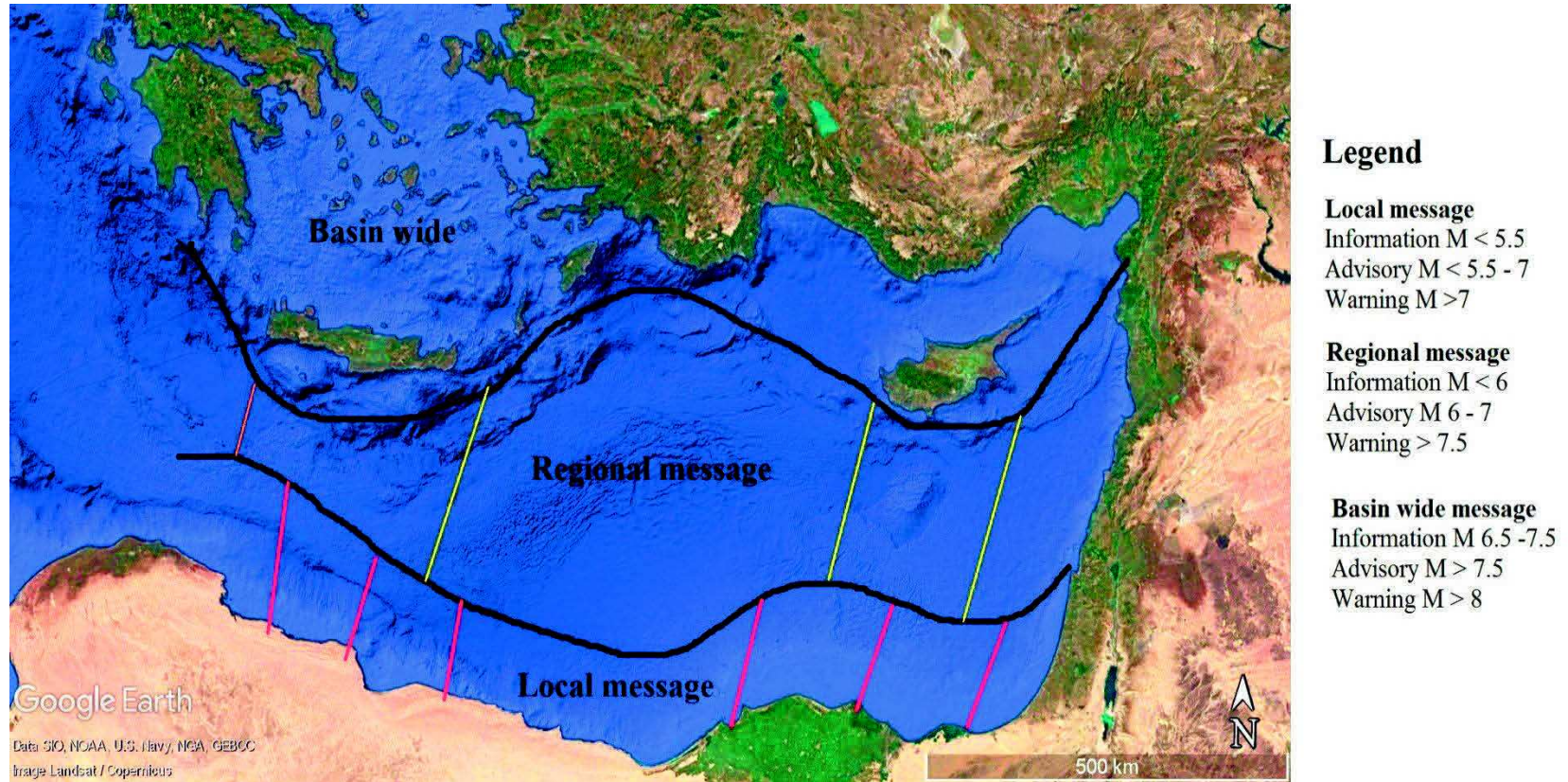
Fig . 80: The message types in case of local, regional, basin-wide with earthquakes magnitude.

REFERENCES

Abdel Aal, A. and A.R. Moustafa (1988). Structural framework of the Abu Gharadig basin, Western Desert, Egypt. Proceedings of the 9th Exploration Conference, Egyptian General Petroleum Corporation, Cairo.

Abdel Aal, A.; Day, R. and Lelek, J. (1992). Structural evolution and styles of the northern Sinai, Egypt. 11th Exploration & Production Conference, Egyptian General Petroleum Corporation, Cairo, Egypt, p. 547-562.

Abdel Aal, A., Price, R.J., Vaital, J.D., Sharallow, J.A., (1994). Tectonic evaluation of the Nile Delta, its impact on sedimentation and hydrocarbon potential. In: EGPC 12th Exploration and Production Conference, Vol. 1, p.19–34.

Abdel Aal, A., El Barkooky, a., Gerrits, M., Meyer, H., Schwander, M., and Zaki, H., (2000). Tectonic evolution of the Eastern Mediterranean Basin and its significance for hydrocarbon prospectivity in the ultradeepwater of the Nile Delta: The Leading Edge, Vol. 19, p. 1086, doi: 10.1190/1.1438485.

Abd El-Aal, A.K. (2008), Simulating time-histories and pseudo-spectral accerela- tions from the 1992 Cairo earthquake at the proposed El-Fayoum New City site, Egypt, Acta Geophys. Vol.56 ,no. 4, p.1025-1042.

Abdel Fattah, A. K., Hussein, H.M. and El Hady, S., (2006). Another look at the 1993 and 1995 Gulf of Aqaba earthquake from the analysis of teleseismic waveforms. Acta Geophysica, Vol.54, no.3, p.260-279.

AFattah, A.K., H.M. Hussein, E.M. Ibrahim and A.S. Abu El Atta, (1997). "Fault plane so- lutions of 1993 and 1995 Gulf of Aqaba earthquakes and their tectonic implications", Annali di Geofisica ,Vol. 40, no. 6, p. 1555-1564.

Abdel-Fattah, R., (1999). Seismotectonic Studies on the Gulf of Suez Region, Egypt. M.Sc. Thesis. Fac. of Sci., Geology Dept. Mansoura Univ.

Abdel-Fattah, A.K., Badawy, A., and Kim, K.Y., (2007). Normal faulting mechanisms in the Western Desert of Egypt: Journal of Seismology, Vol. 11, p. 27–38, doi: 10.1007/s10950-006-9025-z.

Abou Elenean, K.M., (1997), Seismotectonics of Egypt in relation to the Mediterranean and Red Sea tectonics. Ph.D. Thesis, Fac. Sci. Ain Shams Univ., Egypt.

Abou Elenean, K., Arvidsson, R. and Kulhanek, O., (2004). Focal mechanism of smaller earthquakes close to VBB Kottamia station, Egypt. Annals of the Geological Survey of Egypt, XXVII, p.357-368.

Abou Elenean, K. M. (2007), Focal mechanisms of small and moderate size earthquakes recorded by the Egyptian National Seismic Network (ENSN), Egypt, NRIAG J. Geophys., Vol. 6, no. 1, p.119–153.

Abou Elenean, K. M. and Hussein, H. M. (2007): Source mechanism and source parameters of May 28, 1998 earthquake, Egypt, J. Seismol.,Vol. 11, p.259–274.

Abu al-Fida Ismail Ibn Hamwi (born 1273 – died 1331), (1329). The Concise History of Humanity or Chronicles (in Arabic), 2 volumes, pp.1112, Dar El Kutub El Illmiyah (DKI), Beirut, ISBN: 2745104497

Aigner, T. and Reineck, H.E., (1982). Proximality trends in modern storm sands from the Helgoland Bight (North Sea) and their implications for basin analysis. Senckenbergiana maritima, Vol.14 no.5, p.183-215.

Aksu, A. E., Hall, J. & Yaltirak, C. (2005). Miocene to Recent tectonic evolution of the Eastern Mediterranean: new pieces of the old Mediterranean puzzle. Marine Geology, Vol. 221, p. 1–440.

Abd-Allah, A. M. A. (2009) Surface structural investigation of North Western Desert, Egypt, Internal geology report NRIAG, pp.34

Al-Suyuti, Jalal al-Din (15th cent.) Kashf al-salsala 'an wasf al-zalzala. Abd al-Latif Sa'adani (ed), Fez (1971). Also B: BM MS Or.5852, 1768; P: BNP MSS Ar.5929, (1706); C: Cairo NM MS N324; CB: Cambridge Or.8.172, (1760); L: Lahore BMOpuscula 14521.c.37, 1890; for a recent translation in Russian see Buniyatov 1983.

Ambraseys , N., (1962). Data for the investigation of the seismic sea waves in the Eastern Mediterranean. « Bull. Seism. Soc. Am., », Vol.52, no. 4, p. 895-913.

Ambraseys, N.N., Melville, C.P. and Adams, R.D., (2005). The seismicity of Egypt, Arabia and the Red Sea: a historical review. Cambridge University Press.pp.181

Ambraseys, N., (2009). Earthquakes in the Mediterranean and Middle East: A Multidisciplinary Study of Seismicity up to 1900, pp. 947 , Cambridge University Press, ISBN: 9780521872928.

Angelier, J. (1979). Determination of the mean principal directions of stresses for a given fault population, Tectonophysics, Vol.56, p.17-26.

Angelier, J., (1984).Tectonic analysis of fault slip data sets. J. Geophys. Res. 89, p. 5835–5848.

Angelier, J. (1989). From orientation to magnitudes in paleostress determinations using fault slip data. Journal of Structural Geology, Vol.11, p. 37–50, doi: 10.1016/0191-8141(89)90034-5.

Angelier, J., (1991). Inversion directe de recherche 4-D: comparaison physique et mathématique de deux méthodes de détermination des tenseurs des paléocontraintes en tectonique de failles. C.R. Acad Sci., Paris. Vol.312 no.2, p.1213–1218.

Arsenikos, S., Frizon de Lamotte, D., Rooke, N.C., Mohn, G., Bonneau, M. C., Blanpied, C., (2013). Mechanism and timing of tectonic inversion in Cyrenaica (Libya): Integration in the geodynamics of the East Mediterranean', Tectonophysics. Elsevier B.V., Vol.608, p. 319–329. doi: 10.1016/j.tecto.2013.09.025.

ArcGIS Desktop ESRI (2014). Release v. 10.2 Redlands, CA: Environmental Systems Research Institute.(http://desktop.arcgis.com/en/).

Badawy, A., Horvath, F., (1999). Recent stress field of the Sinai subplate region. Tectonophysics Vol.304,p. 385–403.

Badawy, A. (2001). The present-day stress field in Egypt. Ann. Geofis., Vol. 44, p. 557-570.

Bellahsen, N., C. Faccenna, F. Funiciello, J. M. Daniel, and L. Jolivet (2003), Why did Arabia separate from Africa? Insights from 3-D labora- tory experiments, Earth and Plan Sci. Lett., Vol.216, p. 365–381, doi:10.1016/ S0012-821X(03)00516-8.

Ben Menahem, A. (1979), Earthquake catalogue for the Middle East (92 B.C. to 1980 A.D.) Bol. Geof. Teor.ed Applic., Vol.2I, p.245-310.

Ben-Avraham, Z., (1985). Structural framework of the gulf of Elat (Aqaba), northern Red Sea, J. Geophys. Res.-Sol. Ea., Vol.90, p.703–726.

Ben-Avraham, Z., Kempler, D. & Ginzburg, A., (1988). Plate convergence in the Cyprian Arc, Tectonophysics, Vol.146, p. 231–240.

Benetatos, C., Kiratzi, A., Papazachos, C., and Karakaisis, G., (2004). Focal mechanisms of shallow and intermediate depth earthquakes along the Hellenic Arc: Vol. 37, p. 253–296, doi: 10.1016/j.jog.2004.02.002.

Billi, A., C. Faccenna, O. Bellier, L. Minelli, G. Neri, C. Piromallo, D. Presti, D. Scrocca, and E. Serpelloni (2011). Recent tectonic reorganization of the Nubia-Eurasia convergent boundary heading for the closure of the western Mediterranean, Bull. la Soc. Geol. Fr., Vol. 182 no.4, p. 279–303, doi:10.2113/gssgfbull.182.4.279

Bohnhoff, M., Harjes, H.P., and Meier, T., (2005). Deformation and stress regimes in the Hellenic subduction zone from focal mechanisms: Journal of Seismology, Vol. 9, p. 341–366, doi: 10.1007/s10950-005-8720-5.

Borrero, J.C., Sieh, K., Chlieh, M. and Synolakis, C.E., (2006). Tsunami inundation modeling for western Sumatra. Proceedings of the National Academy of Sciences, Vol..103 no.52, p.19673-19677.

Bosworth, W. (2008). North Africa-Mediterranean present-day stress field transition and implications for fractured reservoir production in the eastern Libya basins, Geol. East Libya Vol.4, p.123–138.

Bosworth, W. and Taviani, M. (1996). Late Quaternary reorientation of stress field and extension direction in the southern Gulf of Suez, Egypt: Evidence from uplifted coral

terraces, mesoscopic fault arrays, and borehole breakouts. Tectonics, Vol.15, p. 791-802.

Bott, M. H. P. (1959). The mechanism of oblique-slip faulting. Geological Magazine, Vol.96, p. 109-117.

Bourgeois, J., Pinegina, T. K., Titov, V., Landis, S., and Mann, C. (1999). Bathymetric and topographic effects of the 1969 Ozernoi tsunami: runup evidence from tsunami deposits at Stolbovaya, Kamchatka, Russia, Eos (Transactions, AGU), 80, 46, F751.

Bowman, S.(1990). Radiocarbondating, Berkeley : University of California Press ; [London] : British Museum, ©1990,ISBN: 0-520-07037-2, pp.64.

Bertrand, S., Leroy, S., Cagatay, N., Doner, L., Sancar, U., Akcer, S., Yusal, F., Arz, H., Fagel, N., Oncel, S., Costa, P.,Tomaz, V., Mehta, L., (2005). Sedimentology of Hersek Lagoon, NW Turkey. Relationships with Tsunamis in the sea of Mamara, project annual report, Brunel University West London, pp. 66

Bridge, J.S. (2008). Sedimentary features of tsunami deposits, Sedimentary Geology 211: 94.

Bronk Ramsey, C., (2001). Development of the radiocarbon calibration program: Radiocarbon, Vol. 43, no. 2, p. 355–363.

Bronk Ramsey, C., (2009). Bayesian analysis of Radiocarbon Radiocarbon, Vol. 51, no. 1, p. 337–360.

Bronk Ramsey, C., & Lee, S. (2013). Recent and Planned Developments of the Program OxCal. Radiocarbon, Vol.55(2-3), p.720-730.

Burwell, D, Tolkova, E and Chawla A (2007) Diffusion and dispersion characterization of a numerical tsunami model, Ocean Modelling,19.

Carey-Gailhardis, E. & Mercier, J. -L. (1987). A numerical method for determining the state of stress using focal mechanisms of earthquake populations: application to Tibetan teleseisms and micro seismicity of southern Peru. Earth and Planetary Sciences Letters, Vol. 82, p. 165-179.

Cavazza,W., Roure, F.M., Spakman,W., Stampfli, G.M., Ziegler, P.A., (2004). The TRANSMED Atlas. The Mediterranean region from crust to mantle geological and geophysical framework. A Publication of the Mediterranean Consortiumfor the 32nd International Geological Congress 2004, XXIV, Vol. 141, pp. 44.

Chagué-Goff, C. (2010): Chemical signatures of palaeotsunamis: A forgotten proxy? In: Marine Geology Vol. 271, p. 67–71.

Chenet, P., Colletta, B., Letouzey, J., Desforges, G., Ousset, E. and Zaghloul, E., A., (1985). Décollement and extensional tectonics on the eastern margin of the Suez rift, Symposium on Continental Extensional Tectonics, University of Durham, 1985, abstr. 24.

Cisternas, M., Atwater, B.F., Torrejón, F., Sawai, Y., Machuca, G., Lagos, M., Eipert, A., Youlton, C., Salgado, I., Kamataki, T., Shishikura, M., Rajendran, C.P., Malik, J.K., Rizal, Y., et al., (2005). Predecessors of the giant 1960 Chile earthquake: Nature, Vol. 437, p. 404–407, doi: 10.1038/nature03943.

Cita, M.B., Camerlenghi, A., Rimoldi, B., (1996). Deep-sea tsunami deposits in the eastern Mediterranean: new evidence and depositional models. Sedimentary Geology Vo.l 104, p. 155–173.

Clague, J.J. and Bobrowsky, P.T., (1994). Tsunami deposits beneath tidal marshes on Vancouver Island, British Columbia. Geological Society of America Bulletin, Vol.106 no.10, p.1293-1303.

Constantinescu, L., Ruprechtova, L. and Enescu, D., (1966). Mediterranean-Alpine earthquake mechanisms and their seismotectonic implications. Geophysical Journal International, Vol. 10 no.4, p.347-368.

Cook, H. E., Johnson, P. D., Matti, J. C. & Zemmels, I., (1975). Methods of sample preparation and x-ray diffraction data analysis, x-ray mineralogy laboratory. In: Kaneps, A. G. (Ed.), Initial reports of the DSDP 28, Washington DC, p.997-1007.

CMT catalogue: Centroid Moment Tensor catalogue of Harvard, http://www.seismology.harvard.edusearch.html.

Dalal, N., Torab, M., (2013). Large boulders deposites on the coast of Ras El Hekma, NW, Egypt. storm or tsunami. The 2nd international symposium on Kaz Mountains and Edremit, May 2-4, Edremit-Balikesir- Turkey, pp.8.

Daggett, P.H., Morgan, P., Boulos, F.K., Hennin, S.F., El-Sherif, A.A., El-Sayed, A.A., Basta, N.Z. and Melek, Y.S., (1986). Seismicity and active tectonics of the Egyptian Red Sea margin and the northern Red Sea. Tectonophysics, v.12 5 no.4, p.313-324.

Dahanayake, K. and Kulasena, N., (2008). Geological evidence for paleo-tsunamis in Sri Lanka. Science of Tsunami Hazards, Vol.27 no.2, p.54.

Dawson, A.G. and Shi, S., (2000). Tsunami deposits. Pure & Applied Geophysics, Vol. 157(6-8), p.875.

Dawson, S., Smith, D.E., Ruffman, A. and Shi, S., (1996). The diatom biostratigraphy of tsunami sediments: examples from recent and middle Holocene events. Physics and Chemistry of the Earth, Vol.21(1-2), p.87-92

De Martini, P.M., Barbano, M.S., Pantosti, D., Smedile, A., Pirrotta, C., Del Carlo, P., and Pinzi, S., (2012). Geological evidence for paleotsunamis along eastern Sicily (Italy): An overview: Natural Hazards and Earth System Sciences, Vol. 12, no. 8, p. 2569–2580, doi: 10.5194/nhess-12-2569-2012.

Delvaux, D., Moeys, R., Stapel, G. et al. (1997). Paleostress reconstructions and geodynamics of the Baikal region, Central Asia. Part II: Cenozoic tectonics stress and fault kinematics. Tectonophyscis, Vol.282 (1-4), p.1-38.

Delvaux, D. and Sperner, B. (2003), New aspects of tectonic stress inversion with reference to the TENSOR program. Geological Society, London, Special Publications, Vol. 212, p. 75- 100 , DOI: 10.1144/GSL.SP.2003.212.01.06.

Delvaux, D., and Barth, A., (2010), African stress pattern from formal inversion of focal mechanism data: Tectonophysics, Vol. 482, p. 105–128, doi: 10.1016/j.tecto.2009.05.009.

Dominey-Howes, D.T.M., Papadopoulos, G.A. and Dawson, A.G. (2000), Geological and historical investigation of the 1650 Mt. Columbo (Thera Island) eruption and tsunami, Aegean Sea, Greece. Natural Hazards.

Dunbar, D., LeBlond, P.H.; Murty, T.S. (1989) Maximum tsunami amplitudes and associated currents on the coast of British Columbia. Science of Tsunami Hazards Vol. 7, p. 3-44.

Dupin, J. -M., SASSI, W. & Angellier, J. (1993). Homogeneous stress hypothesis and actual fault slip: a distinct element analysis. Journal of Structural Geology, Vol.15, p.1033-1043

Egyptian National seismic network (ENSN) Bulletin (1998-2004). Earthquakes in and around Egypt. National Research Institute of Astronomy and Geophysics (NRIAG), Egypt.

El-Bastwasy, M.A., (2008). The Use of Remote Sensing and GIS for Catchments Delination in Northwestern Coast of Egypt: An Assessment of water Resources and Soil Potential., Egypt J Remote Sensing Space Sci, p. 3-16.

Emad Mohamed, K., Hassoup, A., Abou Elenean, K.M., Adel Othman, A.A., Diaa-Eldin Hamed, M.K., (2015). Earthquakes focal mechanism and stress field pattern in the northeastern part of Egypt. NRIAG J. Astron. Geophys. Vol.4, p. 205–221.

El-Sayed, A., Korrat, I., and Hussein, H. M., (2004). Seismicity and seismic hazard in Alexandria (Egypt) and its surroundings. Pure Appl. Geophys.,Vol. 161, p.1003–1019,589 doi:10.1007/s00024-003-2488-8.

EMRA Egyptian Mineral Resource map (2008), unpublished geological, personal contact with Mohamed M. Masnour (Director of regional geology department in Egyptian mineral resources authority)

EMSC. Eastern Mediternean seismological center, https://www.emsc-csem.org/#2

ETOPO1 1 min arc-minute global relief model of Earth's surface; https://www.ngdc.noaa.gov/mgg/global/.

Folk, R.L. and Ward, W.C., (1957). Brazos River bar: a study in the significance of grain

Folk, R.L.,(1968), Petrology of sedimentary rocks, in Austin, Texas (HemphilPs Book Store). Journal of Sedimentary Research, Vol. 27(1).

Font, E., C. Nascimento, M.A. Baptista & P.F. Silva (2010): Identification of tsunami - induced deposits using numerical modelling and rock magnetism techniques: A

study case of the 1755 Lisbon tsunami in Algarve, Portugal. In: Physics of the Earth and Planets Interiors Vol.182, p. 187–198.

Frieslander, U. (2000). The structure of the Dead Sea transform emphasizing the Arava, using new geophysical data [in Hebrew, English Abstract], PhD thesis, pp. 43–53, Hebrew Univ., Jerusalem, Israel.

Fuhrman, D.R and Bingham, H.B. (2004). Numerical solutions of fully non-linear and highly dispersive Boussinesq equations in two horizontal dimensions, International Journal for Numerical Methods in Fluids, Vol.44, p.231–255.

Galanopoulos, A.G., (1957). The seismic sea-wave of 9 Iouliou 1956. Praktika Academy Athens, Vol. 32, p. 90–101 (in Greek with Engl. abstr.).

Garfunkel, Z. and Bartov, Y., (1977). The tectonics of the Suez Rift, Israel Geol. Surv. Bull., Vol. 71, p.1- 44.

Garfunkel, Z., (1981). Internal structure of the Dead Sea leaky trans- form (rift) in relation to plate kinematics. Tectonophysics Vol.80, p.81–108.

Garfunkel, Z., (2004). Origin of the Eastern Mediterranean Basin: a reevaluation. Tectonophysics Vol. 391, p. 11–34.

Garziglia, S.,Migeon, S., Ducassou, E., Loncke, L.,Mascle, J., (2008). Mass transport deposits on the Rosetta province (northwest Nile deep-sea turbidite system, Egyptian mar- gin): characteristics, distribution and potential causal processes. Marine Geology Vol. 250, p. 180–198. http://dx.doi.org/10.1016/j.margeo.2008.01.016.

Gaullier, V., Mart, Y., Bellaiche, G., Mascle, J., Vendeville, B., Zitter, T. The Second Leg PRISMED II Scientific Party, (2000). Salt tectonics in and around the Nile Deep-Sea Fan: insights from PRISMED II cruise. In: Vendeville, B., Mart, Y., Vigneresse, J.-L. (Eds.), Salt, Shale and Igneous Diapirs in and Around Europe, Special Publications, Vol. 174. Geological Society, London, p. 111–129.

GEBCO,(2014). Digital Atlas published by the British Oceanographic Data Centre on behalf of IOC and IHO, Bathymetry data 30 arc second.

Gelfenbaum, G. and Jaffe, B., (2003). Erosion and sedimentation from the 17 July, 1998 Papua New Guinea tsunami. In Landslide Tsunamis: Recent Findings and Research Directions p. 1969-1999. Birkhäuser Basel.

Gephart, J. W., and D. W. Forsyth, (1984). An Improved Method for Determining the Regional Stress Tensor Using Earthquake Focal Mechanism Data - Application to the San-Fernando Earthquake Sequence, J. Geophys. Res., Vol. 89, p. 9305-9320.

Gerardi, F. et al. (2012). Geological Record of Tsunami Inundations in Pantano Morghella (South-Eastern Sicily) Both from near and Far-Field Sources." Natural Hazards and Earth System Sciences 12:1185–1200.

Gergawi, A. and El-Khashab, H.M.A. (1968). Seismicity of Egypt, Helwan Observatory Bull., Vol.76.

Geological map of Libya (1985).http://www.sepmstrata.org/page.aspx?pageid=143

GFZ German Research Centre for Geosciences, http://www.gfz-potsdam.de/startseite/

Goto C., Ogawa Y., Shuto N., Imamura N. (1997): Numerical method of tsunami simulation with the leap-frog scheme (IUGG/IOC Time Project), IOC Manual, UNESCO No 35.

Guidoboni, E., (1994). Catalogue of Ancient Earthquakes in the Mediterranean area up to the 10th century, Instituto Nazionale di Geofisica Rome, pp.504 .

Guidoboni, E., and A. Comastri (2005). Catalogue of earthquakes and tsunamis in the Mediterranean area from the 11th to the 15th century, INGV-SGA, Bologna, 1037 pp.

Gunatilake, A. (2005) The Indian Ocean megatsunami of December 2004: the scientific basis of the Catastrophe. Journal of National Science Foundation, Sri Lanka, Vol. 33,p. 69-80

Guidoboni, E. and J. E. E. (2009) Guidoboni, E. and J. E. Ebel. Cambridge University Press.pp.584 doi: 978-0-521-83795-8.

Hamouda, A.Z. (2002), Tsunami data base of the Eastern Mediterranean, Bull. Nat. Inst. Oceanogr. Fish. Vol. 28,p. 437-452.

Hamouda, A.Z. (2006), Numerical compuations of 1303 tsunamigenic propagation towards Alexandria, Egyptian coast, J. African Earth Sciences 44, 37-44, DOI: 10.1016/j.jafrearsci.2005.11.005

Hamouda, A.Z., (2009). A reanalysis of the AD 365 tsunami impact along the Egyptian Mediterranean coast, ActaGeophysica, Vol. 58, no. 4, p. 687–704, doi: 10.2478/s11600-009-0032-7.

Hampton, M.A., Lee H.J. and Locat, J. (1996) Submarine Landslides. Reviews of Geophysics, **34**, pp33–59.

Hany Mohammed Hassan El Sayed, (2013), Impacts on Egyptian Coastal zones Eastern Mediterranean Tsunamigenic Earthquakes and their Geology, Ms., El Azhar University, faculty of science, geology department , Cairo, Egypt, pp.116.

Haraguchi T, Iwamatsu A (2011) Detailed maps of the impacts of the 2011 Japan tsunami: Vol. 1: Aomori, Iwate and Miyagi prefectures. Kokon-Shoin Publishers Ltd, Tokyo

Hartman, G., Niemi, T. M., Tibor, G., Ben-Avraham, Z., Al Zoubi, A., Makovsky,Y., Akawwi,E., Abueladas, A.-R., and Al Ruzouq, R., (2014). Quaternary tectonic evolution of the Northern Gulf of Elat/Aqaba along the Dead Sea Transform, J. Geophys. Res.Sol. Ea., Vol. 119, p. 9183–9205, doi:10.1002/2013JB010879.

Haslett, S.K., Bryant, E.A., 2007. Reconnaissance of historic (post-AD 1000) highenergy deposits along the Atlantic coasts of southwest Britain, Ireland and Brittany, France. Marine Geology Vol.242, p.207–220

Heidbach, O., Tingay, M., Barth, A., Reinecker, J., Kurfeß, D., and Müller, B., (2010). Global crustal stress pattern based on the World Stress Map database release 2008, Tectonophysics, Vol. 482, p. 3–15, doi: 10.1016/j.tecto.2009.07.023.

Hofstetter A, Thio HK, Shamir G (2003). Source mechanism of the 22/11/95 gulf of Aqaba Earthquake and its aftershock sequence. J Seismol Vol.7, p.99–114.

Huntley, D. J. and Clague, J. J., (1996). Optical dating of tsunami-laid sands. Quaternary Research, Vol. 46 no.2, p.127-140.

Hussein, H.M., (1989). Earthquake activities in Egypt and adjacent regions and its relation to geotectonic features in A.R.E. MSc. Thesis. Fac. of Sci., Geology Dept., Mansoura University, Egypt.

Hussein, H., Korrat, I.M and Abdel Fattah, A. K., (1996). The October 12, 1992 Cairo earthquake a complex multiple shock. Bull. Int. Inst. Seis. Earthquake Eng., Vol. 30, p.9-21.

Hussein, H.M., (1999). Source process of October 12, 1992 Cairo earthquake. Ann. Geofis. Vol. 42 no.4, p.665–675.

Hussein, H.M., Korrat, I.M., El Sayed, A., (2001). Seismicity in the vicinity of Alexandria and its implications to seismic Hazard. In: Second International Symposium on Geophysics, 19–20 February 2001. Faculty of Science, Tanta University, Tanta, p. 57–64.

Hussein, H, M., Abu Elenean, K. M., (2008). Source parameters of the significant earthquakes in Egypt, 1992-1998 inferred from P-waves magnitude spectra of teleseismic seismograms. Geofizika journal, Vol. 25, no.1, p.1-26.

Hussein, H.M., Abou Elenean, K.M., Marzouk, I.A., Korrat, I.M., Abu El-Nader, I.F., Ghazala, H., and ElGabry, M.N., (2013). Present-day tectonic stress regime in Egypt and surrounding area based on inversion of earthquake focal mechanisms: Journal of African Earth Sciences, Vol. 81, p. 1–15, doi: 10.1016/j.jafrearsci.2012.12.002.

Ibrahim, E.M. and Marzouk, I., (1979). Seismotectonic study of Egypt. Bull. Helwan Inst. Astro. and Geophysics.

Imamura, F., (1997). Numerical Method of Tsunami Numerical Simulation with Leap-Frog Scheme. Time Project. IUGG/ IOC, UNESCO, Paris

IRIS . Incorporated ReserchInstitutation for seismology, http://ds.iris.edu/seismon.

Ishimura, Daisuke and Takahiro Miyauchi. (2015). Historical and Paleo-Tsunami Deposits during the Last 4000 Years and Their Correlations with Historical Tsunami Events in Koyadori on the Sanriku Coast, Northeastern Japan." Progress in Earth and Planetary Science Vol.2 no.1-16. Retrieved (http://www.progearthplanetsci.com/content/2/1/16).

Ismail, A., (1960). Near and local earthquakes at Helwan from 1903-1950, Helwan Observatory Bull. No. 49.

Jackson J, McKenize D. (1984). Active tectonics in the Alpine– Himalayan belt between western Turkey and Pakistan. Geophys J R Astron Soc Vol. 77, p.185–246.

Jagodziński, R., B. Sternal, W. Szczuciński & S. Lorenc (2009). Heavy minerals in 2004 tsunami deposits on Kho Khao Island, Thailand. In: Polish Journal of Environmental Studies Vol.18 no.1, p. 103–110.

Jones, J. O. (1925). A method for determining thr degree of humification of soil organic matter, jour.AGR. SCI. [ENGLAND] VOL..15, P. 26-29.

Kebeasy, R.M., Maamoun, M., Ibrahim, E., Megahed, A., Simpson, D.W., Leith, W.S., (1987). Earthquake studies at Aswan reservoir. J. Geodyn. Vol. 7, p.173–193.

Kebeasy, R.M., (1990). Seismicity. In: R. Said (Eds). The Geology of Egypt, Balkema, Rotterdam, p. 51-59.

Kelsey, H. M., A. R. Nelson, E. Hemphill-Haley, and R. C. Witter (2005), Tsunami history of an Oregon coastal lake reveals a 4600 yr record of great earth- quakes on the Cascadia subduction zone, Geol. Soc. Am. Bull.,Vol. 117, p. 1009–1032.

Kempler, D. and Garfunkel, Z., (1994). Structures and kinematics in the northeastern Mediterranean: a study of an irregular plate boundary. Tectonophysics,Vol. 234(1-2), pp.19-32.

Kench, P. S., R. F. McLean, R. W. Brander, S. L. Nichol, S. G. Smithers, M. R. Ford, K. E. Parnell and M. Aslam, (2006). Geological effects of tsunami on mid-ocean atoll islands: The Maldives before and after the Sumatran tsunami. Geology, Vol.34, p. 177-180.

Khater, M. (1992). Reconnaissance report on the Cairo, Egypt Earthquake of October 12, 1992. Technical Report NCEER-92-0033, SUNY-Buffalo, Buffalo, NY.

Kokinou, E., Moisidi, M., Tsanaki, I.,Tsakalaki, E.,Tsiskaki, E., Sarris, A., Vallianatos, F., (2008). A seismotectonic study for the Heraklion basin in Crete (Southern Hellenic Arc, Greece), International Journal of Geology, ISSUE 1, Vol. 2, p.9-10.

Korrat, I.M., El Agami, N.L., Hussein, H.M., El-Gabry, M.N. (2005), Seismotectonics of the passive continental margin of Egypt, Journal of African Earth Sciences Vol.41. p. 145–150.

Kortekaas, S. & A.G. Dawson (2007). Distinguishing tsunami and storm deposits: An example from Martinhal, SW Portugal. In: Sedimentary Geology Vol.200, p.208–221.

Kurian N. P., P. Abilash P. Pillai, K. Rajith, B. T. Murali Krishnan and P. Kalaiarasan, (2006). Inundation characteristics and geomorphological impacts of December 2004 tsunami on Kerala coast. Current Science, Vol.90 no.2, p. 240-249

Lavigne, F., C. Gomez, M. Giffo, P. Wassmer, C. Hoebreck, D. Mardiatno, J. Prioyono and R. Paris, R., (2007). Field Observations of the 17 July 2006 tsunami in Java. Nat. Hazards Earth Syst. Sci., Vol.7, p.177-183

Le Pichon, X., Gaulier, J.-M., (1988). The rotation of Arabia and the Levant fault system. Tectonophysics Vol.153, p. 271–294.

Loncke, l., Gaullier, V., Mascle, J., Vendeville, B., (2002). Shallow structure of the Nile Deep Sea Fan: Interactions between structural heritage and salt tectonics; consequences on sedimentary dispersal. CIESM workshop Meditteranean and Black Sea Turbidite systems and Deep Sea Fans, Bucharest, p.5–8 .

Luis, J.F., (2007). Mirone: A multi-purpose tool for exploring grid data: Computers and Geosciences, Vol. 33, p. 31–41, doi: 10.1016/j.cageo.2006.05.005.

Maamoun, M., (1976). La seismicite du Moyen et du proche- orient dans le cadre de la seismotectonique mondiale, These-Doct. Es Science, univ. Louis Pasteur de Strasbourg, France.

Maamoun M, Ibrahim E M (1978). Tectonic acti vity in Egypt as indicated by eart hquakes. Helwan Observatory Bull. No. 170, Helwan.

Maamoun, M., Allam, A., Megahed, A. and El Ata, A., (1980). Neotectonic and seismic regionalization of Egypt, Bull. Int. Instr. Seismol. Earthquake Eng. (Cairo), Vol.18, p. 27-39.

Maamoun, M., Megahed, A. and Allam, A., (1984). Seismicity of Egypt: NRIAG Bull., IV (B), p. 109–160.

Maamoun, M., Megahed, A., Ibrahim, E., (1993). Detailed Studies of 12 October, 1992 Earthquake (Unpublished, Report, NRIAG)

Madder, C. L., (2004). Numerical Modeling of Water Waves. Second ed.CRC Press, Boca Raton, FL, pp. 288.

Madsen, H.B., Bingham, and Liu, H. (2002) A new Boussinesq method for fully nonlinear waves from shallow to deep water, Journal of Fluid Mechanics, Vol.462, p.1–30.

Mahmoud, S., R. Reilinger, S. McClusky, P. Vernant, and A. Tealeb (2005). GPS evidence for northward motion of the Sinai block: Implications for E. Mediterranean tectonics, Earth and Plan. Sci. Lett., Vol.238, p.217-227.

Mahmoud, Y., F. Masson, M. Meghraoui, Z. Cakir, A. Alchalbi, H. Yavasoglu, O. Yönlü, M. Daoud, S. Ergintav, S. Inan, (2013), Kinematic study at the junction of the East Anatolian fault and the Dead Sea fault from GPS measurements, Journal of Geodynamics Vol.67, p. 30– 39.

Malik, J.N., Banerjee, C., Khan, A., Johnson, F.C., Shishikura, M., Satake, K., and Singhvi, A.K., (2015). Stratigraphic evidence for earthquakes and tsunamis on the west coast of South Andaman Island, India during the past 1000years: Tectonophysics, Vol. 661, p. 49–65, doi: 10.1016/j.tecto.2015.07.038.

Maouche, S., Morhange, C. and Meghraoui, M., (2009). Large boulder accumulation on the Algerian coast evidence tsunami events in the western Mediterranean. Marine Geology, Vol.262 no.1, p.96-104

Mascle, J., Benkhelil, J., Bellaiche, G., Zitter, T., Woodside, J., Loncke, L. (2000). The PRISMED II Scientific Party (including V. Gaullier), Marine geological evidences for a Levantine-Sinai plate, a missing piece of the Meditteranean puzzle. Geology Vol. 28 no.9, p. 779– 782.

Matsutomi, H., N. Shuto, F. Imamura and T. Takahashi (2001). Field Survey of the 1996 Irian Jaya earthquake tsunami in Biak Island. Natural Hazards,Vol. 24,p. 199–212.

Mcclusky, S., Balassanian, S., Barka, A., Demir, C., Ergintav, S., Georgiev, I., Gurkan, O., Hamburger, M., Hurst, K., Kahle, H., Kastens, K., Kekelidze, G., King, R., Kotzev, V., (2000). Global Positioning System constraints on plate kinematics and dynamics in the eastern TM , Vol. 105, p. 5695–5719.

McClusky, S., Reilinger, R., Mahmoud, S., Ben Sari, D. and Tealeb, A., (2003). GPS constraints on Africa (Nubia) and Arabia plate motions. Geophysical Journal International, Vol.155 no.1, p.126-138.

McKenzie, D. P. (1972). Active tectonics of the Mediterranean region. Geophysical Journal Royal Astronomical Society Vol. 30, p.109-l 85.

MED_RCMT. MedNet Regional Moment Centroid Moment Tensors, http://www.ingv.it/seismoglo/RCMT.

Megahed, A and Dessokey, M.M.(1988). The Isamailyia (Egypt) earthquake of January 2nd, location, macroseismic survey, radiation pattern of the first motion and its tectonics. Bull. ISSEE, Vol.23, p.143-153

Meghraoui, M., Pondrelli, S., (2012). Active faulting and transpression tectonics along the plate boundary in North Africa. Ann. Geophys. Vol.55 (5), pp.5, http://dx.doi.org/10.4401/ag-4970.

Mercier, J.L., Carey-Gailhardis, E., Sébrier, M., Stein, S., Mercier, J.L., Hancock, P. and England, P., (1991). Palaeostress determinations from fault kinematics: Application to the neotectonics of the Himalayas-Tibet and the Central Andes. Philosophical Transactions: Physical Sciences and Engineering, pp.41-52.

Meshref, W.M., (1990). Tectonic framework of Egypt. In the geology of Egypt edited by Rushdi Said, A.A. Balkema, Rotterdam, Netherlands, p. 133-155

Minoura, K., F. Imamura, T. Takahashi and N. Shuto, (1997). Sequence of sedimentation processes caused by the 1992 Flores tsunami; evidence from Babi Island. Geology, Vol.25, p. 523-526

Mori, N., Takahashi, T., Yasuda, T. and Yanagisawa, H. (2011) Survey of 2011 Tohoku earthquake tsunami inundation and run-up. Geophys. Res. Lett. 38, L00G14.

Mosconi, A., A. Rebora, G. Venturino, P. Bocc, and M. H. Khalil (1996). Egypt–Nile Delta and North Sinai Cenozoic tectonic evolutionary model: A proposal, Production Conference, Cairo, Egypt, Vol. I, p. 203–223.

Mosher, D.C., Austin, J.A., Fisher, D. and Gulick, S.P.S. (2008) Deformation of the northern Sumatra accretionary prism from high-resolution seismic reflection profiles and ROV observations. Marine Geology, Vol. 252, p.89-99.

Moustafa, A.R. and Khalil, M.H. (1989): North Sinai structures and tectonic evolution. M.E.R.C. Ain Shams University Earth Sciences Series, Vol. 3, p. 215-231.

Moustafa, A.R. and Khalil, M.H. (1990), Structural characteristics and tectonic evolution of north Sinai fold belts. In R. Said "Geology of Egypt". A.A. Balkema , Rotterd Brookfield, p. 381-389.

Moustafa, A., Abd-Allah, A., (1992). Transfer zones with en echelon faulting at the northern end of the Suez rift. Tectonics Vol.11, p.499–509.

Moustafa, A. R. (1993). Structural characteristics and tectonic evolution of the east-margin blocks of the Suez rift. Tectonophysics, Vol.223, p. 381-399.

Moustafa, A. and Khalil, M. (1994). Rejuvenation of the eastern Mediterranean passive continental margin in northern and central Sinai; new data from the Themed Fault, Gel.Mag., Vol.p.435-448.

Moustafa, A. R. & Khalil, M. H. (1995). Superposed deformation in the northern Suez rift, Egypt: relevance to hydrocarbons exploration. Journal of Petroleum Geology, Vol. 18, p. 245-266

Moustafa, A.R. (1995). Internal structure and deformation of an accommodation zone in the northern of the Suez rift and Red Sea. Journal of structural geology, Vol.18, p.93-107.

Moustafa, S., (2002). Assessment of ground motion variation for seismic hazard mitigation in the vicinity of Cairo metropolitan area, Ph.D. thesis, Ain Shams Univ. Cairo, Egypt.

Myers, E.P. and Baptista, A.M., (1995). Finite element modeling of the July 12, 1993 Hokkaido Nansei-Oki tsunami. pure and applied geophysics, Vol.144 no.3, p.769-801.

Nakata, T. and Kawana, T., (1995). Historical and prehistorical large tsunamis in the southern Ryukyus, Japan. In Tsunami: Progress in Prediction, Disaster Prevention and Warning, p. 211-221. Springer Netherlands.

Nanayama, F., Satake, K., Furukawa, R., Shimokawa, K., Atwater, B.F., Shigeno, K., and Yamaki, S., (2003). unusually large earthquakes inferred from tsunami deposits along the Kuril trench: Nature, Vol. 424, no. 6949, p. 660–663, doi: 10.1038/nature01864.

Nandasena NAK, Paris R, Tanaka N (2011) Reassessment of hydrodynamic equations: minimum flow velocity to initiate boulder transport by high energy events (storms, tsunamis). Mar. Geol. Vol. 281, p.70–84.

Neev D, Hall JK, Saul J.M. (1982). The Pelusium megashear system across Africa and associated lineament swarms. J Geophys Res. doi:10.1029/JB87Ib02P01015.

NEIC. National Earthquakes Information Center, http//neic.usgs.gov/, http//earthquakes.usgs.gov/regioanl/neic

Nishimura, Y. and Miyaji, N. (1995). Tsunami deposits from the 1993 Southwest Hokkaido earthquake and the 1640 Hokkaido Ko- magatake eruption, northern Japan. In: Tsunamis; 1992-1994, their generation, dynamics, and hazard, (Eds) Satake-Kenji and Imamura-Fumihiko, Pure and Applied Geophysics, Vol.144, 3/4, p. 719–733.

Nocquet, J.M., (2012). Present-day kinematics of the Mediterranean: A comprehensive overview of GPS results: Tectonophysics, Vol. 579, p. 220–242, doi: 10.1016/j.tecto.2012.03.037.

Obura, D., (2006). Impacts of the 26 December 2004 tsunami in Eastern Africa. Ocean & Coastal Management, Vol.49 no.11, pp.873-888..

O'Handley, Robert C. (2000). Modern Magnetic Materials. Hoboken, NJ: Wiley, pp.789, ISBN 9780471155669.

Okada, Y., (1985). Surface deformation due to shear and tensile faults in a half space. The Bulletin of the Seismological Society of America Vol. 75, p.1135–1154.

Orwig R.O. (1982). Tectonic framework of Northern Egypt and the Eastern Mediterranean region, 6th exploration and production conference, Vol. 1, p 193–202.

Ozel, M. N., Necmioglu, O., Yalciner, A.C., Kalafat, D., Mustafa, E. (2011). Tsunami hazard in the Eastern Mediterraneanand its connected seas: Toward a Tsunami warning center in Turkey, Soil Dynamics and Earthquake Engineering, Volume 31, Issue 4, April 2011, Pages 598–610.

Pagnoni, G., A. Armigliato, and S. Tinti. (2015). "Scenario-Based Assessment of Buildings' Damage and Population Exposure due to Earthquake-Induced Tsunamis for the Town of Alexandria, Egypt." Natural Hazards and Earth System Sciences, Vol.15, Isssue 12,2015,p.2669-2695.

Panagiotakis, C., Kokinou, E. and Vallianatos, F., (2008). Automatic $ P $-Phase Picking Based on Local-Maxima Distribution. IEEE Transactions on Geoscience and Remote Sensing, Vol..4 no.68, pp.2280-2287.

Papadopoulos, G.A., Daskalaki, E., Fokaefs, A., and Giraleas, N., (2007). Tsunami hazards in the Eastern Mediterranean: strong earthquakes and tsunamis in the East Hellenic Arc and Trench system: Natural Hazards And Earth System Science, Vol. 7, p. 57–64, doi: 10.5194/nhess-7-57-2007.

Papadopoulos GA, Gra`cia E, Urgeles R, Sallares V., (2014). Historical and pre-historical tsunamis in the Mediterranean and its connected seas: geological signatures, generation mechanisms and coastal impacts. Mar Geol, Vol. 354, p. 81–109.

Papazachos, B., Kiratzi, A., Karacostas, B., Panagiotopoulos, D., Scordilis, E. and Mountrakis, D.M., (1988). Surface fault traces, fault plane solution and spatial distribution of the aftershocks of the September 13, 1986 earthquake of Kalamata (Southern Greece). pure and applied geophysics, Vo.126 no.1, p.55-68.

Papazachos, B.C., (1990). Seismicity of the Aegean and the surrounding area. Tectonophysics Vol.178, p.287–308.

Papazachos, B.C., 1996, Large seismic faults in the Hellenic arc: Annals of Geophysics, Vol. 39, p. 891–903.

Paris, R., F. Lavigne, P. Wassmer, and J. Sartohadi. (2007). Coastal sedimentation associated with the December 26, 2004 tsunami in Lhok Nga, West Banda Aceh (Sumatra, Indonesia). Marine Geology Vol.238, p. 93–106.

Pecharsky, V.K. and P.Y. Zavalij, (2009). Fundamentals of Powder Diffraction and Structural Characterization of Materials. 2009: Springer US., pp.713

Pietrantonio, G., Devoti, R., Mahmoud, S., and Riguzzi, F., (2016). Kinematics of the Suez-Sinai area from combined GPS velocity field: Journal of Geodynamics, Vol. 102, p. 231–238, doi: 10.1016/j.jog.2016.10.003.

Pirazzoli, P.A., Ausseil-Badie, J., Giresse, P., Hadjidaki, E., Arnold, M., (1992). Historical envi- ronmental changes at Phalasarna harbour,West Crete. Geoarchaeology Vol.7, p.371–392.

Pirazzoli, P.A., J. Laborel, and S.C. Stiros (1996). Earthquake clustering in the East- ern Mediterranean during historical times, J. Geophys. Res. Vol.101, p. 6083- 6097.

Poirier, J. P. & Taher, M.A., (1980). Historical seismicity in the near and middle east, North Africa, and Spain from Arabic Documents (VIIth-XVIIIth Century): Bulletin of the Seismological Society of America, Vol. 70, p. 2185–2201.

Pollard, D. D., Saltzer, S. D. & Rubin, A. (1993). Stress inversion methods: are they based on faulty assumptions? Journal of Structural Geology, Vol.15(8), p.1045-1054.

Polonia, A., Bonatti, E., Camerlenghi, A., Lucchi, R.G., Panieri, G., and Gasperini, L., (2013), Mediterranean megaturbidite triggered by the AD 365 Crete earthquake and tsunami: Scientific Reports, 3: 1285, p.2045-2322, doi:10.1038/srep01285.

Power, W. L. (compiler). 2013. Review of Tsunami Hazard in New Zealand (2013 Update), GNS Science Consultancy Report 2013/131. pp. 222 .

Ramsay, J. G., Huber, M. I. and Lisle, R. J. (2000) 'The Techniques of Modern Structural Geology: Applications of continuum mechanics in structural geology, Vol. 3, pp. 1061. doi: 10.1016/S0040-1951(01)00270-0.

Raslan, S.M., (1995). Geomorpholiogical and hydrogeological studies on some localities along the Northwestern Coast of Egypt,M.Sc. Menofia University, pp.172.

Reches, Z., (1987). Faulting of rocks in three-dimensional strain fields. II. Theoretical analysis, Tecttonophysics, Vol. 95, p.133-156.

Reilinger, R., McClusky, S., Vernant, P., Lawrence, S., Ergintav, S., Cakmak, R., Ozener, H., Kadirov, F., Guliev, I., Stepanyan, R., Nadariya, M., Hahubia, G., Mahmoud, S., Sakr, K., et al., (2006). GPS constraints on continental deformation in the Africa-Arabia-Eurasia continental collision zone and implications for the dynamics of plate interactions: Journal of Geophysical Research: Solid Earth, Vol. 111, p. 1–26, doi: 10.1029/2005JB004051.

Reimer, P. J., Baillie, M. G. L., Bard, E., Bayliss, A., Beck, J. W., Blackwell, P. G., Bronk Ramsey, C., Buck, C. E., Burr, G. S., Edwards, R. L., Friedrich, M., Grootes, P. M., Guilderson, T. P., Hajdas, I., Heaton, T. J., Hogg, A. G., Hughen, K. A., Kaiser, K. F., Kromer, B., McCormac, F. G., Manning, S. W., Reimer, R. W., Richards, D. A., Southon, J. R., Talamo, S., Turney, C. S. M., van der Plicht, J., & Weyhenmeyer, C. E. (2009). IntCal09 and Marine09 radiocarbon age calibration curves, 0-50,000 years cal BP. Radiocarbon, Vol.51 no. 4, p. 1111-1150.

Reimer PJ, Bard E, Bayliss A, Beck JW, Blackwell PG, Bronk Ramsey C, Buck CE, Edwards RL, Friedrich M, Grootes PM, Guilderson TP, Haflidason H, Hajdas I, Hatté C, Heaton TJ, Hogg AG, Hughen KA, Kaiser KF, Kromer B, Manning SW, Reimer RW, Richards DA, Scott EM, Southon JR, Turney CSM, van der Plicht J. (2013). Selection and treatment of data for radiocarbon calibration: an update to the International Calibration (IntCal) criteria. Radiocarbon Vol.55 no.4, p. 1869-1887

Riad, S., A. Tealeb, S. Hadidy, N. Basta, A. Mohamed, M.A. Aziz, and H.A. Khalil (2003), Ancient earthquakes from some Arabic sources and catalogue of Middle East historical earthquakes, UNESCO pressed.

Richards, S., Lister, G. and Kennett, B. (2007) A slab in depth: Three-dimensional geometry and evolution of the Indo-Australian plate. Geochemistry Geophysics Geosystems, Vol. 8 no.12.

Richter, D., Tostevin, G., Škrdla, P. and Davies, W. (2009) New radiometric ages for the Early Upper Palaeolithic type locality of Brno-Bohunice (Czech Republic): comparison of OSL, IRSL, TL and 14C dating results ,Journal of Archaeological Science, Vol.36 no.3, p.708-720.

Rizzini, A., Vezzani, F., Coccetta, V., Milad, G., (1978). Stratig- raphy and sedimentation of a Neogene–Quaternary section in the Nile delta area. Mar. Geol. Vol. 27, p. 327–348

Robertson, A.H.F. and Dixon, J.E., (1984). Introduction: aspects of the geological evolution of the Eastern Mediterranean. Geological Society, London, Special Publications, Vol.17 no.1, p.1-74.

Robson, A., (1971). The structure of the Gulf of Suez (Clysmic) rift, with special reference to the eastern side. J. Geol. Soc. Vol.127,p. 247–276.

Ross, D. A., and E. Uchupi, (1977). Structure and sedimentary history of southeastern Mediterranean Sea–Nile Cone area:AAPGBul- letin, Vol. 61, no. 6, p. 872–902.

Rothaus, R.M., Reinhardt, E. and Noller, J., (2004). Regional considerations of coastline change, tsunami damage and recovery along the southern coast of the Bay of Izmit (the Kocaeli (Turkey) earthquake of 17 August 1999). Natural Hazards, Vol.31 no.1, p.233-252.

Said, R. (1962) Tectonic framework of Egypt. IN SAID, R. (Ed.) The Geology of Egypt. Amsterdam, Elsevier. pp. 377.

Sakr, Mohamed A., Kamal A. El-sayed, and Enayat A. Awad. (2011). National Seismic Network and Earthquake Activities in Egypt." 5 th International conference on earthquake geotechanicalengineering,Chile pp.11

Salamon, A., Hofstetter, A., Garfunkel, Z., Ron, H., (2003). Seismotectonics of the Sinai subplate—the eastern Mediterranean region. Geophys. J. Int. Vol.155, p.149– 173.

Saleh, M., Becker, M., (2013). A newvelocity field fromthe analysis of the Egyptian Permanent GPS Network (EPGN). Arab. J. Geosci.Vol.7, Issue11, p.4665 - 4682 http://dx.doi.org/10.1007/s12517-013- 1132-x.

Saleh, M., and Becker, M., (2015). New constraints on the Nubia-Sinai-Dead Sea fault crustal motion: Tectonophysics, Vol. 651, p. 79–98, doi: 10.1016/j.tecto.2015.03.015.

Sandiford, M., Coblentz, D. and Schellart, W.P. (2005) Evaluating slab-plate coupling in the Indo-Australian plate. Geology, Vol.33, p.113-116.

Sangode, S.J., Suresh, N., Bagati, (2001). Godavari source in the Bengal fan sediments: Results from magnetic susceptibility dispersal pattern. Current Science Vol. 80 no.5, p. 660-664.

Sato, H., T. Shimamoto, A. Tsutsumi, and E. Kawamoto. (1995). Onshore Tsunami Deposits Caused by the 1993 Southwest Hokkaido and 1983 Japan Sea Earthquakes. Pure and Applied Geophysics Vol. 144, p. 693–717.

Scordilis, E.M., Karakaisis, G.F., Karacostas, B.G., Panagiotopoulos, D.G., Comninakis, P.E., Papazachos, B.C., (1985). Evidence for transform Faulting in the Ionian Sea: The Cephalonia Island earthquake Sequence of 1983. PAGEOPH, Vol.123, p. 388–397

Sehim, A., Ismail, A., Mahmoud, R., (1992). Proposed structural model, Khalada West Concession, Western Desert, Egypt. In: EGPC Eleventh Exploration & Production Conference, November, 1992-Cairo, p. 79–97.

Selim, E. I. (2012). Subsurface structural trends of the offshoreNile Delta area, Egypt: Evidences from gravity and magnetic data, Environ. Earth Sci. Vol. 68, no. 4, p.1015– 1032, doi: 10.1007/s12665-012-1804-y.

Shah-Hosseini, M., Saleem, A., Mahmoud, A. and Morhange, C., (2016)**.**Coastal boulder deposits attesting to large wave impacts on the Mediterranean coast of Egypt', Natural Hazards. Springer Netherlands, Vol. 83(2), p. 849–865. doi: 10.1007/s11069-016-2349-2.

Shaw, B., Ambraseys, N.N., England, P.C., Floyd, M. a., Gorman, G.J., Higham, T.F.G., Jackson, J. a., Nocquet, J.-M., Pain, C.C., and Piggott, M.D., (2008). Eastern Mediterranean tectonics and tsunami hazard inferred from the AD 365 earthquake: Nature Geoscience, Vol. 1, no. April, p. 268–276, doi: 10.1038/ngeo151.

Shepard, F. P., G. A. Macdonald and D. C. Cox, (1950). The tsunami of April 1, 1946 [Hawaii]. Calif. Univ., Scripps Inst. Oceanography Bull.,Vol. 5, p.391-528.

Sieberg A., (1932). Untersuchungenüber Erdbeben und Bruchschollenban im östlichen Mittelmeergebiet. « Denkschriften der Medizinish-Natur- wissenschaftlichen Gesellschaft zu Jena », vol. 2, Jena.

Sofratome Group (1984). El-Dabaa nuclear power plant, National Power Plant Authority (NPPA), Ministry of Electricity, Egypt, Unpublished report.

Soloviev, S.L., Solovieva, O.N., Go, C.N., Kim, K.S., and Shchetnikov, N.A., (2000). Tsunamis in the Mediterranean Sea 2000 B.C.-2000 A.D, pp. 237, Kluwer academic, Dordrecht/ Boston/ London ISBN: 0-7923-6548-8.

Salamon, A., (2010), Potential tsunamigenic sources in the eastern Mediterranean and a decision matrix for a tsunami early warning system in Israel, Report, pp.52.

Stampfli, G.M., Borel, G.D., Cavazza, W., Mosar, J. and Ziegler, P.A., (2001). Palaeotectonic and palaeogeographic evolution of the western Tethys and PeriTethyan domain (IGCP Project 369). Episodes 24 , p.222-228.

Steckler, M.S., Berthelot, F., Liberis, N., Le Pichon, X., (1988). Subsidence in the Gulf of Suez: implications for rifting and plate kinematics. Tectonophysics Vol.153, p. 249–270.

Stiros, S., Papageorigou, S., (2001). Seismicity of Western Crete and the destruction of the town of Kisamos at AD365, archaeological evidence, Journal of Seismology, Vol.5, p.381-397.

Stiros, S.C., (2001). The AD 365 Crete earthquake and possible seismic clustering during the fourth to sixth centuries AD in the Eastern Mediterranean: a review of historical and archaeological data: Journal of Structural Geology, Vol.. 23, p. 545–562, doi: 10.1016/S0191-8141(00)00118-8.

Stiros, S.C., and A. Drakos (2006). A fault-model for the tsunami-associated, magni- tude> 8.5 Eastern Mediterranean, AD 365 earthquake, Z. Geomorphol. Vol. 146, p. 125-137.

Stiros, S.C., (2010). The 8.5+ magnitude, AD365 earthquake in Crete: Coastal uplift, topography changes, archaeological and historical signature: Quaternary International, Vol. 216, p. 54–63, doi: 10.1016/j.quaint.2009.05.005.

Szczuciński, W., P. Niedzielski, G. Rachlewicz, T. Sobczyński, A. Zioła, A. Kowalski, S. Lorenc and J. Siepak, (2005). Contamination of tsunami sediments in a coastal zone inundated by the 26 December 2004 tsunami in Thailand. Environ. Geol., Vol.49, p. 321–331.

Szczuciński, W., P. Niedzielski, L. Kozak, M. Frankowski, A. Zioła and S. Lorenc,(2007). Effects of rainy season on mobilization of contaminants from tsunami deposits left in a coastal zone of Thailand by the 26 December 2004 tsunami. Environ. Geol.,Vol. 53, p. 253-264.

Ten Brink, U. S., M. Rybakov, A. S. Al-Zoubi, M. Hassouneh, U. Frieslander, A. T. Batayneh, V. Goldschmidt, M. N. Daoud, Y. Rotstein, and J. K. Hall (1999). Anatomy of the Dead Sea Transform; does it reflect continuous changes in plate motion?, Geology, Vol.27, p. 887–890.

Ten Brink, U. S., M. Rybakov, A. S. Al-Zoubi, and Y. Rotstein (2007), Magnetic character of a large continental transform: An aeromagnetic survey of the Dead Sea Fault, Geochem. Geophys. Geosyst., 8, Q07005, doi:10.1029/2007GC001582.

Thenhaus, P.C., R.V. Sharp, M. Celebi, A.B.K. Ibrahim, and H. van de Pol (1993). Reconnaissance report on the 12 October 1992 Dahshour, Egypt, Earth- quake, U.S. Geological Survey, Open-File Report 93-181, Golden, CO.

Tingay, M., Bentham, P., de Feyter, A., and Kellner, A., (2011). Present-day stress-field rotations associated with evaporites in the offshore Nile Delta: Bulletin of the Geological Society of America, Vol. 123, p. 1171–1180, doi: 10.1130/B30185.1.

USAID (2005). United States Agency for International Development

Van den Bergh, G. D., W. Boer, H. de Haas, T. C. E. van Weering and R. van Wijhe, (2003). Shallow marine tsunami deposits in Teluk Banten (NW Java, Indonesia), generated by the 1883 Krakatau eruption. Mar. Geol., 197, 13-34.

Vasseur, G., Etchecopar, A., Philip, H., (1983). Stress state inferred from multiple focal mechanisms. Ann. Geophys. Vol.1, p. 291–298.

Velioglu, D., R. Kian, A. C. Yalciner and A. Zaytsev,(2016), Performance Assessment of NAMI DANCE in Tsunami Evolution and Currents Using a Benchmark Problem, J. Mar. Sci. Eng. 2016, 4(3), 49; doi:10.3390/jmse4030049

Wang, P. & M.H. Horwitz (2007). Erosional and depositional characteristics of regional overwash deposits caused by multiple hurricanes, Sedimentology Vol. 54, p. 545–564.

Wheatcroft, R. A. and J. C. Borgeld, (2000). Oceanic flood deposits on the northern California shelf: large-scale distribution and small-scale physical properties. Cont. Shelf Res., Vol.20, p. 2163-2190.

Yalciner, A., Zaytsev, A., Aytore, B., Insel, I., Heidarzadeh, M., Kian, R., and Imamura, F., (2014). A Possible Submarine Landslide and Associated Tsunami at the Northwest Nile Delta, Mediterranean Sea: Oceanography, Vol. 27, no. 2, p. 68–75, doi: 10.5670/oceanog.2014.41.

Yousef, M. I. (1968). Structure pattern of Egypt and its interpretation. AAPG Bull. Vol.52 no.4, p.601-614.

Zahran, A.A., (2008). Geotechnical Study of Carbonate Rocks on the Area Between Alexandria and El Alamein Along The Mediterranean Sea Coast of Egypt. Ass. Univ. Bull. Environ. Res., Vol.11no.1, p.12.

ZUR_RMT. Zurich Moment Tensors, Swiss Seismological service, ETH-Honggerberg, http//seismo.ethz.ch/info/mt.html.

APPENDICES

Appendix A : Focal mechanism and historical earthquakes

Table 1: The earthquakes events in Egyptian continental margin area Magnitude $M_L \geq 4$

Serial no.	Date	Origin Time (GMT)	Longitude	Latitude	Depth	Magnitude
1	19510130	23:07:24	32.4	33.4	0	5.1
2	19550912	6:09:24	29.8	32.9	33	6.7
3	19870429	04:37.6	30.5	31.7	33	4.6
4	19870409	00:04.6	28.97	32.39	10	4.6
5	19870102	10:14:46	30.48	32.22	24.1	3.9
6	19880609	2:18:24	27.9	32.23	10	4.8
7	19871214	21:50:59	30.72	31.69	10	3.9
8	19920522	23:10:44	30.18	32.01	8	4.1
9	19921105	18:41:49	29.69	30.97	16	4.6
10	19950908	12:13:22	29.7	32.23	13	4
11	19960221	4:59:57	29.03	31.37	15	5.3
12	19980528	18:33:28	27.64	31.45	22	5.5
13	19991011	20:39:34	28.65	31.54	12.1	4.9
14	20001216	142708.04	33.56	33.169	37.3	3.3
15	20000601	164438	29.99	32.58	6	2.8
16	20010612	12:43:26	29.62	31.12	0	4.1
17	20040325	24835	30.54	31.74	24.7	3.4
18	20121019	3:35:12	30.98	32.58	18	5.1
19	20130117	21:17:40	30.6	31.98	10	4.9

Table 2: The focal mechanisms parameters Egyptian continental margin area

Serial no.	Plane 1			Plane 2			P-axis		Taxis		References
	Strike	Dip	Rake	strike	Dip	Rake	Tr.	Pl.	Tr.	Pl.	
1	295	64	-116	162	34	-24	168	60	42	17	Costantinescu et al. (1966)
2	118	69	161	215	68	22	342	2	78	28	Costantinescu et al. (1966)
3	326	40	-7	62	84.00	-5	303.8	8	212	0.7	CMT Harvard solution
4	112	70	157	210.26	68.46	21.57	120.3	21.54	22	22	personal communication with Hussein
5	248	80	-170	156	80	-10.00	112	14	22	0	CMT Harvard solution

152

6	266	54	40	149	58	136	209	3	115	57	Korrat et al., 2005
7	197	40	-4	291	87.00	-130	167	35	52	30	CMT Harvard solution
8	326	40	-7	62	85.00	-130	297	36	182	29	CMT Harvard solution
9	337	48	-40	96	61.00	-130	315	54	214	9	Badawy (2001)
10	123	29	-88	310	61.00	-91	217	73	41	16	Abu Elenean et al. (2004)
11	132	30	-104	328	61.00	-82	257	73	52	16	CMT Harvard solution
12	333	43	87	333	43.07	87	67.2	42.93	243	47	Personal communication with Hesham
13	145	32	-28	259	75.00	-119	136	51	11	25	CMT Harvard solution
14	93	73	-6	184.00	85	-163	50	16	318	8	MED- RCMT
15	3	54	-41	120.00	58	-137	333	52	241	2	ENSN
16	104	50	-107	309	43.00	-71	311	77	155	4	ENSN
17	315	48	-66	101.00	47	-114	297	72	28	0.4	ENSN
18	110	58	164	142.4	58	164	52.4	15.01	148.00	20	EMSC
19	56	56	164	155.1	76.79	35.06	65.1	13.21	326.00	34	EMSC

Table 3: The earthquakes events in Dahshour area $M_L \geq 3.5$

Serial no.	Date (Y/M/D)	Origin Time (GMT)	longitude	latitude	Depth	Magnitude
1	19921012	13:09:59	30.63	29.74	22	5.9
2	19921022	17:38:58	31.108	29.621	10	4
3	19921104	16:29:39	31.133	29.716	19.6	3.5
4	19921105	18:41:51	31.133	29.682	16	4.2
5	19921105	18:46:05	31.101	29.661	20.9	3.6
6	19921105	19:16:47	31.133	29.671	20.74	3.9
7	19921106	2:42:03	31.133	29.7	18	3.7
8	19921107	1:35:03	31.133	29.666	21	3.5
9	19921110	11:17:19	31.133	29.656	17.8	4
10	19930310	19:26:52	31.124	29.726	18.16	3.8
11	19930504	20:56:51	31.123	29.68	21	3.7
12	19930513	8:38:26	31.086	29.687	21.7	3.7
13	19930613	6:16:09	31.116	29.671	17.6	3.9
14	20010612	12:43:26	31.12	29.62	31.12	4.1
15	20050731	16:14:37	31.12	29.67	22.7	4.2
16	20080621	17:59:47	30.6	29.8	6.2	4
17	20080602	17:59:46	30.66	29.73	6.67	4
18	20120216	2:15:00	30.68	29.73	4.11	3.6
19	20140728	8:09:00	30.6	29.77	4.33	3.5

Table 4: The focal mechanisms parameters of Dahshour area $M_L \geq 3.5$

Serial no.	Plane 1			Plane 2			P-axis		T-axis		References
	strike	dip	rake	strike	Dip	Rake	Tr.	Pl	Tr.	Pl.	
1	284.2	65.96	-117.7	284.2	65.96	-117.7	155	59	34	16	NEIC
2	278.65	66.74	-107.81	137.78	28.88	-107.81	159	64	22	20	AbouElenean (1997)
3	312.26	54.48	-59.38	86.72	45.54	-125.52	281	65	21	5	AbouElenean (1997)
4	269.55	54.33	-120.79	135.17	45.74	-54.5	120	22	25	12	AbouElenean (1997)
5	256.66	81.36	-150.22	161.74	60.59	-9.93	123	27	26	14	AbouElenean (1997)
6	259.38	81.55	-145.54	163.62	55.97	-10.22	127	30	27	17	AbouElenean (1997)
7	296.15	61.23	-65.99	73.38	36.80	-126.54	249	65	9	13	AbouElenean (1997)
8	243.19	74.03	-121.46	128.97	34.91	-28.74	117	51	357	23	AbouElenean (1997)
9	263.2	78.73	-138.05	163.24	49.04	-15	132	37	27	19	AbouElenean (1997)
10	113.3	58.74	-79.88	274.32	32.70	-106.14	50	74	196	13	AbouElenean (1997)
11	266.52	78.46	-154.67	171.11	65.22	-12.73	131	26	37	9	AbouElenean (1997)
12	132.43	65.65	-64.73	263.57	34.53	-133.32	81	61	204	17	AbouElenean (1997)
13	135.09	62.58	-50.41	254.2	46.84	-140.85	95	54	198	9	AbouElenean (1997)
14	60.65	53.14	-96.61	251.59	37.37	-81.27	311	77	155	4	ENSN
15	117	21	-117	326	72	-80	250	62	48	26	Emad Mohamed 2010
16	303.12	80.47	-23.13	37.16	67.21	-169.11	258	23	352	9	Abdelazim et al., (2016)
17	48	52	-133	285	55	-48	255	57	347	1	Emad Mohamed (2010)
18	47	74	-160	311	71.00	-17	269	26	178	2	Badreldin, (2016)
19	233	70	-165	233	70.00	-165	95	24	186	4	Badreldin, (2016)

Table 5: The earthquakes events in Cairo-Suez area $M_L \geq 3.5$

Serial no.	Date (Y/M/D)	Origin Time (GMT)	Longitude	Latitude	Depth	Magnitude
1	19740429	20:04:38	30.5	31.7	33	4.6
2	19840329	21:36:06	30.18	32.1	10	4.6

3	19870102	10:14:46	30.48	32.22	24.1	3.9
4	19871214	21:05:09	30.72	31.69	10	3.9
5	19920522	23:10:44	30.18	32.01	8	4.1
6	19931024	5:28:44	30.54	32.205	12	3.4
7	19940928	9:38:37	30.65	32.8	23	3.7
8	19961111	16:01:57	30.31	32.25	6	3.8
9	19961112	3:17:52	30.5	32.25	6	3.9
10	19991228	12:05:10	30.24	31.46	15	3.5
11	20020824	20:01:21	30.14	31.35	19.5	3.5
12	20050416	19:55:13	29.63	31.88	6.4	4.2
13	20060225	1:50:08	27.9	33.3	9.7	4
14	20060609	2:10:09	32.03	27.1	21.73	3.6
15	20060303	20:59:17	27.14	33.19	19.53	3.5
16	20071030	14:43:28	31.81	29.78	20.4	3.8
17	20130325	12:40	29.0234	32.293	20.94	4.2
18	20130822	21:43	28.6846	32.3633	20.8	4.2
19	20130917	15:59	29.7381	31.366	6.5	3.73

Table 6: The focal mechanisms parameters of in Cairo-Suez area

Serial no.	Plane 1			Plane 2			P-axis		T-axis		References
	Strike	Dip	Rake	strike	Dip	Rake	Tr.	Pl	Tr.	Pl.	
1	60.92	85.85	-130.02	326	40.20	-6.43	297	36	182	29	CMT Harvard solution
2	54.59	86	152.47	146.67	62.55	4.51	104	16	7	22	CMT Harvard solution
3	156.14	80.15	-10	247.86	80.15	-170	112	14	22	0	CMT Harvard solution
4	290.52	87.04	-130.08	197	40.17	-4.6	167	35	52	30	CMT Harvard solution
5	60.92	85.85	-130.02	326	40.20	-6.43	297	36	182	29	CMT Harvard solution
6	90.24	54.25	-85.46	262.5	36.00	-96.28	19	80	177	9	AbouElenean et al. (2004)
7	117.05	84.90	-141.77	23.04	51.95	-6.49	347	30	244	22	AbouElenean (1997)
8	94.34	71.5	-89.57	272.98	18.51	-91.29	5	63	184	26	AbouElenean et al. (2004)

9	341.56	38.44	-10.39	79.74	83.56	-127.98	316	39	199	28	AbouElenean et al. (2004)
10	78.6	54.20	-119.37	302.49	45.03	-55.79	290	66	189	5	ENSN
11	298.93	54.93	-58.3	71.86	45.87	-126.81	267	64	7	5	ENSN
12	325.24	68.99	-64.09	91.67	32.90	-138.68	271	58	36	20	Abdelazim et al. (2016)
13	141.57	51.41	-47.42	265.74	54.86	-130.29	116	58	23	2	Abdelazim et al. (2016)
14	266	37.00	-99	97	53	-83.00	37	80	182	8	Emad Mohamed, (2010)
15	81.59	46.96	-151.48	331.24	69.57	-46.74	286	47	31	14	Abdelazim et al. (2016)
16	134	62	-54.00	256	45.00	-139	93	56	199	10	Emad Mohamed, (2010)
17	295	38	-154	185	75.00	-55	132	48	249	22	Badreldin,(2016)
18	243	60	-144	133	59.00	-35	99	46	8	1	Badreldin, (2016)
19	184	84	177	274	87.00	6	49	2	139	7	Badreldin, (2016)

Table 7: The earthquakes events in Gulf of Aqaba area$M_L \geq 3.5$

Serial no.	Date (Y/M/D)	Origin Time (GMT)	Longitude	Latitude	Depth	Magnitude
1	19851231	19:42:41	34.9	29.13	9	4.8
2	19930703	23:34:10	34.821	28.864	18	4.7
3	19930803	12:43:05	34.553	28.729	17	6
4	19930803	16:33:24	34.08	28.36	15	5.7
5	19930807	4:55:40	34.626	28.612	10	4.2
6	19930820	23:09:59	34.612	28.72	2	4.6
7	19931103	18:39:32	34.65	28.7	7	4.9
8	19931108	1:06:02	34.65	28.69	8	4.7
9	19931204	23:34:11	34.799	28.886	10	4.6
10	19951122	4:15:26	34.73	29.07	18.4	7.2
11	19951122	12:47:04	34.74	29.3	15	5
12	19951122	22:16:57	34.21	28.32	15	5.2
13	19951123	18:07:26	34.48	29.31	15	5.7

14	19951124	16:43:46	34.74	28.97	10	4.9
15	19951211	1:32:08	34.75	28.92	19	5
16	19960103	10:05:26	35.248	28.604	10	4.8
17	19960108	13:18:00	34.82	29.38	6	3.8
18	19960116	6:17:00	34.73	29.34	6	4.3
19	19960204	7:23:00	34.94	29.45	6	3.6
20	19970510	23:01:48	34.61	28.28	10	4.9
21	20000308	14:22:25	34.695	28.77	7	4.9
22	20000406	6:37:34	34.83	28.78	12	4.8
23	20010207	3:39:00	35.01	29.26	21	4.2
24	20021110	5:09:45	34.62	28.23	16	3.9
25	20040922	12:00:23	34.6	28.45	10.3	3.2
26	20080404	14:05:20	34.75	28.78	6.8	3.7
27	20091229	6:28:44	34.78	28.71	10.9	3.6
28	20111021	16:36:41	34.74	28.52	8.2	4.2
29	20100715	11:25:00	34.846	34.846	22.27	4.4
30	20111021	12:37:00	34.7344	28.5241	9	3.7
31	20111021	16:36:00	34.7366	28.5224	8.23	4.2
32	20111103	11:08:00	34.829	28.0302	4.7	3.78
33	20111103	11:23:00	35.037	28.0575	15	4.34
34	20131006	8:44:00	34.6313	28.0575	6.14	3.86
35	20140130	6:39:00	34.6335	27.775	20.8	3.55
36	20140315	11:57:00	34.6574	27.8517	11.64	3.5

Table 8: The focal mechanisms parameters of in Gulf of Aqaba zone

serial no.	Strike1			Strike 2			P-axis		T-axis		
	Strike	Dip	Rake	strike	Dip	Rake	Tr.	Pl	Tr.	Pl.	References
1	169.04	64.17	-146.81	63.14	60.48	-30.04	28	41	295	2	AbouElenean (1997)
2	83.53	71.88	-151.1	343.79	62.66	-20.5	306	33	212	6	CMT Harvard solution
3	138.72	35.9	-123	357.43	60.54	-68.49	309	67	72	13	CMT Harvard solution
4	356.13	79.41	-82.81	141.64	12.77	-123.82	275	55	80	34	AbouElenean (1997)
5	86.2	76.13	-148.33	347.78	59.35	-16.18	311	32	214	11	AbouElenean (1997)
6	73.99	80.04	-150.11	338.32	60.60	-11.45	300	28	203	13	AbouElenean (1997)
7	75.45	47.25	-150.94	324.79	69.10	-46.6	280	47	25	13	AbouElenean (1997)
8	92.63	73.21	-143.41	350.53	55.20	-20.59	314	38	220	5	AbouElenean (1997)

9	358.91	54.55	-38.18	113.43	59.77	-137.83	329	50	235	3	CMT Harvard solution
10	293.84	77.43	-148.5	196.24	59.34	-14.66	159	31	62	12	Hofstetter et al. (2003)
11	111.03	77.96	-174.99	19.99	85.10	-12.08	335	12	66	5	CMT Harvard solution
12	294.24	81.15	-163.19	201.58	73.39	-9.24	160	18	66	14	CMT Harvard solution
13	199.44	76.57	7.9	166.45	82.31	166.45	154	4	63	15	Badawy and Horvath (1999)
14	158.64	82.79	148.51	253.04	58.79	8.44	210	16	111	27	Hofstetter et al. (2003)
15	72.09	74.51	11.57	338.96	78.86	164.2	26	3	295	19	AbouElenean (1997)
16	116.24	79.84	140.06	214.64	50.81	13.16	171	19	68	35	Hofstetter et al. (2003)
17	180.27	47.3	-83.94	351.37	43.04	-96.53	149	85	266	2	Hofstetter et al. (2003)
18	2.46	6.48	-72.24	164.6	83.83	-91.98	278	89	98	1	Hofstetter et al. (2003)
19	270.22	64.05	-76.21	60.92	29.16	-116.11	207	68	350	18	MED-RCMT
20	114.17	88.69	149.41	204.95	59.42	1.53	164	20	65	22	MED-RCMT
21	303.34	80.49	-119.89	197.32	31.23	-18.57	183	46	57	29	ZUR-RMT
22	309.85	41.15	-117.48	164.49	54.28	-68.04	129	71	239	7	ZUR-RMT
23	134.95	85.1	-169.32	134.95	85.10	-169.32	0	11	269	4	ENSN
24	318.68	59.53	-122.09	189.73	43.09	-47.91	178	61	71	9	ENSN
25	336.9	58.8	-131.53	216.57	50.19	-42.41	192	55	95	5	Emad Mohamed(2010)
26	146	46	-61	287	51.00	-117	132	69	36	3	Abdelazim et al. (2016)
27	317.2	53.34	-115.58	175.92	43.65	-59.88	169	69	65	5	Abdelazim et al. (2016)
28	352.32	54.09	-74.1	146.41	38.83	-110.73	311	75	71	8	Badreldin, (2016)
29	172	65	-37	280	57.00	-150	133	43	-132	5	Badreldin, (2016)
30	148	49	-145	33	64.00	-47	352	50	93	9	Badreldin, (2016)
31	147	49	-128	15	56.00	-58	341	63	83	6	Badreldin, (2016)
32	162	74	-176	71	86.00	-16	26	14	118	8	Badreldin, (2016)
33	351	85	-161	260	71.00	-5	217	17	124	10	Badreldin, (2016)
34	142	73	-15	237	76.00	-162	100	23	9	2	Badreldin, (2016)
35	195	81	-42	293	49.00	-168	145	35	-110	21	Badreldin, (2016)
36	211	83	-27	305	63.00	-172	165	24	-99	13	Badreldin, (2016)

Table 9: The earthquakes events in North Gulf of Suez $M_L \geq 3.5$

Serial no.	Date (year/M/day)	origin Time (GMT)	Longitude	latitude	Depth	Magnitude
1	19830612	12:00:09	33.13	28.55	24	4.8
2	19921020	1:57:58	33.16	28.51	10	3.8

3	19921027	9:04:46	33.11	28.84	10	3.5
4	19921027	11:02:47	33.18	28.78	17	4.2
5	19950908	12:13:22	32.23	29.7	13	4
6	19960915	5:18:11	33.604	28.254	6	4.3
7	20000625	19:18:48	33.48	28.21	18	4.6
8	20001103	21:19:03	32.84	28.93	23	3.5
9	20040706	12:13:51	32.53	29.5	25	3.5
10	20080910	10:01:58	33.34	28.24	13.9	3.7
11	20100309	19:58	33.707	28.1406	8.09	3.9
12	20101024	20:07	33.3022	28.1806	9.7	3.5
13	20130122	0:35	33.1505	28.4277	23	3.9
14	20130601	11:49	33.1506	28.4178	13.3	5.4
15	20140722	3:03	32.77	29.77	22	4.9

Table 10: The focal mechanisms parameters of in the northern Gulf of Suez

	Plane 1			Plane 2			P-axis		T-axis		
Serial no.	Strike	Dip	Rake	Strike	Dip	Rake	Tr.	Pl.	Tr.	Pl.	References
1	129.14	85.8	-9.96	219.88	80.06	-175.73	84	10	175	4	Morsy et al. (2011)
2	157.17	78.09	-50.7	261.32	40.78	-161.59	105	43	218	23	Morsy et al. (2011)
3	319.71	53.06	-98.95	154.39	37.86	-78.32	195	79	56	7	Morsy et al. (2011)
4	154.91	56.97	-66.03	295.71	40	-122	115	68	228	9	Morsy et al. (2011)
5	166.22	61.81	-68.76	306.77	34.76	-124.06	115	66	241	14	Morsy et al. (2011)
6	121.47	76.8	-109.41	358.52	23.33	-35.22	8	54	227	29	Morsy et al. (2011)
7	257.43	52.24	-129.23	130.57	52.24	-50.77	104	60	14	0	AbouElenean (2007)
8	119.77	46.19	-74.67	278.16	45.9	-105.41	108	79	199	0.1	AbouElenean (2007)
9	322.63	51.85	-70.6	112.95	42.12	-112.92	291	74	39	5	Morsy et al. (2011)
10	259.5	73.44	-148.17	159.46	59.63	-19.29	123	34	27	9	Abdelazim et al. 2016
11	189	59	-61	322	41	-129	148	63	101	10	Badreldin, (2016)
12	284	67	-32	28	61	-154	244	38	-23	4	Badreldin, (2016)
13	193	69	-30	28	61	-156	152	36	-115	4	Badreldin, (2016)
14	171	55	-21	273	73	-143	137	38	39	11	Badreldin, (2016)
15	275	79	-124	169	36	-19	150	45	31	26	Badreldin, (2016)

Table 11: The earthquakes events in South Gulf of Suez ML≥ 3.5

Serial No.	Date (Y/M/D)	Origin Time	Longitude	Latitude	Depth	Magnitude
1	19690324	12:50:51	33.8	27.65	33	4.5
2	19690327	6:15:00	33.9	27.5	33	4.5
3	19690331	7:15:54	33.91	27.61	12	6.7
4	19690423	13:37	33.9	27.6	33	4.6
5	19691230	5:11:03	33.9	27.5	33	4.6
6	19700428	3:20:00	33.6	27.7	33	4.6
7	19701219	22:44:11	33.9	27.5	33	4.4
8	19701008	23:40:00	33.7	27.2	33	4.7
9	19720112	15:44.2	33.82	27.55	36	4.7
10	19720628	9:49:35	33.8	27.7	12	5
11	19730305	23:59:50	33.4	27.74	25	4.4
12	19850228	16:55:47	33.72	27.72	10	4.1
13	19940926	17:27:06	34.02	27.75	19	3.6
14	19950315	9:20:35	33.847	27.706	20	4.1
15	19950406	5:25:04	33.858	27.6	16	3.9
16	19950420	10:41:53	33.816	27.608	15	3.8
17	19950809	20:30:33	33.755	27.66	14	3.6
18	19951211	19:08:25	34.001	27.605	19	5
19	19961217	7:21:20	33.769	27.631	15	3.8
20	19961217	11:31:33	33.758	27.642	12	4.2
21	19991223	8:53:14	33.814	27.526	9	3.9
22	20010820	16:31	33.9	27.5	16	3.6
23	20020213	18:52:10	33.67	28	15	3.7
24	20031011	2:28:06	33.8	28.03	16	3.8
25	20041016	17:47:21	34.91	26.74	12.6	3.5
26	20070520	22:01:51	33.8	27.6	6.1	4.2
27	20111119	7:12:15	34.06	27.7	15	4.6
28	20111120	5:16:04	34.24	27.66	15	4.2
29	20130411	3:56	33.4812	27.8088	4.2	3.5

Table 12: The focal mechanisms parameters of in the southern Gulf of Suez

	Plane 1			Plane 2			P-axis		T-axis		
Serial no.	Strike	Dip1	Rake	strike	Dip	Rake	Tr.	Pl.	Tr.	Pl.	References
1	14.57	27.1	154.81	127.29	78.82	65.15	227	10	26	32	Salamon et al. (2003)
2	153.95	62.9	52.2	33.52	45.30	140.14	270	10	15	55	Salamon et al. (2003)
3	293.65	37.01	-89.08	112.51	52.99	-90.69	19	82	203	8	Huang and Solomon (1987)
4	164.45	79.88	-24.05	258.94	66.34	-168.94	119	24	214	9	Salamon et al. (2003)
5	286.02	44.96	-118.81	286.02	44.96	-118.81	133	70	313	20	Salamon et al. (2003)
6	153.5	90	-17.16	243.5	72.84	-180	107	12	200	12	Salamon et al. (2003)
7	333.32	79.98	-86.05	131.67	10.77	-111.3	248	54	60	34	Salamon et al. (2003)
8	159.77	25.04	-79.69	328.42	65.39	-94.78	229	69	62	20	Salamon et al. (2003)
9	92.55	59.27	-44.54	209.24	52.92	-140.17	58	52	152	4	Badawy and Horvath (1999)
10	288.29	40.28	-99.46	120.61	50.38	-82.07	75	82	205	5	Huang and Solomon (1987)
11	143.88	79.63	-159.24	49.98	79.63	-159.24	8	22	276	7	Hussein (1989)
12	288.15	70.78	9.46	195.01	160.54	81.08	243	7	150	20	Salamon et al. (2003)
13	321.09	88.81	-50.41	52.52	39.61	-178.14	264	34	19	32	AbouElenean (1997)
14	270.14	46.66	-139.63	149.88	61.90	-51.08	111	55	213	9	Abdel Fattah (1999)
15	154.97	44.19	-80.15	46.63	321.37	-99.44	160	83	58	1	Abdel Fattah (1999)
16	125.75	78.02	-49.23	229.28	42.20	-162.01	74	42	186	22	AbouElenean (1997)
17	81.45	51.85	-83.79	251.46	38.58	-97.84	25	82	167	7	Megahed (2004)
18	146.31	47.79	-69.58	297.32	46.04	-111.04	129	75	222	1	R Abdel Fattah (1999)
19	133.6	60.48	-98.76	330.98	30.68	-74.94	105	31	12	5	AbouElenean (1997)
20	317.79	64.72	-172.17	330.98	30.68	-74.94	22	73	230	15	Megahed (2004)
21	323.89	79.21	-140.6	225.15	51.43	-13.86	192	35	89	18	AbouElenean (1997)
22	246.91	61.15	-20.63	347.2	72.02	-149.52	210	34	115	7	AbouElenean (2003)
23	94.12	62.97	-130.75	336.31	47.56	-38.01	314	53	212	9	AbouElenean (2007)
24	29.39	39.36	-134.4	261.09	63.06	-60.15	212	59	331	11	ENSN

25	146.73	55.49	-24.6	69.93	251.27	-142.91	114	40	16	9	ENSN
26	147.3	55	-89.58	326.57	35.00	-90.6	59	80	237	10	Abdelazim et al., (2016)
27	143.26	54.34	-72.75	295.21	39.11	-112.46	103	74	221	8	Abdelazim et al. (2016)
28	154.4	56.1	-65.17	294.7	41.13	-122	117	68	227	8	Abdelazim et al. (2016)
29	154	62	-17	252	75.00	-151	115	31	21	8	Badreldin, (2016)

Table 13: Historical earthquakes list in the northern Egypt and Eastern Mediterranean region

Serial no.	Date	Lat	Long.	probable I Am	Ms	Mw	Reference
1	2200 B.C.	30.75	31.5	7			Badawy 1998 after Seiberg 1932 and Maamoun 1984
2	1210 B.C.	22.5	31.5	6			Badawy 1998 after Seiberg 1932
3	600 B.C.	25.55	33	5			Badawy 1998 after Seiberg 1932
4	220 B.C.	36.5	28.2		7.2		Soloviev et al.,2000
5	227 B.C.	36.36	28.15		7.5		Soloviev et al.,2000
6	142 B.C.	36.7	28		7		Soloviev et al.,2000
7	95 B.C.	30.7	32.5	4	5.2		Ambarseys et al.,1994
8	23±3BC	38.15	22.14				Ambrayseys 2009
9	31 BC	31.75	35.5			6	Reches and Hoexter,1981,Guidoboni,1994, Ambraseys2009
10	53/01/ 24 OR 25 AD	35.2	25.1				Ambraseys 2009
11	115 AD	35.15	36.27			7.4	Ambraseys2009, Guidoboni1994, Meghraoui et al.,2003
12	222	36	28	5			Ambrasey N., 1962
13	320 AD	31.5	30	7	6		Ambraseys 1994
14	365/07/12	35.25	23.6			7.5-8	Ambraseys 1994, Papadimetriou 2008
15	520/10/14	31	31	7		5.8	Ambraseys 1994
16	551/7/09	34	35		7.2		Elias et al.2007 & Anna Fokaefs 2005
17	554/10/14	32	30				Guidoboni 1994
18	749/01/18	32.8	35.5			7.3	Guidoboni 1994, Ambraseys2009, Reches and Hoexter 1981
19	794/04/14	36	26	6			Badawy 1998, Ambraseys 1994, Gudoboni 1994
20	796/04	32	30		6		Maamoun et al.(1984)
21	857/04/30	30	31	9			Ambraseys 1994, Gudoboni 1994
22	885/11/06	30.1	31.2	9			Ambraseys 1994, Gudoboni 1994
23	859/01/27	30.5	31.5				Badawy 1998
24	912	30	31	9			Ambraseys 1994, Gudoboni 1994
25	935/10/4	30.5	31.2	9			Ambraseys 1994, Gudoboni 1994
26	950/07/25	30.2	31.2	9			Ambraseys 1994, Gudoboni 1994
27	963/05/12	35	26			5.4	Ambraseys 1994, Gudoboni 1994
28	951/09/15	32	30	9			Ambraseys 1994, Gudoboni 1994
29	956/1/1	34	32	7			Ambraseys 1994, Gudoboni 1994
30	963/05/12	35	26	6			Ambraseys 1994, Gudoboni 1994
31	1068/03/18	29.65	35	7		6.6	Zilberman et al.,2005, Ambraseys 2009
32	1091/02/12	28	34	7			Ambraseys 1994, Gudoboni 1994
33	1170/06/29	33.15	36.27			7.2	Meghraoui et al.,2003, Maghraoui 2016
34	1068/03/18	29.65	35			6.6	Zilberman et al.,2005, Ambraseys 2009
35	1091/02/12	28	34	7			Badawy 1998, Ambraseys 1994

36	1111/08/31	30.03	31.15	9			Badawy 1998, Ambraseys 1994
37	1195 or 1196	27	34	7			Ambraseys 1994
38	1202/05/20	33.75	35.8			7.6	Maghraoui2016
39	1212/05/01	30.25	35.25			7.9	Klinger et al.,200b, Niemi et al.,2001, Ambraseys2009
40	1222/05/11	34.5	32.5	6			Ambraseys 1994
41	1259/06/06	30	31	8			Badawy 1998, Ambraseys 1994
42	1264/02/20	30	31	7			Badawy 1998, Ambraseys 1994
43	1299/01/08	29.5	30.5	9			Badawy 1998, Ambraseys 1994
44	1303/08/08	34.5	28.5	9		7.3	Badawy 1998, Ambraseys 1994
45	1307/08/10	30.2	31	6			Badawy 1998, Ambraseys 1994
46	1313/02/27	30.5	31.2	6		5.4	Badawy 1998, Ambraseys 1994
47	1335/05/29	30	31	6			Badawy 1998, Ambraseys 1994
48	1352/08/08	20.03	31.15				AL-Maqrizi in Ambraseys 1994 et Emanuela Guidoboni 1994 Catalogue
49	1347/12/08	30	31.2	6			Ambraseys 1994, porir and taher 1981
50	1353/10/16	25	28				Ambraseys 1994, porir and taher 1981
51	1373/10/19	30.2	31.5	6		5.4	Badawy 1998, Ambraseys 1994
52	1385/09/19	30.5	31	6			Badawy 1998, Ambraseys 1994
53	1386/07/17	30.2	31.2	6			Badawy 1998, Ambraseys 1994
54	1392/04/13	35	33				Emanuela Guidoboni 1994 Catalogue
55	1422/01/28	30	31.2	6		5.4	Badawy 1998, Ambraseys 1994
56	1425/06/23	29.5	33.5	7			Badawy 1998, Ambraseys 1994
57	1431/11/06	30	31.2			5.8	Badawy 1998 afterseiberg 1932, Ambraseys 1994
58	1433/12/14	30	31	6			Badawy 1998, Ambraseys 1994
59	1434/11/6	30	31.2	7			Badawy 1998, Ambraseys 1994
60	1438/02/25	35	28	6		5.4	Ambraseys 1994
61	1455/03/05	30.5	31.2	6			Badawy 1998, Ambraseys 1994
62	1458/11/16	30.25	35.25			7.1	Klinger et al.,2000, Ambraseys2009
63	1467/12/15	30	31	6		5.4	Badawy 1998, Ambraseys 1994
64	1476/11/1	30.2	31.2	6			Badawy 1998, Ambraseys 1994
65	1481/02/18	35	30	7			Ambraseys 1994, Porior and taher 1981, Maamoun 1984
66	1483/06/15	30.1	31.2	6			Badawy 1998, Ambraseys 1994
67	1486/10/11	30.5	31.2	6			Badawy 1998, Ambraseys 1994
68	1491/04/21	35	32	6			Ambraseys 1994
69	1498/10/16 or 18	30	31.2	6			Badawy 1998, Ambraseys 1994
70	1500/07/24	36	23	6			Ambraseys 1994, Porior and taher 1981, Maamoun 1984
71	1502/11/17	30.15	31.25	7			Badawy 1998, Ambraseys 1994
72	1508/05/29	35	27	6			Ambraseys 1994
73	1509/04	35	27	6		5.4	Ambraseys 1994
74	1513/03/28	30	31.2	6		5.4	Badawy 1998, Ambraseys 1994
75	1523/04/04	30.25	31.3	6			Badawy 1998, Ambraseys 1994
76	1525/03/09	30.15	31.2	6			Badawy 1998, Ambraseys 1994
77	1527/07/14	30	31.2	6			Badawy 1998, Ambraseys 1994

78	1529/11/12	30.15	31.5	6		5.4	Badawy 1998, Ambraseys 1994
79	1532/07/10	30.2	31.25	6			Badawy 1998, Ambraseys 1994
80	1534/03/25	30.1	31.2	6			Badawy 1998, Ambraseys 1994
81	1537/01/08	32	24	6		5.4	Ambraseys 1994
82	1573/02/4	36.5	35.5	6		5.4	Ambraseys 1994, Porior and taher 1981
83	1576/04/30	30	31.5	6			Badawy 1998, Ambraseys 1994
84	1588/04/07	29.5	31.5	6			Ambraseys 1994, Porior and taher 1980, Badawy1998
85	1592/05/37	37	21	6			Ambraseys 1994
86	1609/04	35	28	6			Ambraseys 1994
87	1613/06	35	27	6			Ambraseys 1994, Porior and taher 1980
88	1633/11/05	37	25	6			Ambraseys 1994
89	1664/11/20	35	35	6		5.4	Ambraseys 1994
90	1693/10/08	32	30.5	4			Maamoun et al. (1984)
91	1694/12/12	29	31	7			Ambraseys 1994
92	1698/10/2	32	30	6			Ambraseys 1994, Porior and taher 1980, Maamoun 1984, Badawy 1998
93	1705/24	33.8	36.15			6.9	Ambraseys2009
94	1710/08/27	29.3	33.25	6			Badawy 1998, Ambraseys 1994
95	1741/01/31	35	28	7			Ambraseys 1994
96	1754/10/18	29.6	32.25	7	5.4		Ambraseys 1994, Porior and taher 1981, Maamoun 1984, Badawy 1998
97	1756/02/13	36	23	6			Ambraseys 1994
98	1759/10/30	33	35.56			7.2	Maghraoui2016, Ambraseys2009
99	1759/11/25	33.75	35.8			7.3	Ambraseys2009
100	1778/06/22	26.2	32.1	6	5.4		Ambraseys 1994, Porior and taher 1981, Maamoun 1984, Badawy 1998
101	1790/05/26	35	25	6			Ambraseys 1994
102	1801/10/10	30	31.2	6			Badawy 1998, Ambraseys 1994
103	1805/07/03	36	24	6			Ambraseys 1994
104	1810/02/17	36	23	7			Ambraseys 1994
105	1814/06/27	29	33	7			Badawy 1998, Ambraseys 1994
106	1825/06/21	30.15	31	6			Badawy 1998, Ambraseys 1994
107	1837/01/01	33.63	35.5			7	Nemenr and Meghraoui,2006, Ambraseys2009
108	1839	28.5	34	7			Ambraseys 1994
109	1846/03/28	35	25	6			Badawy 1998, Ambraseys 1994
110	1846/06/15	30	31	6			Badawy 1998, Ambraseys 1994
111	1847/08/07	29.5	30.75	9			Badawy 1998, Ambraseys 1994
112	1849/07/23	30.15	31.25	6			Badawy 1998, Ambraseys 1994
113	1850/10/27	27	31	7			Badawy 1998, Ambraseys 1994
114	1851/04/03	36	28	6			Ambraseys 1994
115	1856/10/12	35.5	26	7			Ambraseys 1994
116	1858/12/30	30	31.2	6			Badawy 1998, Ambraseys 1994
117	1863/04/22	36.5	28	6			Ambraseys 1994
118	1865/04/11	31.1	30	6			Badawy 1998, Ambraseys 1994
119	1868/02/20	32	33	7			Badawy 1998, Ambraseys 1994
120	1870/06/24	34.5	29.5	7			Badawy 1998, Ambraseys 1994

121	1873/01/12	32.5	33	6		5.8	Badawy 1998, Ambraseys 1994
122	1879/07/11	29	33	7			Badawy 1998, Ambraseys 1994
123	1886/08/27	36	23.5	6			Badawy 1998, Ambraseys 1994
124	1886/11/17	30.15	31.2	6		5.4	Badawy 1998, Ambraseys 1994
125	1887/07/17	36	26	7			Ambraseys 1994
126	1895/12/07	30.1	31.25	6		5.4	Badawy 1998, Ambraseys 1994
127	3/6/1900	29.3	34.6	5			Maamoun et al. (1984)
128	12/28/1908	38	15.3		4.6		Galanopoulos A.,1955
129	1/20/1941	35.10	33.39		5.9		Papadopoulos 2005
130	9/10/1953	34.48	32.47		6.1		Papadopoulos 2005
131	5/15/1979	34.62	24.08			5.8	The euro-Mediterranean tsunami catalogue Alessandra Maramai et al.,2014

Table 14: The 13 earthquakes events Mw ≥ 5 in the Hellenic arc

No.	Date	Time	Long.	Lat.	Depth	Mw
1	19650427	14:09:00	23.5	36.6	13	5.5
2	19910626	11:43:34	21.04	38.34	22	5.2
3	19590709	3:11:00	25.8	36.7	22	7.5
4	8/17/1982	22:29.8	22.9	33.7	23.4	6.3
5	5/28/1998	33:33.4	27.36	31.39	39	5.5
6	4/5/2000	36:58.0	25.83	34.08	15	5.5
7	2/20/2008	27:11.0	21.8	36.31	22.1	6.2
8	7/15/2008	26:44.5	27.34	35.92	34	6.4
9	10/12/2013	11:56.3	23.37	35.37	15	6.8
10	8/29/2014	45:06.0	23.65	36.49	100.3	5.8
11	4/16/2015	07:44.0	26.81	35.03	26.1	6.2
12	7/27/1997	07:52.5	21.064	35.582	13	5.7
13	3/28/2008	16:19.9	25.39	34.89	52	5.7

Table 15: The focal mechanisms parameters of in the Hellenic arc

No.	Strike	Dip	Rake	References
1	191	64	-79	Liotier 1989
2	-105	354	41	Louvari 2000
3	55	40	-90	HRVD
4	36	57	88	HRVD
5	154	44	89	HRVD
6	109	48	99	HRVD
7	250	83	-7	MED_RCMT
8	262	84	-41	NEIC
9	119	88	88	GCMT
10	265	70	170	MED_RCMT
11	65	28	12	MED_RCMT
12	62	80	-175	NEIC
13	99	50	103	MED_RCMT

References

Abdelazim, M., Samir, A., El-Nader, I.A., Badawy, A. and Hussein, H., (2016). Seismicity and focal mechanisms of earthquakes in Egypt from 2004 to 2011. NRIAG Journal of Astronomy and Geophysics, 5(2), pp.393-402.

Abdel-Fattah, R., (1999). Seismotectonic Studies on the Gulf of Suez Region, Egypt. M.Sc. Thesis. Fac. of Sci., Geology Dept. Mansoura Univ.

Abou Elenean, K.M.,(1997), Seismotectonics of Egypt in relation to the Mediterranean and Red Sea tectonics. Ph.D. Thesis, Fac. Sci. Ain Shams Univ., Egypt.

Abou Elenean, K., Arvidsson, R. and Kulhanek, O., (2004). Focal mechanism of smaller earthquakes close to VBB Kottamia station, Egypt. Annals of the Geological Survey of Egypt, XXVII, p.357-368.

Abou Elenean, K. M. (2007), Focal mechanisms of small and moderate size earthquakes recorded by the Egyptian National Seismic Network (ENSN), Egypt, NRIAG J. Geophys., Vol. 6, no. 1, p.119–153.

Abou Elenean, K.M., and Hussein, H.M., (2007). Source mechanism and source parameters of May 28, 1998 earthquake, Egypt: Journal of Seismology, Vol. 11, p. 259–274, doi: 10.1007/s10950-007-9051-5.

Ambraseys , N., (1962). Data for the investigation of the seismic sea waves in the Eastern Mediterranean. « Bull. Seism. Soc. Am., », Vol.52, no. 4, p. 895-913.

Ambraseys, N.N., Melville, C.P., Adam, R.D., (1994). The Seismicity of Egypt, Arabia and the Red Sea: A Historical Review. Cambridge, UK, pp.181.

Ambraseys, N., (2009). Earthquakes in the Mediterranean and Middle East: A Multidisciplinary Study of Seismicity up to 1900, pp.947, Cambridge University Press, ISBN: 9780521872928.

Ambraseys, N.N., Melville, C.P., Adam, R.D., (1994). The Seismicity of Egypt, Arabia and the Red Sea: A Historical Review. Cambridge, UK.

Badawy, A. (2001). The present-day stress field in Egypt. Ann. Geofis., Vol. 44, p. 557-570.

Badawy, A., (1998). Earthquake Hazard Analysis in Northern Egypt, Acta Geodaetica et Geophysica Hungarica, June 1998, Volume 33, Issue 2, p. 341–357.

Badawy, A., Horvath, F., (1999). Recent stress field of the Sinai subplate region. Tectonophysics Vol.304,p. 385–403.

Badreldin , H.Y.Mohamed (2016) Analysis of full waveform moment tensor inverszion of local earthquakes in Egypt, M. Sc., Aswan University, science faculty, pp.170

CMT catalogue: Centroid Moment Tensor catalogue of Harvard, http://www.seismology.harvard.edusearch.html

Costantinescu L., Ruprecrtova, L. and Enescu, D. (1996). Mediterranean- Alpine earthquake mechanisms and their seismotectonic implications Geophys. J .R. Astro. Soc., Vol. 10 ,p.347-368.

Egyptian National seismic network (ENSN) Bulletin (1998-2004). Earthquakes in and around Egypt. National Research Institute of Astronomy and Geophysics (NRIAG), Egypt.

Elias, A., Tapponnie, P., Singh, S.C., King, G.C.P., Briais, A.,Daëron, M., Carton,H., Sursock, A., Jacques, E., Jomaa, R., Klinger, Y., (2007). Active thrusting offshore Mount Lebanon: source of the tsunamigenic AD 551 Beirut–Tripoli earthquake. Geology Vol. 35, p. 755–758. http://dx.doi.org/10.1130/G23631A.1.

EMSC. Eastern Mediternean seismological center, https://www.emsc-csem.org/#2

Galanopoulos, A. G.(1955). The Seismic Geography of Greece, Ann. Geol. Pays Hellen., 6, 83–121 (in Greek).

GFZ German Research Centre for Geosciences, http://www.gfz-potsdam.de/startseite.

Guidoboni, E., 1994, Catalogue of Ancient Earthquakes in the Mediterranean area up to the 10th century, Instituto Nazionale di Geofisica Rome, 504 pp.

Harvard CMT catalog. Centroid Moment Tensor catalog of Harvard, http://www.seismology.harvarrd.edu/CMT search.html.

Hofstetter A, Thio HK, Shamir G (2003). Source mechanism of the 22/11/95 gulf of Aqaba Earthquake and its aftershock sequence.J Seismol Vol.7, p.99–114.

Huang, P.Y., Solomon, S.C., (1987). Centroid depths and mechanisms of midocean ridge earthquakes in the Indian Ocean, Gulf of Aden and Red Sea. J. Geophys. Res. Vol. 92, p.1361–1382.

Hussein, H.M., 1989. Earthquake activities in Egypt and adjacent regions and its relation to geotectonic features in A.R.E. MSc. Thesis. Fac. of Sci., Geology Dept., Mansoura University, Egypt.

Emad Mohamed, K., Hassoup, A., Abou Elenean, K.M., Adel Othman, A.A., Diaa-Eldin Hamed, M.K., (2015). Earthquakes focal mechanism and stress field pattern in the northeastern part of Egypt. NRIAG J. Astron. Geophys. Vol.4, p. 205–221.

Klinger, Y., J. P. Avouac, L. Dorbath, N. Abou Karaki, and N. Tisnerat (2000). Seismic behavior of the Dead Sea fault along Araba valley (Jordan), Geophys. J. Int. Vol.142, p. 769–782

Korrat, I.M., El Agami, N.L., Hussein, H.M., El-Gabry, M.N. (2005), Seismotectonics of the passive continental margin of Egypt, Journal of African Earth Sciences Vol.41. p. 145–150.

Liotier, Y., (1989). Modéˊ lisation des ondes de volume des seˊismes de l'arc Ageen. DEA de l'Universiteˊ Joseph Fourier.Grenoble, France.

Louvari, A ., (2000). A detailed seismotectonic study in the Aegean sea and the surrounding area with emphasis on the information obtained from microearthquakes, PhD thesis, Aristotle University, Thessaloniki, Greece, pp 373.

Maamoun, M., Megahed, A. and Allam, A., (1984). Seismicity of Egypt: NRIAG Bull., IV (B), p. 109–160.

Maramai, A., Brizuela, B. and Graziani, L., (2014). The Euro-Mediterranean Tsunami Catalogue. Annals of Geophysics, Vol.57(4), p.0435.

MED_RCMT. MedNet Regional Moment Centroid Moment Tensors, http://www.ingv.it/seismoglo/RCMT

Megahed, A., (2004). Seismic deformation studies on the northeastern part of Egypt. Ph. D. thesis, Faculty of science, Mansoura University, Egypt.

Meghraoui, M., (2016). Seismotectonic Map of Africa: Episodes, Vol. 39, p. 9–18, doi: 10.18814/epiiugs/2016/v39i1/89232.

Meghraoui, M., Gomez, F., Sbeinati, R., Van der Woerd, J., Mounty, M., Darkal, A. N., Radwan, Y., Layyous, I., Al-Najjar, H., Darawcheh, R., Hijazi, F., Al-Ghazzi, R., and Barazangi, M., (2003). Evidence for 830 years of seismic quiescence from palaeoseismology, archaeoseismology, and historical seismicity along the Dead Sea Fault in Syria, Earth Planet. Sci. Lett., Vol. 210, p. 35-52.

Morsy, M., Hussein, H.M., Abou Elenean, K.M., El-Hady, Sh., (2011). Stress field in the central and northern parts of the Gulf of Suez area, Egypt from earthquake fault plane solutions. J. Afric. Earth Sci. Vol. 60,p. 293–302.

NEIC. National Earthquakes Information Center, http//neic.usgs.gov/, http//earthquakes.usgs.gov/regioanl/neic

Nemer, T. and Meghraoui, M., (2006). Evidence of coseismic ruptures along the Roum fault (Lebanon): A possible source for the AD 1837 earthquake. Journal of Structural Geology, 28(8), pp.1483-1495.

Niemi, R.G., Weisberg, H.F. and Kimball, D.C. eds., (2001). Controversies in voting behavior (p. 1). Washington, DC: CQ Press.

Papadimitriou, E., Karakostas, V., (2008). Rupture model of the great AD 365 Crete earthquake in the southwestern part of the Hellenic Arc. Acta Geophysica Vol.56 no.2,p. 293–312.

Papadopoulos, G. and Fokaefs, A. (2005). ''Strong tsunamis in the Mediterranean Sea: a re- evaluation,'' Journal of Earthquake Technology Vol. 42,p. 159–170 Poirier, J. P. and Taher, M.: 1980, Historical Seismicity in the near and Middle East north Africa and Spain from Arabic documents (VIIth-XVIIth Century), Bull Seismol. Soc. Am. Vol.70, p.185-201. Reborto

Reches, Z., and D. F. Hoexter (1981). Holocene seismic and tectonic ac- tivity in the Dead Sea area, Tectonophysics Vol.80,p. 235–254.

Salamon, A., Hofstetter, A., Garfunkel, Z., Ron, H., (2003). Seismotectonics of the Sinai   subplate—the eastern Mediterranean region. Geophys. J. Int. Vol.155, p.149– 173

Sieberg A., 1932, Untersuchungenüber Erdbeben und Bruchschollenban im östlichen Mittelmeergebiet. « Denkschriften der Medizinish-Natur- wissenschaftlichen Gesellschaft zu Jena », vol. 2, Jena.

Soloviev, S.L., Solovieva, O.N., Go, C.N., Kim, K.S., and Shchetnikov, N.A., (2000). Tsunamis in the Mediterranean Sea 2000 B.C.-2000 A.D, pp. 237, Kluwer academic, Dordrecht/ Boston/ London ISBN: 0-7923-6548-8

Zilberman, E., R. Amit, N. Porat, Y. Enzel, and U. Avner (2005), Surface ruptures induced by the devastating 1068 AD earthquake in the southern Arava valley, Dead Sea Rift, Israel, Tectonophysics, Vol. 408, p.79–99.

ZUR_RMT. Zurich Moment Tensors, Swiss Seismological service, ETH- Honggerberg, http//seismo.ethz.ch/info/mt.html.

Appendix B : XRD Diffraction

Core 1 sample 1

2Theta	d (A)	Height	Area	FWHM	Identified mineral	WT%
17	**6.54906**	14.1	24.2	0.1959	Gypsum	1.767138739
25.207	4.43635	10.4	17.9	0.2284	-	0
26.2	4.27096	80.4	224.4	0.2609	-	
26.878	**4.16509**	7.3	20.4	0.2648	Geothite	0.914901617
29.135	3.84871	7.3	20.4	0.2668	-	
30.344	3.69869	64.1	174.5	0.2688	-	
31.308	3.5876	17.6	47.9	0.3164	-	
31.725	3.54154	15.6	42.3	0.3401	-	
32.31	**3.47908**	13.5	36.7	0.352	Aragonite	1.691941346
33.633	**3.34596**	336.5	1545.2	0.3639	Quartz	42.17320466
34.65	**3.25063**	130	597.2	0.3755	Feldspar (orthoclase)	16.29276852
35.152	**3.20569**	145.5	668.2	0.3813	Albite	18.23536784
37.221	**3.03326**	65.9	338.3	0.3872	Calcite	8.259180348
39.075	**2.89461**	62.2	304.3	0.3949	dolomite	7.795463091
40.166	**2.81908**	12.5	60.9	0.3591	Halite	1.566612357
42.422	**2.67551**	10.4	50.8	0.3412	Pyrite	1.303421481
45.598	2.49811	17.6	86.1	0.3323	-	
46.356	2.45949	46.7	181.3	0.3233	-	
47.353	2.41057	9.4	36.4	0.312	-	
48.189	2.37119	9.4	36.4	0.3063	-	
50.147	2.28426	50.2	165.7	0.3006	-	
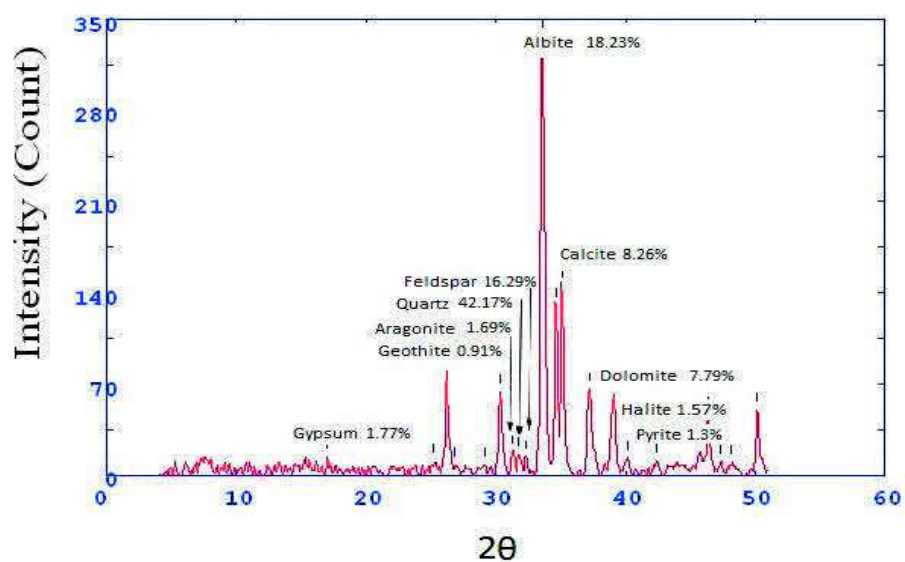
Core 1 sample 2

2Theta	d (A)	Height	Area	FWHM	Identified mineral	WT%
11.008	**10.09211**	13.1	74.7	0.3574	Illite	3.116821318
24.681	4.52938	12.6	51.4	0.3356	-	0
26.207	4.26987	30.8	97.7	0.2652	-	
27.931	4.0111	7.6	24.3	0.2974	-	
29.077	3.85612	21.4	90.1	0.3297	-	
30.351	**3.69791**	10.6	44.6	0.2948	Aragonite	2.522008089
33.57	**3.35211**	154.2	353.1	0.26	Quartz	36.68807994
34.523	**3.26222**	24.6	56.2	0.3908	Feldspar (orthoclase)	5.85296217
35.108	**3.2096**	14.4	33	0.4562	Albite	3.426124197
37.22	**3.03336**	139.9	945.6	0.5217	Calcite	33.28574828
39.053	**2.89614**	40	215.2	0.4159	dolomite	9.517011658
40.031	**2.82818**	11.9	63.9	0.3186	Halite	9.517011658
41.875	**2.70891**	11.6	26.4	0.2213	Pyrite	2.759933381
45.7	2.49284	32.8	355.3	0.9235	-	
47.208	2.41755	15.3	165.4	0.5999	-	
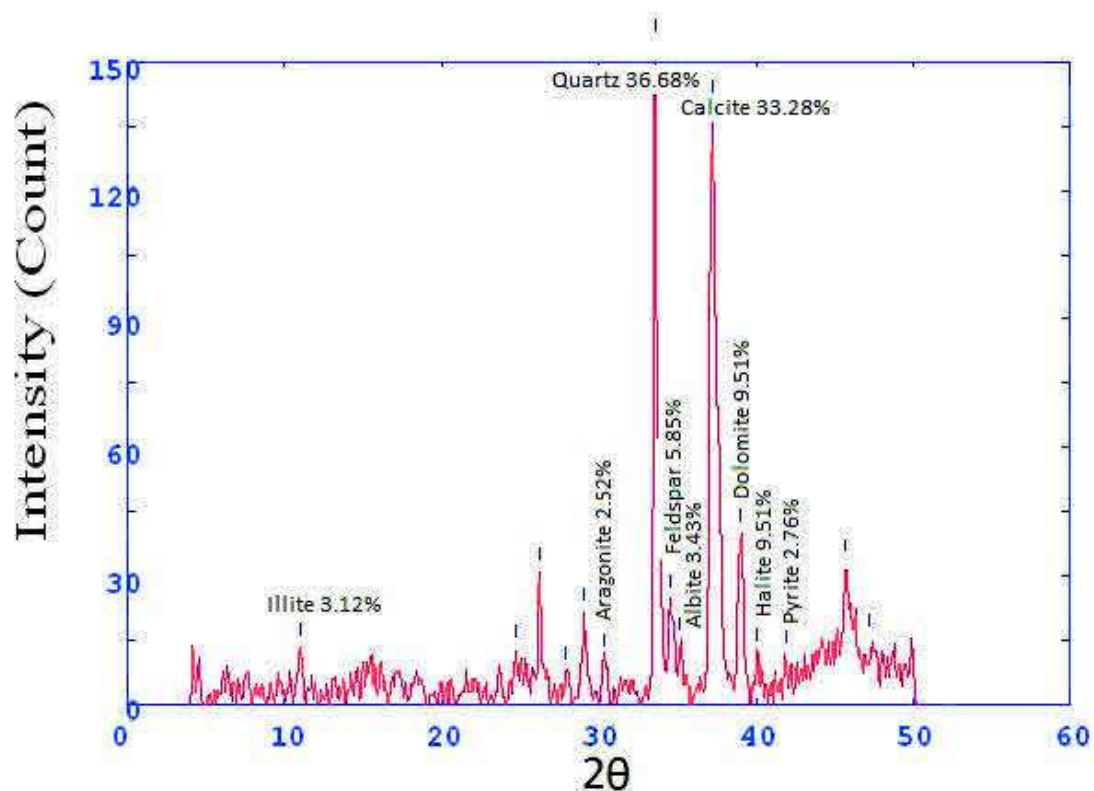
Core 1 sample 3

2Theta	d (A)	Height	Area	FWHM	Identified mineral	WT%
15.408	**7.22089**	12.4	89.9	0.5334	Gypsum	1.651571657
24.948	4.4817	10.4	75.3	0.3984	-	0
26.212	4.26897	70.9	212.5	0.2634	-	
29.054	3.85916	16.6	49.8	0.2498	-	
30.366	3.69605	32.8	82.5	0.2363	-	
31.326	**3.58558**	21.8	54.7	0.2368	Aragonite	2.903569526
33.592	**3.35**	325.3	699.6	0.2373	Quartz	43.32711774
34.646	**3.25106**	133.2	286.5	0.33	Feldspar (orthoclase)	17.74107619
37.218	**3.03354**	196.2	948.1	0.4227	Calcite	26.13212573
39.072	**2.8948**	61.9	261.7	0.3479	dolomite	8.244539158
45.633	2.49629	27.2	406.4	0.9975	-	
46.266	2.464	24.9	371.7	0.7214	-	0
48.712	2.34725	10.4	155.6	0.5833	-	
50.15	2.28412	43.5	242	0.4452	-	
51.246	2.23847	12.5	0	0	-	
52.207	2.20008	11.4	0	0	-	
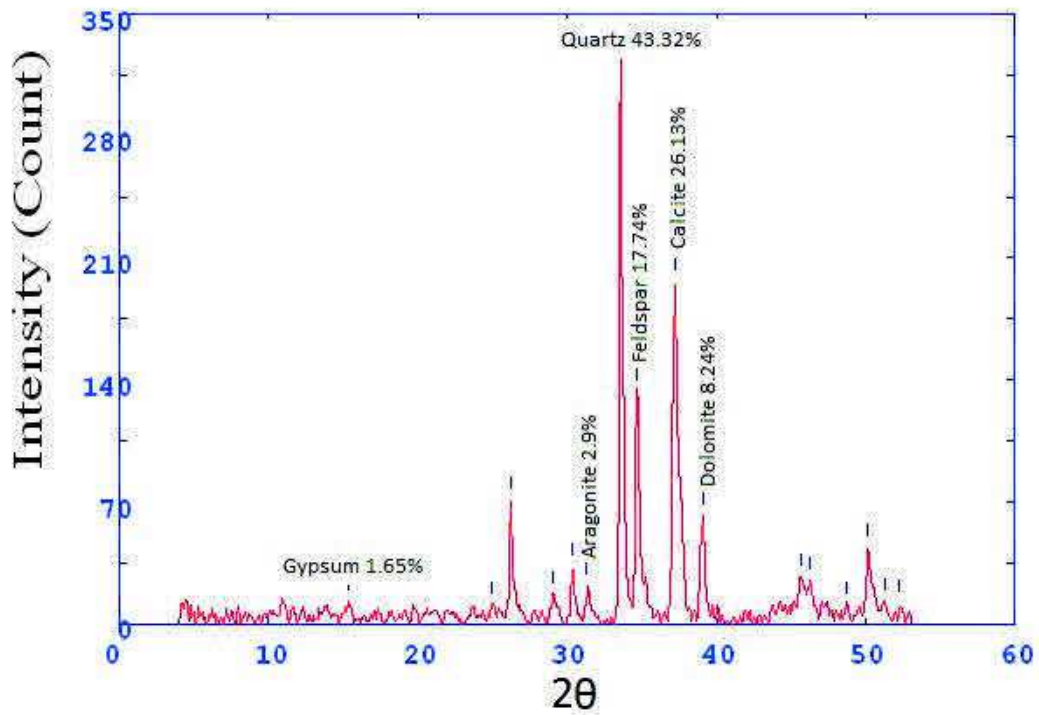
Core 1 sample 4

2Theta	d (A)	Height	Area	FWHM	Identified mineral	WT%
15.354	**7.24607**	15.8	72	0.4291	Gypsum	2.243362204
26.29	4.25668	39.8	142.2	0.3088	-	0
29.193	3.84117	24.4	87.4	0.2846	-	
30.473	3.68344	36.3	87.5	0.2604	-	
31.586	**3.55673**	16.6	40.1	0.2581	Aragonite	2.356950163
33.704	**3.33918**	315	700.4	0.2558	Quartz	44.72525912
34.749	**3.24171**	73.1	162.7	0.353	Feldspar (orthoclase)	10.37909982
35.347	**3.18855**	36.1	80.3	0.4016	Albite	5.12565668
37.347	**3.02339**	185.6	1102.9	0.4502	Calcite	26.35240664
39.207	**2.88523**	62.1	304.6	0.3948	dolomite	8.81726537
43.033	2.6393	16.8	38.6	0.2072	-	
45.94	2.48052	28	202.3	0.5829	-	
46.373	2.45864	21.5	155.5	0.536	-	
50.333	2.27634	37	263	0.4891	-	
51.415	2.23159	8.8	0	0	-	

174
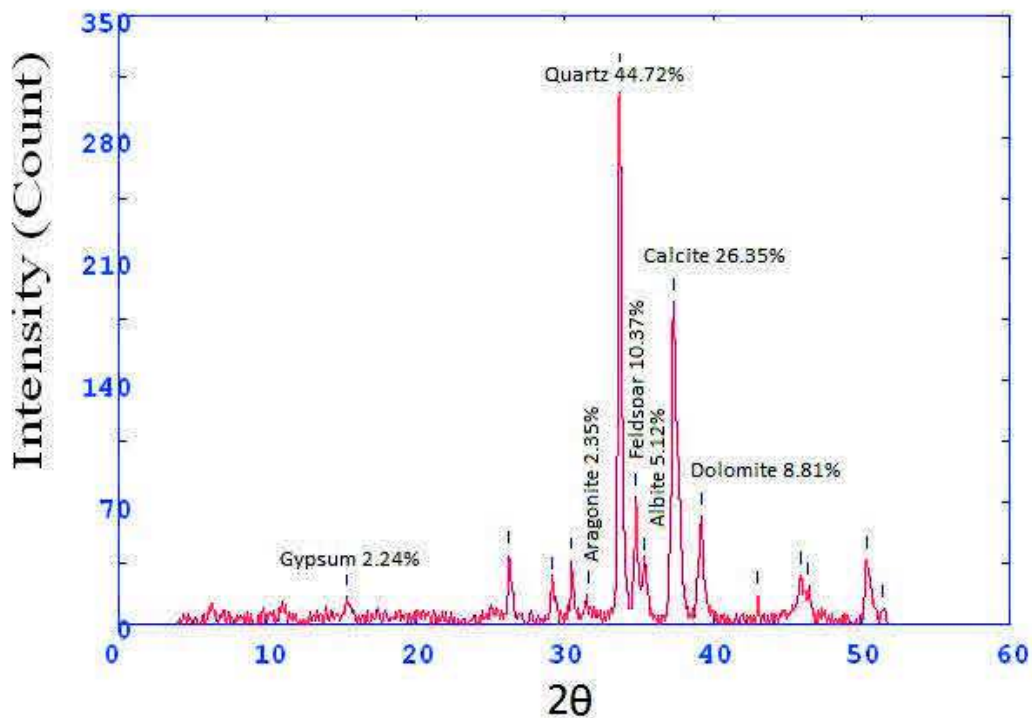
Core 1 sample 5

2Theta	d (A)	Height	Area	FWHM	Identified mineral	WT%
17.139	**6.49624**	16.5	47.7	0.2592	Gypsum	2.160534241
23.727	4.70878	8.4	24.2	0.2634	-	0
24.966	4.47848	11.5	33.2	0.2654	-	
26.259	4.26147	50.3	144.7	0.2675	-	
27.692	4.04493	9.4	27.2	0.2481	-	
29.097	3.85359	9.4	27.2	0.2288	-	
30.417	3.6901	60	63.5	0.1901	-	
31.328	**3.58535**	20.9	22.1	0.2439	Aragonite	2.736676706
33.633	**3.34595**	331.6	1301.9	0.2978	Quartz	43.42019117
34.798	**3.23728**	178.9	702.5	0.3642	Feldspar (orthoclase)	23.42542883
35.294	**3.19323**	37.5	147.3	0.3974	Albite	4.910305094
37.244	**3.03148**	122.2	626.1	0.4307	Calcite	16.00104753
39.1	**2.89278**	56.1	366.2	0.4861	dolomite	7.34581642
42	**2.70119**	21	89.7	0.3611	Pyrite	2.749770852
45.748	2.49039	27.2	218.7	0.6017	-	
46.365	2.45903	18.8	151.4	0.5858	-	
48.1	2.37531	13.6	100	0.57	-	
50.244	2.28014	30.8	93	0.3152	-	0
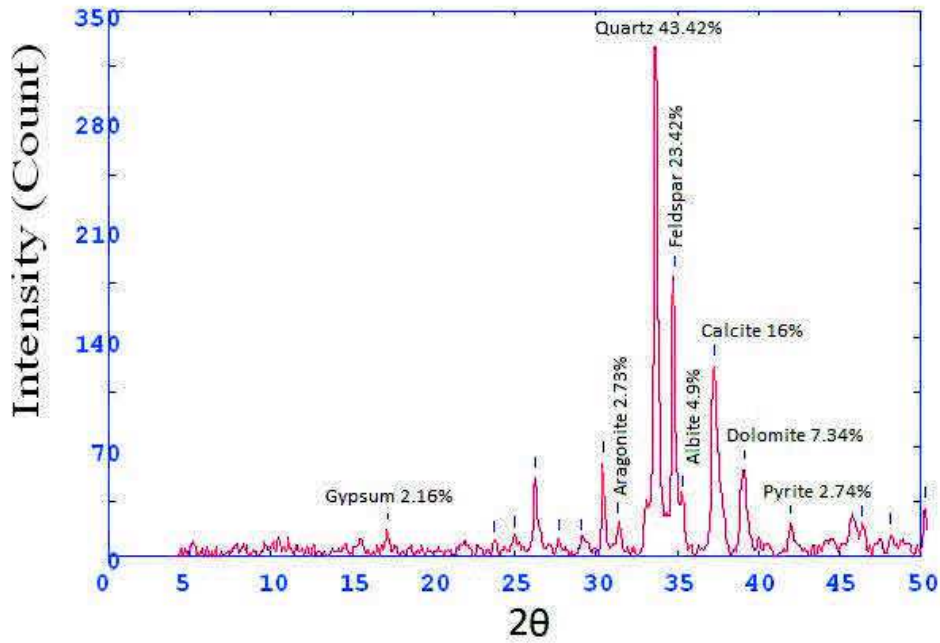
Core 1 sample 6

2Theta	d (A)	Height	Area	FWHM	Identified mineral	WT%
14.926	**7.4528**	140.2	268.1	0.2051	Gypsum	23.04404997
24.139	4.62956	9.8	18.7	0.2147	-	
25.181	4.44076	8.8	16.9	0.2243	-	0
25.877	4.32342	10.8	20.6	0.2435	-	
26.652	**4.19975**	58	176.9	0.2819	Geothite	9.533201841
29.9	3.75237	48.7	138.5	0.2685	-	
30.83	**3.64184**	30.2	85.9	0.2611	Aragonite	4.963839579
33.436	**3.3651**	36	102.5	0.2574	Quartz	5.917159763
34.005	3.31046	305.5	866.3	0.2537	-	
35.087	**3.21139**	39.9	113.2	0.3511	Feldspar (orthoclase)	6.558185404
35.696	**3.15841**	28.2	80.1	0.3998	Albite	4.635108481
37.661	**2.99911**	150.7	858	0.4485	Calcite	24.76988823
39.435	**2.86922**	79.8	607.4	0.4946	dolomite	13.11637081
40.388	**2.80423**	17.6	133.6	0.4097	Halite	2.892833662
42.3	**2.68291**	27.8	122.1	0.3247	Pyrite	4.569362262
46.2	2.46732	31.1	192	0.4667	-	
46.818	2.43654	21.4	132.4	0.3899	-	
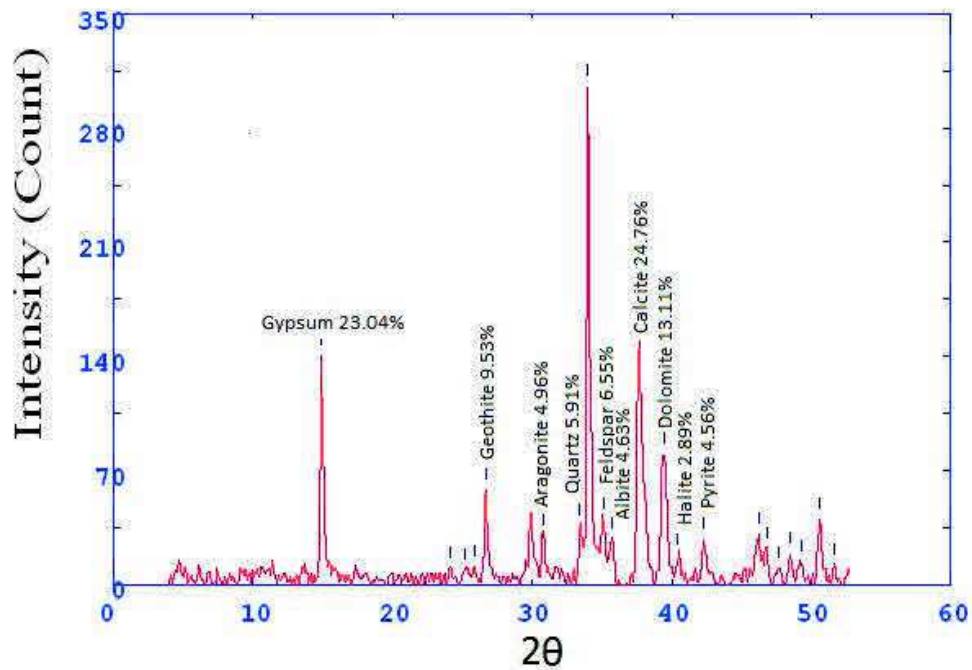
Core 1 sample 7

2Theta	d (A)	Height	Area	FWHM	Identified mineral	WT%
15.414	**7.21807**	11.4	94.4	0.8724	Gypsum	2.366618227
19.4	5.74515	8.2	94.4	0.8724	-	
21.267	5.24597	7.9	27.1	0.1957	-	
22.609	4.93835	8.8	22.9	0.148	-	
24.888	4.49223	10.4	27.2	0.2573	-	
26.255	4.26213	26.7	123.3	0.3665	-	
29.195	3.84093	19.3	85.8	0.3034	-	0
30.36	3.69679	9.4	41.6	0.2881	-	
33.055	**3.40278**	35.8	158.8	0.2805	Aragonite	7.432011625
33.631	**3.34617**	141.8	414.4	0.2729	Quartz	29.43740918
34.689	**3.24714**	30.1	87.9	0.3337	Feldspar (orthoclase)	6.248702512
35.424	**3.18185**	24.9	72.8	0.364	Albite	5.169192443
37.29	**3.02783**	165	698.5	0.3944	Calcite	34.25368487
39.134	**2.89041**	47.8	334.5	0.5099	dolomite	9.923188707
42.034	**2.69908**	24.9	136.3	0.4053	Pyrite	9.923188707
45.792	2.48812	42.1	253.4	0.4755	-	
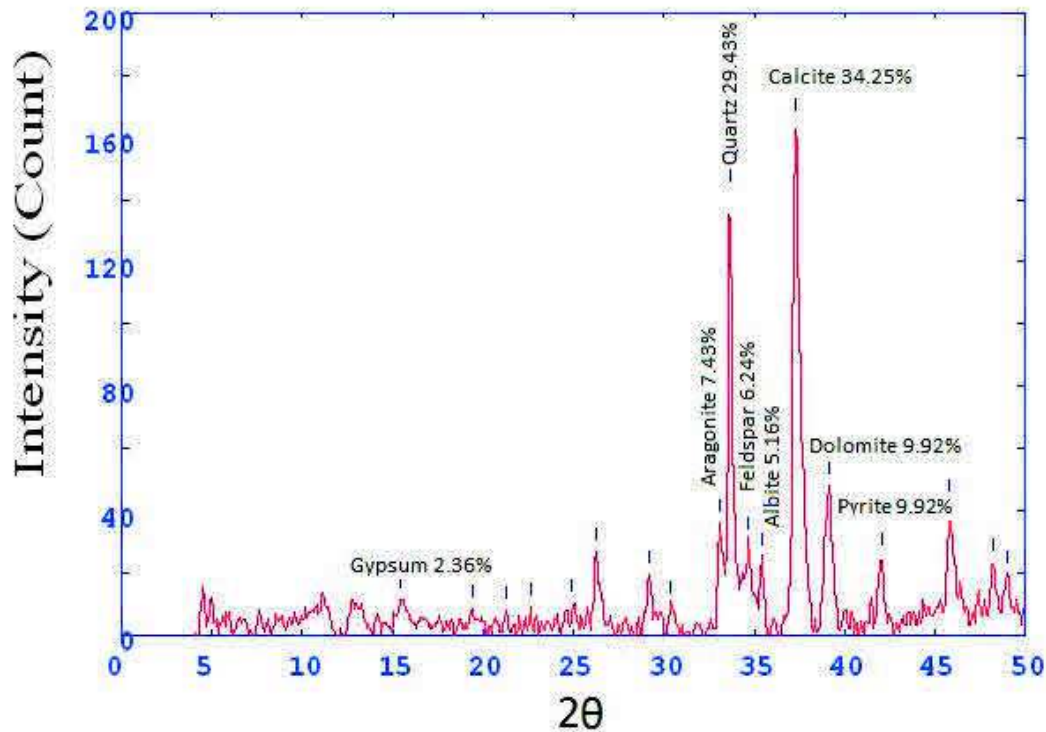
Core 1 sample 8

2Theta	d (A)	Height	Area	FWHM	Identified mineral	WT%
26.28	4.25817	25.9	106.1	0.3271	-	
29.132	3.84901	18.3	102	0.4633	-	
29.949	3.74633	12.9	71.7	0.3677	-	0
30.416	3.69012	12.9	71.7	0.3199	-	
33.126	**3.39576**	49.5	276.4	0.296	Aragonite	10.8220376
33.644	**3.34495**	109.6	390.4	0.2721	Quartz	23.96152164
34.527	**3.26188**	29.7	106	0.3281	Feldspar (orthoclase)	6.493222562
35.088	**3.21137**	21.6	76.9	0.356	Albite	4.722343682
37.262	**3.03002**	183	884.9	0.384	Calcite	40.00874508
39.011	**2.89913**	33.8	163.6	0.3723	dolomite	7.389593354
41.948	**2.70441**	30.2	129.8	0.3606	Pyrite	6.602536073
44.144	2.57606	10.1	40.9	0.3333	-	
45.789	2.48828	43.3	213.1	0.3939	-	
48.033	2.37842	20.3	107.9	0.4705	-	
48.821	2.34234	14.6	77.5	0.464	-	
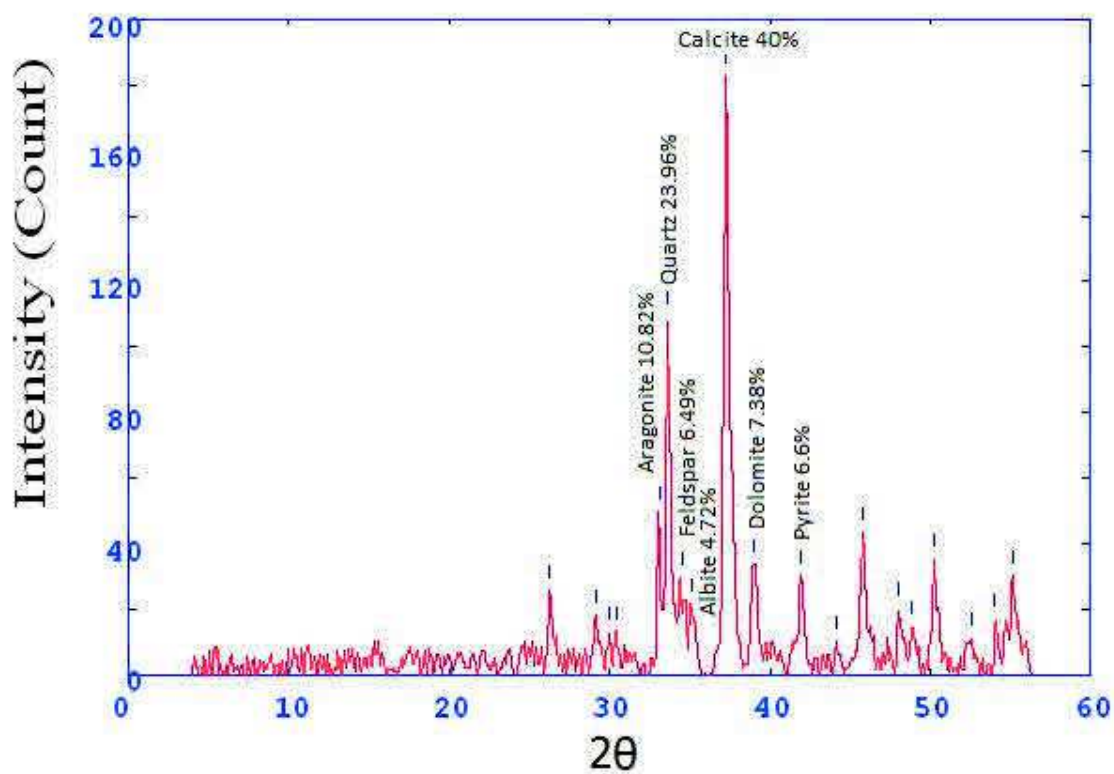
Core 1 sample 9

2Theta	d (A)	Height	Area	FWHM	Identified mineral	WT%
13.14	**8.46016**	20.7	66.9	0.2986	Illite	2.920428894
14.542	**7.64853**	147.8	273.4	0.2206	Gypsum	20.85214447
26.178	4.2745	31.5	90.1	0.2721	-	
28.299	3.95992	9	25.6	0.3067	-	
29.403	3.81438	32.2	122.1	0.3414	-	0
30.366	3.69609	23.1	146.9	0.4859	-	
31.9	3.52268	11.8	100.5	0.7569	-	
32.959	**3.41251**	26.8	227.2	0.5136	Aragonite	3.781038375
33.559	**3.35317**	205.7	585.9	0.2703	Quartz	29.02088036
34.543	**3.26045**	24	68.4	0.2693	Feldspar (orthoclase)	3.386004515
35.288	**3.19374**	64.2	184.6	0.2684	Albite	9.057562077
37.212	**3.03401**	165.2	979.9	0.4741	Calcite	3.68227991
39.087	**2.89373**	26.1	149.9	0.4795	dolomite	3.68227991
39.947	**2.83387**	11.2	64.3	0.5949	Halite	1.58013544
41.903	**2.70715**	17.1	157.3	0.7103	Pyrite	2.412528217
43.866	2.59161	9.6	70.6	0.5639	-	
45.737	2.49095	33.2	187.6	0.4583	-	
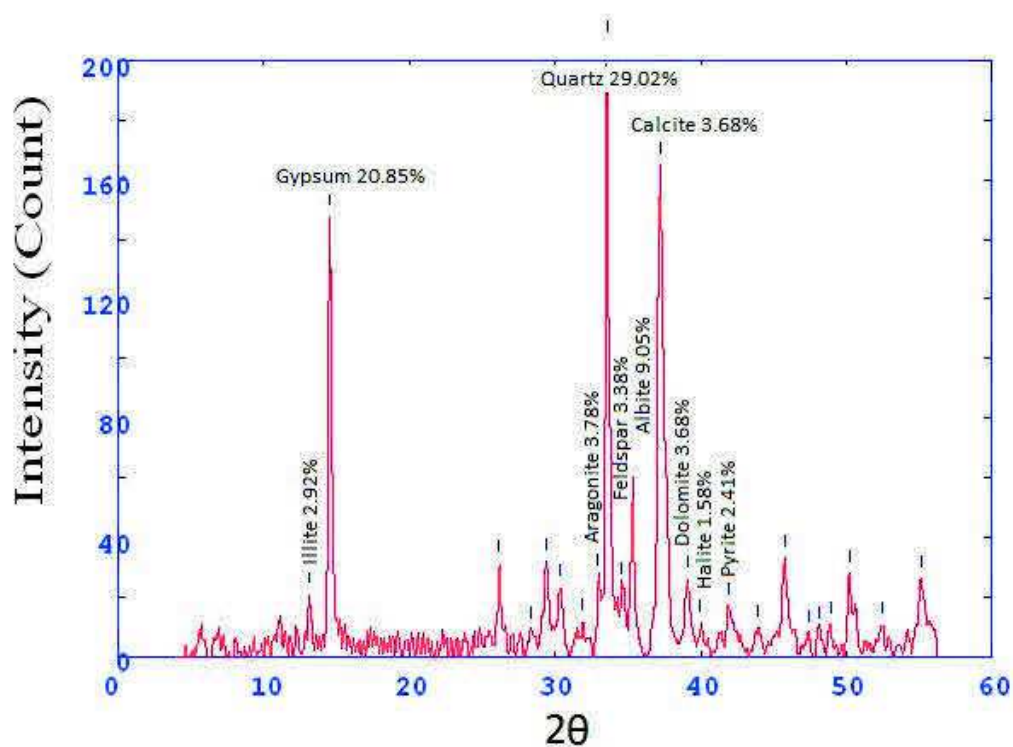
Core 1 sample 10

2Theta	d (A)	Height	Area	FWHM	Identified mineral	WT%
13.156	**8.45006**	23.1	60.7	0.2354	Illite	2.946052799
14.538	**7.65071**	238.4	465.5	0.2324	Gypsum	30.40428517
23.702	4.71352	10	52.5	0.4071	-	
26.2	4.271	35.7	193.4	0.4343	-	
29.422	3.812	43.7	129.9	0.3166	-	
30.363	3.69645	13.7	40.7	0.267	-	0
31.322	3.58594	24.6	54.1	0.2174	-	
32.876	**3.42085**	52.4	114.9	0.2426	Aragonite	6.682821069
33.59	**3.35019**	76.2	225.2	0.2678	Quartz	9.718148195
34.626	**3.25281**	212.3	418.3	0.2266	Feldspar (orthoclase)	27.07562811
37.218	**3.03355**	135.8	993.3	0.6056	Calcite	17.31921949
38.994	**2.9004**	16.7	135.2	0.5603	dolomite	2.129830379
41.867	**2.7094**	29.2	121.8	0.3559	Pyrite	3.724014794
45.747	2.49042	31.2	182.2	0.4542	-	
48.05	2.37766	17.6	56.4	0.2938	-	
48.85	2.34102	15.2	48.9	0.4407	-	
50.217	2.28129	25.1	191.3	0.5876	-	
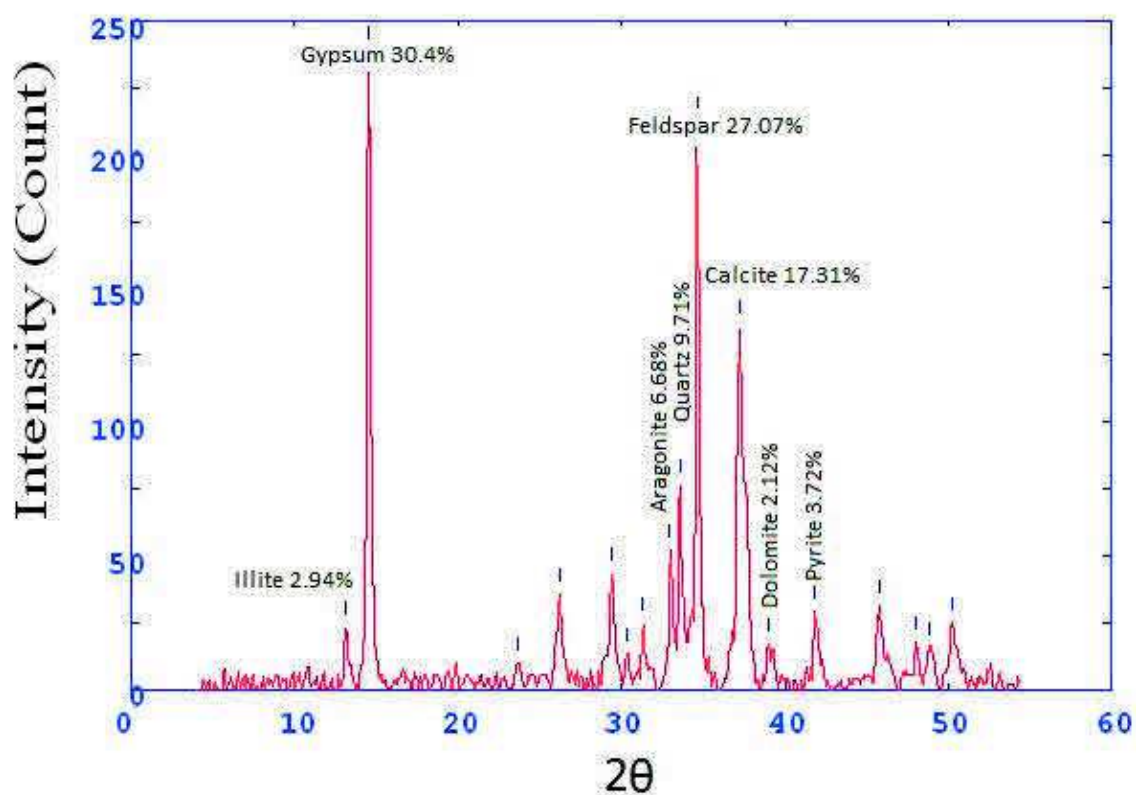
Core 1 sample 11

2Theta	d (A)	Height	Area	FWHM	Identified mineral	WT%
13.205	**8.41877**	22.2	530.9	0.2312	Illite	2.735000616
14.584	**7.62644**	260.8	530.9	0.2312	Gypsum	32.13009733
26.258	4.26164	25	103.6	0.3613	-	-
29.473	3.80552	57.8	122.5	0.2422	-	-
30.302	3.70367	19.7	41.8	0.2409	-	-
32.926	**3.41576**	55	116.6	0.2403	Aragonite	6.775902427
33.645	**3.34479**	218.1	468.5	0.2396	Quartz	26.86953308
34.45	**3.26898**	40.2	86.5	0.4538	Feldspar (orthoclase)	4.952568683
35.381	**3.1856**	16.5	35.4	0.5609	Albite	2.032770728
37.272	**3.02925**	130.5	1114.7	0.668	Calcite	16.07736849
38.936	**2.90455**	25.5	217.7	0.5544	dolomite	3.141554762
41.893	**2.7078**	42.9	244.3	0.4409	Pyrite	5.285203893
45.807	2.48735	34	256.5	0.5778	-	-
48.119	2.37443	25.2	112.3	0.3778	-	-
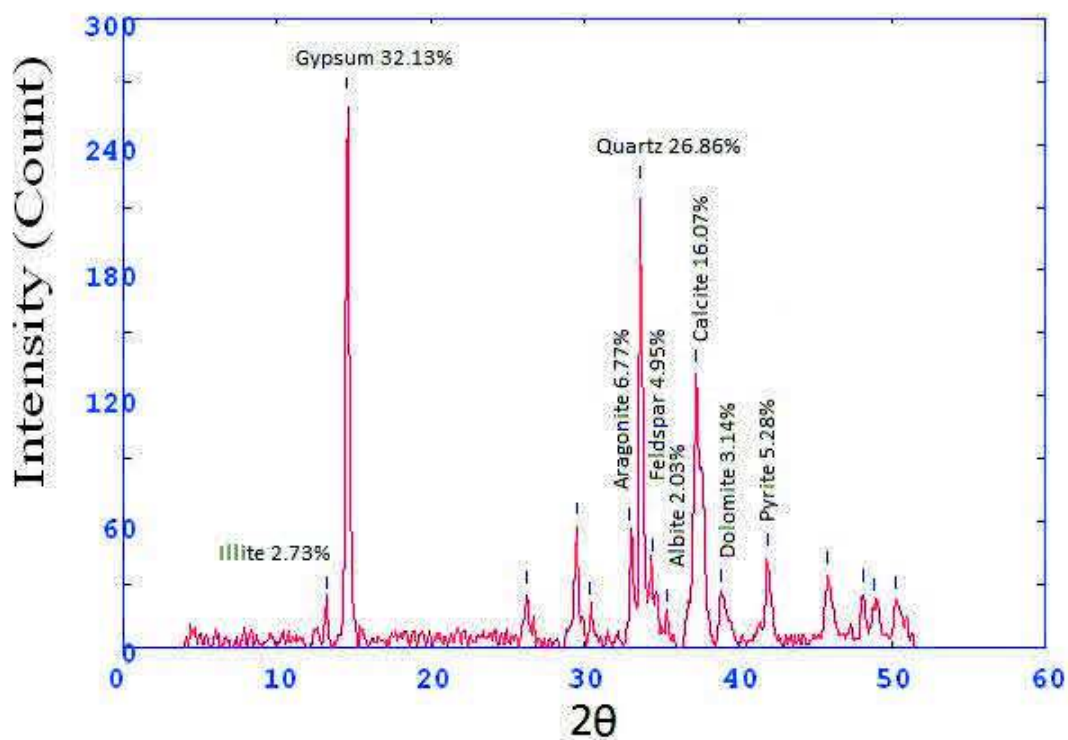
Core1 sample 12

2Theta	d (A)	Height	Area	FWHM	Identified mineral	WT%
29.074	3.85656	27.6	79.1	0.283	Aragonite	3.998261625
33.634	3.34594	27.8	126.2	0.3931	Quartz	4.027234536
35.078	3.21223	29.9	97.3	0.3157	Feldspar (orthoclase)	4.331450094
37.244	3.03147	249.1	988.7	0.3364	Calcite	36.08575981
38.804	2.91402	323.7	1038.5	0.3192	dolomite	46.89265537
39.995	2.83066	17.6	56.4	0.3824	-	-
42.101	2.695	14.6	86.6	0.4457	pyrite	2.115022454
45.716	2.492	28.2	204.7	0.5439	-	-
47.068	2.42434	12.4	90.3	0.4881	-	-
50.233	2.28058	44.5	240.6	0.4322	-	-
52	2.20822	28	135.6	0.3539	-	-
55.133	2.09175	33.5	227.8	0.5053	-	-
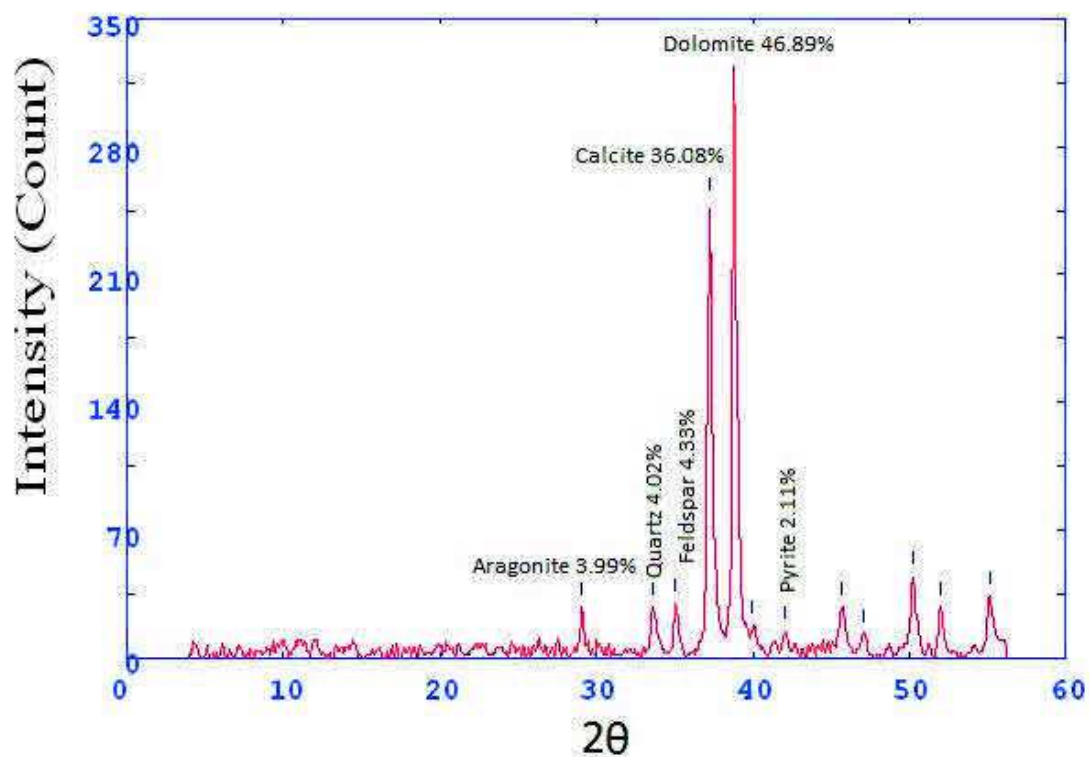
Core 1 sample 13

2Theta	d (A)	Height	Area	FWHM	Identified mineral	WT%
29.053	3.85937	19.5	87.4	0.3652	-	-
29.973	**3.74342**	13.9	62.4	0.3875	Aragonite	2.302849569
33.529	**3.35605**	21.5	97.3	0.4098	Quartz	3.561961564
35.011	**3.21819**	60.4	189.9	0.2922	Feldspar (orthoclase)	10.00662691
37.167	**3.03757**	154.5	744.2	0.3605	Calcite	25.59642147
38.833	**2.9119**	341.2	2226.2	0.4437	dolomite	56.52750166
42.017	**2.70017**	12.1	70.7	0.4667	Pyrite	2.004638834
44.284	2.56835	7.5	43.9	0.4824	-	-
45.674	2.4942	17.4	109.5	0.4981	-	-
47.074	2.42405	17.9	71.5	0.3496	-	-
50.09	2.28668	28	143.2	0.4343	-	-
51.989	2.20866	42.9	175.5	0.3811	-	-
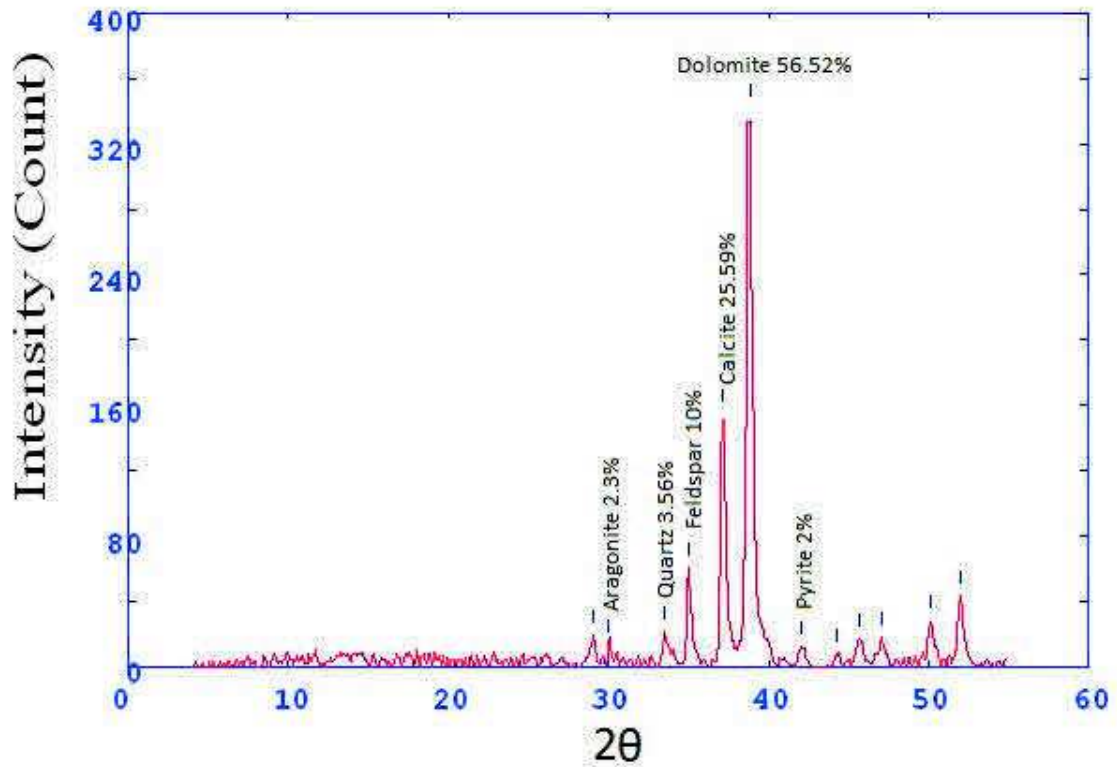
Core 1 sample 14

2Theta	d (A)	Height	Area	FWHM	Identified mineral	WT%
26.237	4.26512	11.8	78.4	0.4812	-	-
29.117	3.85107	20.1	95	0.4278	-	-
30.154	**3.72144**	19	89.9	0.3427	Aragonite	2.887537994
33.592	**3.34998**	53.2	150.4	0.2576	Quartz	8.085106383
35.07	**3.21298**	85.8	249.7	0.2744	Feldspar (orthoclase)	13.03951368
37.227	**3.03281**	125.7	508.3	0.3504	Calcite	19.10334347
38.759	**2.91728**	332.8	1345.4	0.4317	dolomite	50.5775076
40.027	**2.82847**	29.6	218.4	0.5131	Halite	4.498480243
42.201	**2.68892**	11.9	88.7	0.5155	Pyrite	3.11550152
45.652	2.49533	20.5	87.4	0.4439	-	-
47.168	2.41947	21.6	145.3	0.5547	-	-
50.167	2.28341	24.5	172.4	0.5065	-	-
52.025	2.20725	52.7	219.8	0.3621	-	-
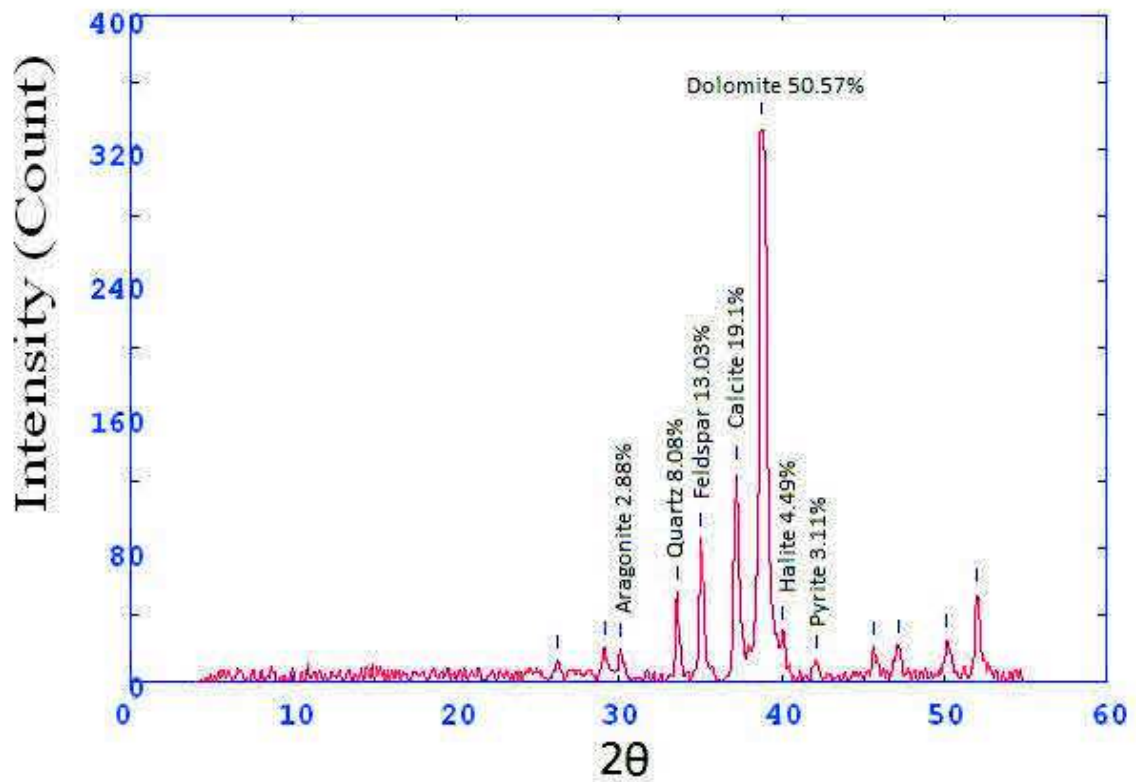
Core 2 sample 1

2Theta	d (A)	Height	Area	FWHM	Identified mineral	WT%
24.68	4.52958	22.1	20.9	0.1821	-	
26.422	4.23575	57.1	160.9	0.2629	Geothite	9.911473702
29.333	3.82326	15.7	44.1	0.2602	-	
30.548	3.67455	25.3	70.6	0.2574	-	
32.097	3.50156	13.8	38.7	0.2614	-	
33.146	3.39375	22.3	62.2	0.2634	Aragonite	3.870855754
33.782	3.33166	190.7	564.2	0.2654	Quartz	33.10189203
34.576	3.25743	19.9	58.7	0.2672	Feldspar (orthoclase)	3.454261413
35.434	3.18101	76.1	238.1	0.269	Feldspar (Albite)	13.20951224
37.425	3.01733	126.8	498.7	0.334	Calcite	22.0100677
39.234	2.88335	56.6	358.6	0.4627	Dolomite	9.824683215
40.2	2.81681	10.2	64.9	0.4647	Halite	1.77052595
42.167	2.691	16.4	84	0.4667	Pyrite	4.287450095
45.824	2.48646	24.7	101.7	0.3456	-	
46.573	2.44863	33.9	134.5	0.3314	-	
48.26	2.3679	10	26.3	0.244	-	
50.434	2.2721	30.8	130.5	0.3732	-	
52.635	2.18346	13.1	105.2	0.5804	-	
54.212	2.12453	13.2	106.7	0.468	-	
55.333	2.08478	21	82.7	0.3556	-	
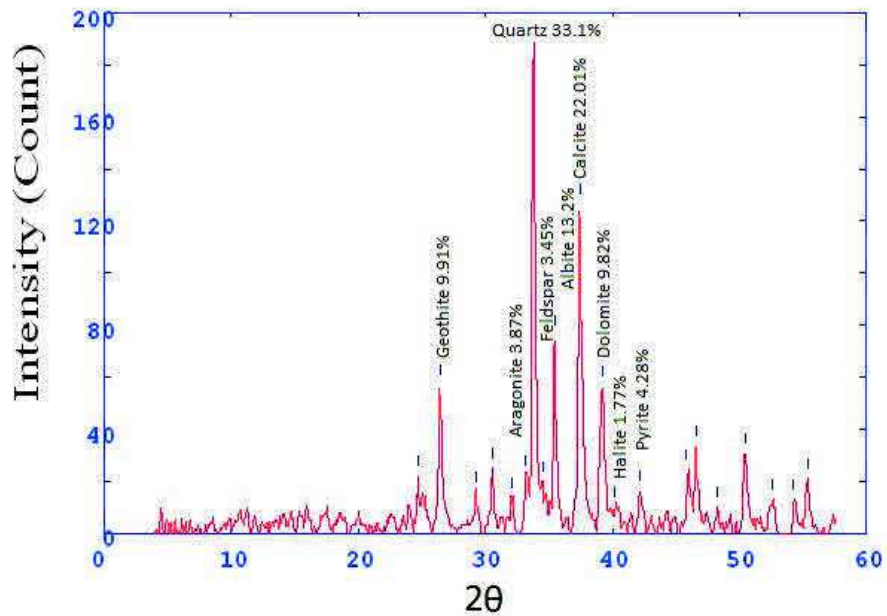
Core 2 sample 2

2Theta	d (A)	Height	Area	FWHM	Identified mineral	WT%
5.947	18.65992	228.2	179	0.1295	Mont.	38.16053512
29.701	3.77699	20.5	100	0.4178	-	
33.605	3.34866	30.4	147.9	0.3617	Quartz	14.71571906
34.224	3.28991	88	326	0.3055	Feldspar (orthoclase)	14.71571906
35.02	3.21734	19.1	70.8	0.3124	Albite	3.193979933
37.863	2.98371	196.8	758.3	0.3193	Calcite	32.909699
39.619	2.8564	20.5	79	0.3379	Dolomite	3.428093645
40.769	2.77913	9.9	38.3	0.3472	-	-
42.6	2.66488	15	70	0.3565	Pyrite	2.508361204
46.392	2.45768	34.1	173.3	0.44	-	-
47.844	2.38727	11.3	57.7	0.3613	-	-
48.673	2.34901	14	42.7	0.2825	-	-
50.811	2.25634	34.1	168	0.4058	-	-
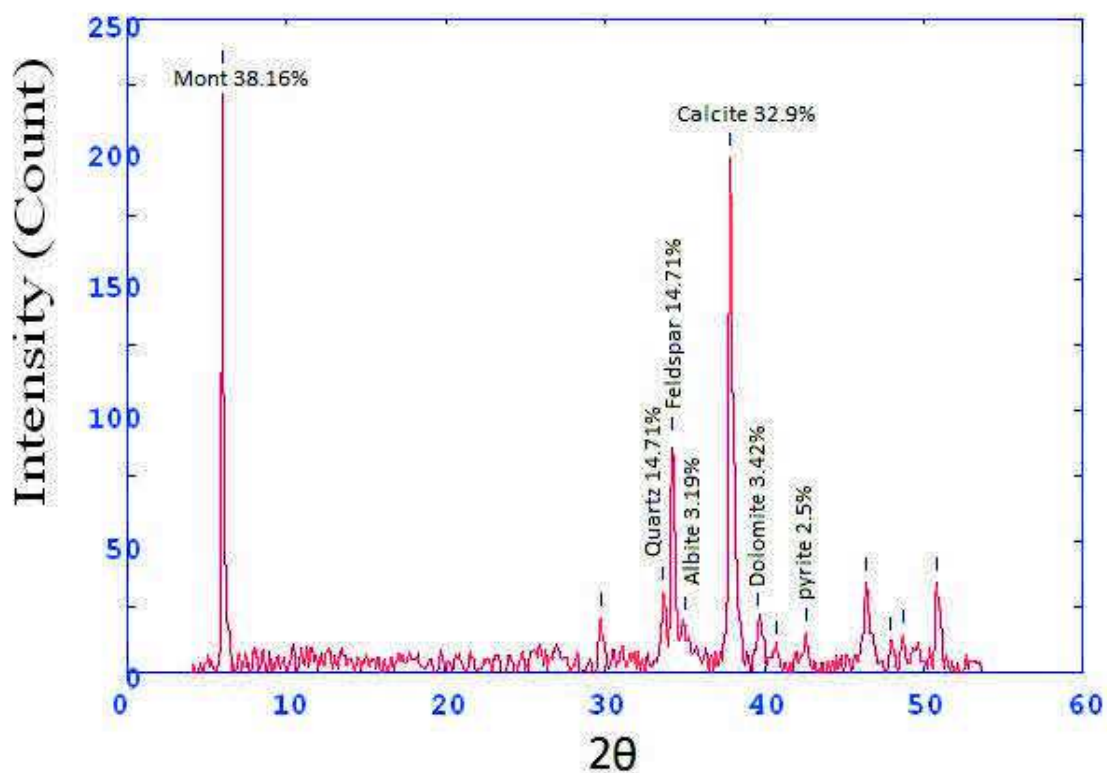
Core 2 sample 3

2Theta	d (A)	Height	Area	FWHM	Identified mineral	WT%
26.26	4.26137	36.7	102.7	0.2462	-	0
29.156	3.84603	19.6	62	0.317	-	
33.048	**3.4035**	34	107.6	0.2939	Aragonite	9.366391185
33.643	**3.34505**	96	290.4	0.2708	Quartz	26.44628099
34.531	**3.26148**	33	99.8	0.3013	Feldspar (Orthoclase)	9.090909091
37.263	**3.03002**	159.3	610.4	0.3318	Calcite	43.88429752
38.783	**2.9155**	11.7	44.8	0.3253	Dolomite	3.223140496
40.069	**2.82563**	11.7	44.8	0.3221	Halite	3.223140496
41.954	**2.70401**	17.3	53.7	0.3189	Pyrite	4.76584022
45.75	2.49027	28.5	183.4	0.4474	-	
48.052	2.37752	16.3	96.4	0.473	-	
48.969	2.33571	14.7	86.9	0.4218	-	
50.234	2.28056	29.1	125.5	0.3706	-	
55.217	2.08884	24.6	121.7	0.3801	-	
58.578	1.97873	24.7	129.5	0.3952	-	
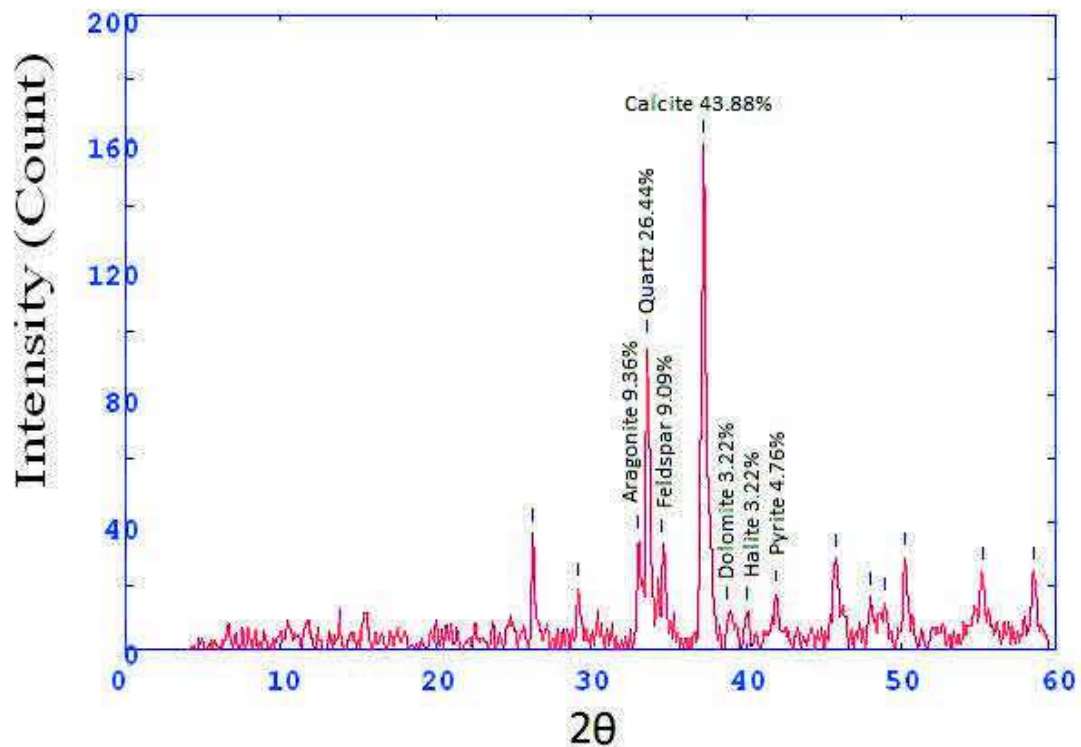
Core 2 sample 4

2Theta	d (A)	Height	Area	FWHM	Identified mineral	WT%
32.758	**3.43282**	64.4	214.7	0.2766	Aragonite	18.14084507
33.525	**3.35641**	72.1	214.7	0.2766	Quartz	20.30985915
34.202	**3.29199**	37.4	111.2	0.4672	Feldspar (orthoclase)	10.53521127
35.104	**3.20995**	6.9	20.6	0.5625	Feldspar (Albite)	1.943661972
37.194	**3.03538**	90.3	833.3	0.6578	Calcite	25.43661972
38.803	**2.91412**	15.3	140.7	0.458	Dolomite	4.309859155
40.019	**2.829**	21.5	68.2	0.2583	Halite	6.056338028
41.825	**2.71197**	47.1	148.9	0.2876	Pyrite	13.26760563
45.678	2.494	34.8	176.7	0.3911	-	
47.013	2.42703	11.8	59.9	0.3525	-	
47.967	2.38153	26.6	105.7	0.3139	-	
48.727	2.34659	22.2	88.1	0.5884	-	
50.7	2.26094	14.3	183.7	0.8628	-	
52.5	2.18866	7.1	69.6	0.6444	-	
54.05	2.13044	6.1	23.1	0.1167	-	
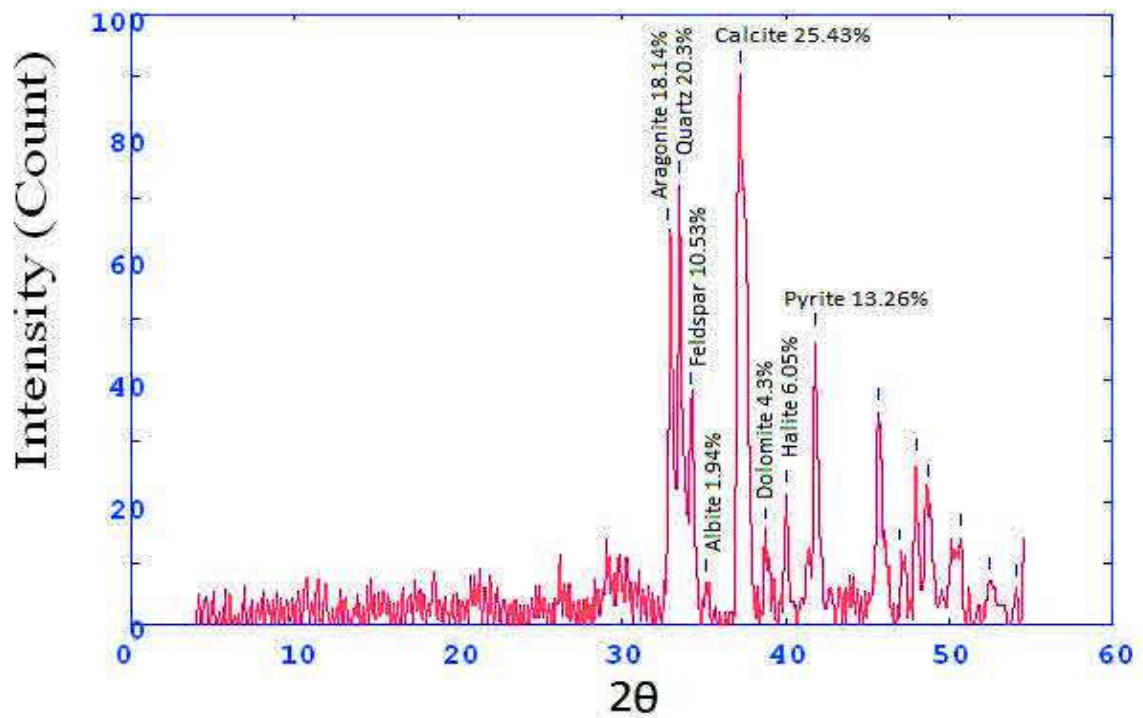
Core 2 sample 5

2Theta	d (A)	Height	Area	FWHM	Identified mineral	WT%
32.945	**3.41386**	70.7	212.3	0.3078	Aragonite	29.60636516
34.155	**3.29636**	36	108	0.4836	Quartz	15.07537688
37.24	**3.03179**	89.7	762.8	0.6595	Calcite	37.56281407
41.806	**2.71316**	42.4	130.2	0.2969	Pyrite	17.75544389
45.687	2.49353	39.6	161.1	0.3731	-	-
47.283	2.41394	10.2	41.6	0.3524	-	-
47.989	2.38048	29.5	121.1	0.3316	-	-
48.924	2.33771	24.4	100	0.6495	-	-
50.5	2.26933	18.2	236.4	0.9674	-	-
52.115	2.20369	9.6	236.4	0.9674	-	-
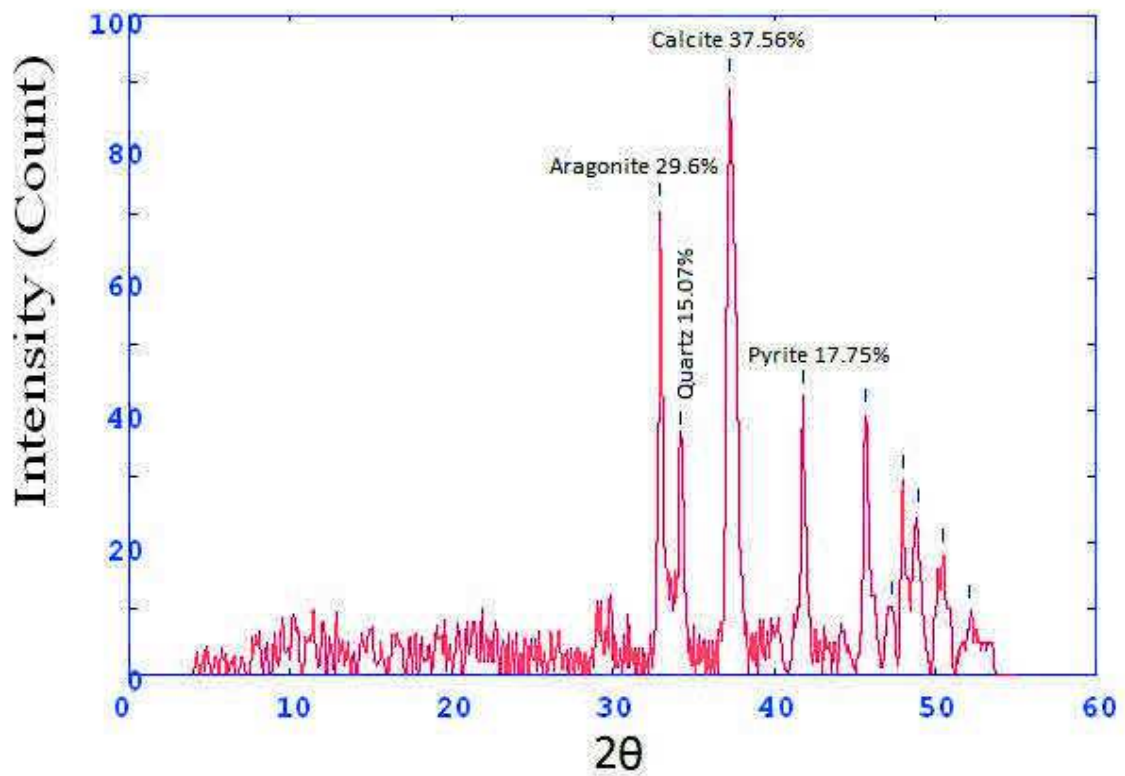
Core 2 sample 6

2Theta	d (A)	Height	Area	FWHM	Identified mineral	WT%
33.091	3.39922	83	337.1	0.3292	Aragonite	25.76039727
34.32	3.28098	53.7	218.4	0.4602	Quartz	16.66666667
37.385	3.02047	118.2	881.1	0.5912	Calcite	36.68528864
40.148	2.8203	18.1	134.5	0.4844	Dolomite	5.617628802
41.967	2.70322	49.2	188.8	0.3775	Pyrite	15.27001862
45.85	2.48512	49.3	247.7	0.4326	-	-
47.347	2.41084	18.1	86.9	0.9047	-	-
47.947	2.38242	36.1	12.3	0.1731	-	-
48.976	2.33538	27.4	19.8	0.2418	-	-
50.347	2.27575	18.8	143.6	0.9735	-	-
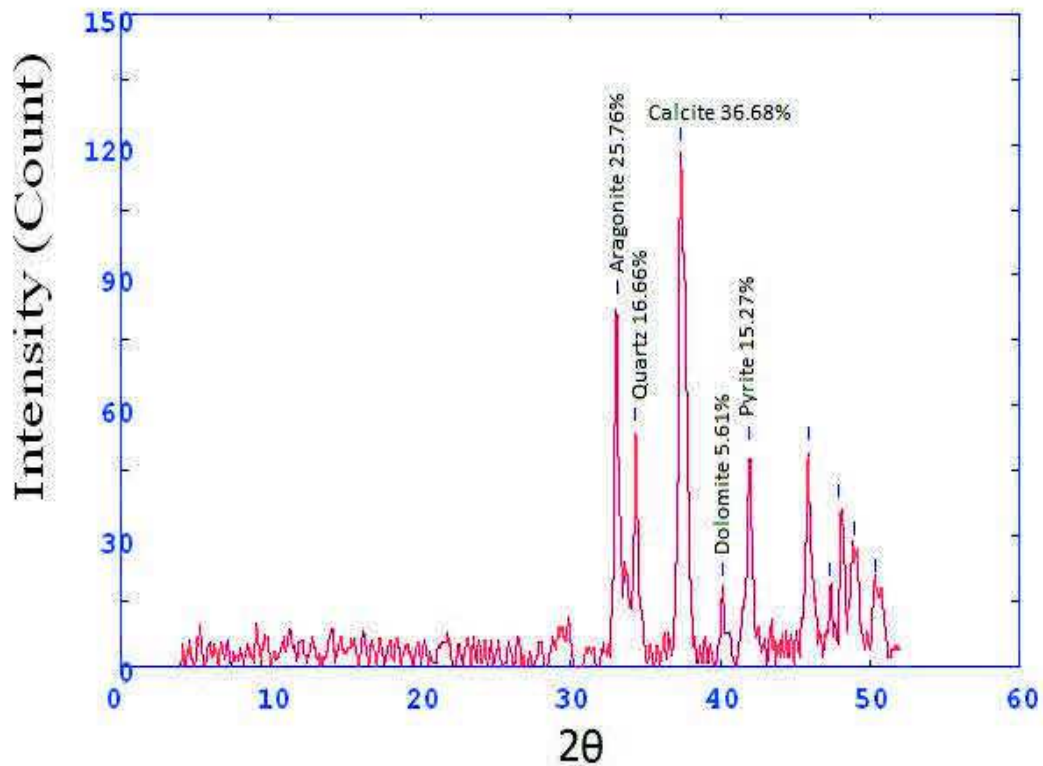
Core 3 sample 1

2Theta	d (A)	Height	Area	FWHM	Identified mineral	WT%
22.341	**4.9968**	12.4	258.9	0.2482	Gypsum	2.094948
23.509	4.75172	14.5	258.9	0.2482	-	
24.829	4.50278	94.1	258.9	0.2482	-	0
28.783	3.89478	64.6	181	0.271	-	
32.033	3.50837	330.8	1764.2	0.374	-	
33.023	**3.40606**	37.1	198	0.3264	Aragonite	6.267951
33.66	**3.34336**	77.9	231.4	0.2789	Quartz	6.267951
35.6	**3.16659**	39.7	118.8	0.3052	feldspar	6.707214
37.467	**3.01407**	61	358	0.4212	calcite	5.575266
38.531	**2.93391**	33	193.7	0.4404	dolomite	2.31458
42.3	**2.68291**	13.7	99.5	0.4596	pyrite	2.31458
44.767	2.54206	36	148.3	0.3118	-	
48.583	2.35309	30.2	170.8	0.4067	-	
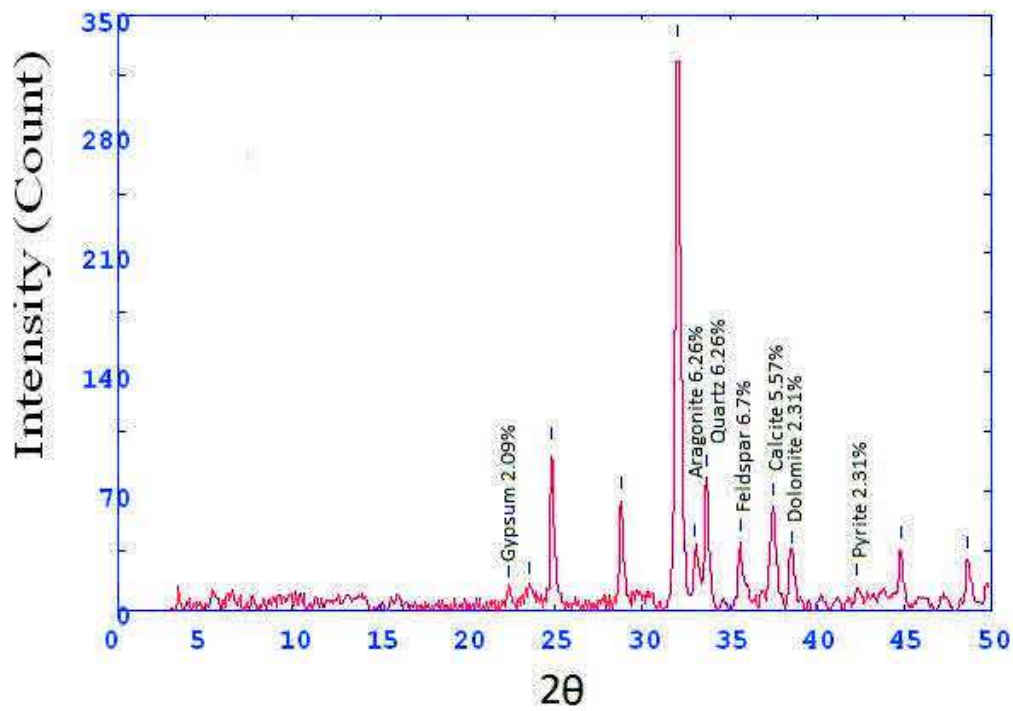
Core 3 sample 2

2Theta	d (A)	Height	Area	FWHM	Identified mineral	WT%
25.081	4.45827	90.2	16182.7	0	-	0
33.583	**3.3508**	124.5	12597.3	5	Quartz	21.08026
34.578	**3.25722**	87.4	8843.6	3.0111	feldspar	14.79851
35.216	**3.20007**	128.8	9830.7	1.0222	feldspar (Albite)	21.80833
37.171	**3.03721**	136.4	2165.3	1.099	calcite	23.09516
39.05	**2.89637**	113.5	17280	1.099	Dolomite	19.21774
40.033	**2.82807**	88	13402.9	1.099	Halite	14.9001
45.633	2.49629	79.4	15474.7	1.099	-	
47.193	2.4183	74.1	14450.9	1.099	-	
50.133	2.28483	79	10121.3	1.099	-	
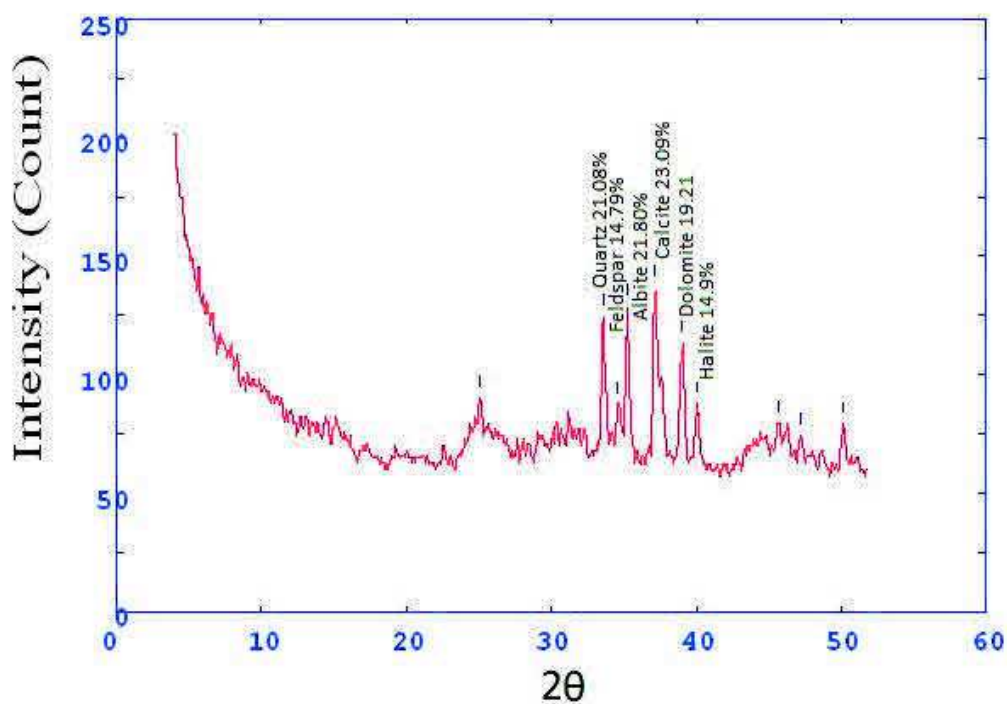
Core 3 sample 3

2Theta	d (A)	Height	Area	FWHM	Identified mineral	WT%
26.237	4.2651	65	141.3	0.2437	-	
30.395	3.69263	29.9	108.1	0.3231	-	0
33.176	**3.39079**	45.9	165.9	0.2885	Aragonite	7.9302
33.613	**3.34793**	274.1	777.9	0.2538	Quartz	47.3566
34.653	**3.2504**	44.2	125.5	0.3469	Feldspar	7.636489
35.348	**3.18846**	26	73.9	0.3934	Albite	4.492053
37.224	**3.03308**	102.1	512.8	0.44	Calcite	17.63994
39.054	**2.89611**	64.6	339.7	0.4255	Dolomite	11.16102
41.917	**2.7063**	21.9	73.7	0.3108	Pyrite	3.78369
45.767	2.48941	26.5	179.3	0.4574	-	
46.471	2.45374	20.8	141	0.3504	-	
48.133	2.37377	19	42.3	0.2433	-	
48.904	2.33862	12.2	27.2	0.3083	-	
50.215	2.28135	25.3	98.7	0.3733	-	
52.367	2.19384	16.3	71	0.3667	-	
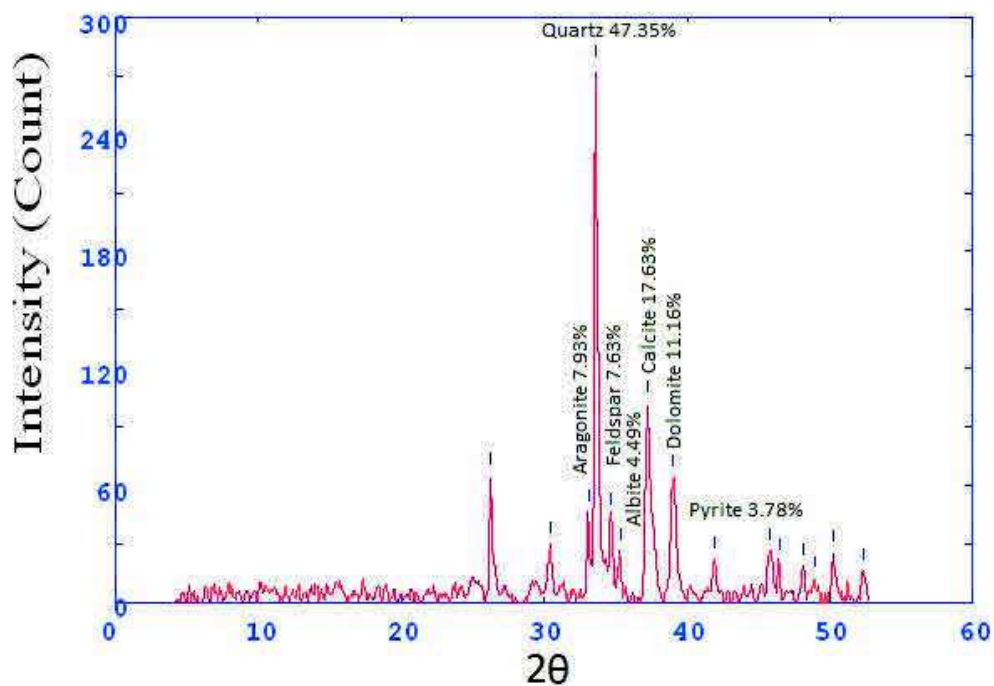
Core 3 sample 4

2Theta	d (A)	Height	Area	FWHM	Identified mineral	WT%
26.276	4.25876	45.2	143.5	0.3076	-	0
29.196	3.84075	15.3	48.5	0.2681	-	
30.421	3.68953	27	60.8	0.2286	-	
32.966	**3.41179**	34.5	77.6	0.2435	Aragonite	5.772126
33.631	**3.3462**	265.4	565.4	0.2583	Quartz	44.40355
34.671	**3.24878**	40.9	87.1	0.3559	Feldspar (orthoclase)	6.842898
35.299	**3.19275**	44.1	93.9	0.4047	Feldspar (Albite)	7.378283
37.264	**3.02987**	153	933.6	0.4535	calcite	25.59813
38.978	**2.90148**	33.7	205.4	0.3847	dolomite	5.63828
41.984	**2.7022**	26.1	114.5	0.3159	pyrite	4.366739
45.75	2.49027	32.5	212.1	0.4647	-	
48.022	2.37893	18.2	65.7	0.3456	-	
50.202	2.28189	35.6	182.6	0.4741	-	
52.621	2.18399	14	85.6	0.4748	-	
54.073	2.1296	16.9	115.4	0.4089	-	
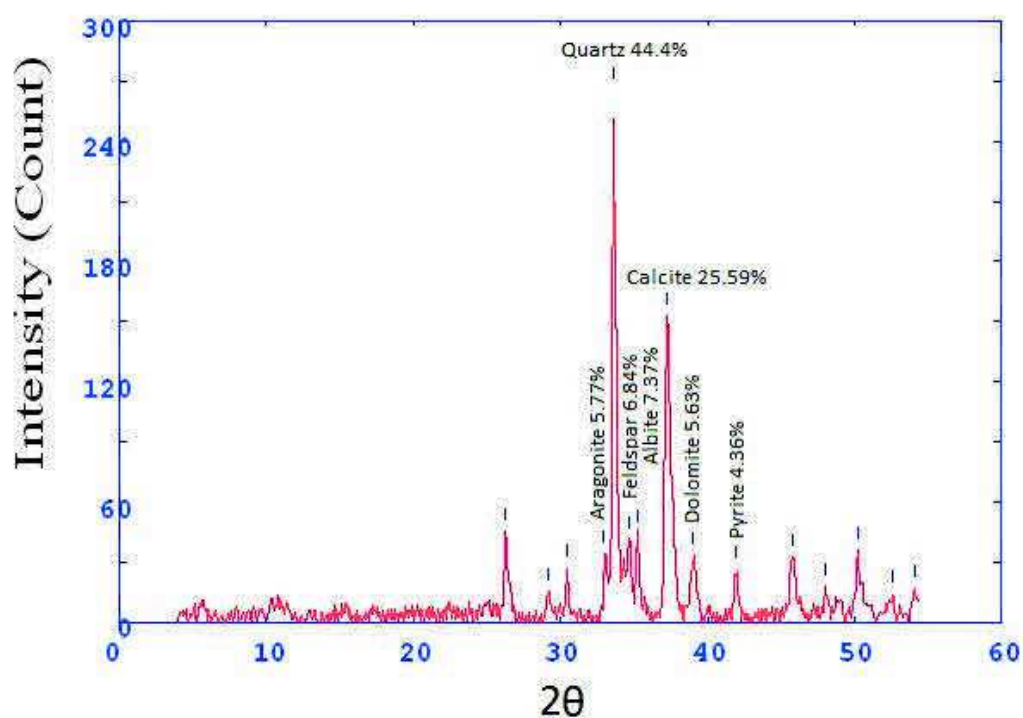
Core 3 sample 5

2Theta	d (A)	Height	Area	FWHM	Identified mineral	WT%
29.34	3.82237	62	12618.7	0	-	0
33.077	**3.40061**	135.4	1153.3	0.5883	Aragonite	28.57143
34.271	**3.2855**	93.9	799.3	0.7727	Feldspar (orthoclase)	19.81431
37.638	**3.00084**	147.2	2238.7	0.9571	calcite	31.06141
41.962	**2.70351**	97.4	2053.3	1.6	Pyrite	20.55286
45.833	2.48598	88.5	7870.7	2.4	-	
47.2	2.41793	55.7	4952.3	2.4	-	
48.133	2.37377	77	12202.7	2.4	-	
48.993	2.3346	74.1	11749.6	2.4	-	
50.315	2.27713	64.9	10287.2	2.4	-	
52.433	2.19125	55.1	11308	2.4	-	
54.681	2.1077	68.2	8512	2.4	-	
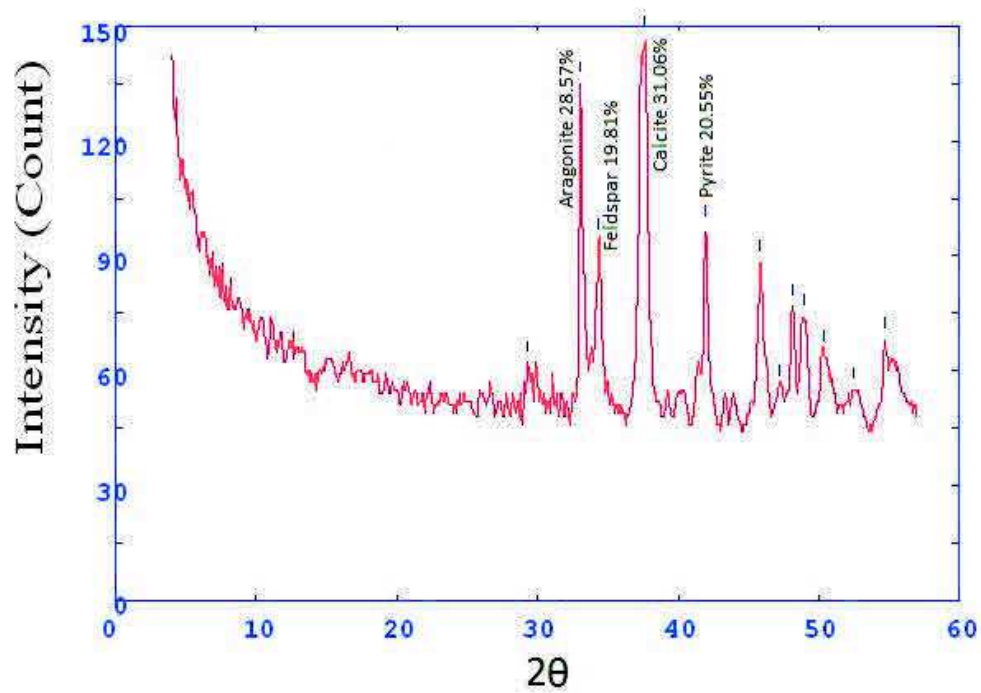
Core 3 sample 6

2Theta	d (A)	Height	Area	FWHM	Identified mineral	WT%
14.55	**7.64437**	132	1633.3	0.9556	Gypsum	12.18387
23.8	4.69447	63	12718.7	0.9556	-	
26.259	4.26147	110.1	1826.7	1.3333	-	
28.283	3.96212	58.1	963.7	1.3333	-	
29.425	3.81158	70.3	1165.4	1.3333	-	
30.395	3.69263	74	15790.7	1.3333	-	
33.013	**3.40701**	115.7	24685.7	0.858	Aragonite	10.67934
33.609	**3.34829**	223.7	1048	0.3827	Quartz	20.64796
34.563	**3.25862**	143.2	671.2	0.6589	Feldspar (orthoclase)	13.21765
35.297	**3.19295**	117.6	551.2	0.7971	Albite	10.85472
37.278	**3.02882**	154.2	2156	0.9352	calcite	14.23297
39.1	**2.89281**	104.3	14274.7	6.8	dolomite	9.6271
40.027	**2.82849**	92.7	12688.9	6.8	Halite	8.556397
41.25	2.7481	65.1	8920.1	6.8	-	
41.927	**2.7057**	82	14721.3	6.8	-	
45.756	2.48998	84.7	11344	6.8	-	
47.285	2.41385	61.3	8213.8	6.8	-	
48.019	2.37909	70.3	9414.5	6.8	-	
48.748	2.34561	71.3	7760	6.8	-	
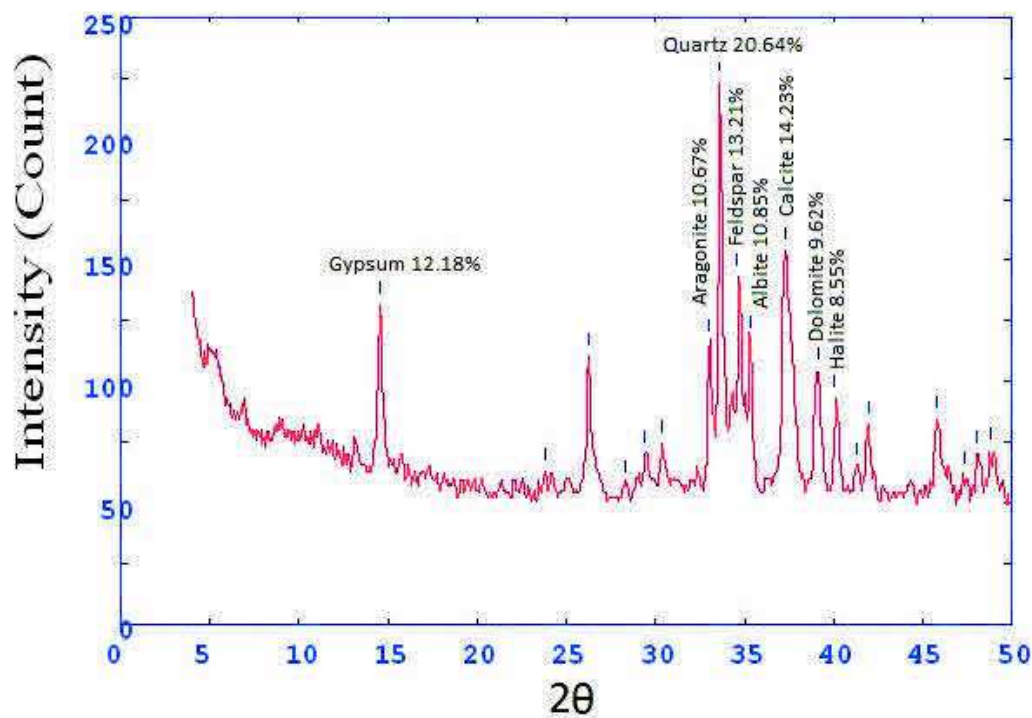
Core 3 sample 7

2Theta	d (A)	Height	Area	FWHM	Identified mineral	WT%
13.166	**8.44383**	79.8	1217.3	0.6667	Illite	8.144519
14.522	**7.65891**	140.5	1217.3	0.6667	Gypsum	14.33966
26.186	4.27326	73.2	12713.3	0.6667	-	
29.429	3.81109	72.6	12608.9	0.6667	-	
30.288	3.70546	76.8	15068	0.6667	-	
33.012	**3.40712**	111.5	21874.5	0.5117	Aragonite	11.37987
33.56	**3.35302**	237	1069.3	0.3567	Quartz	24.18861
34.574	**3.25758**	154	694.7	0.6307	Feldspar (othoclase)	15.71749
37.278	**3.02882**	154.1	2069.3	0.9048	Calcite	15.7277
38.984	**2.90106**	84.1	1129	0.9048	dolomite	8.583384
40.087	**2.82442**	74	993.6	0.9048	Halite	7.552562
41.9	**2.70735**	85.3	14253.3	0.9048	pyrite	8.705858
44.313	2.56673	58.9	9842.8	0.9048	-	
45.8	2.48769	84	12822.7	0.9048	-	
47.345	2.41094	61	9316.6	0.9048	-	
48.1	2.37531	74.5	12541.3	0.9048	-	
48.816	2.34258	66.1	11123.1	0.9048	-	
50.286	2.27836	65.4	11001.8	0.9048	-	
52.333	2.19514	59	9957.3	0.9048	-	
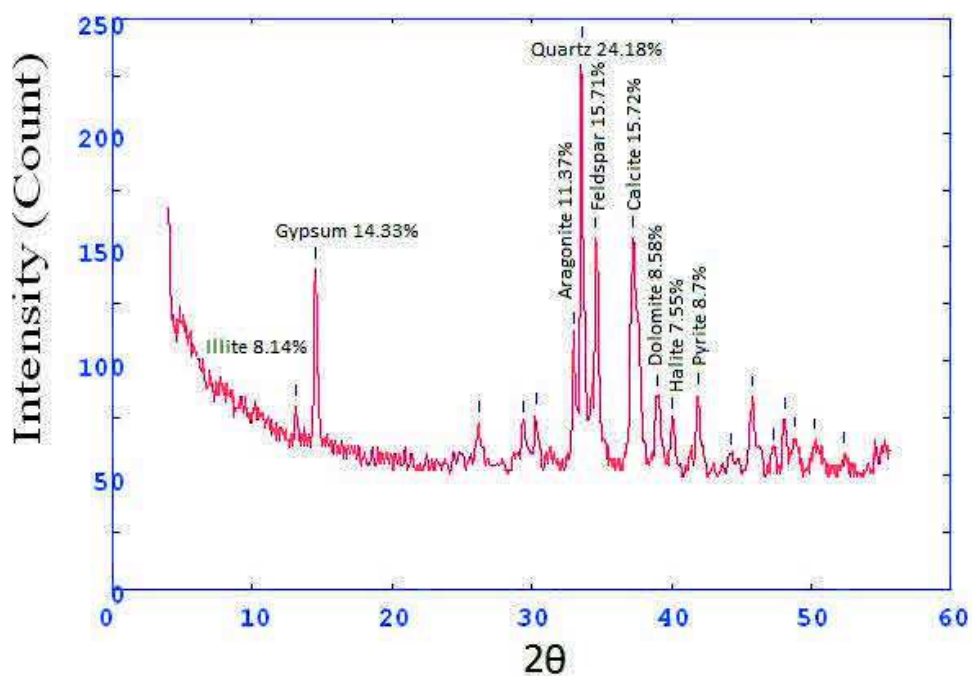
Core 3 sample 8

2Theta	d (A)	Height	Area	FWHM	Identified mineral	WT%
26.447	4.23183	63.2	11172	0	-	
29.952	3.74602	59.3	12373.3	0	-	0
33.179	**3.39041**	132.2	1036	0.563	Aragonite	19.53598
33.856	**3.32457**	98.4	771	0.8111	Quartz	14.54116
34.45	**3.26893**	94.3	738.9	0.9352	Feldspar (orthoclase)	13.93527
35.129	**3.20768**	70.1	549.4	0.9972	Albite	10.3591
37.518	**3.01011**	126.3	2124	1.0593	calcite	18.66411
40.2	**2.8168**	62	12397.3	1.0593	Halite	9.16211
42.013	**2.70037**	93.4	2062.7	1.7222	pyrite	13.80228
45.919	2.48159	82.2	11818.7	1.7222	-	
47.352	2.41065	57.8	8316.8	1.7222	-	
48.147	2.37315	82.4	9737.3	1.7222	-	
48.964	2.33591	72.2	0	0	-	
50.407	2.27323	61.1	0	0	-	
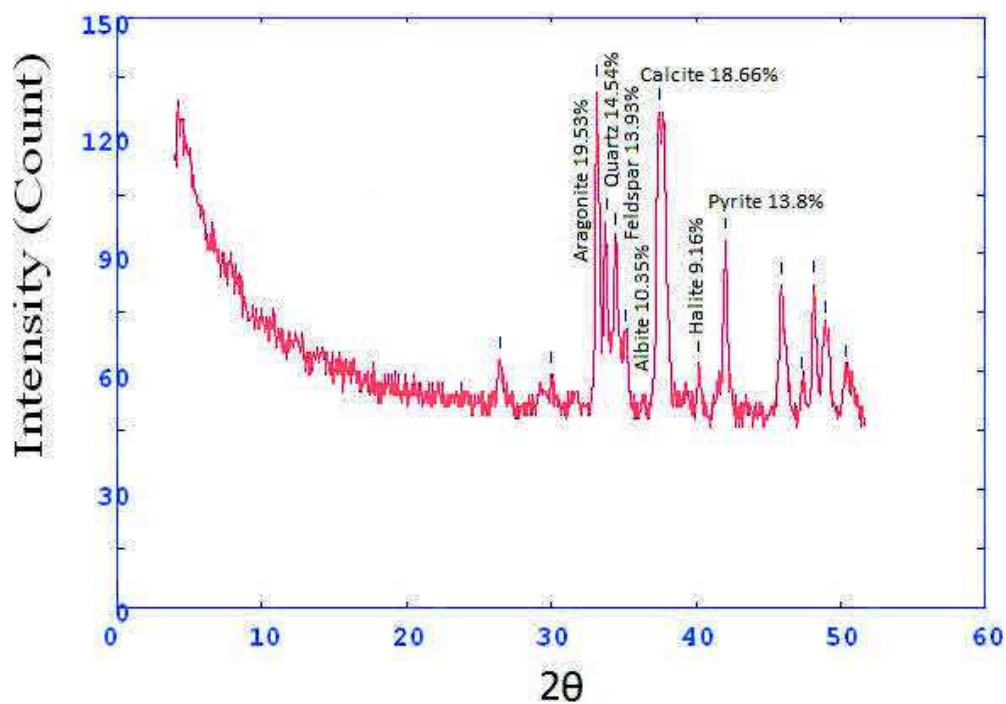
Core 3 sample 9

2Theta	d (A)	Height	Area	FWHM	Identified mineral	WT%
29.776	3.76761	63.4	13272	0	-	0
32.924	**3.41594**	140.3	1076	0.5172	Aragonite	17.68785
33.446	**3.36411**	81	621.4	1.5387	Quartz	10.2118
34.15	**3.29679**	93.4	716.4	2.0495	-	
34.747	**3.24188**	110.6	4132	2.5603	feldspar (orthoclase)	13.94352
37.525	**3.00962**	135.2	2118.7	0.9769	calcite	17.04488
38.812	**2.91343**	84.1	1318.3	0.9769	dolomite	10.60262
39.956	**2.83331**	56.8	889.9	0.9769	Halite	7.160867
41.773	**2.71519**	91.8	13505.3	0.9769	pyrite	11.57337
45.633	2.49629	87.9	12505.3	0.9769	-	
46.993	2.42799	60.9	8666.3	0.9769	-	
47.882	2.38549	82.3	12152	0.9769	-	
48.752	2.34545	68.6	10136.1	0.9769	-	
50.592	2.26548	62.1	9442.7	0.9769	-	
52.253	2.19826	62.2	7386.7	0.9769	-	
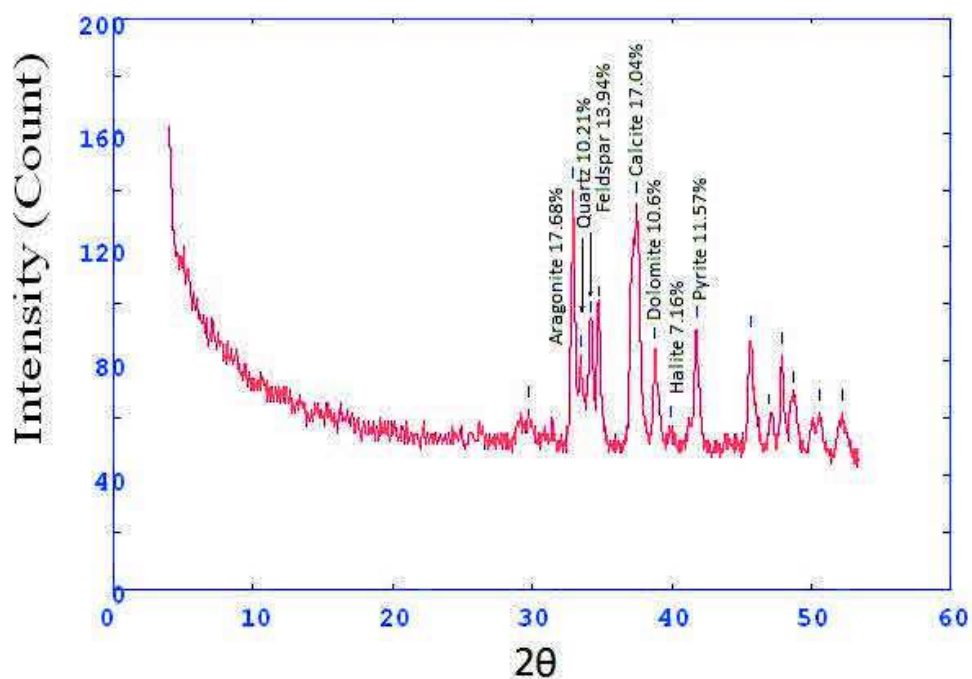
Core 4 sample 1

2Theta	d (A)	Height	Area	FWHM	Identified mineral	WT%
12.995	**8.55463**	108.2	2074.4	0.421	Illite	11.9969
14.5	**7.6705**	329.4	2074.4	0.421	Gypsum	36.5229
23.339	4.78594	11.8	86.1	0.5672	-	
25.977	4.30701	53.8	284.7	0.3977	-	
26.474	**4.22749**	24.6	130.1	0.3204	Geothite	
29.273	3.83091	219.3	603.1	0.2431	-	0
31.24	3.59516	12.6	35.8	0.2209	-	
32.723	**3.43638**	37.8	107.2	0.2347	Aragonite	4.191152
33.409	**3.36782**	113.4	315.8	0.2485	Quartz	12.57346
34.419	**3.27179**	75.6	210.4	0.518	feldspar (orthoclase)	8.382304
36.383	**3.10069**	54.2	150.8	0.6528	Albite	6.009535
36.983	**3.05207**	68.8	695.9	0.7875	calcite	7.62834
39.114	**2.89185**	34.3	134.3	0.3403	dolomite	3.803082
39.865	**2.83952**	27.6	108.1	0.4911	halite	3.060206
41.957	**2.70385**	28	221.2	0.6419	Pyrite	9.080829
44.596	2.5513	10.3	81.1	0.5279	-	
45.519	2.50222	21.6	114	0.4139	-	
47.078	2.42386	11.7	11.4	0.1928	Gypsum	
48.534	2.35536	14.9	95.4	0.4807	Gypsum	
49.875	2.29589	17.6	79.7	0.3828	Gypsum	
51.464	2.22963	13.6	42.5	0.2822	feldspar (orthoclase)	
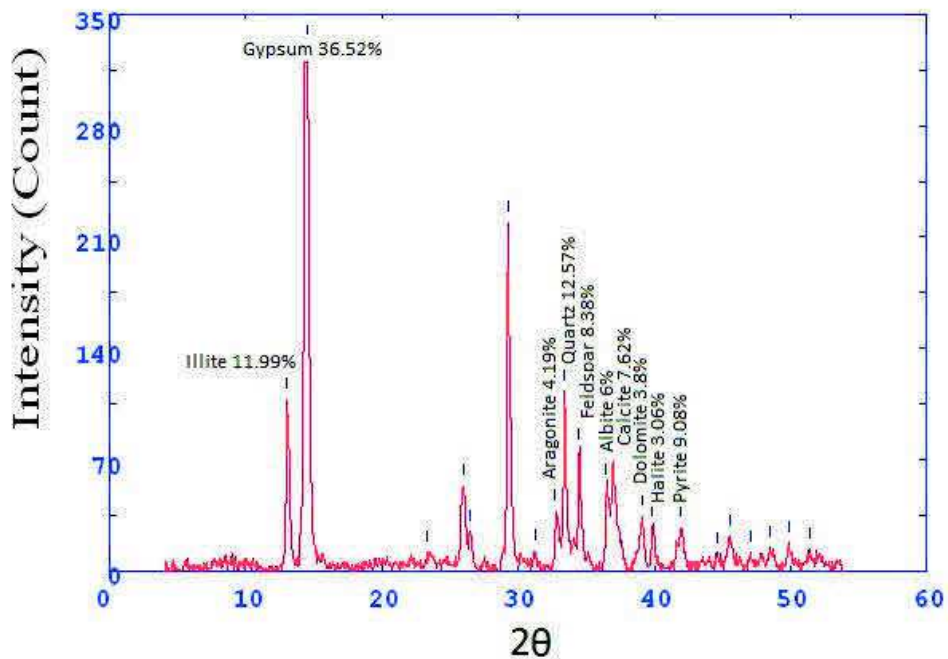
Core 4 sample 2

2Theta	d (A)	Height	Area	FWHM	Identified mineral	WT%
13.631	**8.1568**	8.6	47.9	0.2271	Illite	1.565344
14.954	**7.43883**	18.4	47.9	0.2271	Gypsum	3.349108
26.664	**4.198**	81.9	231.4	0.259	Geothite	14.90717
29.492	3.80305	19.5	90.8	0.3681	-	
30.795	3.64586	23.6	49.8	0.2012	-	0
33.522	**3.35674**	33.6	70.8	0.2302	Aragonite	6.115763
34.025	**3.30859**	184.3	523.8	0.2591	Quartz	33.54569
37.685	**2.99726**	158	621.4	0.3496	calcite	28.75865
39.502	**2.86453**	25.1	141.7	0.3957	dolomite	4.56862
40.572	**2.79205**	16.5	93.3	0.3907	halite	3.003276
42.401	**2.67683**	23	122.1	0.3857	Pyrite	4.186385
46.233	2.46564	35.8	193.6	0.4203	Aragonite	
46.699	2.44242	16.5	89.4	0.3725	Gypsum	
48.478	2.35791	16	64.1	0.3247	Gypsum	
49.3	2.32096	11.4	45.8	0.3437	Gypsum	
50.654	2.26287	36.1	153.2	0.3627	Gypsum	
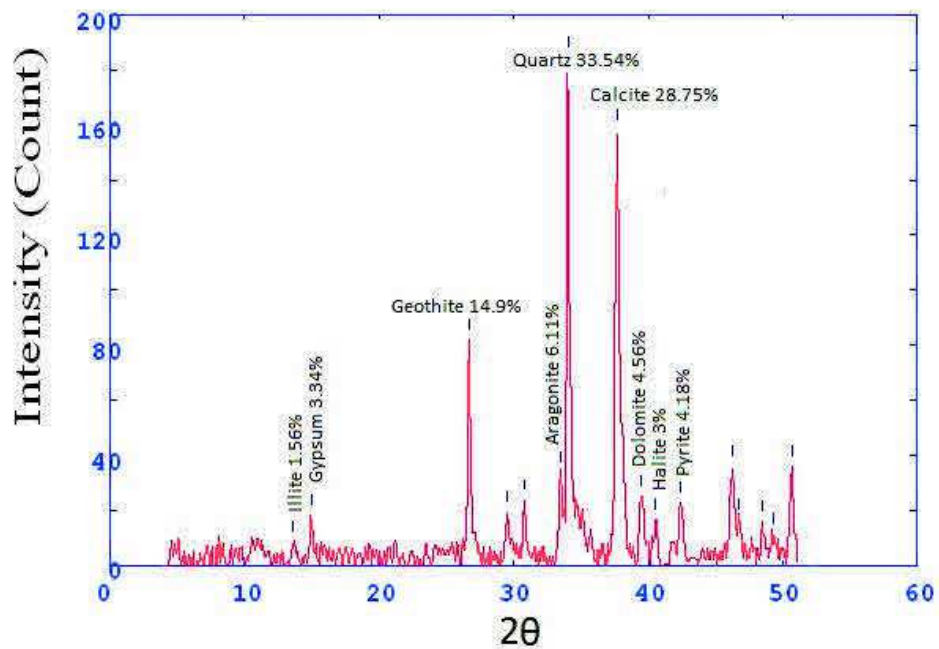
Core 4 sample 3

2Theta	d (A)	Height	Area	FWHM	Identified mineral	WT%
26.082	4.28994	13.5	65	0.3724	-	
29.071	3.85691	13.5	99.1	0.4811	-	0
32.807	**3.42778**	59.7	438	0.407	Aragonite	15.98394
33.471	**3.36169**	66.2	270.5	0.333	Quartz	17.72423
34.152	**3.2966**	33.8	137.9	0.4481	feldspar (orthoclase)	9.049531
37.144	**3.03938**	163.5	1182.2	0.5631	calcite	43.7751
38.943	**2.90403**	11.5	82.8	0.4291	dolomite	3.078983
41.726	**2.71812**	38.8	119.1	0.2951	Pyrite	10.38822
43.811	2.59471	8.6	34.8	0.2911	-	
45.541	2.50108	38.5	202.7	0.4232	-	
47.095	2.42301	14.6	76.6	0.3812	Aragonite	
47.811	2.38882	23.6	92.2	0.3392	Gypsum	
48.608	2.35197	18.2	71.2	0.4174	Gypsum	
49.938	2.29319	19.3	121.8	0.4956	gypsum	
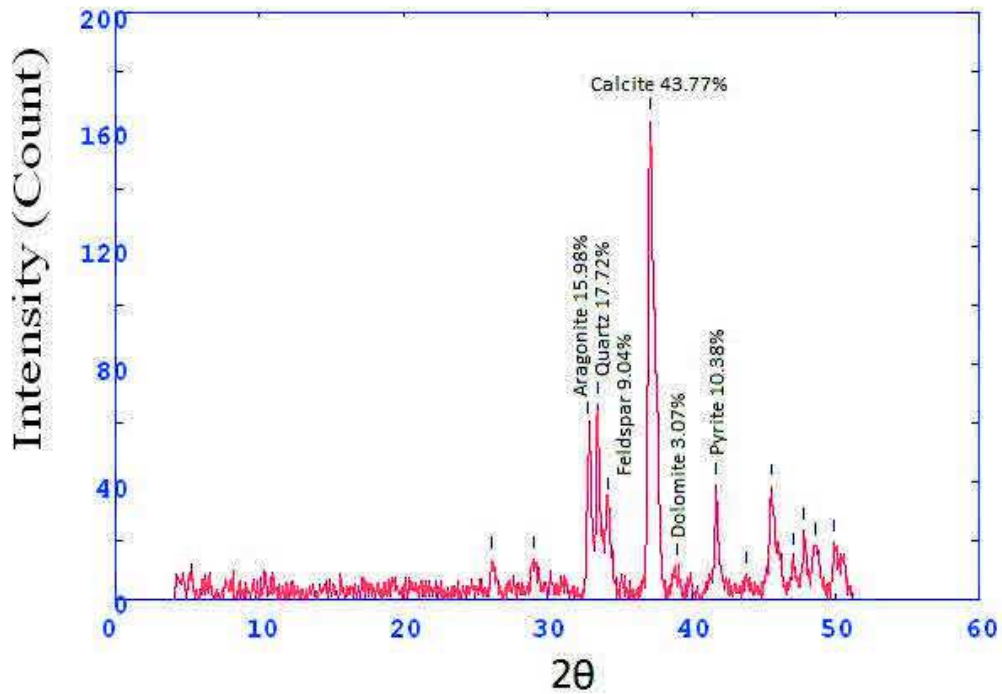
Core 4 sample 4

2Theta	d (A)	Height	Area	FWHM	Identified mineral	WT%
26.125	4.28301	60.1	12293.3	0	-	0
29	3.8662	63	13493.3	0	-	
32.864	**3.42203**	116.8	25010.1	0.3444	Aragonite	17.86752
33.469	**3.36194**	132	1182.7	0.6889	Quartz	20.19275
34.101	**3.30143**	87.2	781.3	0.8713	feldspar (orthoclase)	13.33945
37.427	**3.0172**	121.8	2036	1.0538	calcite	18.6324
38.71	**2.92083**	56.3	940.9	1.0538	dolomite	8.612513
39.933	**2.83483**	59	13505.3	1.0538	halite	9.025547
41.758	**2.71612**	80.6	13326.7	1.0538	Pyrite	12.32981
45.643	2.4958	74.4	12706.7	1.0538	Aragonite	
47.029	2.42625	55.9	9549.3	1.0538	Aragonite	
47.942	2.38269	76.1	12374.7	1.0538	-	
48.715	2.34712	68.9	11202.9	1.0538	-	
49.952	2.29261	64.1	10429	1.0538	-	
52.456	2.19038	59.1	12281.3	1.0538	Aragonite	
54.567	2.11178	59.3	12214.7	1.0538	-	
58.4	1.98422	88	2720	2.4667	-	
60.744	1.91456	61.4	1897.3	2.4667	-	
61.733	1.88682	77	11885.3	2.4667	-	
64.26	1.82013	68	9206.7	2.4667	-	
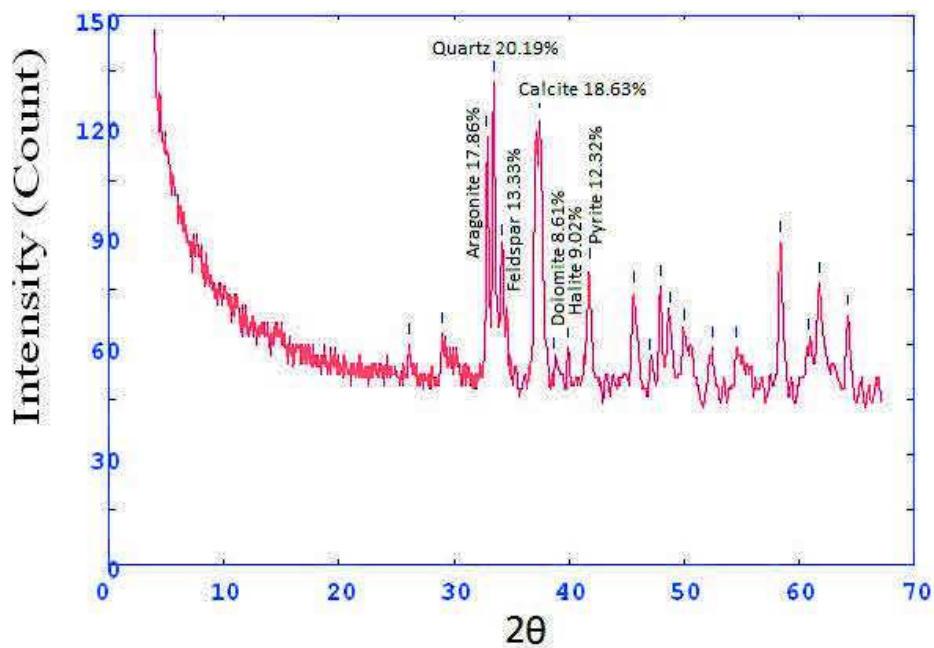
Core 4 sample 5

2Theta	d (A)	Height	Area	FWHM	Identified mineral	WT%
32.977	**3.41066**	62.8	694.7	0.7333	Aragonite	26.9066
34.255	**3.287**	47.5	525.3	0.7742	feldspar (orthoclase)	20.35133
37.589	**3.00465**	79.1	1041.3	0.815	calcite	33.89032
41.805	**2.71324**	44	942.7	1.4667	Pyrite	18.85176
45.667	2.49456	38	6237.3	1.4667	-	
48	2.37997	38	5693.3	1.4667	-	
48.826	2.34211	31.6	4729.1	1.4667	-	
50.667	2.26234	32	4450.7	1.4667	-	
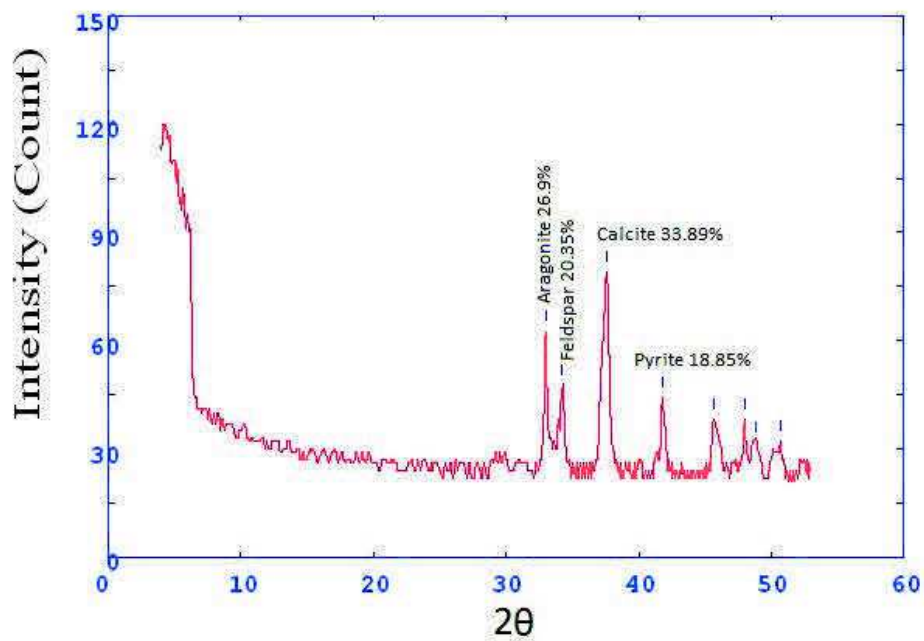
Core 4 sample 6

2Theta	d (A)	Height	Area	FWHM	Identified mineral	WT%
29.167	3.84459	60.4	12160	0	-	
29.826	3.76146	57.5	11584	0.9597	-	
30.889	3.63497	55.6	11191.6	1.4396	-	0
33	**3.40834**	113	2808	1.9194	Aragonite	20.71494
33.588	**3.35031**	66.8	1659.2	1.4523	Quartz	12.24565
34.325	**3.28055**	82.8	2058.6	1.2187	feldspar (orthoclase)	15.17874
37.567	**3.00636**	134.3	2150.7	0.9852	calcite	24.61962
40.033	**2.82804**	63	12472	0.9852	dolomite	11.54904
41.886	**2.70823**	85.6	12698.7	0.9852	Pyrite	15.69203
43.976	2.58545	50.7	7523.2	0.9852	-	
45.744	2.49055	77.1	10422.7	0.9852	-	
48.067	2.37686	71	7892	0.9852	-	
48.883	2.33954	68.7	0	0	Aragonite	
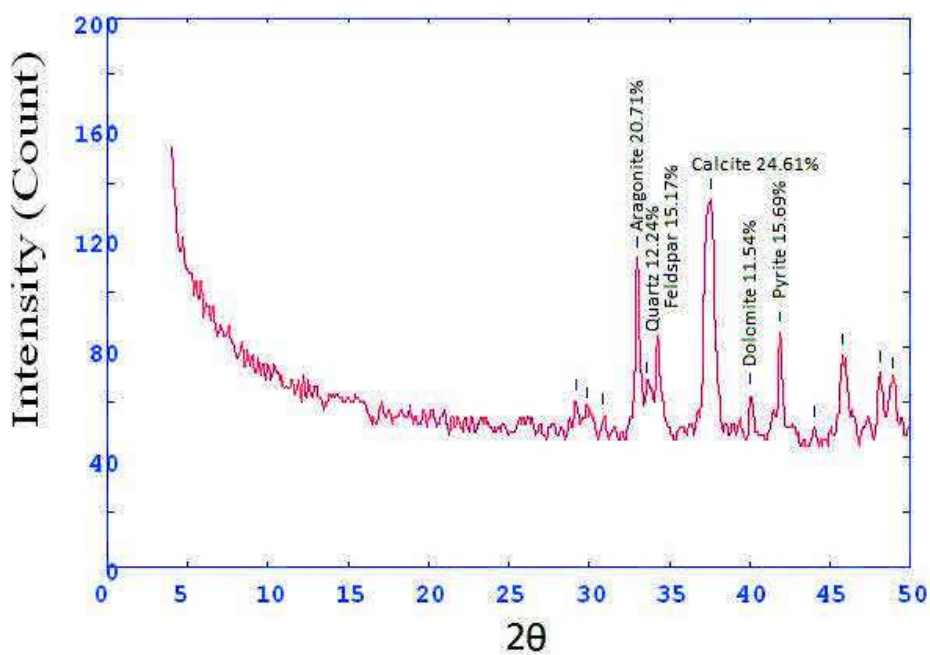
Core 4 sample 7

2Theta	d (A)	Height	Area	FWHM	Identified mineral	WT%
13.147	**8.4559**	79	1170.7	0.3364	Illite	8.072757
14.487	**7.67717**	254.9	1170.7	0.3364	Gypsum	26.04741
22.948	4.8662	62.3	12532	0.3364	-	
26.015	4.30078	74.3	12504	0.3364	-	
29.389	3.81615	79.1	13578.7	0.3364	-	
32.901	**3.41834**	103.4	17747.4	0.4219	Aragonite	10.56611
33.524	**3.3566**	146.4	1085.3	0.5074	Quartz	14.96015
34.11	**3.30055**	80.5	597.2	1.2093	feldspar (orthoclase)	8.226037
36.63	**3.08053**	66.8	495.4	1.5602	Albite	6.826078
37.338	**3.02411**	102	2962.7	1.9111	calcite	10.42305
39.149	**2.88932**	62.2	1807.4	1.9111	dolomite	6.356019
41.833	**2.71147**	83.4	13330.7	1.9111	Pyrite	8.522379
45.75	2.49026	77.1	12605.3	1.9111	Gypsum	
47.111	2.42224	59.2	9673.6	1.9111	Gypsum	
48	2.37997	71	12250.7	1.9111	Gypsum	
48.724	2.34673	63.8	11002	1.9111	Aragonite	
50.6	2.26513	60	12385.3	1.9111	Gypsum	
52.5	2.18866	55.1	12092	1.9111	dolomite	
54.569	2.11169	56.9	12481.3	1.9111	-	
55.433	2.08132	63.8	11328	1.9111	-	
58.5	1.98113	84.5	8129.3	1.9111	-	
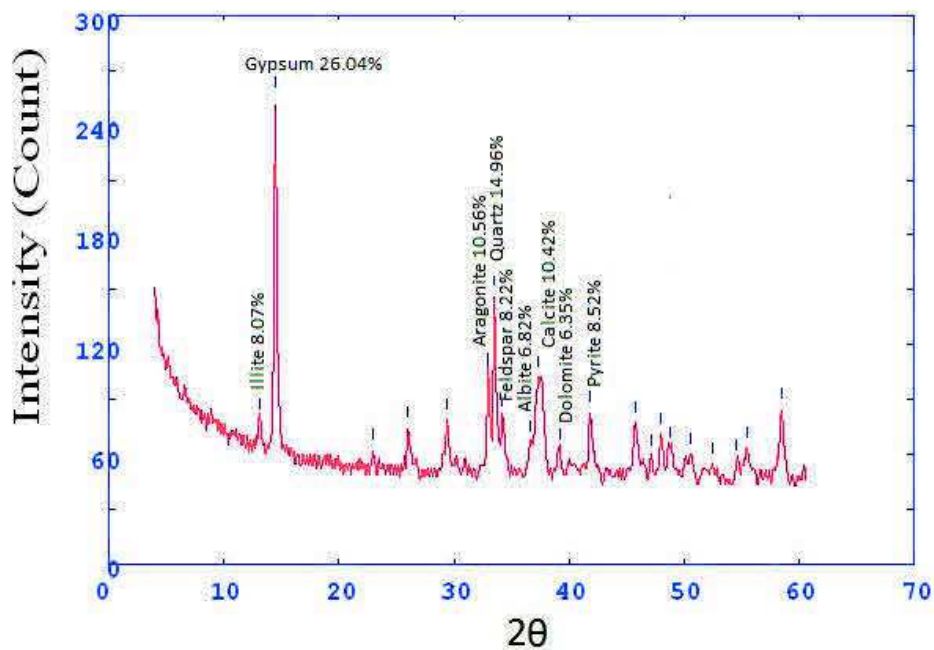
Core 4 sample 8

2Theta	d (A)	Height	Area	FWHM	Identified mineral	WT%
14.54	**7.6496**	73	13630.7	0	Gypsum	15.04844
26.221	4.26761	88.3	11534.7	0	Gypsum	
29.367	3.81897	60.6	12262.7	0	-	
29.803	3.76435	58.8	11903.2	0.9876	-	
30.864	3.6379	54	10929.2	1.4814	-	
33.027	**3.40563**	113.7	2874.7	1.9752	Aragonite	23.43847
34.136	**3.29812**	82.1	2075.9	1.4726	Quartz	16.92435
37.533	**3.00894**	131	1926.7	0.9699	calcite	27.00474
41.879	**2.70863**	85.3	12586.7	0.9699	Pyrite	17.584
45.817	2.48683	76.3	11912	0.9699	Gypsum	
47.136	2.42102	59.2	9256.1	0.9699	gypsum	
48.1	2.37531	70.3	11564	0.9699	gypsum	
48.817	2.34253	64.9	10677.9	0.9699	-	
50.585	2.26573	60.5	9951.3	0.9699	feldspar (orthoclase)	
52.519	2.18792	57.2	7060	0.9699	Aragonite	
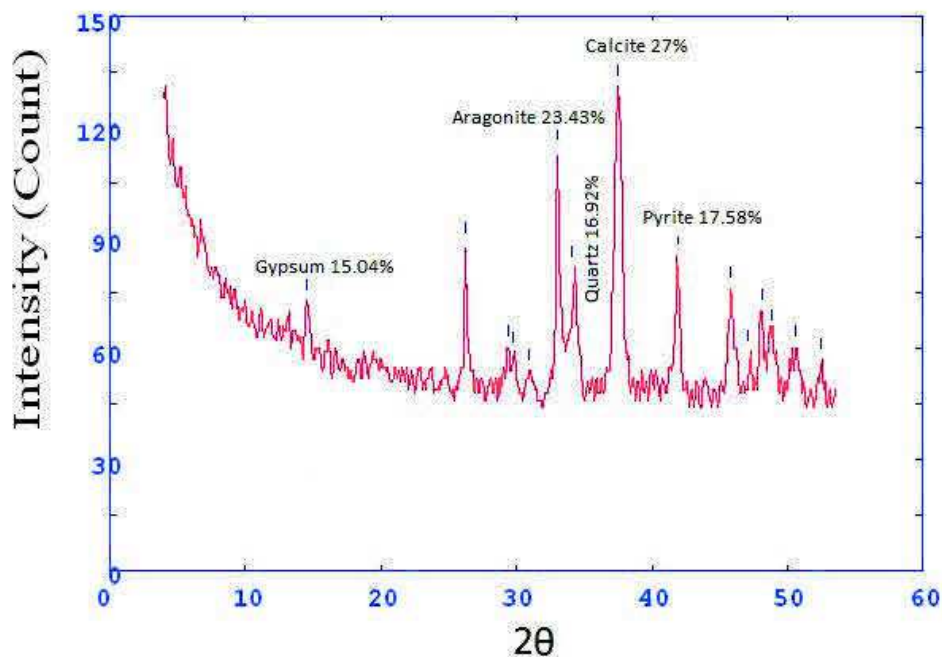
Core 4 sample 9

2Theta	d (A)	Height	Area	FWHM	Identified mineral	WT%
26.3	4.25501	59.3	11653.3	0	-	0
29.083	3.85536	68.3	12318.7	0	-	
32.97	**3.41133**	81.5	14711.3	1.1524	Aragonite	10.51613
33.619	**3.34739**	110.7	3404	2.3048	Quartz	14.28387
34.238	**3.28859**	71.9	2211.8	1.8904	feldspar (orthoclase)	9.277419
34.745	**3.24204**	105.5	3243.1	1.4761	Albite	13.6129
37.274	**3.02914**	215.2	1869.3	0.6474	calcite	27.76774
38.802	**2.91415**	63.7	553.5	0.6474	dolomite	8.219355
40.07	**2.82556**	59.6	517.8	0.6474	halite	7.690323
41.9	**2.70735**	66.9	13498.7	0.6474	Pyrite	8.632258
45.744	2.49055	82.1	11736	0.6474	-	
48.067	2.37686	59	9445.3	0.6474	-	
50.256	2.27963	70.1	7308	0.6474	Aragonite	
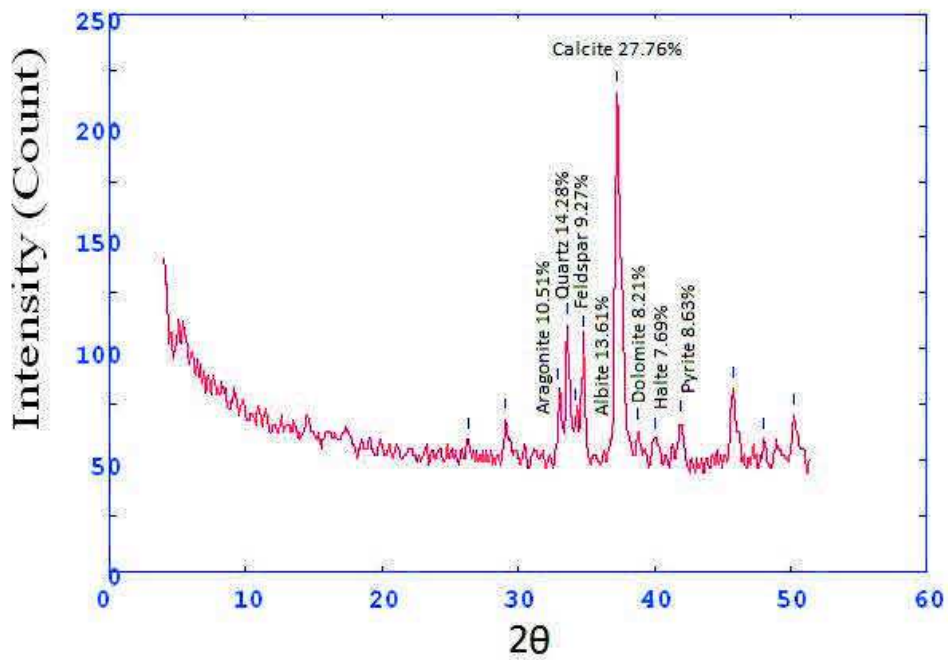
Core 5 sample 1

2Theta	d (A)	Height	Area	FWHM	Identified mineral	WT%
13.212	**8.41467**	116.7	2539.2	0.5017	Illite	24.15649
14.634	**7.60095**	328.4	2539.2	0.5017	Gypsum	67.97764
23.548	4.74408	13.7	41.4	0.2592	-	
26.08	4.29032	91.9	352.2	0.3322	-	
26.724	**4.18869**	25.7	98.3	0.2948	Geothite	5.31981
29.467	3.80626	223	629	0.2574	-	
30.417	3.69007	15.4	43.5	0.2616	-	
33.102	**3.39808**	27.7	78.1	0.2638	Argonite	5.733803
33.6	**3.34918**	91.2	269.5	0.2659	Quartz	18.87808
34.445	**3.26939**	16.4	48.6	0.2844	feldspar (orthoclase)	3.394742
35.369	**3.18667**	16.4	48.6	0.303	Albite	3.394742
36.772	**3.06899**	99.6	394.8	0.3401	Calcite	20.61685
39.325	**2.87692**	35.9	235.8	0.5165	dolomite	7.431174
42.234	**2.68692**	39.8	188.3	0.385	Pyrite	8.23846
43.761	2.5975	9.3	44	0.383	-	
45.713	2.49215	18.2	77.3	0.381	gypsum	
48.1	2.37531	12.6	34.7	0.25	Gypsum	
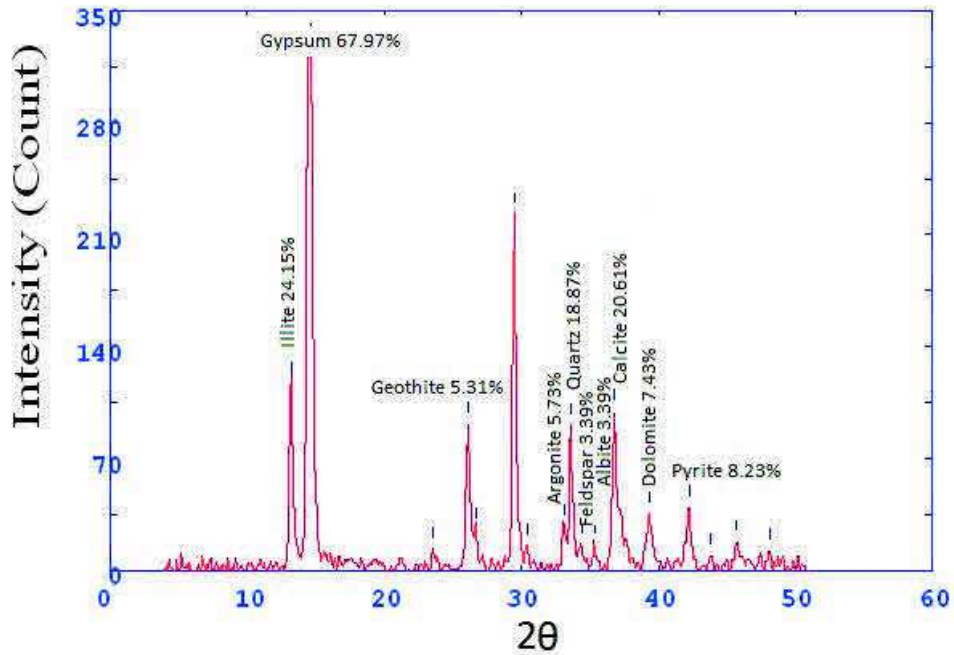
Core 5 sample 2

2Theta	d (A)	Height	Area	FWHM	Identified mineral	WT%
14.591	**7.62305**	53.5	113.8	0.2546	Gypsum	10.33217
25.082	4.45809	10.2	21.6	0.2793	-	0
26.258	4.26177	28	97.5	0.304	-	
29.228	3.83676	12.6	43.7	0.2963	-	
33.112	**3.39712**	45.4	157.7	0.2885	Aragonite	8.767864
33.644	**3.34493**	154.4	558.7	0.273	Quartz	29.81846
34.692	**3.24682**	41	148.5	0.3154	feldspar (orthoclase)	7.918115
35.352	**3.18815**	15.5	56	0.3365	Albite	2.993434
35.728	3.1556	9.2	33.3	0.3471	-	
37.261	**3.03017**	132.2	645.8	0.3577	Calcite	25.53109
39.101	**2.89276**	38.1	217.7	0.4269	dolmite	7.358053
41.982	**2.70227**	37.7	152.7	0.3288	Pyrite	7.280803
43.976	2.58542	7.3	29.5	0.3732	-	
45.848	2.48523	38.7	209.3	0.4176	Gypsum	
48.078	2.37636	20.6	228.5	0.7149	Gypsum	
48.915	2.33813	14.5	160.9	0.5387	Aragonite	
50.217	2.28127	29.9	134.3	0.3626	feldspar (orthoclase)	
52.435	2.19118	14.9	66.5	0.3097	dolomite	
55.167	2.09059	24.2	271.9	0.8289	-	
58.592	1.9783	32.7	156	0.3581	-	
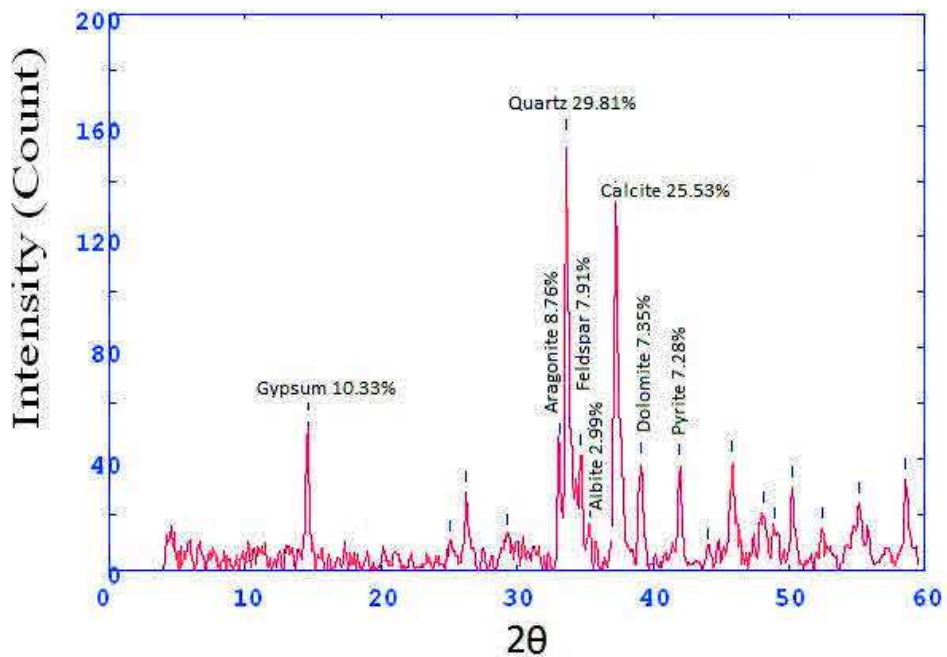
Core 5 sample 3

2Theta	d (A)	Height	Area	FWHM	Identified mineral	WT%
26.344	4.24796	65.2	11717.3	0	-	
29.414	3.81293	62.2	13189.3	0	-	0
29.96	3.74497	61.3	13007.8	0.4405	-	
30.631	3.6649	58.5	12421.6	1.1012	-	
33.156	**3.39279**	141.7	3205.3	1.7619	Aragonite	19.05082
33.732	**3.33647**	126.9	2871.5	1.5878	Quartz	17.06104
34.402	**3.27336**	98.9	2238.7	1.4137	feldspar (orthoclase)	13.29659
35.324	**3.19055**	58.9	1332.4	1.2396	Albite	7.918795
36.078	3.126	55.4	1254.3	1.1526	-	
37.336	**3.02431**	100	2262.1	1.1091	Calcite	13.44447
37.808	2.98789	131.1	2088	1.0656	-	
39.096	**2.89313**	59.6	949	1.6411	dolomite	8.012907
40.101	**2.82345**	56.5	899.5	1.785	Halite	7.596128
41.526	2.73064	61	971	1.9289	-	
42.013	**2.70042**	101.3	2741.3	2.2167	Pyrite	13.61925
45.919	2.48159	87.2	12380	2.2167	-	
47.393	2.40868	64.8	9198	2.2167	-	
48.156	2.37271	91.1	9693.3	2.2167	-	
48.901	2.33874	78.6	0	0	Aragonite	
50.242	2.28021	62.3	0	0	feldspar (orthoclase)	
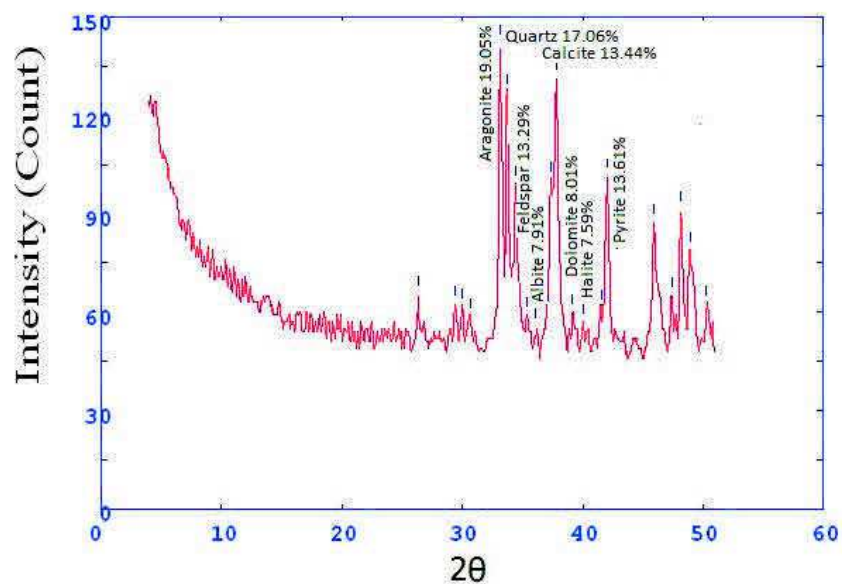
Core 5 sample 4

2Theta	d (A)	Height	Area	FWHM	Identified mineral	WT%
33.085	**3.39984**	126.8	1722.7	1.0667	Aragonite	21.80567
33.553	**3.35377**	76.4	1037.3	1.0883	Quartz	13.13844
34.238	**3.28857**	95.7	1299.7	1.11	feldspar (orthoclase)	16.45744
37.7	**2.99612**	129	2336	1.1533	dolomite	22.18401
40.1	**2.82353**	57.3	12921.3	1.1533	halite	9.853826
41.985	**2.70212**	96.3	1978.7	1.5333	Pyrite	16.56062
45.875	2.48384	90.1	9462.7	5.7	-	0
47.361	2.41017	57.4	6031.1	5.7	-	
48.133	2.37377	85	12134.7	5.7	-	
48.928	2.33751	72.4	10339.1	5.7	Aragonite	
50.299	2.27777	59.4	8481.9	5.7	feldspar (orthoclase)	
50.933	2.25128	62	12364	5.7	-	
52.258	2.19807	57.4	11455.1	5.7	dolomite	
54.742	2.10552	70.1	10548	5.7	-	
55.882	2.06595	59.8	8999	3.3056	-	
56.959	2.03005	57	8583.8	2.1083	-	
58.642	1.97675	99	1229.3	0.9111	-	
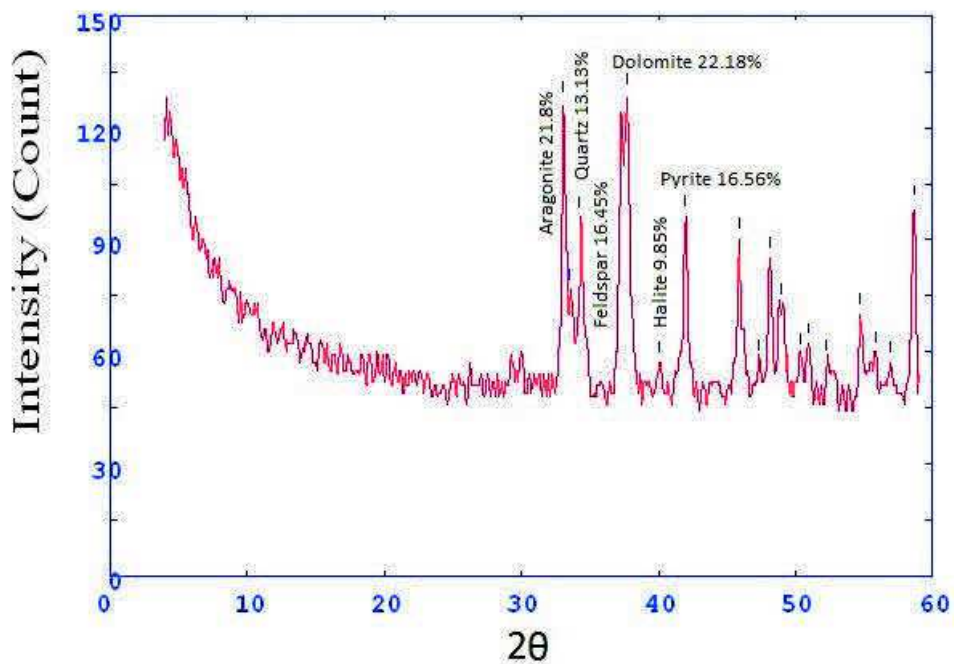
Core 6 sample 1

2Theta	d (A)	Height	Area	FWHM	Identified mineral	WT%
29.301	3.82728	10.3	32.1	0.1989	-	
30.415	3.69027	17.2	32.1	0.1989	-	0
33.11	**3.39737**	74.4	139	0.2336	Aragonite	18.81639
33.641	**3.34522**	122.5	359.2	0.2682	Quartz	30.98128
34.347	**3.27844**	40.5	118.7	0.5226	feldspar (orthoclase)	10.24279
37.707	**2.99559**	93.1	1131.2	0.7769	calcite	23.54578
38.917	**2.90588**	14.5	176.5	0.6549	dolomite	3.667172
40.194	**2.81719**	16.2	107.5	0.5329	halite	4.097117
41.488	2.73305	9.6	63.5	0.4416	-	
41.983	**2.70222**	34.2	139.8	0.3504	Pyrite	8.649469
44.233	2.57114	7.1	39.8	0.3775	-	
45.833	2.48599	36.8	266.8	0.6452	Quartz	
48.14	2.37344	27.6	90.3	0.3078	Pyrite	
49.009	2.33391	21.4	70.1	0.3765	Aragonite	
50.437	2.27198	15.7	51.3	0.4109	Pyrite	
52.466	2.18996	13.9	87.3	0.4453	dolomite	
55.833	2.06759	16.1	408.3	1.6143	-	
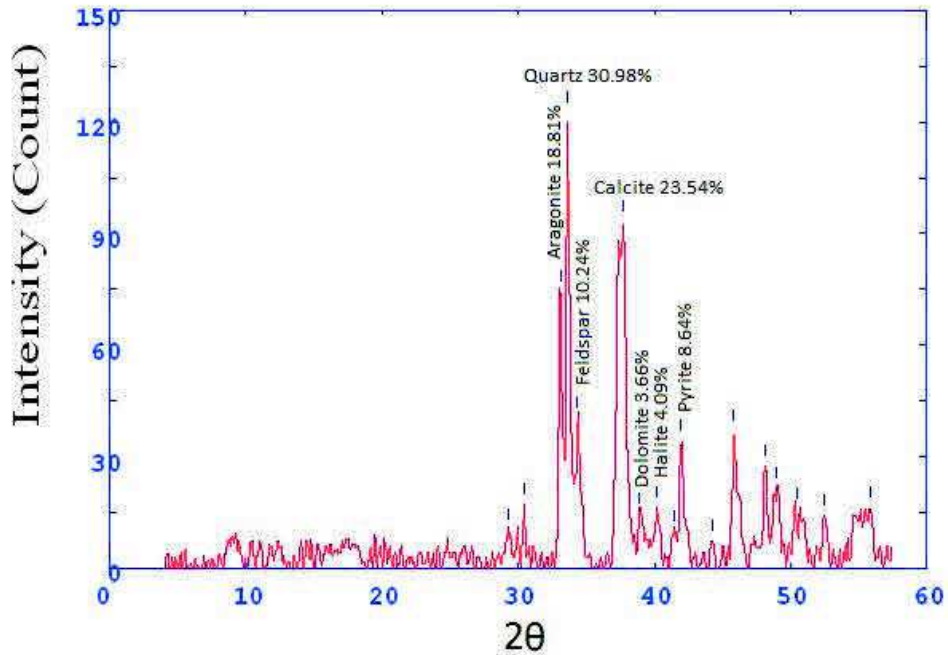
Core 6 sample 2

2Theta	d (A)	Height	Area	FWHM	Identified mineral	WT%
26.215	4.26852	16.7	46.9	0.2115	-	0
29.433	3.81058	13.6	78.4	0.4351	-	
33.044	**3.40397**	75.8	227.4	0.2787	Aragonite	22.27446
33.597	**3.34945**	42.4	127.2	0.4976	Quartz	12.45959
34.296	**3.28317**	43.1	129.2	0.607	feldspar (orthoclase)	12.6653
35.345	**3.18876**	5	15.1	0.6617	feldspar (Albite)	1.469292
36.131	3.1216	5	15.1	0.6891	-	
37.662	**2.99903**	104.9	1051.4	0.7164	Calcite	30.82574
38.839	**2.91146**	14	140.8	0.5365	dolomite	4.114017
39.975	**2.83198**	11.4	114	0.4465	halite	3.349985
41.9	**2.70735**	43.7	180.2	0.3565	Pyrite	12.84161
45.82	2.48666	36.4	318.5	0.6795	-	
47.14	2.42086	15.4	134.4	0.5137	Aragonite	
48.085	2.376	27.3	115.1	0.348	Aragonite	
48.8	2.3433	25.1	105.5	0.7028	feldspar	
50.5	2.26932	14.1	234.4	1.0575	Pyrite	
52.4	2.19254	16	138.7	0.644	dolomite	
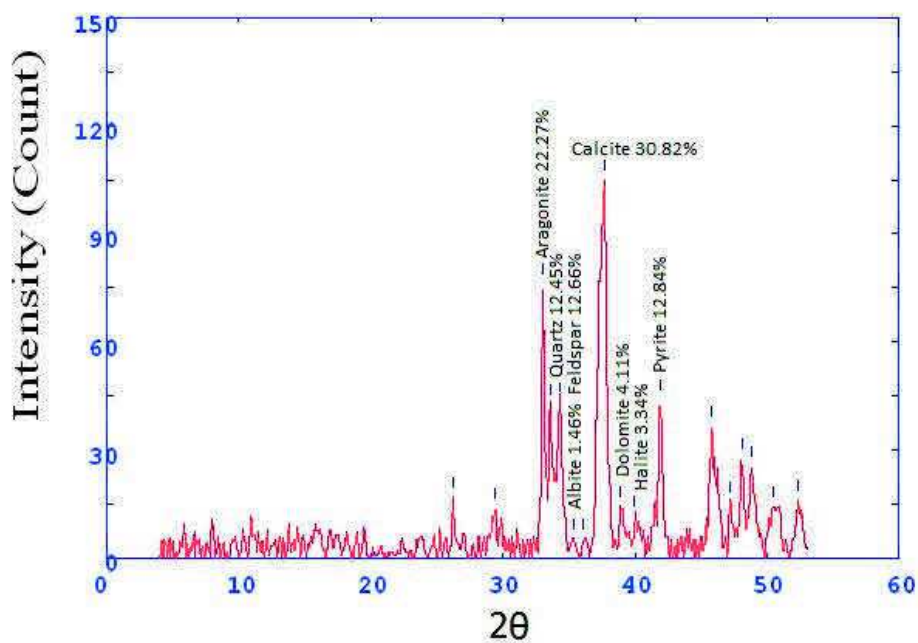
Core 6 sample 3

2Theta	d (A)	Height	Area	FWHM	Identified mineral	WT%
23.867	4.68155	51	9598.7	0	-	
26.267	4.26032	57	9589.3	0	-	0
29.367	3.81897	54.3	9978.7	0	-	
33.047	**3.40366**	82.7	4228	4.1333	Aragonite	17.69741
33.723	**3.33733**	54.7	2798.5	3.3569	Quartz	11.70554
34.352	**3.27801**	65.6	3352.7	2.5806	feldspar (orthoclase)	14.03809
35.071	**3.21287**	56.2	2873.4	1.8042	feldspar (Albite)	12.02654
36.239	3.11261	50	2558.9	1.416	-	
37.227	**3.03277**	89.3	4565.9	1.2219	Calcite	19.10978
37.627	3.00174	91.8	1522.7	1.0278	-	
38.486	2.93721	50.9	844.5	1.0278	-	
39.115	**2.89178**	52.7	873.7	1.0278	dolomite	11.27755
41.922	**2.70598**	66.1	10238.7	1.0278	Pyrite	14.14509
44	2.5841	51	9857.3	1.0278	-	
45.767	2.48941	65.6	9922.7	1.0278	-	
48.033	2.37841	59.3	9829.3	1.0278	Aragonite	
48.999	2.33433	56.8	9418.3	1.0278	-	
50.168	2.28337	55.6	9224	1.0278	Pyrite	
52.533	2.18737	52	6673.3	1.0278	dolomite	
54.1	2.1286	54.4	5157.3	1.0278	-	
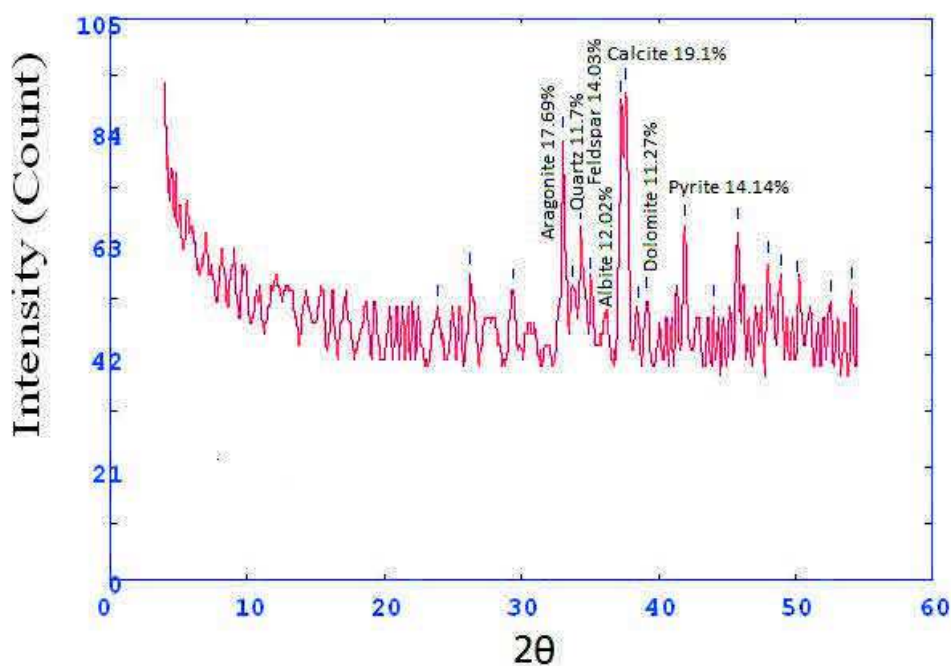
Core 6 sample 4

2Theta	d (A)	Height	Area	FWHM	Identified mineral	WT%
29.874	3.7555	13.3	11.9	0.1432	-	
33.009	**3.4074**	80.9	259.4	0.3146	Aragonite	24.47066
33.509	**3.35803**	28.8	92.4	0.5123	Quartz	8.711434
34.184	**3.29359**	50.3	161.3	0.6111	feldspar (orthoclase)	15.21476
37.54	**3.00843**	99.4	1046.7	0.71	Calcite	30.06655
39.396	**2.87193**	4.8	50.2	0.4886	dolomite	1.451906
40.074	**2.82528**	14.3	46	0.2672	halite	4.325469
41.423	2.73715	13.6	43.6	0.2843	-	
41.904	**2.70708**	52.1	164.8	0.3014	Pyrite	15.75923
45.75	2.49028	35.9	207.5	0.4446	Aragonite	
47.213	2.4173	15.5	89.8	0.4404	Aragonite	
48.034	2.37839	30.6	188.8	0.4362	Aragonite	
48.661	2.34957	25.6	158.1	0.8919	Aragonite	
50.109	2.28589	15.8	97.7	1.1198	feldspar	
50.784	2.25745	15.2	93.8	1.2337	Pyrite	
52.633	2.18353	11	210.9	1.3476	dolomite	
54.683	2.10762	19	137.1	0.4854	Aragonite	
55.61	2.07524	16.2	116.8	0.3883	-	
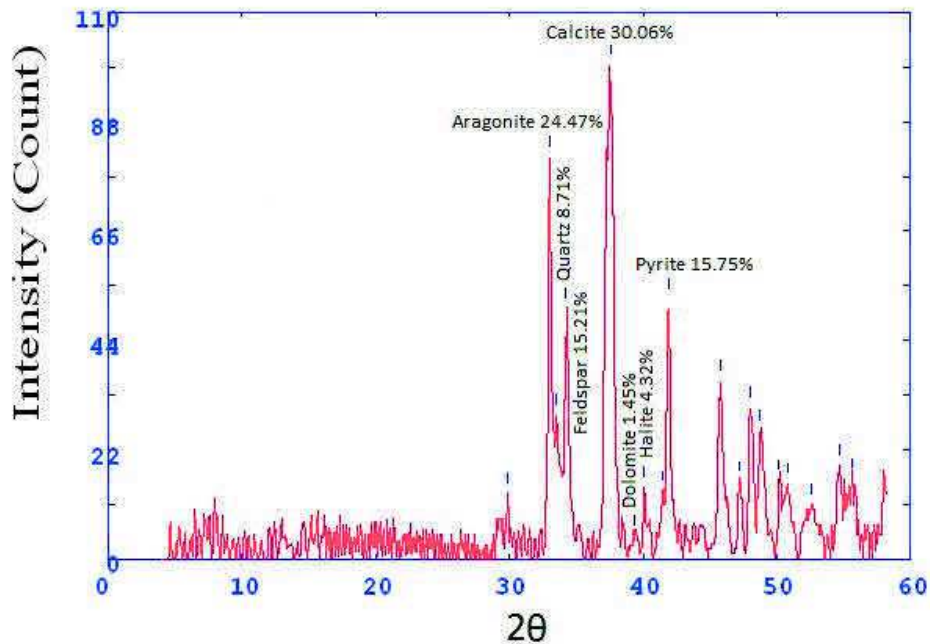
Core 6 sample 5

2Theta	d (A)	Height	Area	FWHM	Identified mineral	WT%
29.108	3.85221	15.7	81	0.2201	-	0
30.352	3.69781	41.5	81	0.2201	-	
32.954	**3.41298**	68.8	134.2	0.226	Aragonite	12.92019
33.59	**3.35016**	194.7	411.6	0.2319	Quartz	36.56338
34.321	**3.28084**	39.7	84	0.4562	feldspar (orthoclase)	7.455399
36.202	**3.1157**	7.3	15.4	0.5684	Albite	1.370892
37.284	**3.02836**	143.6	1363.8	0.6805	Calcite	26.96714
40.085	**2.82456**	41	160.2	0.3105	dolomite	7.699531
41.9	**2.70732**	37.4	116.1	0.3034	Pyrite	7.023474
44.065	2.58048	6.2	19.2	0.3802	-	
45.767	2.48941	48.1	293	0.4569	-	
47.142	2.42075	12.3	75.2	0.3729	Aragonite	
48.022	2.37893	27.5	87.7	0.2888	Aragonite	
48.851	2.34097	20.2	64.3	0.4764	Aragonite	
50.4	2.27353	21.8	183.3	0.664	Pyrite	
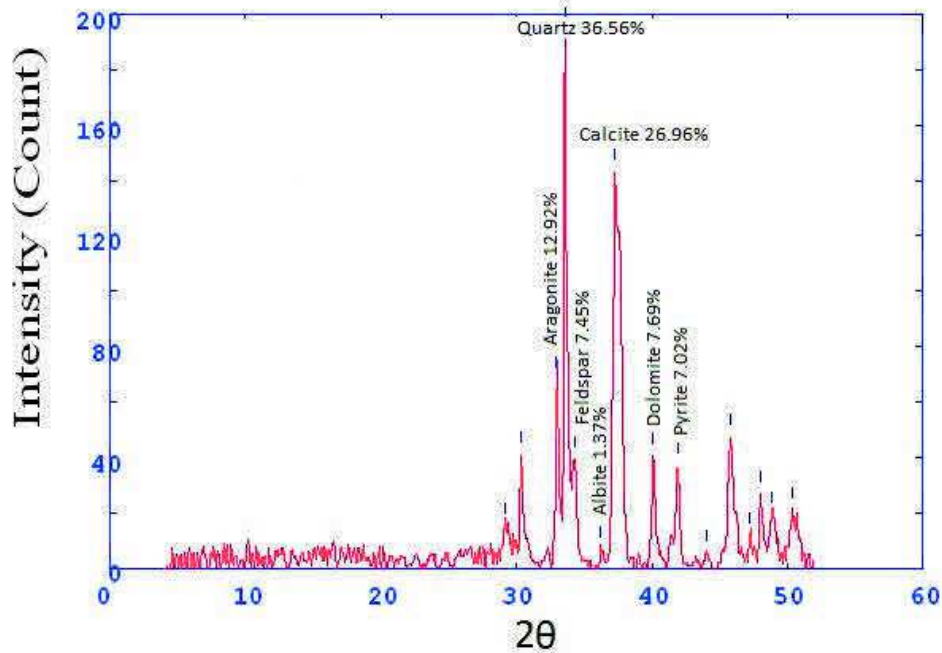
Core 6 sample 6

2Theta	d (A)	Height	Area	FWHM	Identified mineral	WT%
13.083	**8.4971**	28.8	77.7	0.2813	Illite	3.169014
14.609	**7.61383**	21.3	76.1	0.296	Gypsum	2.34375
17.369	6.41117	17.4	89.6	0.4373	-	
23.864	4.68212	13.5	67	0.3772	-	
26.291	4.25642	165.2	458	0.2596	-	
27.655	4.05034	31.1	86.1	0.2552	-	
30.448	**3.68636**	89.9	191.3	0.2508	Aragonite	9.892165
33.633	**3.34597**	329.3	1882.8	0.4046	Quartz	36.2346
34.749	**3.24171**	139.5	797.5	0.3824	feldspar (orthoclase)	15.34991
35.347	**3.18855**	121.9	697.1	0.3712	Albite	13.41329
37.278	**3.02882**	63.4	308.6	0.3601	calcite	6.976232
39.106	**2.89242**	88.8	474.7	0.4111	dolomite	9.771127
40.133	**2.82128**	25.9	138.5	0.8705	halite	2.849912
46.4	2.45727	32	114.2	0.3333	Aragonite, gypsum	
50.219	2.28118	36.6	142	0.3108	Pyrite	
51.244	2.23853	24.9	0	0	Gypsum	
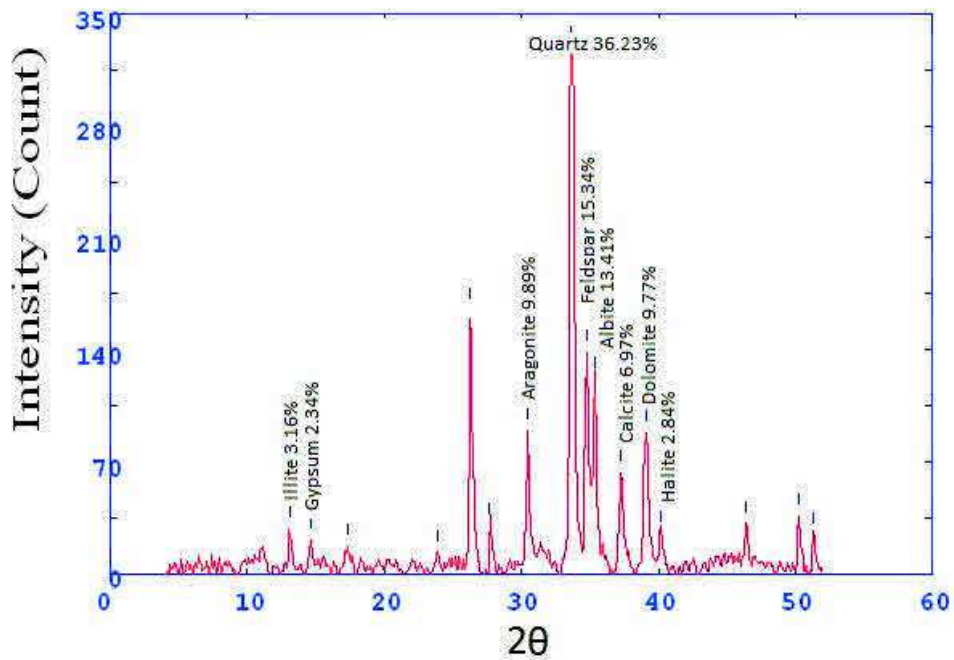
Core 6 sample 7

2Theta	d (A)	Height	Area	FWHM	Identified mineral	WT%
26.275	4.25892	32	96.9	0.2941	-	
29.003	3.8658	14.4	43.6	0.2947	-	0
29.683	3.77913	28.2	84.6	0.2954	-	
30.426	3.68901	13.9	41.9	0.3045	Aragonite	3.020426
33.63	3.34628	147	541.2	0.3136	Quartz	31.94263
34.694	3.24667	34.1	125.7	0.4636	feldspar (orthoclase)	7.409822
35.112	3.20918	26.5	97.6	0.5386	feldspar (Albite)	5.758366
37.265	3.02986	140	1074.2	0.6136	calcite	30.42156
39.072	2.89481	73.8	382.7	0.4123	dolomite	16.03651
39.966	2.83258	13.5	70	0.3169	halite	2.933507
41.913	2.70657	11.4	23.2	0.2215	Pyrite	2.477184
45.833	2.48598	27.8	320.7	0.8956	-	
47.247	2.41566	12.2	140.1	0.7729	Aragonite	
48.837	2.34159	11.3	129.8	0.7116	Aragonite	
50.214	2.28139	29.6	255.5	0.6503	feldspar	
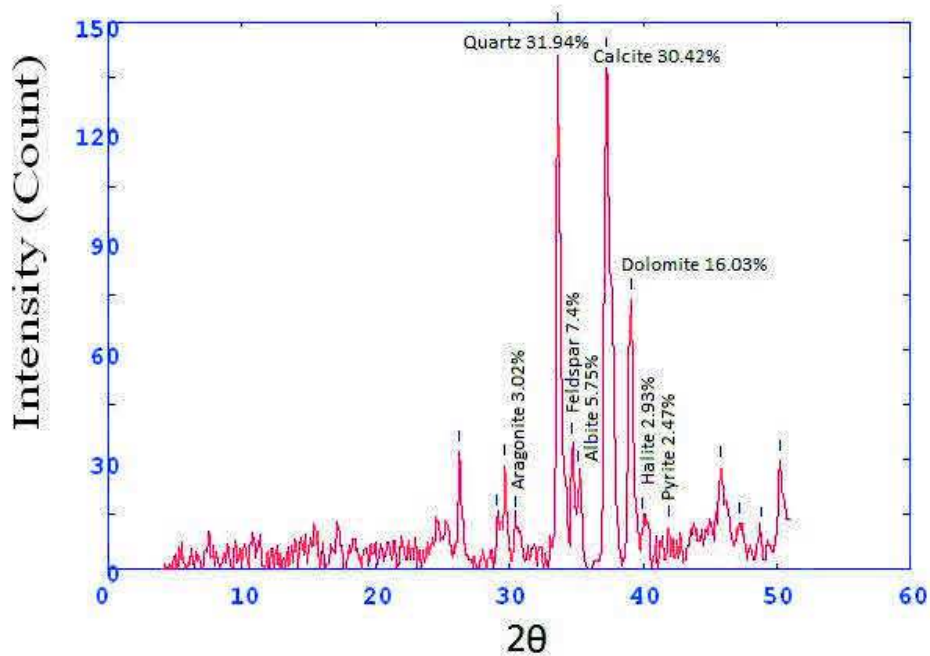
Core 6 sample 8

2Theta	d (A)	Height	Area	FWHM	Identified mineral	WT%
24.891	4.49172	13.9	142.1	0.242	-	0
26.279	4.25843	51.7	142.1	0.242	-	
27.029	**4.1423**	9.5	26.1	0.2925	Geothite	2.071974
27.68	4.04677	8.4	23	0.3051	-	
29.074	3.85659	10.6	29.1	0.3177	-	
30.411	3.69075	24.1	94.3	0.343	-	
33.071	**3.40126**	29.5	115.3	0.2901	Aragonite	6.434024
33.65	**3.34437**	194.9	421.2	0.2373	Quartz	42.50818
34.837	**3.23378**	39.5	85.3	0.3018	feldspar (orthoclase)	8.615049
37.267	**3.02969**	113.4	541.7	0.3663	calcite	24.73282
39.1	**2.89279**	53	266.3	0.3992	dolomite	11.55943
41.996	**2.70143**	18.7	92.2	0.3892	Pyrite	4.078517
45.833	2.48597	25.9	183.8	0.5413	-	
47.385	2.40905	14.5	102.7	0.388	-	
48.137	2.37361	17.5	39.6	0.2346	Pyrite	
48.872	2.34004	13.4	30.3	0.2936	Aragonite	
50.25	2.27988	30	142.2	0.3527	Feldspar	
52.286	2.19697	13.2	73.1	0.4874	Dolomite	
55.017	2.09584	15.1	95.9	0.4776	-	
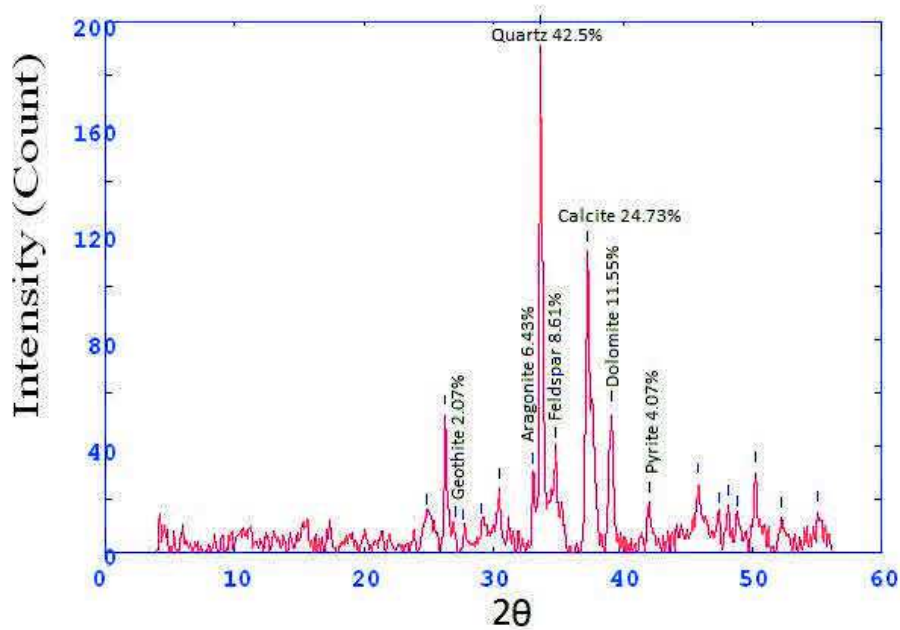
Core 6 sample 9

2Theta	d (A)	Height	Area	FWHM	Identified mineral	WT%
24.559	4.55157	6	112.1	0.3974	-	0
26.334	4.24955	21.7	112.1	0.3974	-	
29.4	3.81471	16.2	102.6	0.4458	-	
31.134	3.60715	10.8	31.9	0.1871	-	
33.062	**3.40212**	75	221.6	0.2165	Aragonite	20.20474
33.685	**3.34095**	106	305.3	0.2459	Quartz	28.55603
34.511	**3.26331**	44.3	127.5	0.4975	feldspar (orthoclase)	11.93427
37.748	**2.99241**	94.1	993	0.7491	Calcite	25.35022
38.956	**2.90306**	9.9	104.8	0.5577	dolomite	2.667026
41.992	**2.70168**	41.9	226.9	0.3664	Pyrite	44.45043
45.886	2.48326	37.7	250.3	0.4643	-	
48.195	2.3709	32.3	196.8	0.4277	Aragonite	
48.909	2.33837	28.4	173	0.6485	feldspar	
50.341	2.27603	26.1	310.1	0.8694	feldspar	
50.842	2.25507	18.8	224.1	1.0566	Pyrite	
52.7	2.18095	9.1	185.8	1.2438	dolomite	
54.817	2.10289	20.1	100.5	0.3489	-	
55.963	2.06319	15.9	79.6	0.4656	-	
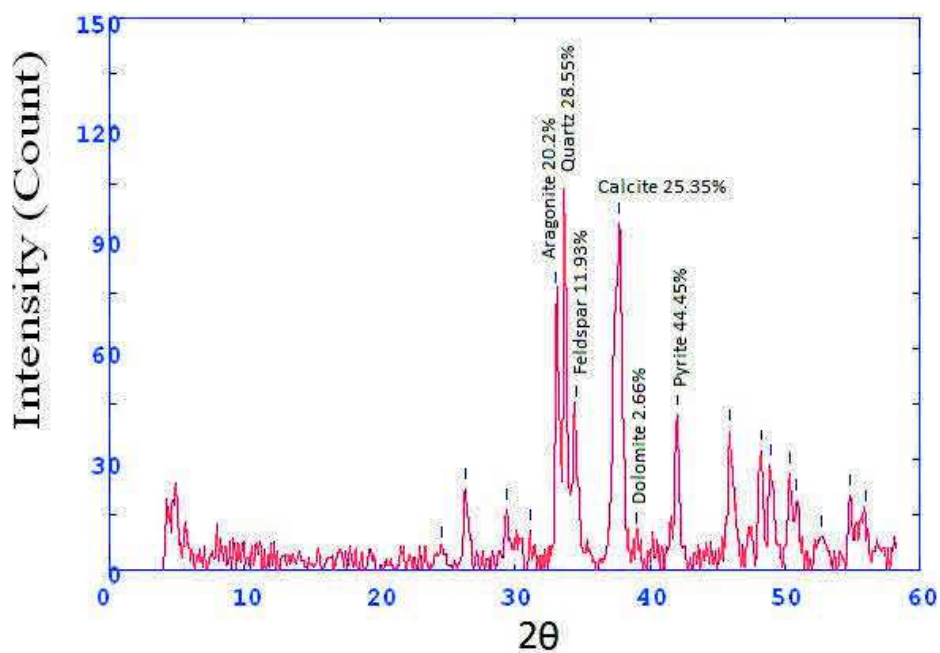
Core 6 sample 10

2Theta	d (A)	Height	Area	FWHM	Identified mineral	WT%
26.275	4.25894	16.1	74.2	0.3697	Geothite	4.054394
29.941	3.74735	16.4	61.8	0.3381	-	
33.133	3.39502	95	282.5	0.2805	Aragonite	23.92344
33.67	3.34239	51.9	154.3	0.4981	Quartz	13.06976
34.373	3.27606	47	139.6	0.607	feldspar (orthoclase)	11.83581
37.71	2.99538	103.6	1005.2	0.7158	Calcite	26.08915
39.029	2.89789	8.9	86.3	0.5725	dolomite	2.241249
40.215	2.8158	29.7	167.3	0.4291	halite	7.479224
42.05	2.69811	44.9	221.2	0.3484	Pyrite	11.30698
45.913	2.48188	40.2	291.7	0.55	-	
47.374	2.40957	13.5	97.8	0.4694	Aragonite	
48.167	2.37222	35.5	178.8	0.3889	Aragonite	
49.043	2.33238	25.6	129.1	0.5595	feldspar	
50.875	2.25369	17.1	173.9	0.7302	feldspar	
52.614	2.18424	14.2	69.1	0.4222	dolomite	
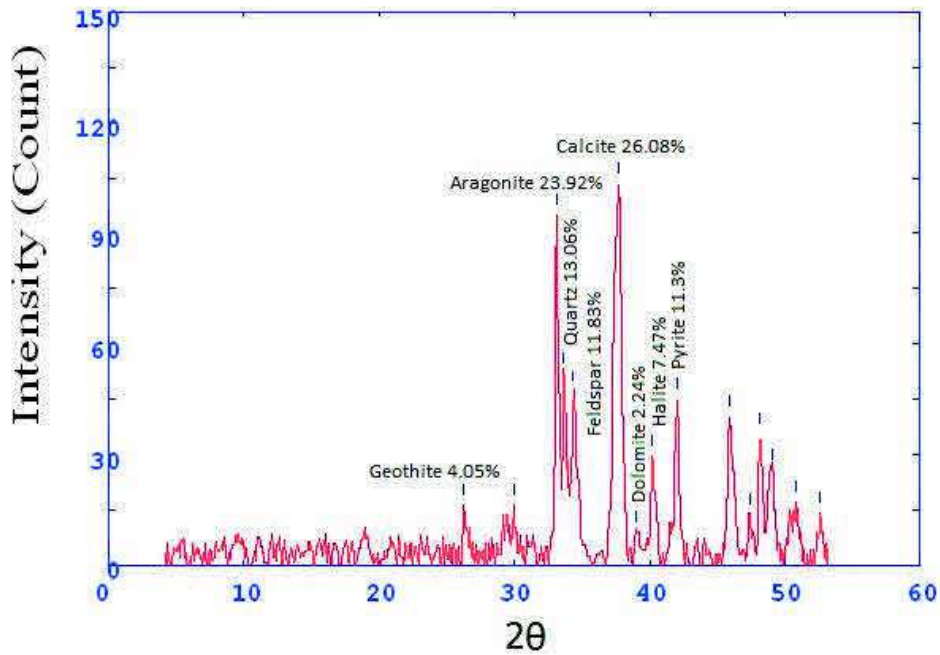
Core 7 sample 1

2Theta	d (A)	Height	Area	FWHM	Identified mineral	WT%
13.112	**8.47866**	73.7	1762.9	0.3861	Illite	9.512132
14.502	**7.66945**	317.4	1762.9	0.3861	Gypsum	40.96541
26.143	4.28013	48.8	294	0.464	Gypsum	
29.396	3.81529	150.4	427.2	0.2441	Gypsum	0
30.305	3.70336	21.3	60.4	0.2477	-	
33.542	**3.35483**	194.7	559	0.2514	quartz	25.12907
34.501	**3.26431**	28.3	81.3	0.2846	feldspar (orthoclase)	3.652555
35.282	**3.19423**	31.8	106.4	0.3179	feldspar (Albite)	4.104285
36.639	3.07974	48.5	162.3	0.3779	gypsum	
37.177	**3.03674**	77.2	454.9	0.4379	calcite	9.963862
39.272	**2.88065**	28.3	166.8	0.3553	dolomite	3.652555
40.044	2.82732	76.4	236.7	0.2727	Feldspar (orthoclase)	
42.192	**2.68945**	23.4	80.1	0.3076	Pyrite	3.020134
45.648	2.49552	18.3	136.3	0.5556	Gypsum	
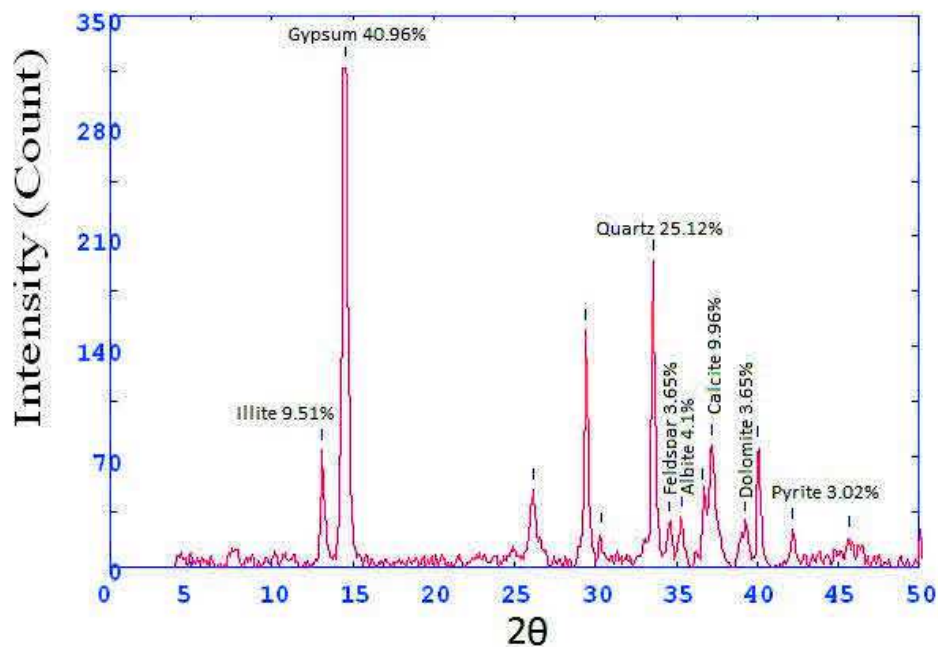
Core 7 sample 2

2Theta	d (A)	Height	Area	FWHM	Identified mineral	WT%
24.849	4.49927	21.8	184.7	0.6198	-	0
26.226	**4.26673**	27.3	138.1	0.4165	Geothite	9.030764
30.233	3.71195	22.5	99.1	0.3589	-	
33.602	**3.34898**	89.1	273.1	0.2922	quartz	29.47403
34.706	**3.24561**	19	58.3	0.3164	feldspar (orthoclase)	6.285147
35.257	**3.19644**	22.7	99.6	0.3406	Albite	7.509097
37.226	**3.03288**	76.4	382.1	0.4324	Calcite	25.27291
39.124	**2.89107**	52.5	269.4	0.4307	Dolomite	17.36685
40.153	**2.81996**	15.3	78.7	0.9224	Halite	5.061197
44.247	2.57041	17.4	325.7	1.4141	quartz	
45.833	2.48598	17.3	280.9	1.1115	-	
47.167	2.41955	16.8	110	0.5568	quartz	
50.233	2.28058	17	110.6	0.4706	Albite	
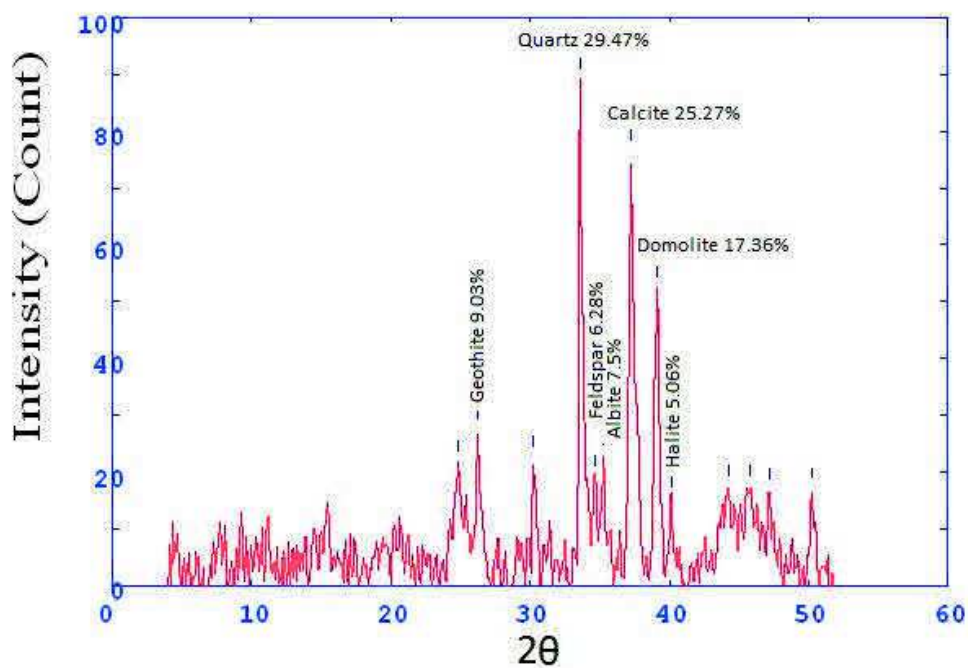
Core 7 sample 3

2Theta	d (A)	Height	Area	FWHM	Identified mineral	WT%
26.211	4.26922	21.2	86.8	0.3373	-	
30.358	3.69709	20.2	112.2	0.466	-	
33.559	**3.35316**	129.6	383	0.2839	quartz	30.38687
34.538	**3.26091**	43.7	129.1	0.2816	feldspar (orthoclase)	10.24619
35.211	**3.20046**	66	205.8	0.2793	Albite	15.47479
37.214	**3.03384**	105.3	423.6	0.3448	calcite	24.68933
39.052	**2.89625**	52.3	377.6	0.5451	dolomite	12.2626
40.155	**2.81984**	12.8	92.8	0.3879	Halite	3.001172
41.942	**2.70479**	16.8	43.7	0.2308	Pyrite	3.939039
45.767	2.4894	19.9	186.1	0.6276	Gypsum	
48.701	2.34777	11.4	97.9	0.4474	feldspar	
50.18	2.28283	23.9	116.2	0.348	Albite	0
52.284	2.19706	14.1	138.5	0.63	Gypsum	
54.055	2.13026	11.6	114.6	0.6233	quartz	
55.033	2.09525	17.7	141.7	0.6166	-	
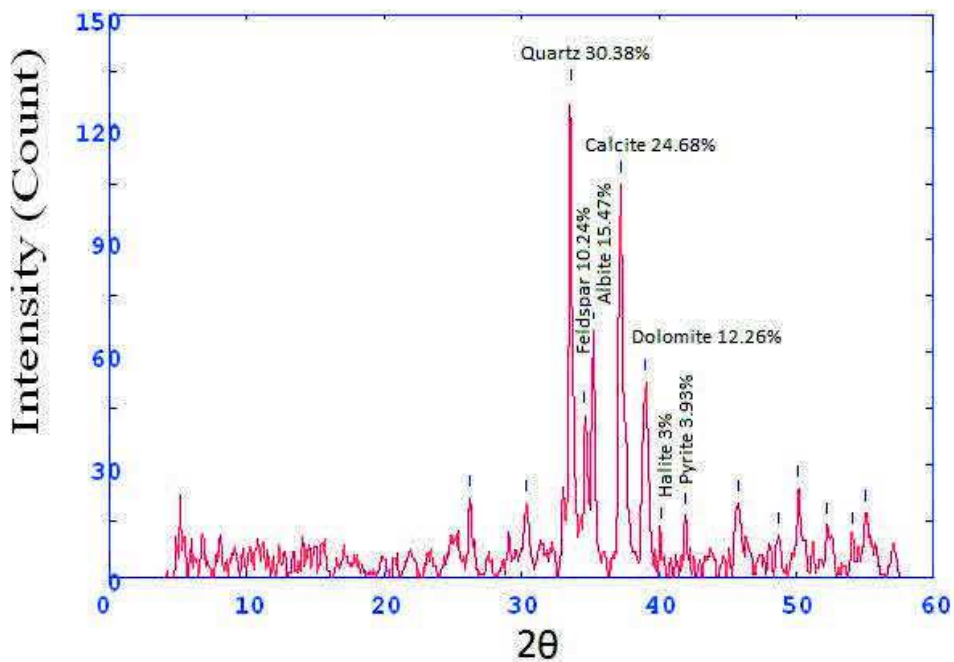
Core 7 sample 4

2Theta	d (A)	Height	Area	FWHM	Identified mineral	WT%
26.19	4.27256	43	100.2	0.2372	-	0
29.066	**3.85759**	18.7	74.9	0.3563	anhydrite	4.066101
30.531	3.67656	13.5	54.1	0.3132	-	
33.012	**3.40712**	22.9	91.4	0.2916	Aragonite	4.979343
33.588	**3.35034**	163.9	483.2	0.27	quartz	35.63818
34.666	**3.24921**	18.2	53.7	0.2884	feldspar (orthoclase)	3.957382
35.217	**3.19992**	16.7	49.1	0.3068	Albite	3.631224
37.228	**3.03275**	152.5	616.2	0.3436	calcite	33.15938
38.934	**2.9047**	35.1	226.1	0.4846	dolomite	7.632094
40.087	**2.82442**	13	83.8	0.4283	Halite	2.826701
41.934	**2.70527**	18.9	92.2	0.372	Magnesite, pyrite	4.109589
44.073	2.58003	10.7	213.9	1.4543	feldspar (orthoclase)	
45.797	2.48785	30.3	173.4	0.4234	Gypsum	
47.989	2.3805	10.9	62.6	0.5535	Pyrite	
48.768	2.34474	11.5	112.4	0.6835	anhydrite	
50.189	2.28246	30.9	164	0.4027	feldspar (orthoclase)	
52.123	2.20336	12	63.6	0.3112	Pyrite	
53.148	2.16389	17.6	39.7	0.2197	-	
55.15	2.09117	25.7	125.4	0.4349	-	
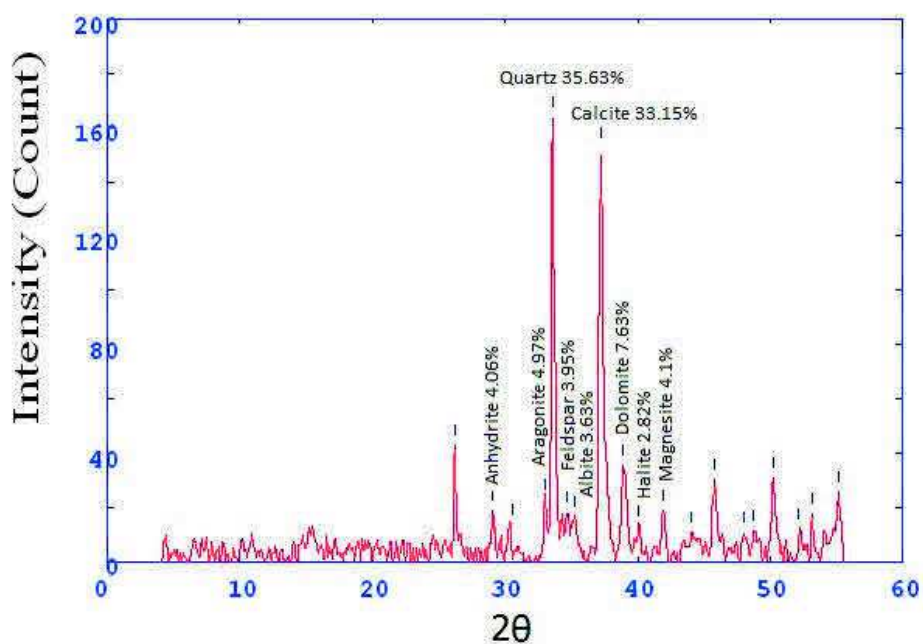
Core 7 sample 5

2Theta	d (A)	Height	Area	FWHM	Identified mineral	WT%
22.3	**5.00587**	7	26.5	0.3264	Gypsum	1.247772
23.5	4.75346	8.3	26.5	0.3264	Gypsum	
26.252	4.26261	13.6	36.2	0.2612	Gypsum	0
29.074	3.85651	18.8	75.9	0.3596	-	
32.87	**3.42148**	47.2	190.8	0.3705	Aragonite	8.413547
33.537	**3.35533**	52.5	215.7	0.3814	quartz	9.358289
34.279	**3.28478**	29.5	121.2	0.4109	feldspar (orthoclase)	5.258467
37.215	**3.03372**	169.5	954.8	0.4405	calcite	30.2139
38.947	**2.90371**	13.4	75.7	0.3464	dolomite	2.388592
40.044	**2.82733**	42.7	125.2	0.2523	Halite	7.611408
41.87	**2.70918**	29.7	114.9	0.3483	Magnesite, pyrite	5.294118
45.733	2.49113	41.4	266	0.466	Aragonite	
47.139	2.4209	12.4	79.5	0.4454	Gypsum	
48.033	2.37842	18.6	100.1	0.4247	Pyrite	
48.812	2.34272	15.1	81.2	0.4447	Gypsum	
50.233	2.28058	29.5	190.8	0.4646	Gypsum	
52.2	2.20035	13.1	64.9	0.3585	Gypsum	
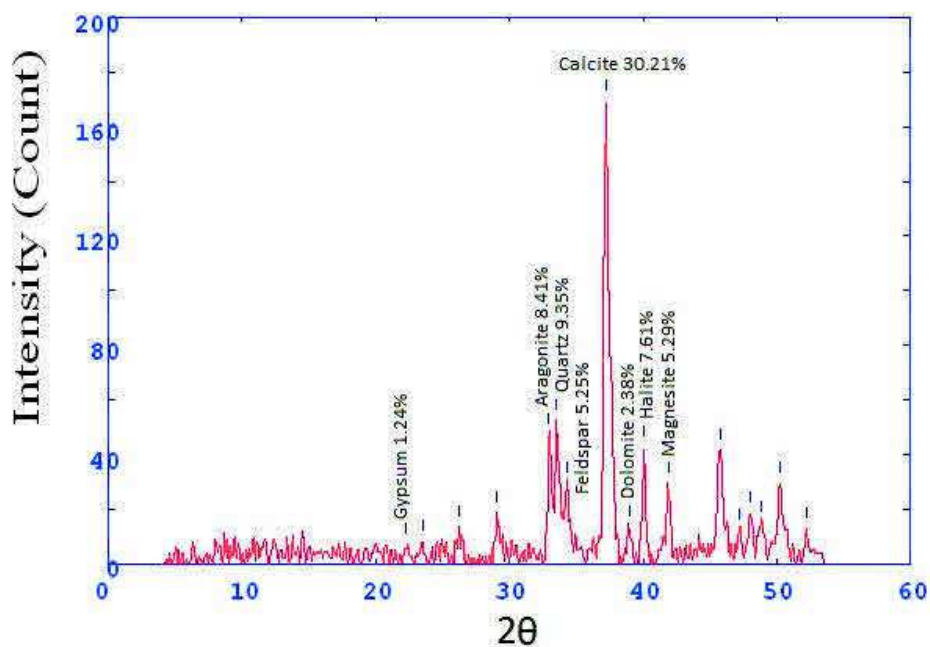
Core 7 sample 6

2Theta	d (A)	Height	Area	FWHM	Identified mineral	WT%
14.494	**7.67379**	35.5	78.4	0.2263	Gypsum	7.011653
26.211	4.26919	44.8	129	0.2502	Gypsum	
29.411	3.81333	20.1	139.2	0.5133	-	0
30.313	3.70237	19.8	137.1	0.3936	-	
32.98	**3.41035**	25.6	176.8	0.3337	Aragonite	5.056291
33.564	**3.35263**	209.8	624.4	0.2738	quartz	41.43788
35.263	**3.19591**	31.8	137.1	0.3543	Albite	6.280861
37.211	**3.03405**	123.7	507.9	0.3458	calcite	24.43215
39.067	**2.89517**	66.7	399	0.4656	Gypsum	13.17401
42.046	**2.69835**	13.2	86.8	0.4398	pyrite	2.60715
45.833	2.48598	23	154.3	0.4812	Gypsum	
46.23	2.4658	19.8	132.8	0.4604	calcite	
47.98	2.3809	8.3	55.9	0.4396	Gypsum	
48.813	2.34268	10.3	68.7	0.398	anhydrite	
50.197	2.28212	36.7	148.7	0.3149	calcite	
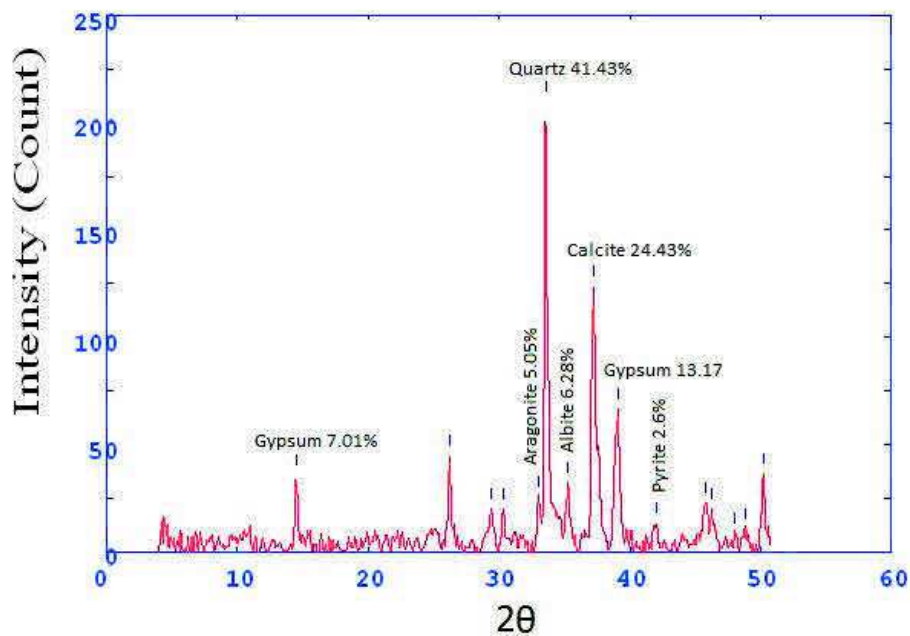
Core 7 sample 7

2Theta	d (A)	Height	Area	FWHM	Identified mineral	WT%
29.354	3.82053	14.2	255.6	0.3246	-	
33.086	**3.39972**	78.2	255.6	0.3246	quartz	35.65891
34.215	3.29073	43.4	141.8	0.5045	-	
37.351	**3.02307**	86.2	823.7	0.6844	calcite	39.30689
39.24	**2.88287**	8.8	83.7	0.5892	dolomite	4.012768
41.465	2.73449	15.3	146.3	0.494	Magnesite, pyrite	
41.933	**2.7053**	46.1	151.6	0.3036	Pyrite	21.02143
43.993	2.58447	6.7	14.5	0.1711	quartz	
45.878	2.4837	36.8	205.5	0.4227	calcite	
47.149	2.42039	14.5	80.9	0.3813	Pyrite	
48.127	2.37407	28.7	122.1	0.3399	-	
48.879	2.33971	22.7	122.1	0.3399	quartz	
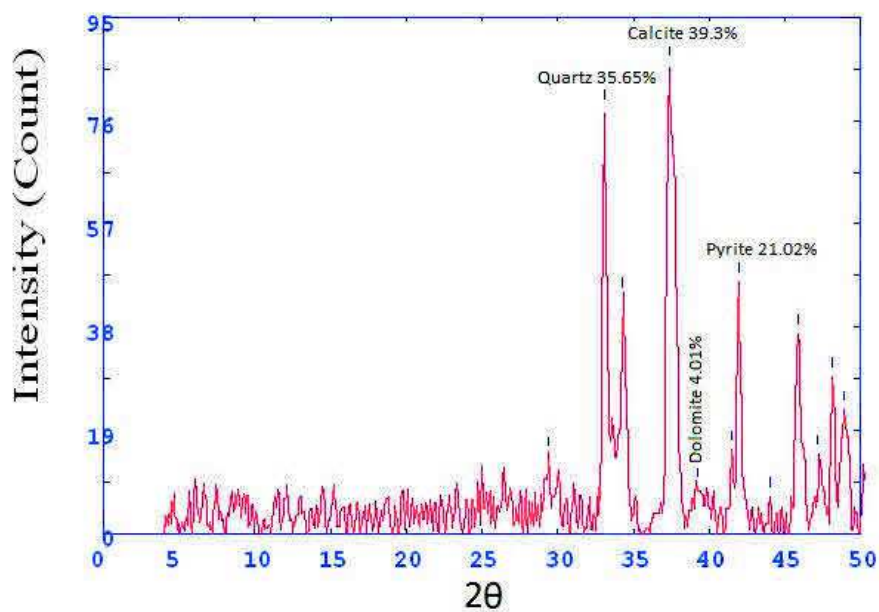
Core 7 sample 8

2Theta	d (A)	Height	Area	FWHM	Identified mineral	WT%
29.167	3.84452	15.5	90.9	0.4459	-	
29.886	3.75409	11.5	67.5	0.3822	-	0
33	**3.40836**	69.5	220.3	0.3185	Aragonite	20.18588
34.176	**3.29437**	44.7	141.7	0.4485	quartz	12.98286
35.166	3.20443	32.3	102.4	0.5135	feldspar	9.381353
37.24	**3.0318**	140.6	951	0.5785	calcite	40.83648
39.992	**2.83086**	17.1	48.6	0.2254	dolomite	4.966599
41.853	**2.71026**	40.1	180.7	0.3353	Pyrite	11.64682
45.7	2.49284	39	224.3	0.4524	Aragonite	
47.211	2.41739	12	68.9	0.376	Pyrite	
48.025	2.3788	31.6	116.7	0.2995	Pyrite	
48.779	2.34423	27	99.9	0.2442	-	
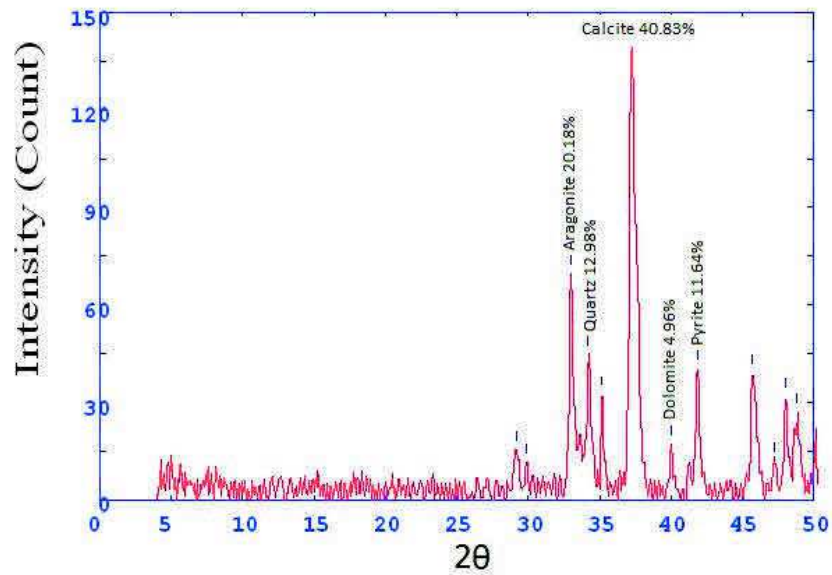
Core 8 sample 1

2Theta	d (A)	Height	Area	FWHM	Identified mineral	WT%
13.117	**8.47535**	84.3	1835.8	0.4044	Illite	14.85462555
14.5	**7.67041**	324.9	1835.8	0.4044	Gypsum	57.25110132
25.98	4.30649	65.1	250.2	0.3347	Gypsum	
26.58	**4.21097**	18.8	72.4	0.293	Geothite	3.31277533
29.386	3.81648	161.1	352.3	0.2513	gypsum	
33.513	**3.35759**	28.3	120.8	0.3605	Quartz	4.986784141
36.678	3.07661	68	217	0.3095	Gypsum	
37.132	**3.04027**	39.8	126.8	0.3925	calcite	7.013215859
39.233	**2.88337**	44.2	273.4	0.4755	dolomite	7.788546256
42.118	**2.69398**	27.2	134.6	0.4495	Pyrite	4.792951542
45.5	2.50321	31.9	178.7	0.4444	Gypsum	
50.167	2.28341	16.6	87.4	0.4167	Quartz	
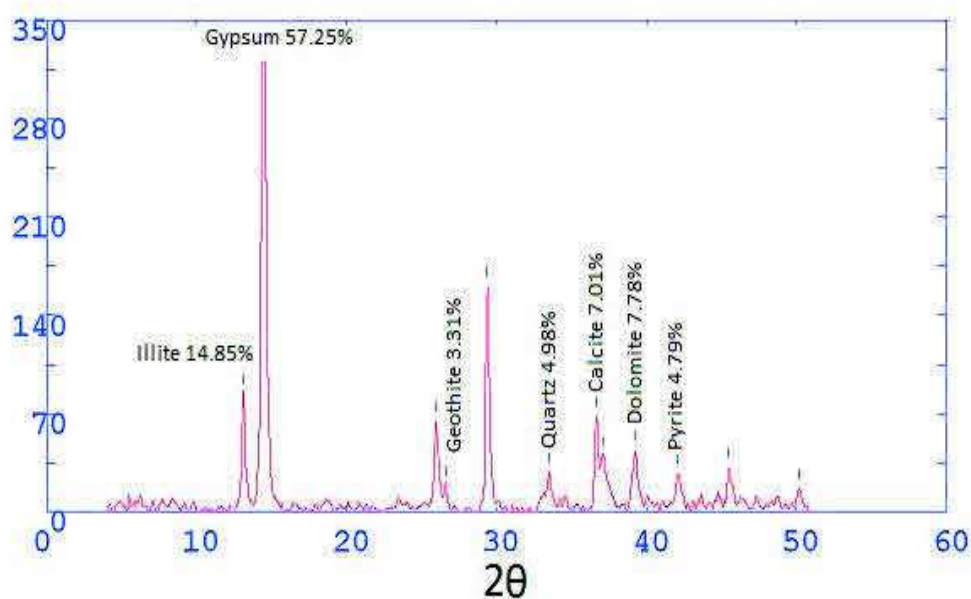
Core 8 sample 2

2Theta	d (A)	Height	Area	FWHM	Identified mineral	WT%
14.441	**7.70171**	11.6	68	0.5052	Gypsum	2.308457711
24.819	4.50464	10	705.3	0.4653	-	
26.074	4.29126	64.5	1883.2	0.4253	Gypsum	
29.087	3.85492	7.5	46.7	0.3822	Gypsum	
30.175	3.71898	37.2	295.9	0.3391	dolomite	
32.936	**3.41473**	26.5	111.1	0.2842	Aragonite	5.273631841
33.439	**3.36488**	285.7	577.9	0.2293	Quartz	56.85572139
34.527	**3.26193**	20.7	55.1	0.2503	feldspar (orthoclase)	4.119402985
35.28	**3.19443**	19.1	734.7	0.2713	feldspar (Albite)	3.800995025
37.205	**3.03457**	101.6	61.5	0.2767	calcite	20.21890547
39.046	**2.89667**	33.1	118.9	0.282	dolomite	6.587064677
39.966	**2.83258**	10	128.1	0.3255	halite	1.990049751
41.975	**2.70273**	20.7	490.7	0.369	Pyrite	4.119402985
44.569	2.55274	15.8	338	0.5075	gypsum	
45.574	2.49939	18.2	119	0.486	calcite	
46.159	2.46937	26.5	59.2	0.4881	Aragonite	
47.917	2.38385	10	118	0.4902	Aragonite	
48.586	2.35295	11.6	146	0.4944	Aragonite	
50.093	2.28656	30.6	123.9	0.2665	calcite	
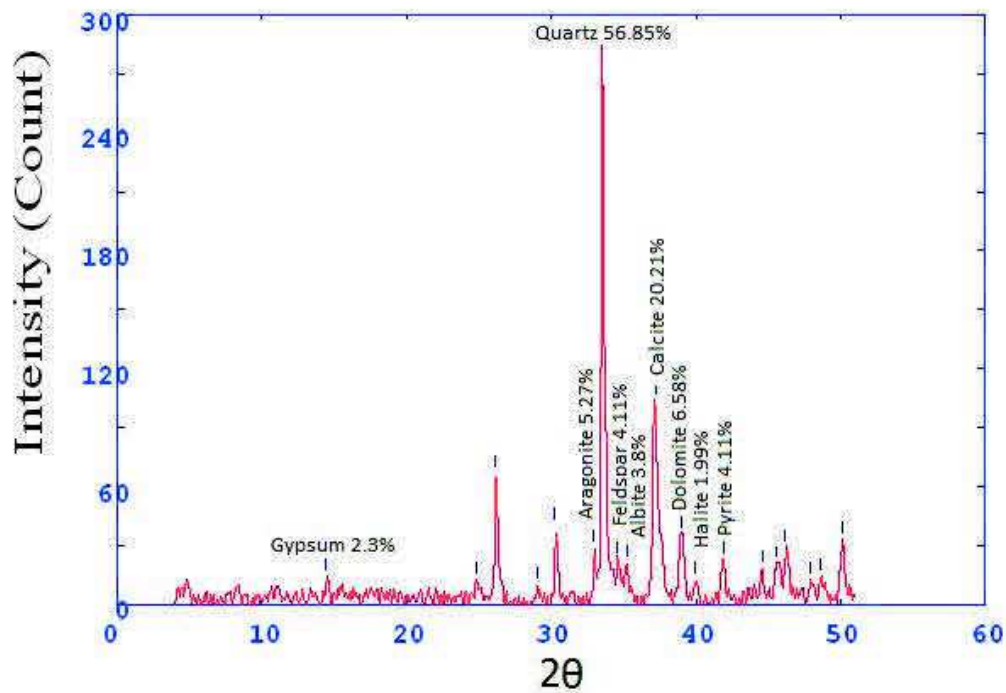
Core 8 sample 3

2Theta	d (A)	Height	Area	FWHM	Identified mineral	WT%
26.214	4.26871	75.3	207.4	0.2619	-	
30.375	3.69505	46.1	167.7	0.2963	-	
32.986	**3.40973**	36.2	131.7	0.3068	Aragonite	5.707978556
33.567	**3.35241**	356.8	1218.4	0.3174	Quartz	56.25985494
34.711	**3.24515**	75.9	259.1	0.3729	feldspar (orthoclase)	11.96783349
37.247	**3.03122**	106.1	520.8	0.4283	calcite	16.72973825
39.084	**2.89395**	37.8	292	0.534	dolomite	5.960264901
41.9	**2.70735**	21.4	115.1	0.4	Pyrite	3.374329864
46.327	2.46093	23	59	0.2442	Aragonite	
48.047	2.37778	18.5	70.6	0.3313	Aragonite	
50.145	2.28435	30.3	122.9	0.3517	feldspar (orthoclase)	
54.1	2.12861	22.2	127.3	0.374	Aragonite	
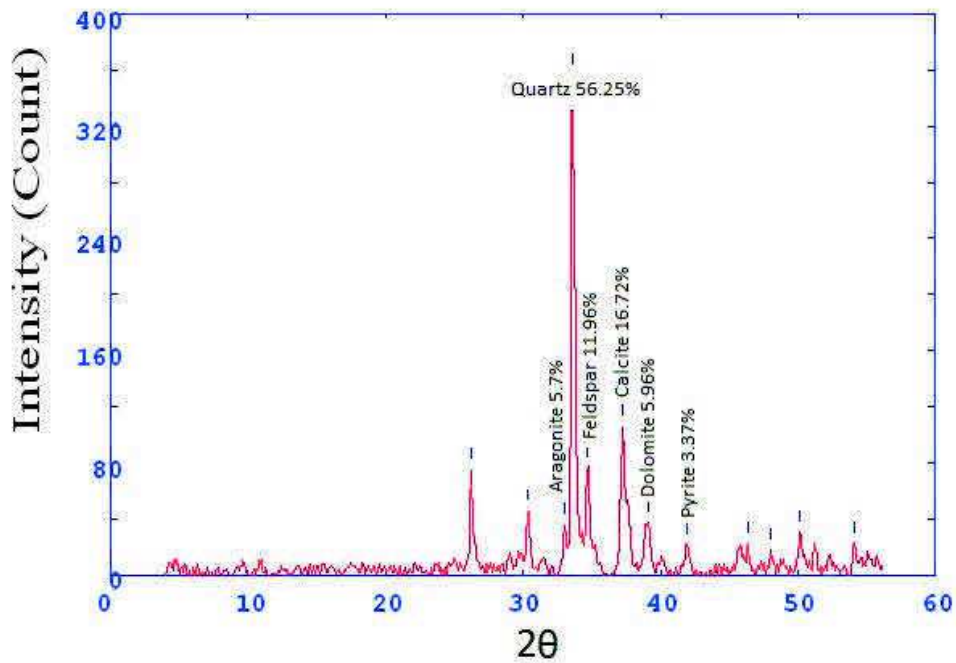
Core 8 sample 4

2Theta	d (A)	Height	Area	FWHM	Identified mineral	WT%
13.125	**8.4702**	313.7	1342.7	0.4503	Illite	28.72447578
14.634	**7.60047**	314.4	2621.8	0.5505	Gypsum	28.78857248
17.307	6.4337	12.6	42.9	0.2941	-	
23.67	4.7199	10.7	36.4	0.2668	-	
26.141	4.28037	67.9	231.1	0.2532	Gypsum	
26.675	**4.19622**	67.9	175.6	0.2395	Geothite	6.217379361
29.437	3.81008	329.6	852.6	0.2489	Gypsum	
33.604	**3.34877**	71	200.7	0.2583	Quartz	6.501236151
34.545	**3.26028**	13.9	39.2	0.2744	feldspar (orthoclase)	1.272777218
36.851	3.06264	71.1	201	0.2824	Gypsum	
37.202	**3.03474**	126.5	382.3	0.2904	calcite	11.58318835
39.347	**2.87539**	115.2	350.3	0.286	dolomite	10.54848457
40.147	**2.82039**	31.9	96.9	0.289	halite	2.920977932
42.272	**2.68459**	37.6	116.7	0.292	Pyrite	3.442908159
44.917	2.53401	41.7	125.4	0.2511	Gypsum	
45.666	2.49458	10.7	32.1	0.2588	Gypsum	
46.387	2.45791	41.5	123.9	0.2665	feldspar (orthoclase)	
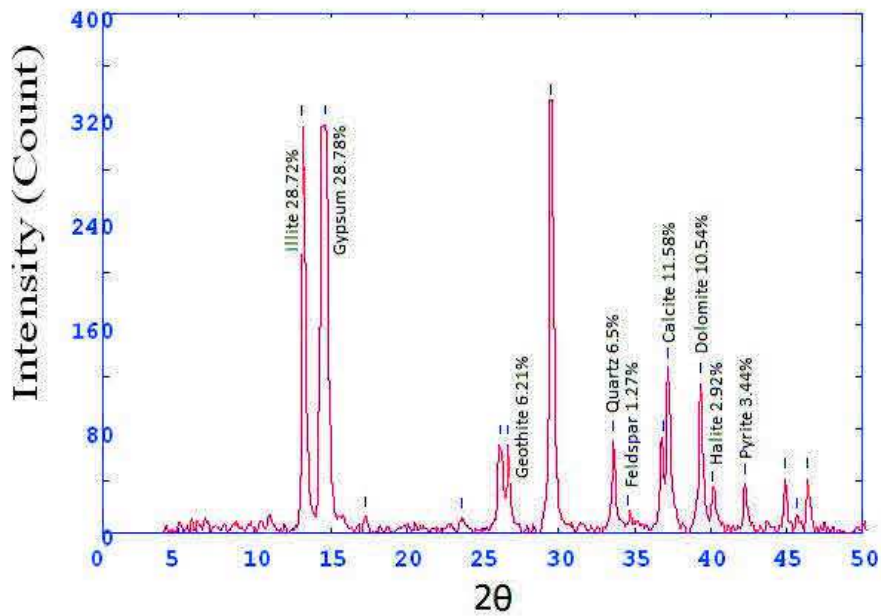
Core 8 sample 5

2Theta	d (A)	Height	Area	FWHM	Identified mineral	WT%
11.214	**9.908**	11.7	68	0.5052	Illite	1.452153407
13.199	8.42294	121.2	705.3	0.4653	Illite	
14.633	**7.60103**	331.4	1883.2	0.4253	Gypsum	41.13193496
17.389	6.40362	8.2	46.7	0.3822	-	
26.197	4.27141	76.1	295.9	0.3391	gypsum	
26.692	**4.19365**	28.6	111.1	0.2842	Geoithite	3.549708328
29.464	3.80659	288.8	577.9	0.2293	gypsum	
30.379	3.6945	27.6	55.1	0.2503	-	
33.611	**3.34811**	256.3	734.7	0.2713	Quartz	31.81084771
34.821	**3.23517**	21.5	61.5	0.2767	feldspar (orthoclase)	2.66848703
35.292	**3.19333**	41.6	118.9	0.282	feldspar (Albite)	170.4918033
36.833	**3.06413**	44.9	128.1	0.3255	calcite	5.572793844
37.241	3.03173	114.4	490.7	0.369	Gypsum	
39.309	**2.87806**	49.1	338	0.5075	Dolomite	6.094079682
42.301	**2.68282**	20.6	119	0.486	Pyrite	2.556782922
43.956	2.58653	10.3	59.2	0.4881	Gypsum	
44.794	2.54056	20.4	118	0.4902	Gypsum	
45.733	2.49112	22	146	0.4944	Gypsum	
50.233	2.28058	24.4	140	0.4323	Quartz	
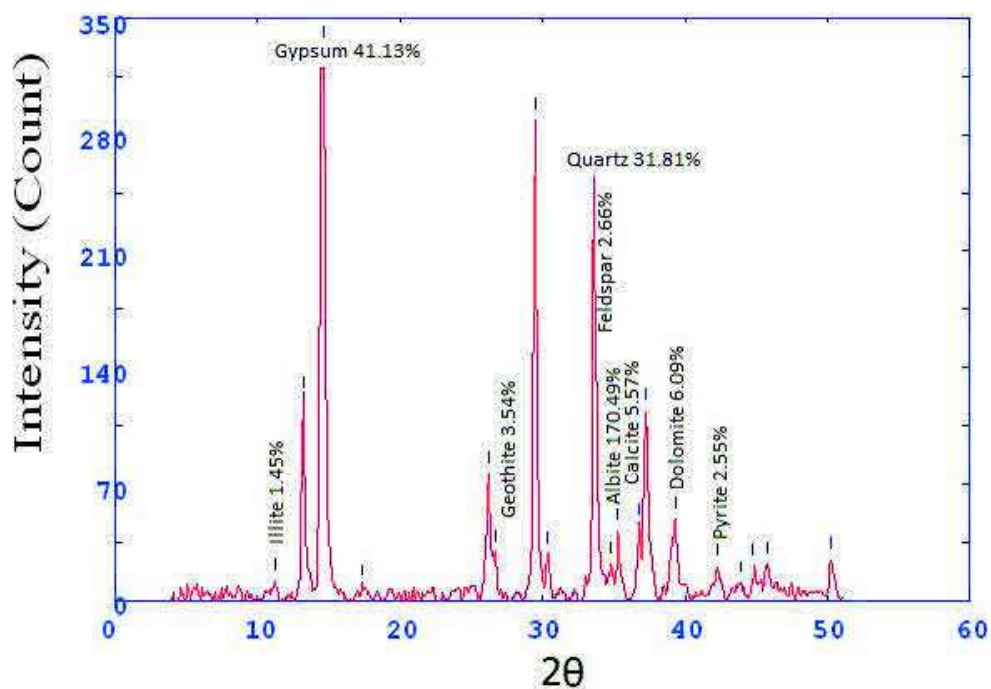
Core 8 sample 6

2Theta	d (A)	Height	Area	FWHM	Identified mineral	WT%
14.419	**7.71334**	11.1	75.4	0.4122	Gypsum	2.149496514
15.481	7.18731	9.8	66.4	0.3705	-	
26.1	4.28703	12.1	76.6	0.3655	Gypsum	
29.035	3.86166	14.3	91	0.2825	-	
30.279	3.70645	22.2	42.9	0.1996	-	
32.814	**3.42716**	56.6	109.3	0.2296	Aragonite	10.96049574
33.507	**3.35825**	184.5	546.1	0.2596	Quartz	35.72811774
34.292	**3.28354**	32.6	96.6	0.4101	-	6.312935709
34.621	**3.25332**	27.5	81.4	0.4854	feldspar (orthoclase)	5.325329202
34.949	**3.22367**	26.9	79.7	0.523	feldspar (Albite)	5.209140201
37.156	**3.03837**	132.2	899.3	0.5606	calcite	25.60030984
38.975	**2.90176**	17.2	117	0.4565	Dolomite	3.330751356
39.632	2.85553	12.6	85.9	0.4044	-	
41.811	**2.71283**	27.8	126.3	0.3523	Pyrite	5.383423703
43.85	2.5925	7.1	35.1	0.3333	gypsum	
45.7	2.49284	31.4	194.5	0.4738	gypsum	
46.203	2.46714	18.9	117.2	0.3613	Aragonite	
47.189	2.41846	8.1	49.9	0.3051	Aragonite	
47.995	2.38019	26	65.8	0.2489	Pyrite	
48.668	2.34926	18.9	0	0	Aragonite	
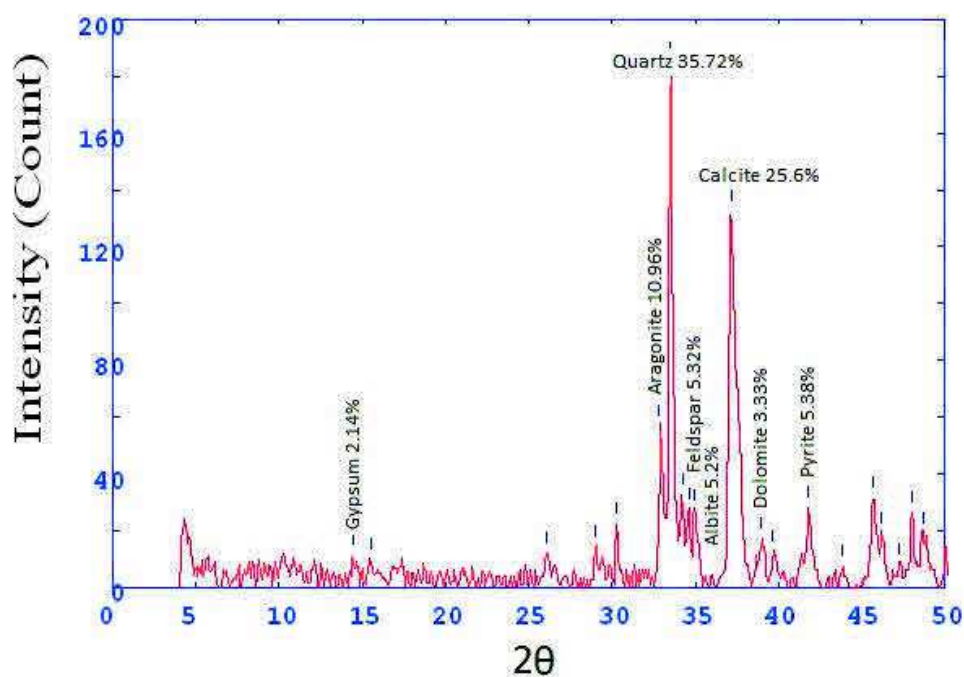
Core8 sample 7

2Theta	d (A)	Height	Area	FWHM	Identified mineral	WT%
14.275	**7.79104**	10.5	92.4	0.5405	Gypsum	2.975347124
15.601	7.13208	12.2	92.4	0.5405	-	
16.979	6.55699	8.1	61.2	0.4369	-	
26.233	4.26563	11.3	51.1	0.3194	Gypsum	
29.283	3.82962	15.1	101.3	0.5155	gypsum	
33.116	**3.39669**	61.8	248.2	0.2997	Aragonite	17.51204307
33.732	**3.3365**	54.2	217.5	0.48	Quartz	15.35845849
34.43	**3.27084**	36.5	146.7	0.5701	feldspar (orthoclase)	10.34287334
37.328	**3.02491**	126.1	1122	0.6602	calcite	35.73250213
39.141	**2.88989**	15.7	139.5	0.4568	Dolomite	4.448852366
39.926	**2.83531**	8.9	78.8	0.3551	halite	2.521960895
40.275	2.81175	9.3	82.4	0.3042	-	
41.986	**2.70208**	39.2	109.8	0.2533	Pyrite	11.1079626
43.504	2.61213	6.9	19.2	0.355	Quartz	
45.867	2.48427	41	231.4	0.4567	Aragonite	
47.343	2.41107	13.3	74.9	0.4543	Gypsum	
48.148	2.3731	27.2	148.8	0.4519	Aragonite	
49.088	2.33039	25.3	138.6	0.4926	Aragonite	
50.376	2.27453	28.4	176.9	0.5333	gypsum	
50.745	2.25906	19.3	119.9	0.4156	Pyrite	
52.567	2.18608	14.6	51.6	0.2978	feldspar (orthoclase)	
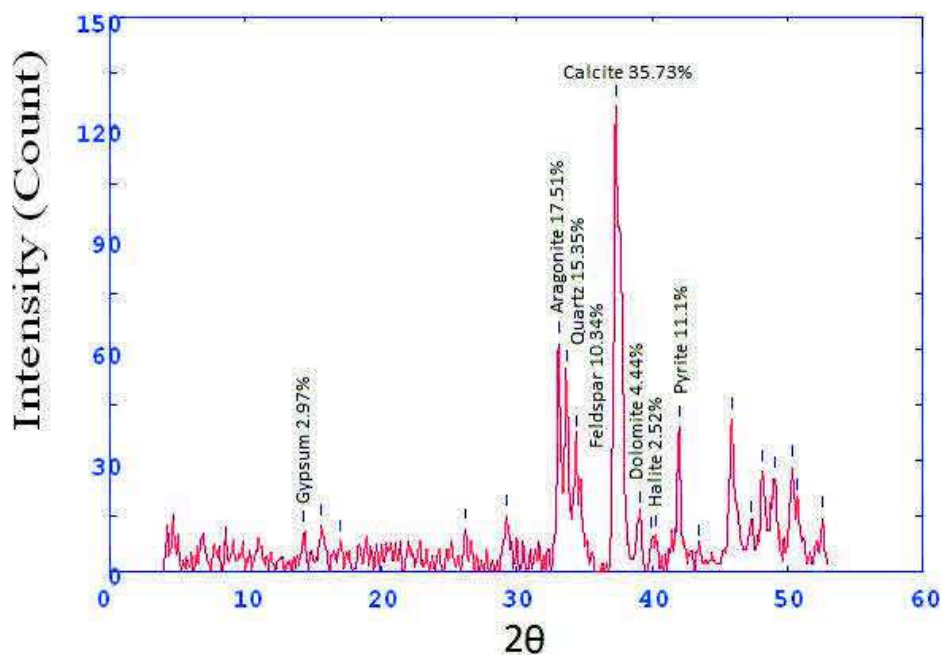
Core 8 sample 8

2Theta	d (A)	Height	Area	FWHM	Identified mineral	WT%
26.291	4.25642	80	11358.7	0	-	
27.547	4.06589	54.2	7696.3	0	-	
29.34	3.82237	62	12396	0	-	
32.979	3.41045	111.8	22344.7	0.8627	Aragonite	16.66169896
33.62	3.34728	132.5	2822.7	1.7254	Quartz	19.7466468
34.316	3.28133	78.8	1679.2	1.3619	feldspar (orthoclase)	11.74366617
37.278	3.02882	142.2	2190.7	0.9983	calcite	21.19225037
39.08	2.89426	58.7	904.4	0.9983	dolomite	8.748137109
40.073	2.82533	62	12428	0.9983	halite	9.239940387
41.891	2.70789	85	12624	0.9983	Pyrite	24.08614338
45.858	2.48474	84.1	11516	0.9983	Aragonite	
48.189	2.37119	68.3	9353.5	0.9983	gypsum	
48.98	2.3352	70.4	8161.3	0.9983	feldspar (orthoclase)	
50.027	2.28936	67.4	0	0	feldspar (orthoclase)	
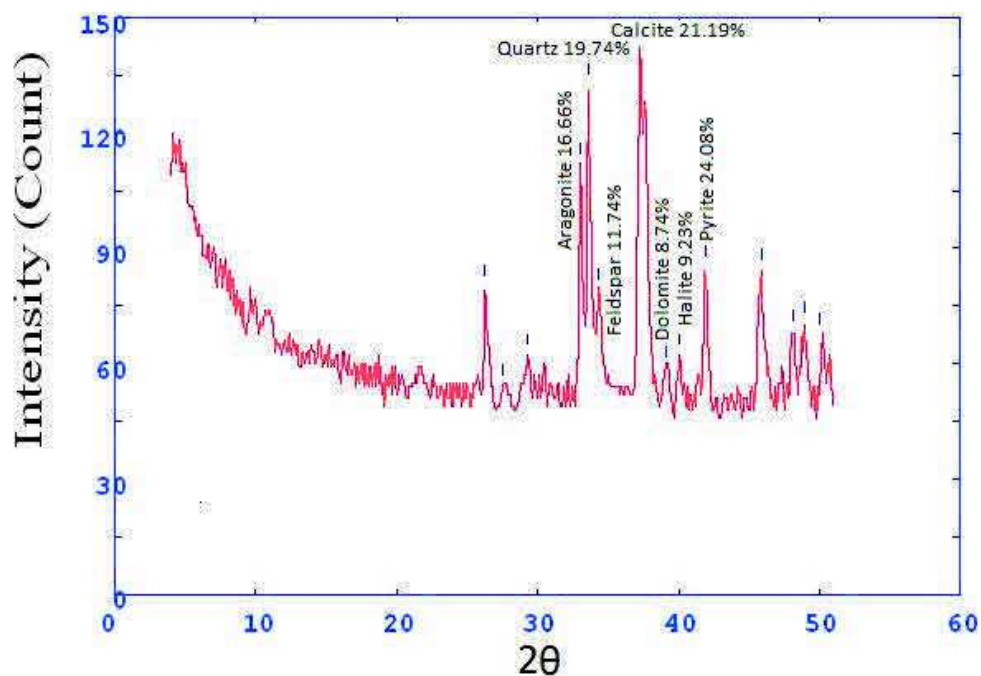
Core 8 sample 9

2Theta	d (A)	Height	Area	FWHM	Identified mineral	WT%
26.234	4.26549	9.5	29	0.2942	-	
29.067	3.85753	11	202.4	1.3297	-	
33.042	**3.40411**	63.9	250.3	0.342	Aragonite	19.5353103
33.686	**3.34089**	54.3	212.4	0.5453	Quartz	16.600428
34.35	**3.27821**	37.5	146.7	0.6469	feldspar (orthoclase)	11.46438398
35.097	**3.21058**	8.4	33	0.6977	feldspar (Albite)	2.568022012
37.255	**3.03059**	101.5	1100.1	0.7485	calcite	31.03026597
37.669	2.9985	87.5	948.1	0.6518	-	
38.996	**2.90019**	15.8	171.7	0.5551	Dolomite	4.830327117
40.075	**2.82521**	8.1	87.7	0.4584	halite	2.47630694
41.887	**2.70817**	37.6	155.8	0.3617	Pyrite	11.49495567
45.783	2.48855	37.1	260	0.5242	-	
47.294	2.4134	8.4	59	0.4413	-	
48.023	2.37889	28.8	118.7	0.3583	Pyrite	
48.954	2.33637	21.7	0	0	feldspar	
50.198	2.28206	18.4	0	0	-	
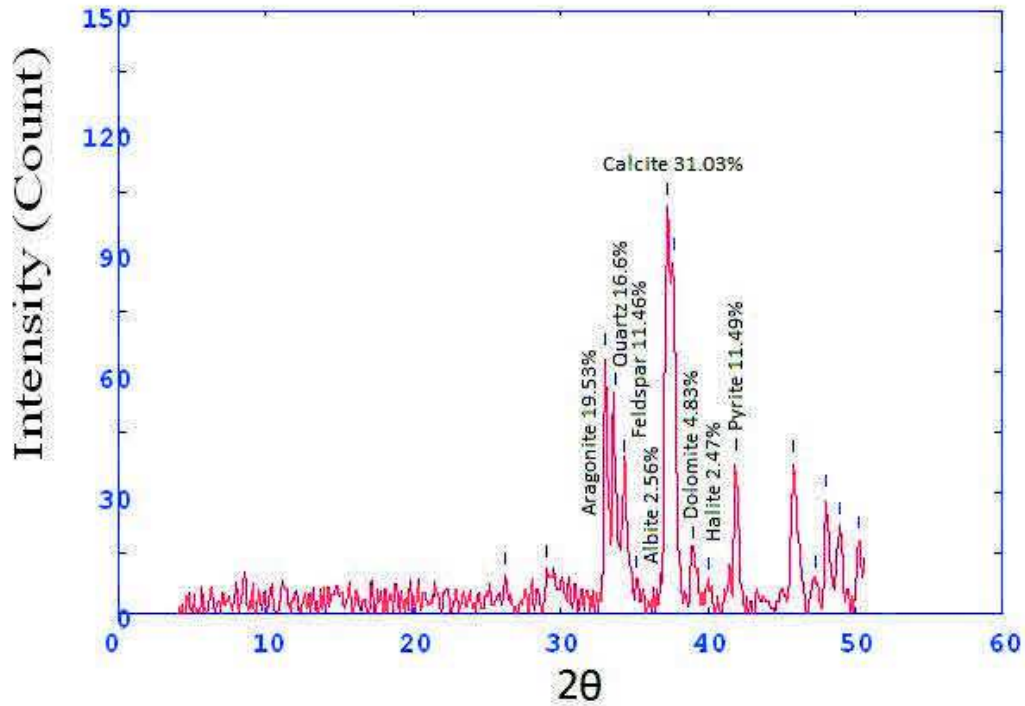
Core 8 sample 10

2Theta	d (A)	Height	Area	FWHM	Identified mineral	WT%
26.167	4.27631	11.5	67.7	0.45	-	0
29.384	3.81679	12.4	163.9	0.9761	-	
33.017	**3.40668**	77.8	247.9	0.2918	Quartz	26.4986376
34.243	**3.28815**	42.7	136.1	0.4985	feldspar (orthoclase)	14.54359673
35.47	**3.17789**	5.3	17	0.6019	feldspar (Albite)	23.24561404
36.369	3.10183	5	15.9	0.6536	-	
37.589	**3.00465**	104	1114.9	0.7053	calcite	35.42234332
39.232	**2.88347**	8	85.4	0.6161	Dolomite	2.72479564
40.033	**2.82806**	16.8	113.5	0.5268	halite	5.722070845
41.9	**2.70733**	39	167.7	0.3471	Pyrite	13.28337875
44.017	2.58315	6.1	9.7	0.1979	-	
45.785	2.48847	41.2	206.2	0.4328	-	
47.247	2.41566	9	44.8	0.4098	-	
48.081	2.3762	27.1	118.8	0.3869	-	
48.883	2.33954	22.8	118.8	0.3869	Pyrite	
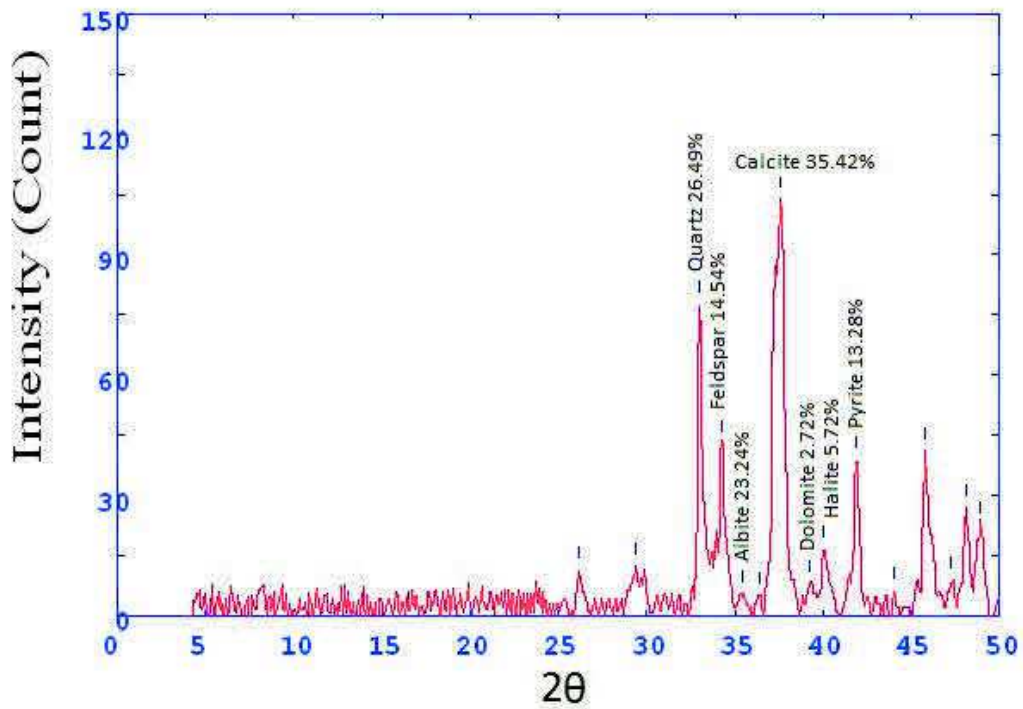
Core 9 sample 1

2Theta	d (A)	Height	Area	FWHM	Identified mineral	WT%
11.058	**10.04719**	19.7	70.4	0.2645	Illlite	5
14.529	**7.65525**	13.8	38.2	0.1372	Gypsum	3.502538
26.22	4.26776	26.1	91.7	0.2111	Gypsum	
27.144	4.12503	22.5	79.2	0.2785	-	
29.141	3.84789	16.4	84.5	0.346	illite	
30.491	3.68126	9.8	50.7	0.3137	Gypsum	
32.782	**3.43042**	44.3	228.6	0.2975	Aragonite	11.24365
33.562	**3.35287**	81.4	252.6	0.2813	Quartz	20.6599
34.191	**3.29299**	26.5	82.3	0.3346	feldspar (orthoclase)	6.725888
34.631	3.25237	69	214.2	0.3879	-	
35.248	**3.19723**	40.7	126.3	0.4411	feldspar (Albite)	10.32995
37.241	**3.03175**	115.4	745.8	0.4944	Calcite	29.28934
38.95	**2.90351**	28.9	165.4	0.4184	Dolomite	7.335025
40.004	2.83001	17.1	98	0.3717	halite	
41.868	**2.70935**	23.3	93	0.325	Pyrite	5.913706
45.719	2.49186	33.2	240.8	0.55	Calcite	
46.434	2.45555	21.8	158.4	0.475	Gypsum	
47.227	2.41664	13.1	95.1	0.4562	Gypsum	
47.932	2.38316	17.1	124.1	0.4375	Pyrite	
48.781	2.34412	21.3	120.2	0.4	gypsum	
50.119	2.28544	24.2	188.8	0.5695	feldspar	
52.3	2.19644	13.2	68.2	0.3	Dolomite	

241
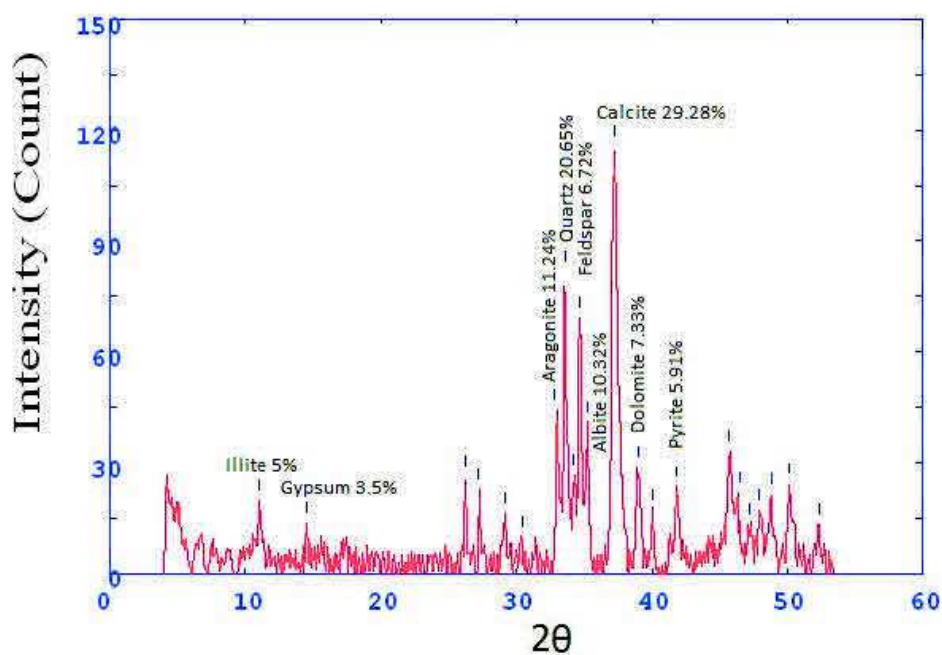
Core 9 sample 2

2Theta	d (A)	Height	Area	FWHM	Identified mineral	WT%
15.402	**7.22381**	13	119.8	0.6363	Gypsum	2.129402
23.733	4.70747	12.9	86.2	0.4821	-	
26.205	4.27016	112.2	325	0.2552	Gypsum	
28.966	3.87064	13.9	60.8	0.2825	-	
30.376	**3.6949**	45.1	219	0.3495	Aragonite	7.387387
33.567	**3.35242**	339.2	1406.8	0.3205	Quartz	55.56102
34.569	**3.25803**	23	95.4	0.3413	feldspar (orthoclase)	3.767404
35.176	**3.20358**	20.9	86.8	0.362	feldspar (Albite)	3.423423
37.202	**3.03475**	80.5	436.3	0.4036	Calcite	13.18591
39.071	**2.89484**	88.8	382.4	0.3469	Dolomite	14.54545
46.272	2.46368	46.5	173.8	0.3152	feldspar (orthoclase)	
48.66	2.34961	13.5	117.5	0.6296	feldspar (orthoclase)	
50.1	2.28625	43.6	199.6	0.3565	feldspar (orthoclase)	
51.121	2.24358	16.8	199.6	0.3565	feldspar (orthoclase)	
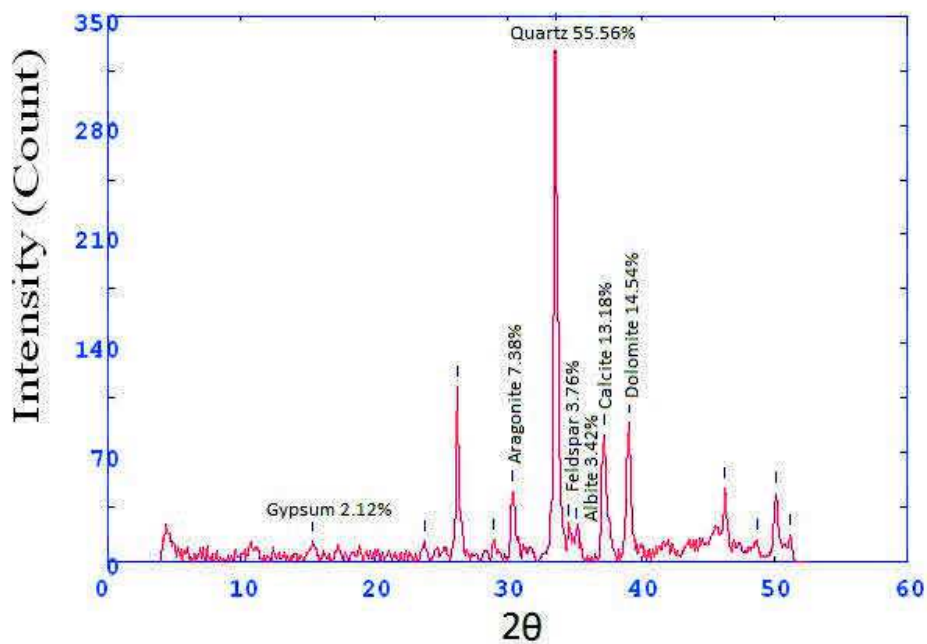
Core 9 sample 3

2Theta	d (A)	Height	Area	FWHM	Identified mineral	WT%
30.434	3.68809	14.2	21.7	0.1935	-	0
32.978	**3.4106**	101.2	155	0.2184	Aragonite	25.33801
33.635	**3.34579**	130.8	286.9	0.2434	Quartz	32.74912
34.402	**3.27336**	59.3	130	0.4794	feldspar (orthoclase)	14.84727
37.73	**2.99385**	48.1	461.6	0.7153	Calcite	12.04306
39.179	**2.88719**	10.1	97	0.5411	Dolomite	2.528793
41.442	2.73592	15.3	147.3	0.454	-	
41.944	**2.70461**	49.9	192.9	0.3669	Pyrite	12.49374
45.8	2.48769	41.6	231.2	0.4759	feldspar (orthoclase)	
47.309	2.4127	17	94.3	0.4063	feldspar (orthoclase)	
48.113	2.37473	41.3	168	0.3368	gypsum	
48.901	2.33874	33.5	136.1	0.2245	gypsum	
50.731	2.25966	12.6	3.3	0.1121	Pyrite	
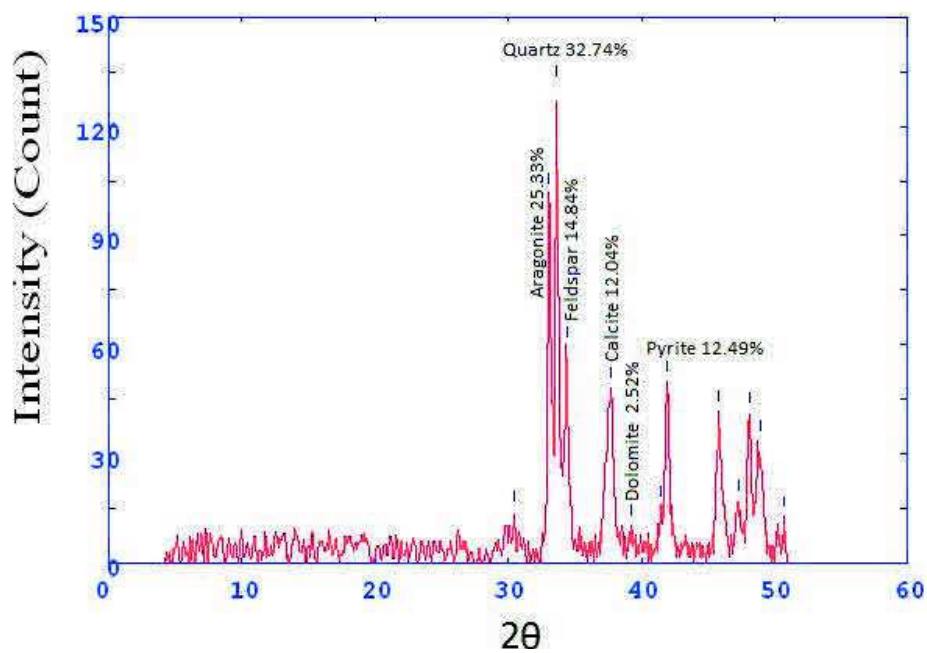
Core 9 sample 4

2Theta	d (A)	Height	Area	FWHM	Identified mineral	WT%
11.053	**10.05114**	18.2	134.2	0.5284	Illite	4.629865
15.595	**7.13484**	17.5	203.4	0.8173	Gypsum	4.451793
22.28	5.01019	7.8	59.8	0.4828	-	
23.863	4.68221	7.5	58	0.4346	-	
24.936	4.4838	19.1	147.3	0.3864	-	
26.288	4.25691	35.4	136.8	0.2901	gypsum	
28.978	3.86902	9.9	38.3	0.3712	-	
30.546	3.67484	12.6	48.8	0.4523	-	
31.473	**3.5692**	13.9	94	0.5064	Aragonite	3.535996
33.651	**3.3443**	108.3	313.3	0.2597	Quartz	27.55024
34.671	**3.24875**	27.7	80	0.3134	feldspar (orthoclase)	7.046553
35.166	**3.20443**	23.9	69.2	0.3402	feldspar (Albite)	6.079878
37.287	**3.02811**	74.7	387.1	0.3671	Calcite	19.0028
39.167	**2.88806**	97.8	488.4	0.3849	Dolomite	24.87917
42.032	**2.69921**	11.1	72.1	0.4696	Pyrite	2.823709
43.927	2.5882	17.5	659.9	2.4667	-	
45.891	2.483	18.1	680.9	1.3996	Aragonite	
46.433	2.4556	21.1	85.4	0.3326	Aragonite	
47.459	2.4055	18.8	75.9	24.9012	Aragonite	
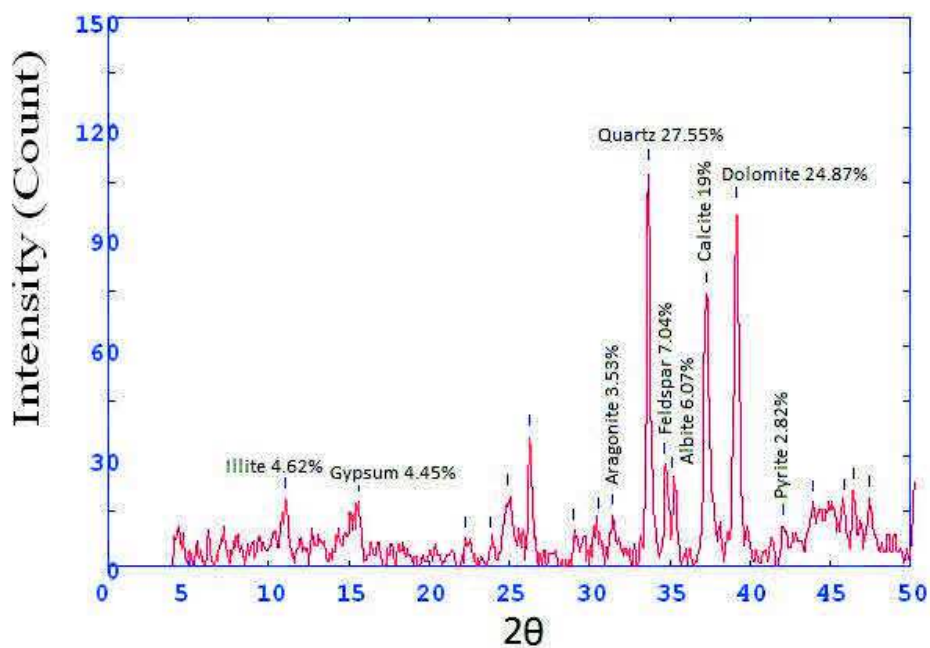
Core 9 sample 5

2Theta	d (A)	Height	Area	FWHM	Identified mineral	WT%
26.189	4.27268	26.9	110.2	0.3512	-	
29.083	3.85544	17	63.2	0.2948	-	
30.367	3.69603	26.1	57	0.2327	-	
32.907	**3.41771**	29.3	63.9	0.2538	Aragonite	6.508219
33.597	**3.34943**	192	565.9	0.2749	Quartz	42.64771
35.259	**3.19621**	22.1	65.2	0.321	feldspar (Albite)	4.908929
37.214	**3.03383**	135.7	551.9	0.3671	Calcite	30.14216
39.117	**2.89157**	34.7	279	0.5248	Dolomite	7.707685
39.965	**2.83271**	16.1	129.3	0.4666	halite	3.576188
41.901	**2.7073**	20.3	98.3	0.4084	Pyrite	4.509107
45.8	2.48769	32.1	133.8	0.3787	-	
46.238	2.46539	19.9	83.1	0.3697	-	
47.284	2.41391	14.4	60	0.3652	Aragonite	
47.981	2.38087	13.8	57.7	0.3641	Aragonite	
48.765	2.34486	14.4	60	0.363	Aragonite	
50.208	2.28164	43	209.1	0.3608	feldspar	
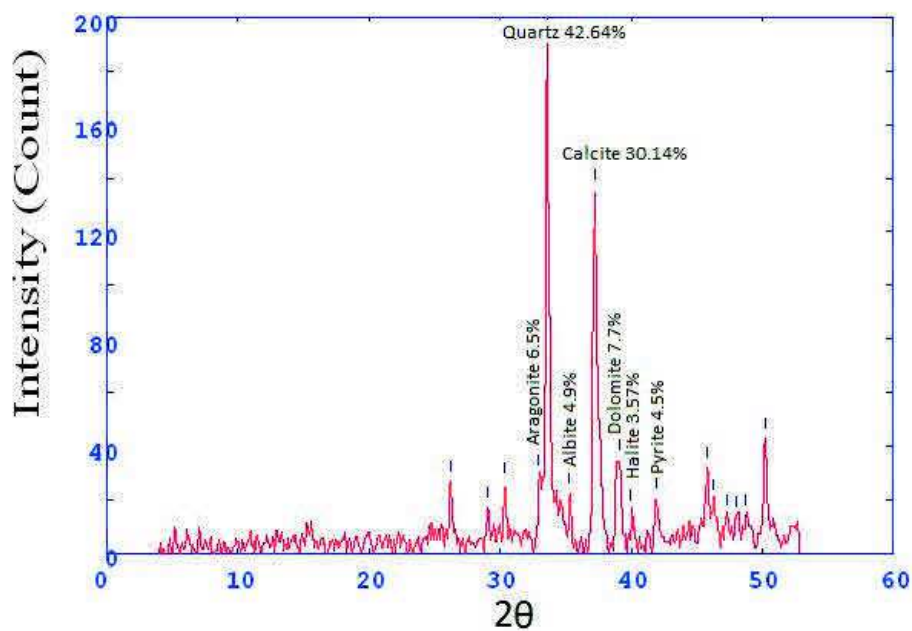
Core 9 sample 6

2Theta	d (A)	Height	Area	FWHM	Identified mineral	WT%
29.167	3.8445	18.9	87.6	0.3487	-	0
29.803	3.76424	11	51	0.3428	-	
32.987	**3.40963**	66.5	268.5	0.337	Aragonite	23.77547
34.259	**3.28667**	36.1	145.6	0.4634	feldspar (orthoclase)	12.90669
37.248	**3.03119**	138.6	1118.4	0.5898	Calcite	49.55309
41.865	**2.70952**	38.5	113.9	0.2779	Pyrite	13.76475
45.742	2.49065	47.1	275.9	0.45	-	
47.294	2.41341	14.1	82.5	0.4383	Aragonite	
48	2.37997	24	128	0.4267	Aragonite	
48.861	2.34051	23.3	128	0.4267	Aragonite	
50.099	2.28629	21.6	128	0.4267	Aragonite	
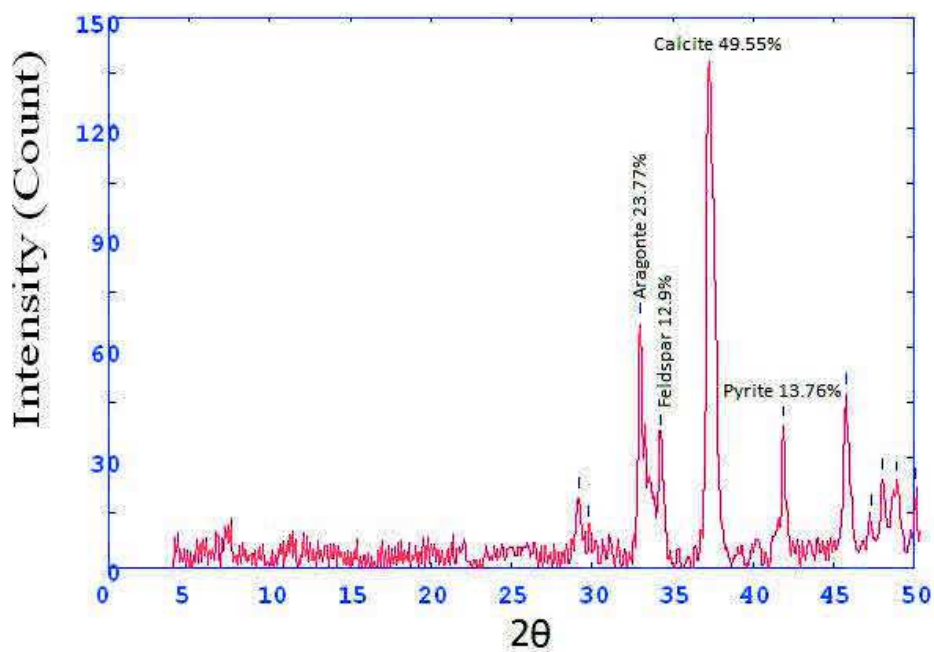
Core 9 sample 7

2Theta	d (A)	Height	Area	FWHM	Identified mineral	WT%
14.584	**7.62642**	55.3	168.6	0.2916	Gypsum	12.28889
26.234	4.26548	23.7	121.8	0.3756	Gypsum	
28.066	3.99216	7.4	56.9	0.4755	-	
29.35	3.82115	12.8	139.4	0.7083	-	
33.029	**3.40545**	81.1	882.8	0.487	Aragonite	18.02222
33.608	**3.34837**	157.7	457	0.2656	Quartz	35.04444
34.232	3.28915	50.6	146.6	0.5187	Quartz	
34.748	**3.24181**	40.1	116.1	0.6453	feldspar (orthoclase)	8.911111
37.261	**3.03012**	53.3	627.4	0.7719	Calcite	11.84444
37.67	2.99843	46.6	548.4	0.7009	-	
39.233	**2.88336**	15.8	144.2	0.6298	Dolomite	3.511111
40.076	2.82514	13	119.3	0.4991	halite	
41.365	2.74077	16.5	151.4	0.4337	-	
41.953	**2.70405**	46.7	225.8	0.3684	Pyrite	10.37778
43.428	2.61645	5	24.4	0.2841	-	
44.267	2.56931	7	10.7	0.1998	-	
45.833	2.48598	40.2	234.5	0.4428	Aragonite	
46.436	2.45546	14.5	84.8	0.4144	-	
47.468	2.4051	13.5	79	0.4003	Aragonite	
48.1	2.37531	36.6	164.6	0.3861	Aragonite	
48.929	2.3375	26.6	119.5	0.6169	Aragonite	
50.767	2.25818	11.2	114	0.8477	Pyrite	
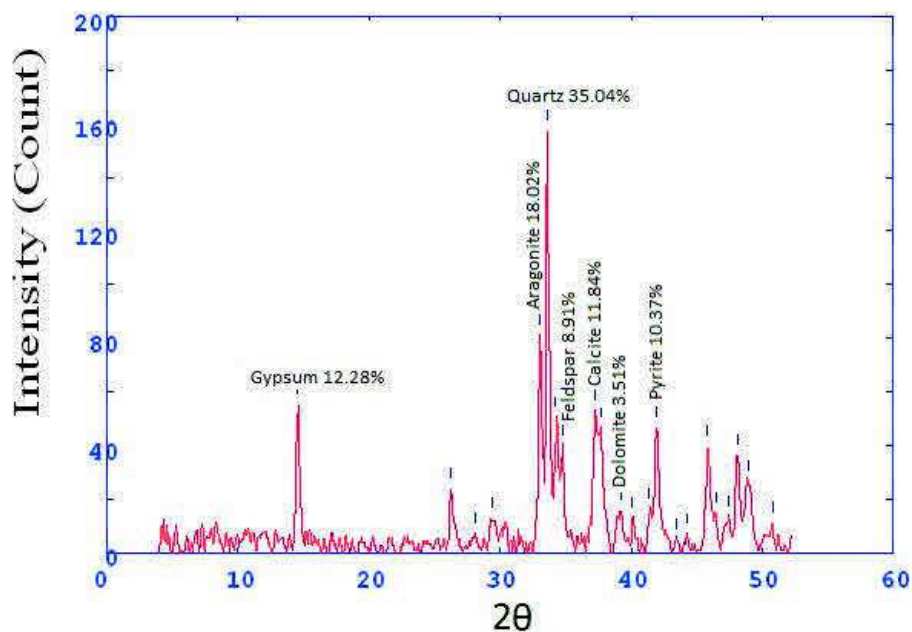
Core 9 sample 8

2Theta	d (A)	Height	Area	FWHM	Identified mineral	WT%
14.61	**7.61338**	17.6	52	0.3002	Gypsum	5.929919
26.367	4.24444	11.3	44.1	0.355	-	
30	3.74012	14.4	52.7	0.3212	-	
31.21	3.59854	10.3	37.6	0.3408	-	
33.147	**3.39367**	87.4	403.1	0.3604	Aragonite	29.44744
34.336	**3.27948**	49	225.8	0.5381	feldspar (orthoclase)	16.50943
37.71	**2.99534**	60.4	625.7	0.7159	Calcite	20.3504
39.272	**2.88065**	9.4	97.6	0.5081	Dolomite	3.167116
40.205	**2.81646**	24.8	82.6	0.3003	halite	8.355795
42	**2.7012**	48.2	188.8	0.3515	Pyrite	16.23989
45.933	2.48086	33.8	200.8	0.4628	Aragonite	
46.429	2.45582	25.7	153.1	0.5298	-	
47.252	2.41545	11.9	70.9	0.5465	Aragonite	
48.074	2.37651	28.8	171.2	0.5632	Aragonite	
48.933	2.33729	31.8	228.6	0.5967	Aragonite	
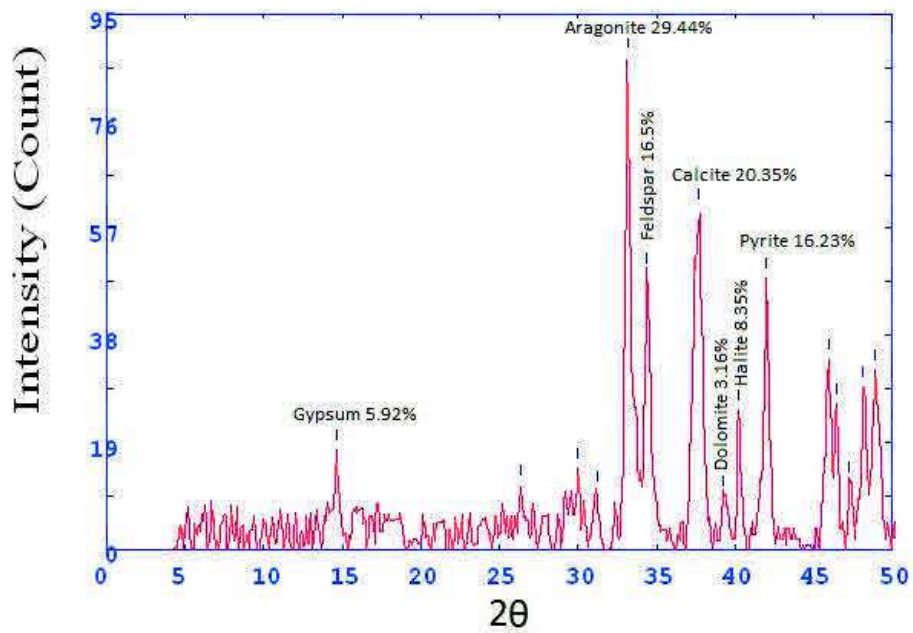
Core 9 sample 9

2Theta	d (A)	Height	Area	FWHM	Identified mineral	WT%
26.234	4.26558	11.4	77.9	0.4278	-	
29.9	3.75241	10.9	263.4	1.8763	-	
33.033	**3.405**	87.5	458.6	0.4214	Aragonite	27.61123
33.592	**3.34993**	53.7	281.6	0.5869	Quartz	16.94541
34.331	**3.27999**	47.2	247.3	0.6697	feldspar (orthoclase)	14.89429
37.633	**3.00123**	59.1	576.2	0.7524	Calcite	18.64942
39.17	**2.88784**	8.5	82.6	0.5478	Dolomite	2.682234
40.154	**2.81986**	12	117.2	0.4455	halite	3.786683
41.385	2.73954	15.3	149.1	0.3944	-	
41.884	**2.7083**	48.9	196.9	0.3432	Pyrite	15.43074
42.779	2.65423	7.4	29.7	0.2994	-	
43.189	2.63021	5.7	23.2	0.2775	-	
44.127	2.57705	8	26.9	0.2556	-	
44.748	2.54307	5.7	19.3	0.393	-	
45.755	2.49003	36.6	273.2	0.5305	Aragonite	
47.209	2.41751	13.1	98	0.4483	Aragonite	
48.056	2.37738	42.1	182.3	0.3661	Aragonite	
48.849	2.34106	29.5	0	0	Aragonite	
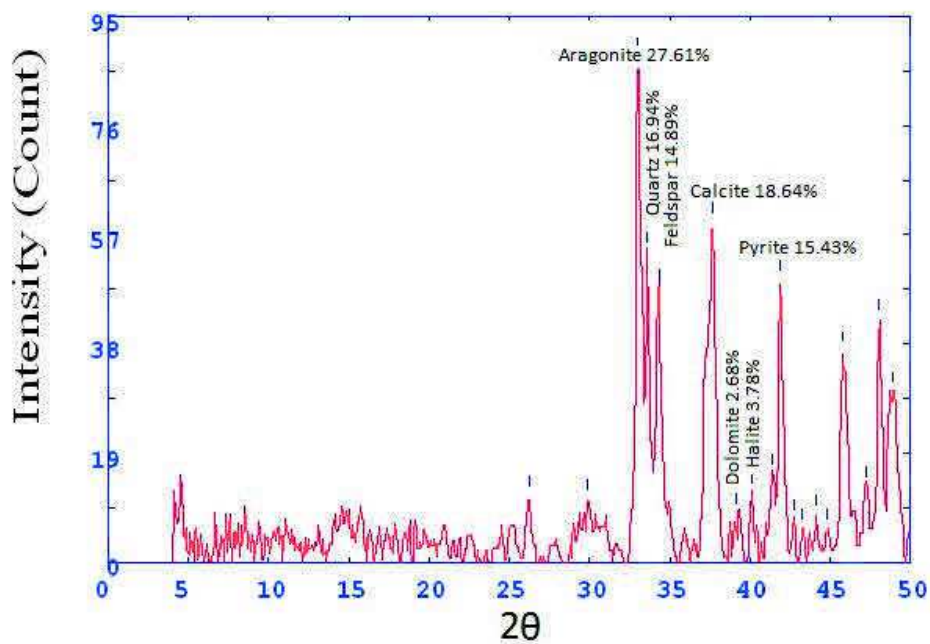
Core 9 sample 10

2Theta	d (A)	Height	Area	FWHM	Identified mineral	WT%
14.538	**7.65074**	67.4	147.2	0.2273	Gypsum	17.95418
29.383	3.81684	17.9	187.2	0.6231	Gypsum	
31.33	3.5851	5.9	73.8	0.5563	-	
33.023	**3.40603**	60.9	248.6	0.3064	Aragonite	16.2227
33.55	**3.35403**	27.8	113.3	0.4844	Quartz	7.405434
34.425	**3.27127**	33	134.7	0.5735	feldspar (orthoclase)	8.790623
37.261	**3.03017**	117.8	1096.6	0.6625	Gypsum	31.37986
39.062	**2.89554**	16.9	157.3	0.5131	Dolomite	4.501865
40.02	**2.82892**	19.9	111.1	0.3637	Halite	5.301012
41.249	2.74817	11.3	63	0.371	-	
41.919	**2.70615**	31.7	170.6	0.3782	Pyrite	8.444326
44.129	2.57694	8.5	69.9	0.5448	-	
45.773	2.48906	42.3	262.4	0.4956	Aragonite	
48.016	2.37922	34.1	107.6	0.2857	Aragonite	
48.773	2.3445	21.4	67.5	0.4283	Aragonite	
50.252	2.27981	26.7	200	0.571	Quartz	
52.233	2.19904	13	101	0.5454	feldspar (orthoclase)	
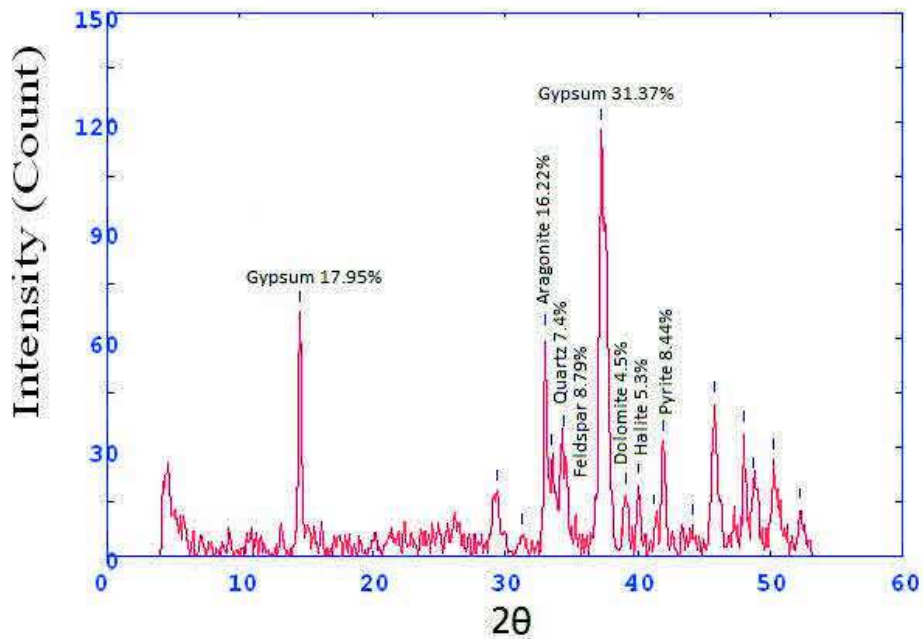
Core 9 sample 11

2Theta	d (A)	Height	Area	FWHM	Identified mineral	WT%
29.133	3.84889	14	40.6	0.2119	-	
33.016	**3.40673**	72.6	233.8	0.3043	Aragonite	21.77564
33.469	**3.36196**	36.3	116.9	0.4946	Quartz	10.88782
34.137	**3.29806**	35.5	114.3	0.5897	feldspar (orthoclase)	10.64787
37.267	**3.0297**	126.7	1273.6	0.6849	Calcite	38.0024
40.112	**2.8227**	20.9	107.9	0.3807	halite	6.268746
41.86	**2.70981**	41.4	169.9	0.3235	Pyrite	12.41752
45.7	2.49285	43.3	227.1	0.4175	Aragonite	
47.212	2.41735	11.7	61.6	0.3753	Aragonite	
47.993	2.38028	28.5	113.4	0.3332	Aragonite	
48.739	2.34603	21	83.4	0.5752	Aragonite	
50.504	2.26917	19.5	236.5	0.8173	Quartz	
52.368	2.19379	14.8	98.6	0.5189	feldspar	
54.466	2.11539	20.6	137.5	0.6595	gypsum	
55.2	2.08942	22	238.9	0.8	-	
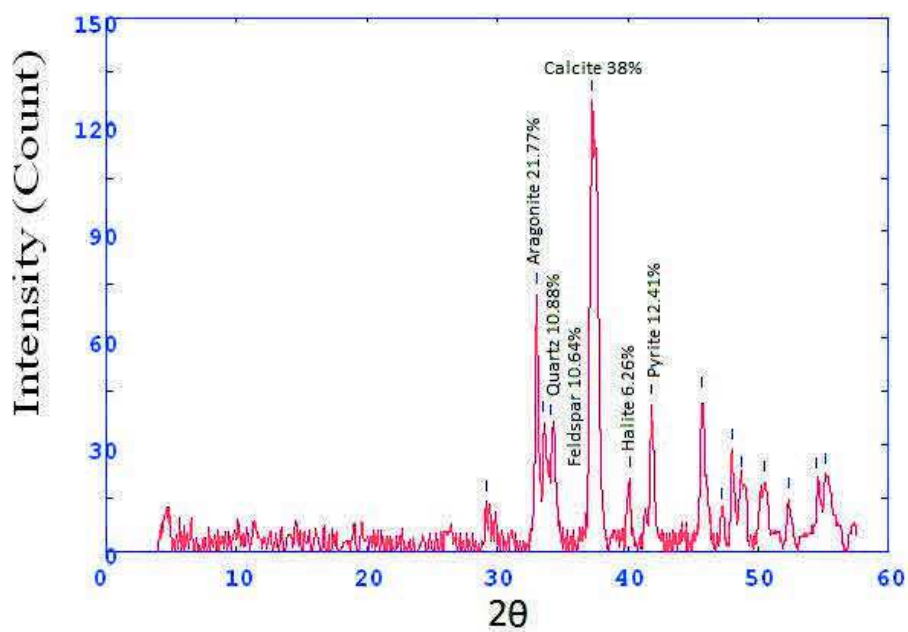
Core 10 sample 1

2Theta	d (A)	Height	Area	FWHM	Identified mineral	WT%
11.078	**10.02865**	18.7	78	0.3655	Illite	2.265294
14.541	7.64914	73.8	212.9	0.2498	Gypsum	8.940036
17.397	6.40068	9.9	28.6	0.2512	-	
23.879	4.67924	8.8	25.4	0.2516	-	
24.974	4.47704	13.2	38	0.2519	-	
26.247	4.26347	90.1	260.5	0.2526	Gypsum	
29.173	3.84374	15.4	44.4	0.2537	Gypsum	
29.447	3.80877	15.4	44.4	0.2542	-	
30.404	3.69162	81.8	233.2	0.2547	-	
31.273	3.59148	14.3	40.7	0.2976	-	
32.003	**3.5116**	9.9	28.2	0.319	Aragonite	1.199273
33.567	**3.35241**	369.7	1580.1	0.3404	Quartz	44.78498
34.559	**3.25895**	51.4	219.5	0.3874	feldspar (othocalase)	13.37371
35.198	**3.2016**	59	252.2	0.4109	feldspar (Albite)	
37.234	**3.03226**	91.3	558.3	0.4345	calcite	11.05996
39.046	**2.89663**	98.9	653.9	0.4639	dolomite	11.98062
40.036	**2.82783**	36.1	238.7	0.5578	halite	4.373107
42.615	**2.66401**	16.7	144.7	0.6517	Pyrite	2.023016
45.605	2.49776	18.6	161.4	0.496	Gypsum	
46.366	2.45895	24.8	115.7	0.3403	Aragonite	
50.172	2.28317	40.4	181.5	0.3299	Gypsum	
51.265	2.23771	13.2	59.2	0.3793	Gypsum	
54.028	2.13123	16	86.1	0.4288	Gypsum	
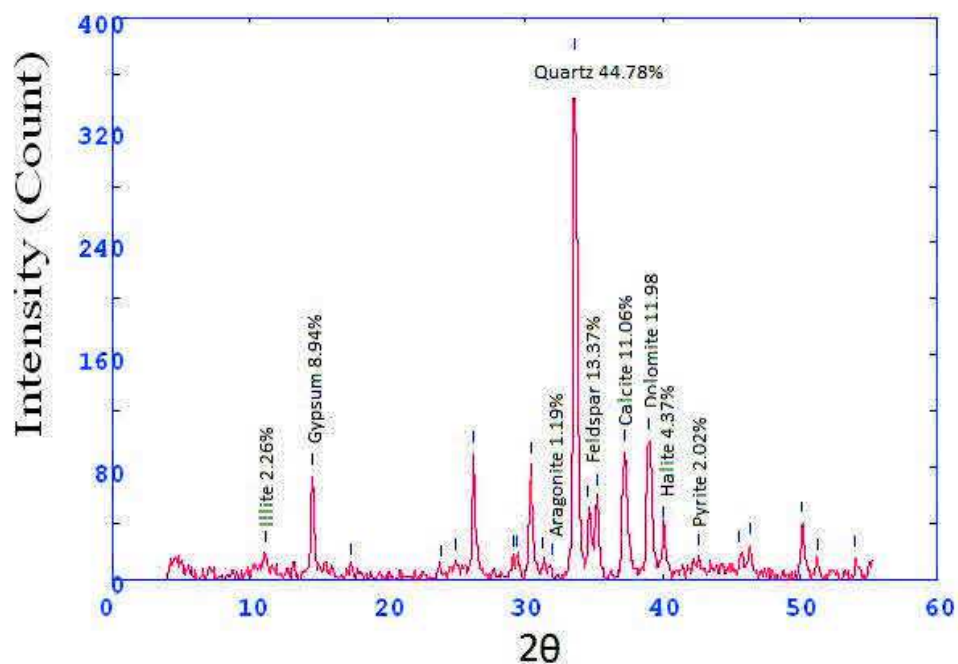
Core 10 sample 2

2Theta	d (A)	Height	Area	FWHM	Identified mineral	WT%
15.329	**7.25803**	16.3	192.2	0.9116	Gypsum	1.351588
24.89	4.49186	17.9	210.1	0.6001	gypsum	
26.221	4.26753	40.8	120.8	0.2887	Gypsum	
29.017	3.86403	10.7	31.8	0.306	feldspar (othocalase)	
30.42	3.68972	34.4	126.1	0.3232	-	
31.361	3.58162	13.4	49.2	0.2888	-	
33.624	3.34682	288.5	801.9	0.2544	Quartz	53.72439
34.737	**3.24275**	49.9	138.7	0.4544	feldspar (othocalase)	33.68715
35.3	**3.19267**	15.2	42.2	0.5545	feldspar (Albite)	
37.283	**3.02838**	61.5	511.1	0.6545	calcite	11.45251
39.056	**2.89595**	65.4	383.4	0.422	Dolomite	12.17877
40.176	**2.81838**	30.3	177.7	0.3728	halite	5.642458
42.333	**2.68088**	9.9	57.8	0.3482	Pyrite	1.843575
45.109	2.52376	21.6	73.8	0.3236	feldspar (othocalase)	
50.312	2.27724	18.6	137.1	0.6012	Gypsum	
52.2	2.20035	12	85.1	0.4994	Gypsum	
54.056	2.13021	8.1	57.4	0.4692	-	
55.317	2.08536	12.1	72.9	0.4389	-	
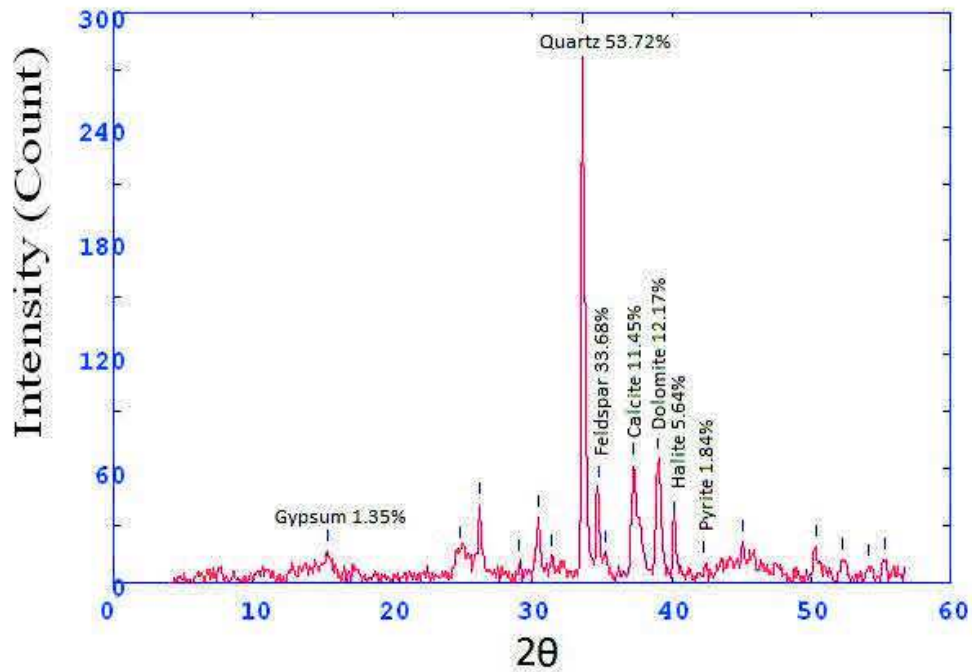
Core 10 sample 3

2Theta	d (A)	Height	Area	FWHM	Identified mineral	WT%
29.478	3.80484	10.4	35	0.3333	-	
31.167	3.60341	7.1	35	0.3333	-	
33.092	**3.39917**	75.6	294.2	0.3123	Aragonite	24.14564
33.643	**3.34503**	28.1	109.2	0.394	Quartz	8.974768
34.323	**3.2807**	43.8	170.2	0.4757	feldspar (othocalase)	8.156425
37.691	**2.99679**	105.9	822.3	0.6391	dolomite	19.72067
40.125	**2.82181**	18.3	57.6	0.3004	halite	3.407821
41.953	**2.70406**	41.4	204.3	0.3833	Pyrite	7.709497
43.417	2.61706	7.4	36.3	0.38	Gypsum	
44.352	2.56459	7.4	36.3	0.3783	Aragonite	
45.861	2.48455	41	168	0.3767	feldspar (othocalase)	
46.307	2.46192	21.7	88.9	0.3676	Aragonite	
47.327	2.41181	14	57.5	0.3586	Aragonite	
48.113	2.37469	34.2	145.1	0.3405	Pyrite	
49.027	2.33309	28.7	121.8	0.5452	Aragonite	
50.8	2.2568	20	180.8	0.75	-	
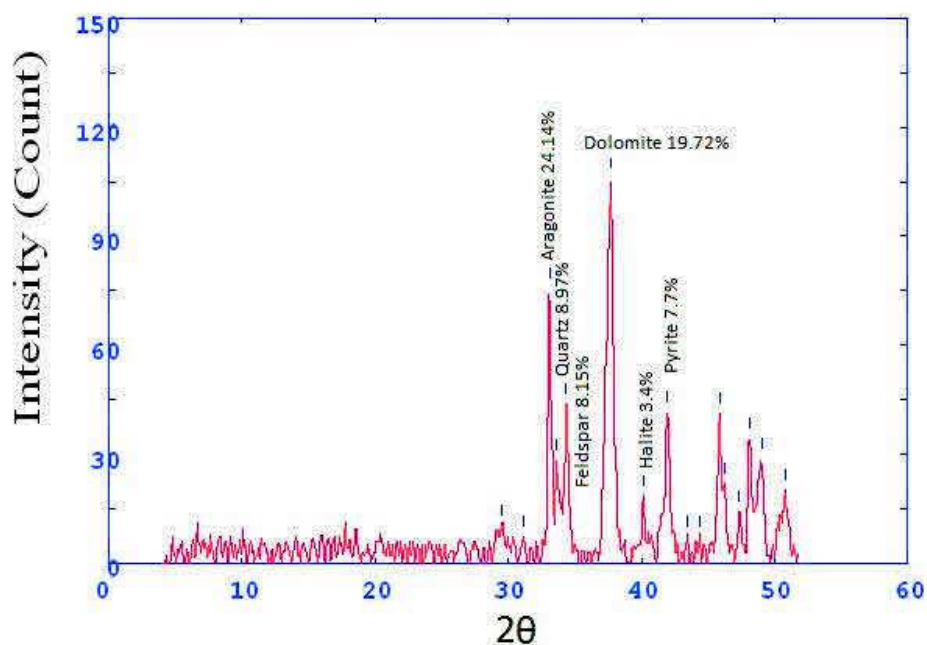
Core 10 sample 4

2Theta	d (A)	Height	Area	FWHM	Identified mineral	WT%
15.458	**7.19766**	11.1	134.3	0.2954	Gypsum	2.007233
26.146	4.27958	42.8	134.3	0.2954	Gypsum	
28.878	3.88215	11.1	34.9	0.2779	Gypsum	
30.274	3.70706	29.4	78.3	0.2605	-	
31.241	3.595	9.4	25.2	0.259	-	
31.917	3.52086	9.4	25.2	0.2583	-	
32.845	**3.42396**	37.5	100.1	0.2579	Aragonite	6.781193
33.488	**3.36003**	274.2	768.1	0.2576	Quartz	49.58409
34.533	**3.26133**	38.4	107.5	0.3209	feldspar (othocalase)	6.943942
37.127	**3.04069**	116.2	551.2	0.3842	calcite	21.01266
39.007	**2.89945**	36.5	178.4	0.4073	Dolomite	6.600362
39.935	**2.83473**	12.8	62.7	0.3423	halite	2.314647
41.811	**2.71282**	26.3	90.9	0.2773	Pyrite	4.755877
45.59	2.49855	21.3	73.9	0.2847	Quartz	
46.295	2.46254	81.4	271.3	0.2921	feldspar (othocalase)	
47.109	2.42234	12	39.9	0.319	Aragonite	
47.953	2.38216	9.4	31.4	0.3324	Pyrite	
48.713	2.34723	11.1	37.1	0.3391	Gypsum	
50.067	2.28768	21.2	87.6	0.3458	Gypsum	
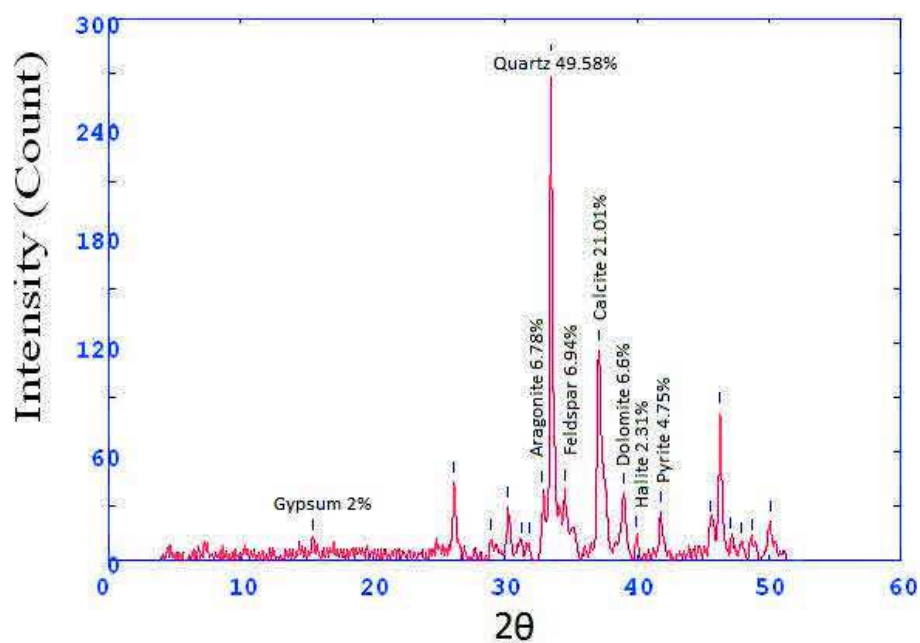
Core 10 sample 5

2Theta	d (A)	Height	Area	FWHM	Identified mineral	WT%
15.619	**7.1242**	10.9	54.8	0.4045	Gypsum	2.42924
26.275	4.25899	56.9	160.3	0.2474	Gypsum	
29.017	3.86397	14.9	42	0.2515	Gypsum	
30.379	3.6945	20.9	48.4	0.2556	dolomite	
31.301	3.58838	4.3	10	0.2575	-	
33.095	**3.39885**	37.8	87.6	0.2595	Aragonite	8.424337
33.624	**3.34688**	171.9	488.2	0.2633	Quartz	38.31068
37.241	**3.03168**	145.7	728.4	0.4444	calcite	32.47158
39.067	**2.89514**	50.4	307.8	0.439	dolomite	11.23245
40.108	**2.82297**	8.6	52.3	0.2873	halite	1.916648
41.902	**2.7072**	23.4	143.3	0.2114	Pyrite	5.215066
42.947	2.64438	32.8	29.2	0.1355	-	
44.023	2.58283	8.6	7.6	0.2922	-	
45.786	2.48843	30.2	162.7	0.4488	Gypsum	
46.469	2.4538	25.6	138	0.4427	Gypsum	
47.366	2.40993	12.3	66.2	0.4397	Aragonite	
48.252	2.36826	13.2	85.6	0.4366	Aragonite	
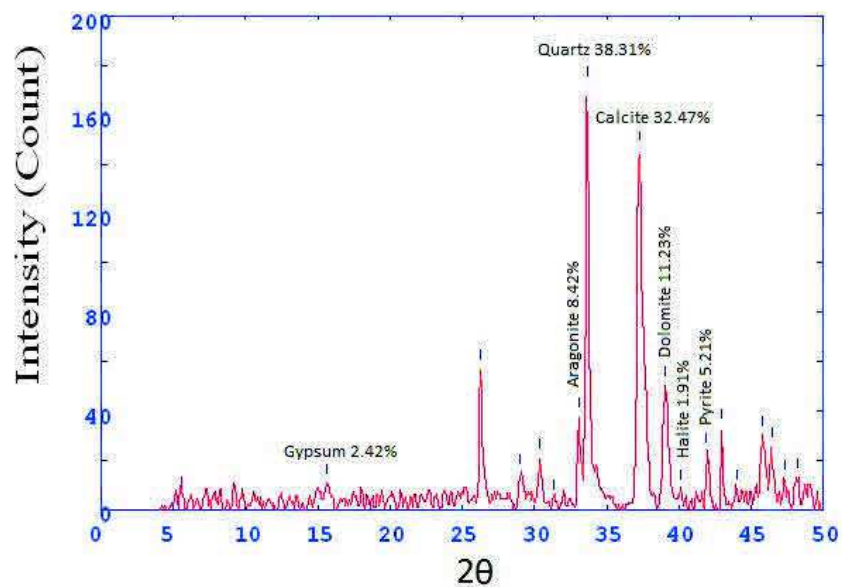
Core 10 sample 6

2Theta	d (A)	Height	Area	FWHM	Identified mineral	WT%
13.44	**8.27245**	92.6	1859.9	0.4128	Illite	9.780313
14.9	**7.46573**	332.9	1859.9	0.4128	Gypsum	35.16054
26.343	4.24818	61.3	370.2	0.4522	Gypsum	
26.888	**4.16359**	25.8	155.7	0.3556	Geothite	2.724968
29.721	3.77448	162.9	355	0.259	Gypsum	
33.276	**3.38084**	21.7	47.2	0.2603	Aragonite	2.291931
33.854	**3.32476**	137.1	389	0.2615	Quartz	14.48035
34.873	**3.23051**	21.7	61.5	0.2837	feldspar (othocalase)	10.29785
35.477	**3.17725**	75.8	232.8	0.3059	feldspar (Albite)	
36.89	3.05951	61.8	189.8	0.3559	-	
37.485	**3.0127**	86.2	407.6	0.406	calcite	9.104351
39.496	**2.86495**	60.8	287.2	0.3541	dolomite	6.421631
40.376	**2.80501**	64.2	241.1	0.3023	halite	6.780735
42.424	**2.67539**	28	184	0.5458	Pyrite	2.95733
45.127	2.52279	12.4	81.6	0.5046	-	
46	2.47746	19	116	0.4633	Gypsum	
46.556	2.44948	13.5	82.1	0.4539	Aragonite	
47.481	2.40446	7.3	44.5	0.4492	Aragonite	
48.826	2.34213	11.4	69.6	0.4468	Aragonite	
50.452	2.27132	21.2	115	0.4444	Pyrite	
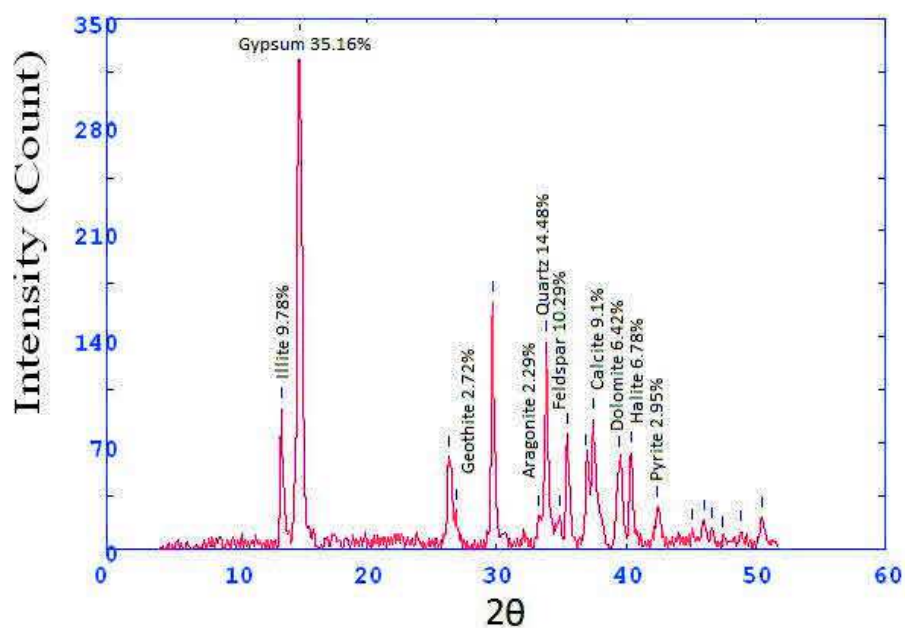
Core 10 sample 7

2Theta	d (A)	Height	Area	FWHM	Identified mineral	WT%
13.245	**8.39388**	166.1	2297.5	0.4949	Illite	15.1981
14.576	**7.63084**	322.2	2297.5	0.4949	Gypsum	29.4812
26.12	4.28388	112.2	566.2	0.3752	Gypsum	
26.649	4.20024	45.8	231.3	0.3342	Gypsum	
29.367	**3.81896**	336.1	1162.3	0.2931	Aragonite	30.75304
33.54	**3.355**	22	167.7	0.6167	Quartz	2.012993
35.586	**3.16786**	6.5	49.3	0.4847	Feldspar (Albite)	0.594748
36.7	**3.07482**	107.4	455.2	0.3527	Calcite	9.827066
39.285	**2.87974**	59.4	217.6	0.3023	dolomite	5.435081
40.054	**2.82666**	25.6	93.8	0.3381	halite	2.342392
42.227	**2.68735**	47.6	211	0.374	Pyrite	4.355385
43.628	2.60502	11.8	52.2	0.3747	-	
44.817	2.53935	22	114	0.3754	-	
45.416	2.50762	15	77.5	0.35	-	
47.389	2.40883	18.8	78	0.3245	Feldspar (Albite)	
51.667	2.22147	19.9	119.6	0.4425	Gypsum	
55.233	2.08825	25.3	256	0.7151	calcite	
58.084	1.99407	25.9	142.6	0.4116	Feldspar (orthoclase)	
61.214	1.90126	61.7	379.2	0.4244	-	
65.95	1.77856	21.2	175.7	0.6341	-	
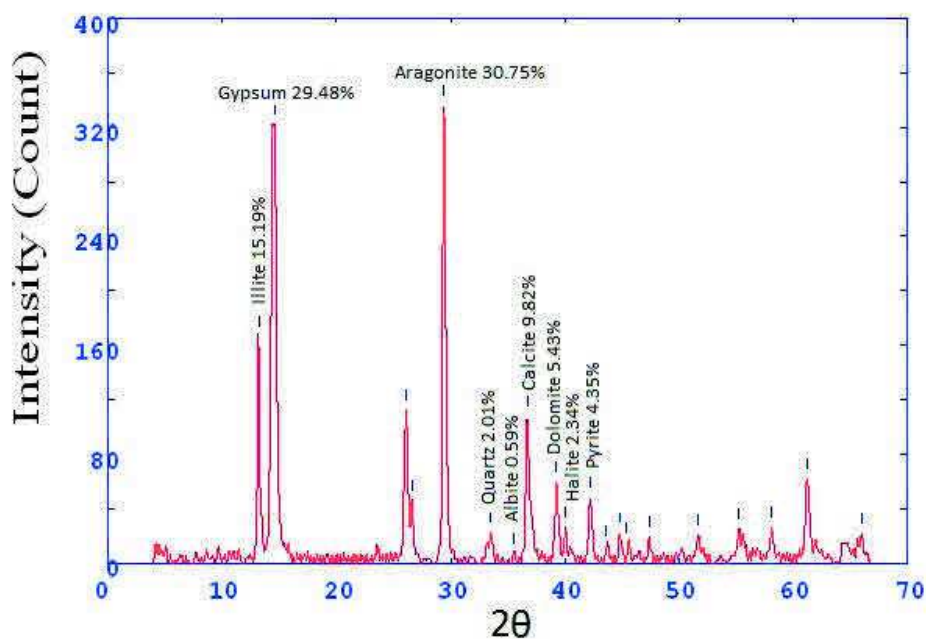
Core 10 sample 8

2Theta	d (A)	Height	Area	FWHM	Identified mineral	WT%
13.133	8.46496	165	2297.5	0.4949	Illite	20.72604
14.576	7.63084	322.2	2297.5	0.4949	Gypsum	40.4723
23.558	4.74198	14.3	58.2	0.2891	-	
26.12	4.28388	112.2	566.2	0.3752	Gypsum	
26.649	4.20024	46.9	236.7	0.3342	Geothite	5.89122
29.367	3.81896	336.1	1162.3	0.2931	Gypsum	
33.54	3.355	22	167.7	0.6167	Quartz	2.763472
36.7	3.07482	107.4	455.2	0.3527	Calcite	13.49077
39.285	2.87974	59.4	217.6	0.3023	dolomite	7.461374
40.054	2.82666	25.6	93.8	0.3381	halite	3.215676
42.227	2.68735	47.6	211	0.374	Pyrite	5.979148
43.74	2.5987	16	71.1	0.3747	Gypsum	
44.817	2.53935	22	114	0.3754	-	
45.751	2.49023	18.2	94.1	0.35	Gypsum	
47.389	2.40883	18.8	78	0.3245	-	
51.667	2.22147	19.9	119.6	0.4425	Gypsum	
55.233	2.08825	25.3	256	0.7151	Gypsum	
58.084	1.99407	25.9	142.6	0.4116	-	
61.214	1.90126	61.7	379.2	0.4244	-	
65.95	1.77856	21.2	175.7	0.6341	-	
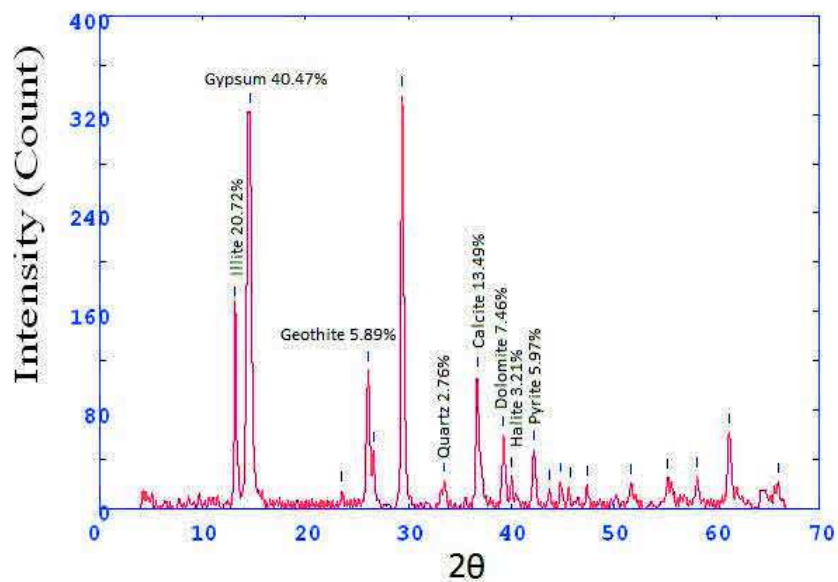
Core 10 sample 9

2Theta	d (A)	Height	Area	FWHM	Identified mineral	WT%
26.145	4.27986	17.5	42.6	0.2766	Geothite	4.995718
29.266	3.83178	16.2	107.1	0.5342	-	
32.967	3.41169	73.3	290.5	0.3406	Aragonite	20.92492
33.547	3.35431	51.7	204.8	0.5615	Quartz	0.147588
34.257	3.28678	49.4	195.6	0.672	feldspar (othocalase)	14.1022
37.573	3.00589	92.1	1041.5	0.7824	calcite	26.29175
38.963	2.90255	19.8	223.7	0.5718	Dolomite	5.652298
40.207	2.81635	8.2	92.3	0.4664	halite	2.340851
41.272	2.74669	11.6	131.7	0.4138	-	
41.851	2.71036	38.3	170.1	0.3611	Pyrite	10.93349
45.747	2.49043	34.2	262.6	0.58	Quartz	
47.133	2.4212	12.8	98.3	0.4744	Aragonite	
48.033	2.37841	30.6	154.5	0.3688	Pyrite	
48.82	2.3424	23.5	118.8	0.6386	Gypsum	
50.152	2.28406	16.6	83.7	0.7734	Gypsum	
50.67	2.26222	19	234.4	0.9083	-	
52.65	2.18287	11.2	90.3	0.5666	calcite	
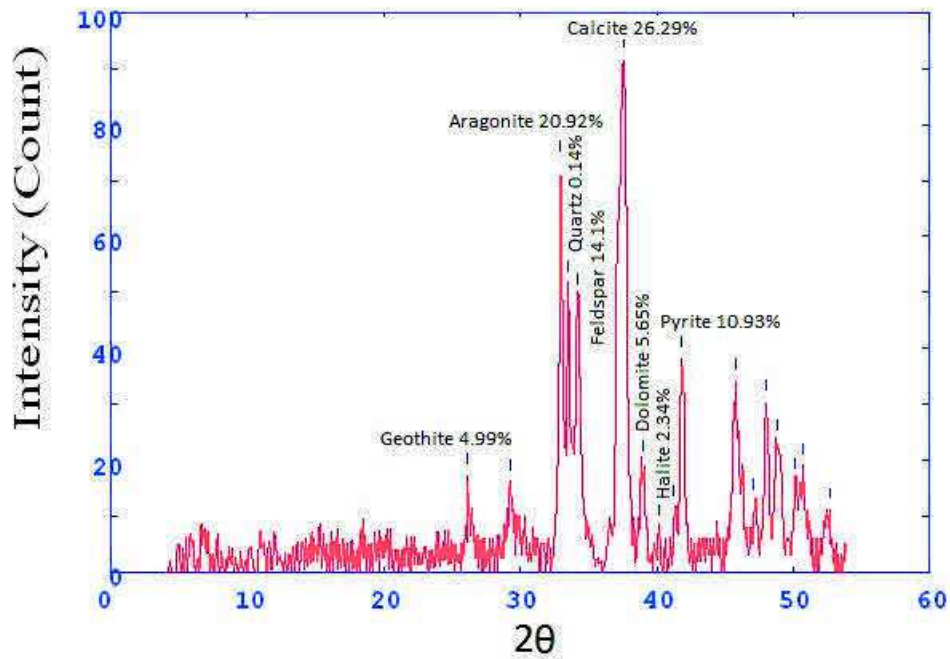
Core 10 sample 10

2Theta	d (A)	Height	Area	FWHM	Identified mineral	WT%
26.334	4.24966	14.8	55.2	0.3062	Geothite	4.766506
29.5	3.8021	14.4	82.4	0.4775	-	
30.065	3.73223	11.1	63.4	0.3829	-	
33.127	3.39568	79.8	246.6	0.2882	Aragonite	25.70048
34.413	3.27241	47.9	148	0.4741	Quartz	15.42673
37.767	2.99101	113.4	1019.1	0.6599	calcite	36.52174
40.236	2.81435	11.1	99.7	0.5267	dolomite	3.574879
42.016	2.70022	43.5	205.5	0.3934	Pyrite	14.00966
45.933	2.48086	40	281.3	0.5578	Quartz	
47.455	2.4057	17.9	125.7	0.5089	Aragonite	
48.233	2.36914	32.2	198.7	0.46	Gypsum	
48.931	2.33737	26.8	198.7	0.46	Aragonite	
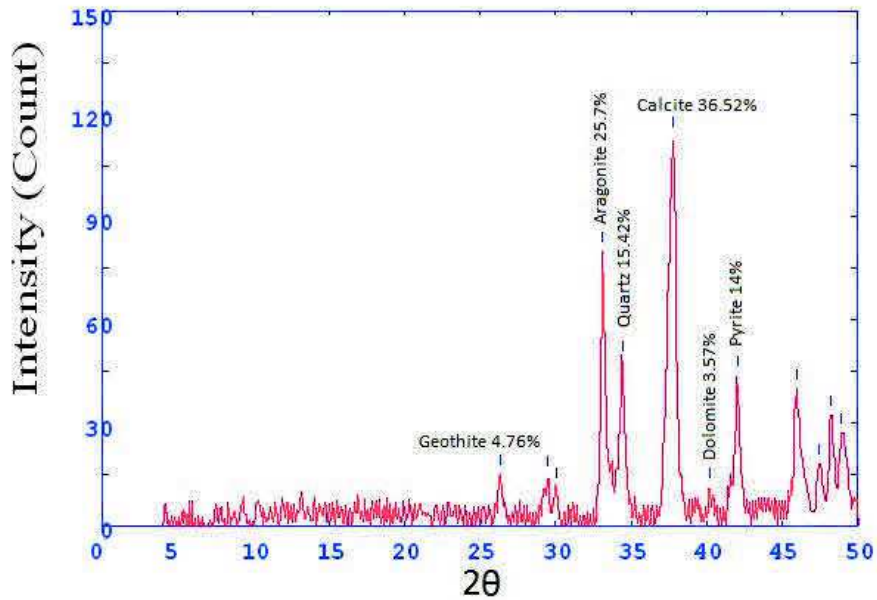
Core 11 sample 1

2Theta	d (A)	Height	Area	FWHM	Identified mineral	WT%
13.085	8.49562	27.5	771.1	0.2181	Illite	4.838142
14.479	7.68149	311.2	771.1	0.2181	gypsum	54.75018
26.025	4.29921	37.7	199.4	0.3953	gypsum	
29.39	3.81604	72.3	157.3	0.2621	gypsum	
32.854	3.42306	25.5	55.6	0.2432	aragonite	
33.534	3.3556	116.9	227.8	0.2243	quartz	20.5665
34.331	3.27999	19.7	38.3	0.2924	feldspar (orthoclase)	3.465869
36.545	3.0874	38.3	74.6	0.3605	gypsum	
37.193	3.03546	39	239.7	0.4968	calcite	6.861365
39.088	2.89366	12.8	78.8	0.3953	dolomite	2.251935
40.017	2.82916	23.7	87.6	0.2938	halite	4.169599
42.168	2.69091	17.6	161.3	0.6133	pyrite	3.096411
43.682	2.602	6.9	63.7	0.59	feldspar (orthoclase)	
45.767	2.48941	14.1	111.3	0.5667	aragonite	
47.947	2.38244	12.8	101	0.4655	gypsum	
48.733	2.34629	25	120	0.3643	aragonite	
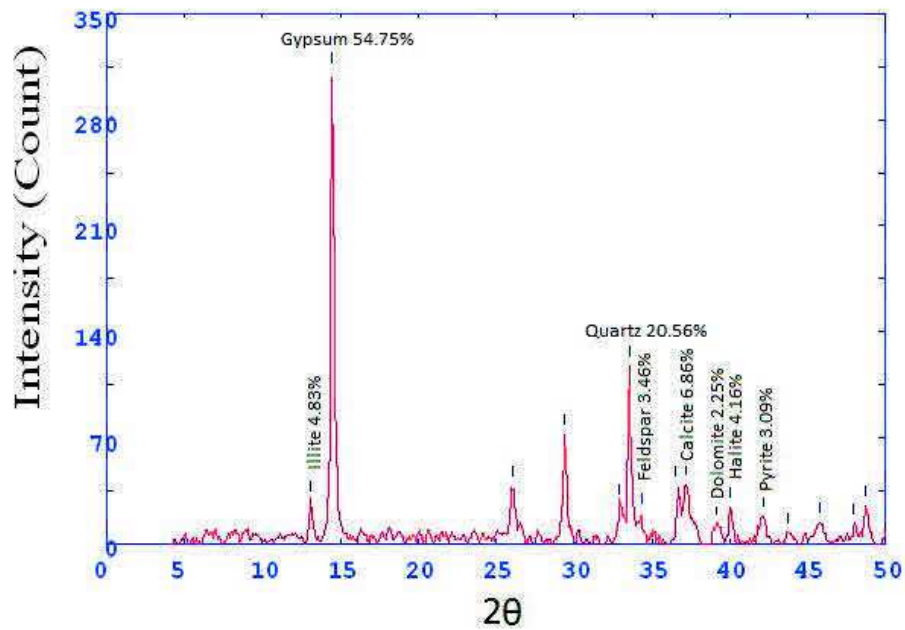
Core 11 sample 2

2Theta	d (A)	Height	Area	FWHM	Identified mineral	WT%
11.431	9.72024	33.2	496.1	0.9852	Illite	7.628676
13.025	8.53509	145	2166.7	0.7899	Illite	
14.567	7.63558	159.5	1492.7	0.5946	gypsum	36.64982
25.992	4.3045	46	174.4	0.3146	gypsum	
26.716	4.18996	26.8	101.5	0.3458	geothite	
29.367	3.81897	171.5	923.7	0.377	gypsum	
33.525	3.35643	59.6	173.8	0.2681	quartz	13.69485
34.433	3.27055	8.1	23.5	0.2858	feldspar (orthoclase)	1.861213
36.686	3.07595	66.6	206.4	0.3036	calcite	15.30331
39.259	2.88158	25.9	105.7	0.3451	dolomite	5.951287
42.149	2.69208	37.4	141.3	0.3329	pyrite	8.59375
44.808	2.53982	18.1	50.7	0.2667	Quartz	4.159007
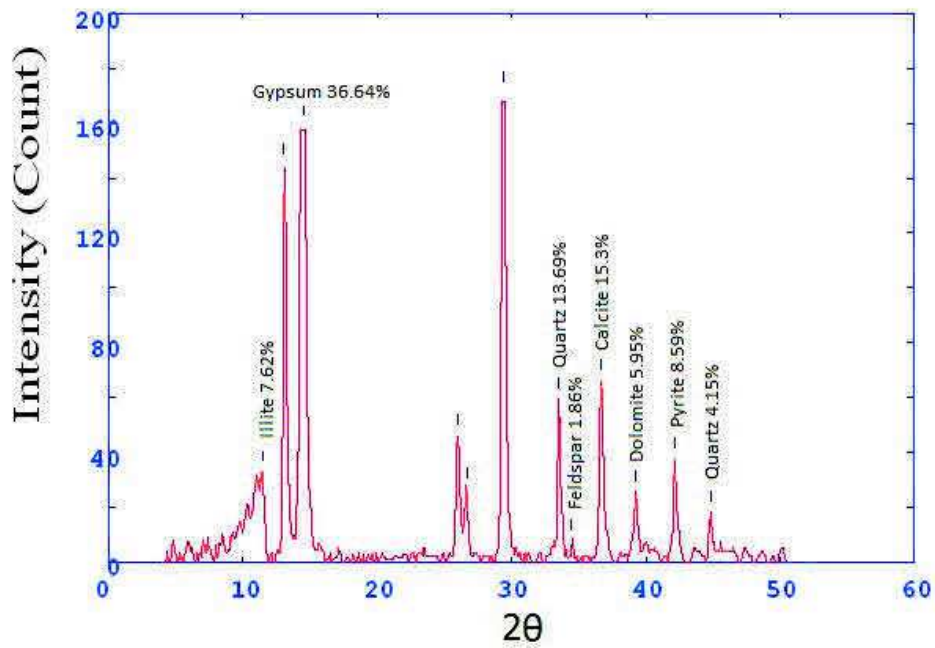
Core 11 sample 3

2Theta	d (A)	Height	Area	FWHM	Identified mineral	WT%
13.078	8.50026	258.4	2934.4	0.5637	Illite	33.25611
14.634	7.60093	322.3	2934.4	0.5637	gypsum	41.48005
15.765	7.05871	15.5	140.9	0.5067	gypsum	0
23.6	4.73375	13.5	74.6	0.4497	gypsum	
26.093	4.28811	117.9	599.8	0.3863	gypsum	
26.683	4.19496	49.6	252.1	0.3521	geothite	
29.5	3.80206	357.3	1249.3	0.3179	gypsum	
30.41	3.69092	30.9	107.9	0.2749	gypsum	
31.19	3.60084	26.5	92.5	0.2534	-	
33.553	3.35371	53	137.3	0.2319	quartz	6.821107
36.733	3.07214	77.7	241.6	0.2968	calcite	10
39.301	2.87863	25.7	147.7	0.456	dolomite	3.307593
40.115	2.8225	7.8	44.7	0.3746	halite	1.003861
42.189	2.68964	32.1	97.3	0.2933	pyrite	4.131274
43.668	2.60276	5.6	16.9	0.1467	gypsum	
44.708	2.54522	8.9	0	0	calcite	
50.081	2.28707	6.7	0	0	gypsum	
51.641	2.22252	10	0	0	-	
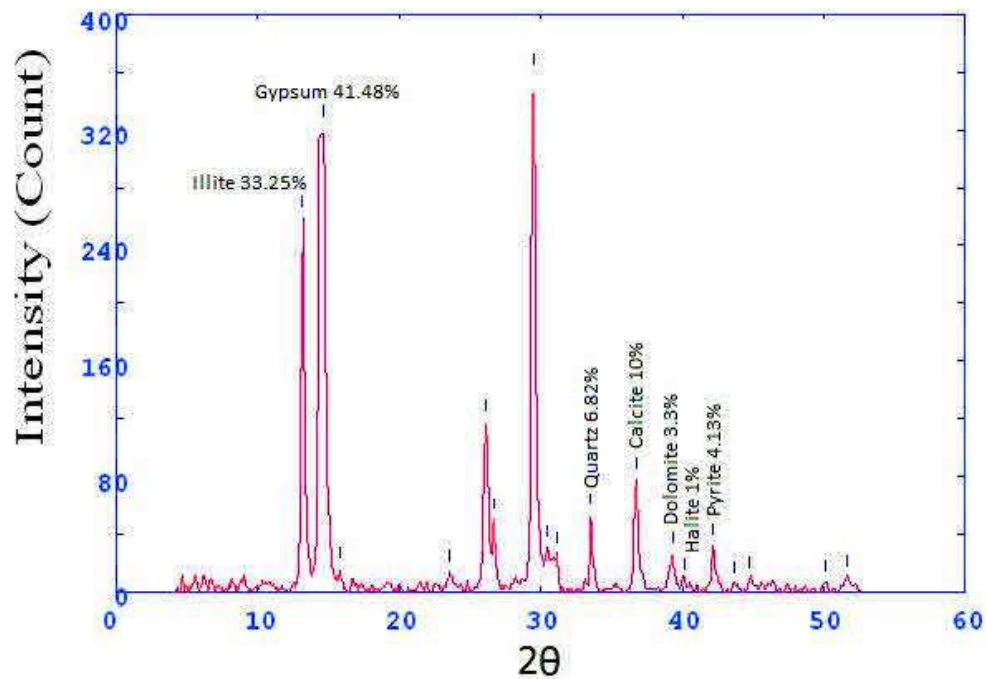
Core 11 sample 4

2Theta	d (A)	Height	Area	FWHM	Identified mineral	WT%
13.15	8.45396	160.8	85.2	0.3255	Illite	17.24212
14.521	7.65931	316.2	85.2	0.3255	gypsum	33.90521
15.978	6.96482	16.1	4.3	0.3255	-	
23.699	4.71427	17.1	85.2	0.3255	-	
26.135	4.28143	143.9	458.1	0.3115	Gypsum	
26.692	4.19364	43.7	139.3	0.2908	Goethite	0
29.515	3.80019	337.2	1044.5	0.2702	gypsum	
33.677	3.34179	115.6	334.5	0.242	Quartz	12.39545
35.434	3.18097	29.9	86.5	0.2725	feldspar (Albite)	3.20609
36.838	3.0637	184.6	724.3	0.303	calcite	3.20609
39.398	2.87178	54.8	439.1	0.5693	dolomite	5.876045
40.234	2.81454	20.3	162.8	0.4656	halite	2.17671
42.31	2.68233	50.4	241.7	0.3619	pyrite	5.404246
43.833	2.59343	8.6	41.2	0.3344	Gypsum	
44.948	2.53235	21.2	91.6	0.3069	gypsum	
50.264	2.27929	22	80.2	0.2841	gypsum	
51.8	2.21615	24	84.9	0.3139	gypsum	
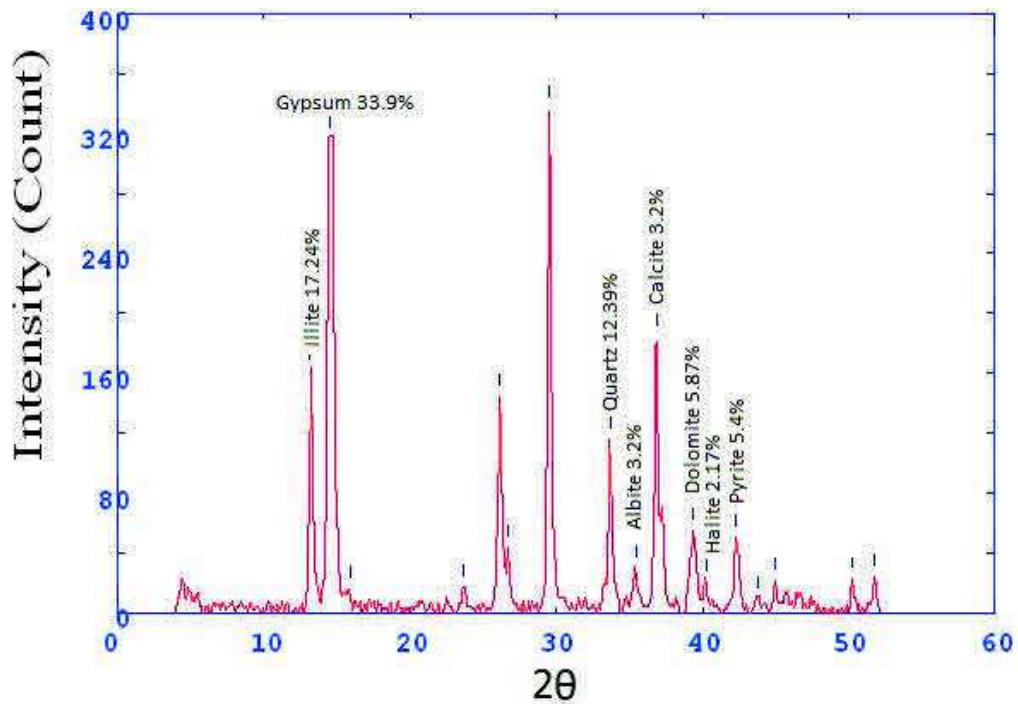
Core 11 sample 5

2Theta	d (A)	Height	Area	FWHM	Identified mineral	WT%
13.046	8.5212	230.9	2673.3	0.5535	Illite	27.12004
14.516	7.66217	317.4	3675.5	0.3844	Gypsum	37.27977
15.741	7.06918	17.2	199	0.2998	-	
23.594	4.73486	20.3	38	0.2152	-	
26.043	4.29618	200.3	581.8	0.2689	gypsum	
26.603	4.20735	63.1	183.3	0.2939	Goethite	
29.434	3.81042	347.1	1220.3	0.319	gypsum	0
33.149	3.39345	17.4	39.1	0.2182	Quartz	2.043693
36.692	3.0755	159.7	633.1	0.3195	calcite	2.043693
39.223	2.88408	53.2	230.7	0.3593	Dolomite	6.248532
40.569	2.79223	11.8	51.3	0.3515	gypsum	
42.126	2.69348	72.8	320.4	0.3437	Pyrite	8.550623
43.591	2.60714	7.6	33.3	0.3206	gypsum	
44.75	2.54296	27.4	95.5	0.2975	gypsum	
45.388	2.50907	12.9	45.1	0.1488	-	
46.368	2.45887	11.8	0	0	gypsum	
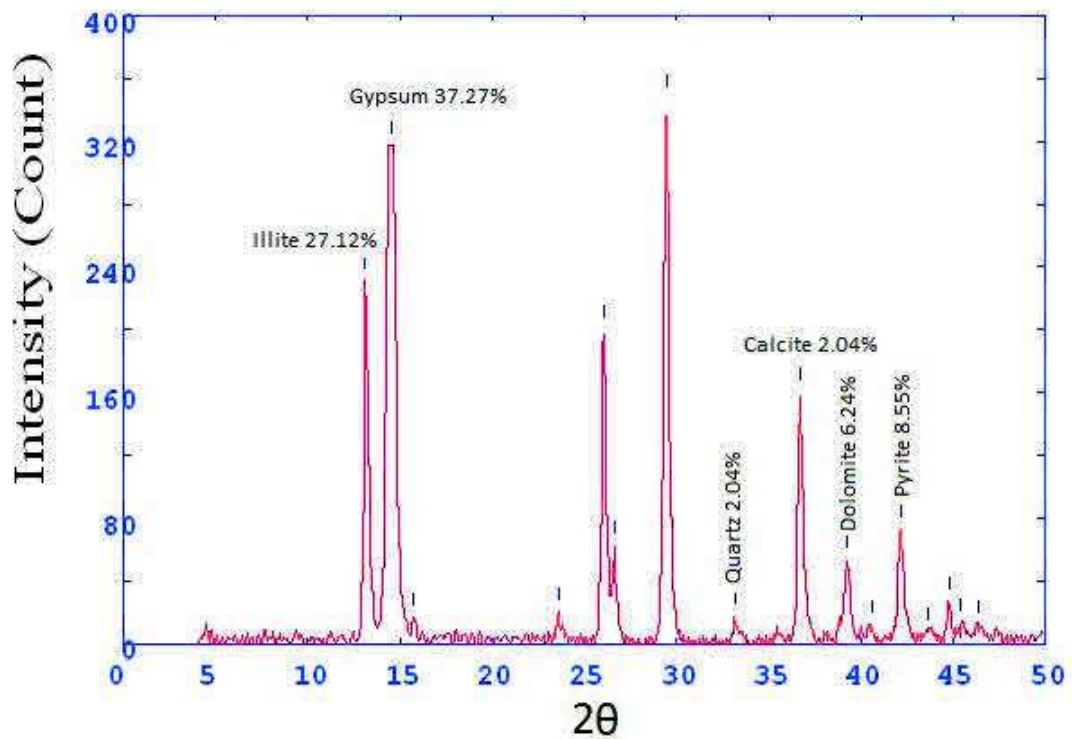
Core 11 sample 6

2Theta	d (A)	Height	Area	FWHM	Identified mineral	WT%
14.568	7.63516	21.9	69.2	0.2894	gypsum	5.968929
26.273	4.25925	14	96	0.5222	gypsum	0
29.873	3.75563	13.9	48.4	0.2814	gypsum	
33.018	3.40653	102.9	399.2	0.3424	aragonite	28.04579
33.566	3.35251	66.6	258.6	0.5313	quartz	18.15209
34.272	3.2854	59.2	229.8	0.6258	orthoclase (feldspar)	16.13519
37.54	3.00842	38.8	150.7	0.4192	calcite	10.57509
39.218	2.88444	8.4	32.7	0.3159	dolomite	2.289452
40.056	2.82654	17.1	39.1	0.2126	halite	0.770384
41.338	2.74252	15.2	34.8	0.2843	-	
41.888	2.70807	52	216.7	0.356	pyrite	192.4512
43.192	2.63004	6.5	27	0.5535	-	
43.94	2.58744	6.5	55.9	0.7509	-	
45.752	2.49017	36.8	212	0.434	gypsum	
47.079	2.42382	18.5	106.2	0.4225	pyrite	
48.052	2.37753	39.6	206.7	0.411	pyrite	
48.757	2.34524	36.2	189	0.5132	gypsum	
50.7	2.26095	6.8	57.9	0.6153	-	
52.433	2.19125	12.6	112.6	0.568	gypsum	
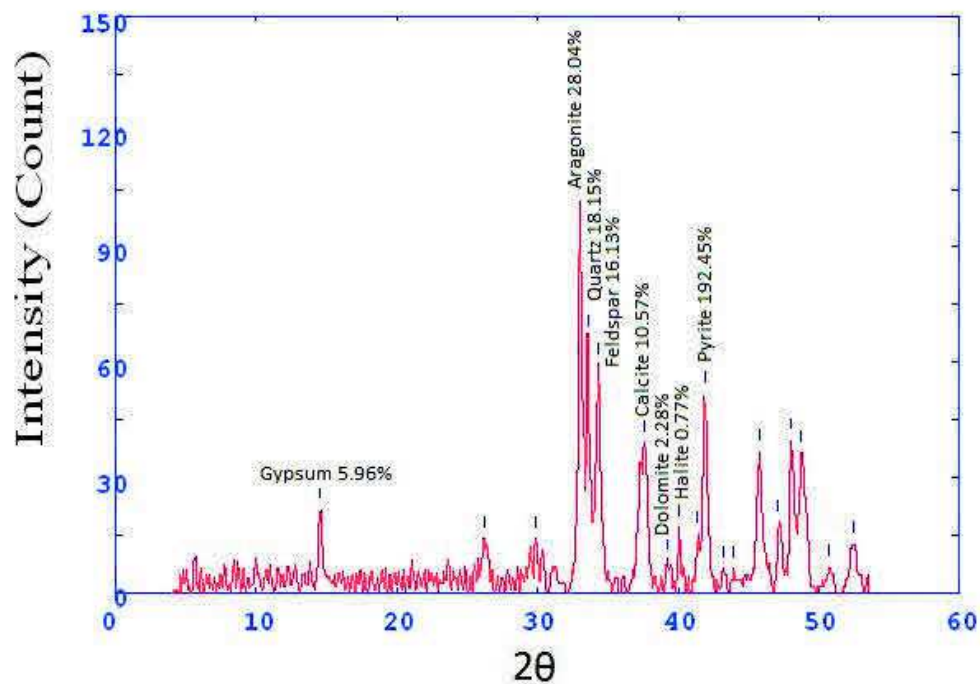
Core 11 sample 7

2Theta	d (A)	Height	Area	FWHM	Identified mineral	WT%
11.154	9.96052	13.3	34.8	0.281	illite	3.207911
13.156	8.44991	163.1	428.7	0.3976	Illite	
14.64	7.59788	322.1	2402.1	0.5142	gypsum	77.68934
23.684	4.71709	9.7	72.2	0.4608	-	
26.081	4.29008	103.9	535.1	0.4074	gypsum	
26.654	4.19956	35.3	181.6	0.3319	Geothite	0
29.479	3.8047	337.3	966.5	0.2563	gypsum	
33.595	3.34968	83.5	314.1	0.2918	quartz	20.13989
35.472	3.1777	11.8	44.4	0.298	feldspar (Albite)	28.77472
36.786	3.06789	119.3	454.8	0.3041	-	
38.081	2.96722	7.5	28.8	0.4539	calcite	1.808973
39.318	2.87737	48.7	376.4	0.6036	dolomite	11.74626
40.061	2.82618	25.7	198.3	0.4921	halite	6.198746
42.256	2.68556	44.8	226.1	0.3806	pyrite	10.8056
43.66	2.60322	11.8	59.5	0.3713	-	
44.83	2.53867	19.3	97.2	0.3621	-	
45.675	2.49415	24.1	101.4	0.3436	gypsum	
50.154	2.28397	18.4	68.3	0.3392	feldspar (Albite)	
51.768	2.21742	22.7	120.6	0.4082	-	
54.089	2.12901	16.2	94.8	0.5283	-	
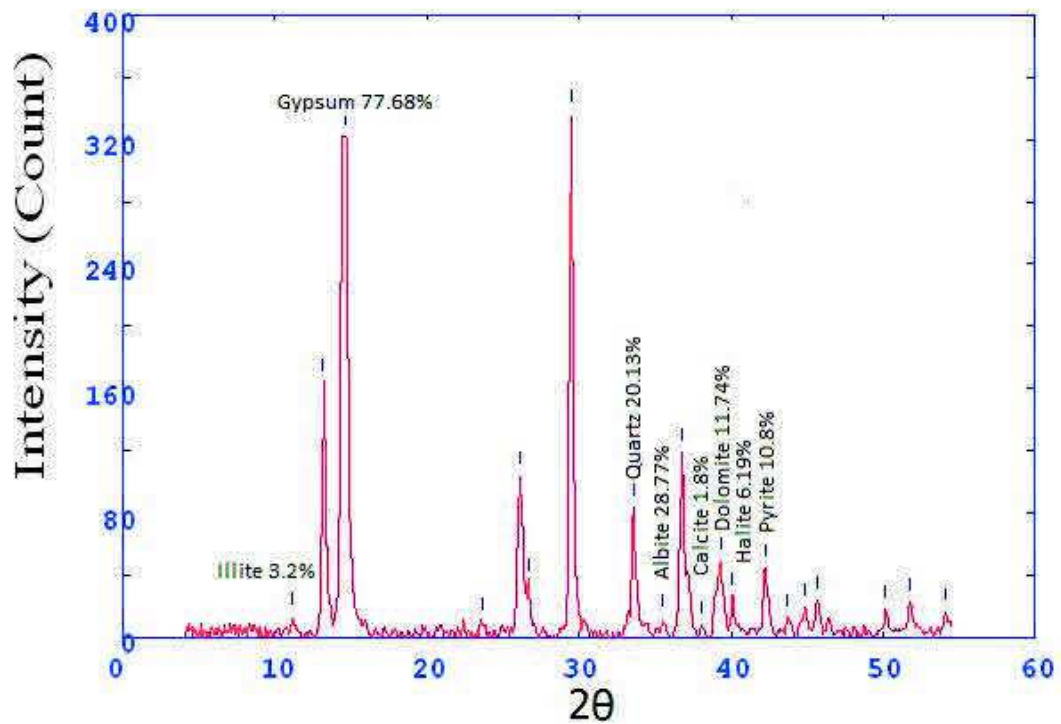
Core 11 sample 8

2Theta	d (A)	Height	Area	FWHM	Identified mineral	WT%
13.194	8.42603	75.4	1795.1	0.3764	Illite	8.070213
14.51	7.66524	323.2	7690.2	0.38	gypsum	34.59274
23.724	4.70933	8.3	198.5	0.3818	-	
26.242	4.26418	71.4	338.3	0.3836	gypsum	0
27.673	4.04778	5.2	24.8	0.3181	-	
29.478	3.80485	136.8	396.4	0.2526	gypsum	
30.387	3.69357	24.9	72	0.2516	-	
33.102	3.39812	33.1	95.9	0.2511	aragonite	3.542759
33.619	3.34734	327.7	925.7	0.2506	quartz	35.07439
35.329	3.19008	35.6	200.3	0.3887	feldspar (Albite)	
36.804	3.06644	39.3	221.4	0.4389	feldspar (Albite)	4.206358
37.246	3.03128	57.9	350.9	0.489	calcite	6.197153
39.151	2.88919	29.1	296.5	0.6689	dolomite	3.114631
40.095	2.8239	25.9	264.2	0.6163	halite	2.772129
41.967	2.70324	22.7	202.1	0.5636	pyrite	2.429626
45.767	2.48941	19.4	145.8	0.53	feldspar (Albite)	
48.1	2.37531	14.5	54.8	0.2686	feldspar (Albite)	
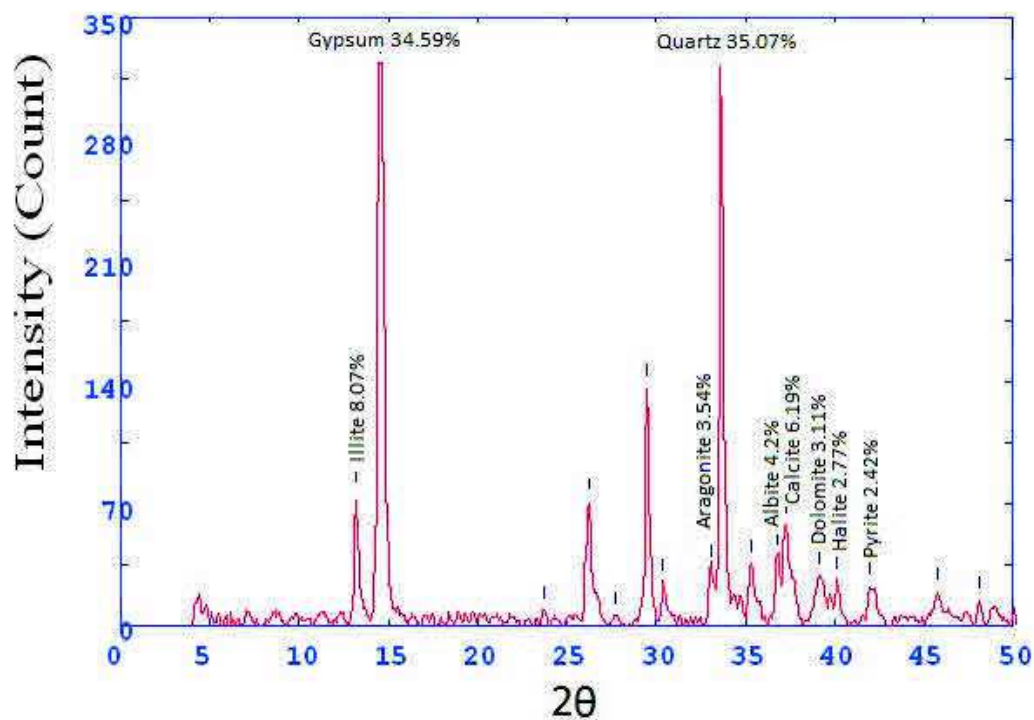
Core 11 sample 9

2Theta	d (A)	Height	Area	FWHM	Identified mineral	WT%
26.162	4.27704	57.1	155.2	0.2525	-	0
29	3.8662	17	52	0.2888	-	
30.362	3.69663	27.2	96	0.2949	feldspar	
32.87	3.42147	45.4	160.6	0.2799	aragonite	7.706671
33.567	3.35241	264.5	753.7	0.265	quartz	44.899
34.575	3.25751	65.3	186.2	0.415	feldspare (orthoclase)	11.08471
35.238	3.1981	35.9	102.2	0.49	feldspar (albite)	6.094042
37.21	3.03418	88.1	658.1	0.5651	calcite	14.95502
39.043	2.89686	39.8	206.7	0.4117	dolomite	6.756069
40.069	2.82562	14.4	74.8	0.3346	halite	2.444407
41.872	2.70909	35.7	101.7	0.2575	pyrite	6.060092
45.748	2.49039	27	132	0.4045	aragonite	
47.269	2.41463	10.4	51	0.379	aragonite	
47.932	2.38316	12.8	62.7	0.3534	feldspar (Albite)	
48.879	2.33973	13.6	66.6	0.3279	feldspar (Albite)	
50.11	2.28585	37.4	120	0.3023	feldspar (Albite)	
52.333	2.19514	12	48	0.3222	feldspar (Albite)	
54.067	2.12982	12	38.7	0.3	aragonite	
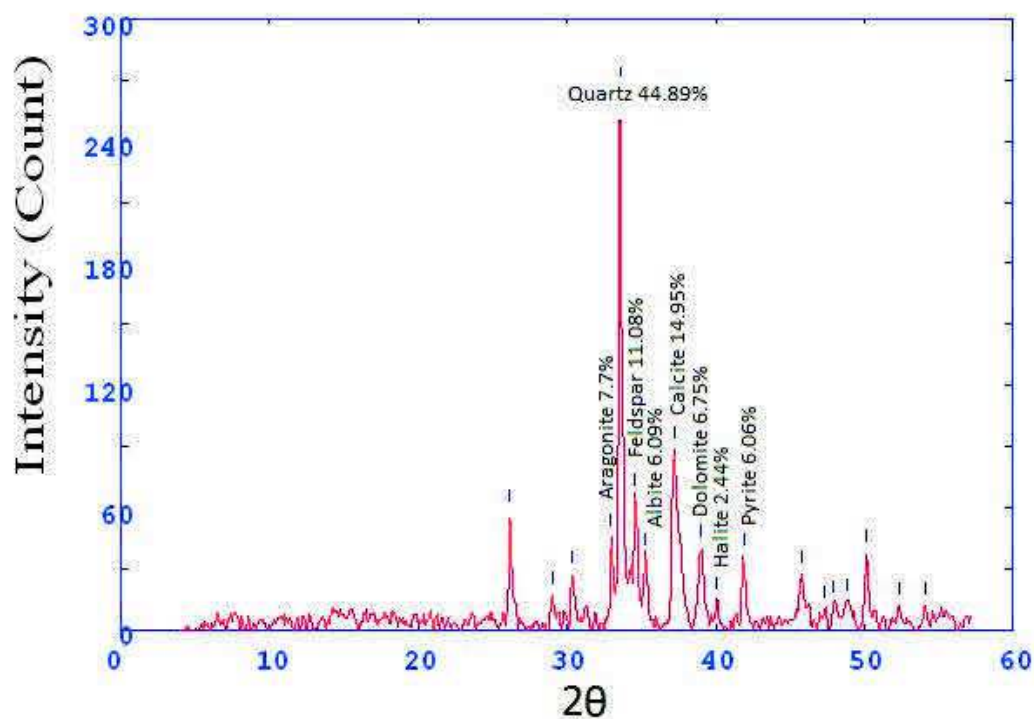
Core 11 sample 10

2Theta	d (A)	Height	Area	FWHM	Identified mineral	WT%
14.569	7.63443	15.3	40.3	0.2568	gypsum	2.32311
15.407	7.22146	11.7	30.8	0.2559	-	
17.058	6.52712	25.3	66.2	0.2549	-	0
22.473	4.96771	8	53.1	0.4604	-	
26.16	4.27743	84.7	249.3	0.2594	gypsum	
29.085	3.85519	13.1	38.5	0.2549	-	
30.32	3.7016	23.8	49.9	0.2505	-	
31.429	3.57404	9.7	20.3	0.2517	-	
32.895	3.41893	35.1	73.5	0.2522	Aragonite	5.329487
33.549	3.35414	218.4	605	0.2528	quartz	33.16125
34.653	3.25035	72.8	201.6	0.3132	feldspar (orthoclase)	5.633161
35.24	3.19796	37.1	102.8	0.3434	feldspar , Albite	5.633161
37.177	3.03676	103.7	497.7	0.3736	calcite	15.74552
38.953	2.90333	79.2	396.6	0.3926	feldspar (orthoclase)	
40.027	2.82849	62.5	312.9	0.3362	halite	9.489827
41.862	2.7097	29	109.6	0.2797	pyrite	4.40328
45.693	2.49319	23.4	88.3	0.2806	gypsum	
46.308	2.46186	41.9	134.2	0.2814	feldspar (orthoclase)	
48.084	2.37607	13.9	59.6	0.3432	pyrite	
48.624	2.35124	12.4	53.3	0.3252	gypsum	
50.167	2.2834	38.1	147.5	0.3071	calcite	
52.271	2.19758	20.2	85.8	0.4221	gypsum	
55.1	2.09292	13.4	120	0.6429	calcite	
57.905	1.99968	19.3	173.2	0.5592	feldspar (orthoclase)	
58.467	1.98216	23.9	145.2	0.4755	feldspar (orthoclase)	
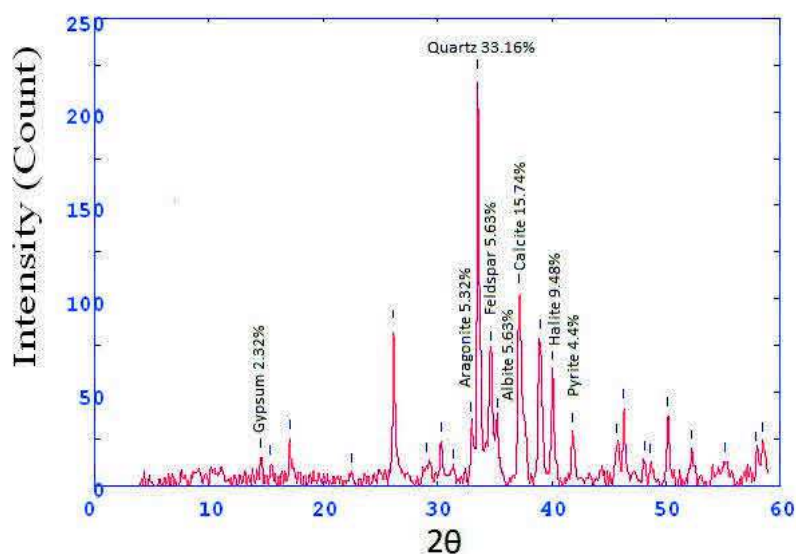
Core 11 sample 11

2Theta	d (A)	Height	Area	FWHM	Identified mineral	WT%
6.57	16.89327	17.1	96	0.4417	Montmorillonite	2.960014
15.768	7.05719	10.3	57.5	0.5417	gypsum	1.782932
23.664	4.72114	14	22.6	0.1632	-	
25.122	4.45102	11.9	19.2	0.205	-	0
26.161	4.27723	85.9	172.9	0.2467	gypsum	
29.054	3.85916	14.4	28.9	0.2544	calcite	
30.316	3.70204	23.5	68.1	0.2621	-	
32.986	3.40978	22	63.8	0.2519	Aragonite	3.808205
33.542	3.35481	265.6	727.6	0.2417	quartz	45.97542
35.17	3.2041	24.5	67.1	0.3417	feldspar (Albite)	4.240956
37.167	3.03756	98.2	482.6	0.4418	calcite	4.240956
39.01	2.89921	62.6	248.4	0.3787	dolomite	10.83607
39.975	2.83198	28.7	114	0.4163	halite	10.83607
41.835	2.71137	25.2	135.5	0.4538	pyrite	4.362126
45.71	2.49235	28.4	146.6	0.416	gypsum	
48.101	2.37529	16.1	83	0.4093	pyrite	
48.887	2.33937	16.1	83	0.4026	gypsum	
50.11	2.28585	31.2	149.1	0.3892	calcite	
52.25	2.19839	16.8	69.8	0.3453	gypsum	
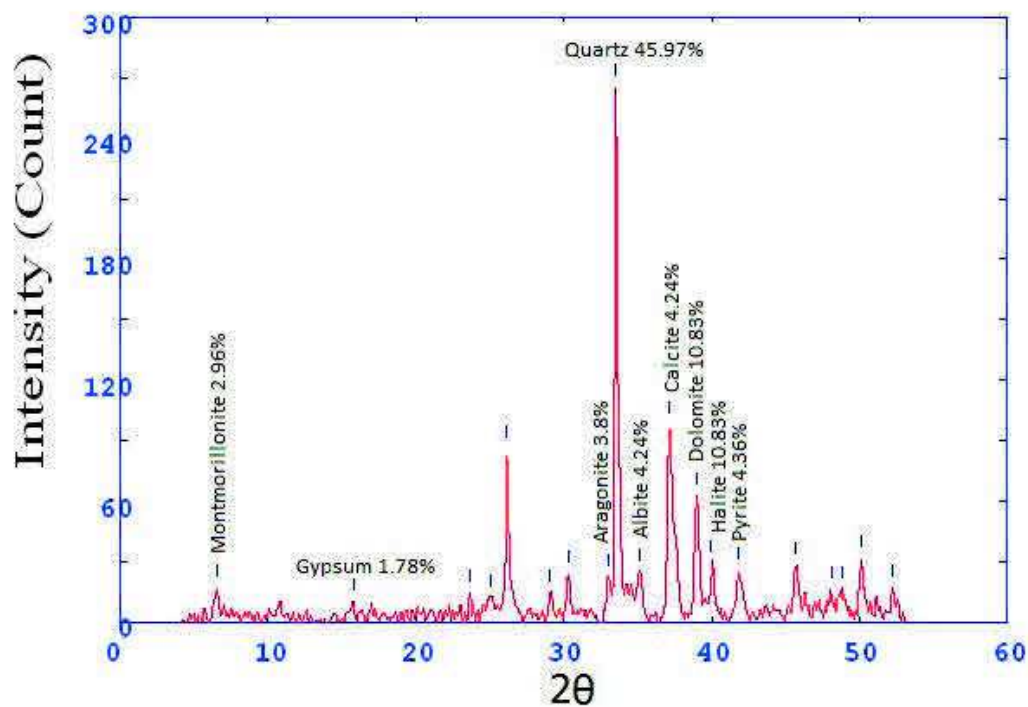
Core 11 sample 12

2Theta	d (A)	Height	Area	FWHM	Identified mineral	WT%
26.225	4.26691	74.8	157.4	0.259	-	
29.169	3.84427	9.1	19.2	0.2647	calcite	0
30.4	3.69211	29.2	84.8	0.2704	-	
31.241	3.5951	9.1	26.5	0.2668	-	
32.981	3.41029	23.2	67.4	0.2633	Aragonite	3.754653
33.611	3.34812	318.1	906.5	0.2561	Quartz	51.48082
34.638	3.25178	42.4	120.7	0.3253	feldspar (orthoclase)	6.861952
35.301	3.19261	11.2	31.8	0.36	feldspar (Albite)	1.812591
37.233	3.03231	109.1	544.6	0.3946	calcite	17.65658
39.101	2.89275	66.8	450	0.4976	Dolomite	10.81081
40.106	2.8231	23.2	156.5	0.4179	halite	3.754653
41.9	2.70737	23.9	99.4	0.3382	pyrite	3.86794
44.166	2.57484	6.1	25.5	0.3266	-	
45.741	2.49074	19.2	79.9	0.315	calcite	
46.35	2.45977	28.8	101	0.2918	-	
47.398	2.40842	8.1	28.5	0.3062	-	
48.061	2.37713	7.1	25	0.3134	pyrite	
48.889	2.33926	5.1	17.9	0.317	gypsum	
50.248	2.27995	30.9	137.8	0.3206	gypsum	
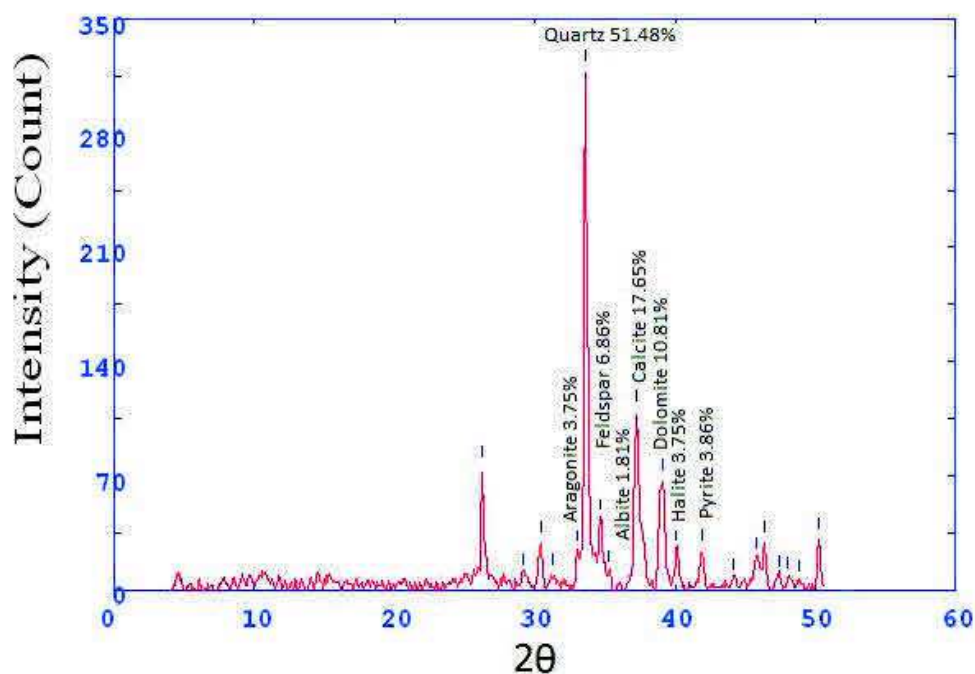
Core 12 sample 1

2Theta	d (A)	Height	Area	FWHM	Identified mineral	WT%
12.975	8.50772	40.1	1397	0.3309	Illite	6.78625825
14.434	7.67568	326.8	1397	0.3309	Gypsum	55.30546624
25.953	4.31094	63.8	328.6	0.412	Gypsum	
29.344	3.82189	80.3	242.9	0.2732	gypsum	
32.85	3.42345	34.9	105.7	0.2686	-	
33.472	3.33165	71.8	207.9	0.264	Quartz	12.15095617
34.307	3.28221	17.5	50.7	0.5412	feldspar	2.961584024
35.42	3.18217	9.3	26.9	0.6799	feldspar(Albite)	1.573870367
36.678	3.07663	66	727.3	0.8185	Gypsum	
37.134	3.03016	62.6	689.7	0.6471	Calcite	10.59400914
39.221	2.88423	27	159.7	0.4758	dolomite	4.569301066
39.789	2.84467	18.5	109.5	0.5747	dolomite	
42.085	2.69597	35.8	339.1	0.6736	pyrite	6.058554747

274
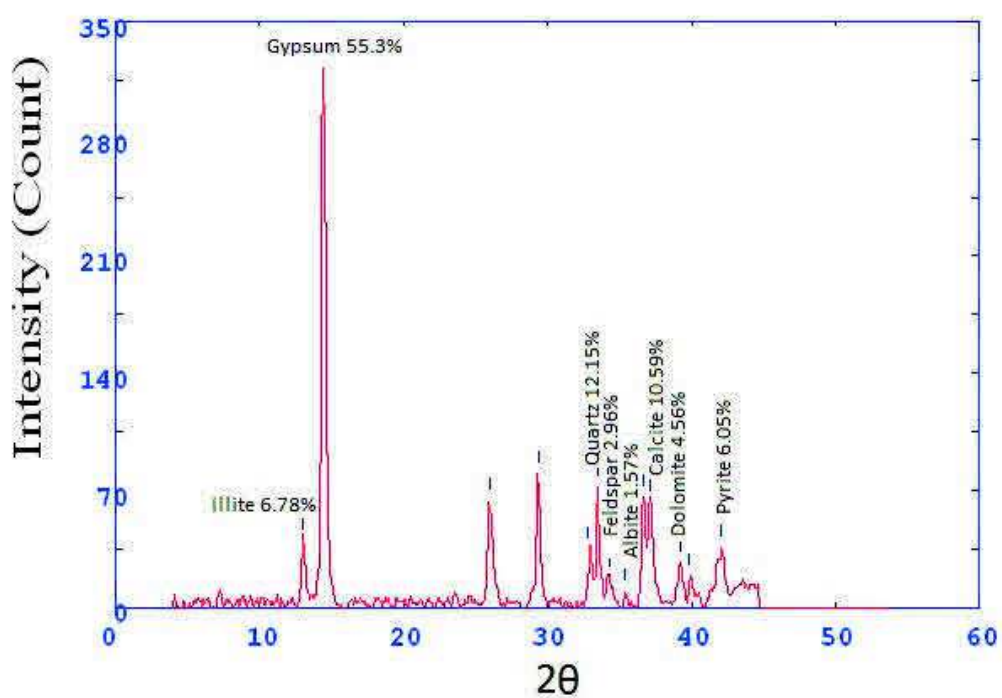
Core 12 sample 2

2Theta	d (A)	Height	Area	FWHM	Identified mineral	WT%
13.249	8.39123	41.4	1689.8	0.3565	Illite	6.461682535
14.633	7.601	331.7	1689.8	0.3565	Gypsum	51.77149992
26.156	4.278	75.1	304	0.3578	Gypsum	
29.53	3.79827	91.1	270.9	0.2799	Gypsum	
33.104	3.39795	75	359.2	0.3984	Aragonite	11.70594662
33.645	3.3448	50.7	242.9	0.3812	Quartz	7.913219916
34.48	3.26622	41.4	198.4	0.3726	feldspar	0.509789293
36.826	3.06465	66	264.3	0.364	Gypsum	
37.354	3.02288	35.2	140.9	0.3218	Calcite	5.493990947
39.414	2.87071	26.9	79.3	0.2796	dolomite	4.198532855
41.993	2.70163	38.4	294.6	0.6176	Pyrite	2.107070392
43.751	2.59808	13.5	103.6	0.5926	Quartz	
45.866	2.48429	33.3	262.5	0.5675	Aragonite	
48.108	2.37493	20.7	163.6	0.5059	Aragonite	
48.862	2.3405	26.4	140.4	0.4444	Aragonite	
51.724	2.21918	11.4	60.8	0.4041	Gypsum	
52.451	2.19058	13.5	75.2	0.3638	Gypsum	
54.733	2.10584	19.9	113.8	0.4712	Aragonite	
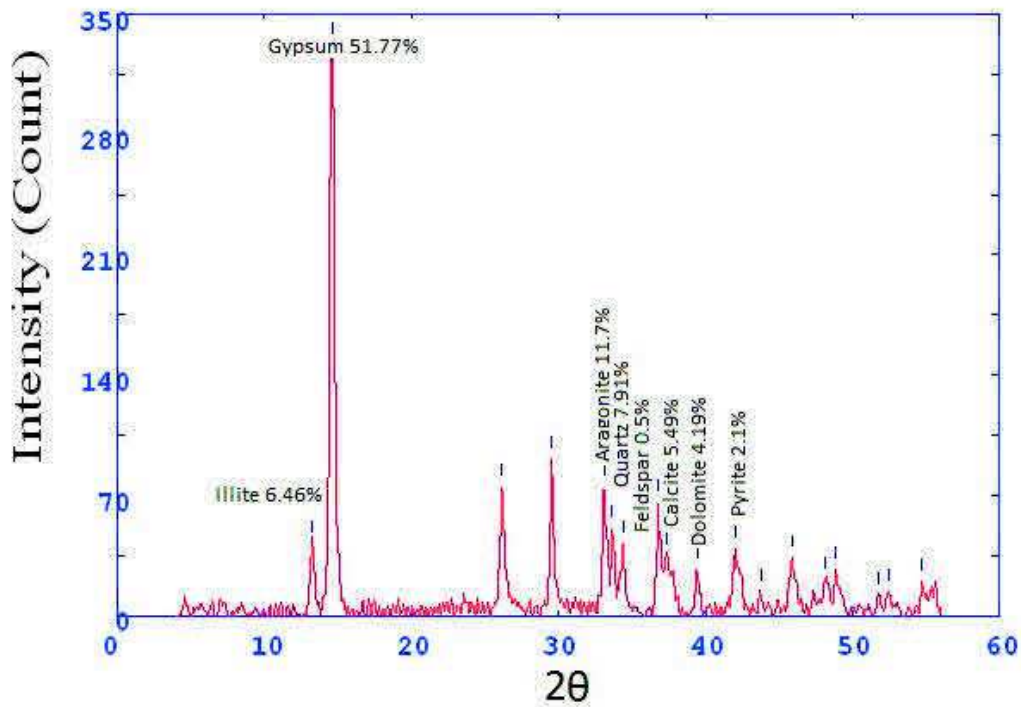
Core 12 sample 3

2Theta	d (A)	Height	Area	FWHM	Identified mineral	WT%
13.22	8.40944	32.3	1019.3	0.28	Illite	4.594594595
14.598	7.61946	326.4	1019.3	0.28	Gypsum	46.42958748
23.634	4.72692	13.1	53.5	0.3608	-	
26.146	4.27965	62.6	248.4	0.3395	Gypsum	
29.513	3.8004	55	205.6	0.2971	Gypsum	
33.045	3.40387	78	291.8	0.2839	Aragonite	11.09530583
33.699	3.33965	117.7	336.1	0.2707	Quartz	16.74253201
34.389	3.27462	44.8	127.8	0.2983	felspar (orthoclase)	6.372688478
36.829	3.06445	58	234	0.3259	Gypsum	
37.329	3.02484	27.1	109.3	0.3217	Calcite	3.854907539
39.394	2.8721	29.8	92.1	0.3175	dolomite	4.238975818
41.958	2.70379	46.9	311.4	0.5299	pyrite	6.67140825
42.369	2.67874	33.3	221.4	0.5348	Gypsum	
45.767	2.48941	30	194	0.5397	Quartz ,Aragonite	
48.142	2.37338	29.8	167.6	0.4552	Aragonite	
48.837	2.34162	26.1	0	0	anhydrite	
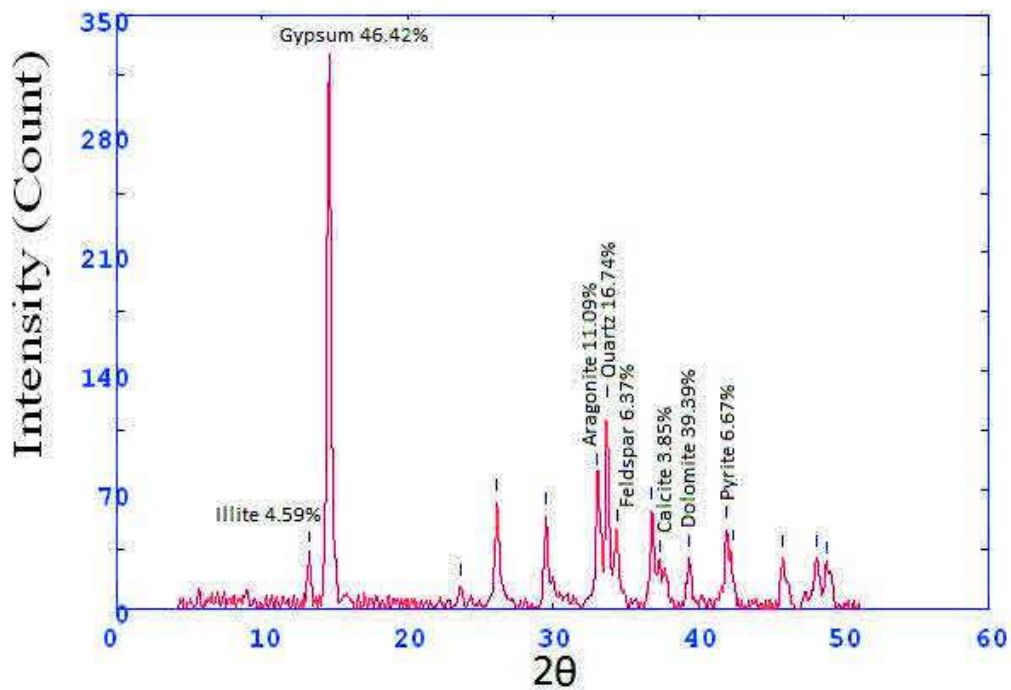
Core 12 sample 4

2Theta	d (A)	Height	Area	FWHM	Identified mineral	WT%
12.973	8.56908	16.3	37.6	0.273	Illite	2.788708298
15.662	7.14458	10.9	37.6	0.273	Gypsum	1.864841745
26.213	4.26888	68.2	182	0.2559	Gypsum	
27.72	4.04102	39	76.1	0.2294	-	
30.387	3.69362	36.7	113.5	0.2593	dolomite	
31.379	3.57967	12	37.1	0.2708	feldspar	
32.976	3.41079	26	80.5	0.2765	Aragonite	
33.603	3.34886	339.4	1126.7	0.2823	Quartz	58.0667237
34.572	3.25774	34.7	115	0.2814	feldspar (orthoclase)	5.936698033
35.329	3.19014	12	39.7	0.281	feldspar (Albite)	
37.212	3.03397	83.9	244.8	0.2806	calcite	14.35414885
39.086	2.89381	59.8	297.9	0.3958	dolomite	10.23096664
40.119	2.82222	17.4	86.5	0.3375	halite	2.976903336
41.88	2.70858	22.1	71.7	0.2791	pyrite	3.78100941
43.986	2.58491	9.8	31.8	0.344	feldspar (orthoclase)	
45.7	2.49284	20	104	0.4088	Quartz	
47.179	2.41894	9.8	51	0.296	Aragonite	
48.026	2.37876	12.7	20	0.1832	pyrite	
50.157	2.28382	31.4	98.6	0.2687	Quartz	

277
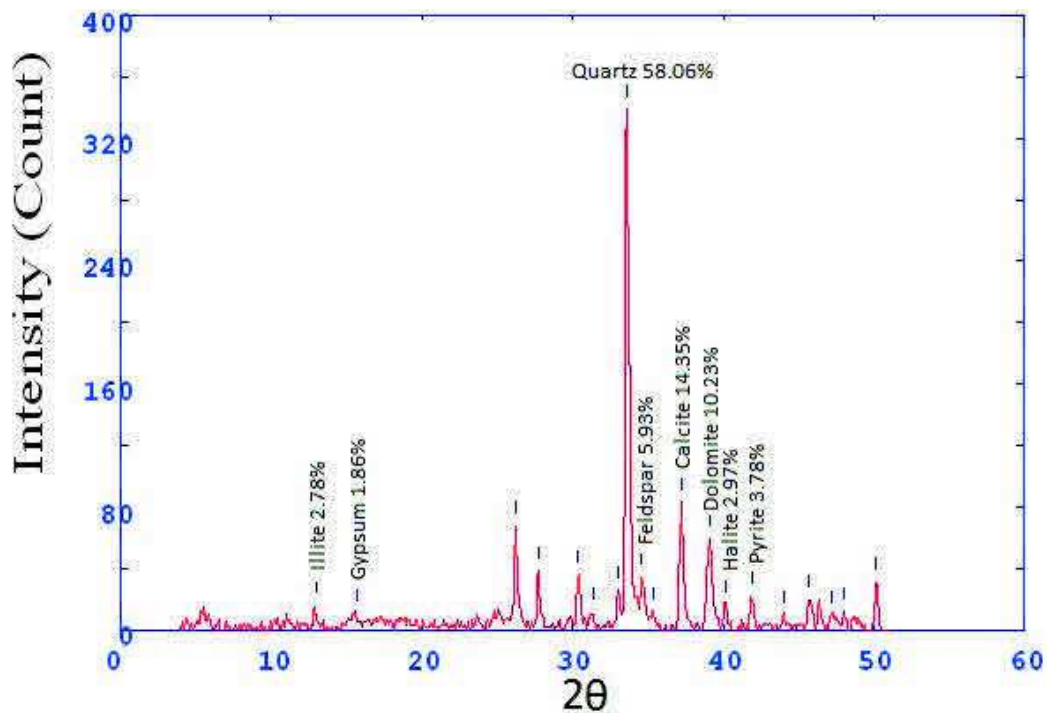
Core 12 sample 5

2Theta	d (A)	Height	Area	FWHM	Identified mineral	WT%
13.223	8.40755	77.2	1993	0.4373	Illite	10.49055578
14.7	7.56674	348.8	1993	0.4373	gypsum	47.39774426
23.675	4.71894	11.9	30	0.291	-	
26.158	4.27775	87.4	358.4	0.3694	gypsum	
26.746	4.18531	19.4	79.4	0.3169	Geothite	2.636227748
29.534	3.79782	163.3	473.3	0.2645	gypsum	
33.08	3.40036	51.5	149.2	0.2733	anhydrite	
33.681	3.34138	56.7	160.1	0.2821	Quartz	7.704851203
34.363	3.27694	25.8	72.8	0.3164	feldspar (orthoclase)	3.505911129
35.476	3.17732	8.7	24.4	0.3336	feldspar (Albite)	
36.869	3.06122	102.4	401.8	0.3507	calcite	13.91493409
37.445	3.01581	47.2	185.3	0.3975	Calcite	
39.4	2.87163	36.6	212.7	0.4442	feldspar (orthoclase)	4.973501834
40.269	2.81216	15.1	87.7	0.5333	halite	2.051909227
42.262	2.68521	39	306.7	0.6223	pyrite	5.299633102
43.778	2.59654	5.4	42.8	0.5143	gypsum	
45.867	2.48427	27	140	0.4063	anhydrite	
47.373	2.40962	6.5	33.8	0.3732	Gypsum	
48.138	2.37354	20	84	0.34	pyrite	
48.914	2.33817	10.8	45.3	0.3467	gypsum	
51.8	2.21615	14	60	0.3533	gypsum	
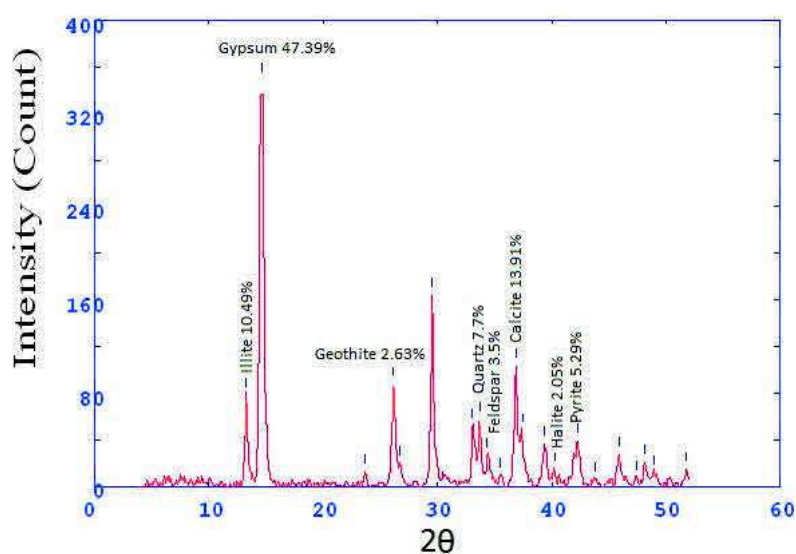
Core 12 sample 6

2Theta	d (A)	Height	Area	FWHM	Identified mineral	WT%
14.572	7.63263	49.6	96.1	0.2098	Gypsum	9.53479431
26.211	4.26917	40.2	113.7	0.257	gypsum	0
28.471	3.9365	5.3	15.1	0.3687	-	
29.216	3.83826	11.2	31.7	0.4245	gypsum	
29.766	3.76882	20	127.1	0.4804	Gypsum	
30.374	3.69514	16	101.3	0.3646	dolomite	
33.022	3.40615	89.2	566.3	0.3068	Aragonite	17.14725106
33.582	3.35088	168.8	361.8	0.2489	Quartz	32.44905805
34.263	3.28627	46.2	99	0.4042	feldspar (orthoclase)	8.881199539
35.173	3.20382	4.8	10.3	0.4819	feldspar (Albite)	
37.151	3.03878	34.8	243.1	0.5596	calcite	6.689734717
39.062	2.89553	37.7	263.6	0.4389	dolomite	7.247212611
40.086	2.82448	40	157.2	0.3181	halite	7.247212611
41.9	2.70735	53.9	177.3	0.3157	pyrite	10.36139946
43.613	2.60592	5.9	19.4	0.3504	-	
45.796	2.48788	37	160	0.3852	gypsum	
46.26	2.46428	16.5	71.3	0.3651	Aragonite	
47.336	2.4114	18.6	80.5	0.3451	Aragonite	
48.033	2.37841	37	145.3	0.3049	pyrite	
48.825	2.34215	25	0	0	gypsum	
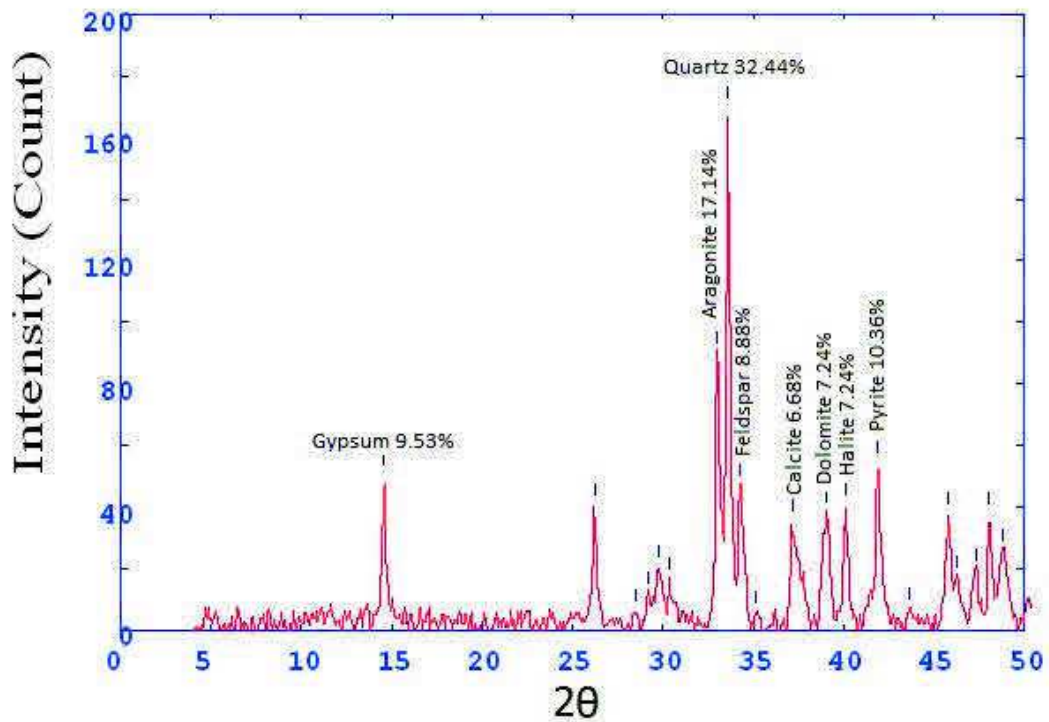
Core 12 sample 7

2Theta	d (A)	Height	Area	FWHM	Identified mineral	WT%
26.233	4.26562	36.5	108	0.2689	gypsum	0
30.393	3.69288	37	104.8	0.2492	dolomite	
33.014	3.40694	57.4	162.8	0.2472	Aragonite	
33.6	3.34922	346.3	1019.9	0.2453	Quartz	62.75824574
34.364	3.27686	27.7	81.4	0.5125	feldspar (orthoclase)	5.019934759
35.293	3.19329	11.1	32.7	0.6462	feldspar (Albite)	2.011598405
37.269	3.02949	68.5	759.2	0.7798	calcite	12.41391809
39.006	2.89948	27.7	306.7	0.5521	dolomite	5.019934759
40.188	2.8176	15.5	172.2	0.4382	halite	2.808988764
41.93	2.70551	55	207.8	0.3243	pyrite	9.967379485
45.793	2.48803	34.7	257.6	0.5446	gypsum	
47.278	2.41419	15.5	115.2	0.4879	Aragonite	
48.05	2.37764	24.7	136.1	0.4313	pyrite	
48.797	2.34341	21	115.8	0.2156	Aragonite	
50.316	2.27706	15.5	0	0	Gypsum	
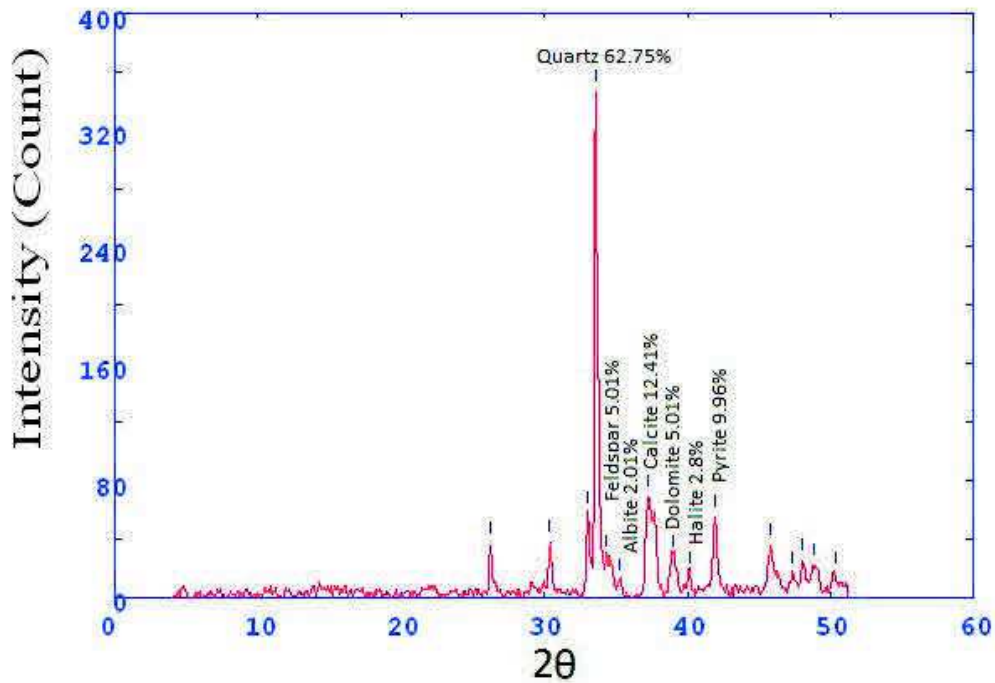
Core 12 sample 8

2Theta	d (A)	Height	Area	FWHM	Identified mineral	WT%
23.767	4.70096	15.4	30.7	0.189	-	
26.236	4.26528	95.3	205.3	0.2405	Gypsum	0
29.135	3.84865	10.5	22.6	0.2464	-	
30.4	3.69209	78.9	219.2	0.2523	dolomite	
32.892	3.41921	36.5	101.4	0.2985	Aragonite	5.916680175
33.567	3.35241	347	1471.6	0.3447	Quartz	56.24898687
34.689	3.24714	38.5	163.5	0.3662	feldspar(orthoclase)	6.240881828
35.261	3.19612	31.3	132.6	0.377	feldspar (Albite)	5.073755876
37.242	3.0316	94.5	424.6	0.3878	calcite	15.31852812
39.11	2.89208	21.7	128.1	0.4701	dolomite	3.51758794
40.079	2.82494	17.8	104.7	0.3671	halite	2.885394716
41.913	2.70657	29.6	89.4	0.2641	pyrite	4.798184471
45.633	2.49631	24	72.5	0.3654	Aragonite	
46.333	2.46061	28	142.3	0.4667	Aragonite	
48.852	2.34092	16.2	126.7	0.5917	gypsum	
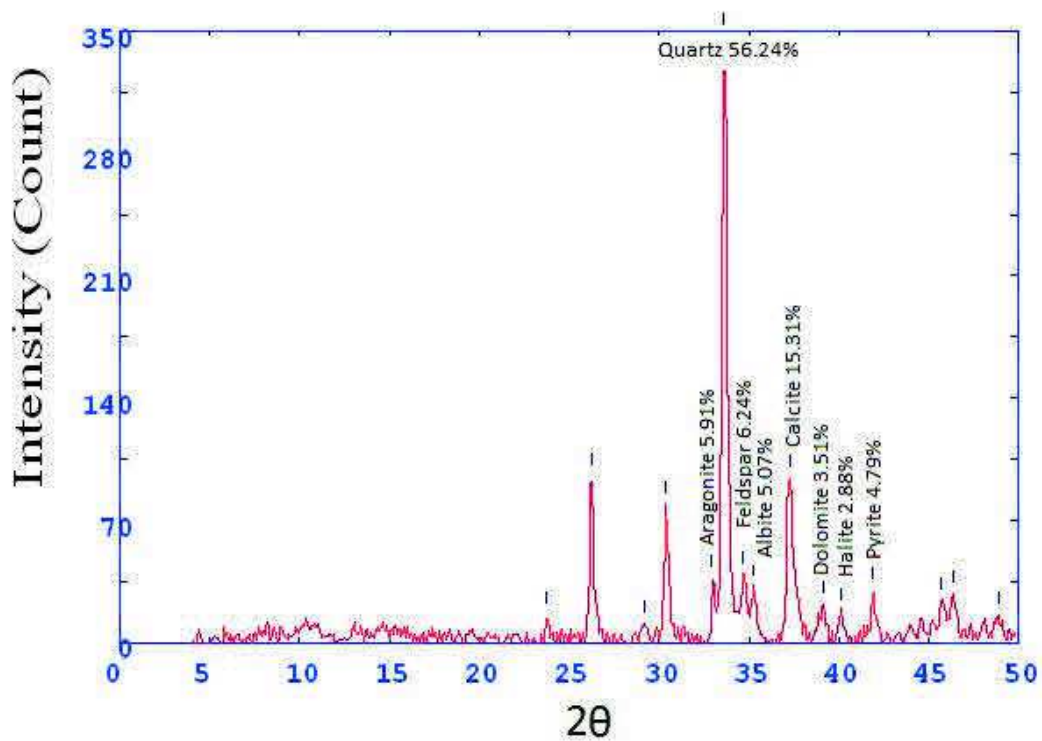
Core 12 sample 9

2Theta	d (A)	Height	Area	FWHM	Identified mineral	WT%
26.273	4.25936	124.3	335.1	0.2414	gypsum	0
29.103	3.85288	9	24.2	0.2596	-	
30.433	3.68813	32.2	103.4	0.2778	dolomite	
31.328	3.58537	7	22.5	0.2766	-	
33.089	3.39942	33.7	108.2	0.2753	Aragonite	
33.64	3.34533	318.5	947	0.2728	Quartz	48.52224254
34.758	3.24088	119.9	356.4	0.3201	feldspar(orthoclase)	18.26630104
35.314	3.19142	24.8	73.8	0.3438	feldspar	3.778184034
37.271	3.02933	122.4	615.8	0.3674	calcite	18.64716636
39.034	2.89748	28.3	196.2	0.4591	dolomite	4.311395491
40.228	2.81493	13	89.6	0.4009	halite	1.980499695
41.954	2.70403	29.5	130.4	0.3427	pyrite	4.494210847
45.698	2.49295	23.8	105.5	0.3124	Aragonite	
46.399	2.45731	26.4	105.7	0.2821	dolomite	
47.367	2.40992	10	40	0.3052	-	
48.108	2.37493	11	43.9	0.3167	pyrite	
48.85	2.34103	12	47.9	0.3224	gypsum	
50.267	2.27914	34.9	157.9	0.3282	pyrite	
51.261	2.23788	11	49.6	0.3824	pyrite	
52.373	2.19359	10	45.2	0.4094	gypsum	
54.166	2.1262	27.2	181.4	0.4365	Aragonite	
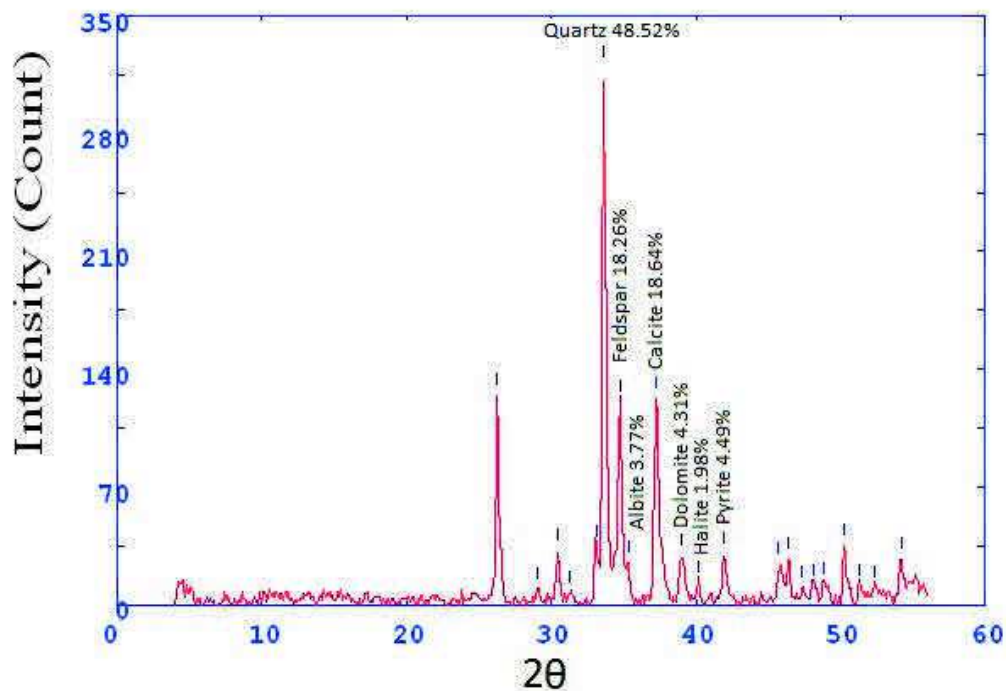
Core 12 sample 10

2Theta	d (A)	Height	Area	FWHM	Identified mineral	WT%
23.8	4.69453	13.1	21.7	0.2221	-	
26.252	4.26269	111.7	252.5	0.2582	gypsum	0
30.426	3.689	45.3	137.8	0.2576	dolomite	
33.029	3.40546	30.9	94	0.2794	Aragonite	4.556850022
33.633	3.34596	359.2	1390.3	0.3011	Quartz	52.97153812
34.743	3.24225	37.5	145	0.3237	feldspar (orthoclase)	5.530157794
35.333	3.18975	91	369.5	0.3464	feldspar (Albite)	13.41984958
37.259	3.03033	68.5	360.7	0.3821	calcite	10.1017549
39.034	2.89751	37.2	238.1	0.471	dolomite	5.485916531
40.066	2.82585	14.4	92	0.4066	halite	2.123580593
41.951	2.70423	22.8	104.2	0.3422	pyrite	3.362335939
45.749	2.49029	16.6	75.9	0.308	Aragonite	3.362335939
46.381	2.45822	48.3	151.6	0.2738	Aragonite	
47.193	2.41828	8.9	27.9	0.2837	gypsum	
48.005	2.37974	10	31.3	0.2887	gypsum	
50.176	2.283	34.8	134.2	0.2937	Aragonite	
51.253	2.23819	6.7	25.8	0.2965	pyrite	
54.109	2.12826	28.4	94.5	0.2993	Aragonite	
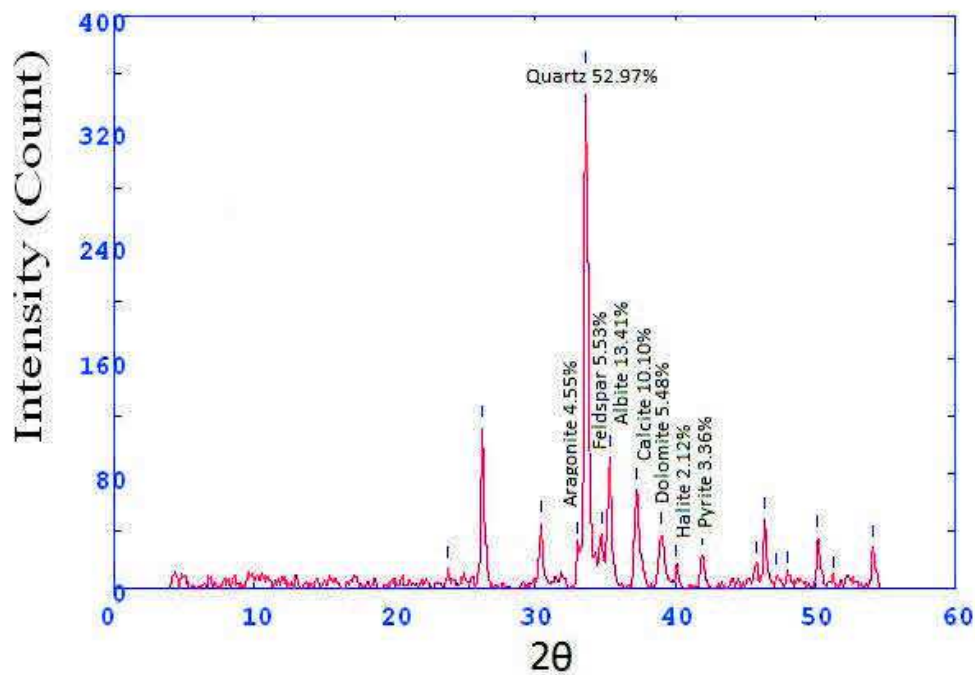
Core 12 sample 11

2Theta	d (A)	Height	Area	FWHM	Identified mineral	WT%
13.099	8.48713	92.9	1562.9	0.3663	Illite	13.18852924
14.504	7.66869	324.1	1562.9	0.3663	Gypsum	46.01078932
25.992	4.26456	39.4	147.3	0.3496	gypsum	
29.378	3.81753	78.9	170.4	0.2584	gypsum	
32.814	3.42716	47.5	102.6	0.2562	aragonite	11.20102215
33.548	3.34424	89.7	258	0.2539	Quartz	12.73424191
34.21	3.29119	24.8	71.4	0.3554	feldspar (orthoclase)	3.52072686
36.592	3.08356	34.1	98.1	0.4061	gypsum	
37.198	3.03507	62.3	307.4	0.4569	calcite	4.840999432
39.25	2.88219	20.7	224.3	0.78	dolomite	2.93867121
39.878	2.83859	12.5	135.1	0.7039	Halite	1.774559909
41.875	2.70886	29.9	251.9	0.6278	pyrite	4.244747303
45.687	2.49353	28.5	121.3	0.3778	gypsum	
47.107	2.42244	14.5	61.9	0.3944	Aragonite	
48.075	2.37647	20.1	94	0.4111	Aragonite	
48.75	2.34554	15.5	0	0	Aragonite	
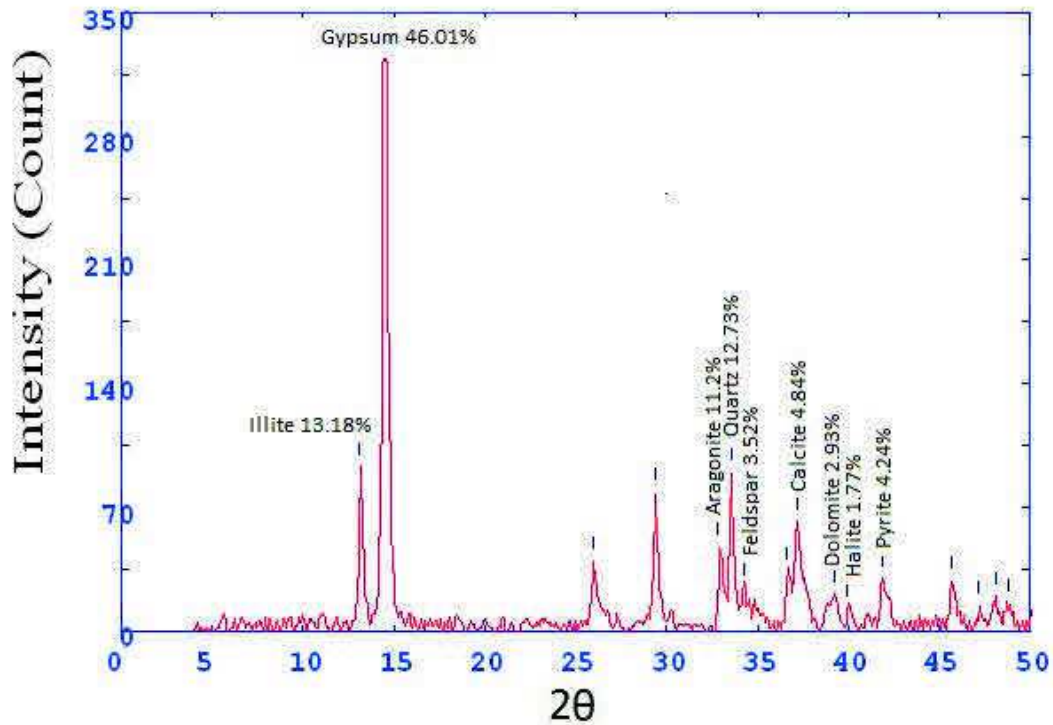
Core 12 sample 12

2Theta	d (A)	Height	Area	FWHM	Identified mineral	WT%
13.115	8.47674	56.2	1615	0.376	Illite	8.27565896
14.567	7.63559	347.8	1615	0.376	gypsum	51.21484317
24.922	4.48631	7.6	35.5	0.3659	-	
26.025	4.29922	68.6	280.9	0.3558	gypsum	
29.42	3.8122	120.6	337.9	0.2577	gypsum	
32.937	3.41472	58.4	163.6	0.2587	aragonite	8.59961714
33.587	3.35048	71.4	200.9	0.2597	Quartz	10.51391548
34.229	3.2894	32.5	91.5	0.2879	feldspar (orthoclase	4.78574584
36.752	3.07062	82.9	254.8	0.3161	gypsum	
37.16	3.03812	45.4	139.7	0.3377	calcite	6.685318804
39.291	2.87933	33.5	142.1	0.3592	dolomite	4.932999558
41.913	2.70654	33.9	332.4	0.6817	pyrite	4.991901046
45.767	2.48941	30.4	177.6	0.4676	gypsum	
47.243	2.41587	8.7	51	0.4096	aragonite	
48.024	2.37886	22.9	100.9	0.3517	aragonite	
48.794	2.34355	19.5	0	0	Aragonite	
51.724	2.21917	8.7	0	0	pyrite	
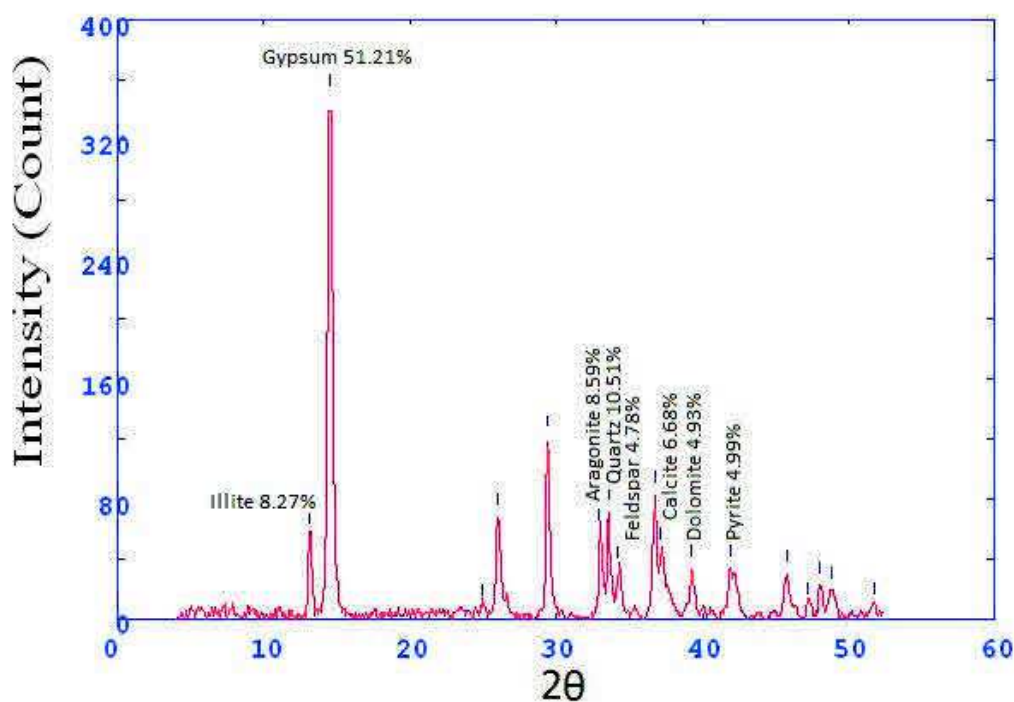
Core 12 sample 13

2Theta	d (A)	Height	Area	FWHM	Identified mineral	WT%
13.078	8.50054	7.4	167	0.2466	Illite	0.980781975
14.516	7.66224	78.7	167	0.2466	gypsum	10.43074884
15.352	7.24701	10.8	22.9	0.2456	-	
24.976	4.47667	9.4	20.1	0.2451	-	
26.196	4.27166	48.8	99.4	0.2446	gypsum	
29.088	3.85475	14.1	28.8	0.2321	-	
29.438	3.80992	14.1	28.8	0.2258	-	
30.316	3.70203	17.8	36	0.2195	-	
32.15	3.49596	14.8	30	0.2366	anhydrite	1.96156395
32.938	3.41462	28.2	57.2	0.2452	Aragonite	3.737574553
33.543	3.35475	211.7	597.2	0.2537	quartz	28.05831677
34.25	3.28748	20.2	56.9	0.239	feldspar (orthoclase)	2.677269715
35.268	3.19543	168.1	341.5	0.2244	feldspar (Albite)	22.2796554
37.197	3.03514	124	577.2	0.344	calcite	16.43472498
38.99	2.90066	53.6	382.3	0.5219	dolomite	7.104042412
39.937	2.83461	20.2	144.1	0.4376	halite	2.677269715
41.249	2.74817	7.4	53.1	0.3954		
41.846	2.71067	27.6	111.9	0.3533	pyrite	3.65805169
45.767	2.48941	26.5	139.6	0.4239	Aragonite	
46.411	2.45673	16.2	85	0.3322		
47.286	2.41381	7.4	39.1	0.2864	Aragonite	
47.995	2.38019	15.9	34.1	0.2406	Aragonite	
48.773	2.3445	8.8	18.8	0.2913	Aragonite	
50.2	2.28199	29.9	120	0.342	feldspar	
51.135	2.24299	12.1	0	0	pyrite	
52.272	2.19751	8.8	0	0	dolomite	

286
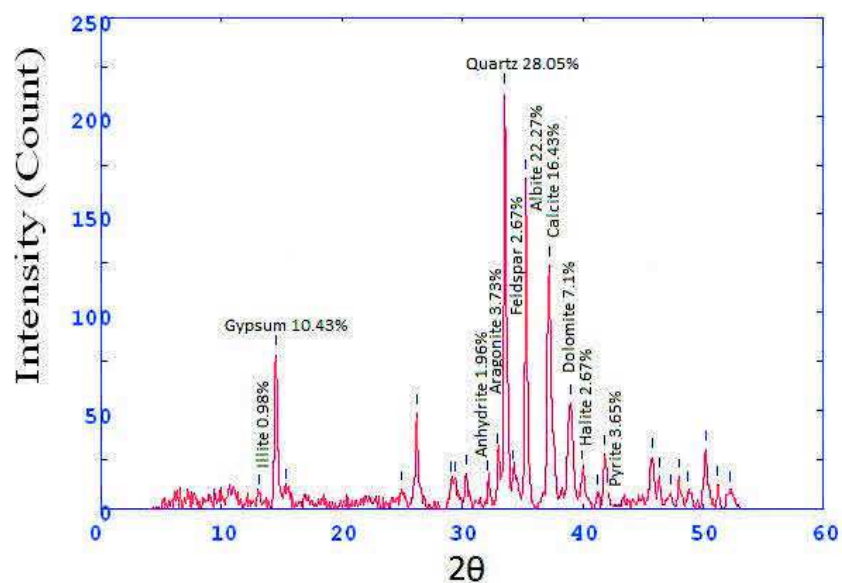
Core 12 sample 14

2Theta	d (A)	Height	Area	FWHM	Identified mineral	WT%
15.202	7.31808	10.6	126.1	0.9042	gypsum	2.703391992
17.34	6.42162	8.1	24.9	0.2794	-	
19.545	5.70319	6.7	22.4	0.3362	-	
22.4	4.9837	6.4	21.8	0.2377	-	
25.083	4.45783	5	17	0.2315	-	
26.261	4.26125	35	70.6	0.2254	gypsum	8.926294313
29.193	3.84117	21.9	111.1	0.4063	-	
33.064	3.4019	49.7	252	0.3292	Aragonite	
33.67	3.34243	120.6	339.5	0.2521	quartz	30.75745983
34.394	3.27409	32.8	92.2	0.3939	feldspar (orthoclase)	8.365212956
37.304	3.02679	174.6	1102	0.5358	calcite	44.52945677
39.271	2.88068	14.2	89.8	0.4252	dolomite	3.621525121
40.158	2.81961	10.9	69.1	0.3698	Halite	2.779903086
41.968	2.70318	28.4	91.2	0.3145	pyrite	7.243050242
45.81	2.48719	44.6	214	0.4	anhydrite ,gypsum	
48.1	2.37532	19.7	91.1	0.3626	pyrite	
48.848	2.3411	15.9	73.4	0.4224	feldspar	
50.233	2.28058	34.9	191.9	0.4822	-	
52.5	2.18866	9.5	85.6	0.6277	gypsum	
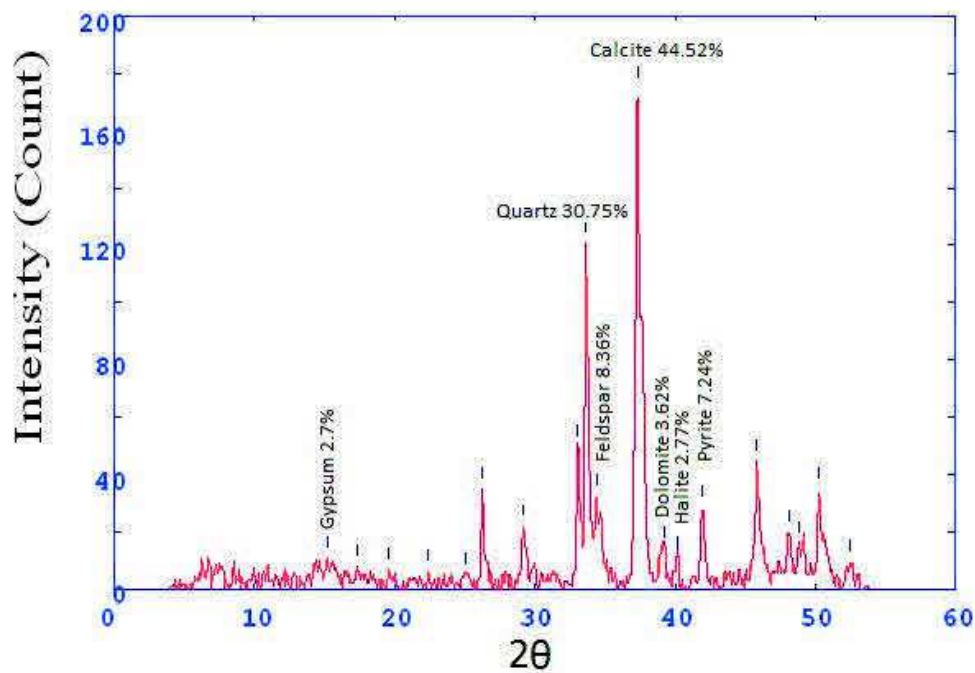
Core 12 sample 15

2Theta	d (A)	Height	Area	FWHM	Identified mineral	WT%
29.25	3.83387	12.1	58.5	0.4441	-	0
32.967	3.41169	68.3	261.1	0.3236	Aragonite	13.36333399
33.533	3.35572	19.3	73.6	0.3487	Quartz	3.776169047
34.259	3.28661	40.8	184.3	0.3738	feldspar (orthoclase)	56.56427314
37.557	3.0371	289.1	897.2	0.7315	calcite	56.56427314
39.934	2.83477	9	37.5	0.334	dolomite	1.760907846
41.844	2.71082	39.9	160.2	0.3362	pyrite	7.80669145
45.7	2.49285	34.4	185.4	0.464	dolomite	6.7305811
47.203	2.41778	10.3	55.6	0.4143	anhydrite, gypsum	2.015261201
47.953	2.38214	23.8	107.5	0.3647	anhydrite	
48.85	2.34101	24	215.3	0.5968	pyrite	
50.734	2.25954	15.7	117.5	0.5868	Quartz	
52.533	2.18736	10.3	90.5	0.6469	Aragonite	
54.578	2.11138	19.8	97.1	0.3789	Aragonite	
55.644	2.07405	19.8	96.5	0.4105	gypsum	
56.638	2.0406	7.5	96.5	0.4105	dolomite	
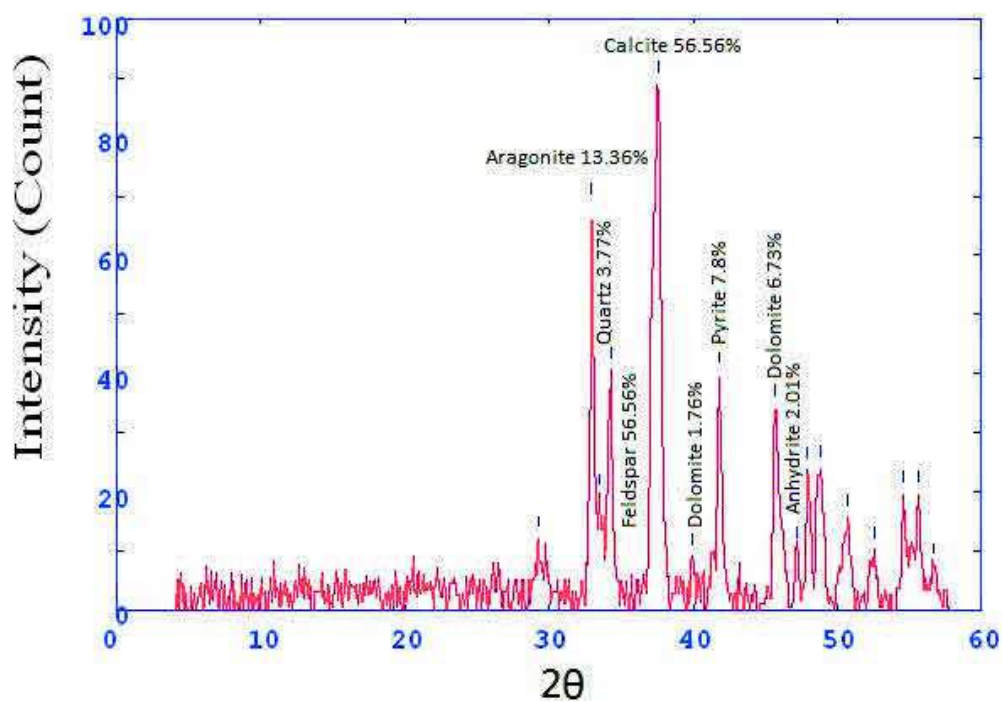
Core 12 sample 16

2Theta	d (A)	Height	Area	FWHM	Identified mineral	WT%
29.46	3.8072	12.1	165.4	0.9856	-	0
33.038	3.40448	79.2	321.7	0.334	anhydrite	13.67454068
33.609	3.34832	52.1	211.7	0.4703	Quartz	13.67454068
34.332	3.27989	48.8	198	0.5384	feldspar (orthoclase)	12.80839895
37.652	3.01981	106.8	815.4	0.6066	calcite	28.03149606
39.21	2.88503	6.8	51.9	0.4611	dolomite	1.784776903
40.113	2.82264	11.9	90.7	0.3883	halite	3.12335958
41.916	2.70639	44.9	171.6	0.3155	magnesite, pyrite	11.7847769
45.785	2.48844	39.1	216.8	0.4512	Gypsum ,anhydrite	
47.34	2.41119	14.2	78.9	0.2768	gypsum	
48.063	2.37704	30.5	168.8	0.1896	pyrite	8.005249344
48.966	2.33582	25.1	138.9	0.146	anhydrite	
50.773	2.25792	16.9	93.9	0.1242	-	
52.309	2.1961	11.9	65.8	0.1133	calcite	
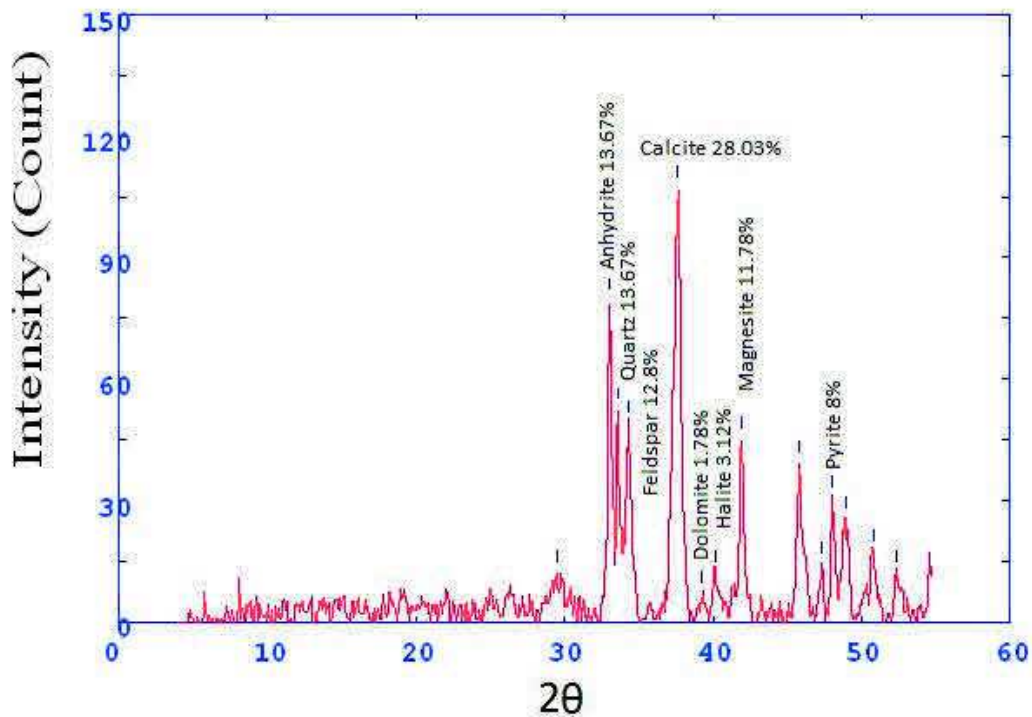
Appendix C: Magnetic susceptibility

Core 1

Depth	Vol. Susc.Meas. in SI
0	35.4155
3	11.3483
6	23.641
9	20.1087
12	21.6678
15	24.4225
18	31.8463
21	28.7108
24	39.7948
27	24.6836
30	22.1004
33	22.1494
36	14.9985
39	13.6771
42	15.7388
45	19.0997
48	7.8488
51	6.3095
54	6.9722
57	14.2959
60	12.3582
63	10.4322
66	11.1242
69	10.6708
72	7.3906
75	14.8381
78	15.666
79	19.9129
82	15.2814
85	21.938
88	17.9912
91	33.2277
94	34.6385
97	36.7415
100	23.6056

Depth	Vol. Susc.Meas. in SI
103	22.9492
106	26.297
109	24.3946
112	23.0851
115	21.1587
116	19.8831
119	16.6158
122	-0.2544
125	6.4037
128	2.5294
131	-1.012
134	-2.3887
137	4.5362
140	20.0711
143	14.5469
146	12.2113
149	11.2123
152	11.3882
155	4.3788
158	20.4468
161	15.972
164	17.5315
167	28.3179
170	12.7604
173	-1.9501
176	0.2273
179	2.0637
182	-0.154
185	2.0596
188	0.917
191	2.4237
194	2.6311
197	6.2455
200	6.3223
203	11.9958

Core 2

Depth	Vol. Susc.Meas. in SI
0	92.2302
3	67.1963
6	67.0557
9	55.7491
12	50.0336
15	35.099
18	15.9848
21	20.3065
24	16.6071
27	11.0456
30	8.048
33	-10.0757
36	-14.9402
39	-23.1475
42	-29.6635
45	-30.489
48	-37.904
51	-39.3286
54	-45.4036
57	-45.1256
60	-52.6906
63	-53.0035
66	-60.471
69	-62.4826
72	-69.5653
75	-70.2672
78	-72.6202
81	-77.4703
84	-79.106
87	-81.4544
90	-84.6462

Core 3

Depth	Vol. Susc.Meas. in SI
0	85.9857
3	75.5464
6	36.3631
9	23.2384
12	22.6146
15	30.1171
18	18.5069
21	18.2813
24	14.1284
27	-17.5925
30	-3.3278
33	-15.0232
36	-25.7192
39	-35.4227
42	-34.3966
45	-40.3256
48	-42.7304
51	-51.5343
54	-49.1112
57	-59.0917
60	-56.8445
63	-82.4599
66	-90.0676
69	-83.5387
72	-87.3392
75	-83.7164
78	-88.5352
81	-88.9396
84	-85.1567

Depth	Vol. Susc.Meas. in SI
87	-85.9368
90	-12.1363
93	46.7013
96	28.3342
99	7.4624
102	-2.211
105	-3.4
108	-16.0372
111	-24.7054
114	-36.0761
117	-43.5013
120	-48.5289
123	-56.7459
126	-62.4998
129	-68.9174
132	-75.5347
135	-70.1256
138	-75.5899

Core 4

Depth	Vol. Susc.Meas. in SI
0	-2.2561
3	79.7528
6	60.717
9	44.5113
12	24.2831
15	13.1494
18	9.2257
21	9.3364
24	4.6543
27	-6.5979
30	-5.575
33	-16.6638
36	-22.7062
39	-25.516
42	-28.661
45	-33.7841
48	-36.9286
51	-44.6097
54	-44.1871
57	-51.9217
60	-55.3367
63	-55.4225
66	-60.2962
69	-63.9697
72	-67.4114
75	-69.4325
78	-72.2006
81	-75.8761
84	-75.5347

Depth	Vol. Susc.Meas. in SI
87	-78.8795
90	-80.8901
93	-82.6987
96	-5.342
99	5.8328
102	5.6805
105	0.1617
108	-6.6066
111	-9.7014
114	-15.9105
117	-20.7532
120	-25.7659
123	-28.73
126	-31.6142
129	-34.4045
132	-38.645
135	-44.1456

Core 5

Depth	Vol. Susc.Meas. in SI
0	-3.3961
3	62.2456
6	42.7024
9	24.7743
12	25.9736
15	12.3827
18	2.3664
21	14.6625
24	0.2578
27	-20.2119
30	-29.2988
33	-26.236
36	-37.5376
39	-42.4224
42	-48.336
45	-52.1048
48	-56.6488
51	-58.8643
54	-62.2233
57	-65.5494
60	-72.5494
63	-75.5494
66	-78.5494
69	-79.5494
72	-82.5494

Core 6

Depth	Vol. Susc.Meas. in SI	Depth	Vol. Susc.Meas. in SI
0	-1.4697	87	68.8786
3	88.8901	90	52.5527
6	42.5665	93	46.816
9	31.5113	96	35.3
12	23.7315	99	38.9507
15	12.5651	102	21.7902
18	5.1015	105	21.0017
21	1.2129	108	15.2076
24	-5.055	111	0.7905
27	-9.1456	114	-3.5678
30	-16.3604	117	-6.6612
33	-18.0722	120	-28.7369
36	-22.5184	123	-35.0991
39	-29.6594	126	-40.1178
42	-33.3271	129	-42.5006
45	-35.2683	132	-46.2134
48	-40.8762	135	-47.6274
51	-42.6926	138	-51.9132
54	-44.8941	141	-53.9644
57	-48.723	144	-56.3652
60	-54.1562	147	-56.3659
63	-57.9524	150	-60.7989
66	-60.498		
69	-60.5087		
72	-65.0771		
75	-7.80E-07		
78	89.4348		
81	80.3898		
84	79.8988		

Core 7

Depth	Vol. Susc.Meas. in SI
0	-13.9242
3	30.0915
6	-9.5663
9	-50.0234
12	-43.0783
15	-37.411
18	3.2867
21	-3.6468
24	-22.1259
27	-14.028
30	-18.2489
33	-17.4961
36	-18.7869
39	-2.3085
42	-1.0119
45	-4.3411
48	9.4708
51	3.6257
54	-3.8509
57	-11.3163
60	-9.5668
63	-23.02
66	-28.4199
69	-30.5984
72	-34.3658
75	-34.3689
78	-2.8301
81	19.4428
84	23.4487

Depth	Vol. Susc.Meas. in SI
87	7.633
90	-25.0462
93	-18.3156
96	-15.5569
99	-35.7075
102	-63.9648
105	-77.2899
108	-85.2653
111	-85.2345
114	-91.2563
117	-93.1243
120	-99.3532
123	-102.3418
126	-105.6144
129	-108.0053
132	-112.6707
135	-115.9342

Core 8

Depth	Vol. Susc.Meas. in SI
0	38.9722
3	-14.9331
6	-9.6561
9	-3.7305
12	-13.0035
15	8.8196
18	20.7144
21	17.3769
24	21.3316
27	17.9929
30	10.7373
33	5.375
36	4.7096
39	2.0758
42	8.6772
45	13.2532
48	9.2902
51	-3.3146
53	-1.5666
56	39.3185
59	46.0818
62	31.7455
65	15.3915
68	6.1511
71	1.6852
74	-6.3113
77	-9.4767
80	-12.0679
83	-9.9136

Depth	Vol. Susc.Meas. in SI
86	-5.7323
89	-4.903
92	-10.0098
95	-17.1532
98	-15.0206
101	-14.9176
104	-13.4481
107	-17.3377
110	-27.7652
113	-22.0026
116	-33.2255
119	-38.6698
122	-41.8553
125	-41.6451
128	-44.0148
131	-44.6451
134	-47.3658
137	-48.3659
140	-52.4569

Core 9

Depth	Vol. Susc.Meas. in SI
0	5.2439
3	36.7042
6	27.3699
9	23.0422
12	30.1755
15	5.7975
18	-10.6901
21	-21.6255
24	-18.6482
27	-7.1892
30	8.6456
33	-11.0567
36	1.3699
39	-9.571
42	-18.5933
45	-21.092
48	-23.2785
51	-35.7834
54	-64.1294
57	-77.3933
60	-81.2924
63	-82.427
66	-87.9229
69	-90.5257
72	-96.2952
75	-96.2553
78	-101.2952
81	-96.2236
84	-96.3622

Depth	Vol. Susc.Meas. in SI
87	-65.3625
88	-4.6783
91	77.4058
94	56.7641
97	47.3133
100	30.7759
103	18.9341
106	16.1364
109	10.8206
112	-1.6926
115	-10.3625
118	-13.6983
121	-17.1065
124	-26.1304
127	-30.1725
130	-34.3796
133	-32.3871
136	-39.3921
139	-45.2488
142	-53.0471
145	-59.3989
148	-64.1355
151	-68.1589
154	-69.7599

Core 10

Depth	Vol. Susc.Meas. in SI
0	3.0575
3	27.2872
6	34.2947
9	30.5114
12	46.7331
15	61.8974
18	22.6822
21	55.5806
24	47.3665
27	34.5577
30	40.2948
33	15.7411
36	20.5933
39	24.4868
42	40.8472
45	29.3653
48	22.7013
51	17.7217
54	10.3803
57	5.026
60	8.4418
63	-3.7673
66	13.0871
69	-2.1255
72	-19.2489
75	-27.0236
78	-27.1255
81	-32.498
84	-36.1286

Depth	Vol. Susc.Meas. in SI
87	-4.1022
90	7.2865
93	4.8089
96	29.4854
99	-2.1246
102	-7.8437
105	-12.962
108	-10.8864
111	-8.114
114	-8.6166
117	-1.8682
120	-2.5214
123	-4.4402
126	1.5388
129	-6.3079
132	-9.6418
135	-9.4396
138	-8.6335
141	-8.9997
144	-7.4746
147	-7.4027

Core 11

Depth	Vol. Susc.Meas. in SI
0	19.0867
3	22.3823
6	40.3152
9	4.181
12	23.1402
15	88.1391
18	41.8879
21	-15.1977
24	-39.0224
27	-40.9884
30	-49.8058
33	-59.7566
36	-63.3642
39	-57.4271
42	-50.2064
45	-66.3742
48	-64.3583
51	-81.9316
54	-86.4522
57	-67.0745
60	-80.1444
63	-83.1323
66	-79.8558
69	-99.0888
72	-106.9114
75	-109.7215
78	-113.7144
81	-118.3216
84	-119.3119
87	-2.6876
90	8.8693
93	-9.3343
96	-22.4976
99	-34.8446
102	-40.8162
105	-46.4278
108	-49.2068
111	-50.8733
114	-51.9776
117	-55.2674
120	-57.5651

Depth	Vol. Susc.Meas. in SI
123	-57.8592
126	-63.0149
129	-63.4328
132	-63.695
135	-64.3087
138	-63.5577
141	-66.5842
144	-68.3904
147	-67.6608
150	-66.7358
153	-69.7756
156	-75.4249
159	-72.0632
162	-73.7894
165	-74.7199
168	-79.3337
171	-81.1817
174	-92.5774

Core 12

Depth	Vol. Susc.Meas. in SI
0	-13.1473
3	-20.8188
6	-34.9227
9	-25.2944
12	-31.6426
15	-58.0905
18	-66.6995
21	-62.7376
24	-82.7483
27	-85.7224
30	-78.7757
33	-31.0866
36	-93.8921
39	-104.6368
42	-106.5748
45	-111.4984
48	-115.7032
51	-117.0992
54	-125.5599
57	-124.0907
60	-122.3836
63	-128.7648
66	-126.0383
69	-128.0413
72	-121.8742
75	-133.0502
78	-136.1706
81	-144.3876
84	-154.5574
87	-7.1808
90	-52.2913
93	-67.0461
96	-67.2825
99	-86.9234
102	-97.8679
105	-96.3793
108	-98.1334
111	-118.7071
114	-117.3532
117	-121.0544
120	-124.1451
123	-126.6062

Depth	Vol. Susc.Meas. in SI
126	-130.3632
129	-133.7748
132	-129.6427
135	-130.3458
138	-133.9567
141	-135.8621
144	-136.6447
147	-141.0215
150	-136.7171
153	-142.427
156	-141.418
159	-144.7899
162	-144.1195
165	-148.3518
168	-153.4596
171	-13.2099
174	-26.5624
177	-38.4516
180	-47.1286
183	-60.4634
186	-67.7871
189	-76.348
192	-81.902
195	-86.1553
198	-86.1355
201	-76.7244
204	-84.3808
207	-91.1654
210	-96.1116
213	-101.6814
216	-111.0636
219	-113.7694
222	-120.5251
225	-124.8399
228	-130.6749
231	-133.7712
234	-138.564
237	-140.4634
240	-141.6178
243	-146.9927
246	-148.7144
249	-152.2589

Continue core 12

Depth	Vol. Susc.Meas. in SI
252	-156.9324
255	-155.7895
258	-156.1258

Appendix D : Grain size analysis

Core 1 sample 1

size	WT%	cumulative WT%
0	1.516	1.516
0.321928	3.475	4.991
0.736965	4.14	9.131
1.736966	7.775	16.906
2.736966	7.971	24.877
3.736966	38.403	63.28
5.64385619	36.72	100
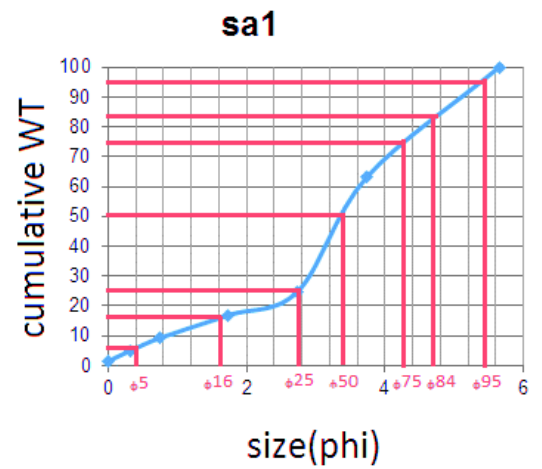
Mean size	sorting
6.33377	8.839632

Core 1 sample 2

size	WT %	Cumulative WT %
0	1.117	1.117
0.321928	3.238	4.355
0.736965	5.785	10.14
1.736966	18.671	28.811
2.736966	24.524	53.335
3.736966	22.838	76.173
5.64385619	23.827	100
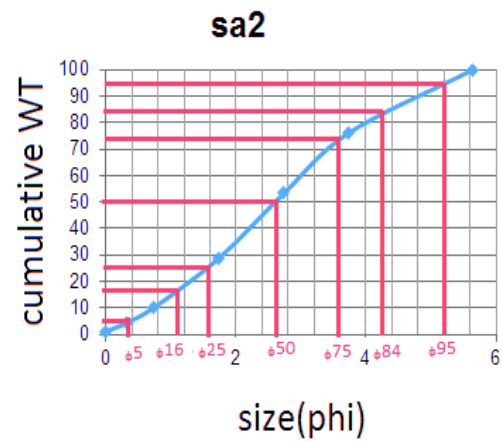
Mean size	sorting
5.09153	8.493642

Core 1 sample 3

size	WT %	cumulative WT %
0	1.651	1.651
0.321928	2.915	4.566
0.736965	3.799	8.365
1.736966	14.429	22.794
2.736966	22.992	45.786
3.736966	27.14	72.926
5.64385619	27.074	100
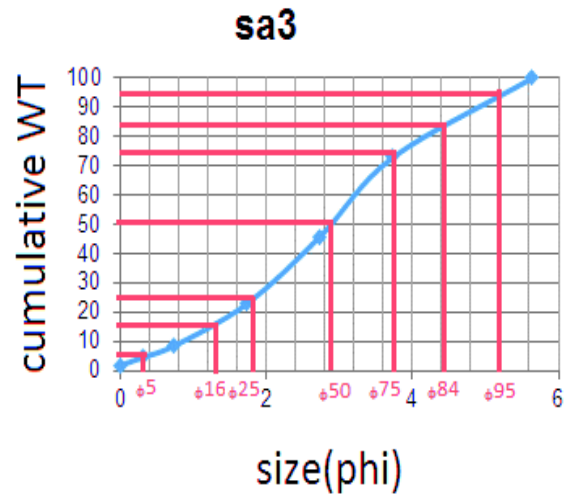
Mean size	sorting
6.580573	9.066486

Core 1 sample 4

size	WT %	cumulative WT %
0	6.945	6.945
0.321928	2.65	9.595
0.736965	3.057	12.652
1.736966	11.249	23.901
2.736966	19.759	43.66
3.736966	29.754	73.414
5.64385619	26.586	100
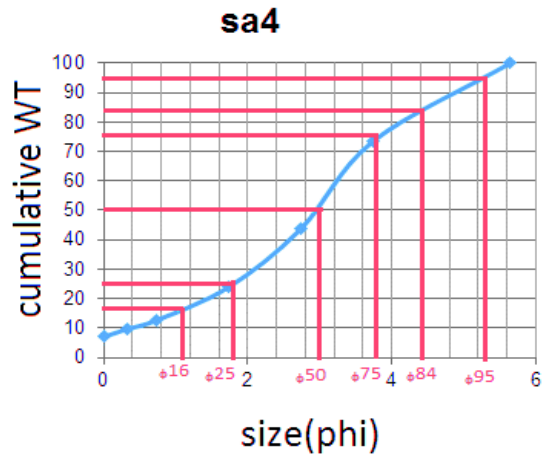
Mean size	sorting
5.4685	8.619654

Core 1 sample 5

size	WT %	cumulativeWT %
0	2.98	2.98
0.321928	2.787	5.767
0.736965	3.64	9.407
1.736966	12.878	22.285
2.736966	22.384	44.669
3.736966	34.527	79.196
5.64385619	20.804	100

Mean size	sorting
5.506978	7.819768
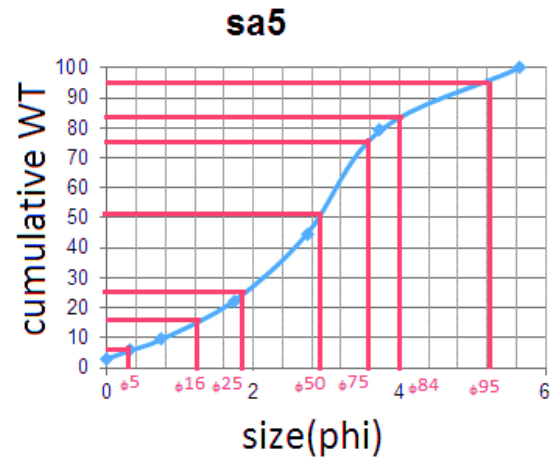
Core 1 sample 6

size	WT%	Cumulative WT%
0	10.958	10.958
0.321928	4.267	15.225
0.736965	5.723	20.948
1.736966	15.118	36.066
2.736966	20.065	56.131
3.736966	25.736	81.867
5.64385619	18.133	100

Mean size	sorting
4.13475	8.08206
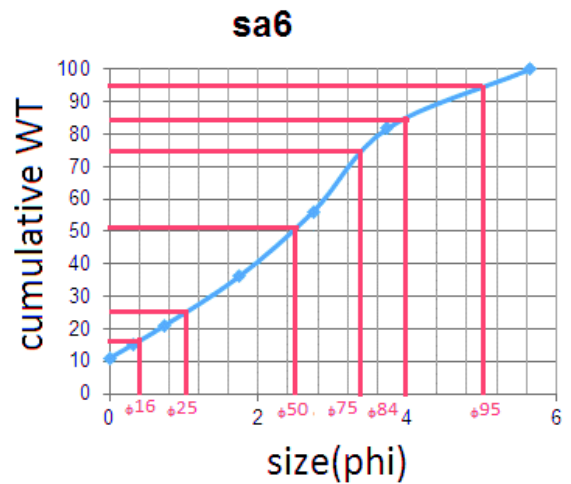
Core 1 sample 7

size	WT %	cumulative WT %
0	20.949	20.949
0.321928	5.501	26.45
0.736965	6.341	32.791
1.736966	14.324	47.115
2.736966	21.165	68.28
3.736966	19.862	88.142
5.64385619	11.858	100

Mean size	sorting
2.881786	7.495146
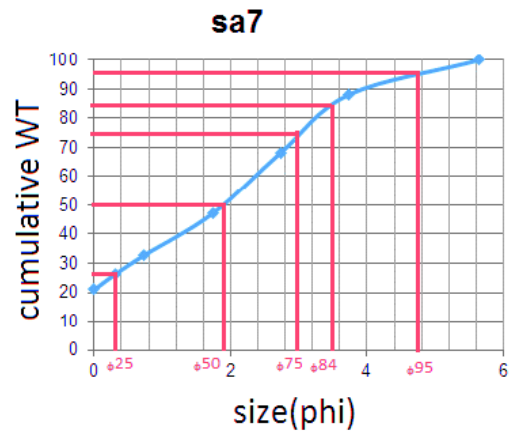
Core 1 sample 8

size	WT %	cumulative WT%
0	20.349	20.349
0.321928	4.215	24.564
0.736965	5.857	30.421
1.736966	15.859	46.28
2.736966	24.085	70.365
3.736966	17.573	87.938
5.64385619	12.062	100

Mean size	sorting
2.818043	7.57713

308
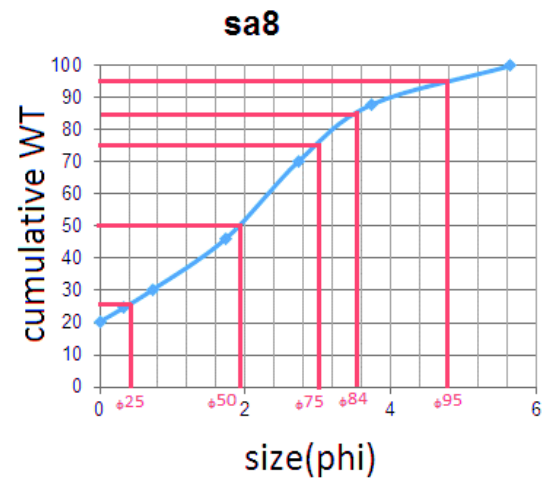
Core 1 sample 9

size	WT %	cumulative WT %
0	13.83	13.83
0.321928	5.279	19.109
0.736965	6.085	25.194
1.736966	15.091	40.285
2.736966	22.453	62.738
3.736966	20.412	83.15
5.64385619	16.85	100

Mean size	sorting
3.5758	8.098216

sa9
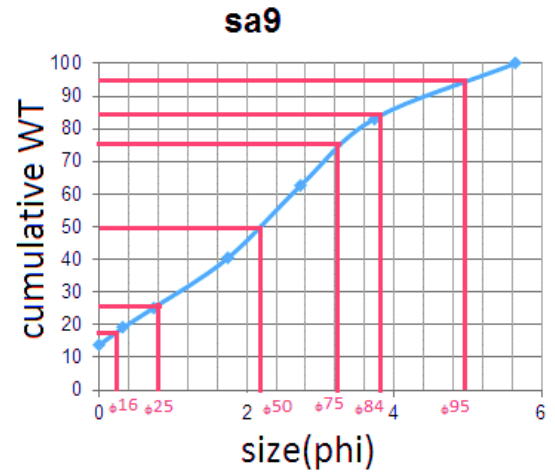
Core 1 sample 10

size	WT %	cumulative WT %
0	10.231	10.231
0.321928	5.149	15.38
0.736965	6.662	22.042
1.736966	20.046	42.088
2.736966	28.617	70.705
3.736966	19.805	90.51
5.64385619	9.49	100

Mean size	sorting
3.482771	7.050196

sa10
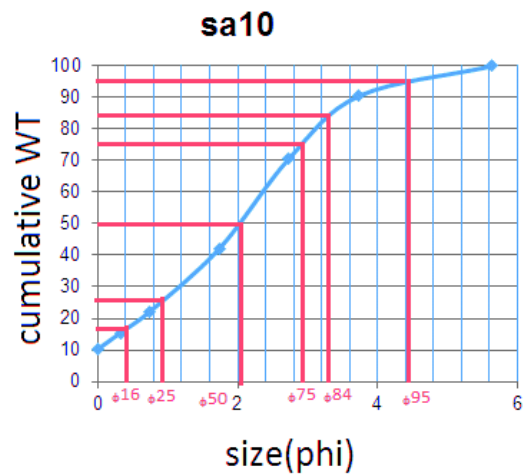
Core 2 sample 1

size	WT%	cumulative WT%
0	4.981	4.981
0.321928	4.598	9.579
0.736965	5.122	14.701
1.736966	11.992	26.693
2.736966	15.448	42.141
3.736966	25.44	67.581
5.64385619	32.419	100

Mean size	sorting
5.255839	9.14149

sa1
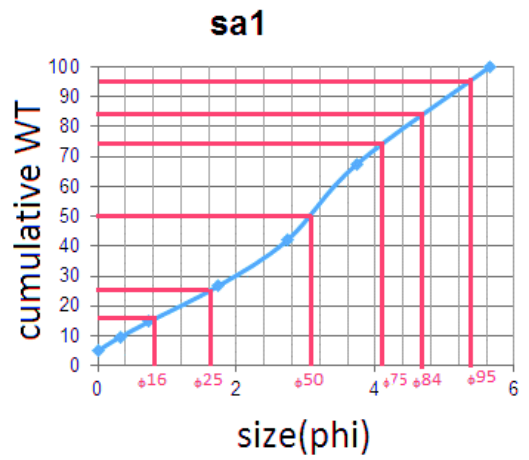
Core 2 sample 2

size	WT %	cumulative WT %
0	17.241	17.241
0.321928	9.81	27.051
0.736965	9.511	36.562
1.736966	16.492	53.054
2.736966	21.986	75.04
3.736966	14.879	89.919
5.64385619	10.081	100

Mean size	sorting
2.610193	7.160603

sa2
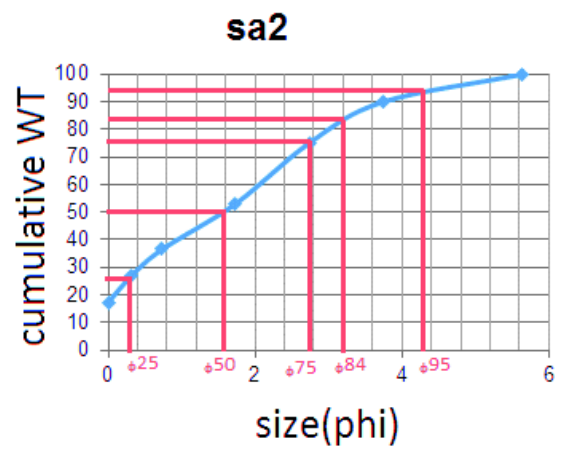
Core 2 sample 3

size	WT %	cumulative WT %
0	7.754	7.754
0.321928	5.239	12.993
0.736965	7.807	20.8
1.736966	17.744	38.544
2.736966	31.624	70.168
3.736966	20.145	90.313
5.64385619	9.687	100

Mean size	sorting
3.714673	7.026248

sa3
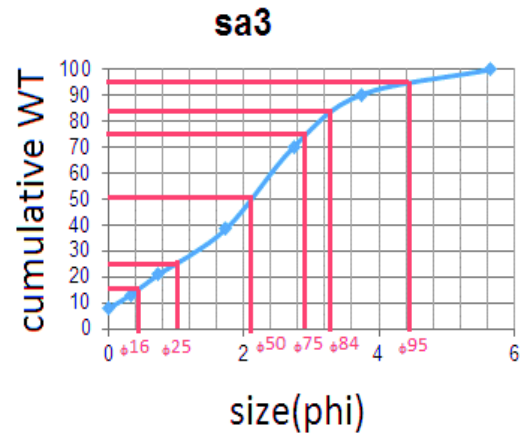
Core 2 sample 4

size	WT %	cumulative WT %
0	9.07	9.07
0.321928	4.529	13.599
0.736965	5.905	19.504
1.736966	12.857	32.361
2.736966	33.027	65.388
3.736966	27.835	93.223
5.64385619	6.777	100

Mean size	sorting
3.919714	6.748145

sa4
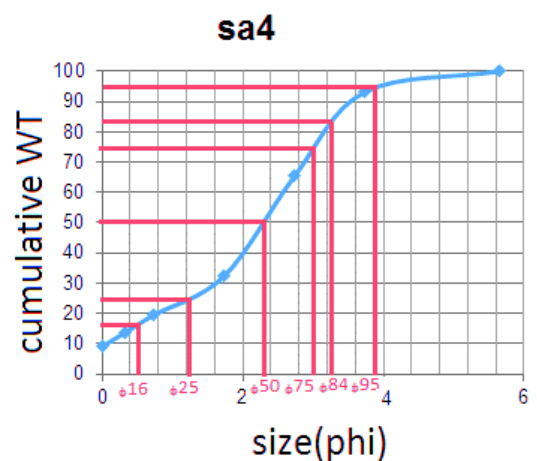
Core 2 sample 5

size	WT%	cumulative WT %
0	16.614	16.614
0.321928	5.16	21.774
0.736965	4.92	26.694
1.736966	11.802	38.496
2.736966	29.354	67.85
3.736966	30.29	98.14
5.64385619	1.86	100

Mean size	sorting
3.23065	6.599271

sa5
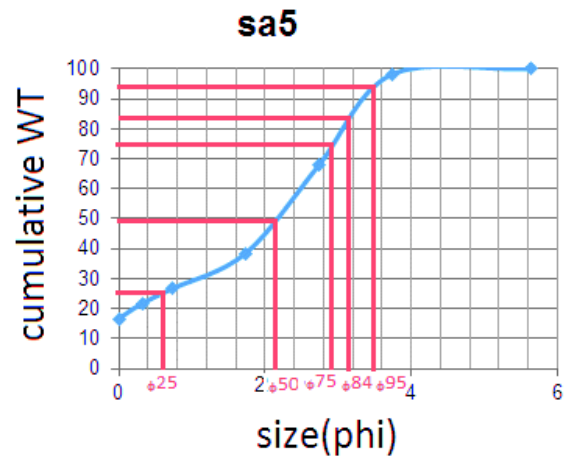
Core 2 sample 6

size	WT %	cumulative WT %
0	11.766	11.766
0.321928	3.518	15.284
0.736965	4.545	19.829
1.736966	10.982	30.811
2.736966	29.922	60.733
3.736966	37.695	98.428
5.64385619	1.572	100

Mean size	sorting
3.973583	6.66662

sa6
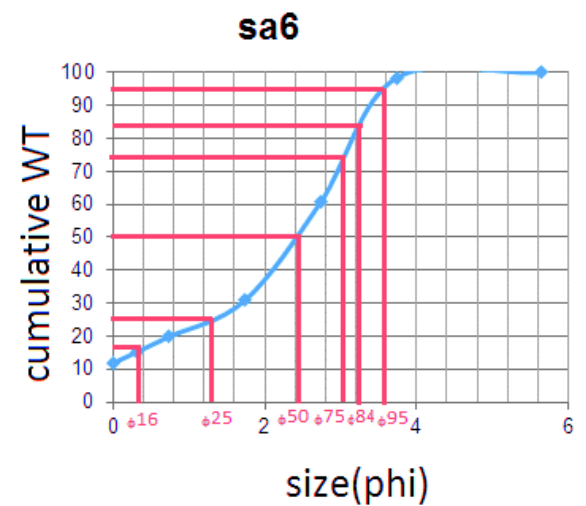
Core 3 sample 1

size	WT%	cumulative WT%
0	12.636	12.636
0.321928	3.975	16.611
0.736965	4.307	20.918
1.736966	7.429	28.347
2.736966	6.665	35.012
3.736966	34.028	69.04
5.64385619	30.96	100

Mean size	sorting
3.0551	7.308591
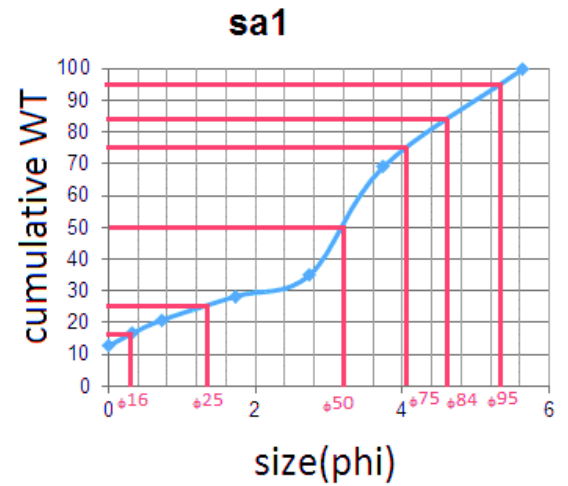
Core 3 sample 2

size	WT %	Cumulative WT %
0	14.221	14.221
0.321928	5.407	19.628
0.736965	7.675	27.303
1.736966	18.575	45.878
2.736966	19.461	65.339
3.736966	18.054	83.393
5.64385619	16.607	100

Mean size	sorting
2.603333	6.83197
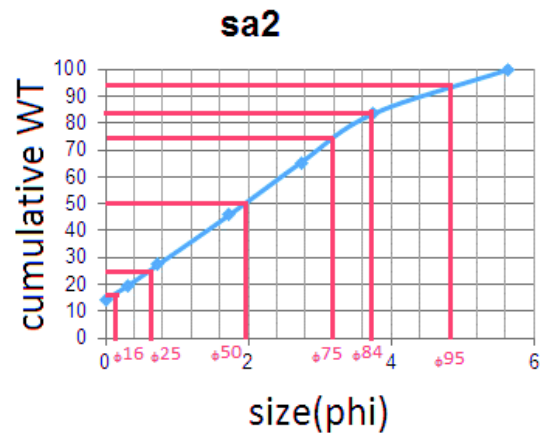
Core 3 sample 3

size	WT%	cumulative WT %
0	9.713	9.713
0.321928	3.923	13.636
0.736965	5.654	19.29
1.736966	16.091	35.381
2.736966	19.215	54.596
3.736966	26.055	80.651
5.64385619	19.349	100

Mean size	sorting
2.411333	6.962644

sa3
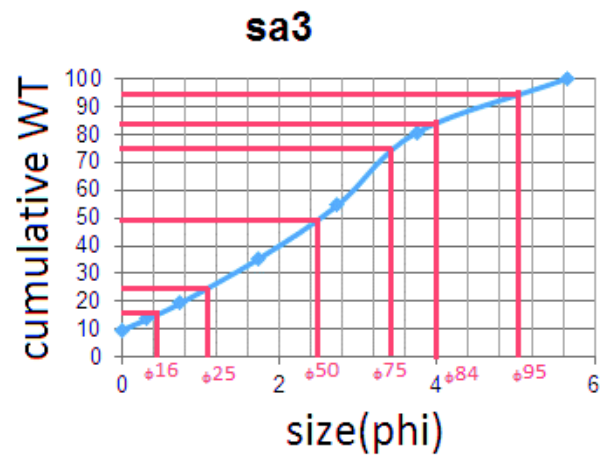
Core 3 sample 4

size	WT%	cumulative WT %
0	10.846	10.846
0.321928	3.598	14.444
0.736965	4.656	19.1
1.736966	12.749	31.849
2.736966	19.323	51.172
3.736966	30.2	81.372
5.64385619	18.628	100

Mean size	sorting
2.26	8.868258

sa4
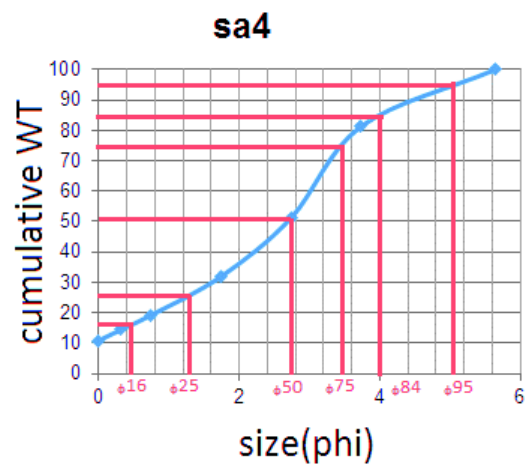
Core 3 sample 5

size	WT%	cumulative WT %
0	12.297	12.297
0.321928	3.562	15.859
0.736965	5.31	21.169
1.736966	14.819	35.988
2.736966	41.575	77.563
3.736966	20.632	98.195
5.64385619	1.805	100

Mean size	sorting
1.133333	5.394
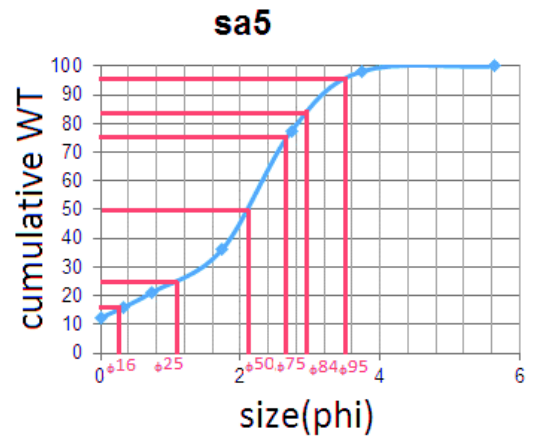
Core 3 sample 6

size	WT%	Cumulative WT %
0	7.58	7.58
0.321928	3.659	11.239
0.736965	5.588	16.827
1.736966	14.779	31.606
2.736966	26.043	57.649
3.736966	24.062	81.711
5.64385619	18.289	100

Mean size	sorting
3.826667	4.614773
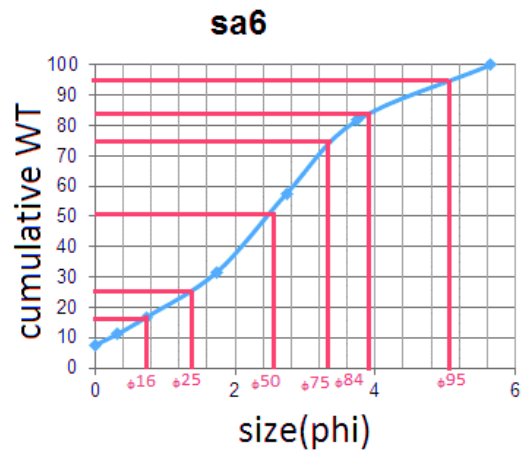
Core 3 sample 7

size	WT %	cumulative WT %
0	13.825	13.825
0.321928	5.019	18.844
0.736965	6.616	25.46
1.736966	15.425	40.885
2.736966	26.575	67.46
3.736966	20.563	88.023
5.64385619	11.977	100

Mean size	sorting
2.168	6.854667
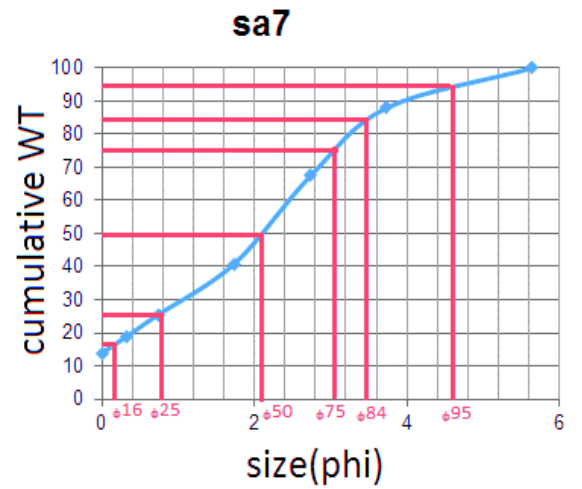
Core 3 sample 8

size	WT %	cumulative WT%
0	10.434	10.434
0.321928	3.548	13.982
0.736965	4.49	18.472
1.736966	10.457	28.929
2.736966	31.902	60.831
3.736966	34.684	95.515
5.64385619	4.485	100

Mean size	sorting
4.503333	8.117197
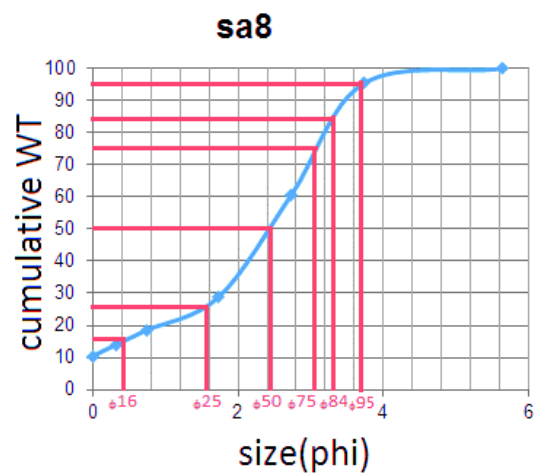
Core 3 sample 9

size	WT%	cumulative WT %
0	17.504	17.504
0.321928	5.288	22.792
0.736965	5.944	28.736
1.736966	12.566	41.302
2.736966	28.547	69.849
3.736966	26.365	96.214
5.64385619	3.7866	100.0006

Mean size	sorting
5.521667	8.403295
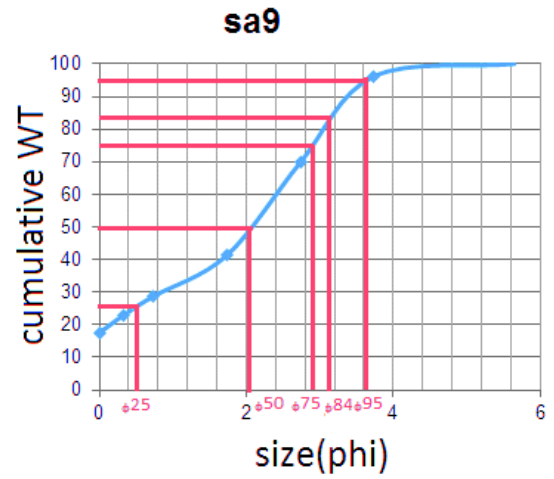
Core 4 sample 1

size	WT%	cumulative WT%
0	20.868	20.868
0.321928	5.971	26.839
0.736965	7.033	33.872
1.736966	14.446	48.318
2.736966	19.609	67.927
3.736966	15.972	83.899
5.64385619	16.101	100

Mean size	sorting
2.61	8.152424
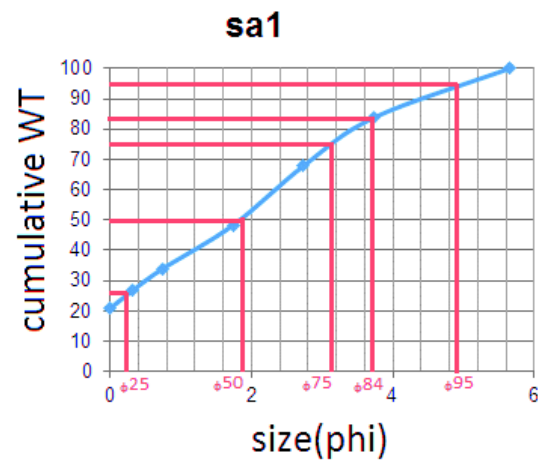
Core 4 sample 2

size	WT %	cumulative WT %
0	10.467	10.467
0.321928	4.664	15.131
0.736965	7.441	22.572
1.736966	18.776	41.348
2.736966	27.045	68.393
3.736966	19.205	87.598
5.64385619	12.402	100

Mean size	sorting
3.612333	7.475674
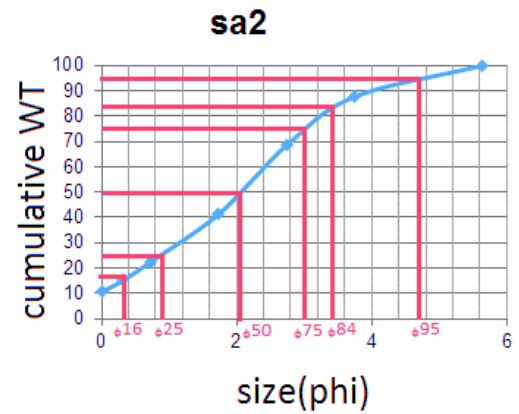
Core 4 sample 3

size	WT %	cumulative WT %
0	4.267	4.267
0.321928	2.509	6.776
0.736965	4.977	11.753
1.736966	17.793	29.546
2.736966	41.518	71.064
3.736966	22.173	93.237
5.64385619	6.763	100

Mean size	sorting
4.417333	6.411205
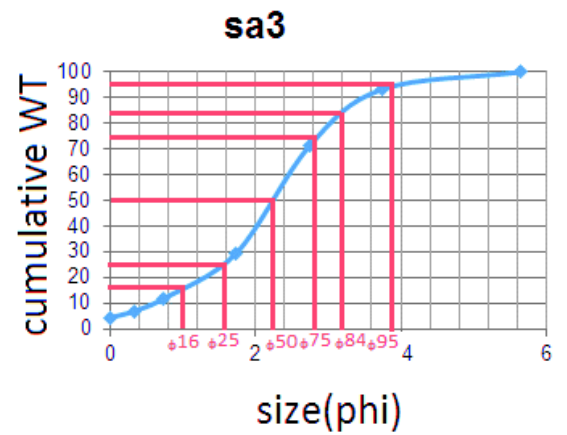
Core 4 sample 4

size	WT%	cumulative WT %
0	1.974	1.974
0.321928	1.521	3.495
0.736965	2.94	6.435
1.736966	13.239	19.674
2.736966	44.122	63.796
3.736966	29.995	93.791
5.64385619	6.209	100
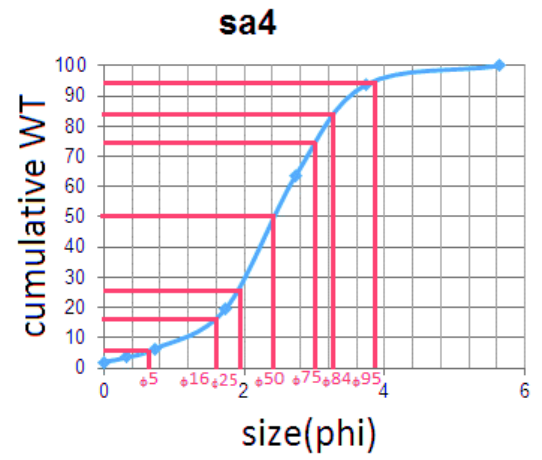
Mean size	sorting
5.139333	6.347348

Core 4 sample 5

size	WT %	cumulative WT %
0	1.492	1.492
0.321928	0.996	2.488
0.736965	2.348	4.836
1.736966	19.587	24.423
2.736966	54.548	78.971
3.736966	18.903	97.874
5.64385619	2.126	100
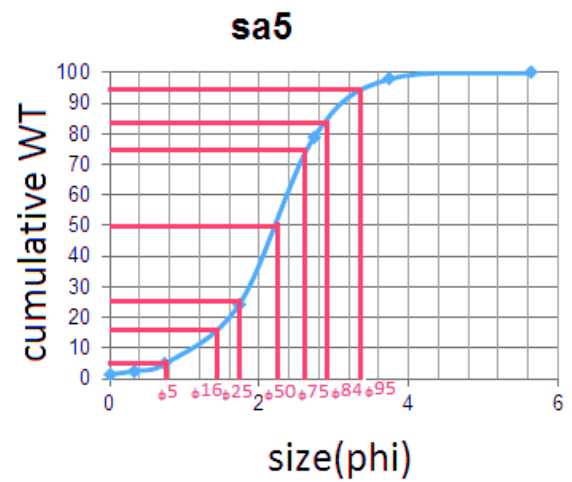
Mean size	sorting
4.651133	5.529535

Core 4 sample 6

size	WT %	cumulative WT %
0	1.98	1.98
0.321928	1.176	3.156
0.736965	2.204	5.36
1.736966	14.286	19.646
2.736966	49.199	68.845
3.736966	29.081	97.926
5.64385619	2.074	100

Mean size	sorting
5.05732	5.918961

sa6
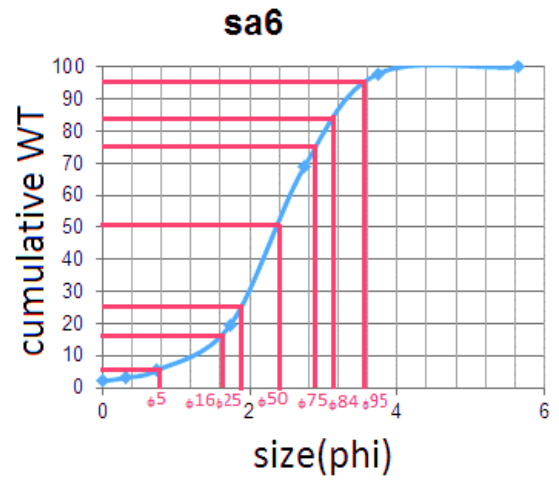
Core 4 sample 7

size	WT %	cumulative WT %
0	5.032	5.032
0.321928	2.25	7.282
0.736965	4.296	11.578
1.736966	17.577	29.155
2.736966	43.282	72.437
3.736966	22.791	95.228
5.64385619	4.772	100

Mean size	sorting
4.3663	6.256008

sa7
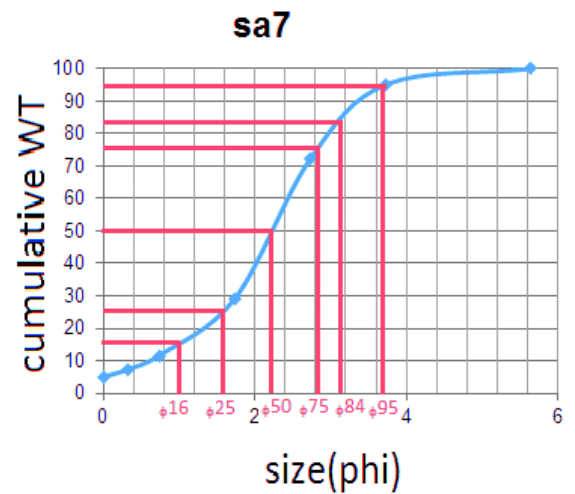
Core 4 sample 8

size	WT %	cumulative WT %
0	3.749	3.749
0.321928	1.338	5.087
0.736965	2.404	7.491
1.736966	12.335	19.826
2.736966	43.912	63.738
3.736966	34.301	98.039
5.64385619	1.961	100

Mean size	sorting
5.112867	6.173006
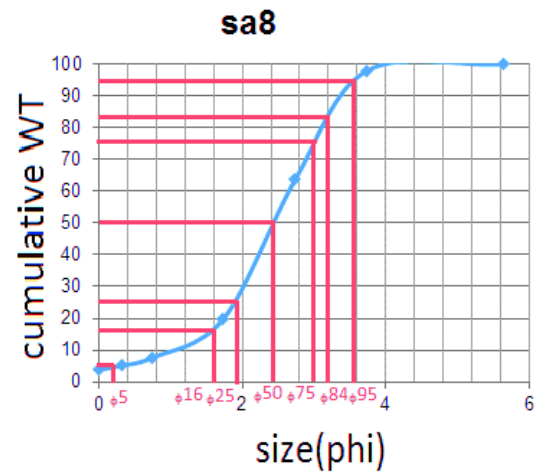
Core 4 sample 9

size	WT%	cumulative WT %
0	28.101	28.101
0.321928	5.886	33.987
0.736965	7.673	41.66
1.736966	17.664	59.324
2.736966	18.281	77.605
3.736966	15.24	92.845
5.64385619	7.155	100

Mean size	sorting
1.95299	6.695535
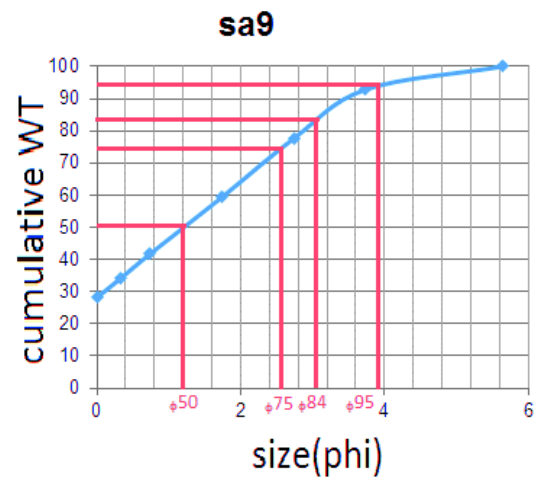
Core 5 sample 1

size	WT%	cumulative WT%
0	17.86	17.86
0.321928	5.667	23.527
0.736965	7.56	31.087
1.736966	17.098	48.185
2.736966	21.178	69.363
3.736966	20.526	89.889
5.64385619	10.111	100

Mean size	sorting
2.74735	7.207403

sa1
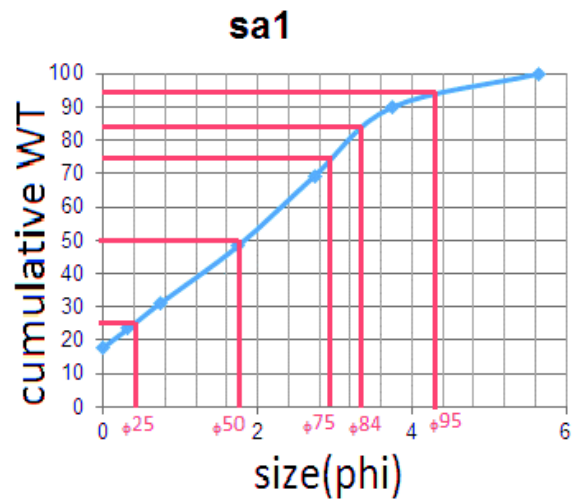
Core 5 sample 2

size	WT %	cumulative WT %
0	14.668	14.668
0.321928	6.026	20.694
0.736965	8.783	29.477
1.736966	18.397	47.874
2.736966	19.26	67.134
3.736966	14.08	81.214
5.64385619	18.786	100

Mean size	sorting
3.194333	8.320795

sa2
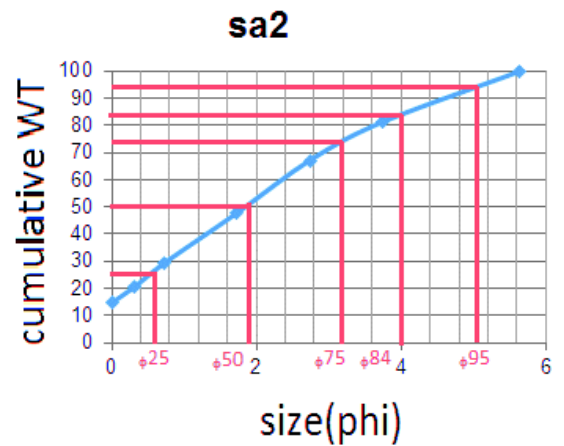
Core 5 sample 3

size	WT %	cumulative WT %
0	9.063	9.063
0.321928	5.166	14.229
0.736965	7.214	21.443
1.736966	16.778	38.221
2.736966	39.002	77.223
3.736966	19.362	96.585
5.64385619	3.415	100

Mean size	sorting
3.444333	6.181198
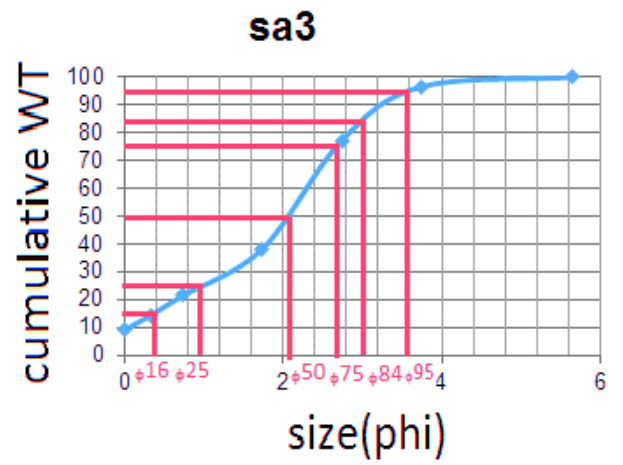
Core 5 sample 4

size	WT %	cumulative WT %
0	8.832	8.832
0.321928	5.005	13.837
0.736965	8.729	22.566
1.736966	23.847	46.413
2.736966	39.947	86.36
3.736966	11.968	98.328
5.64385619	1.672	100

Mean size	sorting
3.143667	5.499894

323
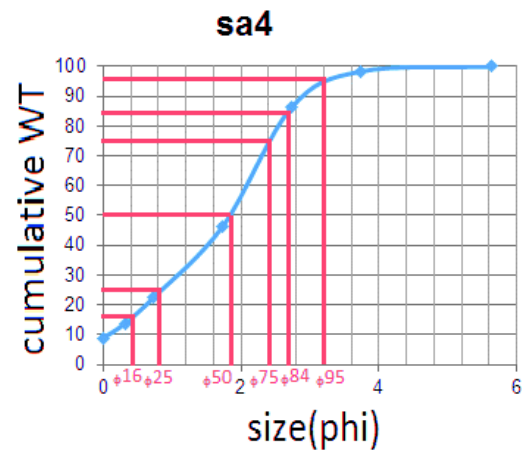
Core 6 sample 1

size	WT%	cumulative WT%
0	12.08	12.08
0.321928	5.501	17.581
0.736965	7.653	25.234
1.736966	20.936	46.17
2.736966	33.546	79.716
3.736966	15.336	95.052
5.64385619	4.948	100
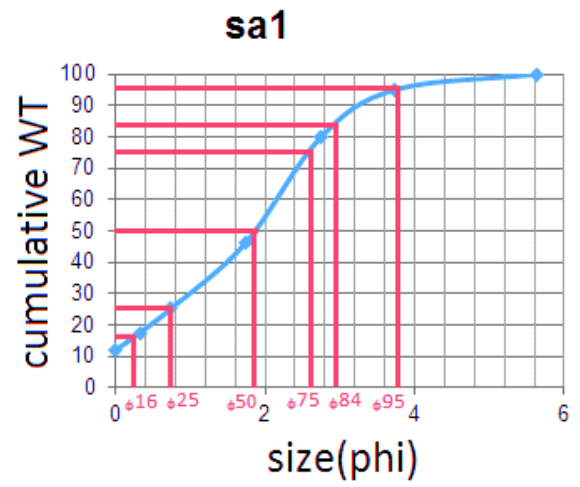
Mean size	sorting
2.9542	6.301268

Core 6 sample 2

size	WT %	cumulative WT %
0	6.629	6.629
0.321928	5.523	12.152
0.736965	10.884	23.036
1.736966	30.902	53.938
2.736966	30.55	84.488
3.736966	11.7	96.188
5.64385619	3.812	100
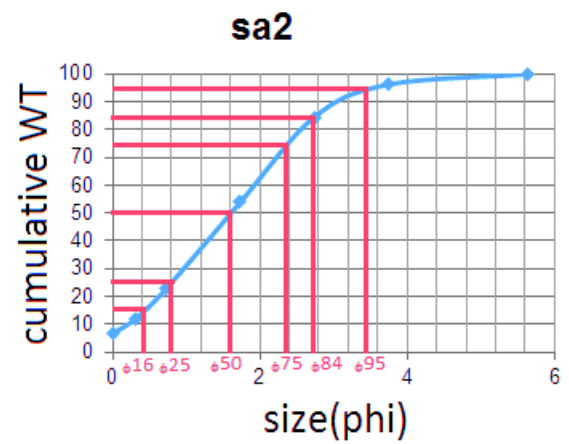
Mean size	sorting
3.016567	5.800123

Core 6 sample 3

size	WT %	cumulative WT %
0	5.373	5.373
0.321928	2.471	7.844
0.736965	4.715	12.559
1.736966	18.741	31.3
2.736966	42.834	74.134
3.736966	23.531	97.665
5.64385619	2.335	100

Mean size	sorting
4.230667	6.066864
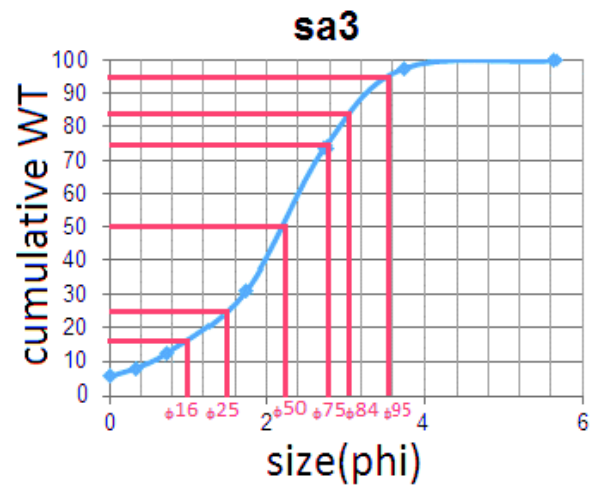
Core 6 sample 4

size	WT %	cumulative WT %
0	7.461	7.461
0.321928	4.024	11.485
0.736965	5.243	16.728
1.736966	12.751	29.479
2.736966	34.17	63.649
3.736966	33.099	96.748
5.64385619	3.252	100

Mean size	sorting
4.14435	6.565728
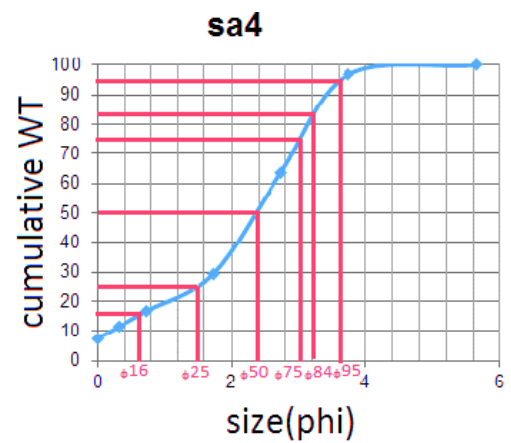
Core 6 sample 5

size	WT %	Cumulative WT %
0	21.232	21.232
0.321928	3.486	24.718
0.736965	4.22	28.938
1.736966	13.023	41.961
2.736966	39.06	81.021
3.736966	16.889	97.91
5.64385619	2.09	100

Mean size	sorting
2.792303	6.09195
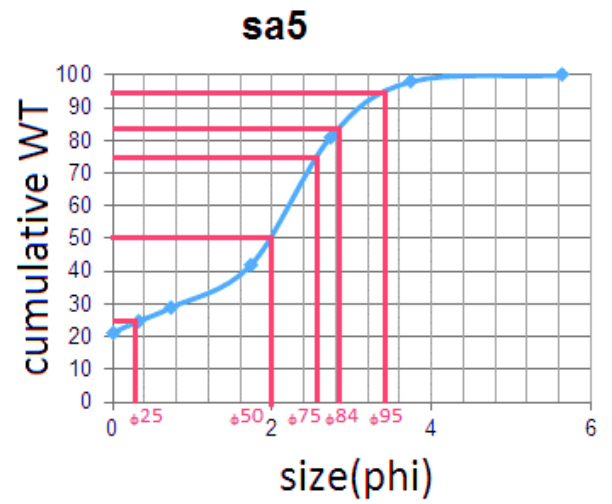
Core 6 sample 6

size	WT %	cumulative WT %
0	5.714	5.714
0.321928	1.877	7.591
0.736965	3.492	11.083
1.736966	8.056	19.139
2.736966	7.149	26.288
3.736966	50.041	76.329
5.64385619	23.571	99.9

Mean size	sorting
5.77684	7.746483
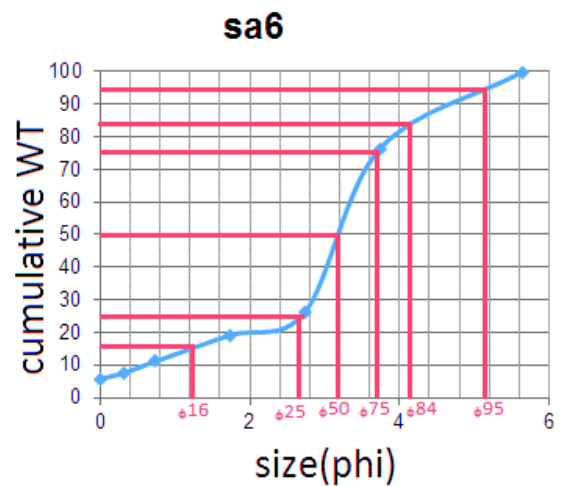
Core 6 sample 7

size	WT %	cumulative WT %
0	6.71	6.71
0.321928	4.838	11.548
0.736965	7.451	18.999
1.736966	18.138	37.137
2.736966	19.345	56.482
3.736966	20.685	77.167
5.64385619	22.833	100

Mean size	sorting
4.407733	8.591306
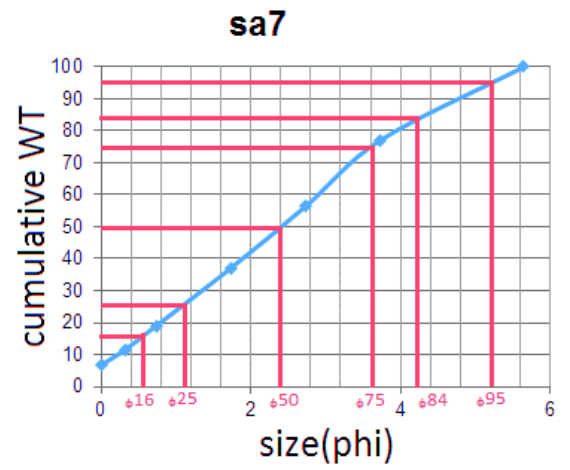
Core 6 sample 8

size	WT %	cumulative WT %
0	12.974	12.974
0.321928	3.688	16.662
0.736965	5.139	21.801
1.736966	13.819	35.62
2.736966	19.25	54.87
3.736966	23.246	78.116
5.64385619	21.884	100

Mean size	sorting
4.124667	8.556376
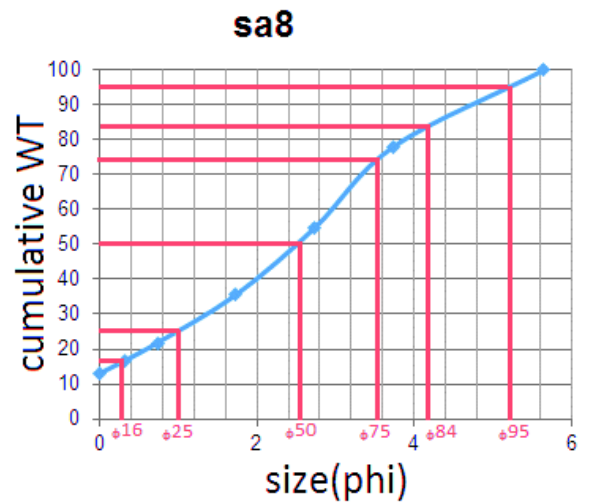
Core 6 sample 9

size	WT %	cumulative WT %
0	20.926	20.926
0.321928	5.227	26.153
0.736965	9.033	35.186
1.736966	23.875	59.061
2.736966	25.999	85.06
3.736966	10.568	95.628
5.64385619	4.372	100

Mean size	sorting
2.126867	6.011352
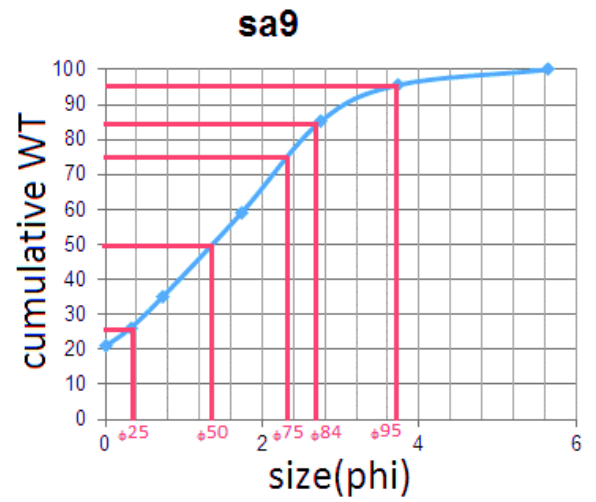
Core 6 sample 10

size	WT %	cumulative WT %
0	8.888	8.888
0.321928	5.284	14.172
0.736965	7.095	21.267
1.736966	18.871	40.138
2.736966	34.261	74.399
3.736966	22.765	97.164
5.64385619	2.836	100

Mean size	sorting
2.158133	5.641148
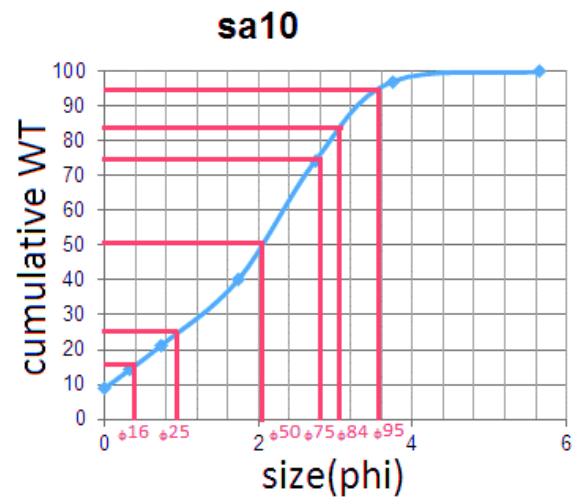
Core 7 sample 1

size	WT%	cumulative WT%
0	19.705	19.705
0.321928	4.66	24.365
0.736965	5.441	29.806
1.736966	12.106	41.912
2.736966	12.109	54.021
3.736966	22.004	76.025
5.64385619	23.975	100

Mean size	sorting
3.559667	8.908765
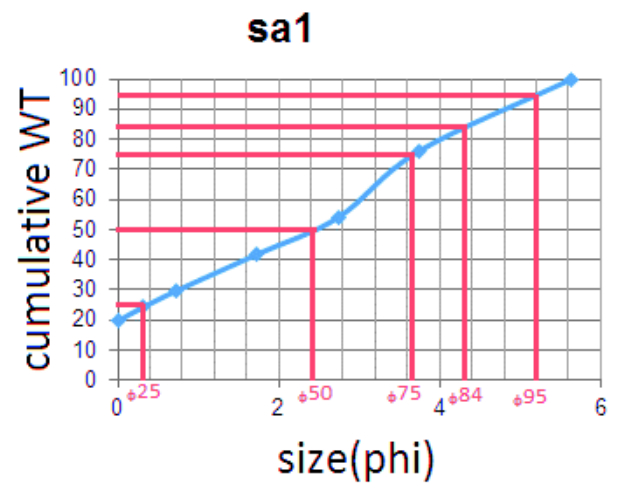
Core 7 sample 2

size	WT %	cumulative WT %
0	1.479	1.479
0.321928	1.991	3.47
0.736965	3.739	7.209
1.736966	18.045	25.254
2.736966	24.221	49.475
3.736966	26.999	76.474
5.64385619	23.526	100

Mean size	sorting
5.427333	8.258818
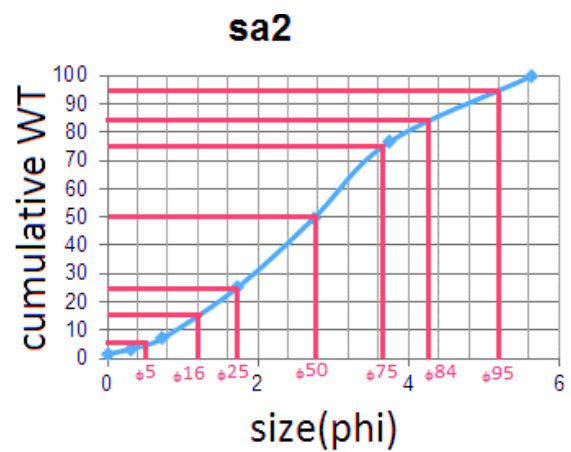
Core 7 sample 3

size	WT %	cumulative WT %
0	7.745	7.745
0.321928	4.267	12.012
0.736965	6.528	18.54
1.736966	14.631	33.171
2.736966	16.548	49.719
3.736966	31.631	81.35
5.64385619	18.65	100
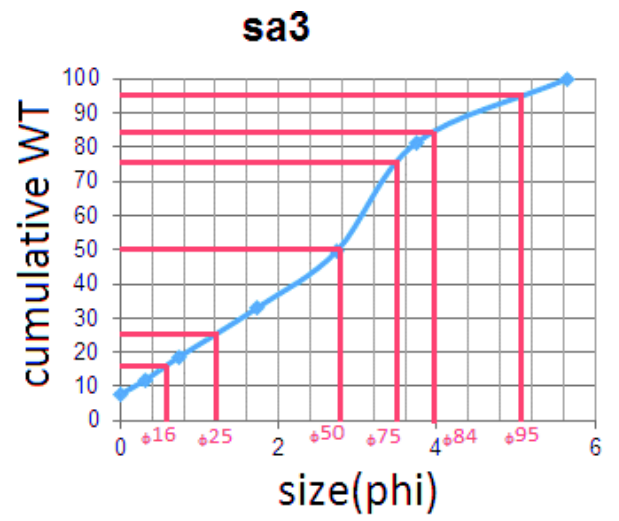
Mean size	sorting
4.609333	7.874689

Core 7 sample 4

size	WT %	cumulative WT %
0	5.017	5.017
0.321928	5.279	10.296
0.736965	9.404	19.7
1.736966	20.586	40.286
2.736966	22.231	62.517
3.736966	21.633	84.15
5.64385619	15.85	100
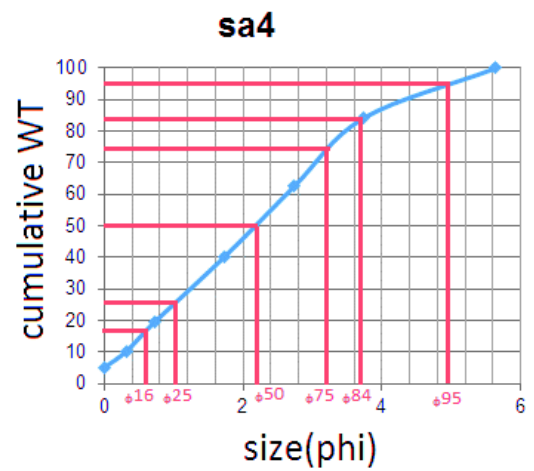
Mean size	sorting
4.035333	7.772455

Core 7 sample 5

size	WT %	cumulative WT %
0	16.421	16.421
0.321928	6.253	22.674
0.736965	6.933	29.607
1.736966	14.186	43.793
2.736966	25.079	68.872
3.736966	20.125	88.997
5.64385619	11.003	100

Mean size	sorting
3.146333	7.327932
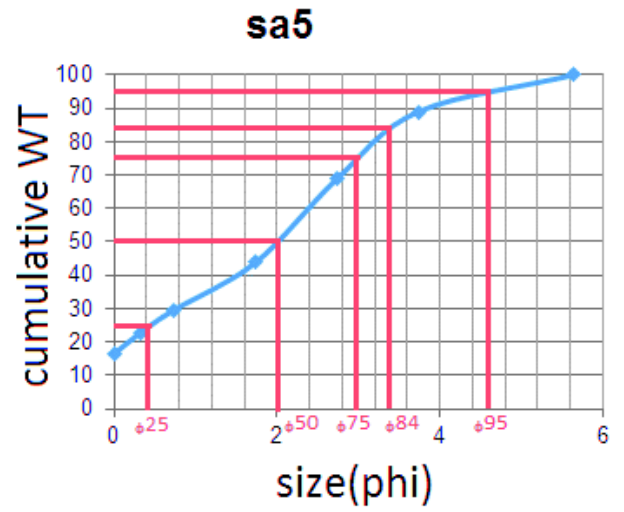
Core 7 sample 6

size	WT %	cumulative WT %
0	17.089	17.089
0.321928	4.37	21.459
0.736965	5.675	27.134
1.736966	14.06	41.194
2.736966	19.277	60.471
3.736966	21.661	82.132
5.64385619	17.868	100

Mean size	sorting
3.145	7.283932
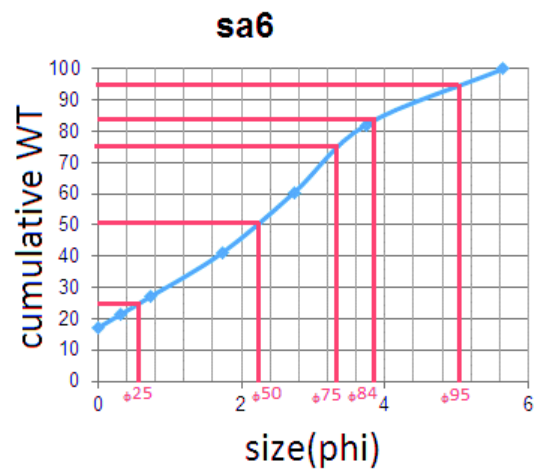
Core 7 sample 7

size	WT %	cumulative WT %
0	2.677	2.677
0.321928	2.189	4.866
0.736965	4.133	8.999
1.736966	12.959	21.958
2.736966	35.526	57.484
3.736966	38.678	96.162
5.64385619	3.838	100

Mean size	sorting
5.089	6.445371

sa7
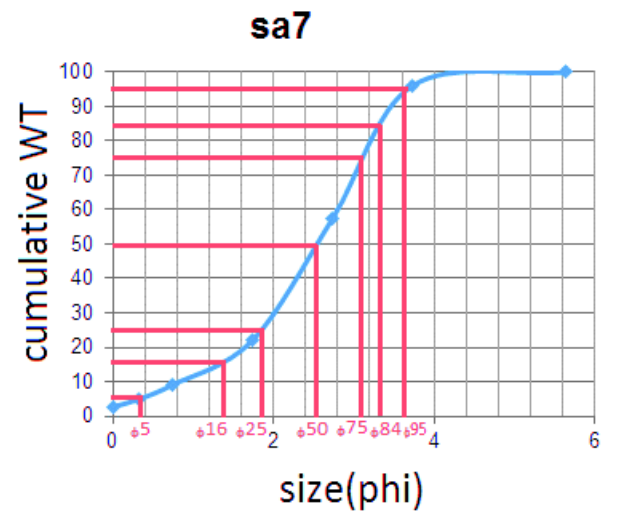
Core 7 sample 8

size	WT %	Cumulative WT %
0	3.342	3.342
0.321928	2.276	5.618
0.736965	4.229	9.847
1.736966	16.873	26.72
2.736966	45.967	72.687
3.736966	25.797	98.484
5.64385619	1.516	100

Mean size	sorting
4.566333	5.950106

sa8
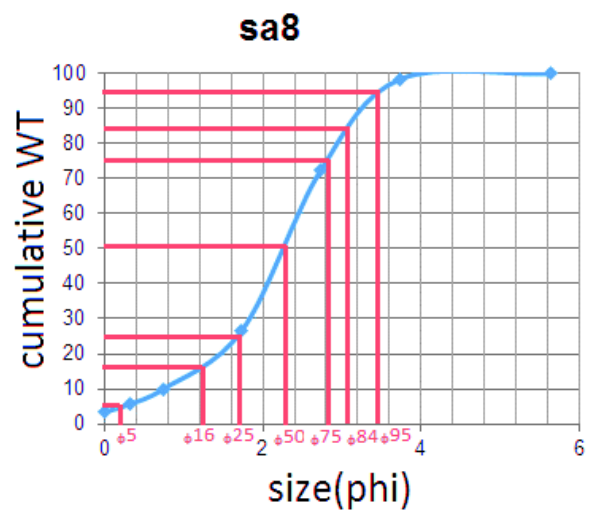
Core 8 sample 1

size	WT %	Cumulative WT %
0	20.675	20.675
0.321928	5.094	25.769
0.736965	5.709	31.478
1.736966	13.476	44.954
2.736966	17.944	62.898
3.736966	20.785	83.683
5.64385619	16.317	100

Mean size	sorting
2.936667	8.100682
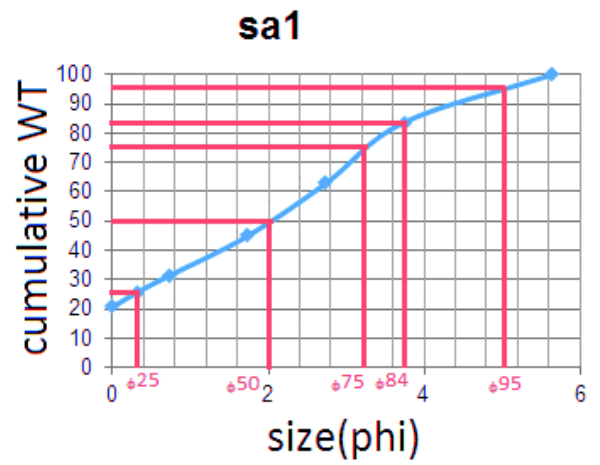
Core 8 sample 2

size	WT %	cumulative WT %
0	11.854	11.854
0.321928	5.719	17.573
0.736965	7.968	25.541
1.736966	17.606	43.147
2.736966	19.204	62.351
3.736966	25.493	87.844
5.64385619	12.156	100

Mean size	sorting
3.563333	7.391894
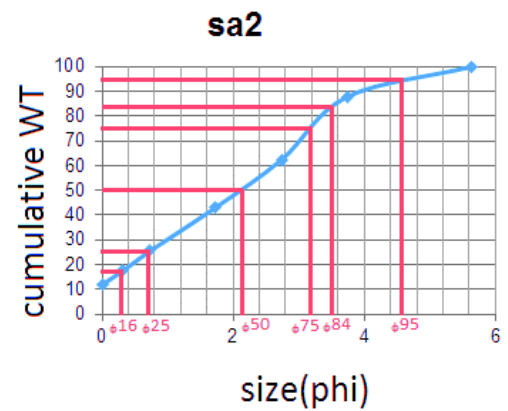
Core 8 sample 3

size	WT %	cumulative WT %
0	12.99	12.99
0.321928	5.506	18.496
0.736965	7.494	25.99
1.736966	16.485	42.475
2.736966	20.307	62.782
3.736966	23.481	86.263
5.64385619	13.737	100

Mean size	sorting
3.54	7.601212

sa3

Core 8 sample 4

size	WT %	cumulative WT %
0	5.575	5.575
0.321928	5.022	10.597
0.736965	10.469	21.066
1.736966	28.401	49.467
2.736966	20.078	69.545
3.736966	15.339	84.884
5.64385619	15.116	100

Mean size	sorting
3.53	7.738227

sa4
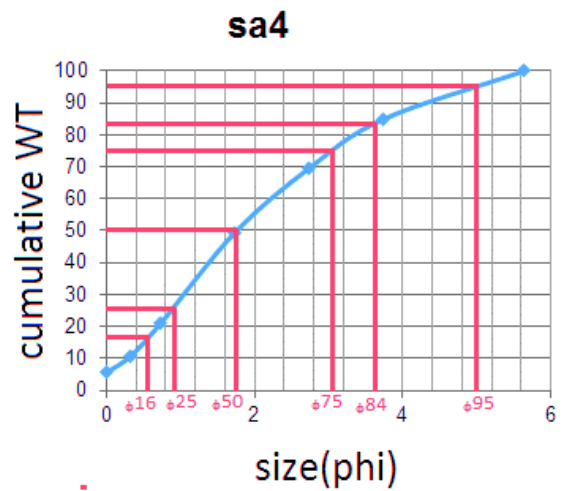
Core 8 sample 5

size	WT %	cumulative WT %
0	7.791	7.791
0.321928	2.314	10.105
0.736965	3.58	13.685
1.736966	13.61	27.295
2.736966	40.906	68.201
3.736966	22.597	90.798
5.64385619	9.202	100

Mean size	sorting
4.473	6.872477

sa5
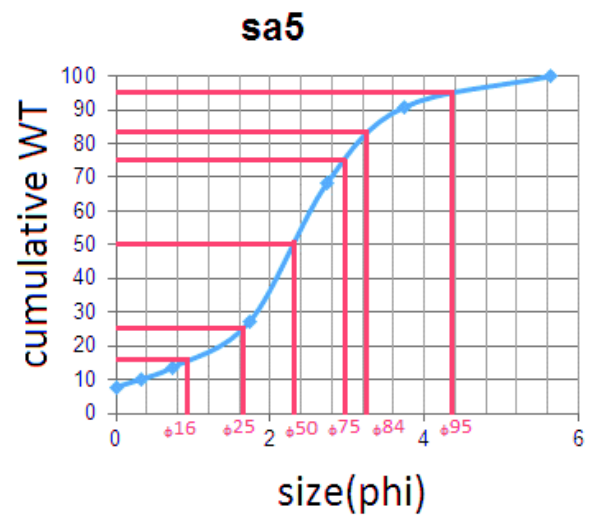
Core 8 sample 6

size	WT %	cumulative WT %
0	2.102	2.102
0.321928	1.637	3.739
0.736965	3.341	7.08
1.736966	14.67	21.75
2.736966	41.881	63.631
3.736966	27.373	91.004
5.64385619	8.996	100

Mean size	sorting
5.066	6.644068

sa6
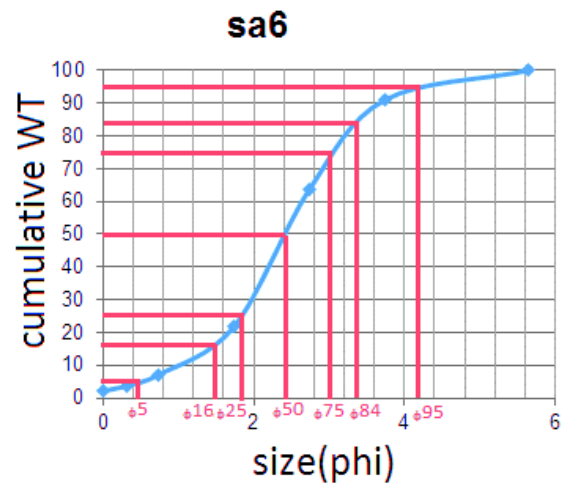
Core 8 sample 7

size	WT %	cumulative WT %
0	2.811	2.811
0.321928	2.381	5.192
0.736965	4.761	9.953
1.736966	18.791	28.744
2.736966	36.495	65.239
3.736966	24.988	90.227
5.64385619	9.773	100

Mean size	sorting
4.643333	6.827212
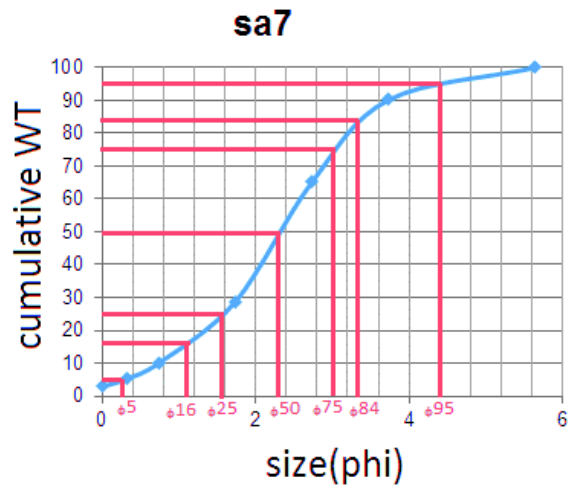
Core 8 sample 8

size	WT %	cumulative WT %
0	4.576	4.576
0.321928	4.191	8.767
0.736965	7.763	16.53
1.736966	24.216	40.746
2.736966	30.117	70.863
3.736966	19.961	90.824
5.64385619	9.176	100

Mean size	sorting
3.853667	6.859189

336
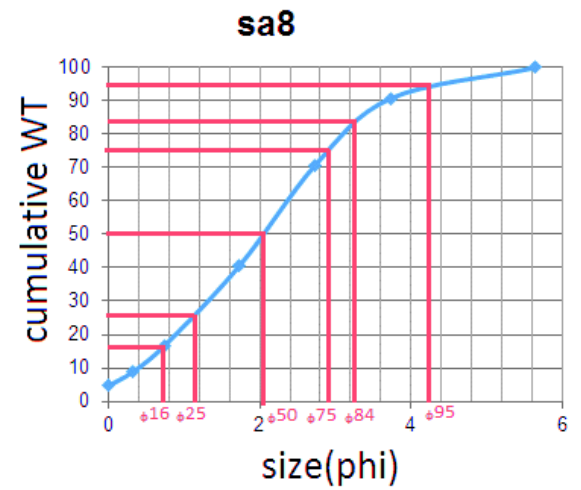
Core 8 sample 9

size	WT %	cumulative WT %
0	5.259	5.259
0.321928	4.712	9.971
0.736965	8.533	18.504
1.736966	23.677	42.181
2.736966	31.706	73.887
3.736966	18.695	92.582
5.64385619	7.418	100
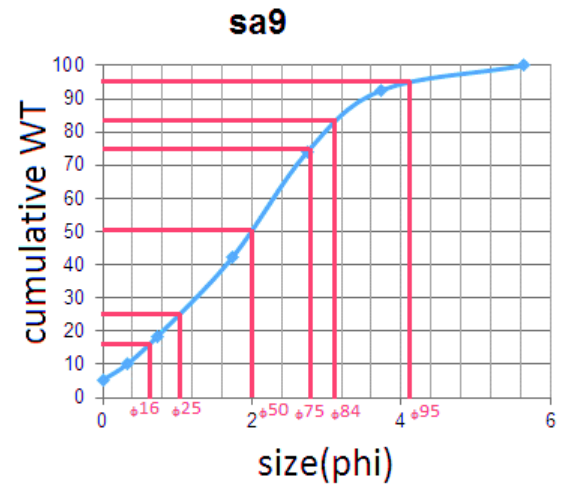
Mean size	sorting
3.786667	6.868432

Core 8 sample 10

size	WT %	cumulative WT %
0	47.888	47.888
0.321928	15.571	63.459
0.736965	10.567	74.026
1.736966	12.851	86.877
2.736966	8.662	95.539
3.736966	4.116	99.655
5.64385619	0.615	100.27
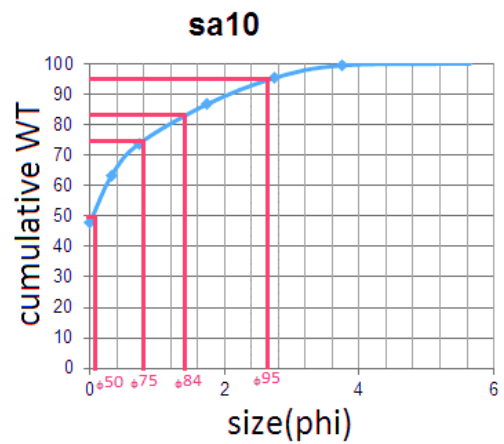
Mean size	sorting
0.343667	3.553182

Core 9 sample 1

size	WT %	cumulative WT %
0	30	30
0.321928	3.948	33.948
0.736965	6	39.948
1.736966	1.616	41.564
2.736966	17.006	58.57
3.736966	17.14	75.71
5.64385619	24.29	100
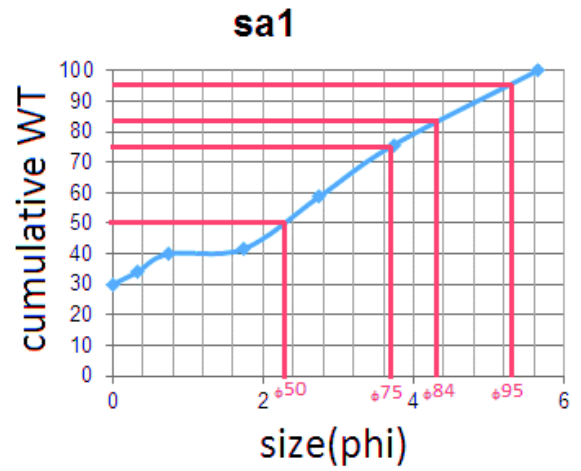
Mean size	sorting
3.281333	9.046121

sa1

Core 9 sample 2

size	WT %	cumulative WT %
0	2.866	2.866
0.321928	1.744	4.61
0.736965	2.286	6.896
1.736966	7.879	14.775
2.736966	8.924	23.699
3.736966	36.107	59.806
5.64385619	40.194	100
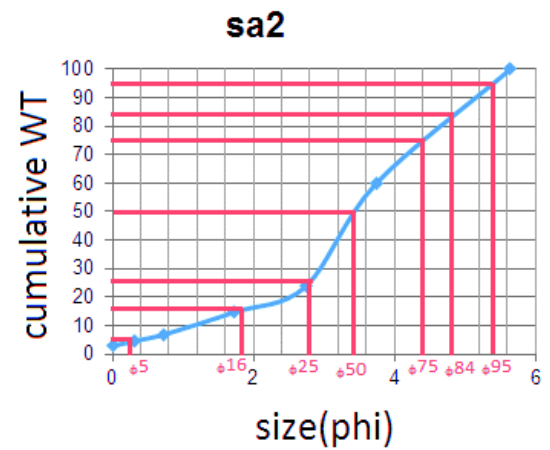
Mean size	sorting
7.052333	8.930379

sa2

338

Core 9 sample 3

size	WT %	Cumulative WT %
0	1.922	1.922
0.321928	0.988	2.91
0.736965	2.487	5.397
1.736966	22.663	28.06
2.736966	62.407	90.467
3.736966	7.156	97.623
5.64385619	2.377	100
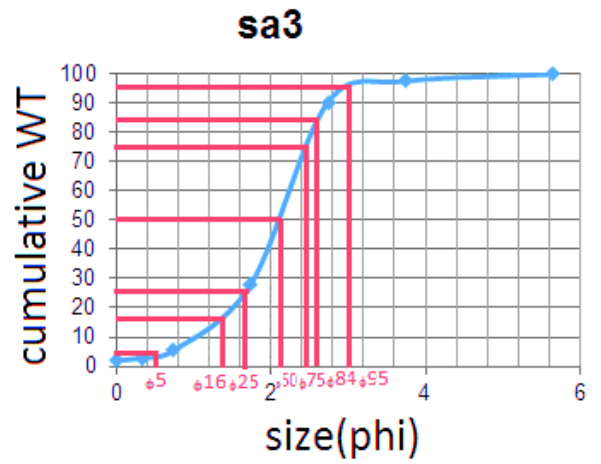
Mean size	sorting
4.39	4.889439

Core 9 sample 4

size	WT %	cumulative WT %
0	13.306	13.306
0.321928	7.608	20.914
0.736965	9.232	30.146
1.736966	17.168	47.314
2.736966	13.067	60.381
3.736966	25.112	85.493
5.64385619	14.507	100

Mean size	sorting
3.279	7.672144

Core 9 sample 5

size	WT %	cumulative WT %
0	5.608	5.608
0.321928	3.922	9.53
0.736965	5.718	15.248
1.736966	18.1	33.348
2.736966	28.262	61.61
3.736966	21.006	82.616
5.64385619	17.384	100
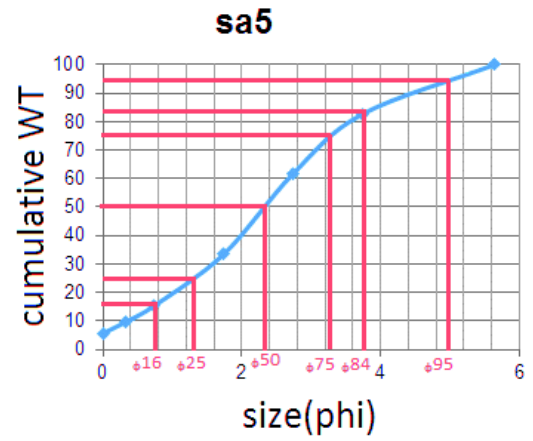
Mean size	sorting
4.378333	8.00303

Core 9 sample 6

size	WT %	cumulative WT %
0	3.909	3.909
0.321928	2.029	5.938
0.736965	3.91	9.848
1.736966	17.192	27.04
2.736966	46.686	73.726
3.736966	24.519	98.245
5.64385619	1.755	100
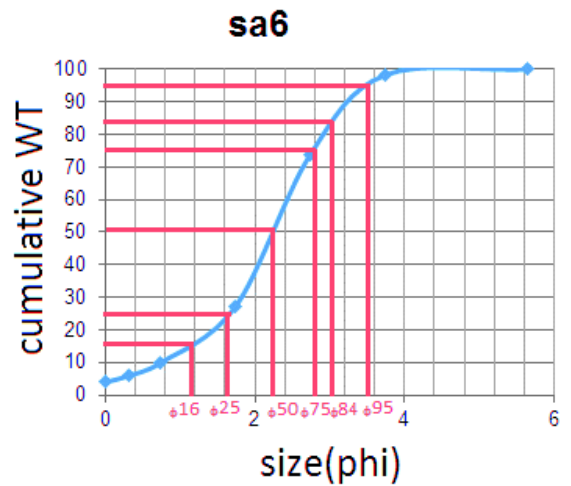
Mean size	sorting
4.378333	7.94303

Core 9 sample 7

size	WT %	cumulative WT %
0	1.839	1.839
0.321928	1.448	3.287
0.736965	2.941	6.228
1.736966	18.49	24.718
2.736966	52.466	77.184
3.736966	13.853	91.037
5.64385619	8.963	100
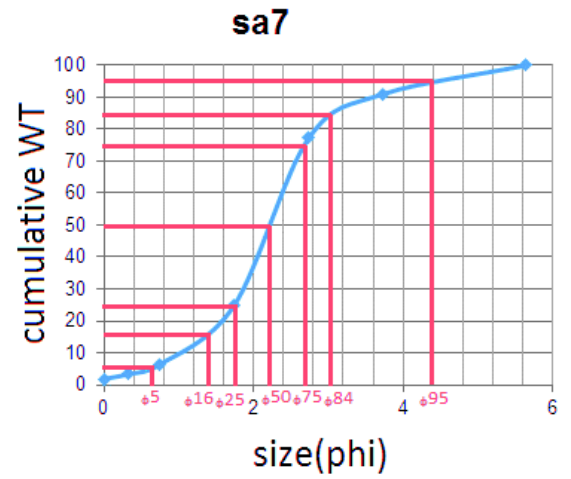
Mean size	sorting
4.645667	5.921045

Core 9 sample 8

size	WT %	cumulative WT %
0	0.434	0.434
0.321928	0.639	1.073
0.736965	2.108	3.181
1.736966	22.012	25.193
2.736966	67.129	92.322
3.736966	4.206	96.528
5.64385619	3.472	100
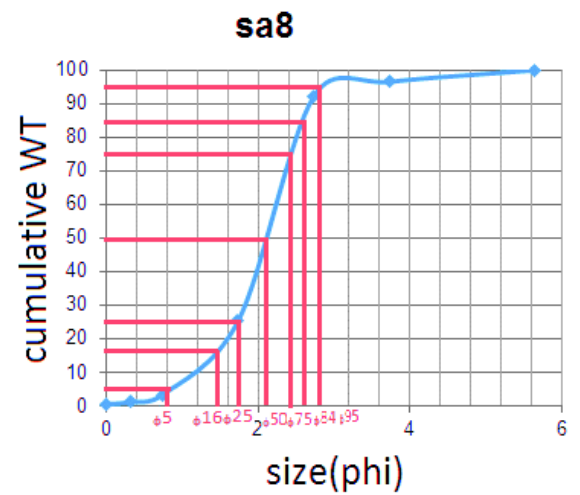
Mean size	sorting
4.746667	6.8925

Core 9 sample 9

size	WT %	cumulative WT %
0	1.408	1.408
0.321928	1.524	2.932
0.736965	3.903	6.835
1.736966	30.593	37.428
2.736966	56.744	94.172
3.736966	3.622	97.794
5.64385619	2.206	100

Mean size	sorting
3.97	4.647561
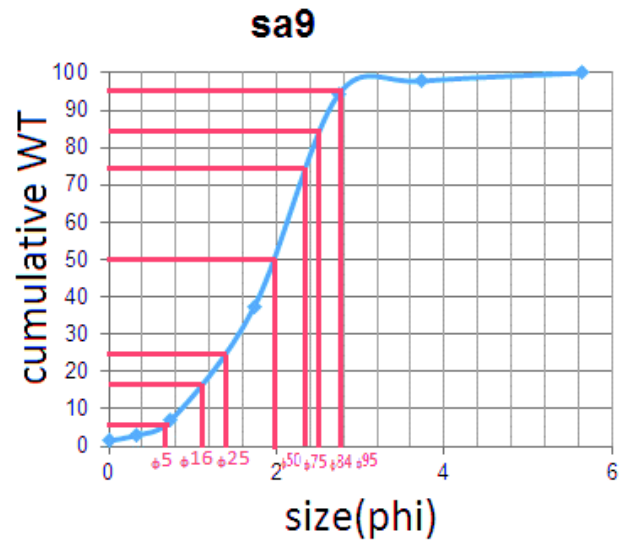
Core 9 sample 10

size	WT %	cumulative WT %
0	3.509	3.509
0.321928	1.295	4.804
0.736965	2.69	7.494
1.736966	17.405	24.899
2.736966	47.067	71.966
3.736966	22.487	94.453
5.64385619	5.547	100

Mean size	sorting
4.756	6.198659
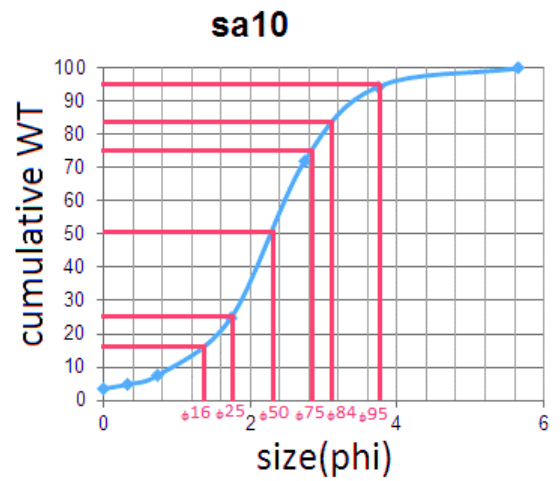
Core 9 sample 11

size	WT %	cumulative WT %
0	3.315	3.315
0.321928	2.344	5.659
0.736965	4.935	10.594
1.736966	16.751	27.345
2.736966	44.147	71.492
3.736966	24.123	95.615
5.64385619	4.385	100

Mean size	sorting
4.538533	6.145212

sa11
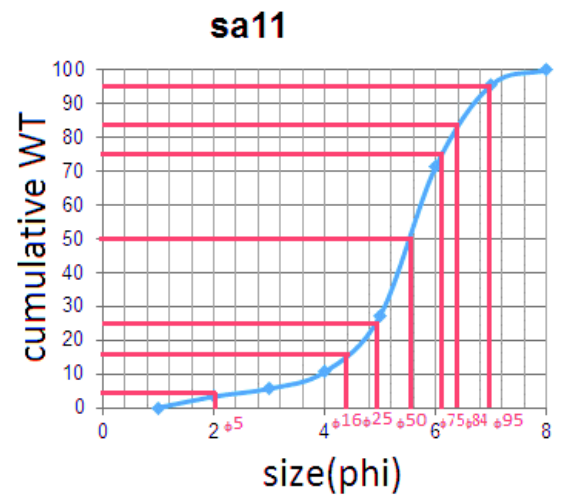
Core 10 sample 1

size	WT %	cumulative WT %
0	6.218	6.218
0.321928	4.247	10.465
0.736965	5.447	15.912
1.736966	10.081	25.993
2.736966	6.807	32.8
3.736966	31.491	64.291
5.64385619	35.709	100

Mean size	sorting
5.437333	9.155152

sa1
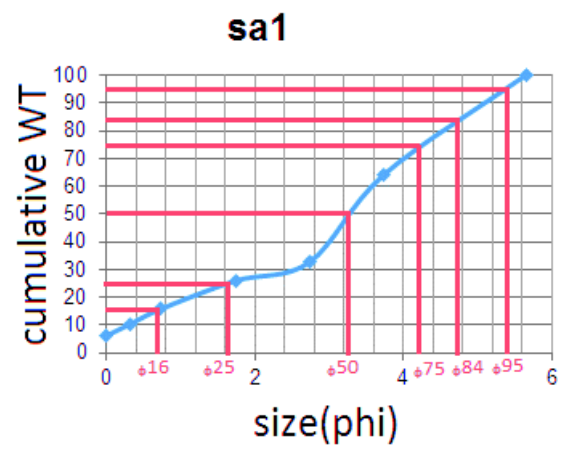
Core 10 sample 2

size	WT %	cumulative WT %
0	11.452	11.452
0.321928	5.568	17.02
0.736965	7.146	24.166
1.736966	15.77	39.936
2.736966	15.462	55.398
3.736966	26.091	81.489
5.64385619	18.511	100
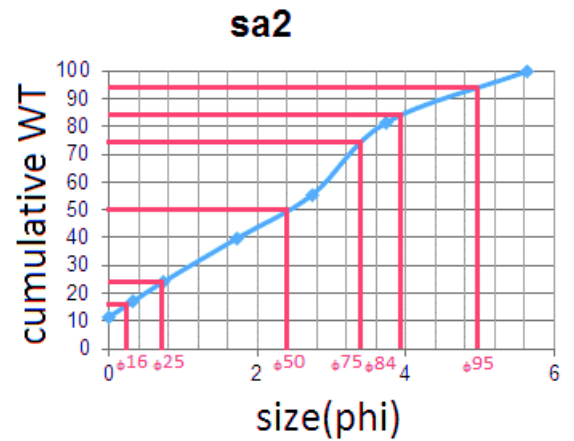
Mean size	sorting
1290.38	8.093182

Core 10 sample 3

size	WT %	cumulative WT %
0	10.549	10.549
0.321928	4.603	15.152
0.736965	6.955	22.107
1.736966	14.546	36.653
2.736966	17.9	54.553
3.736966	23.196	77.749
5.64385619	22.251	100
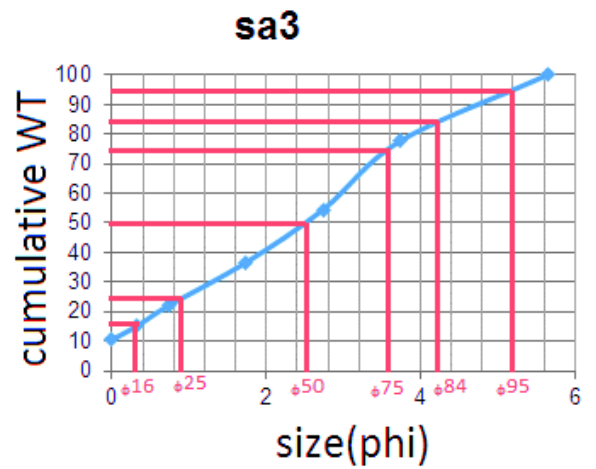
Mean size	sorting
4.99	7.655432

Core 10 sample 4

size	WT %	cumulative WT %
0	13.758	13.758
0.321928	4.032	17.79
0.736965	5.453	23.243
1.736966	14.843	38.086
2.736966	19.629	57.715
3.736966	21.844	79.559
5.64385619	20.441	100

Mean size	sorting
3.501667	7.650432

sa4
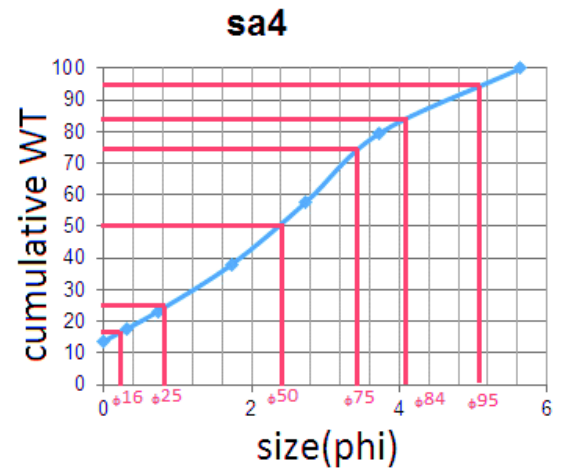
Core 10   sample 5

size	WT %	cumulative WT %
0	10.065	10.065
0.321928	5.696	15.761
0.736965	9.239	25
1.736966	19.811	44.811
2.736966	20.169	64.98
3.736966	20.92	85.9
5.64385619	14.1	100

Mean size	sorting
3.571333	7.642705

sa5

345
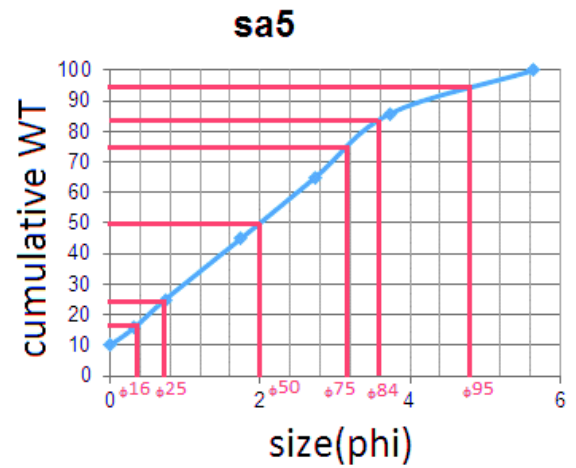
Core 10 sample 6

size	WT %	cumulative WT %
0	22.967	22.967
0.321928	6.79	29.757
0.736965	8.252	38.009
1.736966	14.72	52.729
2.736966	11.574	64.303
3.736966	19.403	83.706
5.64385619	16.294	100

sa6
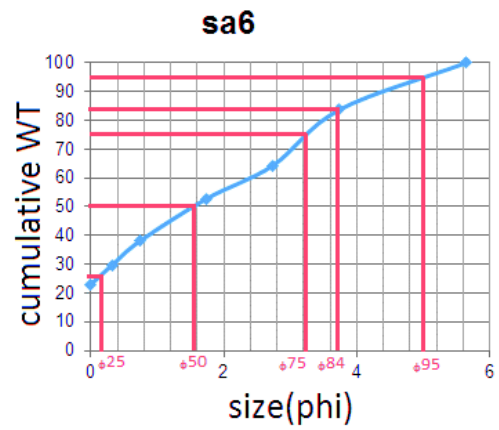
Mean size	sorting
2.558	8.056432

Core 10 sample 7

size	WT %	cumulative WT %
0	22.427	22.427
0.321928	11.185	33.612
0.736965	13.982	47.594
1.736966	23.76	71.354
2.736966	12.991	84.345
3.736966	10.598	94.943
5.64385619	5.057	100

sa7
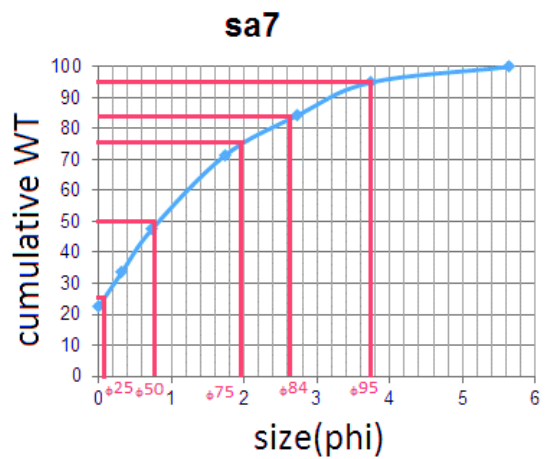
Mean size	sorting
1.598333	5.682985

Core 10 sample 8

size	WT %	cumulative WT %
0	5.061	5.061
0.321928	4.958	10.019
0.736965	8.251	18.27
1.736966	21.226	39.496
2.736966	36.676	76.172
3.736966	19.194	95.366
5.64385619	4.634	100

sa8
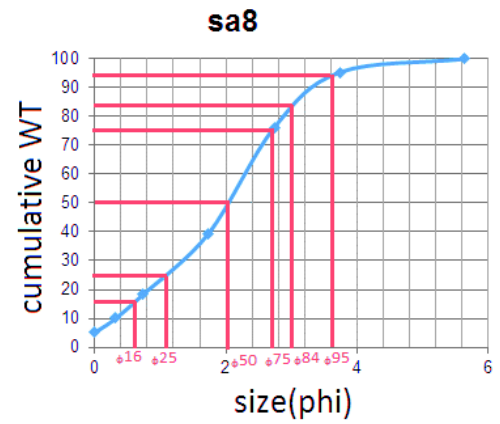
Mean size	sorting
3.072667	6.393205

Core 10 sample 9

size	WT %	cumulative WT %
0	5.049	5.049
0.321928	3.466	8.515
0.736965	6.746	15.261
1.736966	19.703	34.964
2.736966	34.84	69.804
3.736966	22.215	92.019
5.64385619	7.981	100

sa9
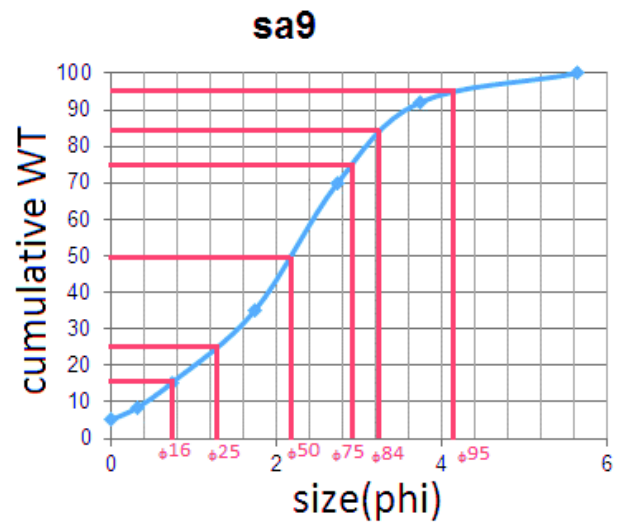
Mean size	sorting
4.067333	6.683636

Core 10 sample 10

size	WT %	cumulative WT %
0	5.379	5.379
0.321928	3.316	8.695
0.736965	5.837	14.532
1.736966	21.458	35.99
2.736966	39.146	75.136
3.736966	23.372	98.508
5.64385619	1.492	100

Mean size	sorting
3.975667	6.014902
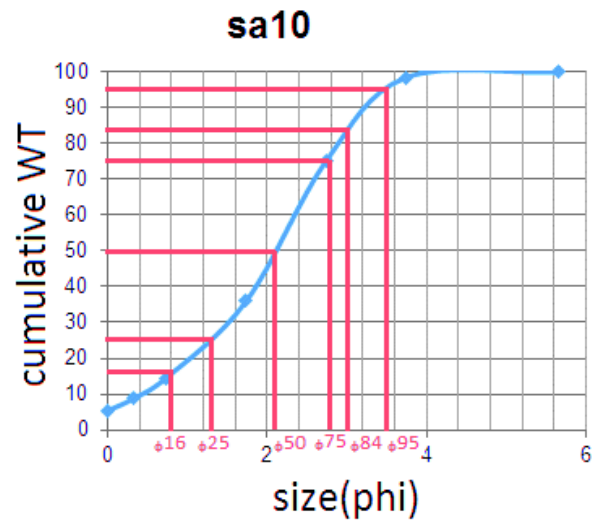
Core 11 sample 1

size	WT%	cumulative WT%
0	11.988	11.988
0.321928	4.821	16.809
0.736965	7.175	23.984
1.736966	23.451	47.435
2.736966	26.101	73.536
3.736966	15.357	88.893
5.64385619	11.107	100

Mean size	sorting
3.0551	7.308591
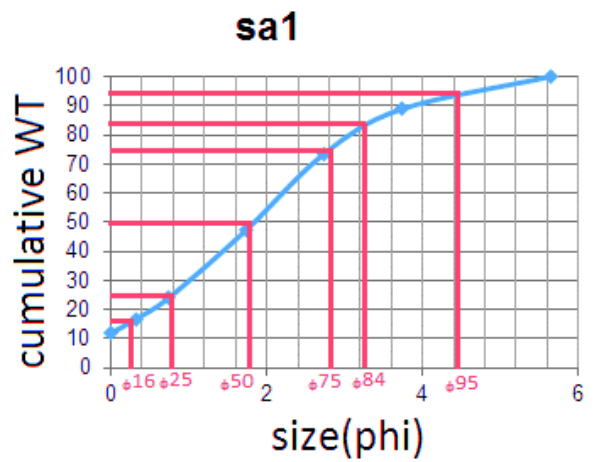
Core 11 sample 2

size	WT %	cumulative WT %
0	10.002	10.002
0.321928	6.29	16.292
0.736965	11.833	28.125
1.736966	32.391	60.516
2.736966	23.359	83.875
3.736966	7.461	91.336
5.64385619	8.664	100
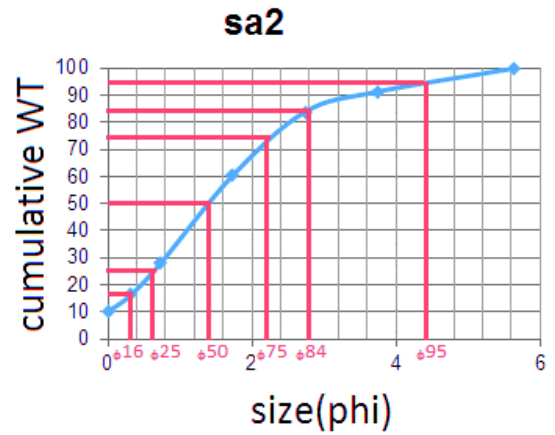
Mean size	sorting
2.603333	6.83197

Core 11 sample 3

size	WT %	cumulative WT %
0	10.086	10.086
0.321928	9.937	20.023
0.736965	15.85	35.873
1.736966	30.433	66.306
2.736966	12.631	78.937
3.736966	9.7	88.637
5.64385619	11.363	100
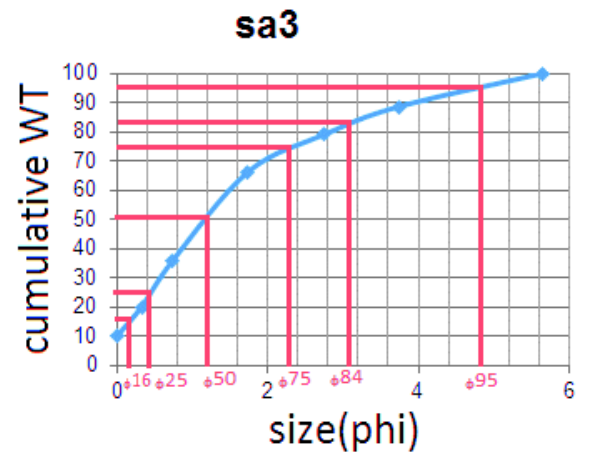
Mean size	sorting
2.411333	6.962644

Core 11 sample 4

size	WT %	cumulative WT %
0	21.078	21.078
0.321928	7.295	28.373
0.736965	10.255	38.628
1.736966	21.391	60.019
2.736966	12.408	72.427
3.736966	9.7	82.127
5.64385619	11.363	93.49

sa4
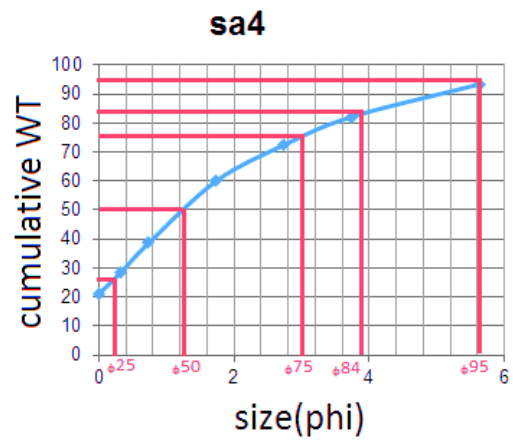
Mean size	sorting
2.26	8.868258

Core 11 sample 5

size	WT %	cumulative WT %
0	40.677	40.677
0.321928	8.696	49.373
0.736965	10.204	59.577
1.736966	17.489	77.066
2.736966	10.146	87.212
3.736966	7.402	94.614
5.64385619	5.386	100

sa5

Mean size	sorting
1.133333	5.394

350
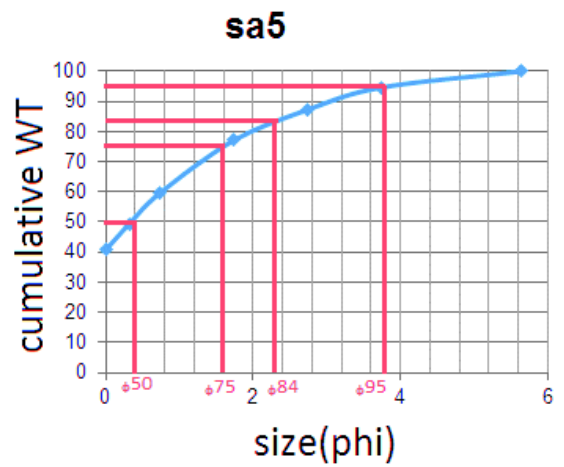
Core 11 sample 6

size	WT %	cumulative WT %
0	0.848	0.848
0.321928	1.313	2.161
0.736965	4.696	6.857
1.736966	34.518	41.375
2.736966	54.704	96.079
3.736966	2.3	98.379
5.64385619	1.621	100
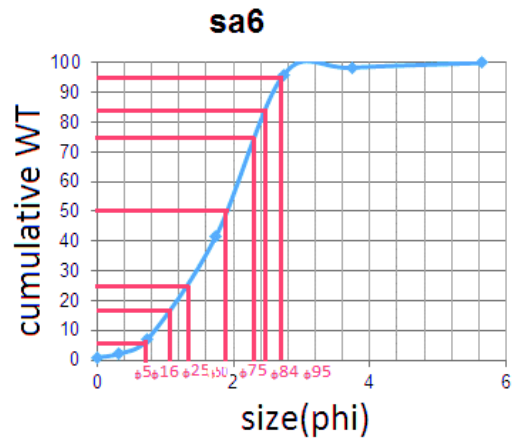
Mean size	sorting
3.826667	4.614773

Core 11 sample 7

size	WT %	cumulative WT %
0	13.269	13.269
0.321928	10.165	23.434
0.736965	14.999	38.433
1.736966	28.467	66.9
2.736966	14.591	81.491
3.736966	8.007	89.498
5.64385619	10.502	100
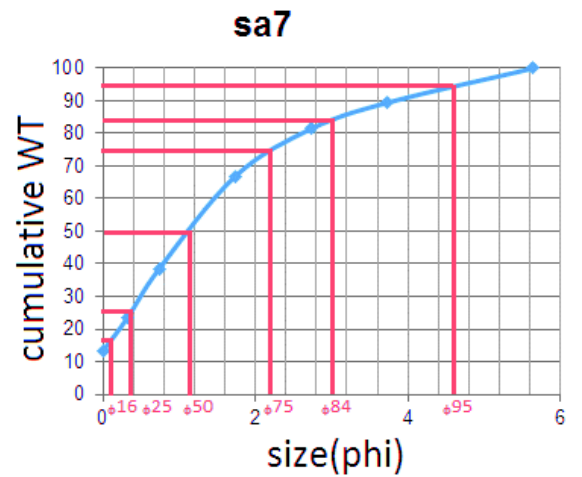
Mean size	sorting
2.168	6.854667

Core 11 sample 8

size	WT %	cumulative WT %
0	7.155	7.155
0.321928	3.783	10.938
0.736965	6.379	17.317
1.736966	17.027	34.344
2.736966	19.941	54.285
3.736966	26.131	80.416
5.64385619	19.584	100

Mean size	sorting
4.503333	8.117197
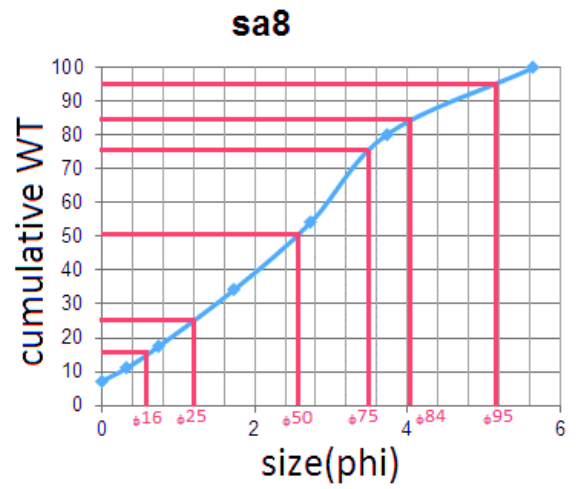
Core 11 sample 9

size	WT %	Cumulative WT %
0	4.078	4.078
0.321928	2.223	6.301
0.736965	3.898	10.199
1.736966	13.951	24.15
2.736966	19.363	43.513
3.736966	30.763	74.276
5.64385619	25.724	100

Mean size	sorting
5.521667	8.403295
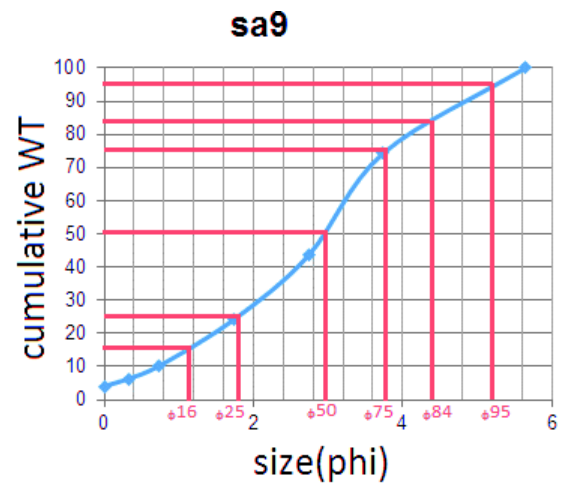
Core 11 sample 10

size	WT %	cumulative WT %
0	7.479	7.479
0.321928	3.866	11.345
0.736965	6.738	18.083
1.736966	16.711	34.794
2.736966	19.754	54.548
3.736966	30.446	84.994
5.64385619	15.006	100

Mean size	sorting
4.395333	7.523212

sa10
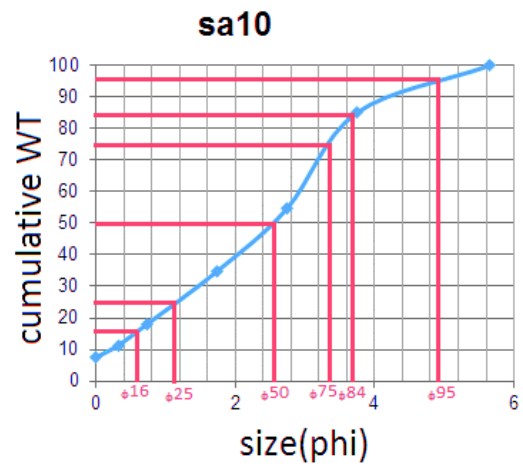
Core 11 sample 11

size	WT %	cumulative WT %
0	13.374	13.374
0.321928	4.919	18.293
0.736965	6.201	24.494
1.736966	14.968	39.462
2.736966	18.022	57.484
3.736966	25.313	82.797
5.64385619	17.203	100

Mean size	sorting
3.802	7.975182

sa11

353
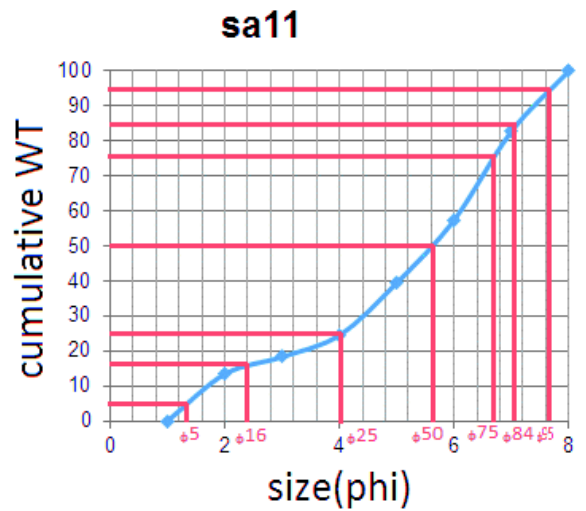
Core 11 sample 12

size	WT %	cumulative WT %
0	10.711	10.711
0.321928	3.694	14.405
0.736965	5.85	20.255
1.736966	14.821	35.076
2.736966	18.712	53.788
3.736966	29.811	83.599
5.64385619	16.401	100

Mean size	sorting
4.276667	7.708561
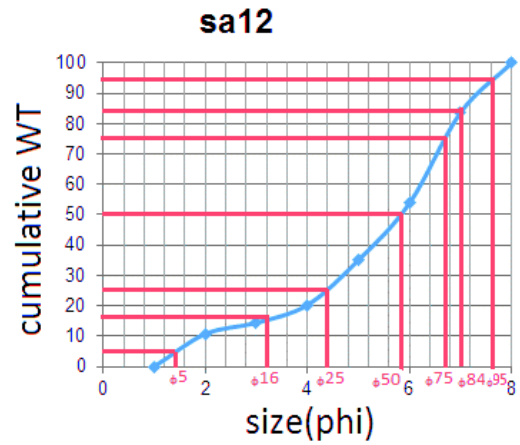
Core 12 sample 1

size	WT %	cumulative WT%
0	9.854	9.854
0.321928	5.75	15.604
0.736965	8.798	24.402
1.736966	20.983	45.385
2.736966	27.509	72.894
3.736966	14.455	87.349
5.64385619	12.651	100

Mean size	sorting
3.075333	7.631083
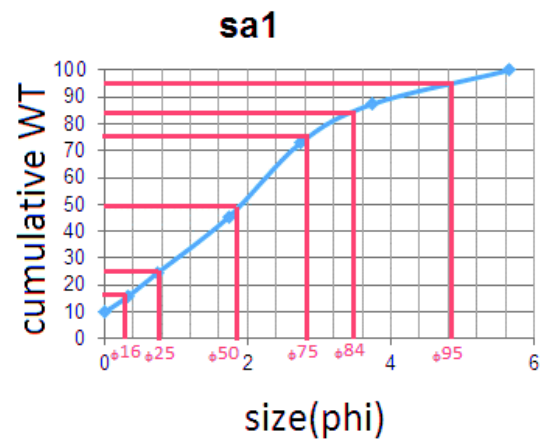
Core 12 sample 2

size	WT %	cumulative WT %
0	4.632	4.632
0.321928	4.193	8.825
0.736965	9.161	17.986
1.736966	43.668	61.654
2.736966	28.44	90.094
3.736966	7.465	97.559
5.64385619	2.441	100
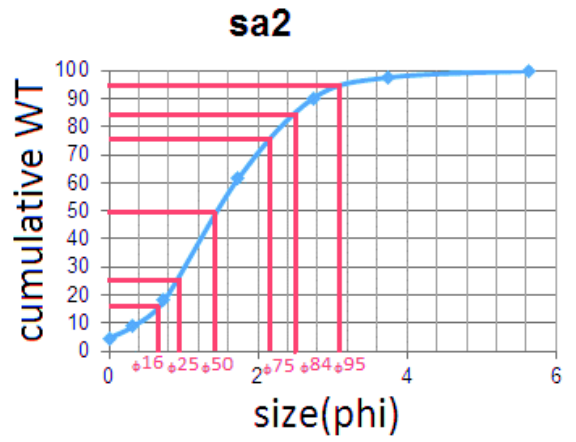
Mean size	sorting
2.826667	5.420303

Core 12 sample 3

size	WT %	cumulative WT %
0	8.819	8.819
0.321928	3.271	12.09
0.736965	5.559	17.649
1.736966	25.105	42.754
2.736966	50.012	92.766
3.736966	4.888	97.654
5.64385619	2.346	100
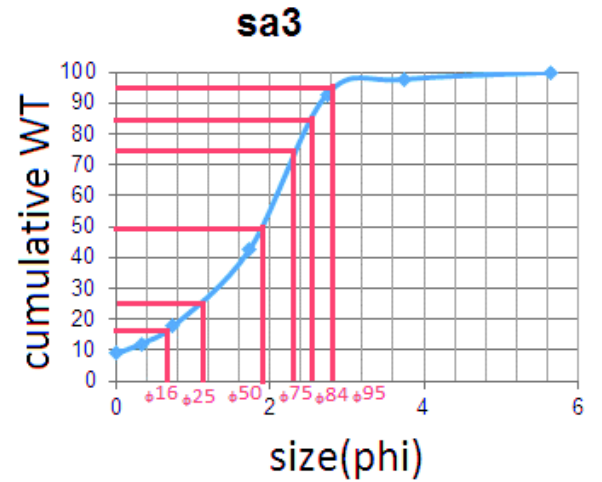
Mean size	sorting
3.339667	5.02425

355

Core 12 sample 4

size	WT %	cumulative WT %
0	2.539	2.539
0.321928	3.144	5.683
0.736965	5.949	11.632
1.736966	15.052	26.684
2.736966	10.793	37.477
3.736966	22.711	60.188
5.64385619	39.812	100

Mean size	sorting
5.936667	9.46303
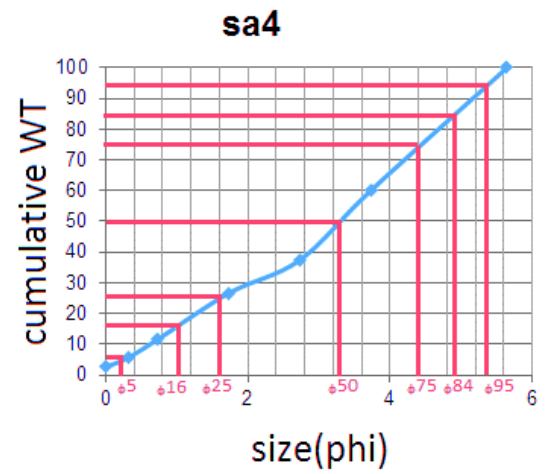
Core 12 sample 5

size	WT %	cumulative WT %
0	4.68	4.68
0.321928	6.167	10.847
0.736965	11.747	22.594
1.736966	32.955	55.549
2.736966	35.854	91.403
3.736966	5.662	97.065
5.64385619	2.935	100

Mean size	sorting
3.553333	4.313409

356
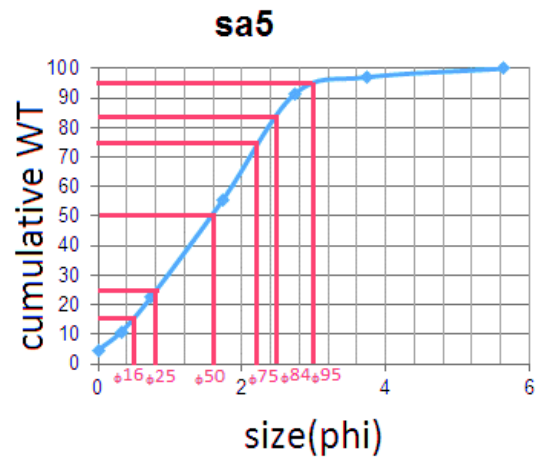
Core 12 sample 6

size	WT %	cumulative WT %
0	11.792	11.792
0.321928	4.069	15.861
0.736965	5.672	21.533
1.736966	14.261	35.794
2.736966	31.853	67.647
3.736966	18.887	86.534
5.64385619	13.466	100

sa6
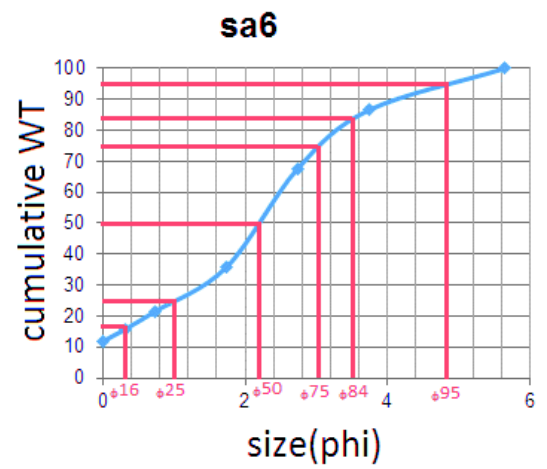
Mean size	sorting
3.71	7.66803

Core 12 sample 7

size	WT %	cumulative WT %
0	15.062	15.062
0.321928	5.53	20.592
0.736965	7.774	28.366
1.736966	21.463	49.829
2.736966	18.533	68.362
3.736966	20.752	89.114
5.64385619	10.886	100

sa7
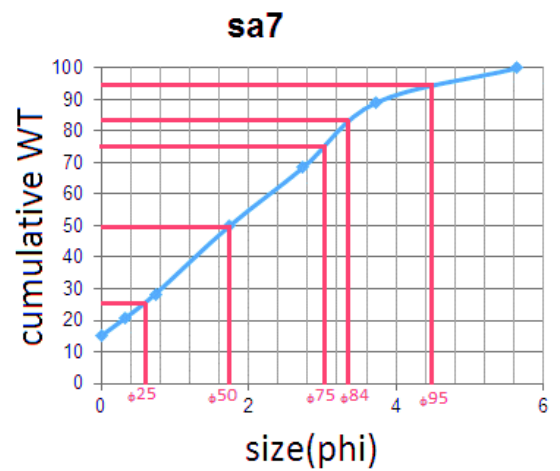
Mean size	sorting
2.964333	7.324447

357

Core 12 sample 8

size	WT %	cumulative WT %
0	2.008	2.008
0.321928	2.098	4.106
0.736965	4.8	8.906
1.736966	15.069	23.975
2.736966	22.651	46.626
3.736966	37.649	84.275
5.64385619	15.725	100

Mean size	sorting
5.293333	7.278864

sa8
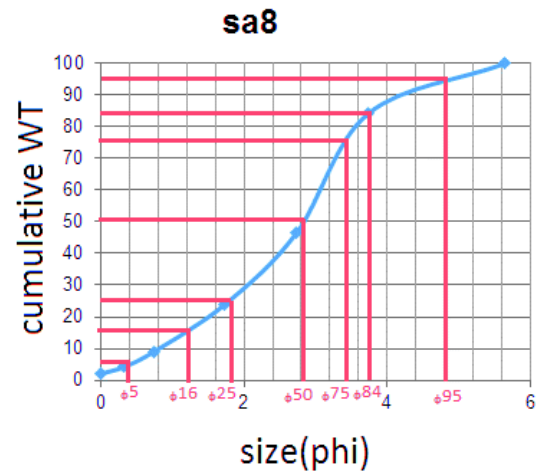
Core 12 sample 9

size	WT %	cumulative WT %
0	0.623	0.623
0.321928	0.674	1.297
0.736965	2.252	3.549
1.736966	13.422	16.971
2.736966	20.545	37.516
3.736966	46.18	83.696
5.64385619	16.304	100

Mean size	sorting
5.926667	7.091667

sa9
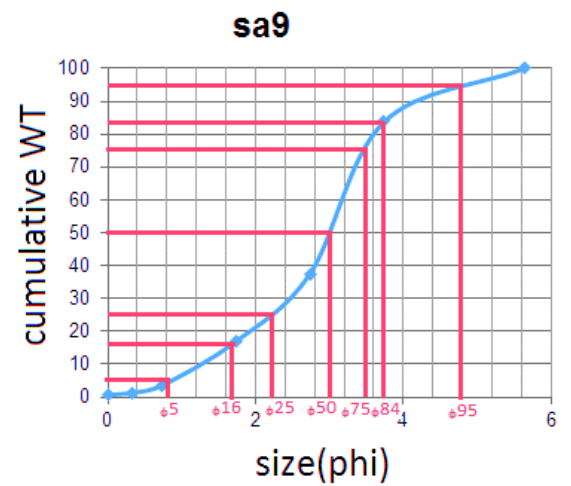
Core 12 sample 10

size	WT %	cumulative WT %
0	1.645	1.645
0.321928	1.656	3.301
0.736965	2.486	5.787
1.736966	5.867	11.654
2.736966	9.46	21.114
3.736966	65.026	86.14
5.64385619	13.86	100

sa10
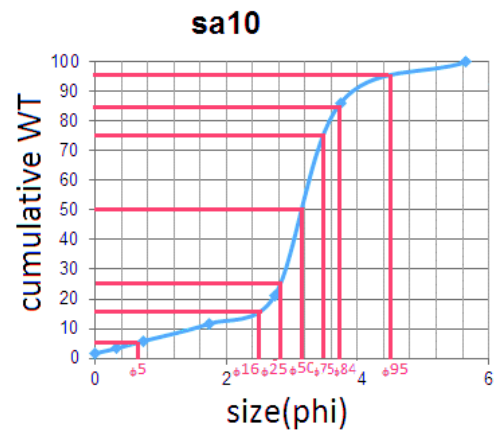
Mean size	sorting
7.02	6.731061

Core 12 sample 11

size	WT %	cumulative WT %
0	18.281	18.281
0.321928	6.467	24.748
0.736965	9.038	33.786
1.736966	20.24	54.026
2.736966	19.068	73.094
3.736966	14.157	87.251
5.64385619	12.749	100

sa11
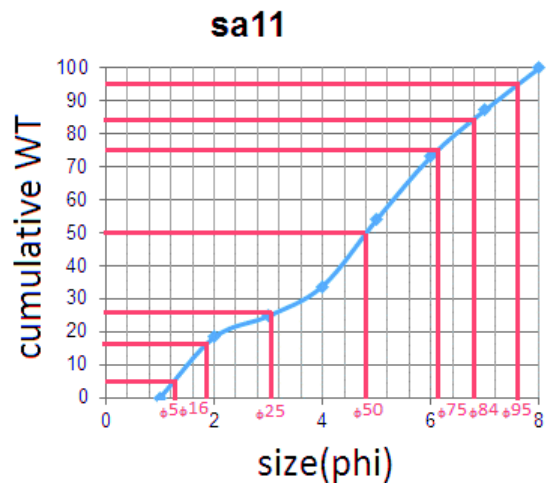
Mean size	sorting
2.56	7.622273

Core 12 sample 12

size	WT %	cumulative WT %
0	12.174	12.174
0.321928	6.325	18.499
0.736965	9.701	28.2
1.736966	27.948	56.148
2.736966	35.438	91.586
3.736966	4.988	96.574
5.64385619	3.426	100

Mean size	sorting
2.57	5.132727
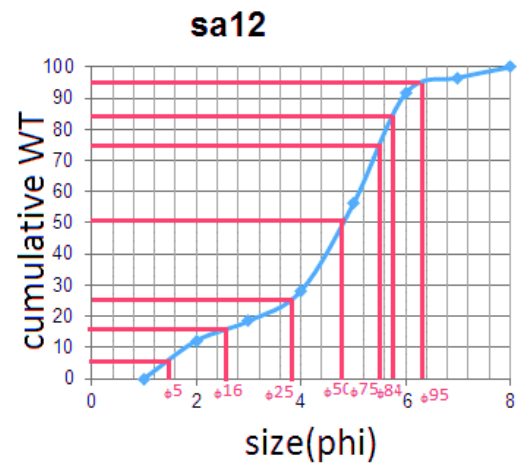
Core 12 sample 13

size	WT %	cumulative WT %
0	12.735	12.735
0.321928	4.881	17.616
0.736965	6.162	23.778
1.736966	14.451	38.229
2.736966	22.015	60.244
3.736966	29.012	89.256
5.64385619	10.744	100

Mean size	sorting
3.713333	7.26053
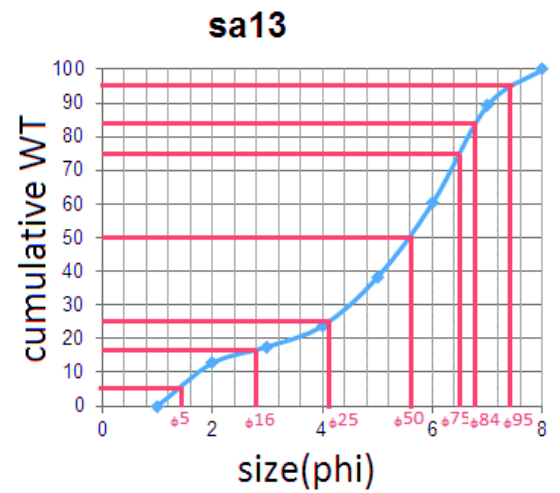
Core 12 sample 14

size	WT %	cumulative WT %
0	2.5	2.5
0.321928	2.196	4.696
0.736965	4.124	8.82
1.736966	16.57	25.39
2.736966	35.652	61.042
3.736966	25.582	86.624
5.64385619	13.376	100
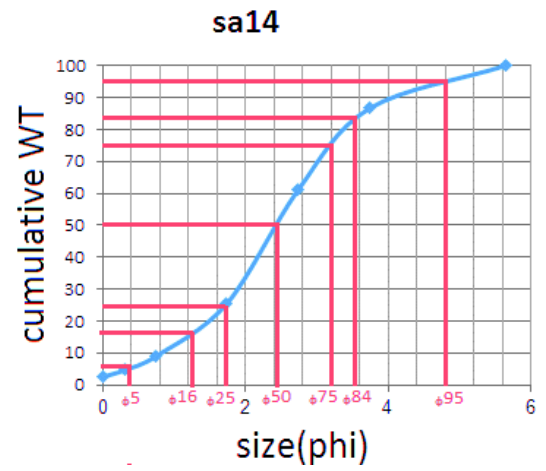
Mean size	sorting
4.916667	7.232955

Core 12 sample 15

size	WT %	cumulative WT %
0	6.321	6.321
0.321928	3.465	9.786
0.736965	5.701	15.487
1.736966	15.566	31.053
2.736966	35.536	66.589
3.736966	29.898	96.487
5.64385619	3.513	100
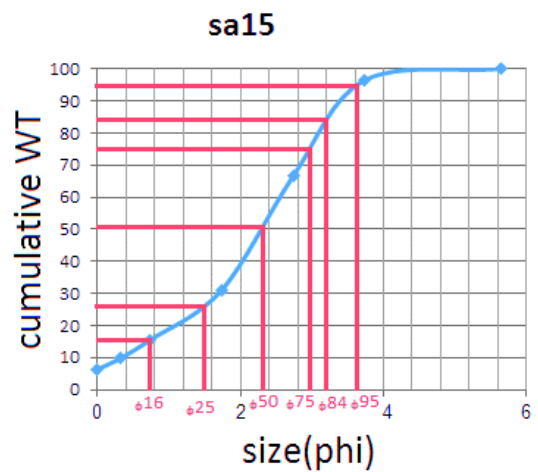
Mean size	sorting
4.136667	6.443788

361

Core 12 sample 16

size	WT %	cumulative WT %
0	4.265	4.265
0.321928	2.435	6.7
0.736965	5.084	11.784
1.736966	15.797	27.581
2.736966	37.109	64.69
3.736966	32.643	97.333
5.64385619	2.667	100

Mean size	sorting
4.543333	6.332348

sa16
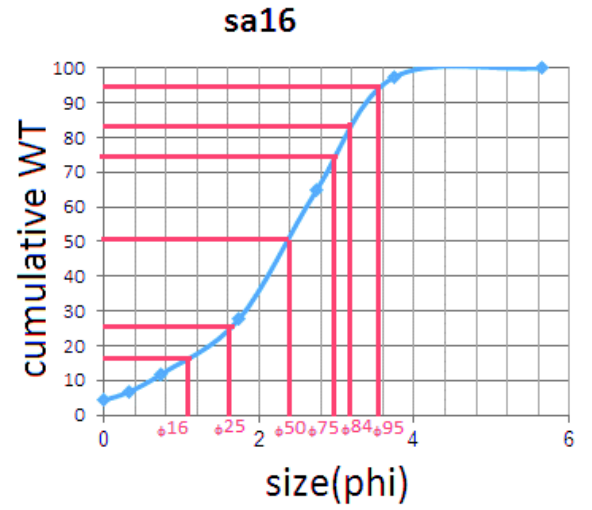
Appendix E : Radiocarbon dating samples calibrated with Oxcal 2009

Table 1: Radiocarbon dating samples and calibrate date in Kafr Saber site using OxCal v4.2 (Bronk Ramsey 2013)

No.	Sample name	Laboratory Name	Type of samples	Depth (m)	Date BP	Calibrated. date
1	RHSX	Poznan	Dendropoma	Boulder	8380 ± 40 BP	7597-6812 BC
2	KSB2S2	Poznan	Dendropoma	Boulder	890 ± 30 BP	940-1446 AD
3	TSU P1 S07B	Poznan	Charcoal	35	110.14±0.3 BP	Modern
4	TSUP1 S09B	CIRAM	Charcoal	53	40560 BP	39000-38250 BC
5	TSU P3S2	CIRAM	charcoal	73	1075 ± 30 BP	890 – 1020 AD
6	TSU P3S3	CIRAM	Charcoal	100	6240 BP	5300 – 5070 BC
7	TSU P4 S4	CIRAM	Charcoal	15	Modern	-
8	TSU P4 S6	Poznan	Charcoal	25	101.42 ± 0.68 BP	1700 – 1920 AD
9	TSU P4 S3	CIRAM	Charcoal	41	Modern	-
10	TSU P4 S5	Poznan	Charcoal	60	15490 ± 70 BP	17200 – 15900 BC
11	TSU P4 S2	CIRAM	Charcoal	61	Modern	-
12	TSU P5S1	Poznan	Charcoal	12	2145 ± 30 BP	360 – 50BC
13	TSU P5S3	Poznan	Charcoal	17	2060 ± 35 BP	180 – 30 AD
14	TSU P5S4	Poznan	Charcoal	33	2590 ± 140 BP	1050 – 350 BC
15	TSU P5S2	Poznan	Charcoal	37	4560 ± 300 BP	4000 – 2400 BC

Figure 1:

Atmospheric data from Stuiver et al. (1998); OxCal v3.5 Bronk Ramsey (2000); cub r:4 sd:12 prob usp[chron]

KS B2S2 : 890±30BP

68.2% probability
1040AD (22.0%) 1090AD
1120AD (11.6%) 1140AD
1150AD (34.6%) 1220AD
95.4% probability
1030AD (95.4%) 1220AD

Radiocarbon determination: 1100BP, 1000BP, 900BP, 800BP, 700BP, 600BP

Calibrated date: 900CalAD 1000CalAD 1100CalAD 1200CalAD 1300CalAD 1400CalAD

Figure 2:

Atmospheric data from Stuiver et al. (1998); OxCal v3.5 Bronk Ramsey (2000); cub r:4 sd:12 prob usp[chron]

TSU P1 S07B : 110±0BP

68.2% probability
1690AD (22.6%) 1710AD
1720AD (8.6%) 1730AD
1810AD (17.4%) 1850AD
1870AD (12.0%) 1890AD
1910AD (7.6%) 1920AD
95.4% probability
1690AD (23.5%) 1710AD
1720AD (9.5%) 1730AD
1810AD (53.7%) 1890AD
1910AD (8.7%) 1920AD

Radiocarbon determination: 300BP, 200BP, 100BP, 0BP

Calibrated date: 1600CalAD 1700CalAD 1800CalAD 1900CalAD 2000CalAD

Figure 3:

Atmospheric data from Stuiver et al. (1998); OxCal v3.5 Bronk Ramsey (2000); cub r:4 sd:12 prob usp[chron]

P1S09B : 40560±180BP

68.2% probability
38800BC (68.2%) 38430BC
95.4% probability
39000BC (95.4%) 38250BC

Relative probability: 0.0, 0.2, 0.4, 0.6, 0.8

Calendar date: 39500BC 39000BC 38500BC 38000BC 37500BC

365

TSU P3S2 : 2000±25BP

Atmospheric data from Stuiver et al. (1998); OxCal v3.5 Bronk Ramsey (2000); cub r:4 sd:12 prob usp[chron]

68.2% probability
40BC (60.5%) 30AD
40AD (7.7%) 50AD
95.4% probability
50BC (95.4%) 70AD

TSU P3S3 : 6240±30BP

Atmospheric data from Stuiver et al. (1998); OxCal v3.5 Bronk Ramsey (2000); cub r:4 sd:12 prob usp[chron]

68.2% probability
5300BC (47.9%) 5200BC
5170BC (14.0%) 5140BC
5110BC (3.2%) 5100BC
5090BC (3.0%) 5080BC
95.4% probability
5300BC (55.1%) 5200BC
5180BC (40.3%) 5070BC

TSU P3S2 : 1075±30BP

Atmospheric data from Stuiver et al. (1998); OxCal v3.5 Bronk Ramsey (2000); cub r:4 sd:12 prob usp[chron]

68.2% probability
900AD (18.9%) 920AD
960AD (49.3%) 1020AD
95.4% probability
890AD (95.4%) 1020AD

366

TSU P4 S5 : 15490±70BP

68.2% probability
16850BC (68.2%) 16250BC
95.4% probability
17200BC (95.4%) 15900BC

Radiocarbon determination

16500BP
16000BP
15500BP
15000BP
14500BP

18000CalBC   17000CalBC   16000CalBC   15000CalBC
Calibrated date

TSU P4 S6 : 101±1BP

68.2% probability
1700AD (27.0%) 1730AD
1810AD (31.2%) 1830AD
1880AD (4.1%) 1890AD
1910AD (5.8%) 1920AD
95.4% probability
1700AD (36.9%) 1730AD
1810AD (35.0%) 1840AD
1880AD (12.8%) 1890AD
1900AD (10.7%) 1920AD

Radiocarbon determination

300BP
200BP
100BP
0BP

1600CalAD   1700CalAD   1800CalAD   1900CalAD   2000CalAD
Calibrated date

TSU P5S1 : 2145±30BP

68.2% probability
350BC (14.7%) 320BC
230BC (1.8%) 220BC
210BC (51.7%) 110BC
95.4% probability
360BC (21.7%) 290BC
240BC (73.7%) 50BC

Radiocarbon determination

2400BP
2300BP
2200BP
2100BP
2000BP
1900BP

400CalBC   200CalBC   CalBC/CalAD   200CalAD
Calibrated date

Table 2: Radiocarbon dating samples and calibrate date in El Alamein site using OxCal v4.2.4 (Bronk Ramsey 2013)

No.	Sample name	Laboratory Name	Type of samples	Depth (m)	Date BP	Calibrated date (2σ)
1	core 1/1sa1	Poznan	charcoal	40	13430±60	13985-14415 BC
2	core 1/1sa2	Poznan	Bone	50	1540±60	403-634 AD
3	core2/1sa6	Poznan	gastropods	75	32000±360	32971-34681 BC
4	core2/1sa4	Poznan	gastropods	77	35500±500	34362-36931 BC
5	core 3/1sa2	Poznan	bivalve	37	45000±2000	43618 BC
6	core 3/1sa1	Poznan	shell	45	33500±600	34218- 37224 BC
7	core 4/1sa1	Poznan	shell	28	31840±350	32887-34447BC
8	core 5/1sa3	Poznan	gastropod +shell	50	446600±1400	442182-448237 BC
9	core 6/1 sa6	Poznan	gastropod	45	34000±400	35002-37441 BC
10	core 6/1sa9	Poznan	coral	60	50000±4000	42776-69225 BC
11	core 6/2 sa1	Poznan	charcoal	80	125±30	1620 AD
12	core 7/1 sa1	Poznan	shell	17	3000±30	293-1113 BC
13	core 9/1sa1	Poznan	gastropod	24	3320±30	1052-1888 BC
14	core 9/1sa5	Poznan	bivalve	55	40000±800	40521-43169 BC
15	core10/1sa3	Poznan	shells	20	4515 ±30	2623-3521 BC
16	core 10/1sa2	Poznan	bone	70	42000±1300	41256-46581 BC
17	core 11/1sa1	Beta analytic	gastropod	20	5230±30	3638-4328 BC
18	core 11/2sa2	Beta analytic	shell	62	16900±60	17869-18741 BC
19	core11/2Sa4	Poznan	gastropod +shell	116	4500±35	2619-3386 BC
20	core 11 2_5	Poznan	gastropod	121	4360±40	2457-3366 BC
21	core11/2sa6	Poznan	gastropod	126	4405±35	2477-3368 BC
22	core11/2sa1	Beta analytic	roots	139	4810±30	2666 - 2817 BC
23	core11/2 sa11	Beta analytic	shells	152	32500±500	33294-36120 BC
24	core 11-2	Beta analytic	charcoal	180	5020±30	3710-3943 BC
25	core 12/1 sa1	Poznan	gastropod	44	5065±30	3367-4072 BC
26	core 12/2sa1	Beta analytic	gastropod	108	4885±35	3097-3950 BC
27	core 12/2sa2	Poznan	gastropod	114	5000±35	3331-4050 BC
28	core 12/2 sa3	Beta analytic	broken shell	117	37940±420	39560 -40811 BC
29	core 12/2sa4	Beta analytic	roots	135	5060±30	3365-4071 BC
30	E1 A1sa1	CIRAM	charcoal	25	130±20	1680-1908 AD
31	E1A1sa2	CIRAM	charcoal	56	190±20	1661-1931 AD

CIRAM Lab. science for art cultural heritage , archeology department http://www.ciram-art.com/en/archaeology.html
contact person : Dr. Armel BOUVIER

Poznan Lab. Poznan Radiocarbon Laboratory, Poland, email: c.fourteen [at]radiocarbon.pl http://radiocarbon.pl/index.php?lang=en.

Beta Analytic radiocarbon dating , Miami, Florida, USA
http://www.radiocarbon.com/, e-mail: lab@radiocarbon.com

OxCal v4.2.4 Bronk Ramsey (2013); r:5; IntCal13 atmospheric curve (Reimer et al 2013) Delta_R(103,161)

Core2/1sa4 R_Date(33500,500)
95.4% probability
36931 (95.4%) 34362calBC

OxCal v4.2.4 Bronk Ramsey (2013); r:5; IntCal13 atmospheric curve (Reimer et al 2013) Delta_R(103,161)

Core2/1sa6 R_Date(32000,360)
95.4% probability
34681 (95.4%) 32971calBC

OxCal v4.2.4 Bronk Ramsey (2013); r:5; IntCal13 atmospheric curve (Reimer et al 2013) Delta_R(103,161)

Core3/1sa1 R_Date(33500,600)
95.4% probability
37224 (95.4%) 34218calBC

371

OxCal v4.2.4 Bronk Ramsey (2013); r:5; IntCal13 atmospheric curve (Reimer et al 2013) Delta_R(103,161)

Core6/2sa1 R_Date(125,30)

95.4% probability

1521 (5.0%) 1592calAD

1620calAD (90.4%) ...

OxCal v4.2.4 Bronk Ramsey (2013); r:5; IntCal13 atmospheric curve (Reimer et al 2013) Delta_R(103,161)

Core6/1sa6 R_Date(34000,400)

95.4% probability

37441 (95.4%) 35002calBC

OxCal v4.2.4 Bronk Ramsey (2013); r:5; IntCal13 atmospheric curve (Reimer et al 2013) Delta_R(103,161)

Core6/1sa9 R_Date(50000,4000)

95.4% probability

69225 (95.4%) 42776calBC

Appendix F

Theory and definitions

1. Seismotectonic methodology

1.1. Focal mechanisms

The description of an earthquake rupture (Fig.1) consists of three angle, the strike angle Φ which is the azimuth (with respect to the North) of the trace of the fault on a horizontal plane such as the Earth's surface; the dip angle δ characterizes the steepness of the fault and the rake or slip angle λ, the direction of motion, within the fault plane and relative to the horizontal of the hanging wall relative to the foot wall.
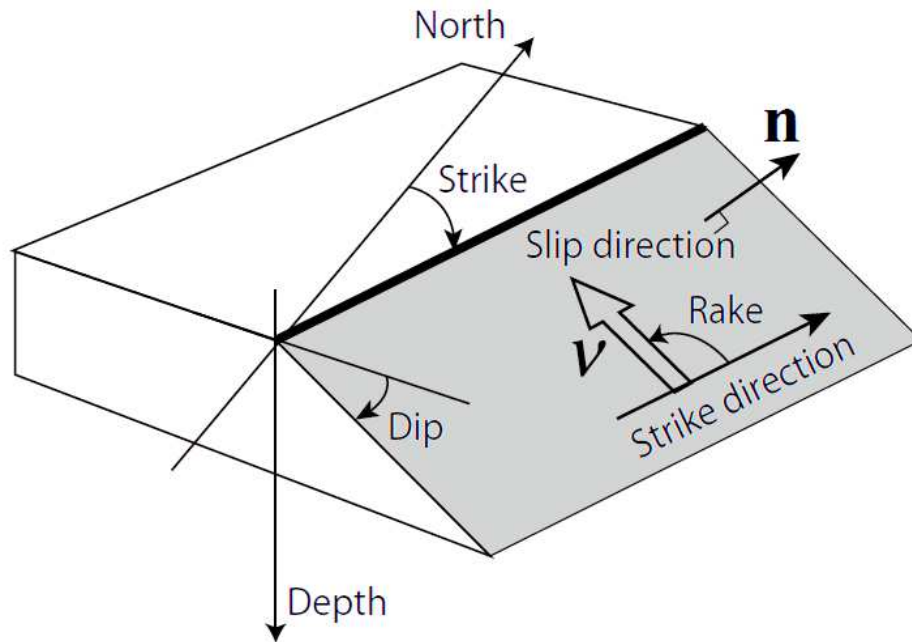
Fig.1 sketch show the geometry of the fault description

The complete characteristic of an earthquake focal mechanism provides important information, including the origin time, epicenter location, focal depth, seismic moment (a direct measure of the energy radiated by an earthquake) and the magnitude and spatial orientation of the 9 components of the moment tensor (Aki and Richards, 1980). From the moment tensor the orientation and sense of slip of the fault is resolved.

The Focal mechanisms are represented as a beach ball (Sykes 1967) in which the lower hemisphere stereographic projections show two black quadrants and two white quadrants separated by great circles arcs oriented 90° from each other. The great circle arcs are the nodal planes, one of which coincides with the fault rupture that generates the earthquake. The strike of the fault is indicated by a line connecting the two points at which the great circle corresponding to the fault intersects the outer edge of the beach ball diagram (fig.2). The dip direction is 90° from strike, in the direction indicated by the bold arrow from the center of the plot to the middle of the great circle arc.

The rake of the hanging wall slip vector (Cronin and Sverdrup 1998) is measured in the fault plane, relative to reference strike of the fault plane. An angle measured through an anticlockwise rotation from the reference strike is considered a positive angle; an angle measured clockwise from reference strike is a negative angle. A slip vector that is directed up relative to strike has a positive rake and a slip vector that is directed down the plane is negative. The range of permissible rake is +180° to -180°.
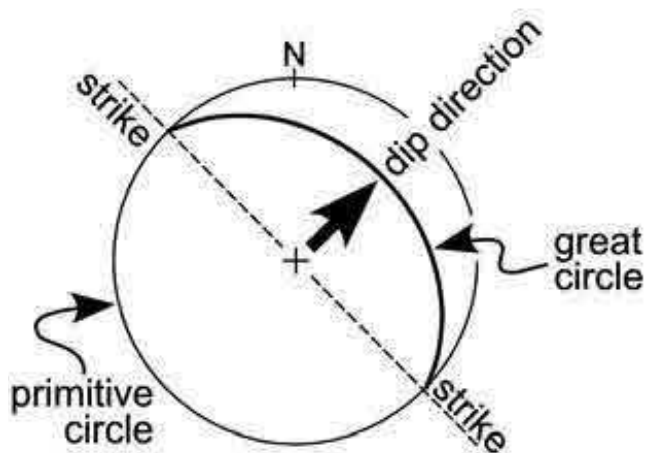
Fig. 2 Strike and dip direction of fault plane in the hemisphere stereographic projections.

According to Aki and Richards (1980), a rake of 90° indicates slip that is entirely reverse with no strike slip component. Similarity, hanging wall slip vectors with negative rake have at least some component of normal slip with rake of -90° indicating slip that is entirely normal with no strike slip component.

1.2. Stress tensor

The stress directions in the Earth's crust are close to vertical and horizontal directions. Anderson (1951) developed a simple scheme connecting the basic stress regimes in the Earth's crust with type of faulting on a pre-existing fault in the crust (Fig. 3). Anderson (1951) distinguishes three possible combinations of magnitudes of principal stresses: the vertical stress is maximum, intermediate or minimum with respect to the horizontal stresses. If the vertical stress is maximum, the hanging wall is moving downwards with respect to the foot wall and the normal faulting is observed along a deeply steeping fault. If the vertical stress is minimum, the crust is in horizontal compression and the hanging wall is moving upwards with respect to the foot wall and reverse faulting is observed along a shallow dipping fault. Finally, if the vertical stress is intermediate, the foot and hanging walls are moving horizontally and the strike slip faulting is observed along a nearly vertical fault.

The Anderson's classification is simple and still proved validity for many seismically active regions and helpful for rough assessment of stress regime (Simpson 1997; Hardebeck and Michael 2006).

Stress is the key in understanding the behavior offaults and other tectonic structures such as deformation processes of the crust. Stress field studies in activezones have widely developed within the last 30 years, by means of in site measurements;faults slip data and focal mechanisms of earthquakes. Focal mechanisms of earthquakeshave long been used to probe the stress field in continental crust (Wallace, 1951; Bott,1959; McKenzie, 1969). This seismological data is considered as an excellent source ofinformation on stress directions and relative stress magnitudes in the crust which alsogives an clear picture of the present-day stress field.
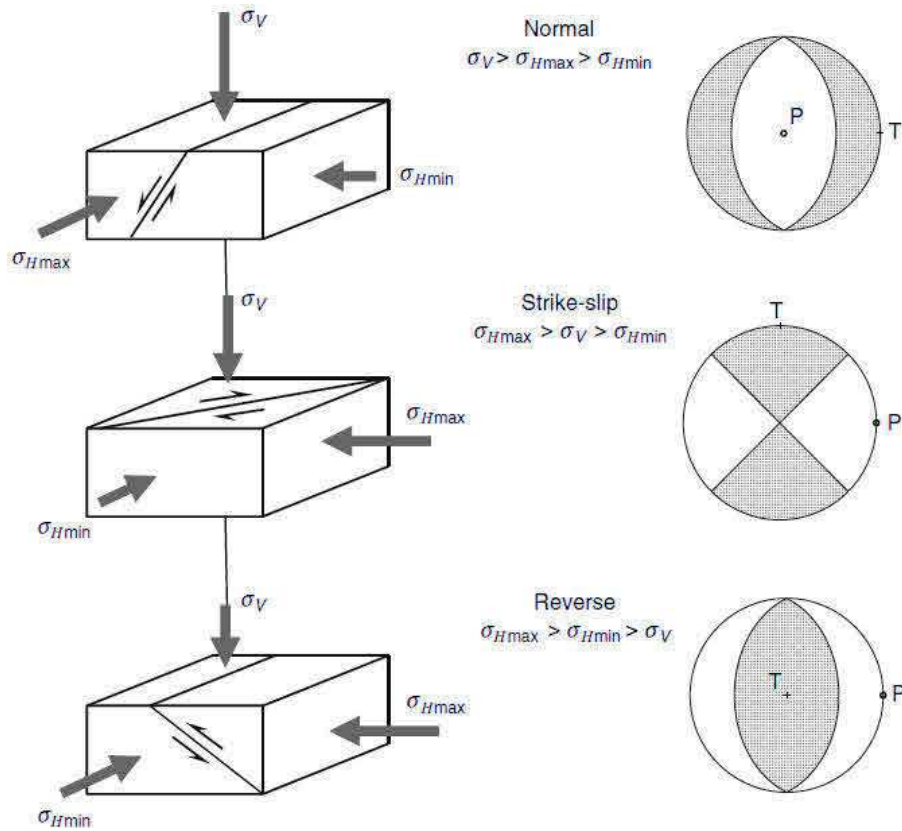
Fig. 3. The classification scheme of stress in the Earth's crust after Anderson 1951 on the left and corresponding faulting regimes in the right.

Stress tensor is describe as the concentration of the internal forces considering not only their magnitude but also the size of the area on which they act (i.e., a force divided by an area that is a stress *(F/A))* (Ramsay and Lisle, 2000; and Parry, 2004). It is related to the familiar concept of a force in a reasonably straight forward way. Hence the forces acting on elements of an elastic solid can be treated with the concept of stress vector and stress tensor. The stress tensor *(σij),* the full specification of the state of stress at a point, is made up of six independent components corresponding to three traction vectors each acts on a surface perpendicular to x, y, and z coordinate axes. These terms represent the complete internal force distribution at a point.

$$\sigma ij = \begin{pmatrix} \sigma 11 & \sigma 12 & \sigma 13 \\ \sigma 21 & \sigma 22 & \sigma 23 \\ \sigma 31 & \sigma 32 & \sigma 33 \end{pmatrix}$$

The diagonal terms of stress tensor are called normal stresses (three components) and the off-diagonal terms are called shear stresses (six components).

Components of stresses on a Fault plane

It is considerable interest to know the direction of the shear stress acts as generally assumed that the shear stress derives the potential slip on the fault plane. To this, one consider a fault plane L which can defined by a unit vector n = (n1, n2,n3 normal to it, and *a,* the stress vector acting on that plane and represent the state of stress on the rock volume. Performing all calculations in the principal stress system, we can easily obtain the total traction acting on the fault surface as:

$$\text{ti} = \boldsymbol{\sigma}\text{ij n} = \qquad\qquad 1$$

Additionally, the traction vector ti can be resolved into shear and normal components. The normal stress component τn (scalar) acting in the direction of n, and causes either tensile (opening) or compressive (shortening) on the weakness plane as function of its sign. In engineering and material science, the convention is that positive stresses are tensional, and compressional stresses are negative. The other one is the shear stress component $\tau s,$ acting along the plane itself (parallel to the fault plane). The two components are perpendicular to each other and related by this relation:

$$\text{t} = \tau n + \tau s \qquad\qquad 2$$

To obtain the normal stress acting on the considered plane, we project the stresses of equations (3) onto the normal n to get:

$$\tau n = (\text{ti.n})\text{n} = [(\sigma n).n]n \qquad\qquad 3$$

The shear traction $\tau s(n, \sigma)$ is found by subtracting the normal traction from the total traction:

$$\tau s = \sigma n - [(\sigma n).n] \ n \qquad\qquad 4$$

Where $\tau s (n, \sigma)$ is the tangential traction on the fault plane with unit normal n due to the deviatoric stress tensor σ in where the deviatoric stress is consider to be a result of tectonic forces as it causes earthquake faulting and seismic wave propagation effects like anisotropy. To find best the deviatoric stress tensor, only orientation of the slip with respect to the orientation of the fault is consider (Michael, 1984).

The Right Dihedron and rotational optimization method

The Right Dihedron method was introduced by Angelier & Mechler (1977) as a graphical method for the determination of the range of possible orientations of $\sigma 1$ and $\sigma 3$ stress axes in fault analysis. These methods developments include (1) the estimation of the stress ratio R, (2) the complementary use of tension and compression fractures and (3) the application of the a compatibility test for data selection and subset determination using a counting deviation. The Right Dihedron method is typically designed for building initial data subsets from the raw data set, and for making a first estimation of the four parameters of the reduced stress tensor. The Improved Right Dihedron method forms a separate module in the TENSOR program (Delvaux and Sperner (2003).

The Right Dihedron method is based on a reference grid of orientations predetermined in as a rectangular grid on the stereonet in lower hemisphere Schmidt projection. For all fault-slip data, compressional and extensional quadrants are determined according to the orientation of the fault plane and the slip line and the sense of movement. These quadrants are plotted on the reference grid and all orientations of the grid falling in the extensional quadrants are given a counting value of 100% while those falling in the compressional quadrants are assigned 0%. This procedure is repeated for all fault-slip data. The counting values are summed up and divided by the number of faults analyzed. The grid of counting values for a single fault defines its characteristic counting net. The resulting grid of average counting values for a data subset forms the average counting net for this subset. The possible

orientations of σl and σ3 are defined by the orientations in the average counting net that have values of 0% and 100%, respectively.

The stress ratio R, defined as equivalent to (σ2 - σ3)/(σ1 - σ3) is one of the four parameters determined in the stress inversion, with the three principal stress axes σ1, σ2 and σ3.

The stress ratio, R controls for any given plane, the direction of shear stress and determines the geometry of the slip on fault planes (Wallace, 1951; Bott, 1959).

Also, the stress ratio R can be obtained with this relation:

$$R= (100-sval)/100$$

where S2val is the counting value of the point on the reference grid nearest to the orientation of *σ2*. This formula is only good valid for large fault populations with a wide variety of fault plane orientations.

The Improved Right Dihedron method allows us a first estimation of the orientations of the principal stress axes and of the stress ratio *R,* and a first filtering of compatible fault-slip data. The selected fault-slip population and the preliminary tensor can be used as a starting point in the iterative inversion procedures like the Rotational Optimization method in the following lines:-

The used Right Dihedron method in combination with the four dimensional iterative Rotational Optimization method for determining the four parameters of the reduced stress tensor using the TENSOR program of Delvaux (1993). The improved version of Right Dihedron method by Delvaux and Spemer (2003) allows not only obtaining the first estimation of the principal stress axes orientation but also estimating the stress ratio R and produces the first filtered focal mechanism data set by application of a compatibility test for data selection and subset determination on the basis of the counting deviation. These results are used as a starting point in the Rotational Optimization inversion procedure. This new iterative inversion method is based on a controlled grid search with rotational optimization of a range of misfit functions with the purpose of minimizing the misfit function. It allows restrictions of the research area during the inversion so that there is no need for the whole grid to be searched. The misfit is defined as the minimum rotation that is necessary to reconcile

the stress tensor with the Observed slip vector direction to all fault plane solutions for a population of earthquakes.

The stress tensor orientation that provides the average minimum misfit is assumed to be the best one for a given populations of focal mechanisms. The TENSOR program (Delvaux and Sperner, 2003) allows to optimize a wide variety of functions, independently or combined according to the nature of tectonic structure used: minimization of deviation angles($\alpha°$) between observed and theoretical slips on fault planes; maximization of shear stress magnitude (τ) on fault planes and shear joints; minimization of normal stress magnitude(σn) on extensional joints (tension veins) and maximization of normal stress magnitude(σn) on compressional joints (cleavage, styloliths).

The TENSOR procedure optimizes the appropriate function by progressive rotation of the tested tensor around each of his axes, and by testing different values of R ratio. The amplitude of rotation angles and values of R ratio tested are progressively reduced until the tensor is stabilized. In fact most stress tensors were computed using an optimized composite function (F5 in TENSOR), with simultaneous minimization of slip deviation angles $\alpha$for fault planes, maximization of τ on fault planes and shear joints and minimization of σn on extension joints. This function has been proved very efficient in paleostress inversion of mixed data sets (Reference). In case of inversion of earthquake focal Mechanism data this function combines the minimization of the misfit angle α (slip deviation) and the maximization of the shear stress magnitude on every fault plane. As a whole the rotational optimization progressively improves the tensor and selects one focal plane for each mechanism on the basis of the slip deviation (e.g., Vasseur et al., 1983; Gephart and Forsyth, 1984; Bergerat et al., 1987) (eventually eliminates focal planes whose slip deviation $\alpha$is more than the threshold value of 30°), the value of composite function (the fault plane will be the one with the smallest value of the composite function the two planes have slip deviation less than 30°) and internal friction criteria (the instability) for each fault plane (Delvaux and Sperner, 2003).

2. Paleotsunami methodology

2.1. Grain size equations

This following equations of calculate mean size, sorting, Skewness, Kurtosis according to Folk (1968).

1. "Mean" - is the average grain-size. Several formulas are used in calculating the mean. The most inclusive graphically derived value is that given by Folk (1968), According to equations:

$$Mz = \frac{\varphi 16 + \varphi 50 + \varphi 84}{3}$$

Where 16, 50, and 84 represent the size at 16, 50, and 84 percent of the sample by weight.

2. Sorting is a method of measuring the grain-size variation of a sample by encompassing the largest parts of the size distribution as measured from a cumulative curve.

Folk (1968) introduced the "inclusive graphic standard deviation", that is calculated as follows:

$$\sigma = \frac{\varphi 84 - \varphi 16}{4} + \frac{\varphi 95 - \varphi 5}{6.6}$$

where 84, 16, 95, and 5 represent the phi values at 84, 16, 95, and 5 percentiles.

The classification scale for sorting:

<0.350: very well sorted;

0.35-0.500: well sorted;

0.5-0.710: moderately well sorted;

0.71-1.00: moderately sorted;

1.00-2.00: poorly sorted;

2.00-4.00: very poorly sorted;

> 4.00: extremely poorly sorted.

3. Skewness is a measures the degree to which a cumulative curve approaches symmetry. Two samples may have the same average grain size and sorting but may be quite different to their degrees of symmetry.

Folk's (1968) "inclusive graphic skewness is determined by the equation:

$$SK1 = \frac{\varphi16 + \varphi84 - 2\varphi50}{2(\varphi84 - \varphi16)} + \frac{\varphi5 - \varphi95 - 2\varphi50}{2(\varphi95 - \varphi5)}$$

Where 5, 16, 50, 84,95 represent the size at 5, 16, 50, 84,95 percent of the sample by weight

Symmetrical curves have a skewness equal to 0.00; those with a large proportion of fine material are positively skewed; those with a large proportion of coarse material are negatively skewed. A verbal classification for skewness suggested by Folk (1968) includes:

+0.10 to -0.10 as nearly symmetrical;

 -0.10 to -0.30 as coarse-skewed;

-0.30 to -1.00 as strongly coarse-skewed.

4. Kurtosis is a measure of "peakedness" in a curve. Folk's (1968) formula for kurtosis is:

$$K = \frac{\varphi95 - \varphi5}{2.44\ (\varphi75 - \varphi25)}$$

where the phi values represent the same percentages as those for Skewness. A normal Gaussian distribution has a kurtosis of 1.00 which is a curve with the sorting in the tails equal to the sorting in the central portion. If a sample curve is better sorted in the central part than in the tails, the curve is said to be excessively peaked, or leptokurtic; if the sample curve is better sorted in the tails than in the central portion, the curve is flat peaked or platykurtic. For normal curves = 1.00, leptokurtic curves have >1.00, and platykurtic curves have <1.00.

2.2. X-ray diffraction theory

Single wavelength incidents to the specimen surface and detector measure the intensity of the diffracted beam. The beam incident angle changes continuously thus a spectrum of diffraction intensity versus the angle between incident and diffraction

beam is produced. This spectrum is compared with database containing over 60,000 diffraction spectra of known crystalline substances. Diffractometer functions are the x-ray diffraction detecting from material and the measuring of diffraction intensity. Fig. 4 illustrated the geometrical arrangement of X-ray source, specimen and detector.

The X-ray radiation generated by an X-ray tube passes through special slits, which collimate the X-ray beam. These slits are commonly used in the diffractometer. They are made from a set of closely spaced thin metal plates parallel to plane to prevent beam divergence in the director perpendicular to the figure plane.
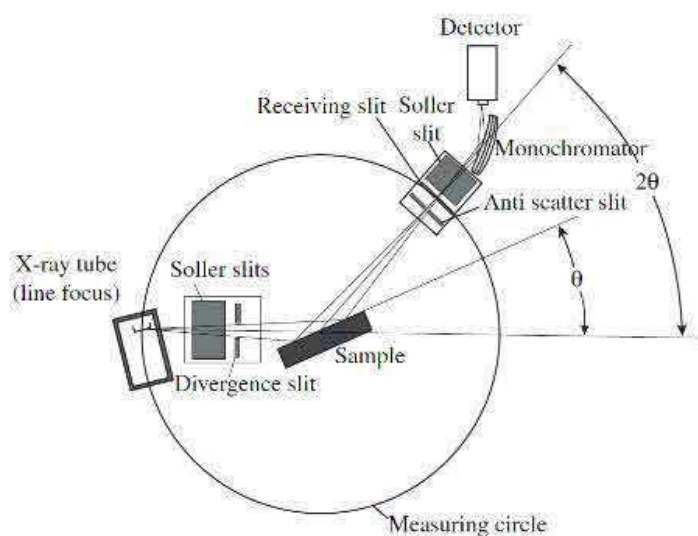
Fig. 4 The geometrical arrangement of an X-ray source, specimen, and detector.

A divergent X-ray beam passing through the slits strikes the specimen. X-rays are diffracted by the specimen and form a convergent beam at receiving slits before they enter a detector. The diffracted X-ray beam needs to pass through a monochromatic filter (or a monochromator) before being received by a detector. Relative movements among the X-ray tube, specimen and the detector ensure the recording of diffraction intensity in a range of 2θ. The θ angle is not the angle between the incident beam and specimen surface; rather it is the angle between the incident beam and the crystallographic plane that generates diffraction. Diffractometers can have various types of geometric arrangements to enable collection of X-ray data.

The technique of thin film X-ray diffractometry uses a special optical arrangement for detecting the crystal structure of thin films and coatings on a substrate. The incident beam is directed to the specimen at a small glancing angle

(usually <1∘) and the glancing angle is fixed during operation and only the detector rotates to obtain the diffraction signals as illustrated in figure 16. Thin film X-ray diffractometry requires a parallel incident beam, not a divergent beam as in regular diffractometry. Also, a monochromator is placed in the optical path between the X-ray tube and the specimen, not between the specimen and the detector. The small glancing angle of the incident beam ensures that sufficient diffraction signals come from a thin film or a coating layer instead of the substrate.
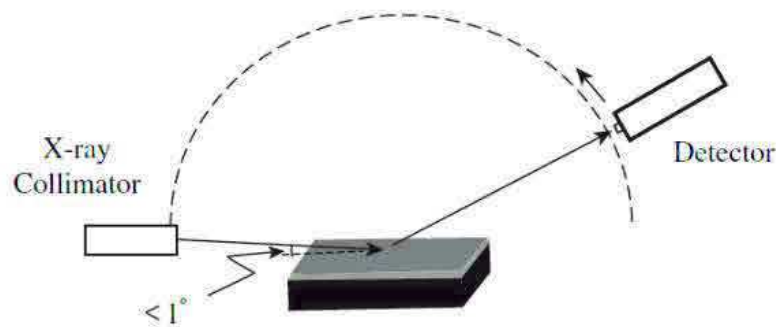
Fig.5 Optical arrangement for thin film diffractometry

3. Tsunami definition and shallow water equation

This items and equations are described from Physics of tsunamis book Boris Levin et al., 2009

The tsunami name originates from two Japanese words translated together as a 'wave in the harbour. The other terms which used from some time ago, such as 'high-tide wave', and 'seismic sea wave' and 'seaquake'

Most tsunamis are caused by submarine earthquakes but not all submarine earthquakes cause tsunamis. Movement on the fault must have a vertical component that generates sufficient displacement to set a tsunami running. Submarine explosions, caldera collapse and massive pyroclastic flows can all cause sufficient displacement of water to generate a tsunami. Underwater landslides or coastal landslides that fall into the ocean can displace enough water to create a tsunami. Sometimes the landslides are caused by earthquakes. Large meteorites have a high probability of landing in the ocean and causing a tsunami given that about two thirds of the surface of the Earth is covered by water.

A tsunami inundation simulation is based on the nonlinear long wave theory namely, the shallow water theory—which considers ocean bottom friction (Madder, 2004). The propagation velocity of long waves a sea water of depth H is determined by the formula $v=$ where g is the fall acceleration of gravity. The tsunami depends on the wave propagation velocity on the sea depth of these waves which is sensitive to the shape of the sea-floor (i.e bathymetery data). Effects peculiar to tsunamis include the capture of wave energy both by underwater ridges and by the shelf, focusing and defocusing exhibited when waves propagate above underwater elevations and depressions. The irregularities of the sea-floor lead to the scattering of tsunami waves.

The propagation velocity of gravitational waves does not depend only on the depth, but on the wavelength. The formula presented above for the velocity of long waves is the limit case (for $\lambda \geq H$) of the more general expression:

$$v = \sqrt{g \tanh(kH)/k}, \text{ where } k = 2\pi/\lambda$$

The tsunami wave amplitude increases by its arrival to the coast and this depend on the relief of the sea-floor. A decrease in the water depth leads to a decrease in the wave propagation velocity and, consequently, to compression of the wave packet in space and an increase of its amplitude. In the case of catastrophic tsunamis, the run-up height reaches 10–30 m, while the wave is capable of inland inundation (runin) of 3–5 km from the coastline. A scheme of the tsunami onshore run-up, explaining the main parameters of this process, is shown in Fig. 6. The maximum wave height can be achieved at the shoreline, at the inundation boundary or at any point in between them. .The process of the simulation process of the tsunami waves applied in this study are shown in Fig.7.
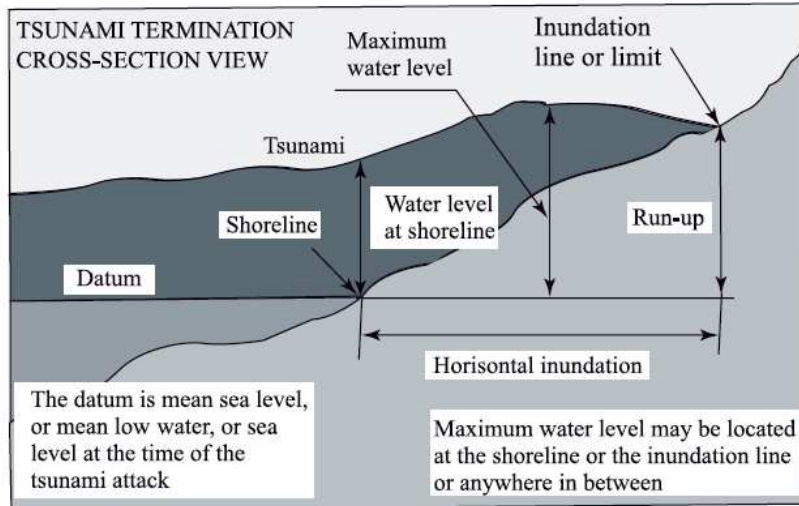
Fig.6 Scheme of tsunami onshore run-up (UNESCO-IOC (2006))
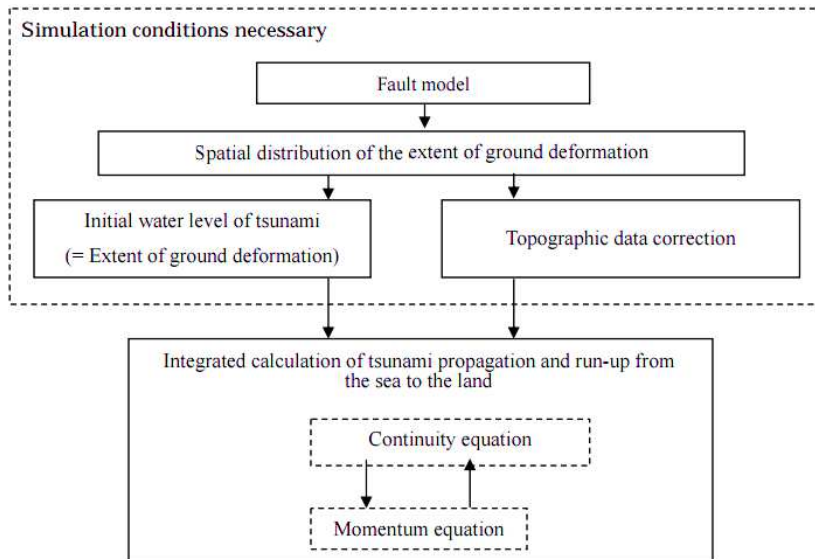
Fig.7 sketch show the simulation process

The linear long wave theory and the nonlinear long wave theory are used as standards for estimating a tsunami in 50-meter or deeper seas and shallower seas, respectively. The long-wave theory consists of the continuity equation found in the principle of mass conservation and the momentum equation found in the principle of momentum conservation. Both of these involve the following governing equations for an integration model that can be found by performing integration from the bottom of the water to the water surface in a vertical direction.

Continuity equation

$$\frac{\partial \eta}{\partial t} + \frac{\delta M}{\delta x} + \frac{\partial N}{\partial y} = 0$$

Momentum equation

$$\frac{\partial M}{\partial t} + \frac{\delta}{\delta x}\left(\frac{MN}{D}\right) + gD\frac{\partial \eta}{\partial x} + \frac{gn^2}{D^{\frac{7}{3}}}M\sqrt{M^2 + N^2} = 0$$

$$\frac{\partial N}{\partial t} + \frac{\delta}{\delta x}\left(\frac{MN}{D}\right) + \frac{\partial}{\partial y}\left(\frac{N^2}{D}\right) + gD\frac{\partial \eta}{\partial y} + \frac{gn^2}{D^{\frac{7}{3}}}N\sqrt{M^2 + N^2} = 0$$

η means changes in the water level from the still-water level. D is the total water depth from the bottom to the surface. g is the acceleration of gravity. n is Manning's roughness coefficient. M, N represents the discharge flux in the direction of x,y. Horizontal flow velocity (u,v) , can be integrated from the bottom of the water (h) to the water surface (η) as the following:

$$M=u(h+\eta)=uD, \quad N=v(h+\eta)=vD$$

This equation assumes that horizontal flow velocity is uniformly distributed in a vertical direction.

Near-field tsunamis concern a 1,000-kilometer by 1,000-kilometer or smaller sea area. Using the rectangular coordinate system is sufficient for this. However, far-field tsunamis propagating over a long distance in the Pacific Ocean as example require the use of the governing equation with the following polar coordinate system. This type of tsunami also requires the dispersion term and Coriolis Effect to be considered as the following equations:-

$$\frac{\partial \eta}{\partial t} + \frac{1}{R\cos\Theta}\left[\frac{\partial M}{\partial \lambda} + \frac{\partial}{\partial \Theta}(N\cos\Theta)\right] = 0$$

$$\frac{\partial M}{\partial t} + \frac{gh}{R\cos\Theta}\frac{\partial \eta}{\partial \lambda} = -fN + \frac{1}{R\cos\Theta}\frac{\partial}{\partial \lambda}\left[\frac{h^3}{3}F\right]$$

$$\frac{\partial N}{\partial t} + \frac{gh}{R}\frac{\partial \eta}{\partial \Theta} = FM + \frac{1}{R}\frac{\partial}{\partial \Theta}\left[\frac{h^3}{3}F\right]$$

$$F = \frac{1}{Rcos\theta}\left[\frac{\partial^2 u}{\partial\lambda\partial t} + \frac{\partial^2}{\partial\theta\partial t}(vcos\theta)\right]$$

M=u(h+η)=uD, N=v(h+η)=vD

In this equation, λ is longitude, θ is latitude, and M and N are the discharge fluxes in the directions of λ and θ , respectively. R is the earth's radius, f is the Coriolis coefficient (f = 2ωsinθ), and ω is the angular velocity of the earth's rotation (7.29×10-5rad/s)

References

1. Seismotectonic methodology

Aki, K. and Richards, P.G., (1980). Analysis of seismological data. Quantitative Seismology. Theory of Methods .

Anderson EM (1951). The dynamics of faulting and dyke formation with applications to Britain, published in New York , Hafner 1972. PP 206.

Angelier, J. & Mechlier, P. (1977). Sur une methode graphique de recherche des contraintes principales egalement utilisable en tectonique et en seismologie : la methode des diedres droits. *Bulletin de la Societe Geologiquede France, Vol.* 7, no.19, p.1309-1318.

Bergerat, F., (1987). Stress fields in the European platform at the time of Africa-Eurasian collision, Tectonics, Vol.61 no.2. p. 99-132.

Bott, M. H. P. (1959). The mechanism of oblique-slip faulting. Geological Magazine, Vol.96, p. 109-117.

Cronin, V.S., and Sverdrup, K.A., (1998), Preliminary assessment of the seismicity of the Malibu Coast Fault Zone, southern California, and related of philosophy and practice, in Welby, C.W., and Growan, M.E.(editors), A Paradox of power--voices of warning and Reason in the Geosciences: Geological Society of America, Reviews in Engineering Geology, p.123-155.

Delvaux, D., Hanon, M., (1993). Neotectonics of the Mbeya area, SW Tanzania. Mus. roy. Afr. centr., Tervuren (Belg.), Dépt. Géol. Min., Rapp. ann. 991–1992, p.87–97.

Delvaux, D., Sperner, B., (2003). Stress tensor inversion from fault kinematic indicators and focal mechanism data: the TENSOR program. In: Nieuwland, D. (Ed.),

New Insights into Structural Interpretation and Modelling: Geol. Soc. Lond. Spec. Publ.,vol. 212, pp. 75–100.

Gephart, J. W., and D. W. Forsyth, (1984). An Improved Method for Determining the Regional Stress Tensor Using Earthquake Focal Mechanism Data - Application to the San-Fernando Earthquake Sequence, J. Geophys. Res., Vol. 89, p. 9305-9320 .
.
Hardebeck JL, Michael AJ (2006) Damped regional-scale stress inversions: methodology and examples for southern California and the Coalinga aftershock sequence. J Geophys Res 111, B11310.

J.G. Ramsay and R.J. Lisle, (2000). The techniques of modern structural geology, volume 3: Applications of continuum mechanics in structural geology: Academic Press, London, pp.1060 ISBN 0-12-576923-7.

Mckenzie, D.P., (1969). The relation between fault plane solutions for earthquakes and the directions of principal stresses. Bull. Seismol. Soc. Am. Vol.59, p. 591–601.

Michael, A. J., (1984). Determination of stress from slip data: Faults and folds, J. Geophys. Res., Vol.89, no. 11, p.517-11,526.

Parry, R H G , (2004), Mohr circles, stress paths and geotectonics, spon Press,London, and New York, pp.263, 2nd ed.

Simpson RW (1997). Quantifying Anderson's fault types. J Geophys Res 102:17909–17919.

Sykes, L., (1967). Mechanism of earthquakes and nature of faulting on the mid ocean ridges: journal of Geophysical Research, Vol.72, p.2131-2153.

Vasseur, G., Etchecopar, A., Philip, H., (1983). Stress state inferred from multiple focal mechanisms. Ann. Geophys. Vol.1, p. 291–298.

Wallace RE (1951). Geometry of shearing stress and relation to faulting. J Geol Vol.59, p.118–130. doi:10.1086/ 625831.

2. Paleotsunami methodology

Folk, R.L., 1968, Petrology of sedimentary rocks, 170 pp, Hemphill's Book Store, in Austin, Texas).

3. Tsunami definition and shallow water equation

Levin, B.W. and Nosov, M., (2009). Physics of tsunamis (Vol. 327). Dordrecht: Springer.

Madder, C. L. (2004). Numerical Modeling of Water Waves, Second ed. CRC Press, Boca Raton, FL, 288pp.

APPENDIX G

Paleotsunami deposits along the coast of Egypt correlate with historical earthquake records of eastern Mediterranean

A. Salama, (1, 2, *), M. Meghraoui (1**), M. El Gabry (2, *),

S. Maouche (3, *), H. Hussein (2, *), and I. Korrat (4)

[1.] EOST-IPGS - CNRS - UMR 7516, Strasbourg, France
[2.] NRIAG, 11421 Helwan, Egypt
[3.] CRAAG, Bouzareah, Algeria
[4.] Mansoura University, Mansoura, Egypt

* Also at *North Africa Group for Earthquakes and Tsunami Studies (NAGET), Ne t40/OEA ICTP, Italy*

**Corresponding author*

Abstract.

We study sedimentary record of past tsunamis along the coastal area west of Alexandria (NW Egypt) taking into account the reported historical inundations and related major earthquakes in the east Mediterranean. The two selected sites at Kefr Saber (~32-km west of Marsa-Matrouh city) and ~10 km northwest of El Alamein village are coastal lagoons protected by 2 to 30-m-high dunes parallel to the shoreline. Field investigations include: 1) Coastal geomorphology along estuaries, wedge-protected and dune-protected lagoons, and 2) identification of paleotsunamis deposits and their spatial distribution using trenching and coring. Five trenches (1.5-m-depth) at Kefr Saber and twelve cores (1 to 2.5-m-depth) at El Alamein are presented with detailed logging including Xrays, grain size and sorting, total organic and inorganic matter, bulk mineralogy, magnetic susceptibility and radiocarbon dating necessary for the identification of tsunamis records. The stratigraphic succession generally of low energy marine and alluvial deposits includes intercalated high-energy deposits made of mixed sand, gravel and broken shells interpreted as catastrophic layers correlated with tsunami deposits. A total of 50 samples of organic deposits, shells and charcoal fragments were collected from both sites, among which 20 samples have been dated. Dated charcoal and shells in deposits above and below the catastrophic layers allow the correlation with the 24 June 1870 (Mw 7.5), 8 August 1303 (Mw ~8) and 21 July 365 (Mw 8 – 8.5), major earthquakes that generated major tsunamis with the inundation of Alexandria and northern Egypt. Major tsunamigenic seismic sources being along the Hellenic subduction zone, the modelling of wave propagation and computed wave heights is consistent with tsunami records in sedimentary layers along the northern coast of Egypt. Our study of paleotsunami deposits documents the size and recurrence of past catastrophes and points out the potential of tsunami hazard over the Egyptian shoreline and the east Mediterranean regions.

Key words: paleotsunami, coring, trenching, coastal geomorphology, northern Egypt

1. Introduction:

Egypt has a well-documented catalogue of earthquakes and tsunamis preserved in a variety of sources due to its long history of civilization. Original documents and archives are considered as the principle sources of macroseismic data for major historical earthquakes and tsunamis (Poirier and Taher, 1980; Maamoun et al., 1984); Ambraseys et al., 1994, 2009; Guidoboni et al., 1994, 2005; Soloviev et al. 2000). The catalogue reports that coastal cities of northern Egypt have experienced tsunamis inducing runup waves and inundations with severe damage (Ambraseys, 2009). While past tsunamis are well documented historically, it appears that there is a lack of holistic investigations for tsunami deposits along the Mediterranean coastlines. The coastal geomorphology with low-level topography, dunes and lagoons along the Mediterranean coastline of northern Egypt constitutes an ideal natural environment for the geological record of past tsunamis.

The Eastern Mediterranean area experienced large earthquakes that can be generally described in the frame of the convergence between the Eurasian and African plates (Taymaz et al., 2004). Major historical tsunamis in the eastern Mediterranean region that affected northern Egypt are triggered by large earthquakes (Papadopoulos et al., 2014) but the possibility of landslide tsunami associated with local earthquakes (El-Sayed et al., 2004) may also exist. Yalciner et al. (2014) estimated that up to 500 km³ landslide volume, with wave height ranging from 0.4 to 4 m, might have taken place offshore the Nile Delta. However, the effects of landslide tsunami are limited to the nearby coastline as shown by the recent

examples of landslide tsunamis in the Mediterranean associated with the eruption of Stromboli volcanic eruption of 30 December 2002 (Tinti et al., 2005).
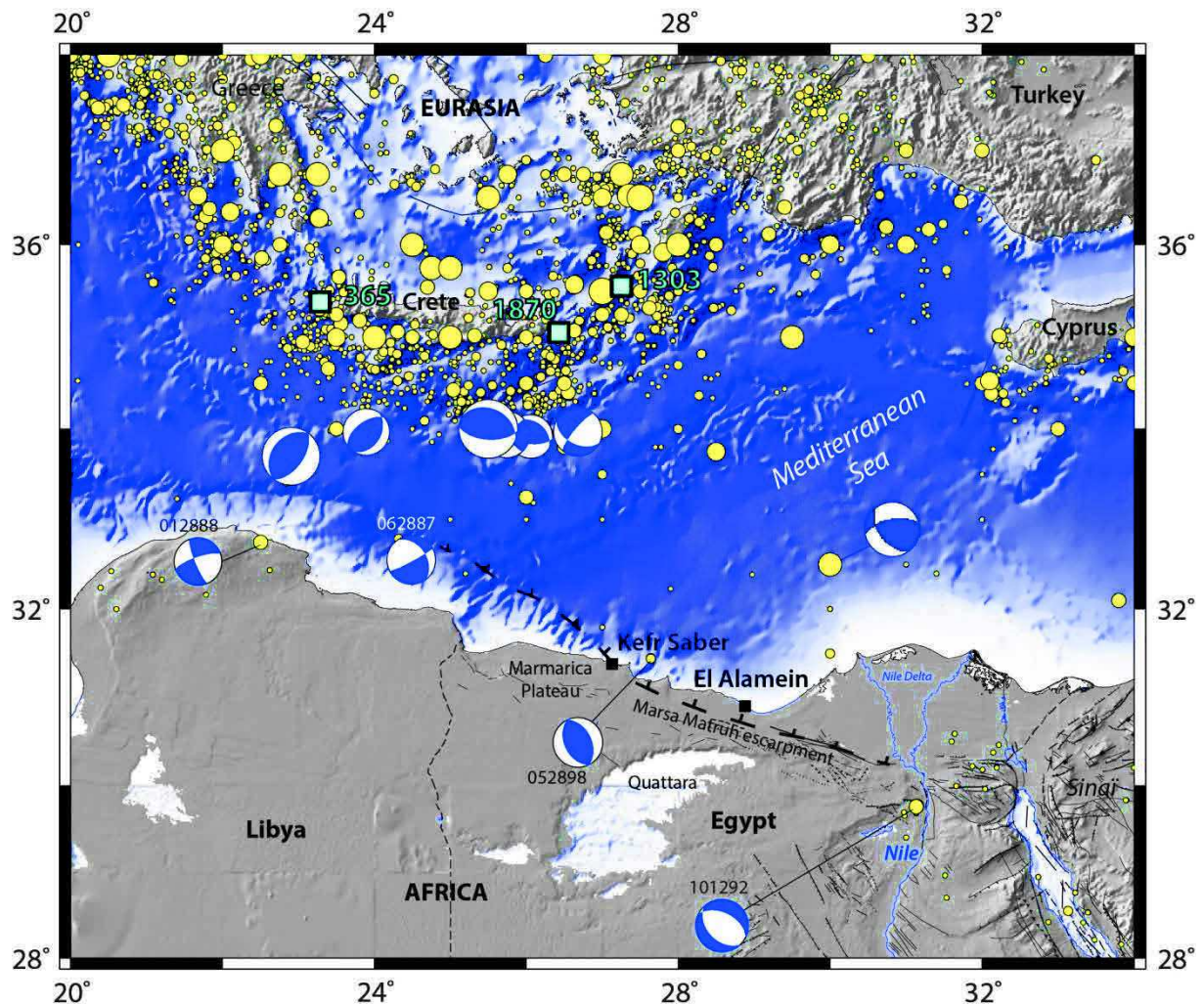
Figure 1: Seismicity (instrumental with M> 5.5) and main tectonic framework of the east Mediterranean regions. Black boxes indicate the paleoseismic sites of Kefr Saber and El Alamein east of the Nile delta. The major historical earthquakes (blue box) of AD 365 (Mw 8 – 8.5), AD 1303 (Mw ~8) and AD 1870 (Mw > 7 – 7.5) are located along the Hellenic subduction zone according to Guidoboni et al. (1994), Stiros (2001) and Ambraseys (2009). Focal mechanisms are CMT-Harvard.

Tsunami research of the past 20 years has led to the discovery of tsunami deposits dating back to thousands of years. For instance, more than 6 soil levels were identified buried below catastrophic sand sheet deposits at Puget Sound coastline (west Washington, USA) due to tsunamis in the past 7000 years (Atwater, 1987). Nanayama et al. (2003) recognized major tsunamis along the eastern coast of Hokkaido (northern Japan) due to extensive coastal inundation and repeated sand sheet layers several kilometers inland; the repetition of this layer evidenced a 500-year tsunami cycle in the period between 2000 and 7000 years BP. Along the coast of South Andaman Island (India), Malik et al. (2011) studied coastal deposits in trenches and identified three historical tsunamis during the past 1000 years comparable to the 2004 Sumatra earthquake tsunami. In the Mediterranean, De Martini et al. (2012) identified two tsunamis deposits during the first millennium BC and another one in 650-770 AD and

108 estimated 385 year average recurrence interval for strong tsunamis along the eastern coast of
109 Sicily (Italy).
110   In this paper, we investigate the paleotsunami deposits in northern coast of Egypt and
111 their correlation with the historical tsunami catalogue of the Eastern Mediterranean. Using
112 coastal geomorphology with trenching and coring, we examine the geological evidence of
113 tsunami deposits using geochemical analysis, magnetic susceptibility and radiocarbon dating
114 to identify the tsunamis records. The obtained results and inferred size of past tsunamis are
115 compared to model wave heights propagation associated with major earthquakes. Finally, we
116 discuss the impact of past tsunamis their dating and correlation with major tsunamigenic
117 earthquakes of the Hellenic and Cyprus subduction zone.
118
119 **2. Major historical tsunamis of the Mediterranean coast of Egypt**
120   Although the tsunamis catalogue of Egypt is not completed yet, Guidoboni et al.
121 (1994, 2005) and Ambraseys (2009) report several large historical earthquakes with tsunamis
122 that caused damage in coastal Egypt and the eastern Mediterranean region (Table 1). Among
123 these events, the tsunamis of 21 July 365, 8 August 1303 and 24 June 1870 caused severe
124 damage to Alexandria city as well as the Mediterranean coast of Greece, Sicily, Libya,
125 Cyprus, Syria, Lebanon and Palestine. These three tsunami events are correlated with the
126 major earthquakes in the Hellenic and Cyprus subduction zones (Papadopoulos et al., 2014).
127

Date	Epicentre	Estimated Magnitude	Comment	Reference
21 July 365	Western Crete	8.3 – 8.5 (M_w)	Tsunami northern Egypt	Stiros and Drakos, 2006; Shaw et al., 2008, Hamouda 2009
18 Jan. 746	Dead Sea Fault	7.5 (M)	Tsunami eastern Medit.	Sieberg, 1932, Ambraseys, 1962
881 - 882	Palestine	?	Tsunami in Alexandria & Palestine	Galanopoulos A., 1957
4 Jan. 1033	Jordan Valley Fault	7.4 (M)	Tsunami northern Egypt	Ambraseys, 1962
18 Jan. 1068	Northern Lebanon	6.9 (M)	Waves in Lebanon Until northern Egypt	Ambraseys, 1962, Soloviev et al., 2000
8 Aug. 1303	Karpathos & Rhodos islands	8 (M)	>8-m-high wave in Alexandria	Abu al-Fida 1329, Ambraseys 2009, Hamouda 2006
24 June 1870	Hellenic Arc	M_L 7.2	Inundation in Alexandria harbour	Ben-Menahem, 1979, Soloviev et al., 2000

128
129 *Table 1: Major earthquakes of the eastern Mediterranean with tsunami wave records in*
130 *northern Egypt. Estimated magnitudes are given in Mw when calculated and in M when*
131 *estimated.*
132
133   Early in the morning of 21 July 365, an earthquake with estimated magnitude ~Mw 8-
134 8.5 located offshore West of Crete generated a major tsunami that affected the eastern
135 Mediterranean coastal regions (Ambraseys et al., 1994; Guidoboni et al., 1994; Stiros, 2001;
136 Shaw et al., 2008). A contemporaneous account from the Roman historian Ammianus
137 Marcellinus (born 325 – 330, died c. 391 – 400; Guidoboni et al., 1994) reports the sudden
138 retreat of the sea and the occurrence of a "gigantic" wave inland with inundation and damage

to the Alexandria harbour and city with ships lifted inland on house roofs; the estimated wave height of this tsunami was calculated by Hamouda (2009) to be larger than 8 m in Alexandria.

On 8 August 1303 a major earthquake with magnitude ~Mw 8 located in between Crete and Rhodos islands generated a tsunami that greatly damaged the coastal cities of the eastern Mediterranean (Guidoboni and Comastri, 2005; Ambraseys, 2009). The contemporaneous Arabic source of Abu-El Fida (1329) report that the Alexandria city and Nile delta were flooded and many houses were damaged in Cairo and northern Egypt. In Alexandria, part of the city walls collapsed, the famous light houses was destroyed and some ships were torn apart carried up inland due to the tsunami waves (Abu-El Fida, 1329). .

On 24 June 1870 a large earthquake affected many places of the eastern Mediterranean region and was felt in Alexandria at around 18 h with no damage in the city but with slight damage in Cairo (Coumbary, 1870; Ambraseys, 2009). In Alexandria coastline and Nile Delta, the sea wave flooded the quays of ports and inland fields.

Among these three reported earthquakes, it appears that the AD 365 and AD 1303 can be classified as very large earthquakes (with Mw $\geq$ 8) that generated major tsunamis with basin-wide impacts, while the 1870 earthquake may be of a lower magnitude (Mw ~7 – 7.5; Soloviev, 2000). However, all studies of the three historical earthquakes refer to tsunami waves with inundation in Alexandria and coastlines of northern Egypt and therefore with the potential of tsunamis record in sedimentary deposits.

3. Coastal geomorphology and site selection of paleotsunami records

The northwest Mediterranean coast of Egypt forms the northern extremity of the Miocene Marmarica homoclinal limestone plateau, which extends west of Alexandria for about 500 km acting as a major catchment area feeding the drainage system (Figure 1). The plateau runs from the Qattara Depression southward to the piedmont plain northward with various elevations reaching ~100 m at Marsa Matrouh escarpment. The landform geomorphology of the study area is characterized by the 60-m-high northern plateau that includes ridges, sand dunes, lagoons, and rocky plains within a 20-km-wide strip along the coastline (Fig 1). The rocks correspond to a veneer of carbonate sand mostly composed of carbonate oolitic grains, entirely composed of Pleistocene limestone ridges (Frihy et al., 2010).
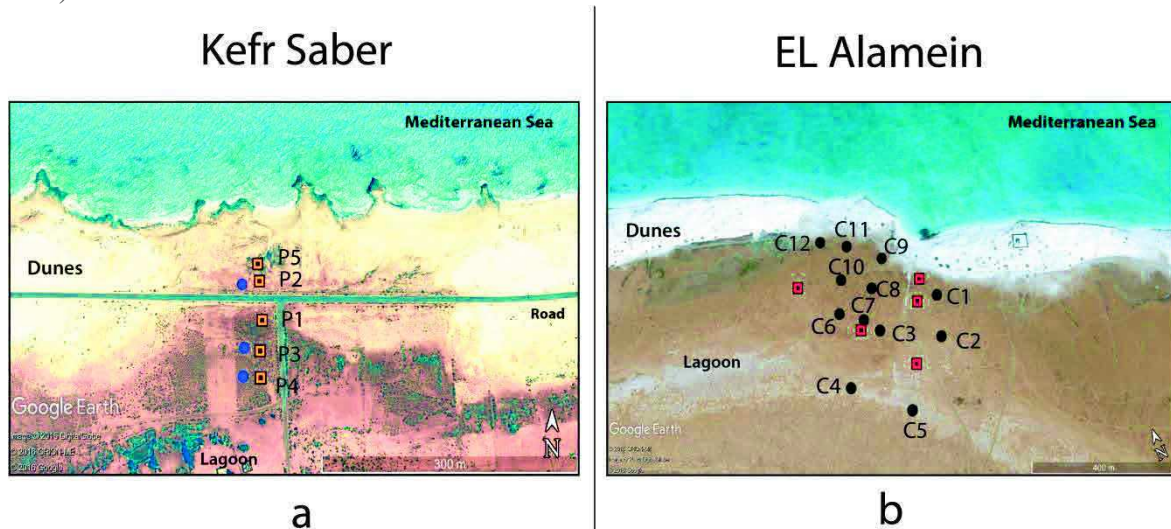
Figure 2: Location of trenches and core sites at (a) Kefr Saber and (b) El Alamein (see also Figure 1).

Coastal dune-ridges constitute an outstanding land feature at several locations parallel to the shoreline and protect inner lagoons from the sea. These dunes are completely weathered where the headlands exist (Abbas et al., 2008). The 2 to 30-m-high coastal beach-dune ridge mainly composed of oolitic and biogenic calcareous sand separates coastal lagoons and sabkhas (salt lake) from the sea, the beach dunes; the beach-dune ridge is developed along the receding Quaternary shorelines and embayment of the Mediterranean Sea (Hassouba, 1995). The lagoons with flat depressions separated from the sea by the coastal dunes (with different heights and sometimes with seawater outltets) are designated sites that may record past tsunami deposits.

The selected sites were chosen taking into account geomorphological and topographic setting, the accumulation of boulders as witness of past tsunami events along the coast (Shah-Hosseini et al., 2016) and the accessibility in order to avoid urbanization and artificial soil reworking. Suitable sites for trenching and coring are therefore located in dry lagoons (during summer season) protected from the sea by 2 to 30-m-high sand dunes. Two sites with ~200 km apart have met the selection criteria for site investigation (Figs. 1 and 2): 1) Kefr Saber located at ~32-km west of Marsa-Matrouh city, and 2) El Alamein site at ~10 km northwest of El Alamein city. Five trenches were dug at Kefr Saber (Fig. 2a), and 12 cores were performed at the Alamein site (Fig. 2b).
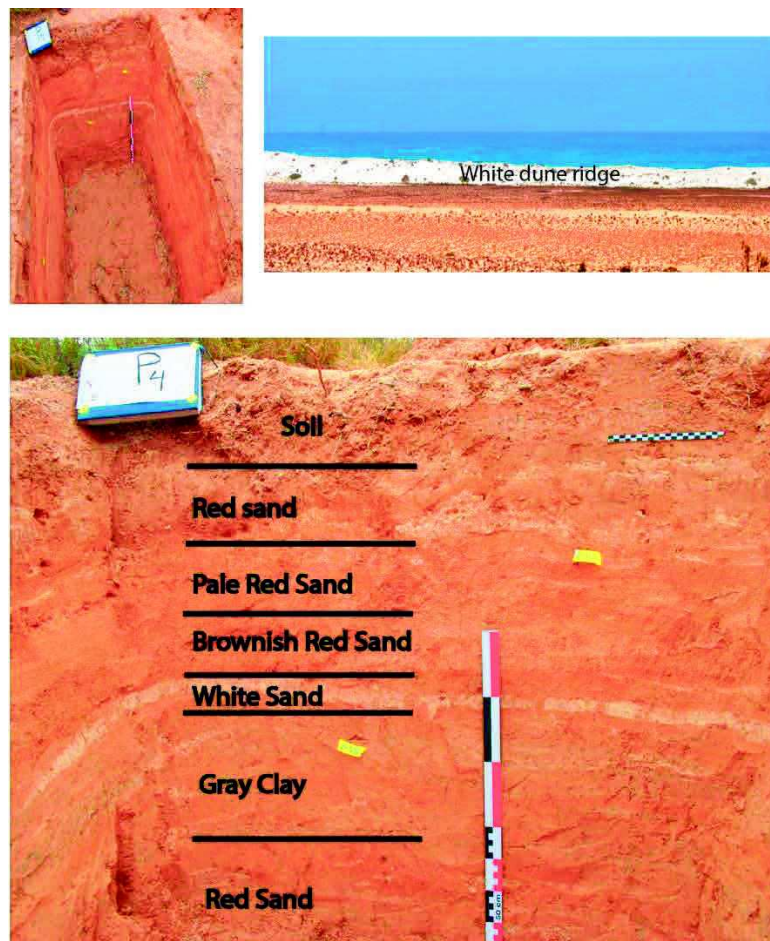
Figure 3: a) Kefr Saber trench size, (b) location in lagoon depression south of dune ridge, and (c) description of sedimentary layers of trench P 4 with carbon dating sampling (yellow flag); the graduated vertical ruler indicates 10 cm scale.

4. Selected sites and used methods for paleotsunami investigations

The trench sizes are ~2 x 1 meter with ~1.5-m-depth and all trench walls exposed fine-grained sedimentary layers and were logged in details. The maximum core depth is ~2.6 m and their distribution in the lagoons was planned to occupy an area from the depression (depo-center) to the edge close to the outlet of seawater in order to observe any thickness variation of tsunami layers.

The core tubes were split in half lengthwise, photographed using both normal and ultra-violet lightning accompanied by detail description of textures and sedimentary structures. The X-ray scanning was performed immediately after core opening and cores were sent to the laboratory of the National Institute of Geophysics and Astronomy (NRIAG, Cairo) for sampling and further analysis. The magnetic susceptibility measurements were operated along cores and samples were collected for radiocarbon dating, physical, chemical and organic matter analyses.
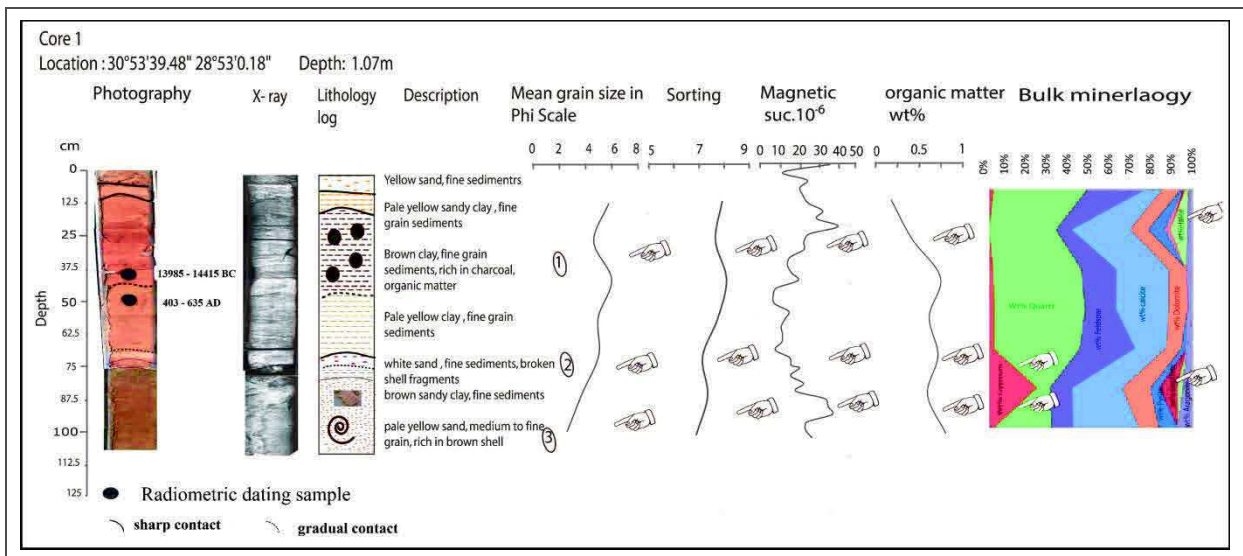
Figure 4: a) Core 1 photography, X-ray scanning, lithology log, magnetic susceptibility, mean grain size, sediment sorting, total organic and inorganic matter and bulk mineralogy. The arrows show the high values of each measurement that may correlate with tsunami deposits.

The magnetic susceptibility was measured for cores at the NRIAG Rock Magnetism laboratory then corrected against air by using Bartington compatible software. 120 samples were collected from cores then analyzed for grain size analysis; X-ray diffraction using Philips PW 1730. The total organic and inorganic measurements were carried out at the laboratory of Central Metallurgical Research & Devolpment Institute (CMRDI) Center of Eltebbin (Egypt). Statistics of the grain-size distribution were calculated using Folk equations (1968) to calculate mean size and sorting of the sediments along the cores.

The Radiocarbon dating of samples were carried out in three laboratories (Poznan laboratory - Poland, CIRAM in Bordeaux, France and Beta Analytical laboratory, USA) to ensure coherency and quality of results (see Tables 2 a and b). The collected samples were made of: charcoal, bones, gastropods, shells and organic matter. The radiocarbon dating results of charcoal and organic matter were calibrated using a recent calibration curve (Reymer et al., 2013) and Oxcal software for the probability density function of each sample age with 2σ uncertainty (Bronk-Ramsay, 2009); furthermore the gastropods and shells were corrected against reservoir effects.

233
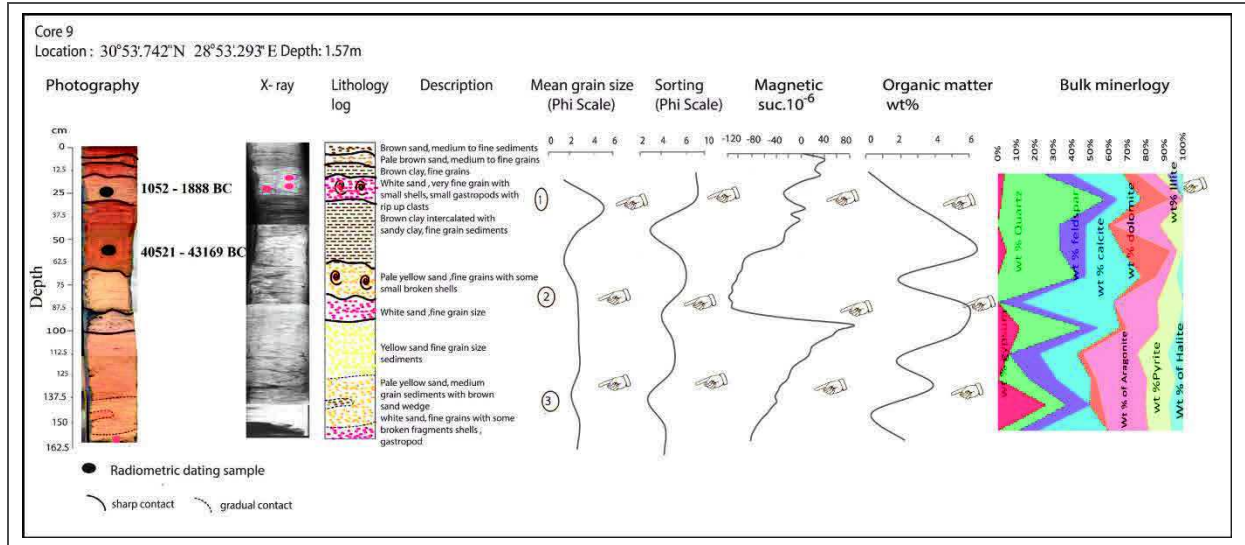
234
235 *Figure 4: b) Core 9 photography, X-ray scanning, lithology log, magnetic susceptibility,*
236 *mean grain size, sediment sorting, total organic and inorganic matter and bulk mineralogy.*
237 *The arrows show the high values of each measurement that may correlate with tsunami*
238 *deposits.(Similar illustrations of cores 2 to 12 are in supplemental materials).*
239

240 **5. Description of trenches and cores sedimentary layers**
241　　　The selected sites revealed a succession of sedimentary units typical of lagoon
242 deposits with fine strata made of a mix of fine gravel, sand, silt and clay. At both Kefr Saber
243 and El Alamein sites, trenches and cores present comparable soft sediment content and
244 stratigraphy, but with some differences due to their distance from the shore, situation in
245 lagoons and with regards to the dune heights.
246　　　*Trenches at Kefr Saber:* Trenches P1, P2, P3 and P4 have quite similar sedimentary
247 succession with fine-grained mostly alluvial deposits made of sandy-silty layers with mixed
248 coarse and white fine sand with broken shells of marine origin (Fig. 3 and trench logs in
249 supplemental material S1). A layer with white mixed sand, gravel and broken shells with
250 variable 2 to 15 cm thickness is found at 30 – 50 cm depth in P1, P2, P3 and P4. The white
251 sandy layer is deeper (larger than 30 cm) in trench P3 and P4 located in the lagoon depo-
252 center. Trench P5 which is close to the dunes and shoreline show a succession of coarse and
253 fine sand and about 30 to 40 cm thick mixed with pebbles. The layer characterized by high-
254 energy sedimentary deposits is interpreted as of tsunami origin.
255　　　Two charcoal samples collected in Trench P1 at 35 cm and 53 cm depth display
256 modern age (younger than 1650 AD) and 39000-38250 BC, respectively. In Trench P2, two
257 other charcoal samples collected at 73 cm and 100 cm depth and both below the tsunami layer
258 1 (Fig.S1-b) indicate 50 - 70 AD and 5300-5070 BC, respectively (see also Table 2a). In
259 Trench P4, four collected charcoal samples at 15 cm, 25 cm, 40 cm and 61 cm depth reveal
260 modern ages (younger than 1650 AD). A fifth charcoal sample located at 60 cm depth
261 provides 17200- 15900 BC. In Trench P5, four charcoal samples are collected with the
262 uppermost located at 12 cm depth is dated at 360 - 50 BC, the second sample at 17 cm depth
263 show 30- 180 AD, the third, and fourth charcoal samples found at 33 cm and 37 cm depth are
264 dated at 350 - 1050 BC and 2400 - 4000 BC, respectively.
265　　　Although the sedimentary deposits in trenches at Kefr Saber and related modern,
266 young and old dates may indicate reworking, the well identified mixed coarse and fine white
267 sand with broken shells of marine origin at ~ 30 - 73 cm depth may well be correlated with

the tsunami deposits of the 21 July 365 earthquake. Furthermore, the radiocarbon calibrated date of shells (Dendropoma) founds in boulders at Kefr Sabr provides 940-1446 AD while another sample in Ras El Hekma (about 100 km east of Kefr Saber) has a calibrated date of 6812 -7597 BC. The Dendropoma sample age at Kefr Saber may correlate with the 8 August 1303 earthquake and tsunami event that dragged large boulders on the shoreline in agreement with the results of Shah-Hosseini et al. (2016). However, the 1303 event is not recognized in the trenches dug in the nearby lagoon sedimentary deposits.

No.	Sample name	Laboratory Name	Type of samples	Depth (m)	Date BP	Calibrated. date
1	RHSX	Poznan		Boulder	8380 ± 40 BP	7320 - 7550 BC
2	KSB2S2	Poznan	Dendroma	Boulder	890 ± 30 BP	1030 – 1220 AD
3	TSU P1 S07B	Poznan	Charcoal	35	110.14±0.3 BP	Modern
4	TSU P1 S09B	CIRAM	Charcoal	53	40560 BP	39000-38250 BC
5	TSU P3S2	CIRAM	charcoal	73	2000 BP	50-70 AD
6	TSU P3S3	CIRAM	Charcoal	100	6240 BP	5300 – 5070 BC
7	TSU P3 S2	Poznan	Charcoal	72	1075 ± 30 BP	890 – 1020 AD
8	TSU P4 S2	CIRAM	Charcoal	61	Modern	-
9	TSU P4 S3	CIRAM	Charcoal	41	Modern	-
10	TSU P4 S4	CIRAM	Charcoal	15	Modern	-
11	TSU P4 S5	Poznan	Charcoal	60	15490 ± 70 BP	17200 – 15900 BC
12	TSU P4 S6	Poznan	Charcoal	25	101.42 ± 0.68 BP	1700 – 1920 AD
13	TSU P5S1	Poznan	Charcoal	12	2145 ± 30 BP	360 – 50BC
14	TSU P5S2	Poznan	Charcoal	37	4560 ± 300 BP	4000 – 2400 BC
15	TSU P5S3	Poznan	Charcoal	17	2060 ± 35 BP	180 – 30 AD
16	TSU P5S4	Poznan	Charcoal	33	2590 ± 140 BP	1050 – 350 BC

Table 2 a: Radiocarbon dating samples and calibrate age at Kefr Saber site using OxCal v4.2.4 (Bronk-Ramsey, 2013).

Cores at El Alamein: The 12 cores extend between 1 and 2.6 m depth and except for cores 1 and 9 which are in Figures 4 a and b, all stratigraphic logs are presented in the supplemental material S2. The core descriptions are as following:
Core 1: This core is located at ~166 m from the shoreline (Figure 2), east of the study area behind the sand dunes and near the outlet of the seawater. The core depth reached ~2.14 m and the stratigraphic section includes 3 tsunami layers recognized as following (Figure 4 a section 1): The first layer is at ~12.5 cm depth with ~34.5 thick, brown clay sediments with poor sorting, fine gain sediments, with high peak in magnetic susceptibility, rich in organic matter, and X-ray image reflects clear lamination. The second layer at ~70 cm depth has ~5 cm thickness, characterized by highly broken shells fragments with extremely bad sorting of sediments granulometry. The third layer at ~75 m depth is ~22 cm thick, pale yellow sand with extremely bad sorting of sediments size, with peak in magnetic susceptibility. The chemical analysis shows the presence of gypsum and minor goethite, and X-ray scanning shows some turbiditic structures in these sediments. A fourth tsunami layer is identified at 158 cm (see also Fig. S2-1, section 2). It is characterized by pale brown silt clay, medium to fine,

296 with broken shells fragments and extremely poor sorting, with a clear high peak of magnetic
297 susceptibility.
298

No.	Sample name	Laboratory Name	Type of samples	Depth (m)	Date BP	Calibrated date (2σ)
1	core 1/1sa1	Poznan	charcoal	40	13430±60	13985-14415 BC
2	core 1/1sa2	Poznan	Bone	50	1540±60	403-634 AD
3	core2/1sa4	Poznan	gastropods	77	35500±500	34362-36931 BC
4	core2/1sa6	Poznan	gastropods	75	32000±360	32971-34681 BC
5	core 3/1sa1	Poznan	shell	45	33500±600	34218- 37224 BC
6	core 3/1sa2	Poznan	bivalve	37	45000±2000	43618 BC
7	core 4/1sa1	Poznan	shell	28	31840±350	32887-34447BC
8	core 5/1sa3	Poznan	gastropod +shell	50	446600±1400	442182-448237 BC
9	core 6/2 sa1	Poznan	charcoal	80	125±30	< 1620 AD
10	core 6/1 sa6	Poznan	gastropod	45	34000±400	35002-37441 BC
11	core 6/1sa9	Poznan	coral	60	50000±4000	42776-69225 BC
12	core 7/1sa1	Poznan	shell	17	3000±30	293-1113 BC
12	core 9/1sa1	Poznan	gastropod	24	3320±30	1052-1888 BC
13	core 9/1sa5	Poznan	bivalve	55	40000±800	40521-43169 BC
14	core 10/1sa2	Poznan	bone	70	42000±1300	41256-46581 BC
15	core10/1sa3	Poznan	shells	20	4515 ±30	2623-3521 BC
16	core11/2sa1	Beta analytic	roots	139	4810±30	2666 - 2817 BC
17	core 11/1sa1	Beta analytic	gastropod	20	5230±30	3638-4328 BC
18	core11/2Sa4	Poznan	gastropod +shell	116	4500±35	2619-3386 BC
19	core11/2sa6	Poznan	gastropod	126	4405±35	2477-3368 BC
20	core11/2 sa11	Beta analytic	shells	152	32500±500	33294-36120 BC
21	core 11/2sa2	Beta analytic	shell	62	16900±60	17869-18741 BC
22	core 11-2	Beta analytic	charcoal	180	5020±30	3710-3943 BC
23	core 11 2_5	Poznan	gastropod	121	4360±40	2457-3366 BC
24	core 12/1 sa1	Poznan	gastropod	44	5065±30	3367-4072 BC
25	core 12/2sa1	Beta analytic	gastropod	108	4885±35	3097-3950 BC
26	core 12/2sa2	Poznan	gastropod	114	5000±35	3331-4050 BC
27	core 12/2 sa3	Beta analytic	broken shell	117	37940±420	39560 -40811 BC
28	core 12/2sa4	Beta analytic	roots	135	5060±30	3365-4071 BC
29	E1 A1sa1	CIRAM	charcoal	25	130±20	1680-1908 AD
30	E1 A1sa2	CIRAM	charcoal	56	190±20	1661-1931 AD

299

Two samples were collected for radiocarbon dating from core 1. The first sample is a charcoal fragment at 40 cm depth and has a calibrated date 13985- 14415 BC (Table 2b). This first and uppermost sample is located within a sedimentary unit of tsunami origin characterized by bad sorting, highly broken shells fragments and peak of magnetic susceptibility. The second sample is a rodent bone at 50 cm depth and provides 403 - 603 AD calibrated age which may correspond to a position in between two tsunami deposits in stratigraphic succession 1 and 2 that may be correlated with the tsunami events of 8 August 1303 above and 21 July 365 below.

Core 2: As shown in Fig. S2 - 1 core 2 is ~90 cm deep located south of core 1 at ~264 m from the shoreline. Two tsunami layers are recognized. The first tsunami layer of brown clay sediments is at ~12.5 cm depth ~12.5 cm thick with extremely bad sorting, corresponding to a small peak at magnetic susceptibility. The layer is rich in organic matter (> 1) comparable with other layers of this core; the geochemical analysis shows minor component of goethite. The second layer is at ~50 cm depth ~15 cm thick, made of yellow sand with silty-clay pockets, rich with broken shells fragments, extremely poor sorting and with peak magnetic suc. It is rich in organic matter comparing to other layer, and the geochemical analysis shows minor component of halite.

Two shell (gastropod) samples were collected at 75 cm and 77 cm depth and have calibrated dates 32971 - 34681 and 34362 - 36931 BC, respectively (Table 2b). These two samples are located in the bottom of the tsunami stratigraphic layer 2 (Fig.S2-1). However, their old age may well be due to a reworked sedimentation during the catastrophic tsunami event.

Core 3: This core is located at 270 m from the shoreline and the outlet of sea water as shown in Fig. S2 - 3. The first tsunami layer is at ~25 cm depth and corresponds to a 26 cm thick pale brown clay with sorted sediments; it is characterized by highly broken shells fragments and sediments rich in organic matter. The second layer at ~70 cm depth is 17.5 cm thick; it is characterized by white sand with laminations at the top and fine sediments at the bottom, with peak of magnetic susceptibility near zero value, and with high organic matter > 2. The third tsunami layer at 106 cm depth is 32 cm thick, characterized by yellow sand with minor illite and broken shells fragments.

Two shell samples were collected for dating at 37 cm and 45 cm depth and show calibrated dates 43618 BC and 34218 - 37224 BC respectively (Fig. S2-2 and Table 2b). These two samples are located within the stratigraphic tsunami layer 2 and may correspond to reworked sediments due to the high energy sedimentation during the catastrophic event.

Core 4: It is located at 435 m from the shoreline and shows stratigraphic units characterized by two tsunami layers (Fig. S2 - 4). The first tsunami layer is white sand at ~12.5 cm depth 7 cm thick with highly sorted sediments. It also shows high broken shells fragments with organic matter > 2. The third tsunami layer is a 35 cm thick pale yellow sand at ~102 cm depth. It is also characterized by yellow sand with minor amount of illite and gypsum and broken shells fragments.

One shell sample collected for dating at 37 cm depth provides a calibrated date 32887 - 34447 BC respectively (Table 2b). This sample located in the stratigraphic tsunami layer 1 (Fig.S2-3) apparently results from high energy reworked sedimentation during the catastrophic event (Fig. S2-4).

Core 5: This is the southernmost core in the El Alamein site at 490 m distance from the shoreline (Fig. S2 - 4). The core reaches 73 cm depth and the sedimentary succession does not show any possible sedimentary catastrophic layer of tsunami origin. According to its content, core 5 may show the limit of inundation area with respect to at least the first and second tsunami layers.

One shell (gastropod) sample collected for dating at 50 cm depth provides 442182 - 448237 BC calibrated age (Table 2b). The relatively old age of the sample may refer to transportation and reworking due to high current waves during a tsunami event.

Core 6: This core is located south of the sand dunes at 320 m from the shoreline. It is characterized by three tsunami layers (Fig. S2 - 5). The first tsunami layer is a pale yellow sand with broken shells fragments at ~5 cm depth and ~24 cm thick with highly sorted sediments rich in organic matter larger than 2.5. The second tsunami layer is at ~58 cm depth ~18.5 cm thick characterized by yellow sand with a minor amount of gypsum and Illite. The third tsunami layer at 130 cm depth ~20 cm thick characterized by white sand with minor amount of goethite and broken shells fragments. It is very rich (larger than 3) in total weight of organic matter.

Kafr Saber

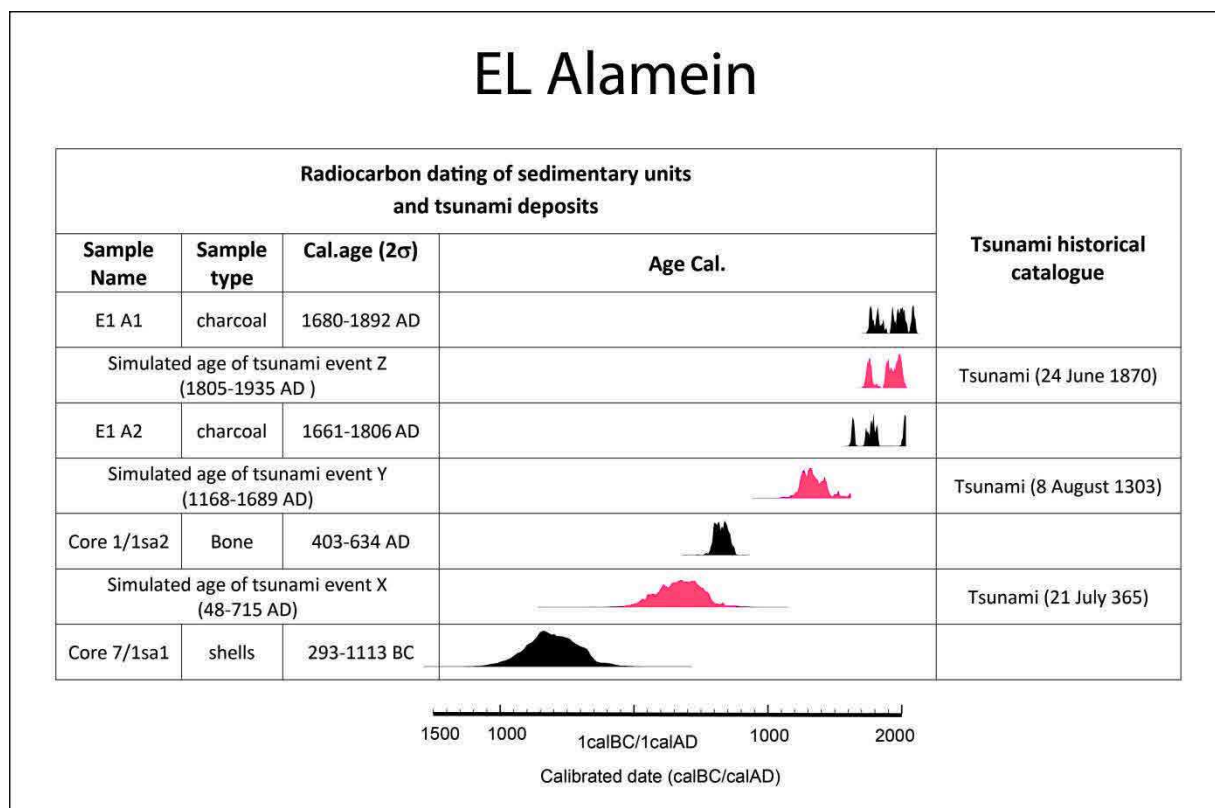| Radiocarbon dating of sedimentary units and tsunami deposit				Tsunami historical catalogue
Sample Name	**Sample type**	**Cal.age (2σ)**	**Age Cal.**	
TSU P3 S2	charcoal	820-1020 AD		
Simulated age of tsunami event X (137-422 AD)				Tsunami (21 July 365)
TSU P5S3	charcoal	30-180 AD		
TSU P3 S1	charcoal	49-59 AD		
TSU P5S4	charcoal	360-50 BC		
TSU P5S4	charcoal	1050-350 BC		
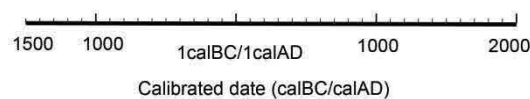
Fig. 5a: Radiocarbon dating calibrated with probability density function (pdf) using Oxcal version 4.2 (Bronk-Ramsey, 2009) and chronology of dated tsunami records in Kefr Saber. Black pdfs refer to the dated samples and red pdfs are simulated dating of three tsunami records. The sedimentary record is correlated with the historical earthquake and tsunami catalogue of the eastern Mediterranean (Guidoboni et al., 1994; Stiros, 2001; Ambraseys, 2009).

Three samples were collected for dating in core 6. The first sample is a gastropod at ~45 cm depth and shows 35002-37441 BC calibrated date. The second and third samples are

coral fragments at ~60 cm and ~80 cm depth that show 42776-69225 BC and modern (younger than 1650 AD) calibrated ages, respectively. The first sample is above the stratigraphic tsunami layer 2 while the second sample was within the stratigraphic tsunami layer 2 (Fig S2-7). These samples may result from reworking due to high current waves transport of tsunamis.

Core 7: This core was located at 273 m from the shoreline. It characterized by stratigraphic units with soft sediments with three tsunami layers within 120 cm depth (Fig. S2 - 6). The first tsunami layer is brown sand with broken shell fragments at ~14 cm depth 6 cm thick with highly sorted sediments. It is characterized by rich with organic matter > 2 and noticeable peak of magnetic susceptibility and the presence amount of gypsum of swampy environment and minor amount of Illite and goethite. The second tsunami layer at 50 cm depth is 20 cm thick characterized by pale brown clay with pebbles at bottom. The third tsunami layer is at 115 cm depth and 15 cm thick characterized by white sand, bad sorting sediments with minor amount of pyrite. One sample of shell only was collected at 17 cm depth for radiocarbon dating and provides 293-1113 BC. This sample predates the 365 AD event.

EL Alamein

		Radiocarbon dating of sedimentary units and tsunami deposits		**Tsunami historical catalogue**
Sample Name	**Sample type**	**Cal.age (2σ)**	**Age Cal.**	
E1 A1	charcoal	1680-1892 AD		
Simulated age of tsunami event Z (1805-1935 AD)				Tsunami (24 June 1870)
E1 A2	charcoal	1661-1806 AD		
Simulated age of tsunami event Y (1168-1689 AD)				Tsunami (8 August 1303)
Core 1/1sa2	Bone	403-634 AD		
Simulated age of tsunami event X (48-715 AD)				Tsunami (21 July 365)
Core 7/1sa1	shells	293-1113 BC		

1500   1000   1calBC/1calAD   1000   2000

Calibrated date (calBC/calAD)

Fig. 5b: Radiocarbon dating calibrated with probability density function (pdf) using Oxcal version 4.2 (Bronk-Ramsey, 2009) and chronology of dated tsunami records in El Alamein. Black pdfs refer to the dated samples and red pdfs are simulated dating of three tsunami records. The three sedimentary records are correlated with the historical earthquake and tsunami catalogue of the eastern Mediterranean (Guidoboni et al., 1994; Stiros, 2001; Ambraseys, 2009).

Core 8: This core is located at 214 m from the shoreline. Three tsunami layers are recognized (Fig. S2 - 7). The first tsunami layer is a pale silty clay at ~14 cm depth 16 cm thick with high organic matter and minor amount of goethite. It is characterized by highly broken shell

fragments and rich in organic matter. The second layer at 52 cm depth and 22 cm thick characterized by pale yellow silty-clay, with low peak of magnetic susceptibility and high organic matter >2.5. The third tsunami layer at 128 cm depth is 9 cm thick characterized by pale yellow sand with highly angular gravel sediments, badly sorted and broken shells fragments. No samples were suitable for dating in this core.

Core 9: It is located at 130 m from the shore line. Three tsunami layers are recognized (Fig. 4 b). The first tsunami layer is white sand at ~16 cm depth and 13 cm thick with high content of organic matter and rip up clasts that appear in X-ray scanning characterized by highly broken shells fragments and rich in organic matter. The second layer at 67 cm depth is 22 cm thick characterized by white sand, with a peak of magnetic susceptibility, high content of organic matter larger than 5. The third tsunami layer at 139 cm depth is 14 cm thick characterized by broken shells fragments and white sand with highly angular sediments that reflect the bad granulometric sorting.

Two samples were collected for dating in core 9. The first sample is a gastropod located at 24 cm depth within the tsunami layer 1 provides 1052-1888 BC calibrated age. The second sample at 55 cm depth is a bivalve (lamellibranch) located below the stratigraphic tsunami layer 1 (and above the tsunami layer 2) dated at 40521-43169 BC calibrated age. These samples may have been transported and sedimented in reworked units due to high current waves of tsunami.

Core 10: It is located at 245 m from the shoreline. Three tsunami layers are recognized (Fig. S2 - 8). The first tsunami layer is a brown silty clay at ~19 cm depth 9 cm thick, with highly organic matter and with rip up clasts and lamination that appear in X-ray scanning. It is characterized by high broken shells fragments and rich in organic matter > 4. The second layer at 48 cm depth and 38 cm thick is characterized by brown sand with broken fragments of shells, with peak of magnetic susceptibility, and high organic matter > 1.5 at the bottom of the layer. The third tsunami layer at 101 cm depth is 28 cm thick characterized by pale yellow sand with high organic rich matter and sediments that reflect the bad sorting.

Two samples were collected for dating in core 10. The first sample located in the stratigraphic tsunami layer 1 is a shell fragment at 24 cm depth that provides 2623 - 3521 BC calibrated age. The second sample located in the stratigraphic tsunami layer 2 is a rodent bone at 70 cm depth showing 41256-46581 BC calibrated age (Table 2b). Both samples may result from reworked sedimentary units due to high current waves of tsunami events.

Core 11: It is located at 151 m from the shoreline. Three tsunami layers are recognized (Fig.S2 - 9). The first tsunami layer is a white sand at ~19 cm depth 10 cm thick, with highly organic matter and characterized by high broken shells fragments and rich in organic matter > 4 with high weight percent of gypsum 50%. The second layer at 76 cm depth 9 cm thick characterized by white sand, with broken fragments of shells, with peak of magnetic susceptibility with organic matter larger than 1.5. The third tsunami layer at 107 cm depth with 21 cm thick characterized by grey silty and sediments reflect the bad sorting and high organic rich matter with minor amount of Illite and gypsum.

Eight samples were collected for dating in core 11. The first sample is a gastropod at 20 cm depth and shows 3638-4328 BC calibrated age. The second sample is a shell at 62 cm depth with a calibrated date of 3710-3943 BC (Table 2 b). These two samples are found in the stratigraphic tsunami layer 1 and 2 respectively (Fig.S2-9). They may correspond to transported samples in reworked sediments due to high wave current of tsunami.

The third, fourth and fifth sample are gastropods found at 116 cm, 121 cm and 126 cm depth with calibrated date 2619-3386 BC, 2457- 3366 BC and 2477-3368 BC, respectively. The sixth sample is a shell found at 152 cm depth with calibrated date 33294-36120 BC. The seventh sample corresponds to roots found at 139 cm depth with 2666-2817 BC calibrated age. The eighth sample is a charcoal found at 180 cm depth with calibrated date 3710-3943

BC (Table 2b). Except for sample 6, samples 3 to 8 belong to sediments with chronological sequence from 2457 to 3943 BC. The six samples are seemed to be transported by high wave current of tsunami.

Core 12: It is located at 127 m from the shoreline. Three tsunami layers are recognized (Fig. S2 - 10). The first layer is ~7.5-cm-thick at ~19-cm-depth and is made of poorly sorted white sandy deposits, and highly broken gastropods and lamellibranch fossils. The high value of organic matter and high peak of magnetic susceptibility reflect a rich content in carbonates and quartz. The second layer is ~13-cm-thick at ~32.5-cm-depth characterized by white sandy deposits intercalated with coarse brown sand horizontal lamination, poor sorting sediments, rich in total organic matter and high peak of magnetic susceptibility. The third layer is ~25-cm-thick at 89-cm-depth made of grey sandy clay, with laminations at the bottom of deposits, vertically aligned gastropods, broken shells fragments, rich in total organic matter and pyrite showing high peak of magnetic susceptibility. A fourth tsunami layer is identified at 151 cm depth core bottom. It is characterized by pale yellow sand, medium to fine, with broken shells fragments and extremely poor sorting, with high peak of magnetic susceptibility, high peak of organic matter > 5.5 and high amount of gypsum.

Five samples were collected for dating in core 12. The first sample is a gastropod found at 44 cm depth with a calibrated date at 3367-3366 BC. The second sample is a shell found at 108 cm depth and shows 3097-3950 BC calibrated age (Table 2b). The third sample is a gastropod found at 114 cm depth with calibrated date 3331-4050 BC. The fourth sample is a shell found at 117 cm depth with calibrated age 39560- 40811 BC. The fifth sample is a gastropod found at 135 cm depth with calibrated age 3365-4071 BC (Table 2b). The first and fourth samples appears off sequence with respect to the other samples and may result from sediment transport and reworking due to high energy tsunami waves. The other samples are in sequence from 2457 to 4071 BC ages comparable to the sedimentary succession of core 11.

6. Summary of results from trenching and coring

The cores and trenches in both Kefr Saber and Alamein sites show three main layers characterized by fine and coarse sand mixed with broken shell fragments that indicate the occurrence of high energy sedimentary deposits in the coastal lagoon environment (Figs. 2 a and b, and Fig. 3). A remarkable observation is the very similar white sandy layer with broken shells found in trenches (see Fig. 3) and in cores with ~200 km apart that we interpret as tsunami deposits due their sedimentary signatures (see details of core descriptions above). According to the radiocarbon dating, this layer may be correlated with the 21 July 365 earthquake in western Crete and related tsunami (Figures 5 a and b).

In most cores (Figs. 4 a and b, and Fig. S2), the first tsunami layer is ~7.5-cm-thick at ~19 cm-depth and is made of poorly sorted white sandy deposits with high broken gastropods and lamellibranch (shell) fossils. The high value of organic matter and high peak of magnetic susceptibility reflect a rich content in carbonates and quartz. The second layer is ~13-cm-thick at ~32.5-cm-depth characterized by white sandy deposits intercalated with coarse brown sand horizontal lamination, poor sorting sediments, rich in total organic matter and high peak of magnetic susceptibility. The third layer ~25-cm-thick at ~89-cm-depth is made of grey sandy clay, with laminations at the bottom of deposits, vertically aligned gastropods, broken shells fragments, rich in total organic matter and pyrite showing high peak of magnetic susceptibility.

In a synthesis of all dated units in trenches and cores, the sedimentary succession provide evidence for the identification of three tsunami deposits with their ages using radiocarbon dating at Kefr Saber and El Alamein sites (Figs 5 a and b). In the case of Kefr Saber trenches (Fig. 5 a and Table 2 a), the dating of charcoal fragments allows the bracket of a tsunami event between AD 30 – 120 (sample TSU P5 S3) and AD 820 – 1020 (sample TSU

P3 S2). From the dating sequence, and using the Oxcal Bayesian analysis (Bronk-Ramsay, 2001) we obtain a simulated age of the tsunami event between AD 137 and AD 422, which includes the AD 365 western Crete earthquake. The dating of sedimentary units at the El Alamein site turned out to be more complex due to the reworked sedimentation with significant alluvial deposits (see the large number of dating larger than 30 ka BC in Table 2 b). The radiocarbon dating (including the Oxcal Bayesian analysis) of shells, bone and charcoals fragments at El Alamein site result in a sequence of ages that allow the bracket of an event X between AD 48 and AD 715, and event Y between AD 1168 and AD 1689, and an event Z between AD 1805 and AD 1935 (Fig. 5b). The three simulated dates of the three tsunami events X, Y and Z include the seismogenic tsunamis of AD 365, AD 1303 and AD 1870.
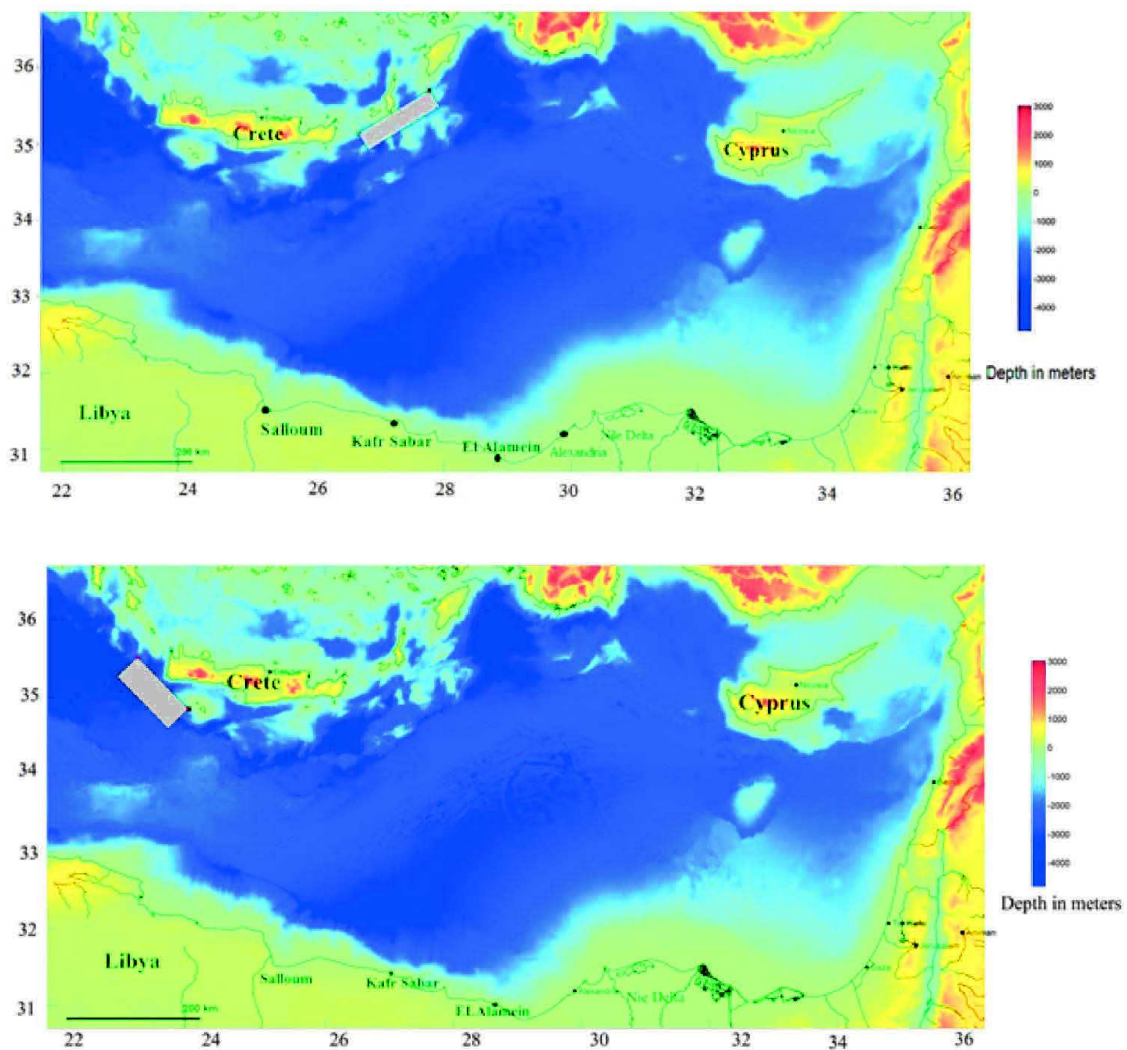
Figure 6: Location and size of tsunamigenic earthquake fault ruptures (box) along the Hellenic subduction zone with a) eastern scenario between Crete and Rhodos (for the AD 1303 and AD 1870 earhquakes), and b) western scenario in western Crete (for the AD 365 earthquake). Bathymetry data from Gebco 2014 (2003).

The three main layers visible in trenches and cores have physical and chemical characteristics that correlate with high energy environmental conditions of tsunami deposits. The three high magnetic susceptibility peaks of the three deposits also correlates with the high

529 value of organic matter and carbonates. We also observe poorly sorted sediments greater than
530 5 in the three layers that according to Folk (1968) mark high energy deposits and tsunami
531 records.
532
533 **The modelling of tsunami waves**
534   The tsunami issue is particularly urgent for the Mediterranean countries that are
535 known to have been affected by tsunamis in the past, several of which had catastrophic size
536 and impact (Papadopoulos et al., 2014). Previous numerical studies of tsunamis modelling and
537 estimation of the wave height runup and the time of wave arrival on a given coastline have
538 been presented for the Hellenic arc (Shaw et al., 2008; Hamouda, 2006, 2009; Tinti et al.,
539 2015; Necmioglu and Ozel, 2015).
540

Fault dimension	Values
Length	124 km
Width	50 km
Strike	54°
Dip	55°
Rake	90°
Coseismic Slip	8 m
Depth	57 km
Mw	8.5
Seismic Moment (N.m.)	$7.1\ 10^{21}$

541
542 *Table 3: Fault geometry and parameters in the east Hellenic arc used for our modelling and*
543 *scenario.*
544
545   These studies present different results due to two reasons: a) the bathymetry data with
546 various resolutions are used in the modelling, and b) the fault rupture and surface deformation
547 with various parameters used in these modelling studies.
548   Here, we present the modelling of wave propagations with two simple scenarios of
549 earthquake-generated tsunamis in the eastern and western Hellenic subduction zone (Fig. 7).
550 For each scenario, we take into account a seismic fault capable of generating an earthquake
551 with magnitude Mw equal to or larger than the highest magnitude (Mw ~ 8.5) consistent with
552 the evaluated earthquake size from historical catalogues (Tables 3 and 4; Stiros, 2001; Shaw
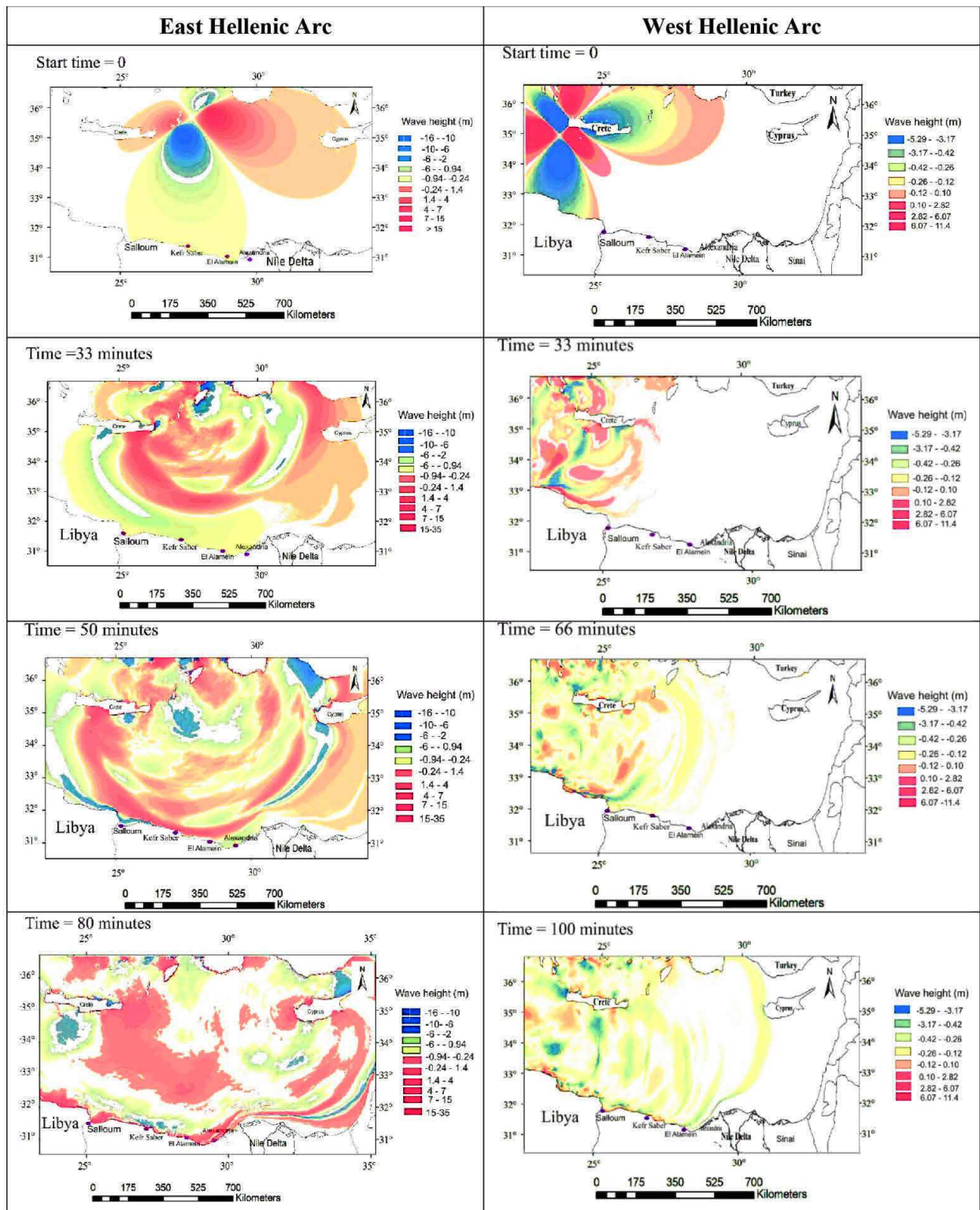553 et al., 2008; Papadopoulos et al., 2014).
554

Fault dimension	Values
Length	115 km
Width	45 km
Strike	133.5°
Dip	45°
Rake	90°
Coseismic Slip	9 m
Depth	40 km
Mw	8.5
Seismic Moment (N.m.)	$7.3\ 10^{21}$

555
556 *Table 4: Fault geometry and parameters in the west Hellenic arc used for our modelling and*
557 *scenario.*

558

559

560

561 *Figure 7: Modeling of wave heights and propagation time in the eastern Mediterranean*
562 *following two worst case scenarios of comparable AD 1303 (eastern Hellenic Arc) and AD*
563 *365 (western Hellenic Arc) earthquakes.*

564

565   The computation is based on the nonlinear shallow water theory using the Mirone
566 software update version 2.7.0, modified on 22 October 2016 (Madder, 2004; Luis, 2006). The
567 digital bathymetric data of the Eastern Mediterranean was obtained from the bathymetric
568 chart of Intergovernmental Oceanographic Commission 2014 (GEBCO, 2003). We use these
569 fault parameters and the Okada (1985) dislocation model in order to create the initial tsunami
570 wave. In this study, grids represent the GEBCO bathymetry (30 arc seconds, 2003) and
571 another grids contains the initial deformation as produced by the dislocation deformation
572 module.
573   In both scenarios, we consider an Mw 8.5 (as worst case) earthquake generated on
574 thrust faults running parallel to Eastern Crete-Rhodos segment consistent with the AD 1303,
575 and to western Crete consistent with AD 365 earthquake (Figures 6 a and b; Papadopoulos et
576 al., 2014). The fault rupture parameters (Tables 3 and 4) of the eastern and western
577 seismogenic segments of the Hellenic subduction zone determine the tsunami initial
578 conditions and associated seafloor coseismic deformation with a 35 m maximum and -15 m
579 initial water elevations (Fig. 7). Snapshot images of Figure 7 obtained from the modelling
580 simulation show the tsunami field wave propagations computed every 0, 16, 33, 66, 100, 150
581 minutes after the tsunami initiation. Our observations indicate that all the Egyptian coastline
582 is affected by tsunami waves but with relatively short time (~50 mn) wave propagation and
583 larger (4 to 10 m) wave heights in the case of the eastern Hellenic arc seismic source (e.g.,
584 AD 1303 earthquake). In the case of the west Crete seismic source, major wave arrives at the
585 Egyptian coast after 100 minutes with 0.86 – 1.76 m wave height at Kafr Saber site and with
586 0.50 m wave height at the El Alamein site.
587   In comparison with the paleoseismic results, the modelling indicate that both Kefr
588 Saber and El Alamein sites recorded the past tsunamis, but with the latter site being better
589 exposed to the eastern Hellenic source of tsunamis than to the western source. In contrast, the
590 Kefr Saber site has a better record of the western Crete tsunami due to its proximity to the
591 western Hellenic seismic sources.
592
593 **Discussions and Conclusions**
594   The identification of tsunami deposits within the stratigraphic layers and results of
595 radiocarbon dating allow the chronological simulation of the three tsunami events (Figs. 5 a
596 and b). Indeed, the dating of the three high energy sedimentary layers deposited along the
597 Egyptian coastline a Kefr Saber and El Alamein correlate with the seismogenic tsunamis
598 generated on the Hellenic subduction zone. The historical seismicity catalogue of the Eastern
599 Mediterranean reports three significant tsunamigenic seismic events of the Hellenic
600 subduction zone that affected the Mediterranean coast of Egypt: 1) The 21 July 365
601 earthquake (Mw 8.3 – 8.5; Stiros and Drakos, 2006; Shaw et al., 2008), 2) the 8 August 1303
602 earthquake (Mw 7.8 – 8.0), and 3) the 24 June 1870 earthquake (Mw 7 - 7.5). The size of past
603 tsunamis can be compared with the thickness of catastrophic sedimentary units in trenches of
604 Kefr Saber and core units of the El Alamein site. It appears that the tsunami deposits of the
605 AD 365 tsunamigenic earthquake have a larger thickness at Kefr Saber site than at the El
606 Alamein site. In return, the thickness of sedimentary layers of the AD 1303 and AD 1870 are
607 thicker at the El Alamein site. These observations can be justified by the proximity of the
608 tsunamigenic source in western Crete and AD 365 earthquake with respect to the Kefr Saber
609 site, and the proximity of the AD 1303 and AD 1870 seismic sources in the east Hellenic Arc
610 with regards to the El Alamein paleotsunami site.
611   The record of past tsunami deposits are favored by the low topography and platform
612 geomorphology along the Egyptian Mediterranean coastline. The coastal environment with
613 similar lagoons and dunes with large areas with relatively flat morphology allowed the
614 deposits of catastrophic marine deposits intercalated within alluvial deposits. The lagoon

shapes elongated along the shoreline at Kefr Saber and El Alamein sites explain the similarity between the sedimentary units and the tsunami deposits. The correlation between the core deposits at El Alamein and trench deposits at Kefr Saber is marked by the dating of tsunami deposits and the correspondence with the AD 365 earthquake. The succession of sudden high-energy deposits with low energy and slow sedimentation may include reworked units with disturbance in their chronological succession. In comparison with the trench results of Kefr Saber, the sedimentary sequence from cores at El Alamein reveals mixed old and young dates likely due to the sedimentary environment with large lagoon and nearby topography with the supply of colluvial and alluvial deposits. Despite the richness of the sediment content in charcoal fragment, bones and shells, the reworking imply significant out of sequence dating and large uncertainties (see table 2 b with 12 dating with ages > 30 ka among 30 samples). Although the results of dated shells would have been suspicious (due to the unclosed mineralogical system), their consistency is pointed out with the comparable nearby radiocarbon dating. On the other hand, 3 modern ages from the Kefr Saber trench units affected the final results of tsunami layer determination.

The study of paleotsunami deposits represents an insight into the occurrence and size of future tsunamis with an estimate of wave heights. Our modelling reveal 4 to 10 m high wave reaching the Egyptian coastline after 50 minutes (Fig. 7) in agreement with the historical seismicity catalogue that indicate the occurrence of great damage in Alexandria region with coastal flooding and inundations. Although the constraint of tsunamigenic seismic sources along the Hellenic subduction zone may include large uncertainties, the changes in the parameters of coseismic ruptures do not affect significantly effect the wave propagation (timing) and heights (less than 20%). The 800 years estimated recurrence time of coseismic slip along the Hellenic subduction zone (with ~5000 years return period for each rupture segment; Shaw et al., 2008) implies the repetition of tsunami catastrophes and the possibility for a forecast programme in the East Mediterranean regions (Titov et al; 2005). These results taking into account the worst case scenarios (earthquakes with Mw ≥ 8.5) are critical for the mitigation of tsunami catastrophes along coastline Egypt.

Supplementary data (See Chapter IV Palotsunami records in Northern Egypt)

Supplementary data associated with this manuscript are:
- Figures S1 a, b c d and e of trench logs of Kefr Saber site,
- Figure S2 – 1 to 10. of core descriptions of El Alamein site.

References

Abbas, M.S., El-Morsy, M.H., Shahba, M.A. and Moursy, F.I., 2008. Ecological studies in coastal sand dune rangelands in the North-West of Egypt, Meeting of the Sub-network on

Mediterranean Forage Resources of the FAO-CIHEAM Inter-regional Cooperative Research and Development Network on Pastures and Fodder Crops, Spai: , p. 389–393.

Abu al-Fida Ismail Ibn Hamwi (born 1273 – died 1331), 1329. The Concise History of Humanity or Chronicles (in Arabic). 2 volumes, 1112 pp, Dar El Kutub El Illmiyah (DKI), Beirut, ISBN: 2745104497.

Ambraseys, N.N., Melville, C.P. and Adam, R.D., 1994. The seismicity of Egypt, Arabia and Red Sea: A Historical Review. Cambridge University Press, 181 pp.

Ambraseys, N., 2009. Earthquakes in the Mediterranean and Middle East: A Multidisciplinary Study of Seismicity up to 1900: Cambridge University Press ,947 pp.

Atwater, B., 1987. Evidence for great holocene earthquakes along the outer coast of Washington state. Science, 236, 942 – 944.

Bronk Ramsey, C., 2001, Development of the radiocarbon calibration program: Radiocarbon, v. 43, no. 2, p. 355–363.

Coumbary, A., Sur le tremblement de terre du 24 juin 1870, Nouvelles Météorologiques, 3, 200-201, Paris.

El-Asmar, H.M., and Wood, P., 2000, Quaternary shoreline development: the northwestern coast of Egypt: Quaternary Science Reviews, v. 19, no. 11, p. 1137–1149, doi: 10.1016/S0277-3791(99)00097-9.

El-Sayed, A., Korrat, I., and Hussein, H. M., 2004. Seismicity and seismic hazard in Alexandria (Egypt) and its surroundings. Pure Appl. Geophys., 161, 1003–1019, doi:10.1007/s00024-003-2488-8.

Folk, R.L., 1968, Petrology of sedimentary rocks, in Austin, Texas (HemphilPs Book Store).

Frihy, O.E., Deabes, E. a., and El Gindy, A. a., 2010, Wave Climate and Nearshore Processes on the Mediterranean Coast of Egypt: Journal of Coastal Research, v. 261, no. 261, p. 103–112, doi: 10.2112/08-1020.1.

GEBCO, 2003. Digital Atlas published by the British Oceanographic Data Centre on behalf of IOC and IHO.

Guidoboni, E., Comastri, A. and Traina G., 1994. Catalogue of Ancient Earthquakes in the Mediterranean area up to the 10th century, INGV-SGA, Bologna.

Guidoboni, E., and A. Comastri (2005). Catalogue of earthquakes and tsunamis in the Mediterranean area from the 11th to the 15th century, INGV-SGA,Bologna, 1037 pp.

Hamouda, A.Z., 2006. Numerical computations of 1303 tsunamigenic propagation towards Alexandria, Egyptian Coast. J. Afr. Earth Sci. 44, 37e44.

Hamouda, A.Z., 2009. A reanalysis of the AD 365 tsunami impact along the Egyptian Mediterranean coast: Acta Geophysica 58, 4, 687–704, doi: 10.2478/s11600-009-0032-7.

Hassouba, A.B.H., 1995. Quaternary Sediments From the Coastal Plain of Northwestern Egypt (from Alexandria to Elomayid): Carbonates and Evaporites 10, 1, 8–44.

Luis, J.F., 2007. Mirone: A multi-purpose tool for exploring grid data. Computers & Geosciences 33, 31–41.

Maamoun, M., Megahed, A. and Allam, A., 1984. Seismicity of Egypt: NRIAG Bull., IV (B), 109–160.

Madder, C. L., 2004. Numerical Modeling of Water Waves. Second ed. CRC Press, Boca Raton, FL, 288 pp.

Malik, J.N., Banerjee, C., Khan, A., Johnson, F.C., Shishikura, M., Satake, K., and Singhvi, A.K., 2015, Stratigraphic evidence for earthquakes and tsunamis on the west coast of South Andaman Island, India during the past 1000years: Tectonophysics, v. 661, no. June 1941, p. 49–65, doi: 10.1016/j.tecto.2015.07.038.

De Martini, P.M., Barbano, M.S., Pantosti, D., Smedile, A., Pirrotta, C., Del Carlo, P., and Pinzi, S., 2012, Geological evidence for paleotsunamis along eastern Sicily (Italy): An

overview: Natural Hazards and Earth System Sciences, v. 12, no. 8, p. 2569–2580, doi: 10.5194/nhess-12-2569-2012.

Nanayama, F., Satake, K., Furukawa, R., Shimokawa, K., Atwater, B.F., Shigeno, K., and Yamaki, S., 2003, Unusually large earthquakes inferred from tsunami deposits along the Kuril trench: Nature, v. 424, no. 6949, p. 660–663, doi: 10.1038/nature01864.

Necmioglu, O. and Ozel, N. M., 2015. Earthquake scenario-based tsunami wave heights in the eastern Mediterranean and connected seas, Pure Appl. Geophys. DOI 10.1007/s00024-015-1069-y.

Okada, Y., 1985. Surface Deformation due to Shear and Tensile Faults in a Half-Space. Bull. Seism. Soc. Amer. 75, 1135–1154.

Papadopoulos, G. A., Gràcia, E., Urgeles, R., Sallares, V., De Mar- tini, P. M., Pantosti, D., González, M., Yalciner, A., Mascle, J., Sakellariou, D., Salamon, A., Tinti, S., Karastathis, V., Fokaefs, A., Camerlenghi, A., Novikova, T., and Papageorgiou, A., 2014, Historical and pre-historical tsunamis in the Mediterranean and its connected seas: Geological signatures, generation mechanisms and coastal impacts: Marine Geology, v. 354, p. 81–109, doi: 10.1016/j.margeo.2014.04.014.

Poirier, J. P. and Taher, M.A., 1980. Historical Seismicity in the near and Middle East, North Africa, and Spain from Arabic Documents (VIIth-XVIIIth Century). Bull. Seismol. Soc. Amer. 70, 6, 2185–2201.

Reimer, P. J., and 24 coauthors (2013). IntCal13 and Marine13 Radiocarbon Age Calibration Curves 0-50,000 Years cal BP. *Radiocarbon, 55*(4).

Shah-Hosseini, M., Saleem, A., Mahmoud, A. and Morhange, C., 2016. Coastal boulder deposits attesting to large wave impacts on the Mediterranean coast of Egypt, Nat Hazards, DOI 10.1007/s11069-016-2349-2

Shaw, B., Ambraseys, N. N., England, P.C., Floyd, M., Gorman, G.J., Higham, T.F.G., Jackson, J., Nocquet, J-M., Pain, C. C., and Piggott, M. D., 2008, Eastern Mediterranean tectonics and tsunami hazard inferred from the AD 365 earthquake: Nature Geoscience, v. 1, no. April, p. 268–276, doi: 10.1038/ngeo151.

Soloviev, S.L., Solovieva, O.N., Go, C.N., Kim, K.S., and Shchetnikov, N.A., 2000, Tsunamis in the Mediterranean Sea 2000 B.C.-2000 A.D:.

Stiros, S. C., 2001. The AD 365 Crete Earthquake and Possible Seismic Clustering During the Fourth to Sixth Centuries AD in the Eastern Mediterranean: A Review of Historical and Archaeological Data. Journal of Structural Geology 23, 545–562.

Stiros, S., and Drakos, A., 2006. A fault model for the tsunami-associated magnitude >8.5 Eastern Mediterranean, AD 365 earthquake. Zeitschrift für Geomorphologie **146**, 125–137.

Taymaz, T., Westaway, R., and Reilinger, R., 2004. Active faulting and crustal deformation in the Eastern Mediterranean region. Tectonophysics 391, 1–9. doi:10.1016/j.tecto.2004.07.005.

Tinti, S., Manucci, A., Pagnoni, G., Armigliato, A., and Zaniboni, F., 2005, The 30 December 2002 landslide-induced tsunamis in Stromboli: sequence of the events reconstructed from the eyewitness accounts: Natural Hazards and Earth System Science, v. 5, no. 6, p. 763–775, doi: 10.5194/nhess-5-763-2005.

Titov, V., F. González, E. Bernard, M. Eble, H. Mofjeld, J. Newman, and A. Venturato (2005), Real-time tsunami forecasting: challenges and solutions, *Natural Hazards 35*, 41-58.

Yalciner, A., Zaytsev, A., Aytore, B., Insel, I., Heidarzadeh, M., Kian, R., and Imamura, F., 2014, A Possible Submarine Landslide and Associated Tsunami at the Northwest Nile Delta, Mediterranean Sea: Oceanography, v. 27, no. 2, p. 68–75, doi: 10.5670/oceanog.2014.41.

Asem Salama

Recherche sur les traces et dépôts de tsunami le long de la côte méditerranéenne de l'Egypte: Contexte sismotectonique et modélisation

Résumé

Sismotectonique, paléotsunami et le tsunami scénarios sont examinés sur la côte du Nord de l'Égypte dans le cadre du tsunami européen ASTARTE projet et le projet IMHOTEP français-égyptiens. La géologie, la géomorphologie, séismicité, des mécanismes focaux, l'inversion de stress calculée et des données GPS utilisée pour identifier le régime de stress de jour présent des zones actives et les zones de tsunamigène. Tranchées et carottes ont été creusées à deux sites. Le balayage de radiographie, la sensibilité magnétique, l'analyse de taille de grain, l'échantillonnage, macrofossile détections, total des matériaux organiques et inorganiques et la datation au carbone est effectuée pour identifier les signatures tsunami. La couche sablonneuse blanche de haute énergie riche en fossiles retravaillés est corrélée avec le 21 juillet 365 dans le Kefr Saber. Les quatre couches sédimentaires de haute énergie à l'El Alamein sont corrélées les tsunamis historiques de 1600 avant J.C., le 21 juillet 365, 8 août 1303, le 24 juin 1870.

Motes-clues: des zones actives, paléotsunamis dépôts, scénarios de tsunamis, Nord de l'Egypte

Résumé en anglais

Seismotectonic, paleotsunami deposits and tsunami scenarios are investigated along the north coast of Egypt in the framework of the tsunami ASTARTE European and the French-Egyptian IMHOTEP projects. The geology, geomorphology, seismicity, focal mechanisms, calculated stress inversion, and GPS data were used to identify the present day stress regime of the main active zones and the tsunamigenic zones. Trenches and cores were dug in Kefr Saber and EL Alamein sites. X-ray scanning, magnetic susceptibility, grain size analysis, sampling, macrofossil detections, XRD analysis, total organic and inorganic matter measurements and carbon dating are carried out to identify the paleotsunami signatures. The high-energy white sandy layer rich in reworked fossils at Kefr Saber are correlated with 21 July 365, while the four characteristic high-energy sedimentary layers at the El Alamein site are correlated with the historical tsunami events of 1600 BC, 21 July 365, 8 August 1303, and 24 June 1870.

Keywords: Active zones, Paleotsunami deposits, tsunamis scenarios, northern Egypt